Projektabschlussbericht
„Felduntersuchungen von Budgets und Konversionen organischer Partikelinhaltsstoffe in troposphärischen Wolkenprozessen (FEBUKO)“
FK 07ATF01

Projektleitung: Prof. Dr. H. Herrmann
Leibniz-Institut für Troposphärenforschung, Leipzig

Teilprojekte

IfT-1 Physiko-chemische Charakterisierung von Luft, Partikeln und Wolkenwasser in Wolkenexperimenten
Projektleiter: Hartmut Herrmann, Alfred Wiedensohler
Institut für Troposphärenforschung, Permoserstrasse 15, D-4318 Leipzig
Tel.: 0341/2352446 Fax: 0341/2352325 E-mail: herrmann@tropos.de
Projektpartner: Hartmut Herrmann, Alfred Wiedensohler, Erika Brüggemann, R. Chemnitzer, Diane Galgon, Thomas Gnauk, Diana Hofmann, Andreas Maßling, Konrad Müller, D. van Pinxteren A. Plewka

IfT-2 Phasenaufteilung von biogenen und anthropogenen organischen Aerosolkomponenten und flüchtiger organischer Substanzen in Wolken
Projektleiter: Stephan Mertes
Institut für Troposphärenforschung, Permoserstrasse 15, D-4318 Leipzig
Tel.: 0341/2352153 Fax: 0341/2352361 E-mail: mertes@tropos.de
Projektpartner: Stephan Mertes, Erika Brüggemann, Thomas Gnauk, Konrad Müller, Antje Plewka

BTU Anteil und Modifikation organischer und reaktiver Substanzen in der Aerosol- und Wolkenwasserphase während des Wolkendurchganges
Projektleiter: Wolfgang Wieprecht
Brandenburgische Technische Universität Cottbus, Arbeitsgruppe Luftchemie
Max-Planck-Strasse 11, D-12489 Berlin
Tel.: 030/63925670 Fax: 030/63925654 E-mail: wie@btu-lc.fta-berlin.de
Projektpartner: Wolfgang Wieprecht, Karin Acker, Detlev Möller

ZUF Aerosolpartikel und Wolkentropfen als Quelle von Peroxyradikalen und Wasserstoffperoxid – Photochemie im atmosphärischen Mehrphasensystem durch organische Chromophore
Projektleiter: Wolfgang Jaeschke
Johann Wolfgang Goethe-Universität, Zentrum für Umweltforschung
Georg-Voigt-Strasse 14, D-60325 Frankfurt a.M.
Tel.: 069/79828147 Fax: 069/79828548
E-mail: jaeschke@zuf.uni-frankfurt.de
Projektpartner: Wolfgang Jäschke, Torsten Salkowski, Werner Haunold

TUD Bestimmung organischer Spezies (Aldehyde, Ketone, Carbonsäuren) in Einzeltropfen zur Bestimmung der zugehörigen Aerosolgrößen und des Wolkenscavengings
Projektleiter: Knut Bächmann
Technische Universität Darmstadt, Institut für Anorganische Chemie
Petersenstrasse 18, D-64287 Darmstadt
Tel.:06131/162373 Fax: 06131/163673
E-mail: baechman@hrzpub.tu-darmstadt.de
Projektpartner: Knut Bächmann, Helge Kramberger, Birgit Svrcina

1 Zusammenfassung

Ein komplexer Datensatz, bestehend aus Gas-, Flüssig- und größenaufgelösten Partikel-Phasen-Komponentkonzentrationen, meteorologischen und Wolkenphysikdaten, wurde aus Feldmessungen erhalten, um die Effekte der Wolkenprozesse auf Änderungen in der chemischen Zusammensetzung der Partikel während der Wolkenpassage zu untersuchen. Aus 14 Messperioden innerhalb 30 Wolkenereignissen wurden drei Ereignisse für eine detaillierte Analyse ausgewählt. Bei verschiedenen Ereignissen konnte ein Einfluss der Wolkenprozesse auf die chemische Partikelzusammensetzung wie z.B. auf organische Komponentengehalte, Sulfat- und Nitratkonzentrationen und auch auf die Partikelgrößenverteilung und Partikelmasse beobachtet werden. Außerdem wurde gefunden, dass der direkte Phasenübergang von polaren organischen Verbindungen aus der Gasphase sehr wichtig ist für das Verständnis der Wolkenwasserzusammensetzung. Es wurde beobachtet, dass Wolkentropfen viel mehr organische Verbindungen enthalten, als aus ihrer Henry-Löslichkeit erwartet wurde, und diese Differenz größer wurde für weniger lösliche Spezies.
Der komplexe Datensatz der FEBUKO Feldexperimente war außerordentlich wichtig für die MODMEP Modellinitialisierung und –validierung. Die SPACCIM Simulationen wurden zur Interpretation der Messungen verwendet und erlauben ein besseres Verständnis der Wolkenpeffekte auf die physiko-chemischen Eigenschaften des atmosphärischen Aerosols.

2 Ziele der Forschung

Im Rahmen des FEBUKO-Verbundprojektes war die Aufklärung von Mehrphasenprozessen unter Aerosolbeteiligung das prioritäre Ziel, das chemische und physikalische Prozesse am Aerosol und im Wolkentropfen zum Schwerpunkt hat. Es sollte den Fragen nach der chemischen Identität der Partikeln, sowie nach deren chemischen Umwandlungen im Wolkenprozess nachgegangen werden. Neben dem Spektrum möglicher Produkte war für das Verständnis realer atmosphärenchemischer Systeme auch die Frage nach dem Ort der Umsetzung (Gasphase, Partikeloberfläche oder innerhalb wässriger Partikeln (aktivierte Aerosole und Wolkentropfen)) zu klären. Die erhaltenen Messdaten sollten als Grundlage für die Einbeziehung von über C_1- und C_2-Verbindungen hinausgehende organische Komponenten bei der Weiterentwicklung von Multiphasenmechanismen dienen und sollten schließlich Eingang in Chemie-Transport-Modelle finden (s.a. Verbundprojekt MODMEP), um die Daten der FEBUKO-Messkampagnen zu interpretieren und zu vergleichen mit den modellierten Daten eines komplexen Multiphasen-Chemie-Modells. Auf diese Weise sollte ein besseres Verständnis der beteiligten Prozesse erreicht werden und die angewendeten Modelle weiter verbessert werden.

3 Durchgeführte Untersuchungen

Am Standort DWD-Station Schmücke (Thüringer Wald) wurden innerhalb der Projektlaufzeit drei Feldexperimente durchgeführt.
Das erste Experiment (Tracer-Experiment, SF6) im Mai 2001 diente der Standortbestimmung, um die optimalen Strömungsverhältnisse der Luftpakete über den Berg zu bestimmen. Der Hauptwindrichtung folgend wurden die Standorte Goldlauter-Pochwerksgrund (vor der Bergstation, 10°45’20’’E, 50°38’25’’N, 605 m NN), Schmücke (Bergstation, 10°46’15’’E, 50°39’19’’N, 937 m NN) und Gehlberg-Pfanntal (nach der Bergstation, 10°47’32’’E, 50°40’21’’N, 732 m NN) für die Durchführung der Wolkendurchgangsexperimente bestimmt (siehe Abbildung 1).
Die zwei Hauptmesskampagnen wurden jeweils im Herbst (24.09. – 08.11.2001 und 16.09.-01.11.2002) durchgeführt. In Tabelle 1 ist eine Zusammenfassung der Parameter und der dafür verantwortlichen teilnehmenden Gruppen dargestellt. An den Talstationen Goldlauter

und Gehlberg wurden identische Sammeltechniken für Spurengase, Partikel-Anzahlgrößenverteilungen (Differential Mobility Particle Sizing (DMPS) – Systeme), Partikeln (5-stufiger BERNER-Impaktor, High-volume Andersen Filtersammler, Denuder-Steamjet-Technik) und meteorologische Parameter eingesetzt. An der Bergstation Schmücke wurde ein 20 m hoher Turm für die Wolkenwasser-Sammler aufgebaut. Verschiedene aktive Wolkenwasser-Sammler (bulk und größenaufgelöst- zweistufig) kamen zum Einsatz (siehe Wieprecht et al., 2005, im Anhang). Im Dachgeschoss des DWD-Stationsgebäudes (in Südwest-Richtung) wurden zwei Counter-flow Virtual Impaktoren (CVI) zur Tropfensammlung und ein Droplet-segregating Inertial Impactor (INT) zur Sammlung von interstitiellen Aerosolpartikeln eingesetzt. Die Anzahlgrößenverteilung der interstitiellen Partikeln und der Tropfenresiduen wurden mittels 2 (DMPS) – Systemen bestimmt. Meteorologische Daten und Spurengasmessungen an der Bergstation wurden von den Mitarbeitern des DWD bzw. UBA durchgeführt.
Für die ausführliche Beschreibung der eingesetzten Messtechnik und gemessenen Parameter siehe Tab. 3-5 in Herrmann et al. (2005a im Anhang) und der meteorologischen Bedingungen siehe Tilgner et al. (2005a, im Anhang).

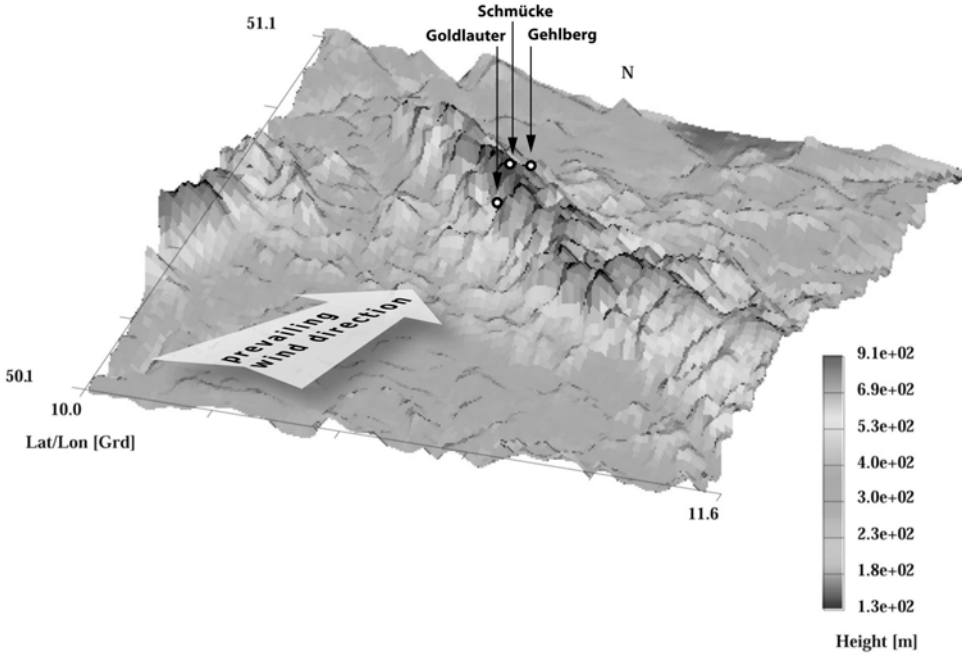

Abb. 1: Untersuchungsgebiet – Thüringer Wald

Spurenkomponenten in der Gasphase
Tracerexperimente mit SF_6 wurden zur Bestimmung des verbundenen Luftstromes von Goldlauter (vor der Bergstation) über die Schmücke (Bergstation) nach Gehlberg (nach der Bergstation) durchgeführt. Standard-Spurengase (O_3, SO_2, NO_x und CO) wurden an allen drei Stationen gemessen, um zusätzliche Informationen zum verbundenen Luftstrom über die Bergstation zu erhalten (O_3, CO). Die anorganischen Komponenten NO_x, andere reaktive Stickstoffverbindungen NO_y, HONO und Salpetersäure sowie Nichtmethan-Kohlenwasserstoffe (NMHC) wurden vor der Bergstation gemessen, um Informationen über den Zustand der ankommenden Luftmasse (Alterung, Kontamination, Oxidationskapazität) zu erhalten. Wasserstoffperoxid (H_2O_2), Carbonylverbindungen und organische Säuren wurden jeweils an den Talstationen bestimmt.

Physikalische Charakterisierung von Aerosol und Wolken
Die Anzahlgrößenverteilungen der Partikeln im Bereich D_p = 3-900 nm wurde an allen drei Messstationen, die Hygroskopizität der Partikeln an der Talstation Goldlauter gemessen. Änderungen in der Partikelgrößenverteilung zwischen den Talstationen ist ein Hinweis auf mögliche Wolkenprozesse. Hygroskopizitätsmessungen liefern Partikelwachstumsfaktoren, die zur Abschätzung des Partikelwassergehaltes benötigt werden, um eine Massenschließung durchführen zu können (für Details siehe Lehmann et al., 2005, im Anhang). An der Bergstation wurden zusätzlich mittels optischer Messungen der Flüssigwassergehalt der Wolke (LWC) und die Verteilung der Wolkentropfen bestimmt. Die Wolkenbasishöhe wurde von der Talstation Goldlauter aus gemessen. Sowohl der LWC als auch die Wolkenbasishöhe sind wichtige Parameter zur Interpretation der experimentellen Ergebnisse (für Details siehe Wieprecht et al, 2005, im Anhang).

Partikelsammlung und –analyse
Partikeln wurden größenaufgelöst mit BERNER Impaktoren und auf Filtern in den Größen PM_1, $PM_{2,5}$ und PM_{10} gemessen, um Vergleiche der Messergebnisse durchführen zu können und genügend Material für die chemischen Analysen, besonders für organische Verbindungen, zur Verfügung zu haben. Zusätzlich wurde die Denuder-Steamjet-Technik an der Talstation Goldlauter angewendet, um Sammelartifakte quantifizieren zu können.
Die chemischen Analysen der Partikelproben wurden durchgeführt von den Filterproben, den Proben der Denuder-Steamjet-Kombination und den größenaufgelösten Proben des 5-stufigen BERNER-Impaktors. Analysiert wurden die ionischen Hauptkomponenten (Chlorid, Nitrat, Sulfat, Natrium, Ammonium, Kalium, Magnesium und Calcium), die Summenparameter OC/EC (OC – organischer Kohlenstoff, EC – elementarer Kohlenstoff) sowie organische Einzelspezies. Eine größenaufgelöste Massenschließung konnte durchgeführt werden (für Details siehe Gnauk et al., 2005 und Müller et al, 2005, im Anhang).

Wolkenwasser
Wolkenwasser wurde mit verschiedenen Wolkenwassersammlern gesammelt und die Komponenten wie bei den Partikeln analysiert (siehe Brüggemann et al., 2005 und van Pinxteren et al., 2005, im Anhang). Zusätzlich wurden Wasserstoffperoxid (siehe Valverde-Canossa et al., 2005, im Anhang), Carbonylverbindungen (siehe van Pinxteren et al., 2005, im Anhang) und wasserlöslicher organischer Kohlenstoff (WSOC), auch als totaler organischer Kohlenstoff (TOC) bezeichnet, als Summe von gelöstem organischen Kohlenstoff (DOC) und partikulärem organischen Kohlenstoff (POC) bestimmt (siehe Brüggemann et al., 2005, im Anhang) bestimmt.

Qualitätskontrolle
Die Qualitätssicherung und -kontrolle während der Messkampagnen wurde mit großer Sorgfalt durchgeführt. Die von UBA, BTU und IfT verwendeten Analysatoren der Standardspurengase wurden in einem von der BTU durchgeführten Test vor jeder Messkampagne verglichen. Die BTU – Gasanalysatoren wurden gegen ein mobiles Kalibrationssystem (welches mit einem US NIST Standard kalibriert wurde) am IFU Institut Garmisch-Partenkirchen kalibriert. Der Vergleich der Instrumente wurde mit einer fünf-Punkt-Kalibration im Bereich von 0-100 nmol mol^{-1} (ppb) für NO_x, O_3 und SO_2, gefolgt von Umgebungsluftmessungen über 24 h, durchgeführt. Kalibrationsgase konnten während der Messkampagne mit einem Environics S 100 Kalibrator bereitgestellt werden, der auch einen Ozongenerator einschloss. Null-Luft wurde mittels eines Ecophysics Pure Air Generator erzeugt, der auch für die täglichen Kalibrationen verwendet wurde.
Die Partikelzähler wurden auf verschiedene Weise kalibriert. Die DMPS-Systeme, die entweder direkt verwendet wurden oder in Verbindung mit den CVI- und INT-Systemen,

wurden gegeneinander vor jeder Messkampagne kalibriert. Die Effizienz der CPCs wurde während einer WMO-Vergleichskampagne bestimmt, die am IfT nach der zweiten Messkampagne stattfand. Die Sammeleffizienz der Partikelsammler, die zur chemischen Charakterisierung der Partikeln verwendet werden (BERNER Impaktoren und Filtersammler), wurde während eines internationalen Sammlervergleiches an der Forschungsstation des IfT in Melpitz (INTERCOMP2000: ten Brink et al., 2004; Müller et al., 2004) bestimmt. Die Sammeleffizienz der Wolkenwassersammler wurde erhalten durch den Vergleich der gesammelten Wokenwasservolumina mit denen, die mit dem Gerber PVM 100 Messgerät erhalten wurden.
Die Masse der gesammelten Partikel wurde bestimmt mit Hochleistungs-Mikrowaagen (Mettler-Toledo UMT-2, Mettler-Toledo AT 261), die zweimal jährlich kalibriert werden. Die Aluminiumfolien wurden vor dem Gebrauch bei 350 °C und die Quarzfilter bei 105 °C für mindestens 2 h bzw. 24 h ausgeheizt, um Blindwerte zu minimieren. Vor der ersten und Endwägung wurden sie bei 50 % und 22 °C mindestens 24 h konditioniert. Die von den verschiedenen Partikelsammlern erhaltene Masse wurde miteinander verglichen. Außerdem wurden die größenaufgelösten Massen vom BERNER Impaktor mit der Partikelmasse, die aus den Anzahlgrößenverteilungen berechnet wurden, verglichen (siehe Gnauk, et al., 2005, im Anhang).
Die analytischen Bestimmungsmethoden zur chemischen Analyse der Partikeln unterlagen auch einer internen Qualitätssicherung, die sowohl Lagerung und Transport der gefrorenen Proben bei -18 °C als auch Blanks und Standardabweichungen umfassen. Seit 1992 nehmen die analytischen Labors der BTU und des IfT erfolgreich an den internationalen Ringversuchen der WMO für die anorganischen Hauptkomponenten teil. Die Methode zur Bestimmung von OC/EC wurde überprüft bei der Teilnahme am internationalen Ringversuch (Round Robin Test 'Carbon Shoot Out') der TU Wien. Außerdem wurden gewonnene Proben geteilt und von verschiedenen teilnehmenden Gruppen analysiert und verglichen (anorganische komponenten: BTU und IfT, organische Komponenten: TUD und IfT).

Messbedingungen
Folgende meteorologischen Bedingungen für die Messungen wurden festgelegt: Windrichtung – 210-250°, Windgeschwindigkeit – 5-12 ms^{-1}, LWC> 0,1 gm^{-3} einer Wolke an der Bergstation sowie wolkenfreie Bedingungen an den Talstationen und kein Niederschlag. Eine ausführliche Beschreibung des orographischen Terrains und der Flussbedingungen sind in Heinold et al. (2005, im Anhang) gegeben. Diese Bedingungen wurden erfüllt an 17 Tagen im Herbst 2001 und an 13 Tagen im Herbst 2002. Bei einigen Ereignissen wurden mehrere kurze kombiniert, so dass 9 Proben in 2001 und fünf Proben in 2002 erhalten werden konnten.

4 Ergebnisse

Auswahl der geeigneten Messereignisse
Vor und während der ersten Messkampagne wurden Tracer-Experimente (SF_6) durchgeführt, um die Trajektorie der Luftströmung zwischen den drei Messstellen zu bestimmen. Die Ergebnisse dieser Experimente halfen, die Grenzwerte für das verwendete Dispersionsmodell zu definieren, um die Strömung der Luft über den Bergrücken zu beschreiben. Die Tracer-Experimente und das Dispersionsmodell sind in Heinold et al. (2005, im Anhang) dargestellt.
Meteorologische Bedingungen wurden bewertet durch synoptische Analysen, basierend auf Satellitenaufzeichnungen, zwei Radiosonden-Aufstiegen pro Tag von Meiningen (etwa 30 km entfernt von der Bergstation) und lokalen meteorologischen Beobachtungen durch den DWD an der Schmücke. Aus der meteorologischen Situations- und den Luftströmungscharakteristiken, die in Tilgner et al. (2005a, im Anhang) und Heinold et al.

(2005, im Anhang) beschrieben sind, wurden drei Wolkenereignisse, die die gestellten Bedingungen (siehe oben) erfüllten, identifiziert und deren Daten zur weiteren Interpretation verwendet. Diese Ereignisse wurden mit E I, E II und E III bezeichnet. Die Hauptdaten für die selektierten Wolkenereignisse sind in Tabelle 2 zusammengefasst.

Betrachtung zu Entrainmenthinweisen
Es wurde versucht, Anzeichen für eine Einmischung von anderen Luftmassen (Entrainment) in den Luftmassenstrom von Goldlauter über die Schmücke nach Gehlberg zu finden. Diese Anzeichen sind zusammengefasst in Tabelle 6 in Herrmann et al. (2005a, im Anhang). In Übereinstimmung mit den Kriterien, die in Colvile et al. (1997) angeführt sind wie die Benutzung von Gasphasen- und Partikelphasen-Tracern, die Übereinstimmung des gemessenen Wolken-LWC mit dem adiabatischen LWC und die Wolkentropfen-Größenverteilungs-Charakteristik, lassen den Schluss zu, dass kein signifikantes Entrainment während der drei ausgwählten Messereignisse aufgetreten ist. Allerdings, das detaillierte Modell, das die Mikrophysik einschließt (beschrieben in Simmel et al., 2005, im Anhang) ergibt, dass Entrainment möglich gewesen sein könnte, was durch Unterschiede zwischen den wolkenphysikalischen Messungen und den Modellabschätzungen besonders bezogen auf den LWC erklärt werden kann. Alle drei Ereignisse sind charakterisiert durch einen verbundenen Luftstrom von Goldlauter über die Schmücke (Wolkenstation) nach Gehlberg.

Hauptergebnisse aus physikalischen Messungen
Das hygroskopische Wachstum der Partikeln mit Durchmessern bei 50, 150 und 250 nm wurde bei 90 % relativer Feuchte mit einem Hygroscopicity-Tandem Differential Mobility Analyser (HT-DMPA) gemessen. Die Ergebnisse sind in Lehmann et al. (2005, im Anhang) diskutiert. Zwei Partikeltypen mit unterschiedlichem Wachstumverhalten wurden gefunden: die eine Gruppe war nahezu hydrophob, die andere war nahezu hygroskopisch. Ein einfaches Wachstums-Modell, basierend auf der Annahme, dass die lösliche Volumenfraktion aus Ammoniumsulfat besteht, wurde angewandt. Dadurch konnte die Verteilung der löslichen Fraktion abgeleitet werden. Die Verteilungen der 150 und 250 nm Partikeln waren bimodal. Ein Peak, der unterhalb von $\varepsilon = 0{,}2$ auftrat, zeigte ein Minimum im Bereich $0{,}2<\varepsilon>0{,}4$ und ein zweites Maximum bei $\varepsilon>0{,}4$. Das hygroskopische Wachstum der Partikeln bei 50 nm unterschieden sich von dem der größeren Partikeln in der Weise, dass manchmal mehr als zwei Wachstums-Moden mit verschiedenen Hygroskopizitäten auftraten. Dies macht die angabe von Wachstumsfaktoren problematisch. Die Verteilung der löslichen Volumenfraktion für die 50 nm Partikeln hatte bei $\varepsilon<0{,}3$ ein Maximum.
Der Einfluss der Verteilung der löslichen Volumenfraktion auf die Aktivierung der Aerosolpartikeln, um Wolkentropfen zu bilden, ist in Mertes et al. (2005a, im Anhang) analysiert. Die Fraktion der Partikeln, die als Wolkenkondensationskerne wirken, hängt stark ab sowohl von der löslichen Volumenfraktion der Partikeln als auch vom Partikeldurchmesser. Eine strenge Korrelation wurde gefunden zwischen der Vergrößerung der löslichen Volumenfraktion bei einer bestimmten Partikelgröße und der Partikelfraktion, die Wolkentropfen bilden kann. andererseits, das interstitielle Aerosol enthält Partikeln, die Bezug nehmend auf die Köhler-Theorie Wolkentropfen bilden könnten, dies aber nicht tun, weil die Oberfläche mit hydrophoben organischen Komponenten benetzt ist.
Die Bildung von zusätzlicher Masse in der Wolke wurde für den Partikelgrößenbereich 60-300 nm beobachtet. Dies wird diskutiert in Mertes et al. (2005b, im Anhang). Die Massenzunahme wird hauptsächlich der Oxidation von SO_2 und der Aufnahme von NH_3 zugeschrieben, obwohl die Bildung von nichtflüchtigen organischen Verbindungen nicht ausgeschlossen werden kann. Ebenso wurde eine Nachtproduktion von ultrafeinen Partikeln beim Auflösen der orographischen Wolke beobachtet.

Hauptergebnisse zum Vergleich der Sammeltechniken

Eine Anzahl verschiedener Geräte zur Sammlung von Partikeln und Wolkenwasser während der Messkampagnen wurden verwendet. Dies erlaubte einen Vergleich der verschidenen Methoden. Die Ergebnisse sind dargestellt in Gnauk et al. (2005, im Anhang), Müller et al. (2005, im Anhang), Brüggemann et al. (2005, im Anhang) und Wieprecht et al. (2005, im Anhang). High-volume Filtersammler und Niederdruck-Impaktoren können positiven und negativen Artefakten unterliegen, die sich in den Differenzen der Ergebnisse zeigen. Für nichtflüchtige Verbindungen, wie Sulfat, wurden ähnliche Ergebnisse erhalten, wobei bei flüchtigeren Verbindungen, wie Nitrat und Ammonium, teilweise Verluste bei der Sammlung mit Impaktoren auftraten. Die Stemjet-Technik, welche diese Probleme nicht hat aber nicht zwischen den Partikelgrößen unterscheiden kann, zeigt höhere Konzentrationen, die mit den gemessenen Wolkenwasserkonzentrationen gut übereinstimmen. Deshalb wurden die mit der Steamjet-Technik erhaltenen Partikelkomponenten-Konzentrationen benutzt, um die mit dem Impaktor erhaltenen größenaufgelösten Konzentrationen zu korrigieren.

Organische Mono- und Dikarbonsäuren, die mit Scrubbern gesammelt wurden, zeigten signifikante Abweichungen um den Faktor 2 bis 3 in den Konzentrationen einiger Proben verglichen mit den Proben des High-volume Filtersammlers und des Impaktors, aber es wurde kein Trend beobachtet (siehe van Pinxteren et al., 2005, im Anhang).

Die verschiedenen Wolkenwassersammler hatten eine Effizienz im Bereich von 45-79 % (siehe Wieprecht et al., 2005, im Anhang).

Hauptergebnisse aus chemischen Messungen

Ein komplexer Datensatz bestehend aus Gas-, Flüssig- und größenaufgelösten Partikel-Phasen-Komponentkonzentrationen, meteorologischen und Wolkenphysikdaten, wurde aus Feldmessungen erhalten, um die Effekte der Wolkenprozesse auf Änderungen in der chemischen Zusammensetzung der Partikel während der Wolkenpassage zu untersuchen (zu Details siehe Gnauk et al, 2005; Müller et al., 2005; Brüggemann et el., 2005; van Pinxteren et al., 2005, im Anhang). Der Datensatz der Talstation vor dem Berg (Goldlauter) wurde verwendet, um das angewandte Modell SPACCIM auf einer realistischen Grundlage zu initialisieren (Tilgner et al., 2005b, im Anhang).

Die PM_{10} Massekonzentration liegt im Bereich von 8-17 µg m^{-3}. Die Hauptkomponenten der Ionen sind Sulfat, Nitrat und Ammonium, die 90% der ionischen Masse ausmachten. Die Konzentration der Komponenten differierte abhängend von der Luftmassenherkunft. In E I (kontinentale Luftmasse) betrug das OC/EC Verhältnis 1,1 und in E II und E III (maritime Luftmasse) wurde 2,5 gefunden. Die Massekonzentration der Partikelgrößenbereiche bis 900 nm, welche mit dem DMPS gemessen wurden, stimmten gut mit den durch Wägung erhaltenen Massen überein. Die chemische Massenbilanz war auch in guter Übereinstimmung mit der durch Wägung erhaltenen Gesamtmasse. Zwischen 10 und 30 % der Masse wurden nicht identifiziert.

Die Partikelkonzentrationen der Dicarbonsäuren waren niedrig in der Nacht und stiegen während des Tages bis zum Abend (in E I und II) um einen Faktor von 2-5. Die Konzentration der Carbonsäuren verringerte sich mit steigender Kohlenstoff (C) -Anzahl. Die höchste Konzentration trat im Größenbereich 0,42-1,2 µm, in dem auch die höchste Partikelmasse gefunden wurde, auf. Die Gasphasen-Mischungsverhältnisse einiger Carbonylverbindungen zeigten einen ähnlichen Tagesgang in der Konzentration wie Ameisen- und Essigsäure. Partikuläre organische Verbindungen biogenen Ursprungs, wie Levoglucosan und Xylitol konnten mit signifikanten Konzentrationen (100 ng m^{-3}) im gleichen Größenbereich wie Oxalsäure nachgewiesen werden, wobei die Konzentrationen von Pinin- und Pinonicsäure sehr niedrig waren (0,5-2,6 ng m^{-3}).

Die Konzentrationen von nichtflüchtigen Spezies wie Sulfat und EC hatten die gleiche Konzentration in der Partikelphase wie im Wolkenwasser. Allerdings, die Konzentrationen

von flüchtigen Komponenten wie Nitrat, Ammonium und organischem Kohlenstoff waren niedriger. Ein Partikelmassezuwachs nach dem Wolkendurchgang (Talstation Gehlberg) wurde hauptsächlich im Größenbereich 0,05-0,14 µm festgestellt. Während E I vergrößerte sich die Konzentration von Sulfat um 20 % und Ammonium um 17 %, während E III nahm die Sulfatkonzentration um 70% und Ammonium um 150 % zu. Die OC-Konzentration erhöhte sich um 20 % im Größenbereich 0,14-0,42 µm (E I). Diese Effekte weisen auf eine Akkumulation von Partikelmasse durch Wolkenprozesse hin. Eindeutige Anzeichen für eine Erhöhung der Konzentration im Akkumulationsmode der Aerosolgrößenverteilung wurden für das Ereignis III erhalten (Mertes et al., 2005a; Brüggemann et al, 2005, im Anhang). Diese Beobachtungen und die Resultate der chemischen Analyse wurden bestätigt durch Modellberechnungen (siehe Tilgner et al., 2005b, im Anhang).
Eine große Anzahl von löslichen organischen Spezies wurden im Wolkenwasser gefunden und ihre zeitliche Variation wurde bestimmt. Carbonylverbindungen und Carbonsäuren trugen 10-17 % im Mittel zur organischen Masse bei. Verschiedene organische Verbindungen wurden in diesem Experiment zum ersten Mal beobachtet: Glycolaldehyd, Pinonaldehyd, Buttersäure, Äpfelsäure und Pininsäure. Das Budget der organischen Verbindungen zeigte auf dem Weg durch die Wolke eine Quelle für Essigsäure. Auch einige Dicarbonsäuren , z.B. Malonsäure, wurden in leicht erhöhter Menge nach dem Wolkendurchgang in einigen der untersuchten Größenbereiche gefunden. Diese Effekte können möglicherweise den Wolkenprozessen zugeordnet werden.

5 Literatur

Colvile, R.N., Bower, K.N., Choularton, T.W., Gallagher, M.W., Wobrock, W., Hargreaves, K.J., Storeton-West, R.L., Cape, J.N., Jones, B., Wiedensohler, A., Hansson, H.-C., Wendisch, M., Acker, K., Wieprecht, W., Pahl, S., Winkler, P., Berner, A. and Kruisz, C. (1997). Meteorology of the Great Dun Fell cloud experiment 1993. Atmos. Environ. 31 (16), 2407-2420.

Müller, K., Spindler, G., Maenhaut, W., Hitzenberger, R., Wieprecht, W., Baltensperger, U., ten Brink, H., 2004. INTERCOMP 2000, a campaign to assess the comparability of methods in use in Europe for measuring aerosol composition. Atmospheric Environment 38, 6459-6466.

ten Brink, H., Maenhaut, W., Hitzenberger, R., Gnauk, Th., Spindler, G., Even, A., Chi, X., Bauer, H., Puxbaum, H., Putaud, J.-P., Tursic, J., Berner, A., 2004. INTERCOMP2000: the comparability of methods in use in Europe for measuring the carbon contnet of aerosol. Atmospheric Environment 38, 6507-6519.

Tab.1: Verantwortlichkeiten für die Messungen

Parameter	Verantwortlich
Meteorologische Routinedaten und Standard-Gasphasenchemie	DWD + UBA +BTU Cottbus + Ift Leipzig 1
Windfeld hochaufgelöst	ZUF Frankfurt
Photolyseraten, andere Strahlungsparameter	IfT Leipzig 1 + ZUF Frankfurt
Probennahme	
Aerosolpartikel mit 2*2 Berner-Impaktoren	IfT Leipzig 1
Aerosolpartikel mit Filtern	BTU Cottbus
Interstitielles Aerosol und (ggf.) interst. Gasphase	IfT Leipzig 2
Tropfenresiduen (CDN)	IfT Leipzig 2
Interstitielle Gasphase	ZUF Frankfurt + IfT Leipzig 2
Lösliche evaporierende Gase	IfT Leipzig 2
Wolkenkondensationskerne (CCN)	ZUf Frankfurt
Wolkenwasser, größenaufgelöst	ZUF Frankfurt + BTU Cottbus
Wolkenwasser bulk (Zweistufen)	BTU Cottbus
Wolkenwasser bulk	BTU Cottbus + IfT Leipzig 1
Peroxyradikale	ZUF Frankfurt
Mikrophysikalische Analytik (Aerosolpartikel und Tropfen)	
Partikelgrößenverteilungen (Luv, Lee)	IfT Leipzig 1
Partikel-Hygroskopizität	IfT Leipzig 1
Größenverteilungen der CDN und interst. Partikel	IfT Leipzig 2
Größenverteilungen der Wolkentropfen	ZUF Frankfurt + BTU Cottbus + IfT Leipzig 2
LWC	BTU Cottbus + ZUF Frankfurt + IfT Leipzig 2
Wolkenbasishöhe	BTU Cottbus
Chemische Gasphasenanalytik	
O_3, SO_2, NO/NO_2, in Luv und Lee	IfT Leipzig 1
O_3, SO_2, NO/NO_2,HNO_3, HONO, NH_3 in der Wolke	BTU Cottbus
$H_2O_{2(g)}$	ZUF Frankfurt
Carbonyle	BTU Cottbus, TU Darmstadt
Organische Säuren	TU Darmstadt
VOC, C3 – C8	UBA
Chemische Analytik in Aerosolpartikel und Wolkenwasser	
Anionen, Kationen, pH	IfT 1 + BTU Cottbus
Übergangsmetalle	ZUF Frankfurt + IfT Leipzig 1
$H_2O_{2(aq)}$	ZUF Frankfurt
OC/EC	IfT Leipzig 1
BC in Tropfenresiduen u. interst. Partikeln	IfT Leipzig 2
Differenzierung org. Materials (TOC, WSOC)	BTU Cottbus + IfT Leipzig 1
Huminstoffe	BTU Cottbus
Org. Säuren	TU Darmstadt + IfT Leipzig 1
Semiflüchtige Verb. (PAH, Alkane, Fettsäuren, Aldeh.)	IfT Leipzig 1 + TU Darmstadt

Tab 2: Wichtigste meteorologische Parameter der drei Hauptereignisse

Date, Event	Time UTC	Wind speed ($m\ s^{-1}$) and direction (deg)	Air pressure (hPa)	Temp. (°C)	LWC ($g\ m^{-3}$)	Cloud base height (m) above upwind site	Relative humidity (%)	
							Upwind site	Downwind site
06-08 Oct 2001 Event EII	10:30 – 14:15	5.0 – 7.8; (6.2) 210 – 230; (221,7)	905.1 – 905.5 (905.3)	9.3 – 11.5 (10.6)	0.000 – 0.251 (0.049)	270 – 340 (318.5)	79 – 94 (85.5)	81.2 – 85.9 (83.6)
	13:15 – 15:15	2.2 – 5.2; (4.0) 200 – 250; (225.8)	902.7 – 903.3 (903.1)	10.5 – 11.0 (10.7)	0.000 – 0.456 (0.153)	90 – 210 (122.2)	100 Constant	86.9 – 89.6 (88.4)
	18:00 – 11:15	2.7 - 9.8; (6.9) 180 – 220; (207.1)	900.9 – 903.0 (901.9)	9.4 – 9.9 (9.6)	0.000 – 0.512 (0.203)	50 – 320 (191.0)	86 – 100 (98.5)	78.5 – 93.6 (89.2)
26/27 Oct 2001 Event EI	22:00 – 13:00	5.1 – 10.9; (8.0) 210 – 230; (216.3)	909.0 – 910.6 (909.8)	5.4 – 7.5 (6.1)	0.109 – 0.665 (0.335)	50 – 210 (115.6)	95 – 100 (99.3)	n/a
16/17 Oct 2002 Event EIII	21:00 – 05:30	7.6 – 12.3; (10.1) 210 – 220; (215.2)	891.1 – 893.3 (892.4)	7.1 – 9.3 (7.9)	0.024 – 0.417 (0.202)	140 – 290 (218.8)	n/a	90.3 – 97.2 (93.2)

Inhaltsübersicht zum Sonderband für „Atmospheric Environment“

“FEBUKO and MODMEP: A combined Study of Aerosol-Cloud Interaction by Field Experiments and Model Devlopment”

Guest Editor: Prof. Dr. Hartmut Herrmann, IfT Leipzig

Liste der enthaltenen Manuskripte (F = enthält FEBUKO-Beiträge und Ergebnisse)

“Link between aerosol hygroscopic growth and droplet activation observed for hill cap clouds at connected flow conditions during FEBUKO” (F)
S. Mertes (**b**), K. Lehmann, A. Nowak, A. Massling and A. Wiedensohler

"Size-resolved soluble volume fractions of submicrometer particles in air masses of different character" (F)
K. Lehmann, A. Massling, A. Tilgner, S. Mertes, D. Galgon and A. Wiedensohler

“Cloud physics and cloud water sampler comparison during FEBUKO” (F)
W. Wieprecht, K. Acker, S. Mertes, J.L. Collett Jr., W. Jaeschke, E. Brüggemann, D. Möller and H. Herrmann

“***Schmücke hill cap cloud and valley stations aerosol characterisation during FEBUKO (I): Particle size distribution and main components” (F)***
E. Brüggemann, T. Gnauk, S. Mertes, K. Acker, R. Auel, W. Wieprecht, D. Möller, J.L. Collett Jr., R. Chemnitzer, C. Rüd, R. Junek and H. Herrmann

“***Schmücke hill cap cloud and valley stations aerosol chemical composition during FEBUKO (II): Organic compounds” (F)***
D. van Pinxteren, A. Plewka, D. Hofmann, K. Müller, H. Kramberger, B. Svrcina, K. Bächmann, W. Jaeschke, S. Mertes, J.L. Collett Jr. and H. Herrmann

“***Non-dissipative cloud transport in Eulerian grid models by the volume-of-fluid (VOF) method”***
D. Hinneburg and O. Knoth

*“**A parcel model for the combined treatment of microphysical and multiphase chemical processes”***
O. Knoth

“***ISSA (Iterative Screening and Structure Analysis) – A new reduction method and its application to the tropospheric cloud chemical mechanism RACM/CAPRAM2.4”***
G. Mauersberger

“Towards a more detailed description of tropospheric aqueous phase organic chemistry: CAPRAM 3.0”
H. Herrmann (**b**), A. Tilgner, P. Barzaghi, Z. Majdik, S. Gligorovski, L. Poulain and A. Monod

“***Numerical simulation of the microphysics of an orographic cloud: Comparison with measurements and sensitivity studies”***
M. Simmel, K. Diehl and S. Wurzler

"***SPACCIM: A parcel model with detailed microphysics and complex multiphase chemistry***"
R. Wolke, A.M. Sehili, M. Simmel, O. Knoth, A. Tilgner and H. Herrmann
"***SPACCIM: Simulations of the multiphase chemistry occurring in the FEBUKO hill cap cloud experiments*** ***(F)***
A. Tilgner, Z. Majdik, A.M. Sehili, M. Simmel, R. Wolke and H. Herrmann

"***Comparison of different model approaches for the simulation of multiphase processes***"
A.M. Sehili, R. Wolke, O. Knoth, M. Simmel, A. Tilgner and H. Herrmann

"H_2O_2 and organic peroxide measurements in an orographic cloud: The FEBUKO experiment" ***(F)***
J. Valverde-Canossa, W. Wieprecht, K. Acker and G. K. Moortgat

Die Druckfahnen der Beiträge zu diesem Sonderband sind beigefügt.

ARTICLE IN PRESS

Available online at www.sciencedirect.com

SCIENCE DIRECT®

ELSEVIER

Atmospheric Environment ▮ (▮▮▮▮) ▮▮▮–▮▮▮

ATMOSPHERIC ENVIRONMENT

www.elsevier.com/locate/atmosenv

Editorial

Introduction to FEBUKO and MODMEP

The FEBUKO and MODMEP projects within the German atmospheric research programme AFO 2000 intended to improve the understanding of tropospheric multiphase processes and especially the interaction of aerosol and clouds with an emphasis on organic compounds. The FEBUKO experiments were carried out at three research sites in the Thüringer Wald in the autumn of 2001 and 2002. The aim was to characterise aerosol and cloud water with respect to their chemical composition and their physical properties upwind, inside of, and downwind a hill cap cloud. The speciation of organic components was one of the most important tasks for the different atmospheric phases. The air masses encountered in the experimental region were anthropogenically influenced and, additionally, were exposed to biogenic emissions on their way from South-West Germany to the Thüringer Wald. In MODMEP the development was directed towards a cloud model which combines a complex multiphase chemistry with detailed microphysics. The description of both is given with high size resolution of the drop spectrum. The influence of simplifications within single components and the kind of their coupling on the simulation results is investigated for different tropospheric situations. Furthermore, techniques are provided and tested which allow an effective implementation of multiphase processes in multidimensional cloud and chemistry-transport models.

The present volume intends to summarise the main results of the FEBUKO field measurements and the model development in MODMEP together with the application of the newly developed mechanisms, models and numerical tools to the interpretation of the FEBUKO experiments. Exceeding this scope, a multiphase model intercomparison has been performed and new chemical multiphase mechanisms, numerical models and tools are now becoming available for a better understanding of aerosol and cloud multiphase processes.

We would like to remark that in these projects field and modelling studies were prevailing. The model development work, however, is heavily based on thorough laboratory studies which will always represent an indispensable prerequisite for the further development of atmospheric models.

FEBUKO and MODMEP were successful projects in our view. However, the results obtained also indicate that much more effort is still needed in the future to address a variety of atmospheric research topics such as (i) the characterisation of tropospheric particles with less artefacts, better time and size resolution, (ii) the improved characterisation of particle phase organics including oligomeric substances, (iii) more detailed descriptions of aerosol and cloud microphysics in models, (iv) a still better treatment of organics in aqueous phase mechanisms, (v) extended sensitivity studies, (vi) the construction of reduced mechanisms and, finally, (vii) the construction of well-founded, and validated chemistry modules for aerosol and clouds to be included into higher scale models.

We would like to thank everybody who has been involved in the effort of FEBUKO and MODMEP at the Institut für Atmosphäre und Umwelt in Frankfurt/Main, the University of Darmstadt, the University of Cottbus, the Max Planck Institut für Meteorologie in Hamburg and the Leibniz-Institut für Troposphärenforschung in Leipzig. We are indebted for the support by the local authorities of Goldlauter and Gehlberg, the German Weather Service DWD and the German UBA with its Schmücke research station for all the support by the UBA staff lead by R. Junek. We thank the handling editors of manuscripts in the IfT, i.e. E. Renner, O. Hellmuth, M. Simmel, and F. Stratmann for their help. We do acknowledge substantial financial support by the BMBF within AFO 2000 under FK 07ATF01 and 07ATF40.

For the present volume the reader is advised that for a number of contributions electronic supplementary material is available under http://www.projects.tropos.de:8088/afo2000g3/FEBUKO_dateien/febuko.html. For any questions, remarks or comments do not hesitate to contact us under herrmann@tropos.de or wolke@tropos.de.

Hartmut Herrmann
(Guest Editor, Coordinator of FEBUKO)
Ralf Wolke
E-mail address: wolke@tropos.de

1352-2310/$ - see front matter
doi:10.1016/j.atmosenv.2005.02.005

3B2v8.06a/w (Dec 5 2003).51c XML:ver:5.0.1 AEA : 5761 Prod.Type:FTP pp.1–16(col.fig.:NIL) ED:S.Latha PAGN:Uday SCAN:Mouli

ARTICLE IN PRESS

Available online at www.sciencedirect.com

SCIENCE DIRECT®

ELSEVIER

Atmospheric Environment ▮ (▮▮▮▮) ▮▮▮–▮▮▮

ATMOSPHERIC ENVIRONMENT

www.elsevier.com/locate/atmosenv

FEBUKO and MODMEP: Field measurements and modelling of aerosol and cloud multiphase processes

H. Herrmann[a,*], R. Wolke[a], K. Müller[a], E. Brüggemann[a], T. Gnauk[a], P. Barzaghi[a], S. Mertes[a], K. Lehmann[a], A. Massling[a], W. Birmili[a], A. Wiedensohler[a], W. Wieprecht[b], K. Acker[b], W. Jaeschke[c], H. Kramberger[d], B. Svrcina[d], K. Bächmann[d], J.L. Collett Jr.[e], D. Galgon[a], K. Schwirn[a], A. Nowak[a], D. van Pinxteren[a], A. Plewka[a], R. Chemnitzer[a], C. Rüd[a], D. Hofmann[a], A. Tilgner[a], K. Diehl[a], B. Heinold[a], D. Hinneburg[a], O. Knoth[a], A.M. Sehili[a], M. Simmel[a], S. Wurzler[a], Z. Majdik[a], G. Mauersberger[b], F. Müller[f]

[a]*Leibniz-Institut für Troposphärenforschung, Permoserstr. 15, 04318 Leipzig, Germany*
[b]*Brandenburgische Technische Universität Cottbus, Lehrstuhl für Luftchemie und Luftreinhaltung, Volmer Str.13, 12489 Berlin, Germany*
[c]*Johann-Wolfgang-Goethe Universität Frankfurt, Zentrum für Umweltforschung, Georg-Voigt-Str. 14, 60325 Frankfurt a.M., Germany*
[d]*Institut für Anorganische Chemie, Technische Universität Darmstadt, Petersenstrasse 18, 64287 Darmstadt, Germany*
[e]*Atmospheric Science Department, Colorado State University, Fort Collins, USA*
[f]*Max-Planck Institut für Meteorologie, Bundesstrasse 53, 20146 Hamburg, Germany*

Abstract

An overview of the two FEBUKO aerosol–cloud interaction field experiments in the Thüringer Wald (Germany) in October 2001 and 2002 and the corresponding modelling project MODMEP is given. Experimentally, a variety of measurement methods were deployed to probe the gas phase, particles and cloud droplets at three sites upwind, downwind and within an orographic cloud with special emphasis on the budgets and interconversions of organic gas and particle phase constituents. Out of a total of 14 sampling periods within 30 cloud events three events (EI, EII and EIII) are selected for detailed analysis. At various occasions an impact of the cloud process on particle chemical composition such as on the organic compound content, sulphate and nitrate and also on particle size distributions and particle mass is observed. Moreover, direct phase transfer of polar organic compound from the gas phase is found to be very important for the understanding of cloudwater composition.

For the modelling side, a main result of the MODMEP project is the development of a cloud model, which combines a complex multiphase chemistry with detailed microphysics. Both components are described in a fine-resolved particle/drop spectrum. New numerical methods are developed for an efficient solution of the entire complex model. A further development of the CAPRAM mechanism has lead to a more detailed description of tropospheric aqueous phase organic chemistry. In parallel, effective tools for the reduction of highly complex reaction schemes are provided.

*Corresponding author. Tel.: +49 341 235 2446; fax: +49 341 235 2325.
E-mail address: herrmann@tropos.de (H. Herrmann).

1352-2310/$ - see front matter
doi:10.1016/j.atmosenv.2005.02.004

Techniques are provided and tested which allow the description of complex multiphase chemistry and of detailed microphysics in multidimensional chemistry-transport models.

Keywords: Hill cap cloud experiment; Aerosol; Cloud water; Trace gases; Physico-chemical analysis

1. Introduction

The interaction of particular matter and trace gases in orographic clouds has been studied before under different aspects in Europe: at Kleiner Feldberg (continental frontal clouds, autumn 1990, Wobrock et al., 1994), at Great Dun Fell (marine orographic clouds, spring 1993 and 1995, Choularton et al., 1997; Bower et al., 1999), at the Puy de Dôme (cloud ice mountain experiment 1998, Wobrock et al., 2001) and at Tenerife (marine orographic clouds, ACE-2, summer 1997, Raes et al., 2000). The interaction between aerosols and clouds has also been studied in the USA, see for example Collett et al. (2002) and Feingold and Kreidenweis (2000). Here, field experiments of aerosol–cloud interactions that were conducted at the Schmücke, a mountain located in central Germany, are described. These studies were coordinated under the code name FEBUKO (Field Investigations of Budgets and Conversions of Particle Phase Organics in Tropospheric Cloud Processes). The experiments were carried out in October 2001 and 2002. From a greater number of observations three cloud events were selected for a detailed analysis and discussed below. Times and duration of the measurement periods for the three events are given in Table 1 together with the principal meteorological parameters observed.

Modelling studies have previously indicated that the interaction of trace gases with the liquid phase of clouds modifies also the chemistry in the gas phase (e.g. Lelieveld and Crutzen, 1991; Kreidenweis et al., 2003). In general, the complexities resulting from the interplay of physical and chemical cloud processes have discouraged investigators from simultaneously treating all aspects of multiphase chemistry with equal rigor. Thus, many models focus either on the complex multiphase chemistry in only a few aggregated drops size classes (Audiffren et al., 1998; Herrmann et al., 2000; Djouad et al., 2003), or on the details of microphysics by assuming strongly simplified chemical mechanisms (Bott, 1999;

Table 1
Meteorological key parameters for the three main events

Date, event	Time UTC	Wind speed ($m\,s^{-1}$) and direction (deg)	Air pressure (h Pa)	Temp. (°C)	LWC ($g\,m^{-3}$)	Cloud base height (m) above upwind site	Relative humidity (%)	
							Upwind site	Downwind site
06–08 October 2001 event EII	10:30–14:15	5.0–7.8; (6.2)[a] 210–230; (221,7)	905.1–905.5 (905.3)	9.3–11.5 (10.6)	0.000–0.251 (0.049)	270–340 (318.5)	79–94 (85.5)	81.2–85.9 (83.6)
	13:15–15:15	2.2–5.2; (4.0) 200–250; (225.8)	902.7–903.3 (903.1)	10.5–11.0 (10.7)	0.000–0.456 (0.153)	90–210 (122.2)	100 Constant	86.9–89.6 (88.4)
	18:00–11:15	2.7–9.8; (6.9) 180–220; (207.1)	900.9–903.0 (901.9)	9.4–9.9 (9.6)	0.000–0.512 (0.203)	50–320 (191.0)	86–100 (98.5)	78.5–93.6 (89.2)
26/27 October 2001 event EI	22:00–13:00	5.1–10.9; (8.0) 210–230; (216.3)	909.0–910.6 (909.8)	5.4–7.5 (6.1)	0.109–0.665 (0.335)	50–210 (115.6)	95–100 (99.3)	n/a
16/17 October 2002 event EIII	21:00–05:30	7.6–12.3; (10.1) 210–220; (215.2)	891.1–893.3 (892.4)	7.1–9.3 (7.9)	0.024–0.417 (0.202)	140–290 (218.8)	n/a	90.3–97.2 (93.2)

[a]Number in parenthesis represent the mean value.

Fahey and Pandis, 2001). The recent development of more sophisticated cloud models that incorporate more comprehensive chemical mechanisms now makes it possible to study the interaction between microphysical and multiphase chemical processes in greater detail (e.g. Leriche et al., 2000, 2003). The rate of chemical conversions in cloud drops is essentially determined by the rate of mass transfer between the gas and the liquid phases. Numerical studies show that much attention must be paid to the dynamics of the inter-phase transfer (Audiffren et al., 1998; Djouad et al., 2003), and that the mass transfer depends strongly on the surface area of the inter-phase boundaries (Fahey and Pandis, 2001; Kreidenweis et al., 2003). Therefore, any description of multiphase processes should consider a sufficiently well-resolved drop size spectrum.

2. Motivation

The aim of the coupled project clusters FEBUKO and MODMEP ("MODelling of MultiphasE Processes: Tools and chemical mechanisms") has been to perform aerosol–cloud interaction hill cap cloud field experiments with special emphasis on the chemical and physical characterisation of particles throughout their transition from CCN (cloud condensation nuclei) to cloud droplets and back to processed particles. Special emphasis was laid on a most detailed characterisation of organic compounds in particles encountered at each stage of the mentioned process chain. Within MODMEP complex models and modelling tools have been developed and the coupled microphysics/chemistry model SPACCIM (Spectral Aerosol Cloud Interaction Model) has been applied for the interpretation of the FEBUKO experiments and a comparison of measured data and modelled data for a complex multiphase chemistry model to assess the current state of performance of multiphase models. In this manner, the comparison of measurements and model simulations led to a better comprehension of the processes involved, while it also provided indications in which way the models might be further improved. In this context, the mechanism CAPRAM 3.0 (Chemical Aqueous Phase Radical Mechanism) has been developed which aims at the better description of aqueous phase tropospheric chemistry including reactions of essentially up to four carbon atoms.

3. Experimental

3.1. Site description

The Thüringer Wald is a low mountain range in central Germany, which extends in south-easterly direction without any important crossing valleys. The research station Schmücke of the German Weather Service (Deutscher Wetterdienst, DWD) and the Federal Environmental Office (Umweltbundesamt, UBA) is located near the summit of the mountain (10°46′15″ East, 50°39′19″ North, 937 m above sea level), which is in the vicinity of the highest peak of the Thüringer Wald (982 m a.s.l.). A model of the terrain is shown in Fig. 1. The air masses encountered at the DWD/UBA station Schmücke (summit site S) are typically composed of aged air, which is first influenced by anthropogenic emissions from Western Europe (Italy, Switzerland, France, Belgium and Germany), and is subsequently exposed to biogenic emissions on its way from the Rhine-Main area to the Thüringer Wald. No anthropogenic aerosol sources exist within 120 km distance toward the south-west. This sector was selected as the area of preferred wind direction for the experiments. In October, the UBA station becomes immersed in clouds on 25 days, on average. In many cases, this is an orographic cloud so that the station is well suited for cloud experiments. The air flow over the station is assessed both by modelling and by tracer experiments. For this purpose, two additional experimental sites were established at Goldlauter (upwind site, U; 10°45′20″ East, 50°38′25″ North, 605 m a.s.l.) and at Gehlberg (downwind site D; 10°47′32″ East, 50°40′21″ North, 732 m a.s.l.). Under conditions of south-westerly winds the air masses are guided from Goldlauter via the summit toward Gehlberg as shown in Fig. 2, which presents a cross section of the mountain range. The orographic terrain and the air flow conditions are further examined in the contribution of Heinold et al. (2005). Between the three measurement sites lies a small road with only occasional traffic. The dominant trees in the region are Norway spruces (8–23 m). Wet deposition occurs on their needles in the presence of clouds, dry deposition occurs at all levels below the cloud. Table 1

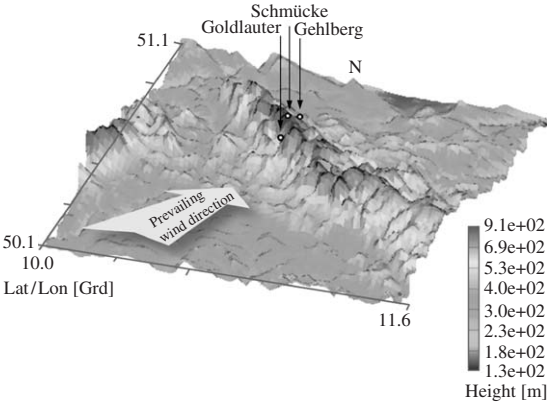

Fig. 1. Map of Central Germany with the marked area of investigations (magnified).

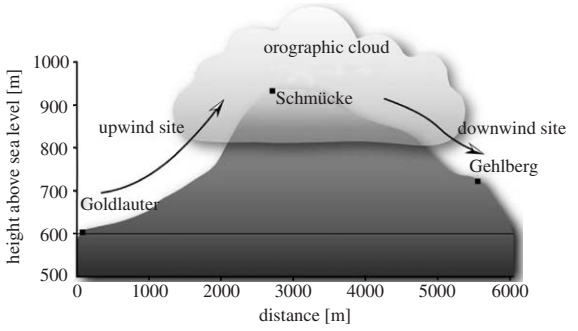

Fig. 2. Cross section of the Thüringer Wald at Goldlauter, Schmücke and Gehlberg.

Table 2
Local climate characterisation of the Thüringer Wald at Schmücke in October based on data for the period 1981–1990

	Climatic mean[a]	October 2001	October 2002
Mean temperature (°C)	5.7	9.2	3.8
Max. temperature (°C)	21.8	19.3	13.6
Min. temperature (°C)	−7.1	1.5	−2.5
Precipitation (mm)	97	80	207
Days with Fog	24.9	28	29
Days with prec. >0.1 mm	17.4	14	23
Days with prec. >1.0 mm	13.2	11	16
Days with snowfall	—	1	10
Mean relative humidity (%)	—	92	97
Sun shine (h)	102	97	44
Wind from SW (%)	57	75	32

[a]Supplied by DWD.

summarises key meteorological data observed during the measurement periods.

3.2. Local climate

Table 2 provides a summary of climatic conditions experienced at the Schmücke station. Fig. 3 further provides the annual ranges of temperature and precipitation. The local climate is characterised by fairly high levels of orographic precipitation, occurring upwind of the mountain range. The precipitation in the higher regions of the Thüringer Wald can reach up to

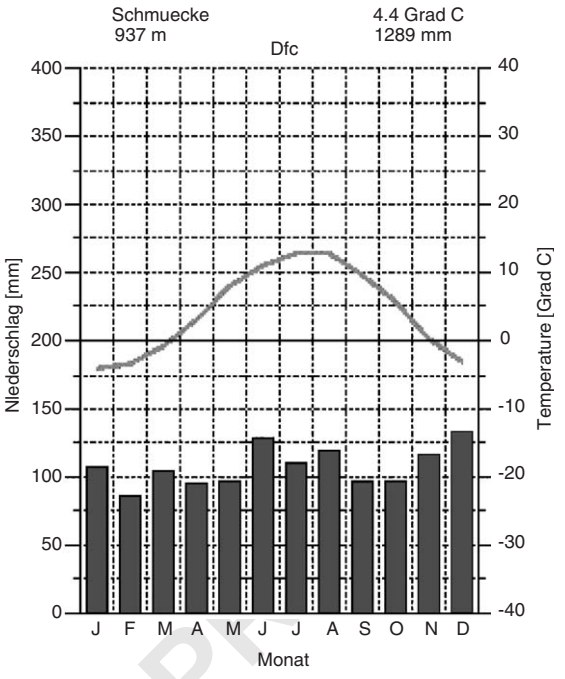

Fig. 3. Local climate diagram for the Schmücke based on data of 1981–1990, modified after http://www.klimadiagramme.de/Deutschland/schmuecke.html

1300 mm annually, and still is about 700 mm during the winter half year. In the downwind regions, the lower regions of the so-called Thüringer Becken, the level of precipitation falls to 200 mm annually. These effects are caused by the prevailing south-westerly winds. Fig. 4 shows the average distribution of wind direction at the station Schmücke. Foggy days are observed at the Schmücke on about 170 days per year. For a number of such events, the fog is in fact better described as an orographic cloud due to the uplift of air from the Goldlauter site toward the Schmücke summit. In October, the wind direction is to 57% from the south-west, in the 210–250° sector of the wind rose. As outlined in Tilgner et al. (2005a, b) and Table 2, this weather situation occurred in October 2001 on 18 days with south-westerly wind being observed in 75% of the cases. In October 2002, the frequencies were 9 days and 32%, respectively. In general, the conditions encountered in October 2001 differed little from the long-term mean, whereas in October 2002 the weather was significantly colder and wetter than the long-term mean. This had consequences for the performance of the experiments, because the necessary experimental conditions were much better achieved in October 2001 than in October 2002.

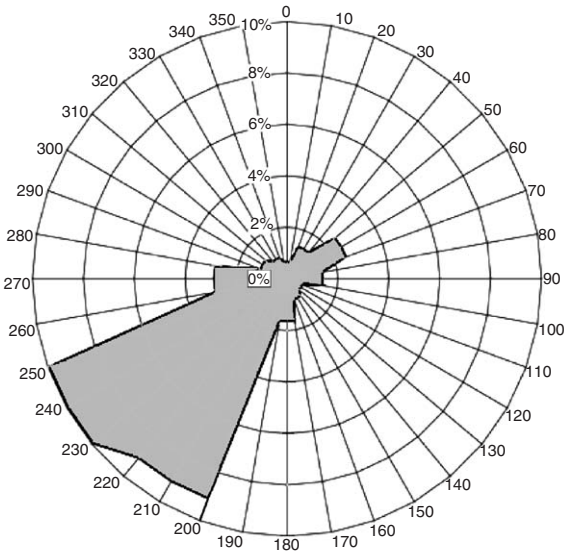

Fig. 4. Wind rose for the Schücke mountain (average of 1981–1990), from weather data of the DWD at the Schmücke research station.

3.3. Sampling equipment, experimental techniques and quality control

Table 3 provides a summary of measurement techniques employed and participating group responsibilities. Tables 4 and 5 list further specifications of individual instruments. Mobile equipment for the sampling of trace gases and particle was installed at the upwind (U) and at the downwind (D) sites. At the summit a 20 m height tower was installed for the placement of cloud water collectors and for the determination of the liquid water content (LWC). A set of different active cloud water collectors was employed for bulk and size-segregated sampling (for details see Wieprecht et al., 2005). Another set of instruments was placed in a window on the top floor of the station building located at the summit, facing the upwind direction, to collect droplets by two counter-flow virtual impactors (CVI) and interstitial aerosol particles by a droplet-segregating inertial impactor (INT), both of which have been described previously by Schwarzenböck et al. (2000). These devices were used in combination with filters to sample residual nuclei from evaporated cloud drops, and with adsorption tubes for the collection of organic carbonyl compounds, respectively. The number size distributions of interstitial particles and of the cloud drop residual particles were determined by means of two differential mobility particle sizing (DMPS) systems. Meteorological data and the main trace measurements at the summit were provided by the staff of the DWD and UBA. Meteorological data at all three sites are necessary to decide whether conditions are suitable for conducting and/or analysing the cloud experiments. The relevant parameters were used for a synopsis of the situation, on the basis of which further action was taken. Altogether 14 cloud events were explored, but only three were found suitable for further investigation (Tilgner et al., 2005a). The key meteorological data for these are summarised in Table 1.

3.3.1. Gas phase trace components

Tracer experiments were performed with SF6 to demonstrate the existence of a connected air flow from the upwind site via the summit to the downwind site. Standard trace gases (O_3, SO_2, NO_x and CO) were measured at all three sites in order to obtain additional data that can be used to asses the air flow over the mountain ridge. Ozone and carbon monoxide were found to provide useful data for his purpose. Other oxidised compounds provide information on the quality of the encountered air masses. The inorganic compounds NO_x, other reactive nitrogen compounds NO_y, nitrous and nitric acids, and non-methane hydrocarbons (NMHC) were measured at the upwind site because they provide information on the extent of ageing, contamination or the oxidation capacity of the encountered air masses. Hydrogen peroxide, carbonyl compounds, and organic acids were measured at the upwind site as well as at the downwind site.

3.3.2. Aerosol and cloud physics parameters

The physical characterisation of the aerosol particles includes measurement of the number size distribution in the range $D_p = 3-900$ nm at all three sites, as well as the hygroscopicity of the particles at the upwind site. Changes in the size distribution between the upwind and the downwind site provide an indication for possible growth by in-cloud processes. Information on the hygroscopicity provides particle growth factors necessary to calculate the particle water content in order to assess the mass balance. At the summit, in addition to the applied methods outlined above for the characterisation of cloud drops, the LWC of the cloud and the size distribution of cloud droplets were determined with optical instruments. The location of the cloud base was determined at the upwind site. Both the liquid water content and the cloud base height were important parameters to asses the suitability of the cloud event for further measurements.

3.3.3. Particle sampling

Berner impactors were used for the collection of size-segregated particles. Particles were also collected on filters in the PM_1, $PM_{2.5}$ and PM_{10} size categories, so as to enable comparison with samples obtained by other techniques, and to provide sufficient material for chemical analysis, especially of organic compounds. In addition, the denuder—steam jet technique was used at

Table 3
Scientific measurements at all sites and responsibilities of participating groups

Measurement	Goldlauter (U)	Schmücke (C)	Gehlberg (D)	Method[a]
Meteorology				
T, r.h., wind speed & direction, $J(NO_2)$, global radiation, pressure, precipitation	BTU	DWD/IfT	IfT	Automatic weather station
Gas phase measurements				
O_3	BTU	UBA	IfT	UV absorption
SO_2	BTU	UBA	IfT	UV fluorescence
NO	BTU	UBA	IfT	Chemiluminescence + PLC
NO_2	BTU	UBA	IfT	Chemiluminescence + PLC
NO_y	BTU	—	—	Gold-converter + chemiluminescence
NO_z	BTU	—	—	
H_2O_2	BTU[1]/ZUF[2]	ZUF	ZUF[2]	1 enzymatic fluoresc.,[2]HPLC
CO	IfT	IfT	IfT	Gas filter correlation—IR
NMHC	IfT/UBA	—	—	GC-FID
Carbonyl compounds	TUD[3]/IfT[4]	IfT[4]	TUD[1]/IfT[2]	[3]GC/[4]HPLC
Organic acids	TUD		TUD	Spray collector—GC
HNO_2	BTU	—	—	Denuder—IC
HNO_3	BTU	—	—	Denuder—IC
HCl	BTU	—	—	Denuder—IC
Aerosol and cloud physics				
Number size distribution Coarse: 20–900 nm Fine: 3–22 nm	IfT	IfT	IfT	TDMPS
Droplet residuals, interstitial particles INT + DMPS	—	IfT	—	CVI + DMPS
Hygroscopicity	IfT	—	—	HDMPS
LWC	—	IfT/BTU	—	Gerber PVM 100
Size distribution (cloud droplets)	—	ZUF/BTU	—	FSSP

Cloud base height	BTU	—	—	Vaisala CTK25 Ceilometer
Tracer experiment	ZUF	ZUF	ZUF	SF_6—GC-ECD
Particle sampling				
Size segregated LV	IfT	—	IfT	5stage-Berner (r.h.—60%)
QF-filter PM_{10} HV	IfT	—	IfT	Sierra-Andersen- HV ($1\,m^3\,min^{-1}$)
QF-filter $PM_{2.5}$ HV	IfT	—	IfT	Digitel DHA-80 ($500\,l\,min^{-1}$)
QF-filter PM_1 HV	IfT	—	—	Digitel DHA-80 ($300\,l\,min^{-1}$)
LV-acidic components	BTU	—	—	Denuder-Steamjet
Interstitial particles, CCN	—	IfT	—	Polycarbonate & quartz filter
Particle analysis				
Mass	IfT	—	IfT	UMT 2 (Mettler)
Ions	BTU/IfT	IfT	IfT	IC, CE
OC/EC	IfT	IfT	IfT	Thermography + NDIR
Metals (Fe, Cu, Mn, Zn)	IfT	IfT	IfT	AAS
BC in CCN & interst. particles	—	IfT	—	PSAP
Semivol. organic comp.	IfT	IfT	IfT	GC-MS, LC-MS
Cloud water				
Size-dependent sampling	BTU/ZUF/CSU	CSU, BSE;		
Bulk sampling	—	BTU/IfT	—	
pH	—	ZUF	—	Mettler 405-60 88TE-S7/120
Conductivity	—	ZUF	—	WTW, LDM/S 2908/06 11.83.
Ions	—	IfT/BTU	—	IC (Metrohm,Dionex), CE (TS)
Organic acids	—	IfT[5]/TUD[6]	—	[5]CE (TS)/ [6]GC (Agilent)
H_2O_2	—	ZUF	—	
WSOC (TOC)	—	IfT/BTU/CSU	—	NDIR; Shimadzu TOC 5000A
OC/EC	—	IfT (CSU)	—	NDIR; Shimadzu TOC 5000A
Carbonyl compounds	—	TUD/CSU	—	GC

[a]Details on the methods applied are reported in the single contributions of this special issue.

Table 4
Analysers for trace gas analysis at the three experiment sites and their properties

Gas analyser (site)	Technique	Detection limit (ppbv)	Time resolution T_{95} (min)
CO MLU 300 (U)	IR-absorption	50	<0.7
CO Ansyco CO11 M (S)	IR-absorption	100	<0.7
CO TE 48C (S)	IR-absorption	100	<0.7
CO ML 9830 (D)	IR-absorption	100	<0.7
O_3 Dasibi 1108 (U)	UV-absorption	1	<2
O_3 APOA 350E (S)	UV-absorption	1	<2
O_3 TE 49 C (D)	UV-absorption	1	<2
SO_2 TE 43 C TL(U)	UV-fluorescence	0.1	<2
SO_2 TE 43 C (S)	UV-fluorescence	1	<2
SO_2 TE 43 C—TL (D)	UV-fluorescence	0.1	<2
NO_x Ecophysics CLD 770 ppt & PLC (U)	Chemiluminescence	0.05	0.5
	Photolytic converter		
NO_x TE 42 C (S)	Chemiluminescence	1	0.5
NO_x ML 9841 A (D)	Chemiluminescence	0.5	0.5
NO_y Ecophysics CLD 770 ppt (U)	Chemiluminescence with Gold converter	0.05	0.5

Table 5
Aerosol samplers in use at the three sites of investigation

Aerosol sampler	Size range	Volume flow ($l\,min^{-1}$)
Berner impactor (five stages)	0.05/0.14/0.42/1.2/3.5/10 μm	75
Sierra-Andersen HVS	PM_{10}	1000
Digitel DHA-80	$PM_{2.5}$	500
Digitel DHA-80	PM_1	300
2 CVI in parallel for CCN[a]	5–50 μm	2*8
INT for interstitial particles	<5 μm	60

PM_1: particulate matter less than 1 μm in diameter.
$PM_{2.5}$: particulate matter less than 2.5 μm in diameter.
PM_{10}: particulate matter less than 10 μm in diameter.
[a]Enrichment factor between 5 and 10 possible.

the upwind site for the purpose of comparison, because it avoids sampling artefacts.

3.3.4. Chemical analysis of particles

The chemical analysis of the particle samples was carried out (i) from filters, (ii) from the denuder-steamjet combination and (iii) in a size-segregated manner from Berner impactors for the main ionic components, the sum parameters OC/EC (OC, organic carbon; EC, elemental carbon) as well as for individual organic compounds. Mass closure was performed in a size-segregated manner (for details see Gnauk et al., 2005; Müller et al., 2005).

3.3.5. Cloud water

Cloud water was sampled using cloud water sampler of different design and analysed like particles extended by hydrogen peroxide, carbonyl compounds, and water soluble organic carbon (WSOC), also called total organic carbon (TOC) as sum of dissolved organic carbon (DOC) and particulate organic carbon (POC).

3.3.6. Quality control

The instruments used for standard trace gases were provided by UBA, BTU and IfT. Quality control was assured by means of intercomparison tests performed by the BTU group. The BTU instruments, in turn, were calibrated prior to the measurement campaign using a mobile calibration system kindly provided by the IFU Institute at Garmisch-Partenkirchen. The calibration of this system is traceable to primary US NIST standards. The intercomparison of instruments included a five point calibration in the range 0–100 $nmol\,mol^{-1}$ (ppb) for each NO_x, O_3 and SO_2, followed by ambient air measurements over a 24 h period. Calibration gases during the campaign were provided by an Environics S

100 calibrator, which also included an ozone generator. Zero air was produced by an Ecophysics Pure Air Generator, which was also used for daily calibration checks.

Particle counting systems were calibrated in different ways. The differential mobility analysers that were used either directly or in conjunction with counter-flow virtual impactors and the detection of interstitial particles were calibrated against each other before each measurement campaign. The efficiency of the condensation particle counters (CPCs) was determined during a WMO calibration workshop organised at the IfT after the second measurement campaign. The collection efficiency of the devices used for collecting particles (Berner impactor, filters, etc.) was determined during an international collector comparison study at the research station Melpitz of the IfT (INTERCOM2000, ten Brink et al., 2004; Müller et al., 2004). The sampling efficiency of the cloud water collectors was checked by comparing the cloud water volume sampled with that determined with the Gerber PVM 100 instrument.

The determination of the mass of collected particles was accomplished by weighing with a high-precision microbalance calibrated twice annually. The foils on which the particles were deposited were treated with deionised water so as to condition the surface, before the first and final weighing was performed at 50% r.h. and 22 °C. The masses of the deposits collected by different sampling devices were compared with each other. The deposits on the individual stages of the Berner impactor were included in the comparison as well as the mass of aerosol particles calculated from the number concentration (Gnauk et al., 2005).

The procedures used for chemical analysis were subjected to regular internal quality assurance tests, which include storage and transport of samples frozen to −18 °C, determination of blanks and control of standard deviations from the mean. During the past 10 years the analytical laboratories of BTU and IfT have successfully taken part in international intercomparison tests organised twice annually by the WMO for the main inorganic components. The methods used to determine organic carbon and elemental carbon were subjected to quality assurance tests by participating in round robin tests organised by the Technical University in Vienna. In addition, duplicate samples were taken and measured for comparison by two of the participating groups (inorganic components: BTU and IfT, organic components: TUD and IfT).

3.4. Measurement regime

A number of specific conditions are required for the measurements: These include a wind direction from the south-west (210–250° sector), and a wind speed at the Schmücke summit of at least 5 m s^{-1} and not exceeding 12 m s^{-1}. Only in this range of wind direction and wind speed the air mass flow can be expected to follow trajectories connecting the three stations (see the contribution of Heinold et al., 2005). If the wind speed is too low, local emission and deposition processes will have a dominant influence on the composition of the air, whereas at wind speeds beyond the indicated range safety rules disallow personnel to be on the tower. Weather forecasts by the DWD and a daily synopsis were used to asses the situation and come to a decision on whether measurements should be performed or not. A second condition required the presence of a cloud at the Schmücke summit with liquid water content greater than 0.1 g m^{-3}, while at the same time both upwind station and downwind station hat to be free of clouds. A third condition was that none of the three sites was expected to experience any precipitation. These conditions were met on 17 days in the year 2001 and on 13 days in 2002. In some cases, several shorter measurement periods were combined. Particle collection by impactors required at least 6 h to obtain sufficient material for chemical analysis. In the year 2001, the experiments permitted nine such samples to be obtained, while in 2002 altogether five samples were collected during the individual sampling periods.

4. Results and discussion

4.1. Selection of suitable measurement periods

Before and during the first experiment tracer experiments were carried out to define the trajectory of the air flow between the three measurement sites. The results of these experiments helped to define the boundaries of the dispersion model used to describe the air flow over the mountain ridge. Both tracer experiments and dispersion model are presented in Heinold et al. (2005).

Meteorological conditions were assessed by synoptic analysis based on satellite images, two radio soundings per day from Meiningen (about 30 km distance from the summit) and local meteorological observations by the German Weather Service at the Schmücke. A detailed overview of the meteorological situation during the FEBUKO measurement periods is given by Tilgner et al. (2005a). From the meteorological situation and the air flow characteristics described by Tilgner et al. (2005a) and Heinold et al. (2005) the three best cloud events were identified and these data were used for the further analysis. They are labelled EI, EII, and EIII. The key data for the selected measurement periods are summarised in Table 1.

4.2. A consideration on entrainment indicators

For comparison with data in the literature for former hill-capped cloud experiments, an effort was made to collect and summarise the indicators for the entrainment of outside air into the air flow during its trajectory from Goldlauter via the Schmücke to Gehlberg. These indicators are summarised in Table 6. In agreement with the criteria suggested by Colvile et al. (1997) such as the conservation of gas phase and particle phase tracers, the agreement of the measured cloud LWC with the adiabatic LWC and the cloud droplet size distribution characteristics, the observations generally support the conclusion that no significant entrainment occurred during the three measurement periods selected for detailed analysis. However, the detailed model that includes the micro-physics as described in the contribution of Simmel et al. (2005) indicates that entrainment may have been possible as it would possible explain differences observed between the cloud physical measurements and model predictions, especially with regard to the liquid water content. Thus, the degree of entrainment at event EI is small, that during event EII may be larger and that the event EIII maybe larger still, Nevertheless, all three events are characterised by a connected air mass flow from the upwind station via the summit toward the downwind station.

4.3. Main findings from physical measurements

The hygroscopic growth of particles with diameters 50, 150 and 250 nm was measured at 90% relative humidity with a hygroscopicity-tandem differential mobility analyser. The results are discussed by Lehmann et al. (2005). At least two types of particles with differing growth behaviour were found: one group was nearly hydrophobic, the other was quite hygroscopic. A simple growth model was applied based on the assumption that the soluble volume fraction consists of ammonium sulphate. Thereby the distributions of the soluble volume fraction were derived. The distributions for 150 and 250 nm particles were bimodal. One peak occurred below $\varepsilon = 0.2$, showed a minimum in the range $0.2 < \varepsilon < 0.4$ and a second maximum at $\varepsilon > 0.4$. The hygroscopic growth of the particles at 50 nm differed from that of the larger particles in that sometimes more than two growth modes with different hygroscopicities were present. This makes the specification of a growth factor problematic (see Lehmann et al., 2005, for details). The distribution of soluble volume for the 50 nm particles peaked at $\varepsilon < 0.3$. The influence of the distribution of soluble volume fraction on the activation of aerosol particles to form cloud drops is analysed by Mertes et al. (2005a). The fraction of particles acting as cloud condensation nuclei depends critically on both the soluble volume fraction of the particles and the particle diameter. A strong correlation was found between the increase of soluble volume fraction with the size of the particles and the fraction of particles that become scavenged to form cloud drops. On the other hand, the interstitial aerosol contained particles that according the Köhler theory should have been formed cloud drops but did not, possibly due to the presence of a hydrophobic organic surface coating. The generation of additional mass in the cloud was observed in the particle diameter range 60–300 nm. This is described by Mertes et al. (2005b). The mass gain is mainly attributed to the oxidation of SO_2 and the uptake of NH_3, although the formation of organic non-volatile compounds cannot be ruled out. Mertes et al. (2005b) have also observed the nighttime production of ultra-fine particles in the outflow of the orographic cloud.

4.4. Main findings from sampling method intercomparison

A variety of devices were used for the collection of particles and cloud water during the campaign. This permitted a comparison of the different methods. The results are reported by Gnauk et al. (2005), Müller et al. (2005), Wieprecht et al. (2005) and Brüggemann et al. (2005). High-volume filters and low pressure impactors may be subject to positive or negative artefacts, which are revealed by the differences of results. For non-volatile components, such as sulphate, similar results were obtained, whereas the more volatile components, such as nitrate and ammonium, frequently experienced losses when they were collected by impactors. The steamjet technique, which avoids these problems but cannot differentiate between particle sizes, resulted in higher concentrations that agreed well with the concentrations observed for cloud water. Therefore, concentrations obtained by the steamjet technique were used to correct the size-segregated concentrations derived from the impactors. Organic mono- and dicarboxylic acids that were collected by scrubbers, showed significant differences by factors up to 2–3 in the concentrations of some analytes compared with samples from high-volume filter and impactors, but no obvious trend. The various methods used to collect cloud water resulted in efficiencies ranging from 45% to 79%. However, the concentrations of analytes differed only by 10%, on average.

4.5. Main findings from chemical measurements

A complex data set consisting of gas, liquid and size-segregated particle phase component concentrations, meteorological, and cloud physics data was provided from field measurements to investigate the effects of in-cloud processes on changes in the chemical composition of particles during cloud passage. The upwind site part

Table 6
Overview on indicators for entrainment during the FEBUKO events

	Remarks	Event EI 26–27 October 2001 22:00–14:00 U-S[b]	S-D[b]	Event EII 06–08 October 2001 3 Parts[a] U-S	S-D	Event EIII 16–17 October 2002 17:00–04:10 U-S	S-D
Potassium (K^+)[f]	1	Constant[c]	Constant	24% Loss	Constant	20% loss	Constant
Sulphate (SO_4^{2-})[f]	1	23% Increase	21% Loss	Constant	Constant	20% loss	Constant
Elemental carbon (EC)[g]	1	Constant	27% Loss	100% Increase	70% Loss	Constant	47% loss
Oxalate ($HOOC\text{-}COO^-$)[g]	2	Constant	Constant	Constant[h]	10% loss[h]	Constant	Constant
Malonate ($HOOC\text{-}CH_2\text{-}COO^-$)[g]	2	Constant	14% Loss	19% Increase[h]	18% loss[h]	19% loss	Constant
Summary for chemical particle tracers		Constant	Constant/loss	Constant	Constant/loss	Constant/loss	Constant
Particles with $25 < D_p < 60$ nm	4	Identical	Identical	Slight shift to smaller sizes	Identical shape, little smaller concentration	Identical shape, little smaller concentration	Identical shape, little smaller concentration
Ozone	6	Minor differences especially in the middle of event		Approximately the same at all sites		Approximately the same between U and C; greater at D	
Cloud LWC[d] range; mean $\pm 1\sigma$ ($g\,m^{-3}$)	5	0.129–0.551; 0.345 ± 0.097		0.002–0.524; 0.203 ± 0.104		0.024–0.417, 0.202 ± 0.052	
LWC from DWD-LM ($g\,m^{-3}$)	6	0.1–0.3 (mean: 0.2)		0.0 (mean: 0.0) 0.0–0.2 (mean: 0.1) 0.0–0.4 (mean: 0.2)		0.3–0.4 (mean: 0.3)	
Cloud LWC compared to adiabatic	5	29% Subadiabatic		42% Subadiabatic		31% subadiabatic	
Correlation LWC = f (CBH[d])	5	Moderate/strong, $r = -0.85$		Moderate, $r = -0.75$		Moderate, $r = -0.62$	
Cloud top height (m agl) from DWD-LM	6	300–1100 (mean: 690)		1000–1100 (mean: 1075) 450 200–1000 (mean: 420)		1500–2100 (mean: 2000)	
Mean Richardson number	6	1.77		1.1		0.5	
	3.6	Stable, slight		Stable-neutral, slight		Less stable, strong	

Table 6 (*continued*)

	Remarks	Event EI 26–27 October 2001 22:00–14:00 U-S[b]	S-D[b]	Event EII 06–08 October 2001 3 Parts[a] U-S	S-D	Event EIII 16–17 October 2002 17:00–04:10 U-S	S-D
Thermal stratification, wind shear							
Cloud droplet size distribution modes	5	Monomodal		Monomodal		Monomodal	
Activation of particles with $D_p > 500$ nm	4	96%		91%		94%	
Indication for effects of entrainment through modelling for	7						
(i) Cloud LWC	7	Weak to moderate		Moderate to strong		Weak to moderate	
(ii) Cloud droplet size distributions	7	Weak		Weak		Very strong	
(iii) Cloud droplet number concentration	7	Weak		Weak		Weak	

(1) See Gnauk et al. (2005) and Brüggemann et al. (2005), (2) See van Pinxteren et al. (2005), (3) See Tilgner et al. (2005a), (4) See Mertes et al. (2005a), (5) See Wieprecht et al. (2005), (6) See Heinold et al. (2005), (7) See Simmel et al. (2005).

(a) Part 1: 06 October 2001, 10:30–14:15, part 2: 07 October 2001, 13:15–15:15, part 3: 07 October–08 October 18:00–11:00, (b) U: upwind station Goldlauter, S: cloud station Schmücke, D: downwind station Gehlberg, (c) constant = changes no bigger than $\pm 10\%$, (d) LWC = liquid water content, (e) CBH = cloud base height, (f) particles sampled by high volume Andersen filter sampler, (g) particles sampled by BERNER impactor, (h) data from part 3 of event EII only, cp. (a).

of the data set was used for the initialisation of the applied SPACCIM model on a realistic basis.

The PM_{10} mass concentrations fell in the range 8–17 $\mu g\,m^{-3}$. The major ionic species, sulphate, nitrate and ammonium, amounted to 90% of the total. The concentration of carbonaceous material differed, depending on the origin of the air mass. In event EI, where the origin was continental, the concentration amounted to 19% of total mass. In EII and EIII, where the air mass had a marine origin, the fraction was 33% of total mass. In these cases, the ratio of the total organic fraction to that of elemental carbon were about 2.5. In air masses of continental origin the ratio was 1.1. The mass concentration of particles ranging in size up to 900 nm, which was derived from differential mobility measurements, agreed well with that determined by weighing. The chemical mass balance also was in good agreement with the total mass obtained by weighing. <10–30% of the material was remained unidentified.

The concentrations of dicarboxylic acids were low at night and arose during the day until noon (in EI and EII) by a factor of 2–5. The concentration of carboxylic acids decreased with increasing carbon number. The maximum concentration occurred in the size range of 0.42–1.2 μm (diameter), where most of particulate mass is concentrated. The gas phase mixing ratios of many carbonyl compounds as formic acid and acetic acid displayed a similar diurnal variation in concentration. Particulate organic compounds of biogenic origin, such as levoglucosan and xylitole occurred with significant concentrations (100 $ng\,m^{-3}$) in the same size range as oxalic acid, whereas the concentrations of pinic acid and pinonic acid were very low (0.5–2.6 $ng\,m^{-3}$).

The concentrations of non-volatile species such as sulphate and elemental carbon were essentially the same in the particle phase and in cloud water, although the concentrations of volatile components, such as nitrate, ammonium and organic carbon, were lower at the upwind site. The increase of particulate concentrations between the upwind and the downwind site occurred primarily in the smallest size range ($0.05 < D_p < 0.14$ μm). During the event EI, sulphate increased by 20% and ammonium by 17%, during the event EIII the percentage increase was 70% and 150%, respectively. The concentration of organic carbon was found to increase by 20% in the size range $0.14 < D_p < 0.42$. These effects indicate accumulation of material by in-cloud reactions. Unambiguous evidence for an increase in concentration in the accumulation mode of the aerosol size distribution was obtained for the event EIII. This observation and the results of chemical analysis were confirmed by model calculations.

A greater number of soluble organic species were found in cloud water and their time dependence was determined. Carbonyl compounds and carboxylic acids contributed 10–17%, on average, to the organic fraction. Several organic compounds were here observed for the first time: glycolaldehyde, pinonaldehyde, butyric acid, malic acid and pinic acid. The budgets of organic compounds on their way through the cloud indicated a source of acetic acid.

Also some dicarboxylic acids, e.g. malonic acid, were found in slightly higher relative abundance at the downwind station, at least for some of the investigated particle size ranges. These effects may potentially be attributed to in-cloud processing of the aerosol.

4.6. Main results from model development and application

The parcel model SPACCIM which combines a complex multiphase chemistry with detailed microphysics has been developed (Wolke et al., 2005) treating a highly size-resolved drop spectrum applying adapted numerical algorithms and implicit time integration methods which integrate all involved processes in a coupled manner and utilise the special structure of large sparse equation systems (Sehili et al., 2005; Simmel et al., 2005).

In the SPACCIM approach, a new coupling scheme between microphysical and multiphase chemical models is implemented. The two codes run separately as far as possible and exchange all information needed at defined times. This approach allows the coupling of a complex multiphase chemistry model with microphysical codes of various types. Two adiabatic air parcel models (Simmel and Wurzler, 2005) with detailed microphysics and interactions between aerosol particles and drops are employed for SPACCIM simulations: one with traditional 1D treatment of the microphysics (water mass only) and one with a two-component treatment of the microphysics (water and aerosol mass). The latter allows drops of the same size to have different aerosol mass contents and, therefore, different gas scavenging properties (Sehili et al., 2005). In the "fully coupled" approach of Knoth (2005), the model equations for the microphysical variables (temperature, water vapour, liquid water content) as well as for all chemical species are considered as one system which is integrated in a coupled manner by an implicit-explicit time integration scheme. Therefore, no splitting error between microphysics and multiphase occurs. The model is based on the discretisation in mass space of the multi-component general dynamic equation using the Discrete Galerkin Method. Finally, a model intercomparison figure out discrepancies as well as similarities between different approaches for the coupled simulation of microphysical and multiphase chemical processes (Sehili et al., 2005).

A new version of CAPRAM has been developed which provides a better description of tropospheric multiphase chemistry of higher organics (Herrmann et al., 2005). The use of very complex multiphase reaction

schemes in higher dimensional models is restricted due to the computational burden. Therefore, the application of tools for the reduction of chemical reaction mechanisms is important. The automated reduction method ISSA (“Iterative Screening and Structure Analysis”) of Mauersberger (2005) achieves a good performance in this context. An application of the ISSA method to the cloud chemical mechanism RACM/CAPRAM 2.4 results in reduction rates of 55% for reactions (46% gas phase, 60% liquid phase), 23% for species, and 23% for phase transfers. Certainly, this reduction will also be applied to CAPRAM 3.0 in the future. An advanced treatment of the description of cloud boundaries has been put forward by the application of the VOF (“Volume of Fluid”) method by Hinneburg and Knoth (2005).

By means of the Lagrangian model SPACCIM, simulations of the hill cap cloud passage experiment FEBUKO were carried out (Tilgner et al., 2005b). Simulations were performed with an air parcel travelling along a predefined trajectory from upwind site through the orographic cloud to downwind site. For the description of the chemical reactions in the atmospheric multiphase system, CAPRAM 3.0 (Herrmann et al., 2005) was applied. The complex data set obtained in the FEBUKO field experiments was of huge importance for the MODMEP model initialisation and validation. Furthermore, the SPACCIM simulations were used for the interpretation of the measurements and allow a better understanding of cloud events effects on the physico-chemical properties of the atmospheric aerosols.

The modelling studies have been shown the importance of dynamic microphysical processes on multiphase chemistry. For all treated events, a significant cloud condensation nuclei (CCN) modification with sizes up to about 400 nm, mass productions up to about 0.7 $\mu g\,m^{-3}$ and acidification caused by cloud processing were identified in the model in agreement with the experimental findings. Final extensive comparisons between modelled and measured concentrations at both sites have been shown to be in good agreements. However, for organic compounds with low solubilities several cloud water measurements show considerably higher concentrations as expected from both (i) their Henry solubilities (van Pinxteren et al., 2005) and (ii) the complex multiphase modelling as performed by SPACCIM. These facts indicated that less soluble organic tropospheric trace gases e.g. aldehydes might potentially be adsorbed on surfaces of cloud droplets and possibly on deliquescent aerosol particles. For that reason, future multiphase chemistry models will include a description of surface layer chemistry as well as heterogeneous reactions. But for all that, the combination of SPACCIM and CAPRAM have been finally allowed an adequate prognosis of cloud water as well as aerosol concentrations of a variety of inorganic and, for the first time, also of a number of organic compounds with up to four carbon atoms during the cloud passage of an air parcel.

5. Summary

The main findings from the coupled FEBUKO and MODMEP projects are to be shortly summarised here. Firstly, the FEBUKO field site Schmücke has been characterised in much detail and it has been demonstrated that connected flow conditions can be observed and verified by tracer experiments and flow models. Great care has to be taken in order to obtain a realistic picture of chemical particle composition including cloud water composition. The coupling of size-resolved sampling and complementary non-size-resolved sampling techniques is urgently required. It is highly desirable to step into the development of real-time or near-real-time particle characterisation techniques especially for cloud processing experiments.

Much more work is required to the individual chemical species in the organic carbon fraction of particles, where about 15% of the organic mass could be accounted for in FEBUKO. Upon activation of particles, budget has been considered and shows good agreement between the upwind and the cloud station in many cases. An important finding is that cloud droplets do contain much more organic compounds then expected from their Henry-solubility and this difference becomes bigger for less soluble species. The same applies for the comparison of measurements and SPACCIM results. A better model picture appears to be required here, e.g. introducing a third reservoir consisting of species absorbed at the droplets surfaces.

During FEBUKO, clearly mass increases for the particles being processed by clouds could be identified under connected flow conditions as averages over observation times of several hours much more extensive than in the material available hitherto. The changes in the experimentally determined aerosol size distributions can be well reproduced by the SPACCIM model. The model results indicate complex interaction of soluble gases and particle constituents the coverage of which even in CAPRAM 3.0 is still far from complete.

6. Uncited reference

Ervens et al., 2002.

Acknowledgements

FEBUKO and MODMEP have been performed within the AFO 2000 research programme of the

German Bundesministerium für Bildung und Forschung. Financial support is gratefully acknowledged under FK 07ATF01 (FEBUKO) and FK 07ATF40 (MODMEP). We would like to thank the reviewers of this contribution for their helpful comments.

References

Audiffren, N., Renard, M., Buisson, E., Chaumerliac, N., 1998. Deviation from the Henry's law equilibrium during cloud events: a numerical approach of the mass transfer between phases and its specific numerical effects. Atmospheric Research 49, 139–161.

Bott, A., 1999. A numerical model of the cloud-topped planetary boundary layer: chemistry in marine stratus and the effects on aerosol particles. Atmospheric Environment 33, 1921–1936.

Bower, K.N., Choularton, T.W., Gallagher, M.W., Colvile, R.N., Beswick, K.M., Inglis, D.W.F., Bradbury, C., Martinsson, B.G., Swietlicki, E., Berg, O.H., Cederfelt, S.-I., Frank, G., Zhou, J., Cape, J.N., Sutton, M.A., McFayden, G.G., Milford, C., Birmili, W., Yuskiewicz, B.A., Wiedensohler, A., Stratmann, F., Wendisch, M., Berner, A., Ctyroky, P., Galambos, Z., Mesfin, S.H., Dusek, U., Dore, C.J., Lee, D.S., Pepler, S.A., Bizjeak, M., Diviak, B., 1999. The Great Dun Fell Experiment 1995: an overview. Atmospheric Research 50, 151–184.

Brüggemann, E., Gnauk, T., Mertes, S., Acker, K., Auel, R., Wieprecht, W., Möller, D., Collett Jr., J.L., Chemnitzer, R., Rüd, C., Junek, R., Herrmann, H., 2005. Schmücke hill cap cloud and valley stations aerosol characterisation during FEBUKO (I): particle size distribution and main components. Atmospheric Environment (this issue).

Choularton, T.W., Colvile, R.N., Bower, K.N., Gallagher, M.W., Wells, M., Beswick, K.M., Arends, B.G., Möls, J.J., Kos, G.P.A., Fuzzi, S., Lind, J.A., Orsi, G., Facchini, M.C., Laj, P., Gieray, R., Wieser, P., Engelhardt, T., Berner, A., Kruisz, C., Möller, D., Acker, K., Wieprecht, W., Lüttke, J., Levsen, K., Bizjak, M., Hansson, H.-C., Cederfelt, S.-I., Frank, G., Mentes, B., Martinsson, B., Orsini, D., Svenningsson, B., Swietlicki, E., Wiedensohler, A., Noone, K.J., Pahl, S., Winkler, P., Seyffer, E., Helas, G., Jaeschke, W., Georgii, H.W., Wobrock, W., Preiss, M., Maser, R., Schell, D., Dollard, G., Jones, B., Davies, T., Sedlak, D.L., David, M.M., Wendisch, M., Cape, J.N., Hargreaves, H.J., Sutton, M.A., Storeton-West, R.L., Fowler, D., Hallberg, A., Harrison, M., Peak, J.D., 1997. The Great Dunn Fell Experiment 1993: an overview. Atmospheric Environment 31, 2393–2405.

Collett Jr., J.L., Bator, A., Sherman, D.E., Moore, K.F., Hoag, K.J., Demoz, B.B., Rao, X., Reilly, J.E., 2002. The chemical composition of fogs and intercepted clouds in the United States. Atmospheric Research 64, 29–40.

Colvile, R.N., Bower, K.N., Choularton, T.W., Gallagher, M.W., Wobrock, W., Hargreaves, K.J., Storeton-West, R.L., Cape, J.N., Jones, B., Wiedensohler, A., Hansson, H.-C., Wendisch, M., Acker, K., Wieprecht, W., Pahl, S., Winkler, P., Berner, A., Kruisz, C., 1997. Meteorology of the Great Dun Fell cloud experiment 1993. Atmospheric Environment 31 (16), 2407–2420.

Djouad, R., Michelangeli, D.V., Gong, W., 2003. Numerical solution for atmospheric multiphase models: testing the validity of equilibrium assumptions. Journal of Geophysical Research 108 (D19), 4602–4614.

Ervens, B., George, C., Williams, J.E., Buxton, G.V., Salmon, G.A., Bydder, M., Wilkinson, F., Dentener, F., Mirabel, P., Wolke, R., Herrmann, H., 2002. CAPRAM2.4 (MODAC mechanism): an extended and condensed tropospheric aqueous phase mechanism and its application. Journal of Geophysical Research 108 (D14), 4426.

Fahey, K.M., Pandis, S.N., 2001. Optimizing model performance: variable size resolution in cloud chemistry modeling. Atmospheric Environment 35, 4471–4478.

Feingold, G., Kreidenweis, S.M., 2000. Does cloud processing of aerosol enhance droplet concentrations? Journal of Geophysical Research 105 (D19), 24,351–24,361.

Gnauk, T., Brüggemann, E., Müller, K., Chemnitzer, R., Rüd, C., Galgon, D., Wiedensohler, A., Acker, K., Auel, R., Wieprecht, W., Möller, D., Jaeschke, W., Herrmann, H., 2005. Aerosol characterisation at the FEBUKO upwind station Goldlauter (I): particle mass, main ionic components, OC/EC, and mass closure. Atmospheric Environment (this issue).

Heinold, B., Tilgner, A., Jaeschke, W., Haunold, W., Knoth, O., Wolke, R., Herrmann, H., 2005. Meteorological characterisation of the FEBUKO hill cap cloud experiments, Part II: tracer experiments and flow characterisation with nested non-hydrostatic atmospheric models. Atmospheric Environment (this issue).

Herrmann, H., Ervens, B., Jacobi, H.-W., Wolke, R., Nowacki, P., Zellner, R., 2000. CAPRAM2.3: a chemical aqueous phase radical mechanism for tropospheric chemistry. Journal of Atmospheric Chemistry 36, 231–284.

Herrmann, H., Tilgner, A., Majdik, Z., Barzaghi, P., Gligorovski, S., Poulain, L., Monod, A., 2005. Towards a more detailed description of tropospheric aqueous phase organic chemistry: CAPRAM 3.0. Atmospheric Environment this issue.

Hinneburg, D., Knoth, O., 2005. Non-dissipative cloud transport in Eulerian grid models by adopting the volume-of-fluid method. Atmospheric Environment (this issue).

Knoth, O., 2005. A parcel model for the combined treatment of microphysical and multiphase chemistry processes. Atmospheric Environment (this issue).

Kreidenweis, S.M., Walcek, C.J., Feingold, G., Gong, W., Jacobson, M.Z., Kim, C., Liu, X., Penner, J.E., Nenes, A., Seinfeld, J.H., 2003. Mopdification of aerosol mass and size distribution due to aqueous phase SO_2 oxidation in clouds: comparisons of several models. Journal of Geophysical Research 108 (D7), 4213.

Lelieveld, J., Crutzen, P.J., 1991. The role of clouds in tropospheric photochemistry. Journal of Atmospheric Chemistry 12, 229–267.

Leriche, M., Voisin, D., Chaumerliac, N., Monod, A., Aumont, B., 2000. A model for tropospheric multiphase chemistry: application to one cloudy event during the CIME experiment. Atmospheric Environment 34 (29/30), 5015–5036.

Leriche, M., Deguillaume, L., Chaumerliac, N., 2003. Modeling study of strong acids formation and partitioning in a

polluted cloud during wintertime. Journal of Geophysical Research 108 (D14), 4433.

Mauersberger, G., 2005. ISSA (iterative screening and structure analysis)—a new reduction method and its application to the tropospheric cloud chemical mechanism RACM/CAPRAM2.4. Atmospheric Environment (this issue).

Mertes, S., Galgon, D., Schwirn, K., Nowak, A., Lehmann, K., Massling, A., Wiedensohler, A., Wieprecht, W., 2005a. Evolution of particle concentration and size distribution observed upwind, inside and downwind hill cap clouds at connected flow conditions during FEBUKO. Atmospheric Environment (this issue).

Mertes, S., Lehmann, K., Nowak, A., Massling, A., Wiedensohler, A., 2005b. Link between aerosol hygroscopic growth and droplet activation observed for hill cap clouds at connected flow conditions during FEBUKO. Atmospheric Environment (this issue).

Müller, K., Spindler, G., Maenhaut, W., Hitzenberger, R., Wieprecht, W., Baltensperger, U., ten Brink, H., 2004. INTERCOMP2000, a campaign to assess the comparability of methods in use in Europe for measuring aerosol composition. Atmospheric Environment 38, 6459–6466.

Müller, K., van Pinxteren, D., Plewka, A., Svrcina, B., Kramberger, H., Hofmann, D., Bächmann, K., Herrmann, H., 2005. Aerosol characterisation at the FEBUKO upwind station Goldlauter (II): detailed organic chemical characterisation. Atmospheric Environment (this issue).

Raes, F., Bates, T., McGovern, F., VanLiederke, M., 2000. The 2nd aerosol characterization experiment (ACE-2). General context and main results. Tellus B 52, 116–126.

Schwarzenböck, A., Heintzenberg, J., Mertes, S., 2000. Incorporation of aerosol particles between 25 and 850 nanometers into cloud elements: measurement with a new complementary sampling system. Atmospheric Research 54, 241–260.

Sehili, A.M., Wolke, R., Knoth, O., Simmel, M., Tilgner, A., Herrmann, H., 2005. Comparison of different model approaches for the simulation of multiphase processes. Atmospheric Environment (this issue).

Simmel, M., Wurzler, S., 2005. Condensation and nucleation in sectional cloud microphysical models based on the Linear Discrete Method. Atmospheric Research (submitted for publication).

Simmel, M., Diehl, C., Wurzler, S., 2005. Numerical simulation of the microphysics of an orographic cloud: comparison with measurements and sensitivity studies. Atmospheric Environment (this issue).

ten Brink, H., Maenhaut, W., Hitzenberger, R., Gnauk, T., Spindler, G., Even, A., Chi, X.G., Bauer, H., Puxbaum, H., Putaud, J.P., Tursic, J., Berner, A., 2004. INTERCOMP2000: the comparability of methods in use in Europe for measuring the carbon content of aerosol. Atmospheric Environment 38, 6507–6519.

Tilgner, A., Heinold, B., Nowak, A., Herrmann, H., 2005a. Meteorological characterisation of the FEBUKO hill cap cloud experiments, Part I: synoptic characterisation of measurement periods. Atmospheric Environment (this issue).

Tilgner, A., Majdik, Z., Sehili, A.M., Simmel, M., Wolke, R., Herrmann, H., 2005b. SPACCIM: simulations of the multiphase chemistry occurring in the FEBUKO hill cap cloud experiments. Atmospheric Environment (this issue).

Wieprecht, W., Acker, K., Mertes, S., Collett Jr., J.L., Jaeschke, W., Brüggemann, E., Möller, D., Herrmann, H., 2005. Cloud physics and cloud water sampler comparison during FEBUKO. Atmospheric Environment (this issue).

Wobrock, W., Schell, D., Maser, R., Jaeschke, W., Georgii, H.W., Wieprecht, W., Arends, B.G., Mols, J.J., Kos, G.P.A., Fuzzi, S., Facchini, M.C., Orsi, G., Berner, A., Solly, I., Kruisz, C., Svenningsson, B., Wiedensohler, A., Hansson, H.-C., Ogren, J.A., Noone, K.J., Hallberg, A., Pahl, S., Schneider, T., Winkler, P., Winiwarter, W., Colvile, R.N., Choularton, T.W., Flossmann, A.I., Borrmann, S., 1994. The Kleiner Feldberg Cloud Experiment 1990. An overview. Journal of Atmospheric Chemistry 19, 3–35.

Wobrock, W., Flossmann, A.I., Monier, M., Pichon, J.-M., Cortez, L., Fournol, J.-F., Schwarzenböck, A., Mertes, S., Heintzenberg, J., Laj, P., Orsi, G., Ricci, L., Fuzzi, S., ten Brink, H., Jongejan, P., Otjes, R., 2001. The cloud ice mountain experiment (CIME) 1998: experiment overview and modelling of the microphysical processes during the seeding by isentropic gas expansion. Atmospheric Research 58, 231–265.

Wolke, R., Sehili, A.M., Simmel, M., Knoth, O., Tilgner, A., Herrmann, H., 2005. SPACCIM: a parcel model with detailed microphysics and complex multiphase chemistry. Atmospheric Environment (this issue).

3B2v8.06a/w (Dec 5 2003).51c XML:ver:5.0.1 AEA : 5762 Prod.Type:FTP pp.1–10(col.fig.:NIL) ED:SabithaRD PAGN:Mamatha SCAN:Mouli

ARTICLE IN PRESS

Available online at www.sciencedirect.com

SCIENCE DIRECT®

ELSEVIER

Atmospheric Environment ▮ (▮▮▮▮) ▮▮▮–▮▮▮

ATMOSPHERIC ENVIRONMENT

www.elsevier.com/locate/atmosenv

Meteorological characterisation of the FEBUKO hill cap cloud experiments, Part I: Synoptic characterisation of measurement periods

A. Tilgner*, B. Heinold, A. Nowak, H. Herrmann

Leibniz-Institut für Troposphärenforschung, Permoserstr. 15, D-04303 Leipzig, Germany

Abstract

The synoptic and local meteorological conditions during the ground-based cloud passage experiment FEBUKO performed at the Schmücke Mountain (Thüringer Wald) during October 2001 and 2002 are reviewed and discussed. A general description of the weather types and a classification of air masses are presented. In the second part the meteorological situations are illustrated in detail for the different experimental cloud events. The main objective of this two-part study is to classify the cloud events with respect to the occurring weather conditions and consistency to the philosophy of cloud passage experiments. Therefore, particular emphasis is placed on the incident flow conditions and on the separation of orographic and non-orographic cloud types. In the case of the flow characterisation, weather charts and calculated backward trajectories are used to determine the horizontal wind pattern and the rawinsonde data for the vertical structure of wind vectors. Additionally, in order to describe the local flow conditions the observed wind speed and direction at the experimental site on the summit are applied for the total of 14 cloud episodes. For the examination of the orographic character and properties of clouds, satellite pictures of different spectral channels, vertical thermodynamic data of the rawinsonde as well as the measured liquid water content and the cloud base height are evaluated. The resulting event evaluation provides a basis for subsequent local analysis of the flow over and/or around the mountain range (Part II of the study). Generally, it is found that more suitable conditions were encountered in October 2001 than in October 2002. Especially for the anticyclonic southwest weather-type, stable incoming flow condition as well as orographically induced clouds could be clearly identified.

Keywords: Febuko; Orographic cloud; Air mass investigation; Meteorological event classification

1. Introduction

The cloud passage experiment FEBUKO (field investigation of budgets and conversions of particle phase organics in tropospheric cloud processes) was performed on and around the Schmücke mountain (937 m asl), Thüringer Wald, Germany, in October 2001 and 2002. The objective was to investigate the physico-chemical aerosol processing within an orographic hill cap cloud. The field campaign was carried out in October due to the utmost probability of the occurrence of warm orographic clouds and the south-westerly incoming flow perpendicular to the mountain range. These two conditions are essential for a successful actualisation of the experimental design (Müller et al., 2005). The philosophy is based on the connected flow

*Corresponding author. Tel.: +49 341 2352406; fax: +49 341 2352325.
E-mail address: tilgner@tropos.de (A. Tilgner).

1352-2310/$ - see front matter © 2005 Published by Elsevier Ltd.
doi:10.1016/j.atmosenv.2005.02.006

between the two valley stations Goldlauter (upwind site) and Gehlberg (downwind site) via Schmücke Mountain (summit) including an orographic hill cap cloud. This kind of overflow can occur especially under a direct incoming flow frontal to the mountain range. Therefore, the analysis of the synoptic scale flow conditions and cloudiness is vital for the characterisation of the encountered cloud events. The main objective of this work is to present the meteorological conditions during FEBUKO, to classify the cloud events with regard to their consistency to the experimental design and completeness of the dataset and to select finally the most adequate periods in terms of local flow conditions. For that purpose a detailed analysis has to be performed by means of an extensive meteorological dataset, including synoptic charts and locally measured parameters, as well as an investigation of the local flow over the mountain range. In principle, just the complete analysis of local and mesoscale meteorological conditions together with flow modelling and tracer examination allows a cloud event classification with respect to the cloud passage philosophy. Therefore, the first part of the meteorological characterisation is focused on the evaluation of large-scale conditions and the event classification. The following second part (Heinold et al., 2005) is mainly devoted to further detailed flow analyses and a final re-evaluation, which then leads to the selection of the most suitable cloud events in terms of their quality for subsequent investigations.

2. Methods and implements

The analysis of synoptic and local scale meteorological conditions during the FEBUKO field campaign provides the basis for subsequent investigations and the resulting evaluation. The description of the large-scale wind field and the air mass characterisation allow statements about frontal processes, the spatial flow over or/and around the mountain range and the origin of the advected aerosol. The observed clouds at the summit can be the result of cloud advection related to frontal systems (preformed clouds), with a long and turbulent history, or directly formed by the orographically induced lifting of moist air. The overflow and formation of the orographic clouds and their microphysical properties are mainly influenced by the buoyancy and the constancy of the synoptic scale wind field.

Synoptic charts from the German Weather Service (DWD) with a time resolution of 12 h were analysed for detection of frontal processes, synoptic scale advection and air mass classification in the lower troposphere. Additionally, backward trajectories calculated by the HYSPLIT model (Rolph, 2003; Draxler and Rolph, 2003) were applied in order to identify the origin and characteristics of air masses reaching the experimental area, the sources for aerosol and constancy of advection. For the analysis and interpretation of the cloud conditions satellite pictures and rawinsonde observations were used. For this purpose satellite pictures of the circumpolar NOAA satellites (source: Deutsches Zentrum für Luft- und Raumfahrt (DLR) and Berliner Wetterkarte e.V.) and the geostationary METEOSAT satellites (source: DWD) with several infrared and visible channels were available. Just a combinative examination of the different spectral channels provides information about cloud properties like the cloud type, cloud height, pattern, dimension and the orographic character. The analysis of the rawinsonde data from the German Weather Service station Meiningen (provided by the university of Wyoming at the associated Webpage) about 30 km upwind of Schmücke mountain was performed in order to investigate the tropospheric thermal stratification and vertical wind structure. From these data conclusions can be drawn about the vertical thermodynamic conditions for the existing clouds. This helps to interpret the satellite pictures especially in terms of extent and cloud type. Furthermore, the meteorological and microphysical dataset of the three sampling stations, containing measurements of temperature, pressure, relative humidity, total precipitation, cloud base height as well as liquid water content and cloud droplet number concentration from the summit (Wieprecht et al., 2005), assist the cloud analysis, the temporal detection of frontal-induced air mass change and the constancy of the local wind.

The procedures mentioned above allow a qualitative classification of the experimental periods. The cloud events which conform to the experimental design, should satisfy the main selection criteria which are: (1) stable south-westerly overflow conditions with respect to the synoptic and local scale wind field, constant backward trajectories and the local meteorological data, (2) the appearance of orographic clouds with stable cloud properties, e.g., cloud base height and liquid water content, (3) the absence of frontal processes, air masses changes and precipitation, (4) the completeness of the data set as well as (5) sufficient experimental time and undivided periods.

As can be seen from item (1) the synoptical characterisation is just the first step for the complete evaluation and the selection of events with the best requirements. But it provides the basis for subsequent examinations such as overflow verification. A final assessment will be presented in Part II (Heinold et al., 2005) based on the present work and the analysis of (1) flow conditions, (2) ozone concentration time courses, (3) dedicated tracer experiments as well as (4) mesoscale and local modelling.

3. Results and discussion

3.1. General synoptic situation and air mass characterisation

The average synoptic situation during October 2001 was characterised by a trough over the east Atlantic close to 20°E and by high pressure over Central Europe resulting in a predominantly south-westerly air flow. In contrast, in October 2002 an expanded trough with small pressure gradients over the northern part of Europe caused an almost zonal flow. Therefore, in general, the conditions in 2001 correlate better with the climatological mean of the monthly air pressure field according to a predominant flow from southwest than those in 2002 (Fig. 1).

3.1.1. Synoptic situation 2001

The synoptic conditions can be divided into five periods with different general weather situations for each case (see Table 1). October 2001 began with a characteristic cyclonic southwest weather type (SWz). During this period the frontal zone was located across Central Europe. The maritime air mass was separated

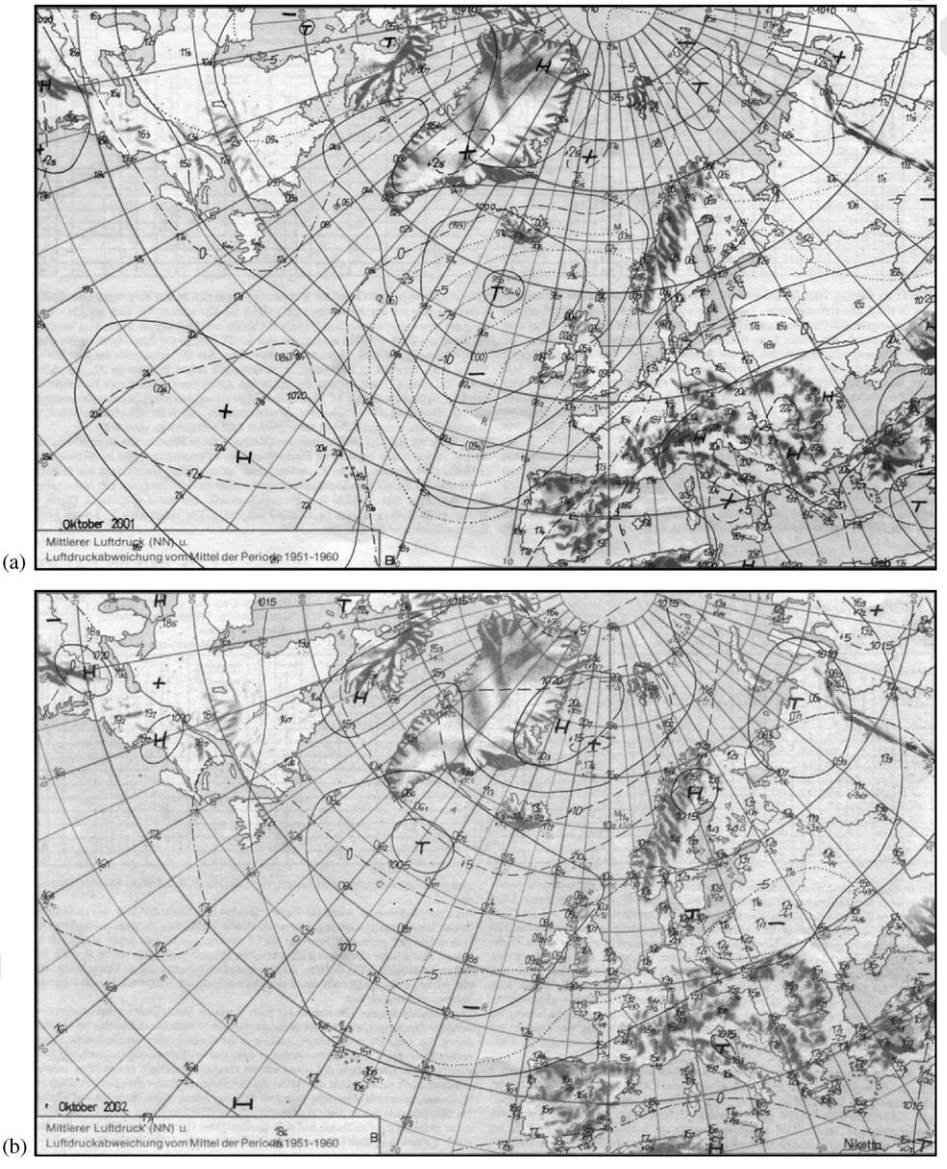

Fig. 1. Mean distribution of air pressure and derivation from the climatological mean over Europe in October 2001 (a) and October 2002 (b) (source: Berliner Wetterkarte, 2001 and 2002).

Table 1
Classification of the general weather situations and the associated air-masses during the FEBUKO field campaign in 2001 and 2002

Period	Date	General weather situation[a]	Predominant air-mass[b]
1a	01–09 Oct. 2001	Anticyclonic southwest (SWa)	Maritime tropical air (mT)
2a	10–13 Oct. 2001	Anticyclonic west (Wa)	Aged maritime sub-tropical (mT_P)
3a	14–20 Oct. 2001	Anticyclonic south (Sa)	Aged maritime sub-polar/-tropic (mP_T,mT_P)
4a	21–25 Oct. 2001	Angular west (Ww)	Aged maritime sub-polar (mP_T)
5a	26–31 Oct. 2001	Anticyclonic west (Wa)	Aged maritime sub-polar (mP_T)
1b	01–03 Oct. 2002	Central European high (HM)	Aged maritime sub-polar (cP_T)
2b	04–07 Oct. 2002	Cyclonic northwest (NWz)	Maritime polar (mP)
3b	08–14 Oct. 2002	High over Norwegian Sea and Fennoscandia (HNFa)	Maritime/continental sub-polar (mP,cP)
4b	15–23 Oct. 2002	Cyclonic southwest (SWz)	Maritime sub-tropic/-polar (mT,mP)
5b	24–31 Oct. 2002	Cyclonic west (Wz)	Maritime polar (mP)

[a]Subjective Hess–Brezowsky classification (Hess and Brezowsky, 1952; revised by Gerstengarbe et al., 1999).
[b]European air-mass classification after Scherhag (1948).

from the subtropical air and embedded atmospheric disturbances affected the weather in Germany. At the western side of the anticyclone over southeast Europe tropical maritime air (mT) was advected into the experimental site with south-westerly flow. From 10 to the 13 October 2001 the Atlantic troughs of low pressure were pushed northwards and Central Europe got into high pressure. Thereafter, the cyclonic southwest conditions turned into anticyclonic west flow with an advection of subtropical maritime air (mT_P). Over the next 7 days the anticyclone shifted slowly to the east and allowed small north-eastward moving atmospheric disturbances to affect the weather in Western Europe. This weather type was characterised by a strongly developed frontal system over the Atlantic and a high-pressure zone widely expanded to the north due to a predominantly southerly flow. The weather charts show an anticyclonic south type (Sa), which was not in agreement with the synoptic requirements of the experimental design, therefore no cloud event suitable for the analysis occurred during this period. On 21 October the anticyclonic south type (Sa) ended by a weakening of the associated anticyclone. Afterwards, an anticyclone which had moved toward the north-east of Europe became dominant for the next 5 days. Within this weather situation (angular west weather type (Ww)) the frontal zone was shifted to the north, therefore the incoming shortwave troughs were pushed northwards. At the western side of the associated anticyclone Mediterranean influenced air masses of maritime origin (mP_T) were advected to the measurement site. The angular west type ended on 25 October due to the shift of the dominant high-pressure area to South-East Europe, on which northern flank cyclones affected the north and centre of Germany until 31 October. During this anticyclonic west weather-type subpolar originated maritime air (mP_T) arrived at Central Europe under a stable south-westerly flow on the backside of the anticyclone. The dominant south-westerly flow was finished by a strongly developed cold front on 31 October 2001.

3.1.2. Synoptic situation 2002

The weather in October 2002 was more cyclonic influenced in comparison to the weather of October 2001. The month began with a short-time Central European high type (HM). The mild and dry weather in an aged subpolar air mass (cP_T) during the first 2 days ended at 3 October with the shifting of the frontal system to the east from Iceland. The associated cold front brought moist maritime polar air mass (mP) to Central Europe. Over the next 4 days the previous influential anticyclone moved toward southeast and the weather was determined by two back-to-back arriving shortwave frontal systems. The advection of cold and moist arctic air masses involving frontal precipitation processes was a characteristic feature for the cyclonic influenced northwest weather type (NWz). To the end of the period a high-pressure area developed over Scandinavia and from 8 to 14 October a high over the Norwegian Sea and Fennoscandia (HNFa) became decisive for the weather. The weather charts for this period show a mixture of southern and later on eastern flow condition within subpolar air masses (cP, mP), which does not conform to the synoptic requirements of the experimental design. The most adequate synoptic weather and flow conditions during the FEBUKO campaign 2002 occurred in the period from 15 to 23 October. Then, the meteorological situation was characterised by a cyclonic southwest weather type (SWz) including a back-to-back arriving low-pressure area over the Atlantic. The advection of air masses changed

depending on the exposure by the dominating cyclone. For this reason in front of the low maritime subtropic air (mT) and on the backside maritime subpolar air (mP) were advected to the experimental site. From 24 October to the end of the month the general weather situation was determined by fast back-to-back shifting troughs within a strong westerly flow associated with predominantly mild and rainy conditions in maritime polar air mass (mP). This cyclonic west weather type (Wz) did not include the required synoptic conditions for the experimental realisation.

3.2. Detailed meteorological description of experimental periods

The following section contains a detailed chronological description of the meteorological conditions at the experimental site such as an explicit cloud analysis and a comparison between the information provided by the previous synoptic examination and the locally measured data for the predefined cloud events (see Table 2).

The non-meteorological selection criteria like the completeness of dataset and the experimental duration will be noted only when relevant. Furthermore, only preselected cloud events will be presented here. The remaining experimental periods as well as the utilised material for all cloud events, including weather charts, satellite pictures, backward trajectories, rawinsonde profiles and locally measured meteorological parameters, are obtainable in the electronic supplementary material (ESM) to this manuscript as well as at the FEBUKO webpage (http://projects.tropos.de:8088/afo2000g3/FEBUKO_dateien/febuko.html).

3.2.1. 2 October 2001

The weather in the experimental area was affected by a low-pressure system with the centre over the Faroe Islands and high pressure over south and east Europe. The resulting intense and stable south-westerly flow and an included shortwave trough were decisive for the weather. Around 10:00 UTC a warm front arrived at the experimental site. Afterwards the advection of warm subtropic air mass strengthened. Therefore, the locally measured meteorological parameters show a significant decrease in the relative humidity at the two valley stations and an analogous reduction of the observed liquid water content at the summit. The satellite pictures (Fig. 2) indicate that the existing cloud had orographic characteristics and was just located over the mountain range (crest cloud). Furthermore, lee-wave clouds in an upper level partly over mountain crest indicate an air flow over the Thüringer Wald. The rawinsonde data prove the existence of unstable atmospheric conditions up to the summit level. The backward trajectories illustrate an extensive constant south-westerly flow with cyclonic bend and an advection of subtropic originated

Table 2
Experimental cloud periods during the FEBUKO field campaign 2001 and 2002

FEBUKO 2001				FEBUKO 2002			
Date	Time (UTC)	Duration	ESM code	Date	Time (UTC)	Duration	ESM code
02-10-2001	08:00–12:45	04 h 45 min	A	03-10-2002	09:00–12:35	03 h 35 min	J
					13:00–15:00		
					17:30–18:10		
06-10-2001	10:30–14:15	03 h 45 min	B	14-10-2002	12:00–13:00	02 h	K
07-10-2001	13:15–15:15	02 h		15-10-2002	06:30–10:45	40 min	
07/08-10-2001	18:00–11:15	17 h 15 min		16-10-2002	03:30–09:30	06 h	
08-10-2001	20:00–21:30	01 h 30 min	C	16/17-10-2002	21:00–05:30	08 h 30 min	L
09-10-2001	08:00–10:45	02 h 45 min		17-10-2002	11:50–12:35	45 min	M
10-10-2001	04:45–10:30	05 h 45 min		18-10-2002	08:00–10:30	02 h 30 min	
11-10-2001	04:00–09:45	05 h 45 min	D	19-10-2002	16:00–16:20	20 min	
					16:35–00:50	08 h 15 min	
21-10-2001	07:15–08:30	01 h 15 min	E	21/22-10-2002	21:30–01:20	03 h 50 min	N
	14:15–16:30	02 h 15 min					
	16:45–19:15	02 h 30 min					
22-10-2001	05:00–13:30	08 h 30 min		23/24-10-2002	21:30–04:35	07 h 05 min	
					06:30–10:05	03 h 35 min	
23-10-2001	09:30–11:00	01 h 30 min	F				
25-10-2001	03:00–05:45	02 h 30 min					
26-10-2001	08:30–16:30	08 h	G				
26/27-10-2001	22:00–13:00	15 h	H				
29-10-2001	09:00–11:00	02 h	I				

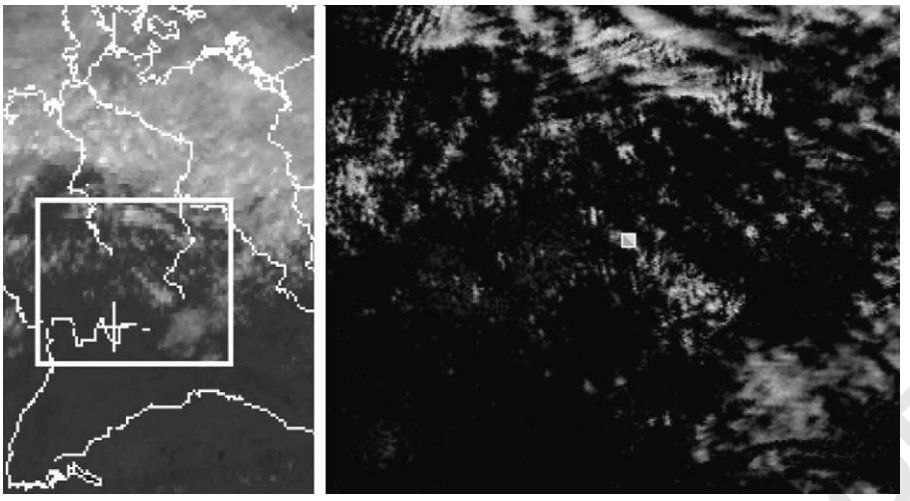

Fig. 2. Meteosat-satellite picture (VIS channel) of Germany with an orographic cloud over ridge of Thüringer Wald (left, source: DWD) and the associated high resolution NOAA picture (corresponding approximately to the marked white frame in the left Meteosat picture) of the area around Schmücke mountain (white quadrate) on 2 October 2001 12:00 UTC (right, source: DLR).

air. The locally measured wind direction was almost constant 210° and the wind speed reached values of up to 15 m s^{-1}. Thereafter, the weather conditions were basically adequate for the realisation of the experimental design. However, this event has significant deficits in dataset completeness and is hence inappropriate for further investigations.

3.2.2. 6–8 October 2001

The weather during this period was determined by a low-pressure system over the British Isles and a wide-range high-pressure system over Central and North Europe including a distinct advection of Mediterranean air masses. This cloud event is subdivided into three sections, in which the third section was the longest one and provided the most advantageous synoptical conditions. On 6 October a trough of low pressure moved in south-westerly direction along the frontal zone to Central Europe. The associated warm front passed over the experimental site around 06:00 UTC and caused a noticeable increase in temperature. The stratus bank as visible in the infrared satellite images was not stable during the cloud event. The height of cloud base over the upwind station quickly grew up to the summit level due to the constant south-westerly advection of warm air masses and the following shift of the existing inversion. After 13:45 UTC the summit came out of the stratus cloud and the measurements were stopped after short time. During the second section the measurement site came into the sphere of Atlantic troughs of low pressure and the weather became rainy. This frontal precipitation continued within the cloud event and the following cloud dissipation lead to the end of this section. The last period offered a more advantageous synoptic situation for the realisation of the experiment. The cloud event began on 7 October at 18:00 UTC. Due to very steady meteorological conditions the measurements lasted for a period of 17.25 h. The backward trajectories show a stable advection of warm subtropic air from south-west and as well the liquid water content as the height of cloud base remained constant. In contrast to the second section there was no rain until the end. The orographic character of clouds is assumed, but is not proved by the satellite images because of expanded mid-level clouds masking the clouds below.

The first two sections are unsuitable for further considerations because of the unstable cloud conditions as well as frontal processes and the resultant short duration. Different from this, the third section provided particularly advantageous and constant synoptical conditions as well as the longest experimental time. Therefore, this section is fulfilling the required conditions.

3.2.3. 23 and 25 October 2001

The general weather situation was dominated by a distinct anticyclone which moved from Scandinavia to Eastern Europe during this period. The location of the high led to a blocking of Atlantic troughs of low pressure, so that the frontal systems were forced to shift northwards around the anticyclone. The incoming frontal disturbances were decelerated over Central Europe and influenced the duration of the field experiments with their cloud bands and associated precipitation. The satellite images document a residue of frontal cloudiness. Especially on 25 October there were noticeable signs of convective processes within the

cloud pattern, which is proved by the rawinsonde data with a characteristic unstable atmospheric stratification. The trajectories indicate that both air masses had an Atlantic origin but were advected in a different way to the experimental site with dissimilar aerosol sources and age. In conclusion, none of the selection criteria are satisfied within this cloud event.

3.2.4. 26 October 2001

A distinct low-pressure area between Iceland and the British Isles and the continental high over southeast Europe affected the weather during this period. Between these two pressure areas a constant south-westerly flow took place. The surface synoptic charts show a small pressure gradient over Germany. Thereafter, the flow was characterised by low wind speeds. The measured wind speed and wind direction were constant around $4\,m\,s^{-1}$ and 210°. An intensive advection of subtropical air masses occurred at the eastside of the Atlantic low and especially the temperature chart for the 850 hPa pressure level illustrates a warm air area reaching up to Scandinavia. The experimental site remained under high pressure over the whole time period and thus it was not influenced by frontal processes. The backward trajectories show a consistent and fast advection of marine air masses from the Mid-Atlantic within the whole troposphere. In the VIS satellite picture of 12:00 UTC (Fig. 3) a bright cloud bank in front of the mountain range can be seen. The associated IR satellite picture illustrates a dark-grey and uniform area that indicates a relatively warm cloud top. From this it follows that the cloudiness was characterised by a low cloud layer of high density and albedo, which implies a stratus nebulous bank. Within the south-westerly flow the stratus bank was obviously formed by uplifting of the moist air mass induced by topography. In the lee of the mountain range cloud evaporation due to the downward motion can be observed over a wide area. The assumption of a stratus cloud is corroborated by the rawinsonde data. These show a striking inversion which separates the boundary layer from the free troposphere and provides the conditions for the formation of stratus clouds. The locally measured LWC amounted to $0.35\,g\,m^{-3}$ on average until 12:00 UTC. The later decrease of the LWC was caused by the shifting of the cloud base height as a consequence of the diurnal variation of the mixed layer height.

As a concluding remark it should be noted that the occurring conditions, in spite of a constant south-westerly flow and a relatively low variability of the locally measured data, did not completely fit to the experimental design because of very stable atmospheric stratification and the preformed clouds. These conditions may be unfavourable in terms of the overflow of the mountain range.

3.2.5. 26/27 October 2001

In contrast to the previous cloud event the experimental site was under influence of frontal processes. The frontal zone had moved eastward during 26 October, therefore frontal disturbances were shifted to Central Europe and affected the weather especially on 27 October. The event began at 22:00 UTC and afterwards a disintegrating occlusion without precipitation reached the experimental site. The occlusion can be identified by means of the locally measured meteorological parameters such as slight decrease in pressure. This process did not end until 06:00 UTC and a following increase of

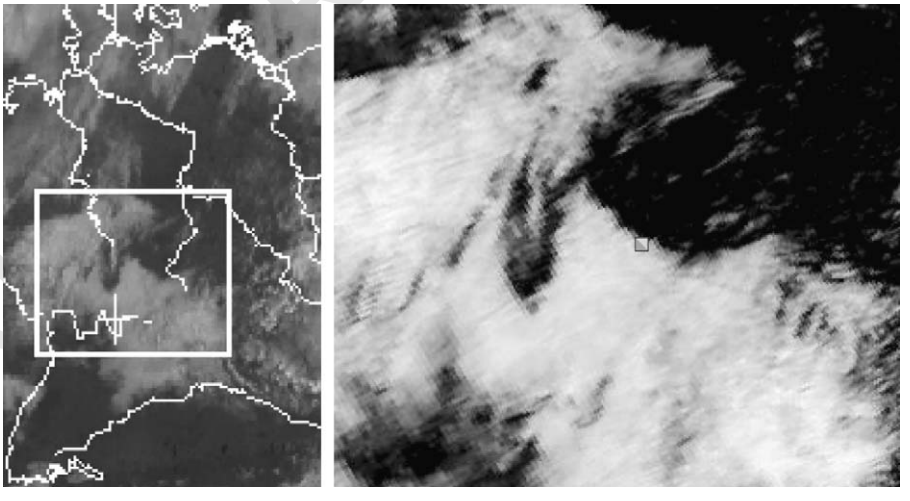

Fig. 3. Meteosat-satellite picture (VIS channel) of Germany with cloud in front of Thüringer Wald ridge (left, source: DWD) on 26 October 2001 12 UTC and the associated high resolution NOAA picture (corresponding approximately to the marked white frame in the left Meteosat picture) of the area around Schmücke mountain (white quadrate) at 11:08 UTC (right, source: DLR).

air pressure at ground level was noticed. The measurement period had to be discontinued because of an incoming precipitation band associated with another occluded front crossing Thüringen around 13:00 UTC. Satellite pictures and the rawinsonde data point to low stratiform clouds in a moist boundary layer. The backward trajectories indicate that the air mass was advected from the Mid-Atlantic. In contrast to the previous event the course of the backward trajectories was less stable and they turned more to Southwest. Particularly after the front passage, the cloud event which lasted 15 h was connected with very stable south-westerly flow conditions.

3.2.6. 3 October 2002

On 3 October 2002, the period of anticyclonic weather ended when the associated anticyclone with the centre over southeast Europe had moved eastward and the weather type changed with a north-westerly upper level flow. The weather at the experimental site was influenced by an incoming trough of low pressure. Its cloud banks and precipitation split the event into three parts. The satellite pictures show structured cloud bands over wide parts of Europe coupled to moving fronts. The frontal processes were mainly affected by a warm front and became fairly weaker during the experimental period while the associated cold front passed over Germany not until the night from 3 to 4 October. The preliminary warm sector was characterised by an advection of subtropic maritime air. In contrast, the cold front brought subpolar air of maritime origin. The backward trajectories illustrate a dissimilar course for the different altitudes and an anticyclonic turn within the last 3 days. Within the warm sector the wind direction was predominantly southwest and turned to west during the last section. The event was characterised by a vertical wind shear and a low level inversion together with stratus clouds. In the daytime the dew-point deficit decreased and the boundary layer stratification became unstable. This event did not fit in further considerations due to the strong partitioning, the precipitation, the vertical wind shear, the frontal-induced clouds and the differences in the air mass origin.

3.2.7. 14–16 October 2002

The weather during this cloud event which consisted of three parts was characterised by two back-to-back arriving shortwave troughs. The first one moved over the Netherlands and Northern Germany to the Baltic Sea and finally dissipated. The second low developed to an elongated low-pressure area from England to Northeast Scandinavia. The occlusion of the first low-pressure area which had passed the experimental site just before the measurement period brought warmer air to Thüringen on 14 October 2002. This caused a gradual warming and the cloud base height was lifted so that the summit came out of cloud after 12:20 UTC. The satellite images show a large-scale cloud pattern. On 15 October the wind slightly turned from 230° to 200° at the summit site indicating the approaching warm front of the second low. Because of expanded mid-level clouds masking the clouds below, the satellite pictures are difficult to interpret. The rawinsonde data illustrate a moist lower troposphere therefore stratus can be assumed. Due to the lifting of the cloud base height in the course of the day the measurements had to be discontinued again. During the third section the experimental site was located within the warm sector of the second low-pressure area which had shifted from the Gulf of Biscaya to the southern North Sea. The surface pressure reached its minimum in this period before it rose again until the end of measurements, when frontal precipitation started. The satellite pictures show frontal mid-level clouds partially masking the low stratus. Thus, there is no information about the orographic character of clouds below. While the course of the backward trajectories of different altitudes was not consistent on 14 and 15 October 2002, the trajectories from 16 October 2002 provide a stable and similar advection of marine air masses from the Mid-Atlantic over France and Germany for all altitudes. Accordingly, the observed velocity was constant at 210° with $10\,m\,s^{-1}$. Therefore, only the third section provides at least some of the required conditions with stable backward trajectories and a stable incoming flow at the summit.

3.2.8. 16/17 October 2002

The weather situation was also determined by the previously described low with its centre over the North Sea and a shifting shortwave trough, which was embedded in the frontal system with associated large scale cloud bands. This shortwave trough moved across Germany in north-easterly direction and became stationary over the Baltic Sea. The warm front passed the experimental site before the measurement period and the coupled cold front arrived after midnight and stagnated above Mid Germany. Due to the occurrence of precipitation the measurements were stopped in the early morning hours. In the satellite pictures the experimental site is capped by bright upper level stratiform clouds (cirrus), but low-level stratus fields can be seen all around the upper level cloud bands. The rawinsonde data indicate a stable tropospheric stratification with a temperature inversion in pressure level of about 900 hPa as well as a moist lower boundary layer, which corroborates the assumption of stratus clouds. Also, the locally measured cloud base height with approximately 100 m below summit level and the LWC values of around $0.2\,g\,m^{-3}$ indicate the stratus clouds. The synoptic scale flow conditions were characterised by the highly constant south-westerly wind directions including wide vertical extent and comparatively high

Table 3
Event classification of the FEBUKO cloud events in 2001 and 2002

Priority	Date	Remarks
1	26–27 Oct. 2001	Stable south-westerly flow conditions, low stratus, longest undivided event
2	06–08 Oct. 2001	Stable south-westerly flow and cloud conditions in the last dominant section
3	16/17 Oct. 2002	Particularly adequate flow characteristics (high wind speed and constant from southwest), sufficient experimental time, stratus cloud
4	02 Oct. 2001	Excellent stable flow conditions, orographic crest cloud, incomplete data set
5	11 Oct. 2001	Less stable incident flow, large-scale cloudiness, relatively short cloud event
6	26 Oct. 2001	Very stable atmospheric stratification, constant synoptic conditions, blocking effects assumed, large preformed orographically induced stratus field
7	08–10 Oct. 2001	Differences between the three short sections, frontal cloud on 9 Oct. 2001 and a low stratus band on 10 Oct. 2001, changing wind direction
8	21–24 Oct. 2002	Orographic cloud on 23–24 Oct. 2002, frontal precipitation, tendency to west winds
9	14–16 Oct. 2002	Stable flow conditions only in the last section, inconsistent backward trajectories, just large-scale cloud pattern
10	23/25 Oct. 2001	Frontal processes, short experimental time, completely different backward trajectories,
11	21–22 Oct. 2001	Strong separation into very short sections, low stability of the meteorological parameters, precipitation processes, different backward trajectories
12	03 Oct. 2002	Strong partitioning into short sections, frontal clouds, occurred precipitation, unstable backward trajectories, distinct wind shear
13	17–19 Oct. 2002	Strong separation into very short sections, completely different weather situations on each day, temperatures around the freezing point, precipitation
14	29 Oct. 2001	Synoptic-scale west wind conditions, insufficient experimental time

wind speeds. The measured wind direction and wind speed average were around 210° and 10 m s^{-1} at the summit. The backward trajectories show a continuous advection of maritime originated air masses from southwest. Because of the long-range transport over Western Europe the aerosol was altered and became more continental. This cloud event was qualified for further considerations particularly with regard to adequate flow characteristics and the sufficient experimental time of about 8.5 h.

4. Overall evaluation

Based on the detailed meteorological analysis, episodes such as 2 October 2001 offer appropriate conditions in terms of stable south-westerly incident flows. In contrast, the split events such as on 23/25 October 2001 and 17–19 October 2002 were mainly characterised by completely different synoptic-scale flows with dissimilar courses of backward trajectories during the experimental time. On 26 October 2001 very stable atmospheric conditions indicate a possible blocking of the incoming flow and air coming from higher levels at the downwind site. Orographic clouds, large-scale clouds showing orographic effects or preformed cloud banks with distinct dissolutions occurred on 2, 10, 11 and 26 October 2001 as well as on 24 October 2002. On a lot of other days orographically induced clouds were also possible, but could not be resolved exactly. Unfortunately, for the most adequate event on 2 October 2001 there are deficits in the completeness of the data set. In consideration of the main criteria the cloud events on 6–8 and 26/27 October 2001 as well as 16/17 October 2002 provides the most suitable conditions. The complete qualitative event classification is summarised in Table 3. The subsequent tracer and flow analysis in Part II (Heinold et al., 2005) has to be focussed especially on these best events.

5. Summary

The synoptic situations during the ground-based cloud passage experiment FEBUKO during October 2001 and 2002 were investigated. After description of weather types for the period of measurements in general a detailed analysis of the synoptic and local scale meteorological conditions was conducted in order to evaluate several cloud events. Thereby, the consistency of the occurring weather conditions to the experimental design with particular respect to flow pattern and the orographic character of clouds was crucial. For the flow characterisation weather charts and calculated backward trajectories as well as rawinsonde data were used. The analysis of backward trajectories has also enabled

us to quantify the transport time and the air mass source regions. Measured wind speed and direction were utilised for describing the local flow conditions. Satellite pictures for different spectral channels, vertical thermodynamic data of the rawinsonde as well as the observed liquid water content and cloud base height have proved as appropriate tools to examine the orographic character and properties of clouds. For stable southwest flow conditions orographic induced clouds could be found which occurred mainly in October 2001 with predominant anticyclonic weather. The resulting event evaluation provides a basis for subsequent local analysis of the flow over and/or around the mountain range and a final event selection, which is given in Part II (Heinold et al., 2005).

Uncited reference

Herrmann et al., 2005.

Acknowledgements

The work was supported by the Bundesministerium für Bildung und Forschung (Project FKZ 07ATF01). We thank the Berliner Wetterkarte e.V., the Deutsches Zentrum für Luft- und Raumfahrt (DLR, Oberpfaffenhofen) and the Deutscher Wetterdienst (DWD, Offenbach) for good cooperation and support. We thank all the colleagues who participated in the FEBUKO experiments.

References

Draxler, R., Rolph, G., 2003. HYSPLIT (Hybrid Single Particle Langrangian Integrated Trajectory) Model access via NOAA ARL READY Website (http://www.arl.noaa.gov/ready/hysplit4.html). NOAA Air Resources Laboratory, Silver Spring, MD.

Gerstengarbe, F.-W., Werner, P.C., Rüge, U., 1999. Katalog der Großwetterlagen Europas (1881–1998)—Nach P. Hess und H. Brezowsky. 5. Auflg., Eigenverlag Potsdam-Institut für Klimafolgenforschung, Potsdam. http://www.pik-potsdam.de/~uwerner/gwl/gwl.pdf.

Heinold, B., Tilgner, A., Jaeschke, W., Haunold, W., Knoth, O., Wolke, R., Herrmann, H., 2005. Meteorological characterisation of the FEBUKO hill cap cloud experiments, Part II: tracer experiments and flow characterisation with nested non-hydrostatic atmospheric models. Atmospheric Environment (this issue).

Hess, P., Brezowsky, H., 1952. Katalog der Großwetterlagen Europas. Berichte des Deutschen Wetterdienstes in der US-Zone 33, Bad Kissingen.

Herrmann, H., Wolke, R., Müller, K., Brüggemann, E., Gnauk, T., Barzaghi, P., Mertes, S., Lehmann, K., Massling, A., Birmili, W., Wiedensohler, A., Wieprecht, W., Acker, K., Jaeschke, W., Kramberger, H., Syrcina, B., Bächmann, K., Collett Jr., J.L., Galgon, D., Schwirn, K., Nowak, A., van Pinxteren, D., Plewka, A., Chemnitzer, R., Rüd, C., Hofmann, D., Tilgner, A., Diehl, K., Heinold, B., Hinneburg, D., Knoth, O., Sehili, A.M., Simmel, M., Wurzler, S., Mauersberger, G., Majdik, Z., Müller, F., 2005. FEBUKO and MODMEP: Field measurements and modelling of aerosol and cloud multiphase processes. Atmospheric Environment (this issue).

Rolph, G., 2003. Real-time Environmental Applications and Display sYstem (READY) Website (http://www.arl.noaa.gov/ready/hysplit4.html). NOAA Air Resources Laboratory, Silver Spring, MD.

Scherhag, R., 1948. Neue Methoden der Wetteranalyse und Wetterprognose. Springer, Berlin.

Wieprecht, W., Acker, K., Mertes, S., Collett Jr., J.L., Jaeschke, W., Brüggemann, E., Möller, D., Herrmann, H., 2005. Cloud physics and cloud water sampler comparison during FEBUKO. Atmospheric Environment (this issue).

3B2v8.06a/w (Dec 5 2003).51c XML:ver:5.0.1 AEA : 5763 Prod.Type:COM pp.1–13(col.fig.:1–4) ED:MangalaK. PAGN:padmini SCAN:geethas

ARTICLE IN PRESS

Available online at www.sciencedirect.com

SCIENCE DIRECT®

ELSEVIER

Atmospheric Environment ▮ (▮▮▮▮) ▮▮▮–▮▮▮

ATMOSPHERIC ENVIRONMENT

www.elsevier.com/locate/atmosenv

Meteorological characterisation of the FEBUKO hill cap cloud experiments, Part II: Tracer experiments and flow characterisation with nested non-hydrostatic atmospheric models

B. Heinold[a,*], A. Tilgner[a], W. Jaeschke[b], W. Haunold[b], O. Knoth[a], R. Wolke[a], H. Herrmann[a]

[a]*Leibniz-Institut für Troposphärenforschung, Permoserstr. 15, 04318 Leipzig, Germany*

[b]*Johann-Wolfgang-Goethe Universität Frankfurt, Zentrum für Umweltforschung, Georg-Voigt-Str. 14, 60325 Frankfurt a.M., Germany*

Abstract

The mesoscale and local flow conditions during the ground-based cloud passage experiment FEBUKO performed at the Schmücke Mountain (Thüringer Wald) during October 2001 and 2002 are investigated and discussed. Several methods are applied to characterise and classify the cloud episodes in terms of the flow conditions and their consistency to the philosophy of cloud passage experiments. For this the flow over the mountain range and a flow that connects the experimental sites are of crucial importance. The resulting selection of events is based on a synoptical evaluation (Part I of the work) and provides a recommendation of events, which are adequate for subsequent investigations. The mesoscale air flow over the complex terrain is characterised by means of non-dimensional flow parameters like Froude number and the non-hydrostatic meteorological model LM. An analysis of the locally measured natural tracer ozone is intended to assure that measurements were performed in identical air masses at the different locations during the 14 cloud events. It is found that the flow connecting the measurement sites is distinctly associated with the flow over and/or around the Thüringer Wald, which in turn is determined by the synoptical flow and the thermal stratification. Furthermore, applications of tracer techniques using the inert SF_6 for studies of transport processes in the experimental site and verification of the location of measurement stations are presented. For the tracer experiments in October 2001 and 2002 an attempt is made to reproduce them with an anelastic non-hydrostatic model in conservation form in order to understand the tracer dispersion.

Keywords: Flow over complex terrain; Febuko; Flow parameters; Flow modelling; Tracer studies

1. Introduction

The purpose of the field experiments during the FEBUKO (field investigation of budgets and conversions of particle phase organics in tropospheric cloud processes) project in October 2001 and 2002 was to subject a physically and chemically completely char-

*Corresponding author. Tel.: +49 341 2352822; fax: +49 341 2352139.

E-mail addresses: heinold@tropos.de (B. Heinold), tilgner@tropos.de (A. Tilgner).

1352-2310/$ - see front matter © 2005 Elsevier Ltd. All rights reserved.
doi:10.1016/j.atmosenv.2005.02.036

acterised air mass to a cloud passage. For this characterisation the gas and particle phase has to be investigated at three locations, i.e. before cloud passage, in the cloud and after cloud passage. A classical situation in which such an experiment can be conducted is the processing of air masses in an orographic hill cap cloud. The ideal location for such an experiment is found at Schmücke Mountain (937 m asl) in the mountain range of the Thüringer Wald. Measurements on the summit and two valley stations (Goldlauter and Gehlberg) are expected to satisfy the conditions mentioned above (Herrmann et al., 2005).

Before analysing the actual field experiments, in which the gas/particle phase and cloud water are investigated, it has to be verified that the chemical and physical properties determined at the elected locations can be attributed to identical air masses (Jaeschke et al., 2001). Statistical wind distributions show that the main direction of flow in the investigation area is between 210° and 240°, i.e., southwesterly. Therefore, the three principal measurement sites are arranged in a line extending from southwest to northeast (Fig. 1). For verification of this approach, several tracer experiments using the inert gas sulphur hexaflouride (SF_6) were performed by the Centre for Environmental Research (Zentrum für Umweltforschung, ZUF) before and during the FEBUKO measurement campaigns. The results of these experiments will be presented here. Computer simulations of meteorological fields provide a more detailed description of local flow conditions during the cloud events. Thereby, statements about the required

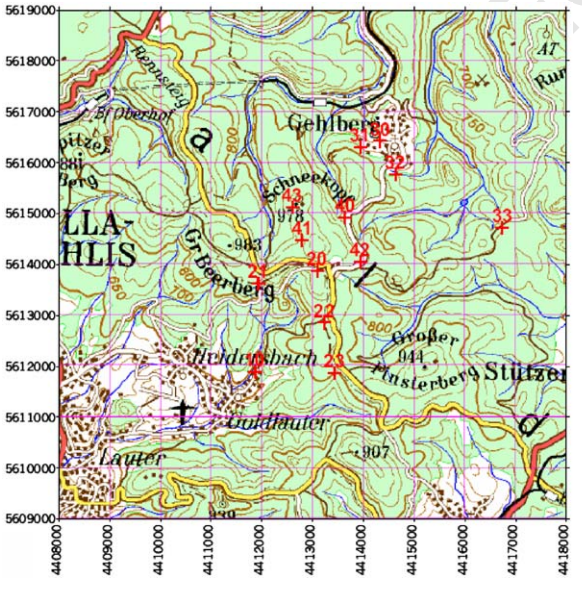

Fig. 1. Location of all sites listed in Table 1 including the main experimental sites (Goldlauter, Schmücke, Gehlberg) (*source*: Thüringer Landesvermessungsamt).

flow over the mountain range as well as orographic blocking and mountain waves are possible. Furthermore, the connected flow between the three experimental sites can be verified by means of transport simulations. The airflow modelling on the mesoscale was performed with the non-hydrostatic Local Model (LM) (Doms and Schättler, 1999), which is the operational regional forecast model of the Deutscher Wetterdienst (DWD). The flow in a closer area around the summit site and the artificial tracer transport were simulated using the anelastic non-hydrostatic All-Scale Atmospheric Model (ASAM). Calculated non-dimensional flow parameters and time series of the natural tracer gas ozone support the flow characterisation by means of atmospheric models.

The synopsis of local and mesoscale meteorological conditions together with flow modelling and tracer examination allows a cloud event classification with respect to the experimental design. The synoptic scale incident flow arriving at the observational sites as well as the meteorological conditions in October 2001 and 2002 including air mass characterisation were already described in Tilgner et al. (2005a). On the basis of these synoptic considerations this work provides a detailed description of local wind fields and advection. After the comprehensive analysis a final selection of cloud events in terms of their quality for subsequent investigations is presented.

2. Methods and experiment

2.1. Flow characterisation with non-dimensional parameters

Flow parameters can be easily calculated from locally measured meteorological data and aid to characterise the flow over a mountain range without numerically expensive models. By means of scale analysis the Froude number *Fr* and the Rossby number *Ro* are found to be the most relevant non-dimensional parameters describing the flow regime in mountainous terrain (Pierrehumbert and Wyman, 1985). There are a variety of quantities termed Froude number that have both different forms and dynamical significance. An overview is given in Baines (1995). The Froude number considered here is defined as $Fr = NH/U$, where U is the characteristic speed of incoming flow, N the Brunt-Väisälä frequency and H the maximum mountain height. This formulation of the Froude number is interpreted as the ratio of the potential energy that enables low-level air to pass over the mountain to the kinetic energy of the flow. It relates to non-linear factors like blocking effects and wave breaking. Numerical simulations performed by Pierrehumbert and Wyman (1985) yield three critical Froude numbers: When $Fr > 0.75$ a disturbance propagates

upstream with time and results in a decelerated low-level flow. Gravity waves begin to amplify. When $Fr \geqslant 1.5$ a stagnant area at the low upstream slope occurs. At $Fr = 2$ the flow is blocked and the stagnant area will extend if Fr further increases.

The values could be validated both in laboratory experiments (Baines, 1995) and in tracer studies (Bruintjes et al., 1995; Vosper et al., 2002; among others). Taking the formation of clouds or precipitation and the associated release of latent heat into account, the critical Froude number at which stagnation sets in is 30–100% higher than under corresponding conditions without clouds (Jiang, 2003; Colle, 2004). But because of uncertainties in determining the variable amount of latent heat release only the "dry" Froude number will be used hereafter.

The Rossby number $Ro = U/fL$, where L is the mountain half-width and f the Coriolis parameter, describe the effect of the Coriolis force. This results in a barrier-jet oriented parallel to the mountain and limits the extent and strength of the upstream blocking in cases of wide mountains ($Ro \ll 1$). For the Thüringer Wald Ro is estimated as $Ro > 10$ with $L \ll 10\,\mathrm{km}$, $U = 10\,\mathrm{m\,s^{-1}}$ and $f = 10^{-4}\,\mathrm{s^{-1}}$. Therefore, the Coriolis effect does not have to be considered in the following.

As seen from the definitions above, the Froude number is directly linked with the atmospheric stratification by the Brunt-Väisälä frequency. The more stable the boundary layer is stratified, the larger the Froude number becomes for a given wind velocity. Hence the blocking effects are more distinctive as mentioned above. The dimensionless gradient Richardson number, or just Richardson number, defined as

$$Ri = \frac{g(\partial\theta/\partial z)}{\theta(\partial U/\partial z)^2} \quad (1)$$

is the ratio of the energy extracted by buoyancy forces to the energy gained from the flow shear. θ is the potential temperature and g the gravitational acceleration. Also taking into account the vertical gradient of wind speed, Ri provides an appropriate measure to characterise the stratification with respect to blocking effects. The thermal stratification determines the sign of the Richardson number. The flow is statically stable if Ri is greater than zero, statically unstable if it is less than zero or else neutral. If Ri is below a critical value of about 0.25, the flow will already become dynamically unstable.

2.2. Description of the atmospheric models

2.2.1. LM

Since the end of 1999 the non-hydrostatic meteorological model LM is run operationally by DWD, but it has also been applied numerous times in scientific work. A detailed description of the LM is given by Doms and Schättler (1999). The model equations are solved on an Arakawa-C grid in horizontal direction and on a Lorenz grid in vertical direction. The LM uses a terrain following a vertical coordinate. It is operated with initial and boundary conditions from the global model GME of DWD. Three model domains, each consisting of 100×100 grid points, are used for the simulations presented in this paper. In order to zoom from a larger domain into a smaller one, one-way grid nesting is applied. While the model grid resolution is gradually increased by a factor of 2.5 the time step is reduced by a factor of 2. The location and extension of the model domains are selected in such a way that all relevant topographic characteristics are taken into account. Due to the prevailing southwest wind direction the experimental site is located northeast from the domain centre. Grid spacing of 7, 2.8 and 1.1 km is used, although only results of the 1.1 km runs will be discussed. The LM is operated with 40 vertical levels of the pressure-based vertical coordinate for the outermost and the second nested domain. Increasing the resolution of the boundary layer 50 levels are chosen for runs with 1.1 km grid spacing. The lowest layers are about 69 and 25 m. The basic characteristics and settings of LM are summarised in Table 1.

2.2.2. ASAM

ASAM, an anelastic non-hydrostatic model in conservation form, is operated to characterise the local flow conditions by simulating the tracer dispersion. It runs on a rectangular Cartesian grid consisting of 99×99 grid points (lower left domain corner is at 50.61°N/10.70°E) in horizontal extension and 80 vertical levels with 100 m horizontal and 20 m vertical grid spacing. Cutting Cartesian grid cells, which lay partially below the boundary, describes the orography. Each grid cell is characterised by the free surface part of its six faces and the free volume of the cell itself. Also, unmodified cells are described that way. A finite volume approach is applied to discretise the model equation in space where only the above-defined cell characteristics are involved in the discretisation scheme. Therefore, this kind of discretisation procedure is also applicable to other orthogonal grids like spherical coordinates providing the face and cell values are defined in the right way. The velocity vector is defined through its normal components on the cell faces, however, for the discretisation a cell centred velocity vector is also introduced. This additional value allows a unified treatment of advection and diffusion for the velocity and scalar components.

For integration in time a two-stage Rosenbrock method is applied which requires the solution of two linear systems in each stage, one system for the computation of an intermediate velocity vector at the cell centre and an elliptic equation to satisfy the anelastic

Table 1
LM configurations, under "model runs": start and simulation time, cloud events and dates of tracer experiments in parenthesises

Grid spacing	7 km (0.0625°)	2.8 km (0.025°)	1.1 km (0.01°)
Domain size/number of layers	$100 \times 100/40$		$100 \times 100/50$
Lower left domain corner	$\varphi_0 = 47.0°$N, $\lambda_0 = 6.0°$E	$\varphi_0 = 49.5°$N, $\lambda_0 = 8.5°$E	$\varphi_0 = 50.1°$N, $\lambda_0 = 10.0°$E
Lowest layer	~68 m		~25 m
Time step	30.0 s	15.0 s	7.5 s
Other settings	• Without parameterisation of moist convection • Grid-scale clouds and precipitation: "1—category ice" scheme		
Model runs	01-10-2001	00:00 UTC + 48 h	02-10-2001 (08:00–12:45 UTC)
	03-10-2001	00:00 UTC + 144 h	06–08-10-2001 (10:30–14:15/13:15-15:15/18:00–11:15 UTC)
	10-10-2001	00:00 UTC + 48 h	11-10-2001 (04:00–09:45 UTC)
	23-10-2001	00:00 UTC + 120 h	26-10-2001 (08:30–16:30 UTC) 26/27-10-2001 (22:00–13:00 UTC)
	29-10-2001	00:00 UTC + 60 h	31-10-2001 (tracer experiment)
	15-10-2002	00:00 UTC + 48 h	16/17-10-2002 (21:00–05:30 UTC and tracer experiment)

constraints. The solution of the linear systems is obtained by iterative methods of conjugate gradient type. By the implicit nature of the Rosenbrock method the problem of small time steps caused by cut cells is avoided.

The whole solution algorithm is parallelised by domain decomposition where the computational domain is split into a number of rectangular subdomains, which are distributed across the number of available processors. Furthermore, this block approach allows one to use different spatial resolution in different blocks. For further details see Hinneburg and Knoth (2005).

For the ASAM simulations the results of LM with 1.1 km horizontal grid spacing are used as initial and lateral boundary conditions in a one-way nesting procedure. The several LM fields are adapted to the respective ASAM grids in different ways. The vertical profiles of wind components and turbulent diffusion coefficients of each LM grid point are stretched or compressed at first depending on a positive or negative altitude difference between ASAM and LM topography. Subsequently, a horizontal interpolation is performed. Layered quantities (e.g. temperature) are horizontally interpolated at first and vertically truncated or extrapolated afterwards.

In order to reproduce the tracer experiments as accurately as possible, ASAM is initialised with a single time-dependent point source of tracer gas, which is positioned in model domain at the upwind site Goldlauter. The settings for model-predicted tracer transport are exactly in accordance with the real ones described in the following.

2.3. Connected flow verification with measured inert gas ozone (O_3)

In the previous parts theoretical flow and stability parameters as well as atmospheric models were presented to investigate the flow over the mountain range. In addition to these studies, the connected flow between the selected measurement stations should be verified by means of tracer concentration profile analyses. For this propose a chemical inert tracer had to be used. Thus, within comparable cloud passage field campaigns, e.g. on the Great Dun Fell (Colvile et al., 1997), ozone was applied, which is highly variable in time and space. Ozone is only produced in the atmosphere and not directly emitted. It has small water solubility with a Henry constant of 1.14×10^{-2} (Kosak-Channing et al., 1983) and is consumed ineffectively in acidic continental clouds. This conclusion is confirmed by the SPACCM (SPectral Aerosol Cloud Chemistry Interaction Model) model results given in Tilgner et al. (2005b). The total of the properties and results mentioned above implicate the applicability of ozone as an inert tracer for the flow analysis.

The concentration profile analysis is based on the measurements at the three sampling stations (Brüggemann et al., 2005). The concentrations were compared with regard to the concurrency of the ozone level and

temporal behaviour as well as their dependency on the locally measured wind speed and direction at the summit site and the atmospheric stratification (see Tilgner et al., 2005a). High correlations between the measured concentration profiles and congruent ozone levels indicate a connected flow as well as slight mixture with ambient air during the cloud passage. The corresponding ozone measurements are obtainable on the FEBUKO website (http://projects.tropos.de:8088/afo2000g3/FEBUKO_-dateien/febuko.html; electronic supplementary material, ESM).

2.4. Tracer experiments

2.4.1. Measuring sites of the tracer experiments

Selection of the sites was determined by the topography of the area, the statistics of wind direction and, additionally, easy access to each site was an important factor. The site for the emission of SF_6 is located north of Goldlauter on a fishing pond at the so-called Pochwerksgrund, which is also the main upwind experimental site. Since the tracer experiments were only performed during main wind directions of between 200° and 240°, all receptor sites are located in a northeast direction from the emission site. According to the pattern of an expanding plume three tiers of receptor sites, tiers 2, 4 and 3, with increasing distance from the emission site were established perpendicular to the expected main flow direction. The out-of-order numbering was chosen in order to assure consistency with site labelling during the main experiment. No measurements took place at sites labelled with number 4. The first tier of sites (tier 2) is located along the Rennsteigstraße and includes the measurement site Schmücke. The second tier (tier 4) surrounds the northeastern edge of the plateau in a half-circle. In the third tier (tier 3), the centre site is located on the western edge of the village Gehlberg where the main downwind station is situated. Tier 3 has two additional sites to the west and east, which are used to investigate the influence of the valleys Schneetiegel and Pfanntal that are the boundaries of the eastern plateau. Table 2 lists all sites with their Gauss–Krüger and geographical coordinates.

2.4.2. Sample collection and determination of SF_6

Each sample at the measuring sites was taken according to a uniform sampling schedule. All samples were each collected in a new 10 l polyethylene bag. Analysis of the samples was performed by GC-ECD (Siemens Sichromat 1-4). Using a syringe, a defined amount of sample gas was removed from the bags and injected into the GC. The detection limit of the method is 0.5 pptv, the precision is >1%. For further details see Strunk et al. (2000). The background concentration of SF_6 in the Thüringer Wald is 4.5 ± 0.5 pptv as determined at the time of tracer release at all receptor sites. The tracer was released at site #10 (Goldlauter) at a rate of approximately $0.3\,g\,s^{-1}$ for a duration of 30 min. Starting with the release, sample collection starts at all sites as described above.

Between May and October 2001 four tracer experiments were conducted on 16 and 18 May 2001, 7 June 2001, and 31 October 2001. During the FEBUKO measuring campaign 2002 one tracer experiment took place on 16 October. Further experimental details are compiled in Table 3.

3. Results and discussion

3.1. Results of the flow characterisation with non-dimensional parameters

The parameters were calculated by means of rawinsonde data from Meiningen (about 30 km upwind from Schmücke Mountain). The flow speed was

Table 2
Location of emission site and receptor sites during tracer experiments around mountain Schmücke

Number	Location	Gauss–Krüger coordinates		Geographical coordinates	
10	Goldlauter (SF_6 emission)	4411989	5612244	10°45′20″	50°38′25″
20	Schmücke (937 m)	4413089	5613882	10°46′15″	50°39′19″
21	Mühltiegel (930 m)	4411926	5613624	10°45′16″	50°39′10″
22	Borsten Platz (880 m)	4413230	5612860	10°46′23″	50°38′46″
23	Mordfleck (820 m)	4413429	5611868	10°46′34″	50°38′14″
40	Güldene Brücke (865 m)	4413640	5614930	10°46′42″	50°39′53″
41	Jägerstein (963 m)	4412785	5614475	10°45′59″	50°39′38″
42	Seiffartsburg (900 m)	4413937	5614054	10°46′58″	50°39′25″
43	Schneekopf (981 m)	4412599	5615127	10°45′49″	50°39′59″
30	Gehlberg (718 m)	4414329	5616427	10°47′16″	50°40′42″
31	Schneetiegel (718 m)	4413935	5616310	10°46′56″	50°40′38″
32	Pfanntal (738 m)	4414633	5615773	10°47′32″	50°40′21″
33	Zwei Wiesen (729 m)	4416737	5614719	10°49′20″	50°39′48″

Table 3
Experimental details of tracer experiments. SF_6 emission at Goldlauter, Pochwerksgrund in 3 m agl

Date	16-05-2001	18-05-2001	07-06-2001	31-10-2001	16-10-2002
Time	11:00–11:30	13:00–13:30	11:30–12:00	10:00–10:15	10:00–10:30
($l\,min^{-1}$)	3	3.8	2.98	3	3
($g\,min^{-1}$)	19.5	24.8	19.4	19.5	19.5
Incoming flow at Pochwerksgrund					
Wind direction (deg)	130	130	120	—	120
Wind speed ($m\,s^{-1}$)	2	2	1.5–2	4–7	6
Incoming flow at Schmücke mountain					
Wind direction (deg)	225	250	240	208	212
Wind speed ($m\,s^{-1}$)	2–3	5–6	2–3	8–10	9–11

averaged between the values of summit level and Meiningen level and the effective mountain height is about 484 m. The calculated Froude numbers and the Richardson numbers and associated remarks are listed in Table 4.

As can be seen from Table 4 the flow is mainly affected by the atmospheric stratification. For example, on 2 October 2001 the small Froude number and the negative Richardson number indicate that there was no blocking during this period. On the other hand, for the case of 26 October 2001 even stagnation of air flow had to be expected because of the very stably stratified boundary layer and a low mean wind speed. It is evident that in spite of large Richardson numbers (very stable stratification) high wind speeds can prevent blocking effects on 8 and 27 October 2001 as well as on 16 October 2002. Therefore, from the periods that also provide most adequate meteorological conditions (Tilgner et al., 2005a), on 2, 8 and 27 October 2001 and on 16/17 October 2002 the Froude numbers show that the flow passed over the mountain ridge. However, on 26 October 2001, for a cloud event with advantageous meteorological conditions, the large Froude number ($Fr = 1.58$) indicates a stagnant flow.

3.2. Results of modelling the mesoscale incoming flow

The results of LM simulations of five out of 14 cloud events were chosen to be presented here as examples. For 2, 6–8, 26 and 26/27 October 2001 as well as 16/17 October 2002 the mesoscale flow conditions at Thüringer Wald will be described with regard to orographic effects on flow pattern like channelling of flow, upstream blocking and gravity waves. The five periods have been already shown to provide the most adequate synoptic conditions (Tilgner et al., 2005a). A more detailed description of these periods as well as the results for some other events are available online (ESM).

The mesoscale simulations clarify whether the mountain ridge was overflowed and air masses were lifted up from valleys so that orographic clouds could be formed or whether the air tended to pass around rather than over the mountain range at the experimental site. Due to blocking air tries to flow around the Thüringer Wald and the air masses at the summit and downwind site originate from higher levels. Gravity waves indicate air passage over a mountain range in a stably stratified atmosphere with air parcels being triggered to oscillate by the vertical orographically induced deflection.

3.2.1. 2 October 2001

On 2 October 2001 the wind blew constantly from southwest with wind speeds up to $12\,m\,s^{-1}$. The stable flow conditions are also reflected in the LM results. Fig. 2a presents the horizontal surface winds for the innermost domain for 2 October 2001 at 12:00 UTC. As seen, the flow structure is very homogeneous with wind speeds of 10–20 kn (~5–11 $m\,s^{-1}$). Due to the strong wind the orography hardly has an effect on the flow. Only downstream from the Rhön does channelling of flow occur along the Werra valley and a little deceleration can be detected just before the ridge. The experimental site itself is located in a zone of straight southwesterly flow and the air passes over the mountain range. In consequence of the overflow the LM predicts lee waves evident from the ups and downs of isentropes in Fig. 3a. This is in agreement with rawinsonde data and also satellite pictures in Tilgner et al. (2005a) prove the model-predicted lee waves.

3.2.2. 6–8 October 2001

The flow conditions from 6 October 2001 to the early morning hours on 8 October 2001 were characterised by low wind speeds of about 5 kn (~2.6 $m\,s^{-1}$) and unstable winds from south on windward side. On the ridge and downwind the modelled surface wind turns to southwest. The different wind directions indicate that the air passes around rather than over the mountain range. But on 8 October 2001, the blocking weakens because the wind speed slightly increases and the wind direction

Table 4
Froude number *Fr* and Richardson number *Ri* for the cloud events in 2001 and 2002

Date/time (UTC)	U (m s^{-1})	$d\Theta/dz$ (K m^{-1})	dU/dz (s^{-1})	N^2 (s^{-2})	*Fr*	*Ri*	Overflow	Stability
							y: yes, n: no	
02-10-2001, 12:00	10	−0.0028	0.0181	−1.e-4	→0.0	−0.29	y	Unstable
06-10-2001, 12:00	6	0.0079	0.0085	3.e-4	1.24	3.71	y (decelerated)	Stable
07-10-2001, 12:00	4	0.0117	0.0046	4.e-4	2.22	18.96	n (stagnation)	Stable
08-10-2001, 00:00	9	0.0088	0.0129	3.e-4	0.96	1.79	y (decelerated)	Stable
08-10-2001, 12:00	7	0.0009	0.0085	3.e-5	0.36	0.41	y	Stable
09-10-2001, 00:00	10	0.0048	0.0275	2.e-4	0.62	0.22	y	Stable
09-10-2001, 12:00	8	−0.0003	0.0051	−1.e-5	→0.0	−0.38	y	Unstable
10-10-2001, 00:00	7	0.0135	0.0210	5.e-4	1.51	1.05	y (slightly stagnant)	Stable
10-10-2001, 12:00	7	−0.0024	0.0068	−8.e-5	→ 0.0	−1.74	y	Unstable
11-10-2001, 00:00	10	0.0090	0.0188	3.e-4	0.85	0.88	y (decelerated)	Stable
11-10-2001, 12:00	6	0.0003	0.0047	1.e-5	0.26	0.53	y	Stable
21-10-2001, 00:00	6	0.0161	0.0165	6.e-4	2.02	2.04	n (stagnation)	Stable
21-10-2001, 12:00	8	0.0066	0.0130	2.e-4	0.92	1.34	y (decelerated)	Stable
22-10-2001, 00:00	8	0.0035	0.0204	1.e-4	0.69	0.29	y	Stable
22-10-2001, 12:00	6	−0.0006	0.0043	−2.e-5	→0.0	−1.06	y	Unstable
23-10-2001, 12:00	3	0.0063	0.0027	2.e-4	2.54	30.79	n (stagnation)	Stable
25-10-2001, 00:00	6	0.0065	0.0018	2.e-4	1.13	0.73	y (decelerated)	Stable
26-10-2001, 12:00	5	0.0080	0.0039	3.e-4	1.58	18.58	y (slightly stagnant)	Stable
27-10-2001, 00:00	8	0.0123	0.0135	4.e-4	1.22	2.35	y (decelerated)	Stable
27-10-2001, 12:00	9	0.0065	0.0137	2.e-4	0.81	1.18	y (decelerated)	Stable
03-10-2002, 00:00	5	0.0191	0.0131	7.e-4	2.71	3.86	n (stagnation)	Stable
03-10-2002, 12:00	4	0.0095	0.0079	3.e-4	2.46	5.15	n (stagnation)	Stable
14-10-2002, 12:00	—	—	—	—	—	—	—	—
15-10-2002, 00:00	6	0.0025	0.0149	1.e-4	0.73	0.38	y	Stable
15-10-2002, 12:00	—	—	—	—	—	—	—	—
16-10-2002, 00:00	8	0.0054	0.0090	2.e-4	0.78	2.30	y (decelerated)	Stable
16-10-2002, 12:00	8	0.0060	0.0194	2.e-4	0.83	0.55	y (decelerated)	Stable
17-10-2002, 00:00	11	0.0062	0.0214	2.e-4	0.67	0.46	y	Stable
17-10-2002, 12:00	9	0.0007	0.0115	2.e-5	0.26	0.19	y	Stable
18-10-2002, 00:00	6	0.0051	0.0086	2.e-4	1.15	2.41	y (decelerated)	Stable
18-10-2002, 12:00	6	0.0	0.0158	0.0	0.00	0.00	y	Stable
19-10-2002, 12:00	6	−0.0012	0.0006	−4.e-5	→ 0.0	−113.75	y	unstable
20-10-2002, 00:00	5	0.0036	0.0143	1.e-4	1.02	0.62	y (decelerated)	Stable
22-10-2002, 00:00	8	0.0103	0.0132	4.e-4	1.15	2.03	y (decelerated)	Stable
24-10-2002, 00:00	6	0.0041	0.0253	1.e-4	0.90	0.22	y (decelerated)	Stable
24-10-2002, 12:00	7	0.0005	0.0034	2.e-5	0.27	1.39	y	Stable

changes from south to southwest on the lee side during daytime (Fig. 2b).

3.2.3. 26 October 2001

On 26 October 2001, the meteorological conditions were generally very stable including a stable atmospheric stratification. But the stable conditions seem to be unfavourable with respect to the overflow of the Thüringer Wald. As can be seen in Fig. 2c the local flow at 09:00 UTC is directed from south on the windward side with channelling of airflow in the Werra valley. Northwest and southeast of the mountain range the air tends to flow around the ridge. The vertical cross-section of isentropes (Fig. 3b) shows air falling down from higher altitudes to the downwind site in a hydraulic jump. This refers to overturned gravity waves and results in different air masses at the experimental sites.

3.2.4. 26/27 October 2001

The event on 26/27 October 2001 provides more appropriate flow conditions. This episode was characterised by a front passage which ended just around 06:00 UTC on 27 October 2001 and divided the flow situation into two periods. At the beginning the modelled flow was southeast with wind speeds of about 5 kn (~2.6 m s^{-1}). Channelling occurs in the upper Werra valley and the upwind flow runs parallel to the Thüringer Wald. Northwest and southeast of the

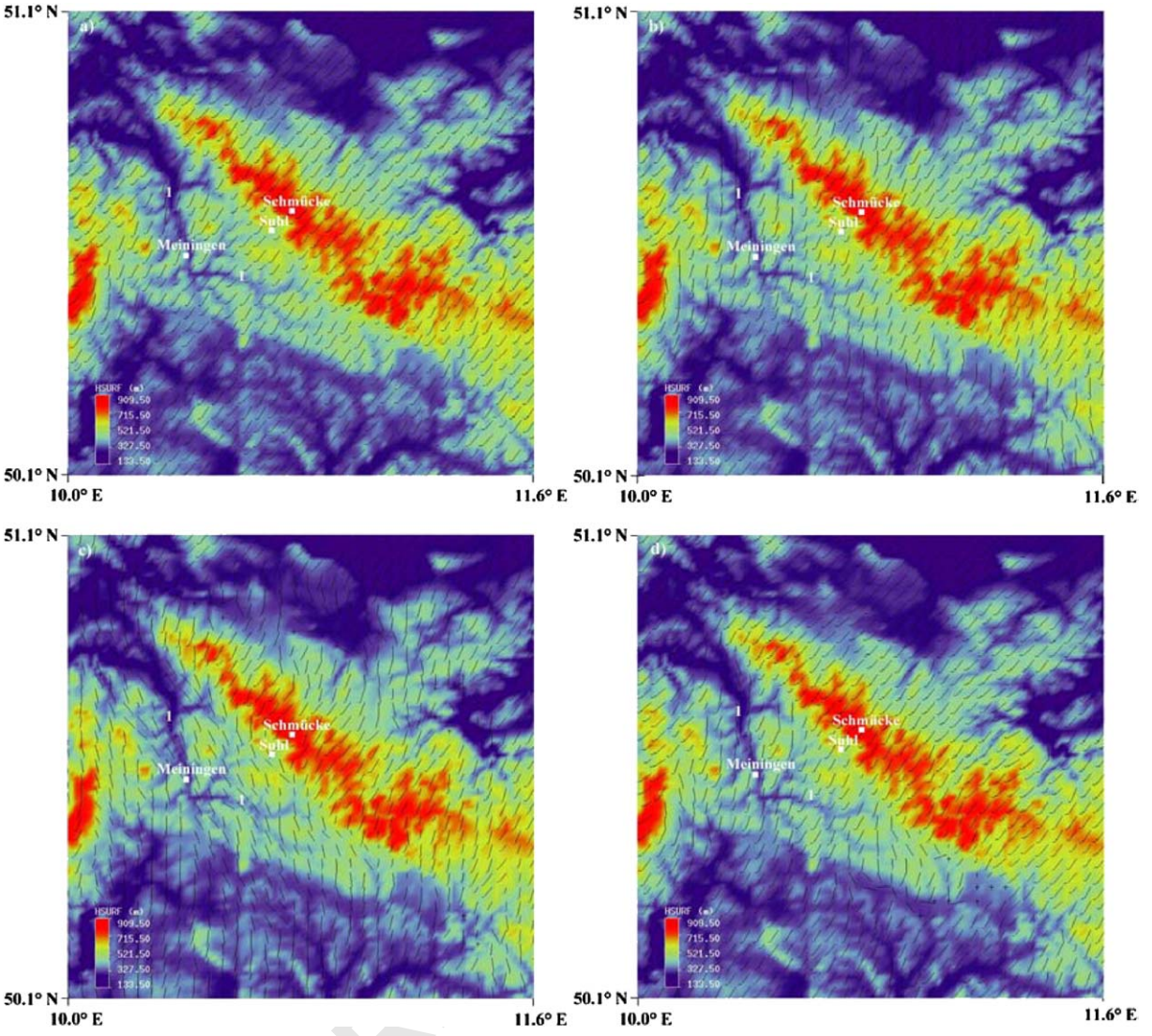

Fig. 2. Horizontal cross-section of the topography and the surface wind plotted at every third grid point for the innermost LM domain for (a) 02-10-2001 at 12:00 UTC, (b) 08-10-2001 at 09:00 UTC, (c) 26-10-2001 at 09:00 UTC and (d) 27-10-2001 at 09:00 UTC. The wind barbs are in knots. 1: Werra valley.

mountain range the flow is deflected around. Evidently, there is a strong blocking effect due to low wind speeds. After the end of frontal processes the wind direction gradually changes, the wind speed increases and thus the flow conditions are expected to become appropriate. From 09:00 UTC the wind pattern is characterised by predominantly southwesterly flow (Fig. 2d). Therefore, the air passes over the mid-mountain range including the experimental site only with little blocking effects in the second period of this event. On 27 October 2001 the LM simulates several wave regimes, lee waves with small amplitude up to an altitude of 2000–2500 m asl and vertically propagating gravity waves in atmospheric layers above (Fig. 3c).

3.2.5. 16–17 October 2001

A comparable flow situation as on 2 October 2001 also exists from 16–17 October 2002. High wind speeds up to 20 kn ($\sim$11 m s^{-1}) as well as a less complex flow pattern with only minor channelling in the Werra valley and negligible upwind deceleration meet the required flow conditions. In this case the air flow crossing the Thüringer Wald does not include any noticeable wave

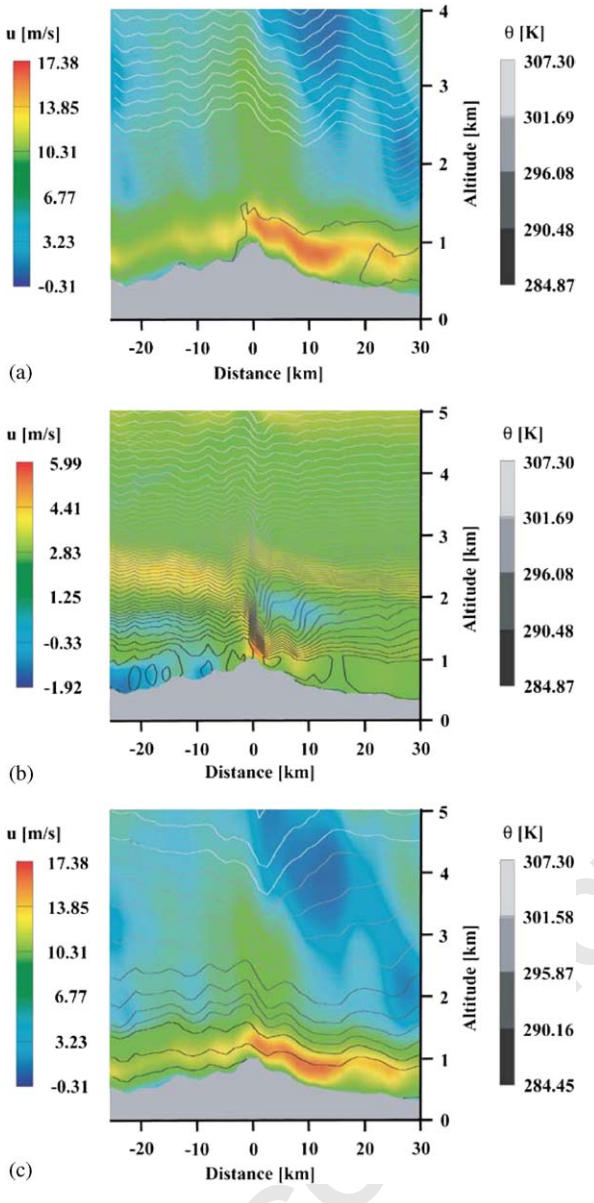

Fig. 3. Vertical southwest–northeast cross-section trough the Thüringer Wald at mountain Schmücke of isentropes (K) and zonal wind speed ($m\,s^{-1}$) from the inner LM domain for (a) 02-10-2001 at 12:00 UTC, (b) 26-10-2001 at 12:00 UTC and (c) 27-10-2001 at 09:00 UTC. Flow comes from the left.

regime. Obviously, the necessary atmospheric conditions for the formation of gravity waves are not satisfied.

As a result the most suitable mesoscale flow conditions were established on 2 and 8 October 2001 as well as on 16/17 October 2002. On 2 October and 26/27 October 2001 gravity waves occurred and signalised air passage over the mountain range. But in the 26/27 October 2001 case air coming from higher levels and the distinct stagnation point to an unfavourable event.

3.3. Results of the connected flow verification with ozone

Especially, for days with constant southwesterly flow conditions, high wind speeds and less stable stratification strong correspondence between the measured ozone concentration profiles is found. This can be seen, for example, on 9 October 2001 (Fig. 4). This day was characterised by a constant wind direction of about 220° and comparable moderate wind speeds. Mainly before 14:00 UTC there are good correlations that means connected flow conditions between the upwind and downwind sites. Thereafter, the concentration levels differ from each other up to 20 ppb. The explanation for this fact is the formation of a near ground inversion so that flow blocking occurred and the flow became disconnected. For other days (concentration profiles in the ESM) not only the dependency on thermal stratification but also on the high flow parameters could be noticed. The results of the ozone studies are in good agreement with the theoretical flow parameters. In the 9 October case the Froude number (Table 4) at 00:00 and 12:00 UTC implies a connected flow and only at 24:00 UTC the flow parameter points at a disconnection. The ozone concentration analysis proves these results.

The results of the cloud event periods mentioned above are presented in Table 5. The percentage deviation of the downwind site ozone concentrations from the upwind site measurements with a time resolution of about 4 h is presented. On 7/8 October 2001 just at the beginning of the cloud event higher deviations of about + 63% between the two sites can be recognised. However, during the event the mean deviation decreases down to about + 10%. These ozone level differences of about + 10% can be explained by, e.g. uncertainties of measuring instruments, cloud processing and entrainment. Therefore, equivalent concentration courses including small deviations are an indication of a connected flow.

The detailed investigation of flow conditions allows one to validate the presented methods against each other. It is evident both from the LM results (Fig. 2) and the analysis of Froude numbers that air could easily flow over the Thüringer Wald with minor or without deceleration on the 2 ($Fr \to 0.0$) and 8 October 2001 ($Fr = 0.96/0.36$) as well as on 16/17 October 2002 ($0.26 \leqslant Fr \leqslant 0.83$). Also, the blocked flow on 26 October 2001 predicted by flow parameters is in agreement with LM results. For the 27 October 2001 case a decreasing Froude number during daytime reflects the change from strong orographic effects to a less complex flow pattern modelled by LM. Generally, in all cases with sufficient overflow conditions the flow between the experimental sites was connected as well. This follows from the consistency of ozone concentration profiles of the three experimental sites during the cloud events mentioned above. The validation shows that the comparison of

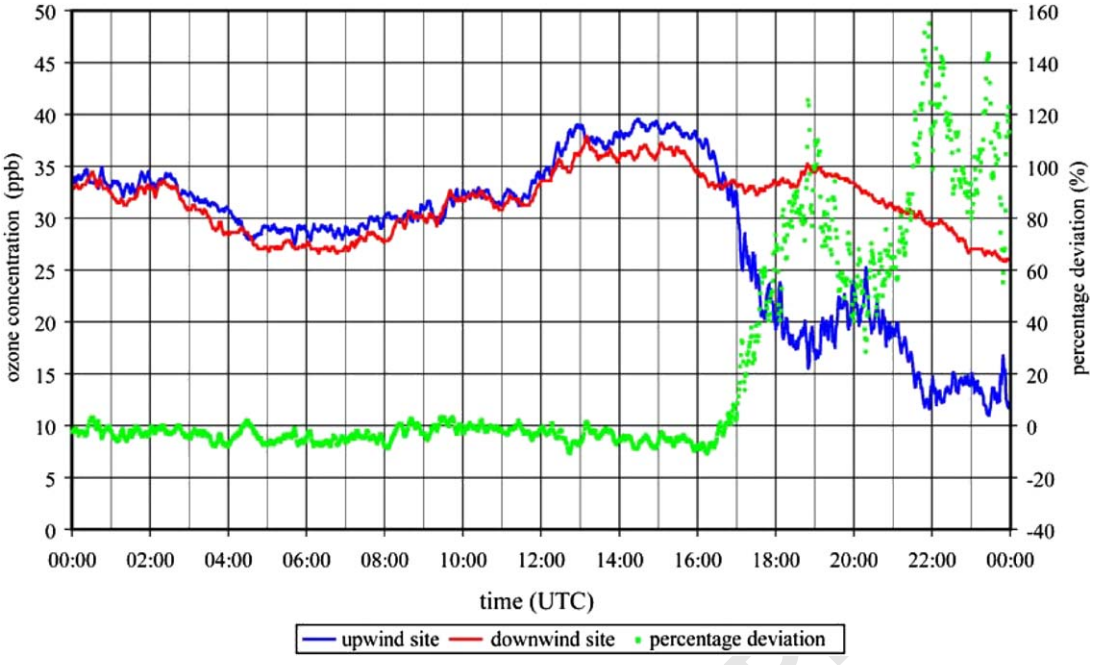

Fig. 4. Measured ozone concentrations at upwind and downwind sites on 09-10-2001 and the percentage deviations of the downwind site ozone concentration relative to the upwind site measurement.

Table 5
Mean percentage deviation of the downwind site ozone concentration from the upwind site level for five pre-selected cloud events

Event Interval	02-10-2001 08:00–12:30UTC	07/08-10-2001 18:00–11:15UTC	26-10-2001 08:30–16:30UTC	26/27-10-2001 22:00–13:00UTC	16/17-10-2002 21:00–05:30UTC
1	−3.6% [08:00–12:30]	+62.7% [18:00–22:00]	+8.6% [08:30–12:30]	+4.9% [22:00–02:00]	+10.4% [21:00–01:00]
2	—	+9.6% [22:00–02:00]	+7.4% [12:30–16:30]	+6.8% [02:00–06:00]	+11.8% [01:00–05:30]
3	—	+10.7% [02:00–06:00]	—	+27.9% [06:00–10:00]	—
4	—	+11.8% [06:00–10:00]	—	+21.4% [10:00–13:00]	—
5	—	+12.0% [10:00–11:15]	—	—	—
Mean	−3.6%	+22.8%	+8.0%	+9.4%	+10.7%

ozone concentration series is an adequate method for time resolved overflow investigations.

3.4. Measurement and modelling results of the tracer experiments

In the diagrams of Fig. 5 results of the tracer experiments on 31 October 2001 and 16 October 2002 are shown as examples. The indicated SF_6 concentrations were measured in the air samples taken at 13 sites in 5-min intervals. The data were measured up to 60 min after tracer release. Results of all experiments (see also ESM) confirm that during southwesterly flows identical air masses are prevailing at the main station Schmücke and the two valley stations.

Moreover, the results of the tracer experiments help to validate the more quantitative flow characterisation with non-hydrostatic atmospheric models. For 31 October 2001 as well as for 16 October 2002 the LM predicts homogenous flow patterns with minor deceleration effects and air passage over the Thüringer Wald. These modelling results are also consistent with the assumptions obtained from the analysis of Froude numbers, which are 0.37 for the 31 October 2001 case and 0.55 for the 16 October 2002 case. The adequate flow conditions are caused by relatively high wind speeds of about $10\,m\,s^{-1}$ and wind directions between 208° and 212° as well as a weak atmospheric stratification.

A comparison with the tracer movement and dispersion modelled with ASAM reveals some differences (Fig.

5). While the dependencies of SF_6 concentration on time and also the order of concentration are almost consistent, the simulated plume is narrower and tends to disperse too far east in the predicted than in the measured cases. Therefore, the simulated SF_6 concentrations are considerably lower at the western and northwestern but much higher at the southeastern receptor sites. The reasons are differences between the real and modelled wind directions with a stronger west component in the modelling results as well as the fact that the results are obviously determined rather by wind speed than by diffusion. The effect is more distinctive on 31 October 2001 when the artificial tracer plume even passes by the Schmücke Mountain (Figure A37, ESM). There is no tracer material simulated at northwestern sites, because of too strong a westerly wind component in the initial LM run.

The ASAM results show that channelling of the flow from Goldlauter to Schmücke Mountain is the main orographic effect in the experimental area and supports the assumption of connected flow conditions.

4. Summary

The mesoscale and local flow conditions during the ground-based cloud passage experiment FEBUKO during October 2001 and 2002 were studied. At first, the flow regimes were characterised by means of the non-dimensional parameters the Froude and Richardson numbers which were calculated from rawinsonde data for each cloud period. Moreover, the mesoscale flow conditions over the complex terrain of Thüringer Wald were simulated with the non-hydrostatic meteorological model LM for some pre-selected cloud events. The LM modelling was used to quantify the topographic effects on airflow like blocking, channelling of airflow and gravity wave activities. The corresponding results prove the statements about the overflow of the mountain range provided by the analysis of Froude numbers. It was found that the connected flow as well as the tendency of air to pass over or around the Thüringer Wald is mainly determined by the speed and direction of the synoptical flow and by the atmospheric stratification. In order to verify that the flow between the experimental sites was connected and thus the measure-

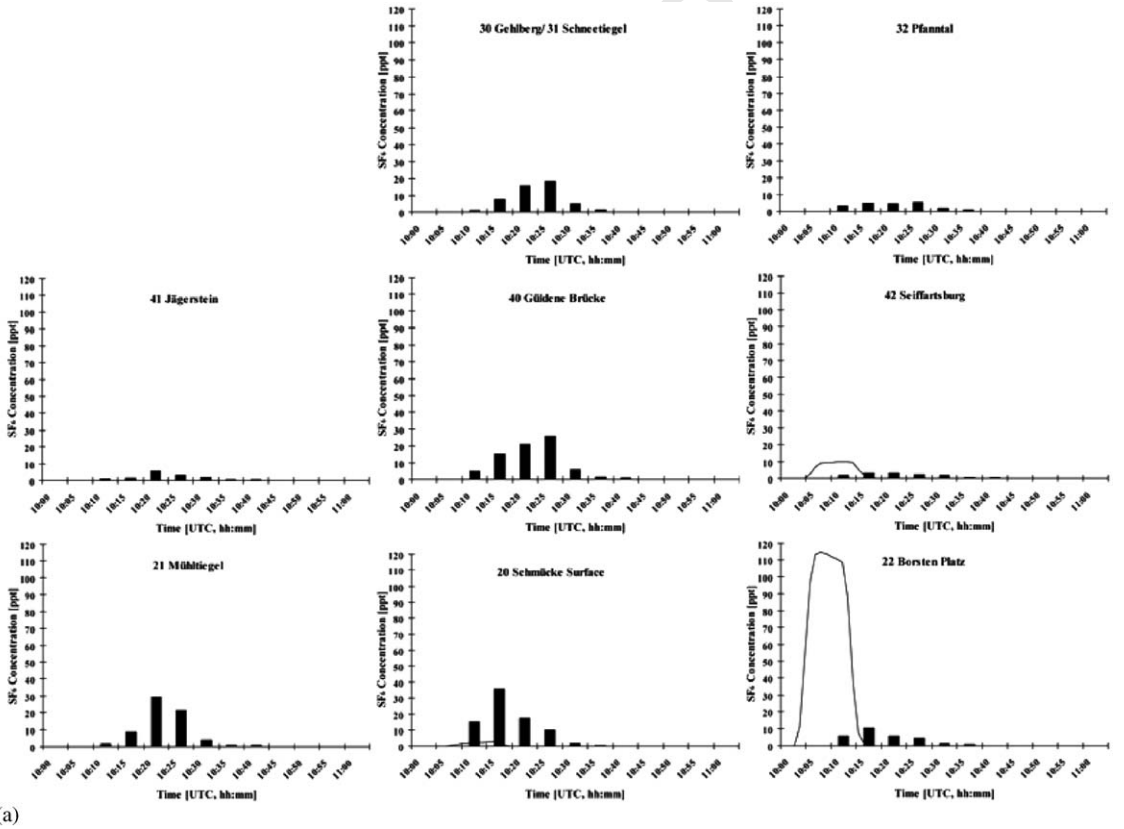

Fig. 5. Comparison between measured (bars) and simulated (lines, results of ASAM after 45 min simulation time) SF_6 concentrations (ppt) at different receptor sites for (a) 31-10-2001 and (b) 16-10-2002.

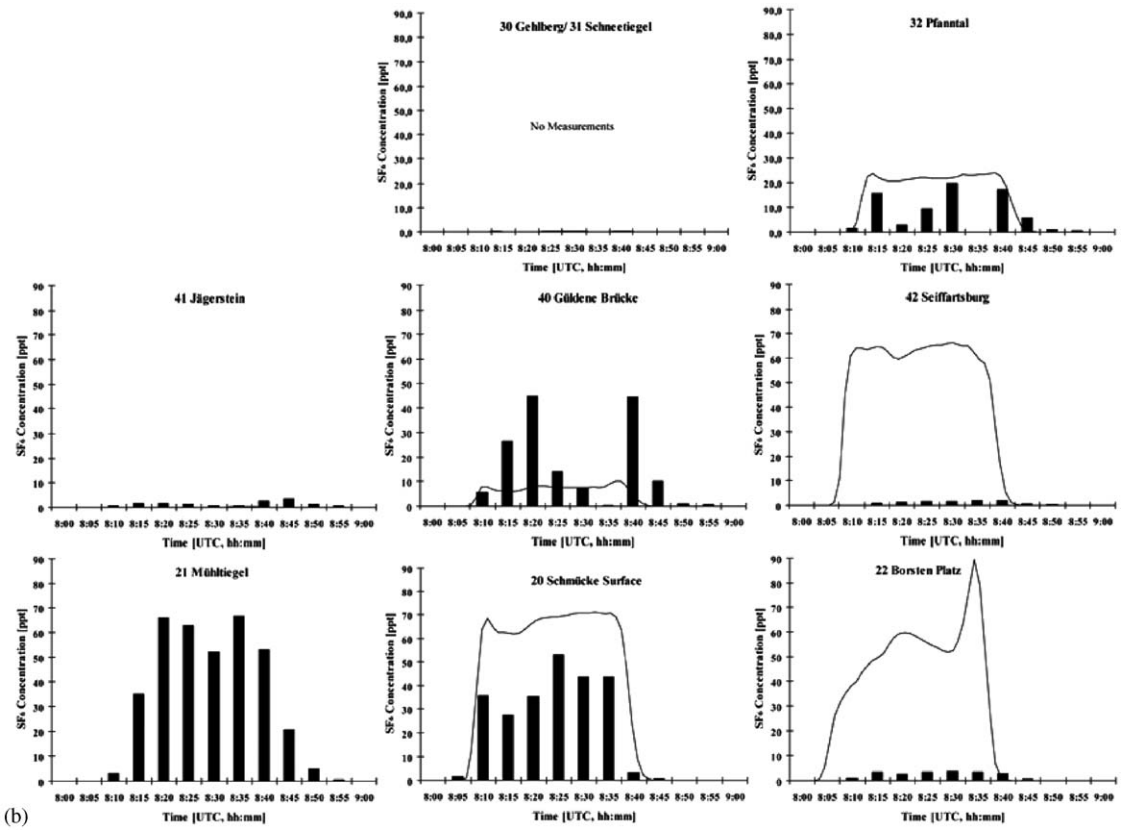

Fig. 5. (*Continued*)

ments were performed in identical air masses during the cloud events time series of the natural tracer ozone from the different locations were analysed. For the verification of the connected flow tracer experiments with SF_6 were also conducted before and during the field campaigns in 2001 and 2002. For these tracer dispersion studies that confirm the correct location of the experimental sites an attempt was made to reproduce them by means of an anelastic non-hydrostatic model in conservation form. The modelled tracer transport supported the understanding and visualisation of the advection of air masses in the experimental area.

On the basis of selection criteria given in Tilgner et al. (2005a), the corresponding classification of cloud episodes with regard to most suitable synoptical conditions, the completeness of data set (Part I of the paper) and the local flow analysis conducted in this work a final selection can be performed now. Due to the required synoptic conditions, a sufficient duration and adequate flow characteristics the events on 26/27, 6–8 October 2001 and on 16/17 October 2002, hereafter referred to as E I, E II and E III, are recommended as most suitable for subsequent investigations of the chemical and physical properties of air masses observed during FEBUKO 2001 and 2002. A comprehensive ranking of the first six events of the meteorological classification (Tilgner et al., 2005a, b) is available online (ESM).

Acknowledgements

The work was supported by the Bundesministerium für Bildung und Forschung (Project FKZ 07ATF01). We thank the Deutscher Wetterdienst (DWD, Offenbach), the John von Neumann Institute for Computing (Jülich) and the Thüringer Landesvermessungsamt (Erfurt) for good cooperation and support.

References

Baines, P.G., 1995. Topographic Effects in Stratified Flows. Cambridge University Press, Cambridge.

Brüggemann, E., Gnauk, T., Mertes, S., Acker, K., Auel, R., Wieprecht, W., Möller, D., Collett, J.L., Chemnitzer, R., Rüd, C., Junek, R., Herrmann, H., 2005. Schmücke hill cap cloud and valley stations aerosol characterisation during

FEBUKO (I): particle size distribution and main components. Atmospheric Environment (this issue).

Bruintjes, R., Clark, T., Hall, W., 1995. The dispersion of trace plumes in mountainous regions in Central Arizona: comparisons between observations and modeling results. Journal of Applied Meteorology 34, 971–988.

Colle, B.A., 2004. Sensitivity of orographic precipitation to changing ambient conditions and terrain geometries: an idealized modeling perspective. Journal of Atmospheric Science 61, 588–606.

Colvile, R.N., Bower, K.N., Choularton, T.W., Gallagher, M.W., Beswick, K.M., Arends, B.G., Kos, G.P.A., Wobrock, W., Schell, D., Hargreaves, K.J., Storeton-West, R.L., Cape, J.N., Jones, B.M.R., Wiedensohler, A., Hansson, H.-C., Wendisch, M., Acker, K., Wieprecht, W., Pahl, S., Winkler, P., Berner, A., Kruisz, C., Gieray, R., 1997. Meteorology of the Great Dun Fell cloud experiment 1993. Atmospheric Environment 31, 2407–2420.

Doms, G., Schättler, U., 1999. The Nonhydrostatic Limited-area Model LM (Lokal-Modell) of DWD. Part I: Scientific Documentation (Version LM-F90 1.35). Deutscher Wetterdienst (DWD), Offenbach.

Herrmann, H., Wolke, R., Müller, K., Brüggemann, E., Gnauk, T., Barzaghi, P., Mertes, S., Lehmann, K., Massling, A., Birmili, W., Wiedensohler, A., Wieprecht, W., Acker, K., Jaeschke, W., Kramberger, H., Syrcina, B., Bächmann, K., Collett, J.L., Galgon, D., Schwirn, K., Nowak, A., van Pinxteren, D., Plewka, A., Chemnitzer, R., Rüd, C., Hofmann, D., Tilgner, A., Diehl, K., Heinold, B., Hinneburg, D., Knoth, O., Sehili, A.M., Simmel, M., Wurzler, S., Mauersberger, G., Majdik, Z., Müller, F., 2005. FEBUKO and MODMEP: field measurements and modelling of aerosol and cloud multiphase processes. Atmospheric Environment (this issue).

Hinneburg, D., Knoth, O., 2005. Non-dissipative cloud transport in Eulerian grid models by the volume-of-fluid (VOF) method. Atmospheric Environment (this issue).

Jaeschke, W., Beltz, N., Schütz, L., 2001. Measuring strategies of the SFB field experiments CLEOPATRA, FELDEX and NORDEX. In: Jaenicke, R. (Ed.), Dynamics and Chemistry of Hydrometeors. Wiley-VCH, Weinheim, pp. 9–34.

Jiang, Q., 2003. Moist dynamics and orographic precipitation. Tellus 55A, 301–316.

Kosak-Channing, L.F., Helz, G.R., 1983. Solubility of ozone in aqueous solutions of 0–0.6 M ionic strength at 5–30 °C. Environmental Science and Technology 17, 145–149.

Pierrehumbert, R.T., Wyman, B., 1985. Upstream effects of mesoscale mountains. Journal of Atmospheric Sciences 42, 977–1003.

Strunk, M., Engel, A., Schmidt, U., Volk, C.M., Wetter, T., Levin, I., Glatzel-Mattheier, H., 2000. CO2 and SF6 as stratospheric age tracers: consistency and the effect of mesospheric SF6-loss. Geophysical Research Letters 27, ,341–344.

Tilgner, A., Heinold, B., Nowak, A., Herrmann, H., 2005a. Meteorological characterisation of the FEBUKO hill cap cloud experiments, Part I: synoptic characterisation of measurement periods. Atmospheric Environment (this issue).

Tilgner, A., Majdik, Z., Sehili, A.M., Simmel, M., Wolke, R., Herrmann, H., 2005b. SPACCIM: simulations of the multiphase chemistry occurring in the FEBUKO hill cap cloud experiments. Atmospheric Environment (this issue).

Vosper, S.B., Mobbs, S.D., Gardiner, B.A., 2002. Measurements of near surface flow over a hill. Quarterly Journal of the Royal Meteorological Society 128, 2257–2280.

3B2v8.06a/w (Dec 5 2003).51c XML:ver:5.0.1 AEA : 5764 Prod.Type:FTP pp.1–11(col.fig.:NIL) ED:MangalaK. PAGN:hashmath SCAN:Global

ARTICLE IN PRESS

Available online at www.sciencedirect.com

SCIENCE DIRECT®

ELSEVIER

Atmospheric Environment ▮ (▮▮▮▮) ▮▮▮–▮▮▮

ATMOSPHERIC ENVIRONMENT

www.elsevier.com/locate/atmosenv

Aerosol characterisation at the FEBUKO upwind station Goldlauter (I): Particle mass, main ionic components, OCEC, and mass closure

T. Gnauk[a,*], E. Brüggemann[a], K. Müller[a], R. Chemnitzer[a], C. Rüd[a], D. Galgon[a], A. Wiedensohler[a], K. Acker[b], R. Auel[b], W. Wieprecht[b], D. Möller[b], W. Jaeschke[c], H. Herrmann[a]

[a]*Leibniz-Institut für Troposphärenforschung e.V., Permoserstr. 15, D-04318 Leipzig, Germany*
[b]*Brandenburgisch-Technische Universität, Abt. Luftchemie, Volmerstr. 13, D-12489 Berlin, Germany*
[c]*Zentrum für Umweltforschung der Johann Wolfgang Goethe-Universität, Georg-Voigt-Str. 14, D-60325 Frankfurt, Germany*

Abstract

This contribution presents characterisation efforts of the gas phase and particle phase main components during the FEBUKO orographic cloud passage experiments in autumn 2001 and 2002 in the Thüringer Wald (Germany). Three events out of a total of 14 were chosen as the best events considering all meteorological conditions. Gas phase and size-segregated particle phase data obtained from physical (dry size distribution) and chemical (particle mass, main ions, OCEC, and water-soluble metals) measurements are presented for the upwind site. The total particulate mass concentration (PM_{10}) was found to be between 8 and 17 $\mu g\,m^{-3}$. Particles with an aerodynamic diameter up to 1.2 μm contribute about 80% of the mass concentration. About 90% of the total ion concentration consists of nitrate, sulphate and ammonium. The OC concentration in all three events amounts to about 1.0 $\mu g\,m^{-3}$, whereas EC concentrations were between 0.40 and 1.0 $\mu g\,m^{-3}$. The contribution of OC and EC to stage mass ranged from 5% to 35% and from 2% to 17%, respectively. The water content of particles was estimated to be 16–18%. Physical and chemical mass closure is discussed in detail and the results are in a reasonable agreement. The complex data set obtained for each event can be used in the initialisation of models for the multiphase processes during and after the cloud passage of the characterised air mass.

Keywords: Size-segregated particle characterisation; Major ions; OCEC; Physical and chemical mass closure

1. Introduction

The atmospheric aerosol plays an important role in the trace material cycle of the atmosphere and may influence radiation forcing and atmospheric chemistry. Aerosols can also act as condensation nuclei in the cloud formation. Formed clouds continuously process particles and thus modify their chemical composition (Hallberg et al., 1994; Kreidenweis et al., 2003; Hegg et al., 2004). Therefore, it is particularly important to determine the size-segregated physical and chemical properties of the atmospheric aerosol. At present, only a

*Corresponding author. Tel.: +49 341 235 2156; fax: +49 341 235 2325.
E-mail address: gnauk@tropos.de (T. Gnauk).

1352-2310/$ - see front matter © 2005 Elsevier Ltd. All rights reserved.
doi:10.1016/j.atmosenv.2005.02.007

limited number of studies are available measuring size-segregated particle composition with emphasis on organic species in Europe (e.g. Nunes and Pio, 1993; Mészáros et al., 1997, 1998; Neusüß et al., 2000a, b, 2002; Maenhaut et al., 2002; Pakkanen et al., 2003; Bardouki et al., 2003; Lammel et al., 2003; Plewka et al., 2004).

Size-segregated aerosol sampling and characterisation at the upwind site of the summit (Mount Schmücke) was part of the FEBUKO/MODMEP research projects within the German Atmospheric Research Programme AFO 2000 Programme (www.afo-2000.de). The main goal of the FEBUKO field studies was to put a basis for the further development of tropospheric cloud chemistry models. A complex experimental data set was obtained by two field campaigns in 2001 and 2002. This data set was used as a realistic initialisation dataset for the newly developed applied models (SPACCIM, CAPRAM 3.0). The model calculations are capable of reproducing the flow of the approaching air mass from the upwind site above the summit with its orographic cloud to the downwind site. The air masses of the experimental region were typically from an anthropogenic influenced origin which has been exposed to biogenic emissions on their way from the Rhein-Main area to the Thüringer Wald. For a more detailed description and results of the FEBUKO experiments see Herrmann et al. (2005a), Brüggemann et al. (2005), van Pinxteren et al. (2005), Tilgner et al. (2005b).

2. Experimental set-up

Aerosol sampling was performed at the upwind site in the village of Goldlauter (U site, 605 m asl, 10°45′20″E, 50°38′25″N), Thüringer Wald (Germany), during October 2001 and 2002. A more detailed overview of the FEBUKO experimental design is given by Herrmann et al. (2005a), and the meteorological characterisation during the campaigns by Tilgner et al. (2005a) and Heinold et al. (2005). Hence, only a short description of the specific experimental set-up for particle and trace gases characterisation is given here.

Different collectors were applied to obtain samples for the chemical characterisation of particles. For the size-resolved particle sampling, BERNER impactors (BI, cut-offs: stage 1: 0.05–0.014, stage 2: 0.14–0.42, stage 3: 0.42–1.2, stage 4: 1.2–3.5, stage 5: 3.5–10 μm, aerodynamical particle diameter) were used which were conditioned at 60% RH to minimise bounce-off effects. Humidity was controlled by a sensor placed directly in front of the sampling inlet of the impactors and automatically regulated by changing the temperature of the sampling inlet line for each impactor. Two impactors, one with tedlar foil for major ion analysis and the other with aluminium foil for carbon analysis (OC: organic carbon, EC: elemental carbon, TC: total carbon), were operated in parallel (flow volume: 75 l min^{-1}). Additionally, ANDERSEN (HVA) for PM_{10} and DIGITEL (DF) high-volume filter samplers for PM_1 and $PM_{2.5}$ equipped with quartz fibre filter (Munktell MK 360) were used for high-volume samples (940, 300 and 500 l min^{-1}, respectively). The total mass on the filter was determined using a microbalance. The filter samples were equilibrated 24 h at about 50% RH and 20 °C prior to weighing (Plewka et al., 2004). Recent study (INTERCOMP2000) shows a good agreement between the measurements using Munktell quartz fibre and other filters (Hitzenberger et al., 2004). The quartz fibre filter samples were used to identify and quantify organic particle constituents (Müller et al., 2005), some of water-soluble metals (Fe, Cu, Mn, and Zn), and for the comparison of mass and ion analysis. Furthermore, particles for anionic analysis were collected by the Steamjet (StJ) technique with online analysis by IC (Dionex), cf. Acker et al. (2003). The number size distribution of particles was measured by a Tandem Differential Mobility Particle Sizer (T-DMPS) for the particle size range between 3 and 900 nm. In the T-DMPS, particles were dried and classified at relative humidity below 10% (Birmili et al., 1999).

Standard trace gases mixing ratios (NO, NO_2, O_3, SO_2, and CO) were recorded by ambient trace gas monitors (Herrmann et al., 2005a). The concentrations of the trace gases (HCl, HONO, and HNO_3) were measured online by a Wet Effluent Diffusion Denuder (WEDD) using IC (Dionex) (Acker et al., 2001) and H_2O_2 by means of a H_2O_2-Analyser Model UD8801. The measured trace gas mixing ratios/concentrations are given in Table I (Electronic supplemental material, ESM), as well as a brief discussion of the temporal evolution during the events.

The collected particles were chemically analysed by ion chromatography (Metrohm) and capillary electrophoresis (Spectrophoresis1000) for the main ionic components (Brüggemann and Rolle, 1998; Neusüß et al., 2000a). OCEC was determined by a two-step thermographic method (C-mat 5500, Ströhlein), see Plewka et al. (2004). The metals in the BI and HVA samples were analysed using atomic absorption spectrometry (Perkin Elmer) (Chemnitzer, 2002; Rüd, 2003). Table II (ESM) lists the measured size-segregated concentrations for particulate mass, Cl^-, NO_3^-, SO_4^{2-}, Na^+, NH_4^+, K^+, Mg^{2+}, Ca^{2+}, OC, EC, water-soluble Fe, Cu, Mn, and Zn (PM_{10}). In addition, the sum of all impactor stages (corresponding to PM_{10}), the HVA PM_{10} concentrations and the total (without cut-off) concentrations of Cl^-, NO_3^- and SO_4^{2-} by StJ are shown.

Quality control was achieved through successful participation in international ring analysis initiatives by WMO-EPA each year since 1991 (http://www.marble.asrc.cestm.albany.edu/qasac/) for ion analysis. The

OCEC method used in this study was involved in the International Round Robin Test Carbon Shoot out Stage I (Schmid et al., 2001) and Stage II (Puxbaum, TU Vienna, unpublished) and in the INTERCOMP2000 campaign (ten Brink et al., 2004).

3. Results and discussion

A set of total 14 events from campaign 2001 and 2002 was selected for detailed analysis. The best conditions (defined by a connected flow upwind-summit-downwind site) were fulfilled during three events. These are E I: 26/27-October 2001, E II: 06–08-October 2001, and E III: 16/17-October 2002 (Tilgner et al., 2005a; Heinold et al., 2005). These events were chosen for further discussion. The complex data set of the particle and gas phase concentrations from the upwind site is used for the initialisation of the complex multi-phase chemistry model SPACCIM (Wolke et al., 2005) and its application with CAPRAM3.0 (Herrmann et al., 2005b; Tilgner et al., 2005b).

3.1. Particle mass

The total mass concentration of particles on the impactor foils (PM_{10}: sum of the five BI stages) based on gravimetric measurements amounts to between 8 and 17 $\mu g\,m^{-3}$. This is comparable to other measurements at rural sites in Germany and middle Europe (Table 1) but is lower than near-city measruements. For example, the PM_{10} mean value in Melpitz was about 33 $\mu g\,m^{-3}$ in 1995 (Müller et al., 2005) and the range during an autumn campaign in 1997 was found to be 13–47 $\mu g\,m^{-3}$ (Neusüß et al., 2002; Plewka et al., 2004). For Waasmunster (B—July 1994–November 1995), a mean value of 38 and for Ispra (I—February 2000–December 2000) of 29 $\mu g\,m^{-3}$ was determined (Putaud et al., 2004). At urban sites, the PM_{10} mean values were 24, 38, and 47 $\mu g\,m^{-3}$ in Zurich (CH—January 1998–March 1999), Gent (B—May 1993–July 1994) and Bologna (I—2002), respectively (Putaud et al., 2004).

For E I and E II, a distribution of particle mass in the five BI size ranges was found (Fig. 1) to be a typical aged central European aerosol (Neusüß et al., 2000a, b). E III shows more maritime-influenced aerosol recognisable by elevated sea salt fractions in the coarse mode on stages 4 and 5 (Fig. 3). Ninety six hour backward trajectories of the sampled air masses were produced with HYSPLIT from the NOAA ARL Website (http://www.arl.noaa.gov/ready/), see Tilgner et al. (2005a).

Table 1
Mean PM_{10} concentration for rural sites

Site	Period	PM_{10} ($\mu g\,m^{-3}$)
Westerland (G)	2001	20[a]
Zingst (G)	2001	17[a]
Neuglobsow (G)	2001	16[a]
Waldhof (G)	2001	16[a]
Schmücke (G)	2001	10[a]
Deuselbach (G)	2001	15[a]
Brotjacklriegel	2001	10[a]
Schauinsland (G)	2001	10[a]
Chaumont (CH)	Jan98–Mar99	11[b]
Monagrega (CH)	Mar99–Jul00	18[b]
Illmitz (A)	Oct99–Oct00	24[b]
Schmücke (G)	Oct01, Oct02	8–17[c]

[a]Beilke et al., 2002.
[b]Putaud et al., 2004.
[c]This work.

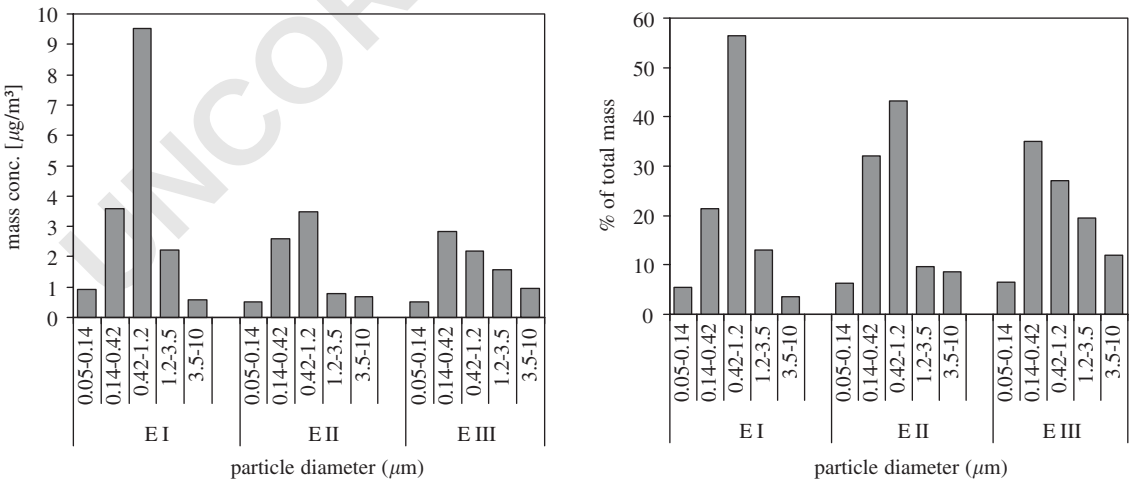

Fig. 1. Size-segregated mass concentration and percentage of stage mass to total mass concentration at upwind site.

Particle mass concentrations were measured also by DIGITEL (PM_1 in 2001/$PM_{2.5}$ in 2002) and a HVA filter sampler (PM_{10}). The comparison of all three samplers is presented in Fig. 2. BI ($PM_{1.2}$) vs. DF (PM_1) shows a reasonable agreement. A slight excess of the BI mass can be caused by the higher cut-off. The particle mass of BI ($PM_{3.5}$) vs. DF ($PM_{2.5}$) shows excess values of about 50% for the DF. Moreover, BI (PM_{10}) vs. HVA (PM_{10}) shows even an excess of >100% for the HVA. These differences could be attributed to positive and negative artefacts of the respective sampling techniques. Losses of volatile components by BI sampling cannot be fully excluded, especially for smaller particles, because of pressure drop (Neusüß et al., 2000a). Bounce-off effects in the upper stages of impactor might also contribute to mass losses (Wang and John, 1988; Hillamo and Kauppinen, 1991). Quartz fibre filters can adsorb gaseous components from the sample air stream forming excess mass (Cadle and Mulawa, 1990) and react with gaseous compounds (Zhang and McMurry, 1991). Additionally, high-volume filter samplers exhibit a much flatter curve of particle deposition efficiency (Schaap et al., 2004; Hitzenberger et al., 2004).

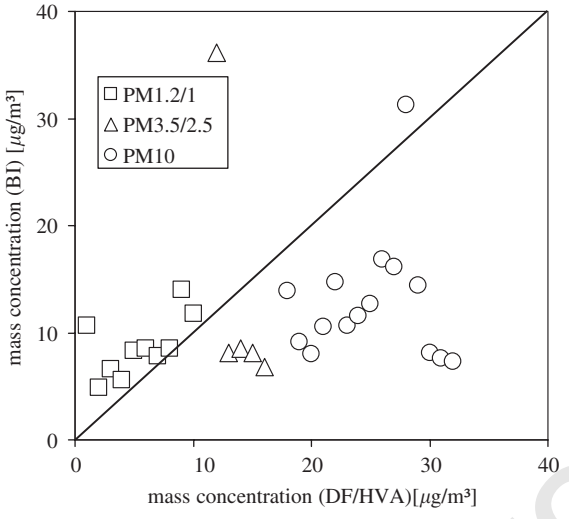

Fig. 2. Comparison of mass concentration measured by BERNER impactor (BI—$PM_{1.2}$, $PM_{3.5}$, and PM_{10}), Digitel filter sampler (DF—PM_1 and $PM_{2.5}$), and High-Volume Andersen filter sampler (HVA—PM_{10}).

3.2. Ionic components

The total concentrations of major ionic components (summed up to PM_{10}) reach 6.55 (E I), 2.67 (E II) and 2.53 $\mu g\,m^{-3}$ (E III). The total concentration of ion mass of E I is about twice higher than E II and E III. The contribution of ions to particle mass (PM_{10}) is about 40% (E I) and 30% (E II and E III). In Fig. 3, the concentrations of size-segregated main ionic components for the three events are presented. The major components are nitrate, sulphate, and ammonium (about 90% of the total ionic concentration).

For E I, the highest ionic concentration was found on stage 3 followed by stages 2, 4, 5 and 1. Nitrate has the highest concentration, followed by sulphate and ammonium with maximum on stage 3 (0.42–1.2 μm). The other components (Cl^-, Na^+, Mg^{2+}, Ca^{2+}) show the highest concentration (from sea salt and soil) on the stages 4 and 5 (1.2–10 μm) and stages 2 and 3 (0.14–1.2 μm) for K^+ (wood burning). In E II, the sulphate concentration was the highest on stages 3 followed by 2 and in E III on stages 2 followed by 3. The order of nitrate concentration was found to be stage 3>2>4 for E I and II but it was in a reverse order for E III (stage 4>2>3).

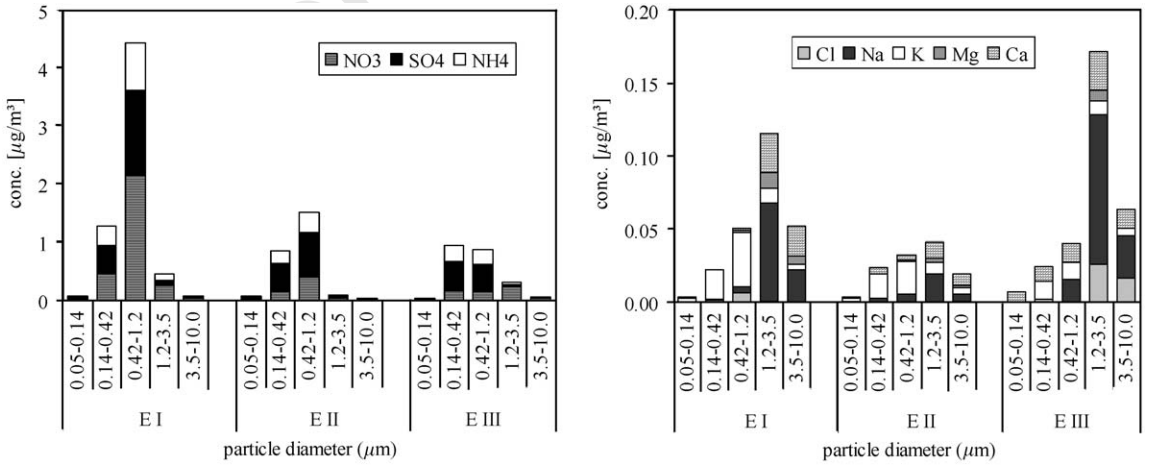

Fig. 3. Size-segregated particle concentration of main ion components for the three events at upwind site.

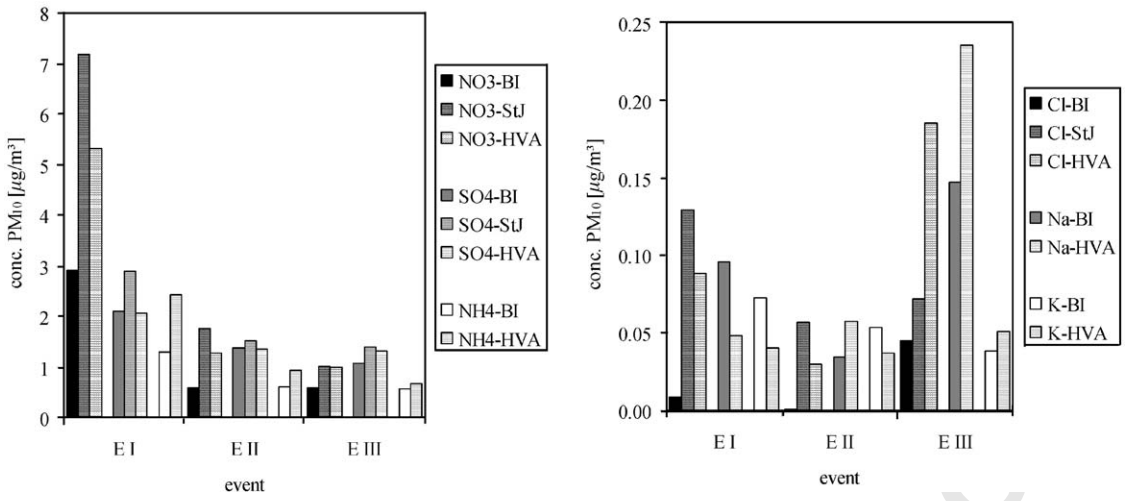

Fig. 4. Comparison of ion concentration (PM_{10}) measured by BERNER impactor (BI), Steamjet technique (StJ), and High-Volume Andersen sampler (HVA).

Together with the very high concentrations of sea salts components (sodium, chloride, magnesium and calcium) on stage 4, it can be assumed that the aerosol for E III was of marine origin.

Fig. 4 shows the comparison for some ionic components measured by BI, HVA and StJ sampler (PM_{10}). It can be seen that there are some discrepancies between the samplers except for sulphate which is determined in relative good agreement for all three events. Differences can originate from different collection techniques, from contamination of the samples or inaccuracy in the chemical analysis. The analytical error for all components is on average below 10% but it can be as high as up to 50% near the detection limit.

The particulate concentration of chloride and nitrate was typically higher in the StJ than in BI samples. This is due to the sampling performance of StJ (denuded gases, particles are absorbed in water vapour without cut-off) excluding adverse effects as discussed for BI or HVA sampling. Based on StJ values, chloride found in BI samples was much lower and about 30% and 50% lower in HVA samples for E I and E II, respectively. In E III, the chloride loss for BI amounts to about 40% and for HVA an excess of 150% can be observed. The particulate chloride of the HVA samples minus the gaseous HCl concentration shows an excess of about 30%. This is an indication of a possible adsorption of gaseous HCl on the HVA filter sample (gaseous HCl concentration in E III is 4–8 fold higher than in E I and E II, see Table I—ESM). The discrepancies of nitrate concentration between the different samplers were about −60%, −70%, and −40% for BI and −25%, −25%, and 0% for HVA (all based on StJ) for E I, E II and E III, respectively. The measured particulate ammonium concentrations from BI were about 50% (EI), 35% (EII), and 15% (EIII) lower than from HVA. However, it cannot be checked if there is a NH_4^+ loss for BI and/or an excess for HVA. Losses of ammonium nitrate during both filter and impactor sampling are discussed in Chang et al. (2000). The cations (Na^+, K^+, Mg^{2+}, and Ca^{2+}) cannot evaporate and do not have gaseous precursors in the atmosphere. The different concentration of these between BI and HVA samples in E III could be explained with the higher mass concentration sampled by HVA filter sampler, mainly in the larger particle size range (because of the flat collection efficiency curve), see Figs. 2 and 3. There is a possibility of contaminations from re-suspended soil materials (alkaline and alkaline-earth oxides and silicates).

In order to compensate the sampling errors the ionic concentrations of volatile components were adapted at the StJ values including the measured mass size distribution to initialise the model calculations, see Tilgner et al. (2005b) for further details.

3.3. OCEC

The carbonaceous particle fraction forms an important part of the aerosol mass. Considering PM_{10} (sum of all impactor stages), the fraction of TC in E I (12%) was lower than in E II (19%) and E III (18%). This was due to the smaller OC fraction during E I while the EC fractions were more or less constant during all three events between 5% and 6%.

Fig. 5 shows the measured OCEC concentration and the contribution to the mass on each impactor stage. The total OC concentration (PM_{10}) for all three events (E I, II and III) was about 1.0 µg m^{-3}. Total EC

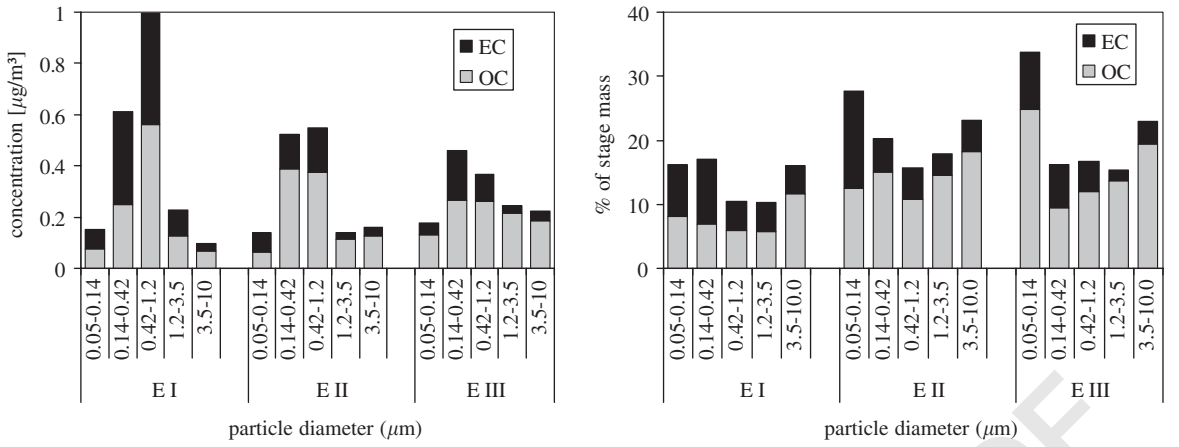

Fig. 5. Size-segregated OCEC concentration and the percentage of stage mass for the three events at upwind site.

concentrations were 1.0, 0.45, and 0.40 μg m^{-3} for EI, II and III, respectively. The total OC/EC ratios were 1.1 (E I), 2.4 (E II) and 2.6 (E III). Air masses of E II and E III showed similar OCEC values whereas E I showed smaller OC and lower EC/OC ratio than the other two events. The OC/EC ratio is an important parameter considering the activation of the particles as a CCN and cloud droplet formation (Mertes et al., 2005; Brüggemann et al., 2005). OC influences particle growth or surface tension depending on its chemical composition. Therefore, the detailed analysis of OC fraction to determine most of organic single species is desirable (see Müller et al., 2005).

Size-segregated analysis for E I shows that a TC fraction accounts 16–17% on stages 1, 2 and 5 compared to only 10% on stages 3 and 4. E II and E III show their highest TC fraction on stage 1 with approximately 30% followed by stage 5 with 23%. TC fractions on stages 2 and 4 were in the range of 15–20%.

OC/EC ratios for E I were especially low in the range of 0.7–1.3 (except stage 5) as well as the stage 1 for E II. Low OC/EC ratios from small particles indicate fresh diesel vehicle emissions (Turpin and Huntzicker, 1995; Plewka et al., 2004) in the narrow valley of the upwind site possibly caused by lorries and cars of the inhabitants. One thing to note is that OC/EC ratios also may be influenced by different separation and analytical methods resulting in different OCEC fractions (Schmid et al., 2001; ten Brink et al., 2004). The fraction on stage 3 for E I indicates an aged air mass influenced by traffic and possibly industrial EC emissions. The E II air mass is more OC dominated (OC/EC = 2.8, 2.2, 4.4, 3.6; stages 2–5). The OC/EC ratio in E III rises up to 7.7 at stage 4 and 5.5 at stage 5. The OC/EC ratio generally increases during particle ageing. A part of aged organic materials is called secondary organic aerosol (SOA) formed by oxidised VOCs. Therefore, OC/EC ratios can be used to estimate SOA concentrations (e.g. Strader et al., 1999). Higher OC fractions in the coarse particle size range ($PM_{1.2-10}$) can originate from biogenic (e.g. plant wax abrasion and pollen) or anthropogenic sources (tire abrasion and re-suspension). The differentiation can be performed using the Carbon Preference Index (CPI_{odd}), the ratio of odd and even alkanes (see Müller et al., 2005). In PM_{10} filter samples from E I and E II CPI_{odd} of about 0.9 were determined. This suggests anthropogenic sources (fuel alkanes) on the highest loaded stages but does not exclude fractions of biogenic alkanes on the coarse stages as found in other studies (Herrmann et al., 2005a, b).

3.4. Mass closure

Mass closure includes the comparison of the gravimetric mass determined by weighing the particle samples using a microbalance with the physically calculated mass or the chemically determined mass consisting of all components determined. Average particle number size distributions from events I, II, and III are discussed in detail and figures of volume and number size distributions are presented in Brüggemann et al. (2005) and Mertes et al. (2005).

3.4.1. Physical mass closure

The masses corresponding to each size range were calculated from the continuously measured dry particle size distributions by the procedure described in Neusüß et al. (2000b, 2002). The T-DMPS measured size distributions were averaged over the whole event time. Particle diameters at 60% RH are estimated from DMPS size distributions at 10% RH using growth factors (fg) derived from the simultaneously measured hygroscopic particle growth factor using a HTDMA (Hygroscopicity Tandem Differential Mobilility Sizer) (Lehmann et al., 2005). From the mean dry particle number distributions the volume distributions were

calculated using the wet diameters. The mass distribution can be calculated from the volume distribution by means of the corresponding wet densities. For this purpose, wet densities were calculated from averaged dry densities (estimated from the compounds found by chemical analysis) using the growth factors: $\rho_{wet} = [(fg^3-1)/fg^3] \cdot \rho_{H_2O} + 1/fg^3 \cdot \rho_{dry}$. The used densities are: carbonaceous material (OM 1.65, EC 1.8), ions 1.7, unidentified fraction 2.2, and water 1.0 g cm^{-3}. The growth factors for 50, 150, and 250 nm particles, determined by a HTDMA, were found to be 1.08, 1.07, and 1.19 for E I; 1.07, 1.10, and 1.15 for E II, and 1.07, 1.08, and 1.11 for E III, respectively (Lehmann et al., 2005). The resulting mass distribution was integrated up to the corresponding impactor stage diameter. The wet size distribution corresponds roughly to the range up to 1 μm diameter, so the first three impactor stages can be compared.

Mass closure between BI and T-DMPS shows reasonable agreement (Fig. 6). The relative differences between calculated T-DMPS and BI mass concentrations are about −45%, 60%, and 50% for E I, −45%, 30%, and 50% for E II, and −60%, 10%, and 30% for E III on the size ranges of 0.05–0.14, 0.14–0.42, and 0.42–1.2 μm, respectively (positive bias means higher BI mass concentration). Neusüß et al. (2000b) found deviations of less than 10% to about 70% (often in the range of 30–40%) between gravimetric and number-derived mass concentrations due to measurement uncertainties.

3.4.2. Chemical mass closure

For the purpose of the chemical mass closure, the sum of OC has to be converted to organic mass (OM). OC to OM conversion factors between 1.2 and 2.6 were typically used, e.g. in Turpin et al. (2000). In this study, a conversion factor of 2.1 representing non-urban aerosol was applied (Turpin and Lim, 2001). A differentiation between the single size ranges (lower conversion factors for fresh fine particles and higher factors for more coarse aged particles) was not considered because of insufficient knowledge of the chemical composition of OC fraction (about 15% are identified, see Müller et al., 2005).

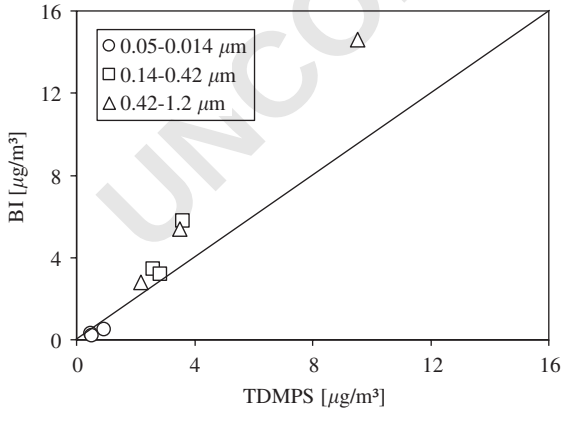

Fig. 6. Mass closure between gravimetric determination and calculation of particle mass from the number size distribution.

The water content was estimated by the following approach (Neusüß et al., 2002): $m_{H_2O} = m_{dry}(((\rho_{wet}/\rho_{dry})f)-1)$ with m_{H_2O}—resulting water content, m_{dry}—chemical measured mass concentration, ρ_{wet}—density of wet particles, ρ_{dry}—density of dry particles, $f = (D_{wet}/D_{dry})^3$—volume growth factor (for spheric particles), $D_{wet,dry}$—diameter of wet or dry particles. As a first approximation, an average volume growth factor $(1.1)^3 = 1.33$ was used (Neusüß et al., 2000b). The density ratio ρ_{wet}/ρ_{dry} was estimated from the fractions of measured components. The value of ρ_{dry} was determined from fractions of compounds (NH_4NO_3 and $(NH_4)HSO_4$: $\rho_{dry} = 1.7$ g cm^{-3}), OM (oxalate: $\rho_{dry} = 1.65$ g cm^{-3}), EC (soot: $\rho_{dry} = 1.8$ g cm^{-3}), and undetermined mass (SiO_2: $\rho_{dry} = 2.2$ g cm^{-3}). The value of ρ_{wet} was calculated by the following approach: $\rho_{wet} = (1-(1/f))\rho_{H_2O} + (1/f)\rho_{dry}$. The water content was found to be in the range of about 16–18%. The mean hygroscopic growth factor derived from available measurements in the size range up to $D_p = 50$, 150, and 250 nm was used also for more coarse particle fractions. Hysteresis effects could not be taken into account in this calculation. Therefore, results from this calculation are only approximate values. Nevertheless, this gives a rough idea on the water content of particle samples.

Size-segregated chemical mass closure for all events is shown in Fig. 7. The unidentified mass (UM) fraction from E I for all size ranges was higher than that of E II and E III. The percentage of UM for the three events was about 20% in average and as high as 50% for E I (stage 1). Such high fraction of UM, especially on the fine particle stages 1 and 2, was not observed from other measurement campaigns (e.g. Herrmann et al., 2005a, b). In all events, stage 3 shows the lowest UM portion of about 10% which can be explained by crust material that was not analysed and possibly transported over long distances because of the long lifetime of such fraction. On stages 4 and 5, a higher portion of coarse particles (20–35%) produced by abrasion and resuspension can contribute to the UM. Chemical analysis performed during the FEBUKO campaigns should be able to explain most of the mass fraction from fine particles (stage 1) as it is unlikely to contain crust materials such as silicates, silicon dioxide and metal oxides. However, higher UM portion (about 50%) from E I (stage 1) was observed and no explanation can be given at this moment. Investigations (joint project "Suspended dust" of IfT, Leipzig and Sächsisches Landesamt für Umwelt und Geologie, Dresden) from the size-segregated chemical composition of fine parti-

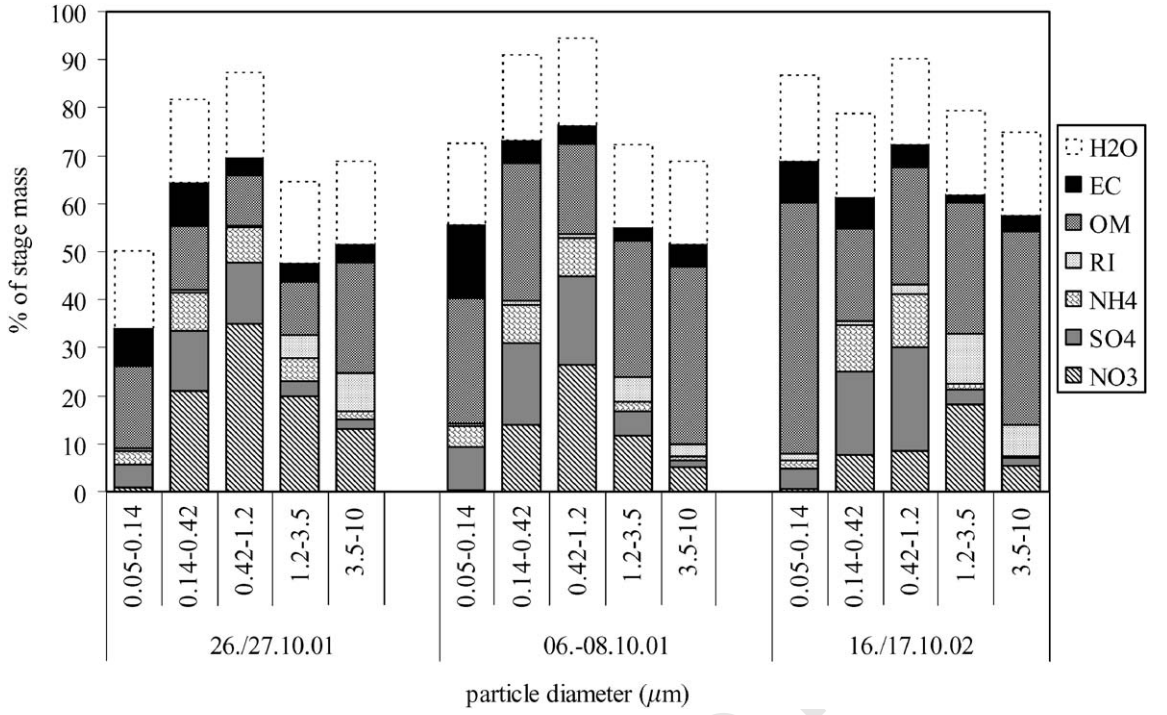

Fig. 7. Chemical mass closure (OM: organic material, RI: remaining ionic components).

cles in Saxony including metal analysis by PIXE (Proton Induced X-ray Emission) show that these components amount only to a minor portion on stage 1 and cannot be responsible for the large UM fraction. After all, the stage 1 mass of E I includes only 5% of the total sample mass and single components are only traces. Therefore, the 50% UM fraction amounts only to 3% of the total mass and does not contribute significantly to the total mass balance. Nevertheless, the chemical mass closure of particle components is quite well for the BI stages 2–5 (0.14–10 μm). The observed losses of volatile components (mainly nitrate) for BI measurements (Fig. 4, in comparison to StJ and HVA) lead to the conclusion that the part of UM fraction should be lower than that estimated by this method.

4. Summary

Detailed measurements of the gas and particle phase constituents allowed good chemical and physical characterisation of the air mass flow from the upwind site to the cloud-covered summit and to the downwind site.

The total mass concentration of particles (PM_{10}) measured by BERNER impactor was between 8 and 17 $\mu g\,m^{-3}$ and is comparable to other measurements at rural sites. More than 80% of the PM_{10} mass consists of particles with a diameter below 1.2 μm. The comparison of mass concentration sampled by BERNER impactor (BI), high-volume DIGITEL (DF), and ANDERSEN (HVA) filter collectors shows a sufficient agreement with slight surplus of the BI (BI-$PM_{1.2}$/DF-PM_1) and excess values of about 50% for the DF (BI-$PM_{2.5}$/DF-$PM_{3.5}$) and >100% for the HVA (BI-PM_{10}/HVA-PM_{10}).

The total concentration of ionic mass of E I was about twice higher than from E II and E III. The major ionic components are nitrate, sulphate, and ammonium which amount to 90% of the total ionic concentration. In E I nitrate had the highest concentration but in E II and E III sulphate was the dominant component. The comparison of particulate ionic concentrations measured by BI, HVA, and Steamjet technique shows great losses of volatile components (chloride, nitrate, and ammonium) from BI. The sulphate concentration was determined in relative good agreement by the different collectors.

The fraction of TC concentration in total mass concentration was lower for E I (12%) than for E II (19%) and E III (18%). The EC portion was about equal in all three events between 4% and 5%. The OC/EC ratio was smallest for E I (1.1) but it was much higher for E II (2.4) and E III (2.6). In E II and E III, the air mass is more OC dominated indicating SOA formation at the small particles (0.05–0.14 μm).

The physical mass closures derived from T-DMPS results show sufficient agreement with gravimetrically determined mass concentrations from BI. The chemical

mass closure of particle components is reasonably good for the size ranges 0.14/0.42/1.2/3.5/10 μm but in the fine particulate range (0.05–0.14 μm) the portion of unidentified material is very high, especially for EI and E II.

Based on the data presented here, a separate data set was provided for each chosen event to initialise the model calculations with all measured concentrations, see Tilgner et al. (2005b) for further details.

5. Uncited references

Pio and Lopes, 1998.

Acknowledgements

This work was supported financially by the German BMBF (AFO2000, project 07ATF01). For the support at the field and laboratory work we thank H. Bachmann, B. Gerlach, S. Haferkorn, N. Heim, A. Kappe, E. Neumann, K. Pielok, and A. Thomas.

References

Acker, K., Möller, D., Wieprecht, W., Auel, R., Kalaß, D., Tscherwenka, W., 2001. Nitrous and nitric acid measurements inside and outside of clouds at Mt. Brocken. Journal of Water, Air and Soil Pollution 130, 331–336.

Acker, K., Wieprecht, W., Möller, D., 2003. Distribution of reactive nitrogen compounds between atmospheric gas and aerosol phase. In: ten Brink, H., Baltensberger, U. (Eds.), Composition and Size Evolution of the Secondary Aerosol. EUROTRAC-2 Subproject AEROSOL Final Report, GSF Munich, pp. 197–203.

Bardouki, H., Liakakou, H., Economou, C., Sciare, J., Smolik, J., Ždimal, V., Elefteriadis, K., Lazaridis, M., Dye, C., Mihalopoulos, N., 2003. Chemical composition of size-resolved atmospheric aerosols in the eastern Mediterranean during summer and winter. Atmospheric Environment 37, 105–208.

Beilke, S., Berg, R., Bieber, E., Uhse, K., Wallasch, M., 2002. Jahresbericht 2001 aus dem Messnetz des UBA: Messungen von Feinstaub im Messnetz des Umweltbundesamtes. Texte 69/02, pp. 3–27 (ISSN 0722-186X).

Birmili, W., Stratmann, F., Wiedensohler, A., 1999. Design of a DMA-based size spectrometer for a large particle size range and stable operation. Journal of Aerosol Science 30, 549–553.

Brüggemann, E., Rolle, W., 1998. Changes of some components of precipitation in East Germany after the unification. Water, Air, and Soil Pollution 107, 1–23.

Brüggemann, E., Gnauk, T., Mertes, S., Acker, K., Auel, R., Wieprecht, W., Collett Jr., J.L., Chemnitzer, R., Rüd, C., Junek, R., Herrmann, H., 2005. Schmücke hill cap cloud and valley stations aerosol chemical composition during FEBUKO (I): standard trace gases, main components and metals. Atmospheric Environment 123, 12 (this issue).

Chang, M.C., Sioutas, C., Kim, S., Gong Jr., H., Linn, W.S., 2000. Reduction of nitrate losses from filter and impactor samplers by means of concentration enrichment. Atmospheric Environment 34, 85–98.

Chemnitzer, R., 2002. Bestimmung von Metallen in troposphärischen Partikeln und Wolkentröpfchen mittels Atom-Absorptionsspektrometrie. Diplomarbeit Technische Universität Bergakademie Freiberg.

Electronic supplemental material: (http://www.projects.tropos.de:8088/afo2000g3/FEBUKO-dateien/font!.html/).

Hallberg, A., Noone, K.J., Ogren, J.A., Okada, K., Heintzenberg, J., Svenningsson, I.B., 1994. The influence of aerosol particle composition on cloud droplet formation. Journal of Atmospheric Chemistry 19, 153–171.

Hegg, D.A., Covert, D.S., Jonson, H., Khelif, D., Friehe, C.A., 2004. Observations of the impact of cloud processing on aerosol light scattering efficiency. Tellus 56B, 285–293.

Heinold, B., Tilgner, A., Jaeschke, W., Haunold, W., Knoth, O., Wolke, R., Herrmann, H., 2005. Meteorological characterisation of the FEBUKO hill cap cloud experiments, Part II: tracer experiments and flow characterisation with nested non-hydrostatic atmospheric models. Atmospheric Environment (this issue).

Herrmann, H., Wolke, R., Müller, K., Brüggemann, E., Gnauk, T., Barzaghi, P., Mertes, S., Lehmann, K., Massling, Birmili, W.A., Wiedensohler, A., Wieprecht, W., Acker, K., Jaeschke, W., Kramberger, H., Svrcina, B., Bächmann, K., Collett Jr., J.L., Galgon, D., Schwirn, K., Nowak, A., vanPinxteren, A., Plewka, A., Chemnitzer, R., Rüd, C., Hofmann, D., Tilgner, A., Diehl, K., Heinold, B., Hinneburg, D., Knoth, O., Sehili, A.M., Simmel, M., Wurzler, S., Mauersberger, G., Majdik, Z., Müller, F., 2005a. FEBUKO and MODMEP: field measurements and modelling of aerosol and cloud multiphase processes. Atmospheric Environment (this issue).

Herrmann, H., Tigner, A., Barzaghi, P., Majdik, Z., Gligorovski, S., Poulain, L., Monod, A., 2005b. Towards a more detailed description of tropospheric aqueous phase organic chemistry: CAPRAM 3.0. Atmospheric Environment (this issue).

Hillamo, R.E., Kauppinen, E.I., 1991. On the performance of the Berner low pressure impactor. Aerosol Science and Technology 14, 33–47.

Hitzenberger, R., Berner, A., Galambos, Z., Maenhaut, W., Cafmeyer, J., Schwarz, J., Mueller, K., Spindler, G., Wieprecht, W., Acker, K., Hillamo, R., Mäkelä, T., 2004. Intercomparison of methods to measure the mass concentration of the atmospheric aerosol during INTERCOMP2000—influence of instrumentation and size cuts. Atmospheric Environment 38, 6467–6476.

Kreidenweis, S.M., Walcek, C., Kim, C.H., Feingold, G., Gong, W., Jacobson, M.Z., Liu, X., Penner, J., Nenes, A., Seinfeld, J.H., 2003. Modification of aerosol mass and size distribution due to aqueous-phase SO_2 oxidation in clouds: comparisons of several models. Journal of Geophysical Research 108 (D7), 4213.

Lammel, G., Brüggemann, E., Gnauk, T., Müller, K., Neusüss, C., Röhrl, A., 2003. A new method to study aerosol source contributions along the tracks of air parcels and its application to the near-ground level aerosol chemical

composition in central Europe. Journal of Aerosol Science 34, 1–25.

Lehmann, K., Massling, A., Tilgner, A., Mertes, S., Galgon, D., Wiedensohler, A., 2005. Size-resolved soluble volume fractions of submicrometer particles in air masses of different character. Atmospheric Environment (this issue).

Maenhaut, W., Cafmeyer, J., Dubtsov, S., Chi, X., 2002. Detailed mass size distribution of elements and species, and aerosol chemical mass closure during fall 1999 at Gent, Belgium. Nuclear Instruments and Methods in Physics Research 189, 238–242.

Mertes, S., Galgon, D., Schwirn, K., Nowak, A., Lehmann, K., Massling, A., Wiedensohler, A., Wieprecht, W., 2005. Evolution of particle concentration and size distribution observed upwind, inside and downwind hill cap clouds at connected flow conditions during FEBUKO. Atmospheric Environment (this issue).

Mészáros, E., Barcza, A., Gelencsér, A., Hlavay, J., Kiss, G., Krivászcy, Z., Molnár, A., Polyák, K., 1997. Size distribution of inorganic and organic species in the atmospheric aerosol. Journal of Aerosol Science 28, 1163–1175.

Mészáros, E., Molnár, A., Ogren, J., 1998. Scattering and absorption coefficients vs. chemical composition of fine atmospheric aerosol particles under regional conditions in Hungary. Journal of Aerosol Science 29, 1171–1178.

Müller, K., van Pinxteren, D., Plewka, A., Svrcina, B., Kramberger, H., Hofmann, D., Bächmann, K., Herrmann, H., 2005. Aerosol characterisation at the FEBUKO upwind station Goldlauter (II): detailed organic chemical characterisation. Atmospheric Environment (this issue).

Neusüß, C., Pelzing, M., Plewka, A., Herrmann, H., 2000a. A new analytical approach for size-resolved speciation of organic compounds in atmospheric aerosol particles: methods and first results. Journal of Geophysical Research 105 (D4), 4513–4527.

Neusüß, C., Weise, D., Birmili, W., Wex, H., Wiedensohler, A., Covert, D.S., 2000b. Size-segregated chemical, gravimetric, and number distribution-derived mass closure of the aerosol in Sagres, Portugal during ACE-2. Tellus 52B, 169–184.

Neusüß, C., Wex, H., Birmili, W., Wiedensohler, A., Koziar, C., Busch, B., Brüggemann, E., Gnauk, T., Ebert, M., Covert, D.S., 2002. Characterization and parameterization of atmospheric particle number-, mass-, and chemical-size distributions in central Europe during LACE 98 and MINT. Journal of Geophysical Research 107, 8127.

Nunes, T.V., Pio, C.A., 1993. Carbonaceous aerosols in industrial and coastal atmospheres. Atmospheric Environment 27, 1339–1346.

Pakkanen, T.A., Kerminen, V.M., Loukkola, K., Hillamo, R.E., Aarnio, P., Koskentalo, T., Maenhaut, W., 2003. Size distribution of mass and chemical components in street-level and rooftop PM_1 particles in Helsinki. Atmospheric Environment 37, 1673–1690.

Pio, C.A., Lopes, D.A., 1998. Chlorine loss from marine aerosol in a coastal atmosphere. Journal of Geophysical Research 103, 25263–25272.

Plewka, A., Gnauk, T., Brüggemann, E., Neusüß, C., Herrmann, H., 2004. Size-resolved aerosol characterisation for a polluted episode at the IfT research station Melpitz in Autumn 1997. Journal of Atmospheric Chemistry 48, 131–156.

Putaud, J.-P., Raes, F., van Dingenen, R., Baltensberger, U., Brüggemann, E., Facchini, M.-C., Decesari, St., Fuzzi, S., Gehrig, R., Hansson, H.-C., Hüglin, C., Laj, P., Lorbeer, G., Maenhaut, W., Mihalopoulos, N., Müller, K., Querol, X., Rodriguez, S., Schneider, J., Spindler, G., ten Brink, H., Törseth, K., Wiedensohler, A., 2004. A European aerosol phenomenology: 2. Chemical characteristics of particulate matter at kerbside, urban, rural, and background sites in Europe. Atmospheric Environment 38, 2579–2595.

Rüd, C., 2003. Bestimmung von Metallen in Aerosolpartikeln und Wolkenwasser mittels Atom-Absorptionsspektrometrie. Diplomarbeit Universität Leipzig.

Schaap, M., Spindler, G., Schulz, M., Acker, K., Maenhaut, W., Berner, A., Wieprecht, W., Streit, N., Müller, K., Brüggemann, E., Putaud, J.-P., Puxbaum, H., Baltensperger, U., ten Brink, H.M., 2004. Artefacts in the sampling of nitrate studied in the, INTERCOMP' campaign of EUROTRAC-AEROSOL. Atmospheric Environment 38, 6449–6487.

Schmid, H., Laskus, L., Abraham, H.J., Baltensperger, U., Lavanchy, V., Bizjak, M., Burba, P., Cachier, H., Crow, D., Chow, J., Gnauk, T., Even, A., ten Brink, H.M., Giesen, K.-P., Hitzenberger, R., Hueglin, C., Maenhaut, W., Pio, C., Carvalho, A., Putaud, J.-P., Toom-Sauntry, D., Puxbaum, H., 2001. Results of the "carbon conference" international aerosol carbon round robin test stage I. Atmospheric Environment 35, 2111–2121.

Strader, R., Lurmann, F., Pandis, S.N., 1999. Evaluation of secondary organic aerosol formation in winter. Atmospheric Environment 33, 4849–4863.

ten Brink, H., Maenhaut, W., Hitzenberger, R., Gnauk, Th., Spindler, G., Even, A., Chi, X., Bauer, H., Puxbaum, H., Putaud, J.-P., Tursic, J., Berner, A., 2004. INTERCOMP2000: the comparability of methods in use in Europe for measuring the carbon contnet of aerosol. Atmospheric Environment 38, 6507–6519.

Tilgner, A., Heinold, B., Nowak, A., Herrmann, H., 2005a. Meteorological characterisation of the FEBUKO hill cap cloud experiments, Part I: synoptic characterisation of measurement periods. Atmospheric Environment (this issue).

Tilgner, A., Majdik, Z., Sehili, A.M., Simmel, M., Wolke, R., Herrmann, H., 2005b. SPACCIM: simulations of multiphase chemistry occuring in the FEBUKO hill cap cloud experiments. Atmospheric Environment (this issue).

Turpin, B.J., Huntzicker, J.J., 1995. Identification of secondary organic aerosol episodes and quantitation of primary and secondary organic aerosol concentrations during SCAQS. Atmospheric Environment 23, 3527–3544.

Turpin, B.J., Lim, H.-J., 2001. Species contribution to PM2.5 mass concentrations: revisiting common assumptions for estimating organic mass. Aerosol Science and Technology 35, 602–610.

Turpin, B.J., Saxena, P., Andrews, E., 2000. Measuring and simulating particulate organics in the atmosphere: problems and prospects. Atmospheric Environment 34, 2983–3013.

van Pinxteren, D., Plewka, A., Hofmann, D., Müller, K., Kramberger, H., Svrcina, B., Bächmann, K., Jaeschke, W., Mertes, S., Collett Jr., J.L., Herrmann, H., 2005. Schücke hill cap cloud and valley stations aerosol chemical

composition during FEBUKO (II): organic compounds. Atmospheric Environment (this issue).

Wang, H.-C., John, W., 1988. Characteristics of the Berner impactor for sampling inorganic ions. Aerosol Science and Technology 8, 157–172.

Wolke, R., Sehili, A.M., Simmel, M., Knoth, O., Tilgner, A., Herrmann, H., 2005. SPACCIM: a parcel model with detailed microphysics and complex multiphase chemistry. Atmospheric Environment (this issue).

Zhang, X., McMurry, P.H., 1991. Theoretical analysis of evaporative losses of adsorbed or absorbed species during atmospheric aerosol sampling. Environmental Science and Technology 25, 456–459.

3B2v8.06a/w (Dec 5 2003).51c XML:ver:5.0.1 AEA : 5765 Prod.Type:FTP pp.1–13(col.fig.:NIL) ED:DeepaRani PAGN:gopal SCAN:

ARTICLE IN PRESS

Available online at www.sciencedirect.com

SCIENCE DIRECT®

ELSEVIER

Atmospheric Environment ▮ (▮▮▮▮) ▮▮▮–▮▮▮

ATMOSPHERIC ENVIRONMENT

www.elsevier.com/locate/atmosenv

Aerosol characterisation at the FEBUKO upwind station Goldlauter (II): Detailed organic chemical characterisation

K. Müller[a,*], D. van Pinxteren[a], A. Plewka[a], B. Svrcina[b], H. Kramberger[b], D. Hofmann[a], K. Bächmann[b], H. Herrmann[a]

[a]*Leibniz-Institut für Troposphärenforschung, Permoserstr. 15, 04318 Leipzig, Germany*
[b]*Technische Universität Darmstadt, Institut für Anorganische Chemie, Petersenstrasse 18, 64287 Darmstadt, Germany*

Abstract

An extensive set of gaseous and particulate organic compounds was quantified before an orographic cloud passage at the upwind site of the research region in Thüringer Wald. Samples were collected with two different time resolutions, 2 h for gaseous species and spray absorber samples and the whole cloud event duration to determine the concentrations of ketones, aldehydes, monocarboxylic acids, dicarboxylic acids (DCA), hydrocarbons, biogenic sugars and alcohols in both the gas and particle phase.

The measurement of different groups of organic compounds delivered size-segregated concentrations at the upwind site of a cloud experiment. The size distribution of DCA showed a peak in the mass-rich impactor stage 3 (0.42–1.2 μm). The concentrations of DCA from the filters, the impactor foils as well as the spray absorber samples decreased with increasing C-number. The time resolved measurements revealed an increasing mixing ratio from night time to midday for carboxylic and DCA, and related carbonyl compounds.

The biogenic compounds xylitol (up to 103 ng m^{-3}), levoglucosan (up to 62 ng m^{-3}) and pinonaldehyde (up to 34 ng m^{-3}) were the compounds found in highest concentrations in the particle phase beside the oxalate (up to 104 ng m^{-3}).

The organic trace gases with the highest mixing ratios identified were formaldehyde (up to 1.47 ppbv), acetaldehyde (up to 0.84 ppbv) and acetone (up to 0.65 ppbv), acetic acid (up to 0.43 ppbv) and formic acid (up to 0.41 ppbv).

Keywords: Filter; Impactor; Spray collector; Carbonyl compounds; Acids; Organic semivolatiles

1. Introduction

One of the main aims of field investigations of budgets and conversions of particle phase organics in tropospheric cloud processes (FEBUKO) is the better understanding of the role of organic compounds in cloud chemistry and their changes as well as the influence on the particles—air–cloud droplets system. In this experiment, meteorological, physical and chemical data were collected at three sites in the Thüringer Wald to characterise the connected flow between the sites and the changes in composition of organic and inorganic components of the gas and particle phase as well as their concentration in the cloud droplets. The collection of gaseous and particulate compounds was accomplished

*Corresponding author. Tel.: +49 341 2 35 2157; fax: +49 341 2 35 2361.
E-mail address: konrad@tropos.de (K. Müller).

1352-2310/$ - see front matter © 2005 Elsevier Ltd. All rights reserved.
doi:10.1016/j.atmosenv.2005.02.008

during the cloud events (i.e. mountainous site was in the cloud) considering the preferred wind direction.

The model input parameters (meteorology, gas phase compounds, physical and chemical characterisation of particles) for the further investigation of particle–cloud interaction were measured at the upwind site of the experimental region in Goldlauter (U), a town of Suhl, prior to air mass lifting, particle activation and cloud formation (Herrmann et al., 2005b). A nearly identical experimental setup was applied at the downwind site in Gehlberg (D). In previous experiments, studies of organic compounds on atmospheric multiphase chemistry were restricted to phenol and nitrophenols (GDF, 1993; Lüttke and Levsen, 1997) and formaldehyde, formic and acetic acid (Winiwarter et al., 1994; Laj et al., 1997) in clouds and air.

The determination of further organic compounds in the particle phase as well as in the gas phase of the investigation point U is reported here because the role of organics during the activation of particles to cloud condensation nuclei is not well understood up to now. Chemical analysis is focused here on size-segregated and time-resolved determination of dicarboxylic acids (DCA) and the determination of selected biogenic marker compounds. Most of the investigated compounds are water soluble with the exception of higher alkanes and long-chain carbonyl compounds. In parallel, carbonyl compounds and carboxylic acids from the gas phase were analysed. Interactions between these gaseous compounds and cloud droplets are well known. Carbonyl compounds are precursors of carboxylic and DCA and the formation of DCA is one of the transfer paths of gaseous compounds to the particulates, which can occur faster in clouds.

DCA are a main fraction of atmospheric organic aerosols and frequently found in many parts of the world (Saxena and Hildemann, 1996; Röhrl and Lammel, 2001). Their sources remain largely unknown, but primary emissions from automobile exhaust (Kawamura and Kaplan, 1987) or biomass burning (Narukawa et al., 1999) and secondary formation by either gas-phase or liquid-phase oxidation from different precursor compounds are discussed in literature (Satsumabayashi et al., 1990; Kawamura and Ikushima, 1993; Ervens et al., 2003; Warneck, 2003). Most of the studies dealing with the analytical determination of organic acids utilise quartz filters for particle sampling and relatively long sampling periods (many hours up to days). This practice limits both the available information about the temporal evolution of concentrations during a time interval of only a few hours (as is the case for the cloud events investigated in this study) and about the size distribution of the compounds. To overcome this problem, in this work different techniques have been applied in parallel. Berner impactors gave size-resolved information over the entire cloud event, whereas scrubbers sampled the bulk aerosol in 2-h intervals.

Carbonyl compounds are the first stable oxidation products of anthropogenically emitted hydrocarbons and of biogenic terpenoid emissions (Carlier et al., 1986; Singh et al., 1995). Several of these carbonyl compounds are water soluble and may also react in cloud water (Grosjean and Wright, 1983).

The treatment of organics in current tropospheric chemistry models is much restricted. The development of the CAPRAM 3.0 aqueous phase mechanism (Herrmann et al., 2005a) and of SPACCIM (Tilgner et al., 2005b; Wolke et al., 2005) considers a number of organic species which were previously not treated in such models. The data obtained for carbonyl compounds, carboxylic and DCA in the present study provides the basis for the model initialisation and act as a model validation dataset for the summit Schmücke and the downwind site in Gehlberg (van Pinxteren et al., 2005).

2. Experimental

The upwind station Goldlauter (605 m a.s.l.) is located outside the village at the beginning of a valley leading the air mass to the mountain site Schmücke and later to the downwind site Gehlberg at wind directions between 210° and 250°. During the three selected events out of 14 cloud events the filter and impactor sampling for particulates was operated in parallel. Additionally, gas-phase sampling was carried out to collect aldehydes and ketones as well as organic acids by scrubbers. The three events (E I: 26/27 October 2001, 15 h; E II: 6/8 October 2001, 23 h; E III: 16/17 October 2002, 8.5 h) chosen for further discussion have fulfilled the flow connection criterion.

2.1. Gas phase sampling of carbonyl compounds

In this experiment, two methods of collection and analysis of carbonyl compounds were applied. Solid sorbent cartridges are used with 2,4-dinitrophenylhydrazine (DNPH) as the derivatisation reagent on Silicagel 60 (Merck, Germany, 125–200 μm) on the one hand (Müller et al., 2005) and sep-Pak tC18 tubes (Waters, Millipore Corp.), which are coated with pentafluoro-benzylhydroxylamine (PFBHA) on the other hand. The cartridges were exposed for 2 h at a flow rate of 2.0 and 0.5 l min^{-1}, respectively. For ozone removal, both techniques used KI scrubbers. The sampling trains consisted of a pump and a flow controller. The sampling tubes were stored in a freezer until the analysis.

2.2. Aerosol sampling

For the time-resolved sampling of the bulk aerosol phase (both gas and particle phase), custom-made scrubbers (Kramberger, 2003) similar to the design of Cofer et al. (1985) were used. Their sampling efficiencies were determined by serial connection of scrubbers and were generally >95% for short chain carboxylic acids at the applied flow rates (8 l min^{-1}) and even higher for DCA.

The collection of size segregated particles was performed by a pair of humidity controlled low-pressure Berner-type five-stage impactors (Neusüß et al., 2000) covering aerodynamic diameters (d_p) from 0.05–10 μm (lower cut-offs at $D_p = 0.05$, 0.14, 0.42, 1.2 and 3.5 μm). In front of the impactors, seven parallel tubes (1.5 m × 1 cm) were used after an isokinetic inlet to regulate the relative humidity to 60 ± 5% by heating or cooling the tubes. One impactor was operated with Tedlar foils (for the analysis of ionic components), the other was operated with aluminium foils (for mass determination and OC/EC analyses).

For the sampling of bulk particulate matter (PM), a high-volume sampler (General Metal Works, Inc., PM_{10}) and two Digitel DHA-80 high-volume samplers ($PM_{2.5}$ and PM_1), all using Munktell quartz fibre filters (MK 360) were applied at environmental conditions on the top of the measurement container. The inlet height for all samplers was about 4 m above the ground. Denuders for the separation of gaseous and particulate components were not applied here. Positive sampling artefacts according to Mader et al. (2003) were possible.

2.3. Analysis of carbonyl compounds

During the field experiment up to 35 carbonyl compounds in air were determined with the PFBHA method and the DNPH method. Dicarbonyls and hydroxycarbonyls were determined by the PFBHA method only. These secondary compounds, oxidation products of biogenic hydrocarbons, are of great interest because they might transfer into the aqueous phase during a cloud passage and they are reported as precursors of oxalic acid (Crahan et al., 2004).

Desorption from the DNPH cartridges was made by 3 ml acetonitrile in the laboratory before a gradient HPLC analysis (Müller et al., 2005) using a Waters RP18 column (300*3.9 mm, 4 μm, 60 Å) in a Thermoquest HPLC (AS3000) at 45 °C with UV/VIS detection at 360 and 380 nm (UV3000HR). External 3-point calibrations for 29 compounds were made daily using gravimetric standards.

The PFBHA cartridges were eluted with 1 ml hexane. A fraction (25–100 μL) of this solution was injected using a programmed temperature vaporiser (PTV, solvent-vent mode) into the GC. PFBHA derivatives were detected with an electron capture detector. For identification, a GC-MS system (Varian, Saturn 2100 T) was used. Also dicarbonyl and hydroxycarbonyl compounds were detected. The complete method was described by Schlomski (2000) and Moortgat et al. (2002).

2.4. Analysis of organic acids

While the gas-phase monocarboxylic acids (MCA) were determined from the scrubber samples, the analysis of the particulate DCA took place from samples obtained by three different sampling systems: impactor, scrubber, and quartz fibre filter.

For the analysis of impactor samples, the substrates were cut into small pieces and extracted with deionised water (BARNSTEAD nanopure). After filtration through pre-cleaned syringe filters (Acrodisc 13, 0.45 μm pore size, PALL), the analysis of the extract was carried out by capillary electrophoresis (CE) with indirect UV detection (Spectra Phoresis 1000, Thermo Separation Products). Short-chain DCAs (C_2–C_5) together with some hydroxylated analogues were determined by this method. Details of this method can be found in Neusüß et al. (2000).

For the analysis of the scrubber samples, the salicylate system described in Mainka et al. (1997) was optimised and coupled with a pre-column enrichment under inert gas (water evaporation using a nitrogen stream) to achieve better detection limits. Both MCAs (C_1–C_4) and DCAs (C_2–C_9) were determined from scrubber samples.

From the bulk filter samples, short-chain DCAs (C_4–C_9) and terpenoic acids (pinic and pinonic acid) were determined by a GC-MS method together with various other organic compounds.

2.5. Analysis of further organic compounds on particles

For the GC-MS analysis of organic compounds, the quartz fibre filters were Soxhlet-extracted with CH_2Cl_2/MeOH (4:1) for 22 h. The Soxhlet tubes were extracted with CH_2Cl_2 for 24 h prior the use to obtain low blank values. The sample extract was concentrated to a volume of about 600 μl and separated into three fractions of about 200 μl each. The first fraction was used for the determination of the nonpolar compounds alkanes, pinonaldehyde and ketones. The polar compounds, like DCA and terpenoic acids, were methylated with BF_3-MeOH, as follows: the fraction was evaporated to dryness, 300 μl of BF_3–MeOH were added and heated to 56 °C for 10 min. After cooling, the solution was extracted three times with *n*-hexane. The extracts were combined and evaporated to a small-defined volume. The third fraction for the determination of sugars and alcohols was silylated with BSTFA (*N*,O-bis(trimethylsilyl)-trifluoracetamide) as follows: the fraction was

evaporated to dryness, then 100 µl of BSTFA and 100 µl acetonitrile were added, the mixture was shaken and then heated to 80 °C for 1 h. After cooling, the solution was evaporated to dryness and then dissolved in 200 µl CH_2Cl_2. The individual fractions were spiked with 1-chlorhexadecane as internal standard for quantification. Response factors of this internal standard and the other compounds were used to calculate the concentrations. A more detailed description was given in Plewka et al. (2003).

3. Results

3.1. Carbonyl compounds

The concentration of main carbonyl compounds was summarised in Table 1. Acetaldehyde and acetone are the main compounds besides formaldehyde. The observed concentration of all compounds (Electronic Supplemental Material—ESM, Table 4) was rather low depending on the radiation intensity which is an important parameter of secondary formation of carbonyl compounds. Primary emissions from vegetation are low at the time of the experiment due to the temperatures. Traffic influences and emissions from households are not important. The short-chain carbonyl compounds with their high water solubility were fast deposited on wet surfaces. The results are comparable to other measurements in rural regions at similar temperatures (7–14 °C) and the low level of global radiation ($<300\ W\ m^{-2}$).

Atmospheric mixing ratios of oxalic acid precursor compounds measured during the FEBUKO field experiment at the upwind site (U) ranged from <0.005 (d.l., detection limit) to 0.06 ppb for glyoxal, from <0.005 (d.l.) to 0.085 ppb for methylglyoxal, from 0.006 to 0.145 ppb for glycolaldehyde, from <0.005 (d.l.) to 0.105 ppb for and hydroxyacetone. The concentrations are not as high as measured in July in Papstthum (Moortgat et al., 2002: glyoxal 0.01–0.13 ppb, methylglyoxal 0.03–0.19 ppb, glycolaldehyde 0.01–0.2 ppb, hydroxyacetone 0.02–0.16 ppb); however, they fit well into the autumnal and rural to semi-urban area of the experimental site U. In the following section, profiles of selected compounds which are water soluble will be presented and discussed.

The profiles of E I and E II (Fig. 1) proceeded from the evening until the next midday (duration of cloud events) whereas E III was a night event only. During E I, an increase for glycolaldehyde, methylglyoxal and hydroxyacetone up to midday took place as well as for

Table 1
Most abundant carbonyl compounds concentrations during the events E I–E III

Mean time (UTC) Derivatization method	Formal-dehyde ppbv DNPH	Acetalde-hyde ppbv DNPH	Acetone ppbv DNPH	Propanal ppbv DNPH	Heptanal ppbv DNPH	Methyl glyoxal ppbv PFBHA	Acrolein ppbv PFBHA
E I 26–27 Oct. 01							
26-Oct 23:00	0.86	0.48	0.39	0.077	0.046	0.020	0.040
27-Oct 01:00	0.93	0.49	0.38	0.079	0.017	0.020	0.049
27-Oct 03:00	0.75	0.46	0.44	0.066	0.030	0.021	0.037
27-Oct 05:00	0.69	0.31	0.37	0.058	0.027	0.015	0.032
27-Oct 07:00	0.74	0.35	0.38	0.056	0.020	0.022	0.040
27-Oct 09:00	1.17	0.65	0.58	0.069	0.029	0.032	0.043
27-Oct 11:00	1.47	0.84	0.51	0.064	0.027	0.060	0.045
27-Oct 13:00	0.98	0.52	0.50	0.090	0.031	0.060	0.066
E II 07–08 Oct. 01							
07-Oct 19:00	0.38	0.37	0.24	0.014	0.019	n.m.	n.m.
07-Oct 21:00	0.64	0.41	0.35	0.035	0.029	0.036	0.022
07-Oct 23:00	1.21	0.72	0.30	0.042	0.045	0.055	0.028
08-Oct 01:00	1.38	0.73	0.32	0.024	0.027	0.043	0.020
08-Oct 03:00	0.46	0.30	0.26	0.022	0.017	0.053	0.018
08-Oct 05:00	0.44	0.34	0.37	0.034	0.038	0.064	0.023
08-Oct 07:00	0.54	0.46	0.41	0.037	0.028	0.077	0.026
08-Oct 09:00	0.65	0.60	0.59	0.062	0.034	0.121	0.027
08-Oct 11:00	0.91	0.67	0.65	0.116	0.039	0.147	0.027
E III 16–17 Oct. 02							
16-Oct 22:00	0.59	0.51	0.65	0.023	0.018	0.018	0.010
17-Oct 00:00	0.36	0.28	0.29	0.020	0.015	0.016	0.008
17-Oct 02:00	0.34	0.22	0.23	0.027	0.015	0.015	0.008
17-Oct 04:00	0.17	0.12	0.30	0.035	0.014	0.019	0.015

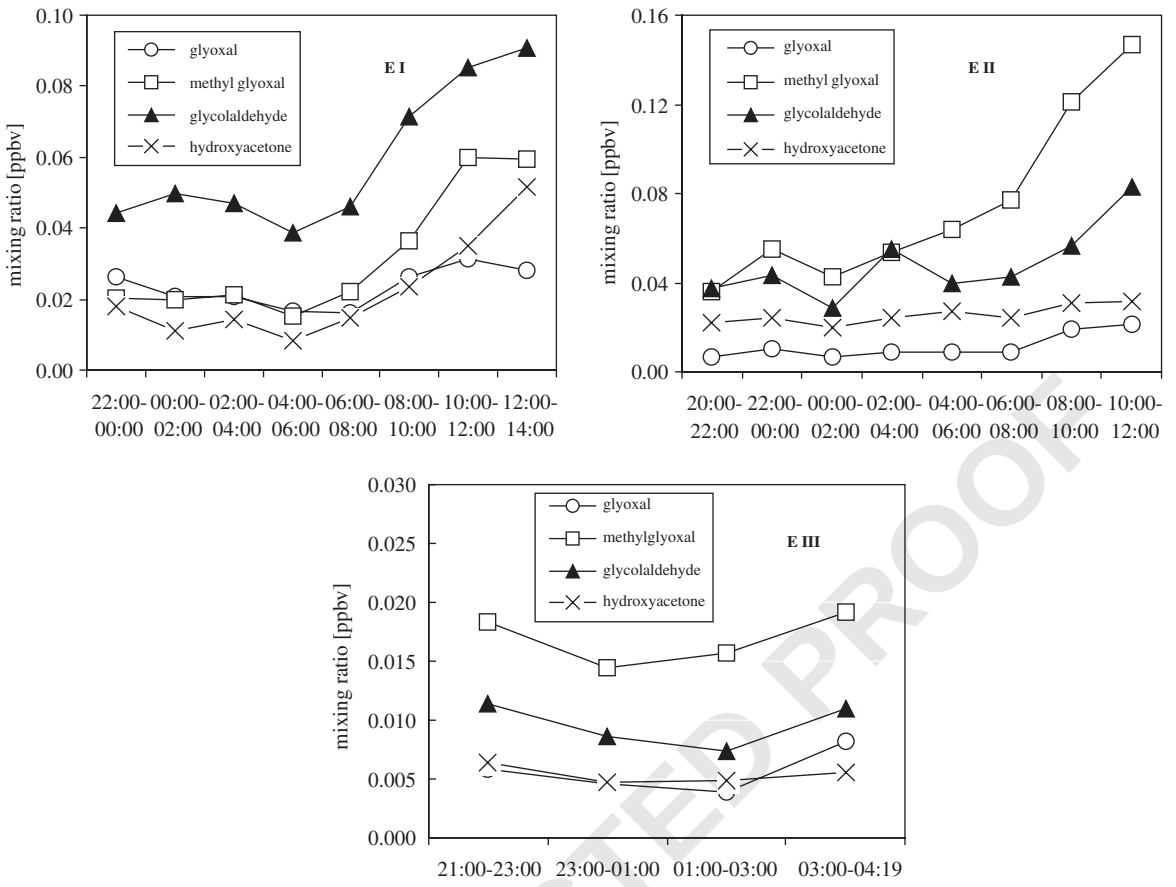

Fig. 1. Variation of mixing ratios of selected carbonyl compounds during E I, E II and E III.

formaldehyde. During E II, this increase was observed in a similar manner, except for hydroxyacetone. The observed night peaks of formaldehyde and acetaldehyde could have their origin in transports from the Stuttgart/Würzburg region. In the four samples of E III, a nearly constant mixing ratio was observed. This observation is not unexpected because it was the night time and the low temperature event. In E I, other components of aerosol were found in higher concentrations than in E II (Gnauk et al., 2005). The differences between the two first events were on one hand the initial concentrations of glyoxal and on the other hand the difference in the increase of the carbonyl compounds. Both are smaller in the event E II, which cannot be connected with the global radiation, since it is even higher in E II. Anthropogenic influences can explain the higher values. They were measured during the night from 26–27 October 2001, the night of Friday to Saturday, which had obviously more traffic on the roads than from Sunday to Monday (7–8 October 2001). In addition, a carbon monoxide peak can be constituted only in E I at 11:00, which hints for an increased traffic volume.

3.2. Carboxylic and dicarboxylic acids

Due to their low vapour pressure, DCAs are only emitted at the high temperatures of combustion processes and more likely formed by photochemical oxidation of volatile precursors. In contrast, short-chain MCAs are emitted in several biogenic processes.

Detected mixing ratios for MCAs during the FEBUKO field campaigns 2001 and 2002 are generally in the range that is expected and documented for rural areas and conditions of low photochemical activity (Table 2 and ESM, Table 1). Particularly, values for acetic and formic acid resemble literature values for the free troposphere (Helas et al., 1992; Chapman et al., 1995; Talbot et al., 1997) and are about one order of magnitude lower than those detected with the same sampling method and analytical system during the summer months in the urban atmosphere (Kramberger, 2003).

From the time-resolved scrubber measurements, an increase of MCAs mixing rations was observed from night to midday during the events I and II, while during the night event E III nearly constant mixing ratios were

Table 2
Organic compounds in aerosol particles during FEBUKO events (all data in ng m^{-3})

Event	I	II	III	Event	I	II	III
Alkanes				*Dicarboxylic acids*			
C20	0.3	0.3	NA	Oxalic[a]	70.0	45.1[d]	32.2
C21	0.3	0.2	NA	Oxalic[b]	35.3	30.6	23.6
C22	0.5	0.4	NA	Malonic[a]	14.8	7.7[d]	7.5
C23	0.6	0.4	NA	Malonic[b]	25.6	14.3	5.2
C24	1.6	1.7	NA	Succinic[a]	8.4	3.5[d]	8.7
C25	1.0	0.8	NA	Succinic [b]	20.6	7.1	2.9
C26	1.0	0.7	NA	Succinic[c]	13.9	2.1	11.0
C27	0.8	0.6	NA	Glutaric[a]	0.9	0.3[d]	2.3
C28	0.7	0.6	NA	Glutaric [b]	23.1	15.1	<DL
C29	0.9	1.0	NA	Glutaric[c]	1.3	0.2	1.2
C30	0.5	0.4	NA	Adipic[c]	3.2	1.1	47.9
C31	0.5	0.5	NA	Pimelic[c]	0.3	0.1	<DL
Carbonyl compounds				Suberic[a]	1.6	<DL	2.0
Pinonaldehyde	3.4	5.2	33.6	Suberic[c]	0.6	0.2	2.3
6,10,14-Trimethylpentadecanone	0.5	0.5	0.6	Azelaic[a]	2.2	1.8[d]	18.9
Alcohols and sugars				Azelaic[c]	2.1	1.1	7.2
Hexadecanol	0.4	1.1	9.0	Tartronic[b]	3.8	1.9	0.3
Octadecanol	3.4	2.9	14.6	Malic[b]	10.9	10.8	5.9
Levoglucosan	62.0	56.4	58.4	Tartaric[b]	4.5	3.9	0.8
Xylitol	47.0	2.4	103.1	Citramalic[b]	1.7	2.0	<DL
Terpenoic acids				Maleic[b]	6.8	1.2	<DL
Pinic	0.9	0.7	1.4				
Pinonic	1.4	0.5	2.6				

<DL: concentration below detection limit.
[a]Determined from scrubber samples, averaged over event.
[b]Determined from impactor samples, summed up over all impactor stages.
[c]Determined from filters.
[d]Only part 3 of the event; NA: not available due to high blanks.

observed (Fig. 2). A slight increase of the photochemical activity during the events I and II in the morning hours is the favourable cause for this.

In Table 2, the concentrations of DCAs for E I–E III are given. Some acids were determined in parallel from different sampling systems and with different analytical methods (see the experimental section). For the time-resolved scrubber samples time-weighted average values for the whole event are given. As the scrubbers were not operated during the first two parts of event II, only the third part was considered in this case. For the size-resolved impactor samples the concentrations were summed up over the five stages. Succinic and glutaric acid were quantified together with their branched isomers, which hampers a direct comparison with the other values. All DCA data can be found in detail in ESM, Tables 1 and 2. A comparison of the data reveals differences up to a factor of 2–3 in some cases. Similar deviations were reported by other authors who compared filter-based sampling techniques with impactors for the determination of DCAs (Kerminen et al., 1999; Kerminen et al., 2000; Mochida et al., 2003). Evaporative losses of DCAs due to the reduced pressure on the lower impactor stages were suggested as one possible reason (Kerminen et al., 2000; Mochida et al., 2003). Negative artefact formation on filters due to chemical reactions during sampling was proposed as another possible reason (Kerminen et al., 1999). These sampling artefacts are likely to be at least some of the sources of uncertainty also in our study. Therefore, in cases when one single value is needed for a given species, the average over the results from the different procedures seems to be the most suitable solution. This was done for the initialisation of model calculations by Tilgner et al. (2005b).

Within the substance class of DCA, oxalic acid is the most abundant, followed by malonic and succinic acid. This relative abundance is commonly found in the atmospheric aerosol. Longer-chain DCAs usually showed significantly lower concentrations. Among the hydroxylated acids, malic acid (hydroxysuccinic acid) showed increased concentrations. In Table 3, literature data for particulate DCAs at rural or remote locations in Europe are given. Generally, the concentrations of the

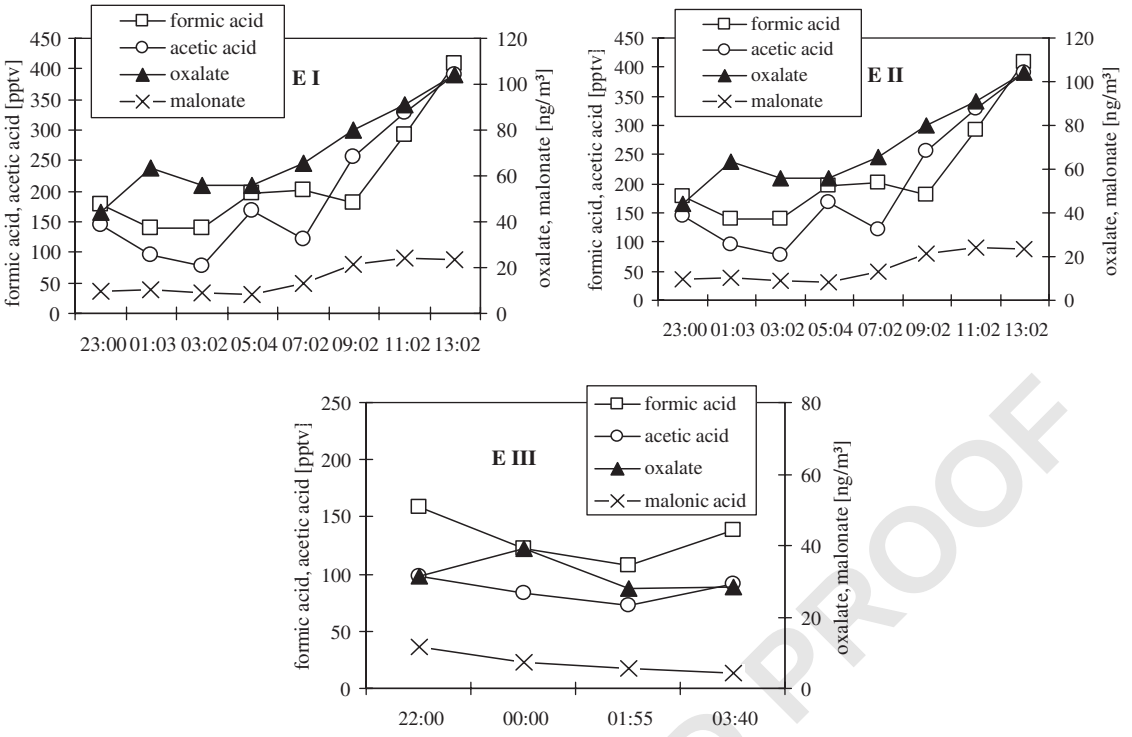

Fig. 2. Variation of mixing ratios and concentrations of the most important acids and diacids during E I, E II and E III.

short-chain diacids (C2–C5, including hydroxylated derivatives) found at the upwind station in this study fit well into most of the reported ranges. The same applies to the longer-chain acids, where the available data are, however, much sparser. Two notable exceptions are the concentrations of adipic and azelaic acid during E III. They are much higher than the 2001 concentration (E I and E II) and the reported values from the Fichtelgebirge (Plewka et al., 2003). Similarly high concentrations were also found for other events at the beginning of the 2002 FEBUKO field campaign, which are not reported here. These unexpectedly high concentrations decreased during the following weeks and arrived at the level of the preceding year at the end of the campaign. Kawamura et al. (1996) found similar results during long-time measurements of azelaic acid in remote areas and there is some evidence that seasonally specific precursor substances are emitted by trees during the autumnal stage of vegetation. The difference between both field campaigns may be induced by the different average temperatures in the previous months and thereby delayed period of vegetation in 2002, whereas the corresponding effect in 2001 was completed before the start of the field campaign. As adipic acid shows a similar behaviour during the 2002 campaign, we conclude that it may also be produced from specific biogenic sources during autumn.

In Fig. 3, the size distributions of the four most abundant DCA (oxalic, malonic, succinic, and malic acid) are shown. The concentration profiles over the sampled size range look clearly different for the three investigated events. During E I, highest concentrations are found on impactor stage 3 ($D_p = 0.42-1.2\,\mu m$), indicating a dominant accumulation mode for all four diacids. For E II, besides the highest concentrations on stage 3, a relative increase of concentrations on impactor stage 2 ($D_p = 0.14-0.42\,\mu m$) can be seen. During E III, the size distributions look quite different due to less distinct differences between concentrations of stages 2, 3, and 4 (stage 4: $D_p = 1.2-3.5\,\mu m$). The observation of a dominant accumulation mode for DCA is reported by various authors (Krivacsy and Molnar, 1998; Neusüß et al., 2000; Yao et al., 2002). Also, strong supermicron modes were found, especially for marine air masses, indicating an association of diacids with sea salt (Kerminen et al., 1999; Mochida et al., 2003; Neusüß et al., 2000). This seems to be the case for event III with relatively elevated concentrations in the coarse particle fraction.

The temporal profile of particulate oxalic and malonic acid during the three events can be found in Fig. 2.

Table 3
Literature data of particulate organic compounds at non-urban locations in Europe , min–max (mean), all concentrations in ng m^{-3}

Location									Reference
Various organic compounds	Alkanes	Pinonaldehyde	Levoglucosan	Pinic acid	Pinonic acid				
Fichtelgebirge, GER	0.23–9.71	0.3–1.4		0.2–6.3	0.3–2.3				Plewka et al. (2003)
Abies forest, GRE	5.5								Alves and Pio (2000)
Melpitz, GER	14–200								Plewka et al. (2004)
Hyytiälä, FIN		6.6		7.5	12.5				Alves et al. (2002)
Forest sites[a]		0.2–32.0			0.2–71.0				Kavouras and Stephanou (2002)
Gent, BEL[b]			121–1133						Zdráhal et al. (2002)
Gent, BEL[c]			4.1–34.6						Zdráhal et al. (2002)
Pertouli, GRE		0.01–13.2		0.4–4.4	1–25.7				Kavouras et al. (1999a)
Tábua, POR	0–2.2	0–13.2		0.4–82.7	1.5–97.7				Kavouras et al. (1999b)
San Bernardino, USA		(1.0)		(0.5)	(0.8)				Yu et al. (1999)
Pertouli, GRE		0.12–0.87							Pio et al. (2001)
Dicarboxylic acids	Oxalic acid	Malonic acid	Succinic acid	Glutaric acid	Adipic acid	Pimelic acid	Suberic acid	Azelaic acid	
Kap Arkona, GER	21–432 (147)	<3.7–41 (18)	(<19)	<4.8–66 (11)					Röhrl and Lammel (2001)
Merseburg, GER	<4.4–157 (57)	<7.5–21 (4.8)	<4.4–18 (4.2)	<9.6					Röhrl and Lammel (2001)
Falkenberg, GER	173–699 (251)	15–128 (64)	8.7–100 (25)	6.5–70 (21)					Röhrl and Lammel (2001)
Sonnblick, AUT	(153)	(22)	(14)	(2.7)	(4.4)				Limbeck and Puxbaum (1999)
Melpitz, GER	31–85	4–46	8–27						Plewka et al. (2004)
Crete Island, GRE[b]	(68.6)		(3.3)	(2.5)					Bardouki et al. (2003)
Luuki, FIN[d]	10–250	0–18	0–30						Kerminen et al. (2000)
Tihany, HUN[e]	14–44								Kiss et al. (1997)
Mace Head, IRE[b]	<5–125 (39)	<2–8 (3)							Kleefeld et al. (2002)
Sevettijarvi, FIN	<2.8–58 (8.6)	<0.2–15 (1.5)	<0.6–41 (2.9)	<0.2–24 (2.5)					Ricard et al. (2002)
Veszprém, HUN[b]	(129)	(30)	(33)						Meszaros et al. (1997)
Fichtelgebirge, GER			3.2–16.0	0.6–1.8	1.6–3.3	0.4–1.4	0.2–1.1	0.2–2.5	Plewka et al. (2003)
Other dicarboxylic acids	Tartronic acid	Malic acid	Tartaric acid	Maleic acid					
Rural Germany[f]		<2.5–194 (34)	<0.2–23 (4.0)	<0.2–13 (3.2)					Röhrl and Lammel (2002)
Melpitz, GER	0–10.2	0–37.4							Plewka et al. (2004)
Melpitz, GER		3.1–14	<0.1–1.5						Carvalho et al. (2003)
Hyytiälä, FIN		0.1–8.0	<0.1–0.7						Carvalho et al. (2003)
Sevettijarvi, FIN		<0.2–36 (3.3)							Ricard et al. (2002)

[a]Two sites: Tábua, Portugal, and Pertouli, Greece.
[b]Winter season.
[c]Summer season.
[d]$PM_{2.3}$, estimated from figure.
[e]Estimated from figure.
[f]Two sites: Merseburg and Falkenberg.

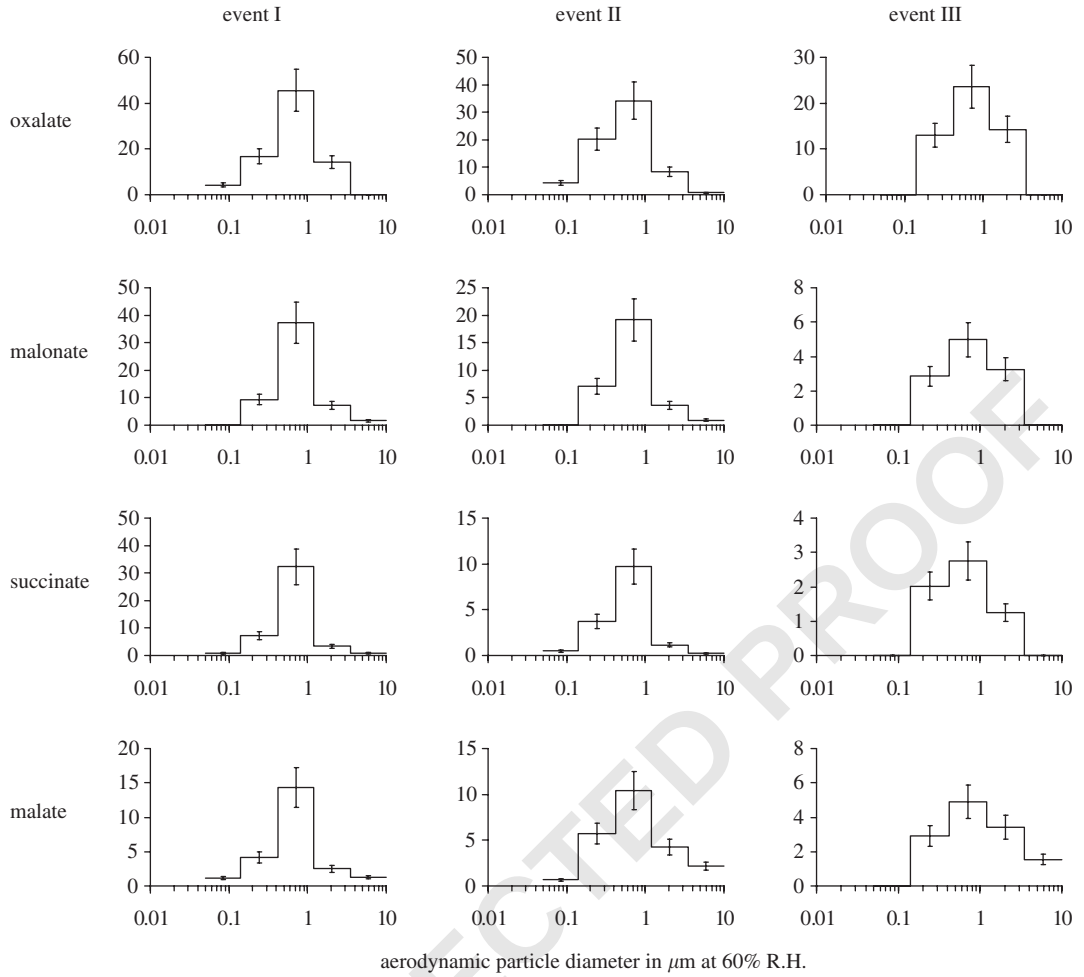

Fig. 3. Size distributions ($\Delta C/\Delta \log D_p$ in ng m^{-3}) of the most abundant dicarboxylic acids. Error bars represent the analytical error.

Apart from a dissertation thesis (Kramberger, 2003), this is to our knowledge the first report about continuous determination of particulate DCAs with good time resolution (2 h). From E I and E II, which started during the night and continued into daytime, it can be seen, that the concentrations of oxalic and malonic acid show a clear increase in the morning hours up to the maximum value at the end of the event around midday. During E III, which was shorter and only during the night, the concentrations were much more stable. Reasons for the increasing concentrations might lie in enhanced emissions or enhanced photochemical production during the day hours. Kawamura and Kaplan (1987) discuss automobile exhaust as source for DCAs. While local emissions are unlikely to account for the observations, anthropogenic emissions on the air trajectory might be important. For example the highly industrialised Rhine-Main-area or the Stuttgart–Würzburg-region in a distance of about 120–200 km might influence the chemical composition of the aerosol particles reaching Goldlauter. Photochemical activity due to increasing solar radiation could also contribute to the findings. Ervens et al. (2003) treat the formation of oxalic acid in a complex multiphase chemistry model from glyoxal as one gaseous precursor compound. As can be seen from Fig. 1 the glyoxal concentrations show a similar profile with increasing concentrations during the day hours. Formation pathways from different precursors are likely for the short-chain DCAs, which can all attribute to the observed day/night profile.

3.3. Non methane hydrocarbons (NMHC)

The NMHC measured during the events E I and E II are important for the determination of anthropogenic influences to the site of investigation. The concentration of long-chain alkanes, determined from filters, are low (Tables 2 and 3) in comparison to our own measurements at urban and suburban sites in Germany, but high against remote measurements (Schneider and Gagosian, 1985; Sicre and Peltzer, 2004).

Particles containing alkanes result both from fossil fuel combustion and primary biogenic processes (vascular plant waxes, pollen, etc.). Interestingly, clues about the origin of alkane aerosol are obtained from the ratio of the concentration of *n*-alkanes of odd numbers to even numbers of carbon atoms. Land-based vegetation preferentially releases alkanes with odd carbon numbers in the C19-C35 range with a maximum at C29 and C31, whereas alkanes of anthropogenic or marine origin lack such a preference. The CPI_{odd} (carbon preference index) was calculated as the ratio of odd and even numbered *n*-alkanes and has a value of about 0.9 that hints to mainly anthropogenic sources of alkanes.

3.4. Particle-bounded compounds of biogenic origin

The concentrations of determined organic compounds in the filter particulates are presented in Table 1. Highest concentrations of single organic compounds were detected for xylitol, pinonaldehyde and levoglucosan. Xylitol is widely distributed throughout the nature in fruits, berries and hardwood. Levoglucosan is known to be derived solely from the breakdown of polysaccharide materials during biomass burning and therefore serve as excellent indicator for the contribution of biomass burning to the overall aerosol mass (Simoneit et al., 1999). The measured and averaged concentrations of 59 ng m^{-3} are slightly higher than the summer concentrations of 19.1 ng m^{-3} in Ghent (Belgium), but lower than the winter concentrations of 420 ng m^{-3} there (Pashynska, et al., 2002). The two measured alcohols are probably of biogenic origin and are contained in plant waxes (Sicre and Peltzer, 2004). The pinonaldehyde concentrations are similar during E I and E II, but during E III were the concentrations ten times higher than in E I and E II. For the other terpene oxidation products, pinic and pinonic acid, also the highest concentrations were found during E III. These terpene oxidation products, especially pinonaldehyde, have high vapour pressures and therefore the gas phase concentrations are much higher than the particle phase concentrations. Ambient conditions like the temperature can strongly influence the particle phase concentration. Only a few data are known from literature and are summarised in Table 3. From Yu et al. (1999) and Kavouras et al. (1999a), different distributions between gas and particle phase are reported for pinonaldehyde, pinic and pinonic acid. Trimethylpentadecanone is described as a photo-oxidation product of phytol of chlorophyll and the detected concentrations are very low (Alves and Pio, 2000). These authors also measured alkanes in an Abies forest in central Greece and found a concentration of 5.5 ng m^{-3} and agree with the presented concentrations here.

4. Summary

At the upwind site of a hill-capped cloud, a set of data was collected for organic compounds in the gas phase and in PM. High time resolution and size class information were delivered for the DCA.

The concentrations of organic gaseous and particulate compounds are generally in the range that is expected and documented for rural areas and conditions of low photochemical activity. Minor anthropogenic influences can be fixed from the gas phase and particle composition. The low radiation intensity and the temperatures are further aspects influencing the concentrations of investigated compounds.

For acetic acid and formic acid mixing ratios, one order of magnitude lower than in urban summer samples were detected. For DCA (oxalic, malonic and succinic acid) and the main carboxylic acids (formic and acetic acid) 2-h samples show increasing concentrations during the first events from night to midday. A nearly identical variation is found for carbonyl compounds (formaldehyde, propanal, methyl glyoxal and glycolaldehyde). DCA are distributed mainly in the accumulation mode (0.14–1.2 μm) of the investigated size classes.

Uncited references

Hartmann et al., 1989; Montgomery, 1991; Müller, 1997; Narukawa et al., 2003; Sanhueza et al., 1992; Sempéré and Kawamura, 1994; Tilgner et al., 2005a; Wang and John, 1988.

Acknowledgements

This work was financially supported by the German BMBF (AFO2000, project 07ATF01). We thank H. Bachmann, S. Haferkorn, N. Heim, A. Kappe, E. Neumann, C. Sedello, and A. Thomas for their support in the field and laboratory work.

Appendix A. Electronic Supplemental Material

The online version of this article contains additional supplementary data. Please visit doi:10.1016/j.atmosenv.2005.02.008.

References

Alves, C., Carvalho, A., Pio, C., 2002. Mass balance of organic carbon fractions in atmospheric aerosols. Journal of Geophysical Research 107 (D21), 8345.

Alves, C.A., Pio, C., 2000. Particulate size distributed organic compounds in a forest atmosphere. Environmental Science & Technology 34, 4287–4293.

Bardouki, H., Liakakou, H., Economou, C., Sciare, J., Smolík, J., Zdímal, V., Eleftheriadis, K., Lazaridis, M., Dye, C., Mihalopoulos, N., 2003. Chemical composition of size-resolved atmospheric aerosols in the eastern Mediterranean during summer and winter. Atmospheric Environment 37 (2), 195–208.

Carlier, P., Hannachi, H., Mouvier, G., 1986. The chemistry of carbonyl compounds in the atmosphere—a review. Atmospheric Environment 20, 2079–2099.

Carvalho, A., Pio, C., Santos, C., 2003. Water-soluble hydroxylated organic compounds in German and Finnish aerosols. Atmospheric Environment 37 (13), 1775–1783.

Chapman, E., Kenney, D.V., Busness, K., Thorp, J., Spicer, C.W., 1995. Continuous airborne measurements of gaseous formic and acetic acids over the western North Atlantic. Geophysical Research Letters 22, 405–408.

Cofer, W.R., Collins, V.G., Talbot, R.W., 1985. Improved aqueous spray absorber for collection of soluble atmospheric trace gases. Environmental Science & Technology 19, 557–560.

Crahan, K.K., Hegg, D., Covert, D.S., Jonsson, H., 2004. Oxalic acid production in the costal marine atmosphere. Sixth Conference on Atmospheric Chemistry: Air Quality in Megacities: http://ams.confex.com/ams/pdfpapers/70442.pdf.

Ervens, B., George, C., Williams, J.E., Buxton, G.V., Salmon, G.A., Bydder, M., Wilkinson, F., Dentener, F., Mirabel, P., Wolke, R., Herrmann, H., 2003. CAPRAM 2.4 (MODAC mechanism): an extended and condensed tropospheric aqueous phase mechanism and its application. Journal of Geophysical Research 108 (D14), 4426.

Gnauk, T., Brüggemann, E., Müller, K., Chemnitzer, R., Rüd, C., Galgon, D., Wiedensohler, A., Acker, K., Auel, R., Wieprecht, W., Möller, D., Jaeschke, W., Herrmann, H., 2005. Aerosol characterisation at the FEBUKO upwind station Goldlauter (I): particle mass, main ionic components, OC/EC, and mass closure. Atmospheric Environment, this issue.

Grosjean, D., Wright, B., 1983. Carbonyls in urban fog, ice fog, cloudwater and rainwater. Atmospheric Environment 17, 2093–2096.

Hartmann, W.R., Andreae, M.O., Helas, G., 1989. Measurements of organic acids over central Germany. Atmospheric Environment 23, 1531–1533.

Helas, G., Andreae, M.O., Hartmann, W.R., 1992. Behavior of atmospheric formic and acetic acid in the presence of hydrometeors. Journal of Atmospheric Chemistry 15, 101–115.

Herrmann, H., Tilgner, A., Barzaghi, P., Majdik, Z., Gligorovski, S., Poulain, L., Monod, A., 2005a. Towards a more detailed description of tropospheric aqueous phase organic chemistry: CAPRAM 3.0. Atmospheric Environment, this issue.

Herrmann, H., Wolke, R., Müller, K., Brüggemann, E., Gnauk, T., Barzaghi, P., Mertes, S., Lehmann, K., Massling, A., Birmili, W., Wiedensohler, A., Wieprecht, W., Acker, K., Jaeschke, W., Kramberger, H., Syrcina, B., Bächmann, K., Collett Jr., J.L., Galgon, D., Schwirn, K., Nowak, A., van Pinxteren, D., Plewka, A., Chemnitzer, R., Rüd, C., Hofmann, D., Tilgner, A., Diehl, K., Heinold, B., Hinneburg, D., Knoth, O., Sehili, A.M., Simmel, M. Wurzler, S., Mauersberger, G., Majdik, Z., Müller, F., 2005b. FEBUKO and MODMEP: Field measurements and modelling of aerosol and cloud multiphase processes. Atmospheric Environment, this issue.

Kavouras, I.G., Stephanou, E.G., 2002. Direct evidence of atmospheric secondary aerosol formation in forest atmosphere through heteromolecular nucleation. Environmental Science & Technology 36, 5083–5091.

Kavouras, I.G., Mihapolous, N., Stephanou, E.G., 1999a. Formation and gas/particle partitioning of monoterpenes photo oxidation products over forests. Geophysical Research Letters 26, 55–58.

Kavouras, I.G., Mihalopoulos, N., Stephanou, E.G., 1999b. Secondary aerosol formation vs. primary organic aerosol emission: in situ evidence for the chemical coupling between monoterpene acidic photooxidation products and new particle formation over forests. Environmental Science & Technology 33, 1028–1037.

Kawamura, K., Ikushima, K., 1993. Seasonal changes in the distribution of dicarboxylic acids in the urban atmosphere. Environmental Science & Technology 27, 2227–2235.

Kawamura, K., Kaplan, I.R., 1987. Motor exhaust emissions as a primary source for dicarboxylic acids in Los Angeles ambient air. Environmental Science & Technology 21, 105–110.

Kawamura, K., Kasukabe, H., Barrie, L.A., 1996. Source and reaction pathways of dicarboxylic acids, ketoacids and dicarbonyls in arctic aerosols: one year of observations. Atmospheric Environment 30 (10–11), 1709–1722.

Kerminen, V.M., Teinila, K., Hillamo, R., Mäkelä, T., 1999. Size-segregated chemistry of particulate dicarboxylic acids in the arctic atmosphere. Atmospheric Environment 33, 2089–2100.

Kerminen, V.M., Ojanen, C., Pakkanen, T., Hillamo, R., Aurela, M., Merilainen, J., 2000. Low-molecular-weight dicarboxylic acids in an urban and rural atmosphere. Journal of Aerosol Science 31 (3), 349–362.

Kiss, G., Gelencser, A., Krivacsy, Z., Hlavay, J., 1997. Occurrence and determination of organic pollutants in aerosol, precipitation, and sediment samples collected at Lake Balaton. Journal of Chromatography A 774 (1–2), 349–361.

Kleefeld, S., Hoffer, A., Krivacsy, Z., Jennings, S.G., 2002. Importance of organic and black carbon in atmospheric

aerosols at Mace Head, on the West Coast of Ireland (53 degrees 19′N, 9 degrees 54′W). Atmospheric Environment 36 (28), 4479–4490.

Kramberger, H., 2003. Carbonsäuren und dicarbonsäuren in atmosphärischen Mehrphasenprozessen—Analytische Entwicklungen und feldexperimentelle Untersuchungen. Ph.D. Thesis, Technische Universität Darmstadt.

Krivacsy, Z., Molnar, A., 1998. Size distribution of ions in atmospheric aerosols. Atmospheric Research 46, 279–291.

Laj, P., Fuzzi, S., Facchini, M.C., Lind, J.A., Orsi, G., Reiss, M., Maser, R., Jaeschke, W., Seyffer, E., Helas, G., Acker, K., Wieprecht, W., Möller, D., Arends, B.G., Möls, J.J., Colvile, R.N., Gallagher, M.W., Beswick, K.M., Hargreaves, K.J., Storeton-West, R.L., Sutton, M.A., 1997. Cloud processing of soluble gases. Atmospheric Environment 31, 2589–2598.

Limbeck, A., Puxbaum, H., 1999. Organic acids in continental background aerosols. Atmospheric Environment 33, 1847–1852.

Lüttke, J., Levsen, K., 1997. Phase partitioning of phenol and nitrophenols in clouds. Atmospheric Environment 31, 2649–2655.

Mader, B.T., Schauer, J.J., Seinfeld, J.H., Flagan, R.C., Yu, J.Z., Yang, H., Lim, H.-J., Turpin, B.J., Deminter, J.T., Heidemann, G., Bae, M.S., Quinn, P., Bates, T., Eatough, D.J., Huebert, B.J., Bertram, T., Howell, S., 2003. Sampling methods used for the collection of partice-phase organic and elemental carbon during ACE-Asia. Atmospheric Environment 37, 1435–1449.

Mainka, A., Ebert, P., Kibler, M., Prokop, T., Tenberken, B., Bächmann, K., 1997. Development of new methods for the analysis of carboxylic acids and carbonyl compounds in size classified raindrops by CE for application in modelling atmospheric processes. Chromatographia 45, 158–162.

Meszaros, E., Barcza, T., Gelencser, A., Hlavay, J., Kiss, G., Krivacsy, Z., Molnar, A., Polyak, K., 1997. Size distributions of inorganic and organic species in the atmospheric aerosol in Hungary. Journal of Aerosol Science 28 (7), 1163–1175.

Mochida, M., Umemoto, N., Kawamura, K., Uematsu, M., 2003. Bimodal size distribution of C-2-C-4 dicarboxylic acids in the marine aerosols. Geophysical Research Letters 30 (13), 1672.

Montgomery, D.C., 1991. Desing and Analysis of Experiments, third ed. Wiley, Singapore.

Moortgat, G.K., Grossmann, D., Boddenberg, A., Dallmann, G., Ligon, A.P., Turner, W.V., Gäb, S., Slemr, F., Wieprecht, W., Acker, K., Kibler, M., Schlomski, S., Bächmann, K., 2002. Hydrogen peroxide, organic peroxide and higher carbonyl compounds determined during the BERLIOZ campaign. Journal of Atmospheric Chemistry 42, 443–463.

Müller, K., 1997. Determination of aldehydes and ketones in the atmosphere—a comparative long time study at an urban and a rural site in Eastern Germany. Chemosphere 35, 2093–2106.

Müller, K., Haferkorn, S., Grabmer, W., Wisthaler, A., Hansel, A., Kreuzwieser, J., Cojocariu, C., Rennenberg, H., Herrmann, H., 2005. Biogenic carbonyl compounds from a coniferous forest in Germany. Atmospheric Environment, submitted.

Narukawa, M., Kawamura, K., Takeuchi, N., Nakajima, T., 1999. Distribution of dicarboxylic acids and carbon isotopic compositions in aerosols from 1997 Indonesian forest fires. Geophysical Research Letters 26, 3101–3104.

Narukawa, M., Kawamura, K., Okada, K., Zaizen, Y., Makino, Y., 2003. Aircraft measurement of dicarboxylic acids in the free tropospheric aerosols over the western to central North Pacific. Tellus Series B—Chemical and Physical Meteorology 55, 777–786.

Neusüß, C., Pelzing, M., Plewka, A., Herrmann, H., 2000. A new analytical approach for size-resolved speciation of organic compounds in atmospheric aerosol particles: methods and first results. Journal of Geophysical Research—Atmospheres 105, 4513–4527.

Pashynska, V., Vermeylen, R., Vas, G., Maenhaut, M., Claeys, M., 2002. Development of a gas chromatographic/ion trap mass spectrometric method for the determination of levoglucosan and saccharidic compounds in atmospheric aerosols. Application to urban aerosols. Journal of Mass Spectrometry 37, 1249–1257.

Pio, C.A., Alves, C.A., Duarte, A.C., 2001. Identification, abundance and origin of organic particulate matter in a Portuguese rural area. Atmospheric Environment 35, 1365–1375.

Plewka, A., Hofmann, D., Müller, K., Herrmann, H., 2003. Determination of biogenic organic compounds in airborne particles by solvent extraction, derivatisation and mass spectrometric detection. Chromatographia 57 (Suppl.), 253–259.

Plewka, A., Gnauk, T., Neusüß, C., Brüggemann, E., Herrmann, H., 2004. Size-resolved aerosol characterization for a polluted episode at the IfT research station Melpitz in autumn 1997. Journal of Atmospheric Chemistry 48, 131–156.

Ricard, V., Jaffrezo, J.L., Kerminen, V.M., Hillamo, R.E., Sillanpaa, M., Ruellan, S., Liousse, C., Cachier, H., 2002. Two years of continuous aerosol measurements in northern Finland. Journal of Geophysical Research—Atmospheres 107 (D11).

Röhrl, A., Lammel, G., 2001. Low molecular weight dicarboxylic acids and glyoxylic acid: seasonal and air mass characteristics. Environmental Science & Technology 35, 95–101.

Röhrl, A., Lammel, G., 2002. Determination of malic acid and other C-4 dicarboxylic acids in atmospheric aerosol samples. Chemosphere 46, 1195–1199.

Sanhueza, E., Santana, M., Hermoso, M., 1992. Gas- and aqueous-phase formic and acetic acids at a tropical cloud forest site. Atmospheric Environment 26A, 1421–1426.

Satsumabayashi, H., Kurita, H., Yokouchi, Y., Ueda, H., 1990. Photochemical formation of particulate dicarboxylic acids under long-range transport in central Japan. Atmospheric Environment 24, 1443–1450.

Saxena, P., Hildemann, L.M., 1996. Water-soluble organics in atmospheric particles: a critical review of the literature and application of thermodynamics to identify candidate compounds. Journal of Atmospheric Chemistry 24, 57–109.

Schlomski, S., 2000. Development of analytical methods for the determination of carbonyl compounds in the atmosphere. Ph.D. Thesis, TU Darmstadt.

Schneider, J.K., Gagosian, R.B., 1985. Particle size distribution of lipids in aerosols off the coast of Peru. Journal of Geophysical Research 90 (D5), 7889–7898.

Sempéré, R., Kawamura, K., 1994. Comparative distributions of dicarboxylic acids and related polar compounds in snow, rain and aerosols from urban atmosphere. Atmospheric Environment 28, 449–459.

Sicre, M.A., Peltzer, E.T., 2004. Lipid geochemistry of remote aerosols from the southwestern pacific ocean sector. Atmospheric Environment 38, 1615–1624.

Simoneit, B.R.T., Schauer, J.J., Nolte, C.G., Oros, D.R., Elias, V.O., Fraser, M.P., Rogge, W.F., Cass, G.R., 1999. Levoglucosan, a tracer for cellulose in biomass burning and atmospheric particles. Atmospheric Environment 33, 173–182.

Singh, H.B., Kanakidou, M., Crutzen, P.J., Jacobs, D.J., 1995. High concentrationsand photochemical fate of oxygenated hydrocarbons in the global troposphere. Nature 78, 50–54.

Talbot, R.W., Dibb, J.E., Lefer, B.L., Scheuer, E.M., Bradshaw, J.D., Sandholm, S.T., Smyth, S., Blake, D.R., Blake, N.J., Collins, J.E., Gregory, G.L., 1997. Large-scale distributions of tropospheric nitric, formic, and acetic acids over the western Pacific Basin during wintertime. Journal of Geophysical Research 102, 28,303–28,313.

Tilgner, A., Heinold, B., Nowak, A., Herrmann, H., 2005a. Meteorological characterisation of the FEBUKO hill cap cloud experiments, Part I: synoptic characterisation of measurement periods. Atmospheric Environment, this issue.

Tilgner, A., Majdik, Z., Sehili, A.M., Simmel, M., Wolke, R., Herrmann, H., 2005b. SPACCIM: simulations of the multiphase chemistry occurring in the FEBUKO hill cap cloud experiments. Atmospheric Environment.

van Pinxteren, D., Plewka, A., Hofmann, D., Müller, K., Kramberger, H., Svrcina, B., Bächmann, K., Jaeschke, W., Mertes, S., Collett Jr., J.L., Herrmann, H., 2005. Schmücke hill cap cloud and valley stations aerosol chemical composition during FEBUKO (II): organic compounds. Atmospheric Environment, this issue.

Wang, H.-C., John, W., 1988. Characteristics of the Berner impactor for sampling inorganic ions. Aerosol Science and Technology 8, 157–172.

Warneck, P., 2003. In-cloud chemistry opens pathway to the formation of oxalic acid in the marine atmosphere. Atmospheric Environment 37, 2423–2427.

Winiwarter, W., Fierlinger, H., Puxbaum, H., Facchini, M.C., Arends, B.G., Fuzzi, S., Schell, D., Kaminski, U., Pahl, S., Schneider, T., Berner, A., Solly, I., Kruisz, C., 1994. Henry's law and the behavior of weak acids and bases in fog and clouds. Journal of Atmospheric Chemistry 19, 173–188.

Wolke, R., Sehili, A.M., Simmel, M., Knoth, O., Tilgner, A., Herrmann, H., 2005. SPACCIM: a parcel model with detailed microphysics and complex multiphase chemistry. Atmospheric Environment, this issue.

Yao, X.H., Fang, M., Chan, C.K., 2002. Size distributions and formation of dicarboxylic acids in atmospheric particles. Atmospheric Environment 36, 2099–2107.

Yu, J., Griffin, R.J., Cocker, D.R., Flagan, R.C., Seinfeld, J.H., Blanchard, P., 1999. Observation of gaseous and particulate products of monoterpene oxidation in forest atmospheres. Geophysical Research Letters 26, 1145–1148.

Zdráhal, Z., Oliveira, J., Vermeylen, R., Claeys, M., Maenhaut, W., 2002. Improved method for quantifying levoglucosan and related monosaccharide anhydrides in atmospheric aerosols and application to samples from urban and tropical locations. Environmental Science & Technology 36, 747–753.

3B2v8.06a/w (Dec 5 2003).51c XML:ver:5.0.1 AEA : 5766 Prod.Type:FTP pp.1–13(col.fig.:NIL) ED:S.Latha PAGN:Dini SCAN:Global

ARTICLE IN PRESS

Available online at www.sciencedirect.com

SCIENCE DIRECT®

ELSEVIER

Atmospheric Environment ▮ (▮▮▮▮) ▮▮▮–▮▮▮

ATMOSPHERIC ENVIRONMENT

www.elsevier.com/locate/atmosenv

Evolution of particle concentration and size distribution observed upwind, inside and downwind hill cap clouds at connected flow conditions during FEBUKO

S. Mertes[a,*], D. Galgon[a], K. Schwirn[a], A. Nowak[a], K. Lehmann[a], A. Massling[a], A. Wiedensohler[a], W. Wieprecht[b]

[a]*Leibniz-Institut für Troposphärenforschung, Permoserstr. 15, 04318 Leipzig, Germany*

[b]*Brandenburgische Technische Universität Cottbus, Lehrstuhl für Luftchemie und Luftreinhaltung, Volmer Str.13, 12489 Berlin, Germany*

Abstract

The concentration and size distribution of atmospheric particles were traced upwind, inside and downwind a hill cap cloud within the ground-based cloud passage experiment FEBUKO, which was carried out at the mountain ridge Thüringer Wald (Germany) during October 2001 and 2002. Three cloud events were examined in detail for which the connected flow between all three sites was meteorologically confirmed and the influence of entrainment and local sources on particle concentration and size distribution was only of minor importance. Modifications of the number size distributions between 60 and 300 nm particle diameter that are attributed to cloud processing were observed comparing upwind and downwind dry particle size distributions. Despite a small interference of droplet deposition, a maximum in-cloud mass production of $0.38\,\mu g\,m^{-3}$ was found accounting for 5% of the upwind aerosol mass. The corresponding mass production rate was estimated to $1.16\,\mu g\,m^{-3}\,h^{-1}$. A formation of new ultra-fine particles was detected in the outflow of the orographic clouds during nighttime yielding number concentrations up to $300\,cm^{-3}$ at a pre-existing dry particle surface area of about $300\,\mu m^2\,cm^{-3}$. At a more than twice as high particle surface area, i.e. when adsorption of condensable gases on existing particles became more important, no new particle formation was observed. Whereas the in-cloud mass production proceeded rather continuously throughout the cloud events, the particle production occurred during periods of 15 min up to 2 h within the cloud events. In the absence of actinic radiation, ternary nucleation of gaseous substances outgassing from the evaporating droplets at high relative humidity is hypothesized as the most likely particle formation mechanism but the reason for the temporary appearance of the particle production is not known.

Keywords: Particle number size distribution; Cloud processing; In-cloud mass production; New particle formation

1. Introduction

The scientific understanding of the interaction between atmospheric particles and clouds is crucial to evaluate the direct and indirect aerosol forcing on climate (Charlson et al., 1992). The part of the aerosol population that forms cloud droplets, the cloud condensation nuclei (CCN), can be physically and chemically modified by cloud processing influencing their solar radiative properties after cloud dissipation (Lelieveld and Heintzenberg, 1992; Yuskiewicz et al.,

*Corresponding author. Tel.: +49 341 235 2153; fax: +49 341 235 2361.

E-mail address: mertes@tropos.de (S. Mertes).

1352-2310/$ - see front matter © 2005 Published by Elsevier Ltd.
doi:10.1016/j.atmosenv.2005.02.009

1999). After droplet evaporation the size and soluble mass of some former CCN will have increased (Alkezweeny, 1995; Leaitch, 1996) which reinforces their potential to cool the atmosphere in two ways. First, these particles scatter the incoming solar radiation more efficiently, because they grow earlier and larger with respect to ambient relative humidity (RH). Second, they can be activated to cloud droplets at lower supersaturations than before which can lead to clouds with higher droplet concentrations (Bower and Choularton, 1993) that exhibit higher albedo and longer lifetime. The major mechanisms that change the particle size by cloud processes are assumed to be the liquid-phase oxidation of SO_2 to SO_4^{2-} by O_3 and H_2O_2 (Bradbury et al., 1999; Kreidenweis et al., 2003) and the uptake of HNO_3, HCl and NH_3 (Flynn et al., 2000). The modification of the aerosol size distribution by cloud processing was empirically addressed by ground-based hill cap cloud experiments at Great Dun Fell, United Kingdom (Birmili et al., 1999b; Bower et al., 1997) and on Tenerife, Spain (Bower et al., 2000). By comparing upwind and downwind dry particle size distributions, changes of aerosol sizes were detectable only for the smallest activated particles with diameters between 100 and 300 nm, because their relative diameter increase by adding soluble mass is largest.

During the hill cap cloud experiments at Great Dun Fell, another modification of the downwind particle size distribution was observed in the size range below 25 nm, which was attributed to the production of ultra-fine particles at the evaporative stage of the clouds (Birmili et al., 1999b; Wiedensohler et al., 1997). These formation mechanisms have been hypothesized to be binary or ternary nucleation of outgassing trace substances like HNO_3, HCl and NH_3 with H_2O (Korhonen et al., 1997, 1999) at high RH and low temperatures in the outflow region of the cloud, which might be a non-negligible particle source in the boundary layer.

As a contribution within the framework of the joint project FEBUKO (field investigations of budgets and conversions of particle-phase organics in tropospheric cloud processes), this work focuses on the particle size (mass) and number modification due to cloud processing. Measurements from the FEBUKO ground-based cloud experiment are presented, which was carried out at the low mountain ridge Thüringer Wald (Germany). In refinement to the past studies, results of interstitial and cloud residual particle concentration and size distributions are considered.

2. Experimental

The field experiments were conducted at the low mountain ridge Thüringer Wald in October 2001 and 2002. The Thüringer Wald extends from south–east to north–west at a length of 60 km. The in-cloud station Schmücke (937 m asl, summit site) is situated on a saddle of the ridge. The upwind and downwind stations Goldlauter (605 m asl) and Gehlberg (732 m asl) are located southwest and northeast at air distances of about 3 km from the summit site, respectively. Measurements were carried out after cloud formation at southwesterly winds (liquid water contents $>0.1\,g\,m^{-3}$, wind direction between 190° and 230° and wind speed between 5 and $12\,m\,s^{-1}$ at the summit site) as long as upwind and downwind site remained underneath cloud base and no rain was observed at all three measuring sites. An overview of all experimental activities and about the topographic situation is given in Herrmann et al. (2005).

2.1. Measurements at upwind and downwind sites

At the upwind site the aerosol inlet faced the main wind direction 6 m above ground. The sampled aerosol particles were first dried below 30% RH and then distributed to a condensation particle counter (CPC, TSI-3010) and a twin differential mobility particle sizer (TDMPS, Birmili et al., 1999a) to measure particle concentration (dry particle diameter $d_p > 12$ nm) and dry particle size distribution ($3\,nm < d_p < 22\,nm$ and $22\,nm < d_p < 900\,nm$), respectively. At the downwind site, the aerosol was collected by a PM10 inlet 6 m above ground and dried to 50% RH. Particle concentration and dry particle size distribution were determined with a second CPC TSI-3010 and an identical TDMPS. Due to the dry sheath air, the RH inside the TDMPS systems at the upwind and downwind site was around 10%. The time resolution of the number concentration, number size distribution measurements was 15–80 s and 15 min at the upwind and 120 s and 15 min at the downwind site.

2.2. Measurements at the summit site

Inside cloud, interstitial particles and cloud droplets were separately collected by a droplet segregating interstitial inlet (INT) and a counterflow virtual impactor (CVI, Ogren et al., 1985). Both inlets are designed to separate droplets and interstitial particles at a diameter of 5 μm (Schwarzenböck et al., 2000). Details of the CVI sampling principle are described in Mertes et al. (2005). The CVI and INT were positioned outside two windows located at the upright wall of the top floor of a research building. The windows faced the favoured southwest direction (215° which was close to the centre of the accepted wind direction range) at a height of 15 m, i.e. the inlets were situated above the canopy. Upon sampling, the droplets were evaporated in the CVI system in a particle free and dry carrier air releasing dry residual particles (RH < 10%). At the INT sampling

system interstitial particles were dried to 50% RH. Downstream the INT and CVI, two CPC TSI-3010 and two differential mobility particle sizers (DMPS) measured the residual and interstitial particle concentration ($d_p > 12$ nm) and dry size distribution (22 nm < $d_p < 900$ nm). The dry sheath air reduced the RH inside the DMPS systems down to < 10%. The time resolution of the simultaneous particle number concentration and size distribution measurements at both inlets was 10 s and 15 min, respectively.

In order to determine the droplet concentration a forward scattering spectrometer probe (FSSP-100, Baumgardner, 1983) was operated on the top platform of a 20 m high scaffold located 10 m apart from the research building. The results of the FSSP-100 are averaged to 10 s values.

Prior to the field experiment, all CPCs, TDMPS and DMPS systems (part of the TDMPS in the out of cloud sites) were inter-compared. The CPCs agreed within 5% (particle concentration) and the TDMPS, DMPS within 10% (particle concentration per size bin). No relative shifts with regard to particle size were observed between the different TDMPS and DMPS systems.

3. Results

The synoptic and flow modelling evaluation (Heinold et al., 2005; Tilgner et al., 2005a) confirmed best connected flow conditions for three of 14 examined cloud events, numbered E I, E II and E III (Table 1). At this point it is stressed that the term connected flow conditions does not necessarily imply that exactly the same air parcel was traced from the upwind site along the summit site to the downwind. It rather means that the same air mass passed all three sites and thus the aerosol characterized at the upwind and downwind site was representative for the cloud input and cloud processed particles, respectively.

From backward trajectories analyzed by Tilgner et al. (2005a) it can be concluded that maritime air masses originating from the Atlantic Ocean that were influenced by the western European continent prevailed at the measurement site. For E II the air mass arrived from the western Mediterranean Sea and travelled over the south of France between 01:00 and 05:00. The clouds from each of the three events showed a strong orographic influence but were temporarily mixed with advected stratus clouds at heights above the summit level (Tilgner et al., 2005a).

3.1. Evolution of particle number concentration

The time series of particle number concentrations during all three cloud events are presented in Fig. 1. In the lower part of the diagrams (a)–(c) it becomes obvious that the residual particle concentration resulting from the CVI sampling is in good agreement with the insitu droplet concentration obtained from the FSSP for droplet diameters D larger than 5 μm. This finding confirms that the CVI collected droplets with a high number sampling efficiency and that no undesired droplet break-up appeared during CVI collection. In E I and E III the upwind, downwind, and interstitial particle concentration show the same time pattern. Moreover, the sum of the interstitial particle and droplet concentration determined at the summit site matches the downwind particle concentration in both cloud events and the upwind concentration in E III. In E I, the upwind particle concentration was found to be higher with regard to the summit and downwind site during the last few hours of the event. Consequences for the further analysis will be discussed in the next paragraph describing the dry particle number size distributions. The observed identical particle concentration time pattern at all three sites and the conservation of the number concentration supports the meteorological evaluation of a connected airflow above the mountain ridge and implies only a minor influence of entrainment

Table 1
Additional information regarding the three presented cloud events

	E I (26–27.10.2001)	E II (07–08.10.2001)	E III (16–17.10.2002)
Time period, duration (h)	21:45–12:45, 15	18:00–08:00, 14	21:00–04:00, 7
Mean temperature (°C)	6.1	9.6	7.9
Mean wind speed ($m\,s^{-1}$)	8.0	6.9	10.1
Mean wind direction (°)	216.3	207.1	215.2
Mean cloud base height below summit site (m)	216	141	113
Mean LWC ($g\,m^{-3}$)	0.335	0.203	0.202
Mean effective droplet radius (μm)	6.2	5.3	4.4
Mean droplet concentration (cm^{-3})	408	311	435

All parameters are measured on the summit site except the cloud base height (ceilometer at the upwind site).

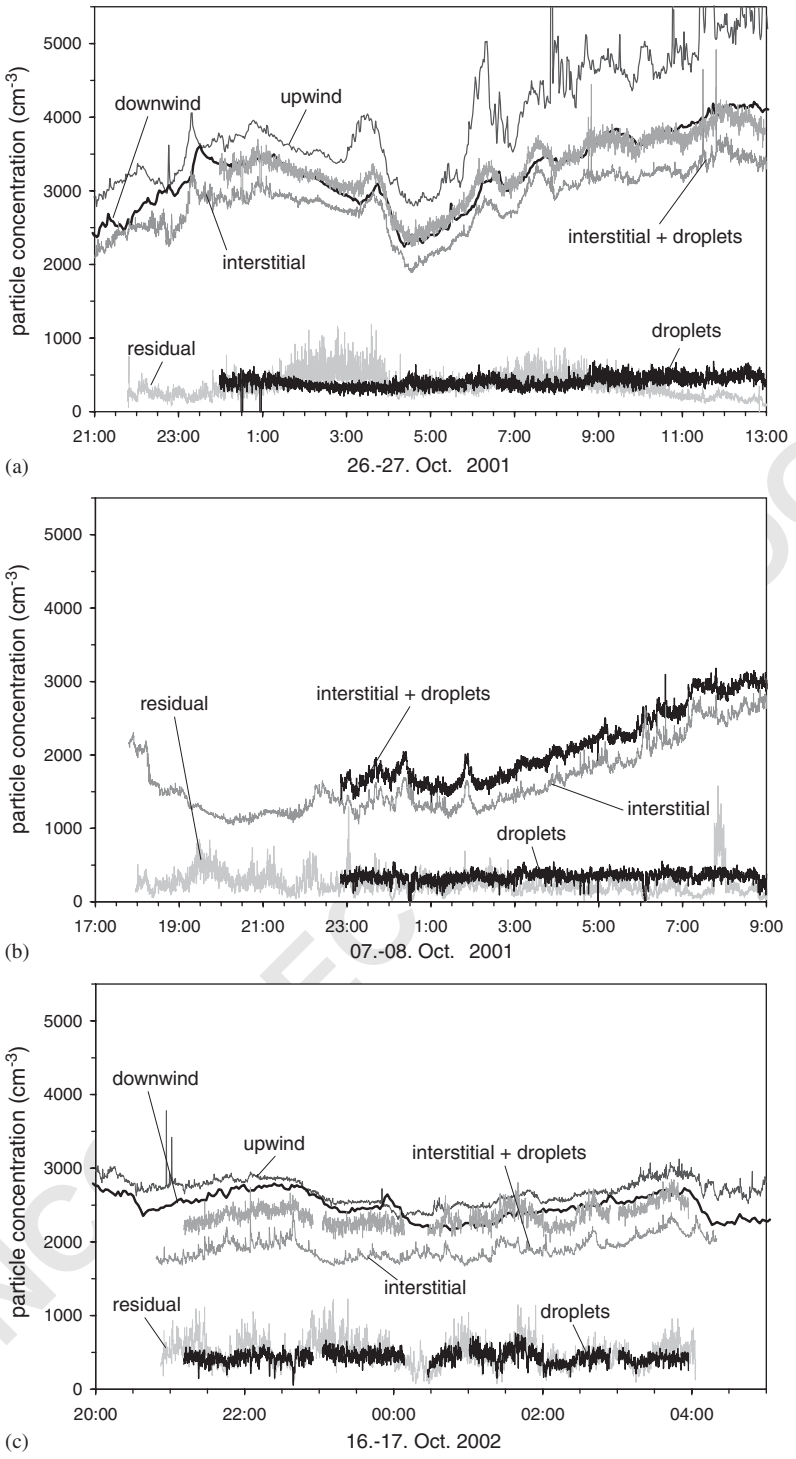

Fig. 1. Time series of particle number concentrations measured upwind, downwind and inside cloud (residual, interstitial) for the cloud events (a) E I, (b) E II, (c) E III. Moreover, time series of droplet concentration with $D > 5\,\mu m$ and the total particle concentration on the summit site (interstitial + droplets) are shown.

and droplet deposition on the total particle number budget. Unfortunately, no upwind and downwind particle concentration was measured during E II (Fig. 1b), but the influence of entrainment for this event will be subsequently examined on the basis of the particle number size distributions.

Using the time shift of the particle number concentration time series, the transit times of the air masses between the measurement locations were determined for E I and E III. On average, the air needed 8 min to travel from the upwind to the summit site and 16 min from the upwind to the downwind site.

3.2. Evolution of the dry particle number size distribution

Mean particle number size distributions (PNSD) of the three selected cloud events measured upwind, downwind and inside cloud (interstitial, residual) are depicted in Fig. 2. In addition, the sum of interstitial and residual PNSD is indicated representing the total particle number size distribution on the summit site. Error bars that take into account the 10% relative DMPS deviations and the Poisson error which is only perceivable at low counting statistics are added to the PNSD measured at the summit and downwind site. The shape of the upwind PNSD in E I and E II (Fig. 2a and b) looks very similar with a strong Aitken-mode and a less pronounced accumulation mode centred at $d_p = 70$ and 200 nm. For E III, the two modes are more separated and located at smaller particle diameters of $d_p = 30$ and 160 nm, respectively. The PNSD measured in-cloud reveals that most Aitken mode particles remained in the interstitial phase, whereas most accumulation mode particles were activated to droplets and are found as residual particles.

At connected flow conditions changes of the cloud downwind PNSD compared to the cloud upwind PNSD may be caused by the sum of different processes. Beside cloud associated particle nucleation and in-cloud aerosol mass production that are subject of this study there might occur entrainment of a different aerosol population, droplet deposition and particle emissions between upwind and downwind site. Droplet deposition would affect the large diameter size range of particles that form cloud droplets. Hence, droplet losses would have much more impact for the downwind particle mass than for downwind particle number and will be taken into account during the discussion of in-cloud mass production. New particle production that is not cloud related can be ruled out for the selected cloud events, because they all persisted mostly during nighttime, i.e. no photochemical reactions and no OH production took place. An excess of particles with diameters between $d_p = 70$ and 110 nm was observed in the PNSD during E I (Fig. 2a) compared to the summit and downwind PNSD that explains the enhancement of the upwind particle concentration in Fig. 1a. The sole occurrence of the particle excess at the upwind site, gives evidence that it is caused by a small local emission which became substantially diluted to be no more observable at the other two sites or traversed the mountain ridge in an air parcel that did not pass the summit and downwind site. Entrainment, defined as mixing of subsaturated air from above into the cloud top that might additionally contain a different aerosol population is common even for air flow across a hill. For cap clouds the entrainment influence is mostly restricted to the upper cloud regions and the entrained air is not mixed down to the hill surface until downwind of the summit. Colvile et al. (1997) gave different indicators to identify whether entrainment affects the surface measurements of a hill cap cloud experiment. For all three events, the monomodal droplet size distribution and a LWC closely correlated with cloud base height (Wieprecht et al., 2005), identical ozone concentration time series at all three sites (Brüggemann et al., 2005; Heinold et al., 2005) and the particle number closure shown above give evidence that entrained air did not substantially penetrate to the summit surface. The air flow continuity across the mountain ridge and the absence of a large entrainment impact on the particle number size distribution is also confirmed by the equity of the lower end of the Aitken mode in the size range between $d_p = 25$ and 60 nm (especially for E I), which is neither affected by nucleation scavenging (cf. residual particle PNSD) nor by cloud associated particle production. In event E III, the shape of the dry PNSD in this size interval is also preserved but slightly decreases in concentration from the upwind to the downwind site (Fig. 2c). A slight shift to smaller sizes of this particle diameter range was observed for E II (Fig. 2b). These differences might be attributed to a slightly increasing entrainment influence during E III and particularly during E II. More empirical indications to estimate the existence and influence of entrainment during the three cloud events are discussed in Herrmann et al. (2005).

3.3. Scavenged aerosol fraction

The number fraction of aerosol particles that indeed undergo nucleation scavenging as a function of particle size (scavenged fraction SF) can be derived by the interstitial and residual PNSD according to Eq. (1), where N_{res} and N_{int} denote residual and interstitial particles.

$$SF = \frac{\frac{dN_{res}}{d \log d_P}}{\frac{dN_{res}}{d \log d_P} + \frac{dN_{int}}{d \log d_P}}. \quad (1)$$

The SF curves of all three cloud events are illustrated in Fig. 3 (this time in a linear x-scale up to 600 nm). For large particles SF was always close to one, which again

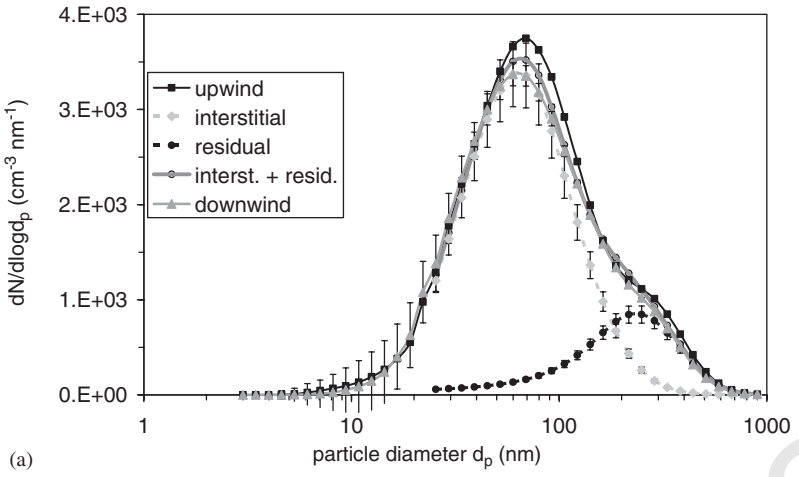

(a)

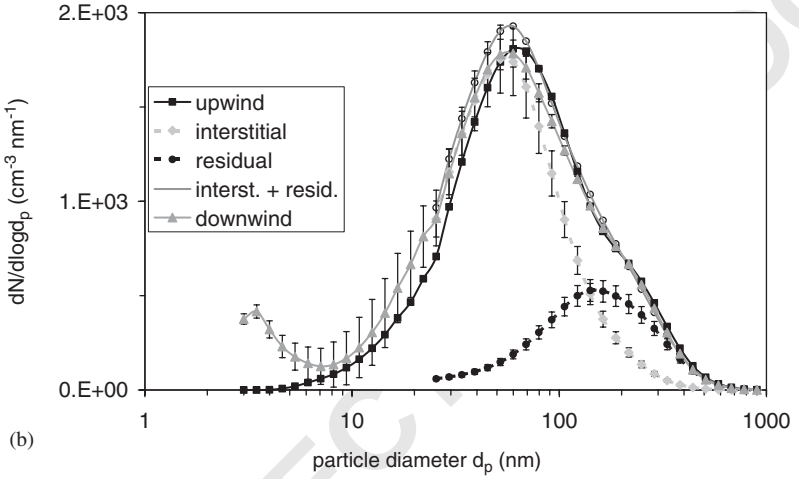

(b)

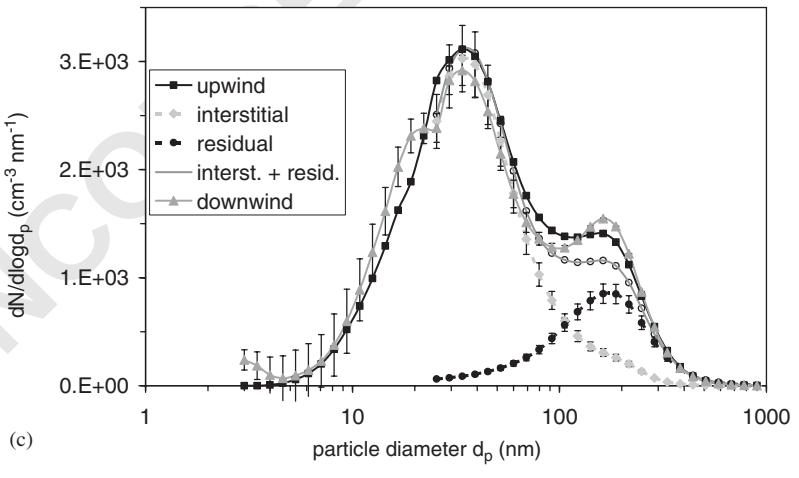

(c)

Fig. 2. Dry particle number size distributions determined upwind, downwind and inside cloud (interstitial, residual) averaged over the cloud events (a) E I, (b) E II, (c) E III.

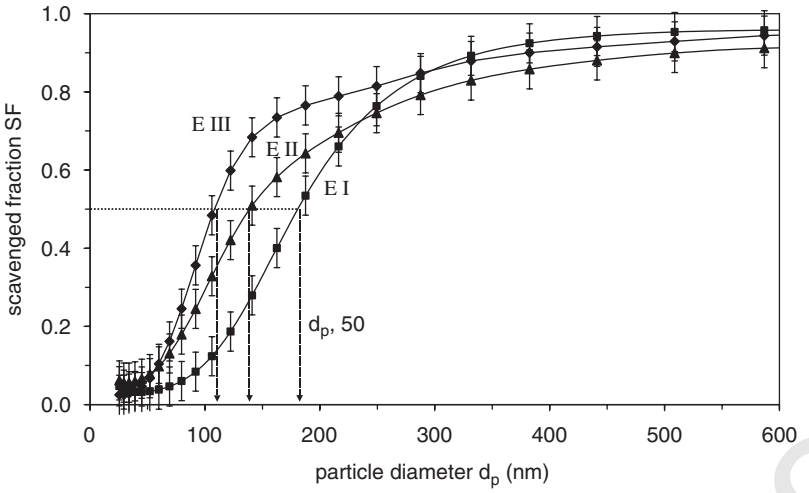

Fig. 3. Scavenged fractions SF as function of the dry particle diameter determined for the cloud events E I, E II and E III derived from Eq. (1). Error bars are estimated from the experimental uncertainties. Arrows indicate the respective 50% activation diameters $d_{p,50}$.

Table 2
Particle mass and number concentration of cloud-processed particles derived from particle number size distributions at the upwind, summit and downwind site

Parameter	Event	Upwind	Summit	Downwind
Mass concentration ($\mu g\,m^{-3}$)	E I	16.5	14.9	13.3
	E II	6.1	5.7	5.1
	E III	6.4	6.4	6.4
Number concentration of cloud Processed particles (cm^{-3})	E I	542	512	485
	E II	368	369	358
	E III	568	493	570

indicates the limited impact of entrainment. The increase of SF is rather steep for E I and E III but appeared at different particle sizes, whereas for E II the scavenged fraction rises less sharp. Particle activation (SF > 0.1) was observed down to $d_p = 60$ nm (E II, E III) and 100 nm (E I). Droplet activation diameter $d_{p,50}$ (defined for SF = 0.5) of 180, 140 and 110 nm are inferred for E I, E II and E III. The shape of the SF function as well as the derived $d_{p,50}$ are similar to results obtained from measurements at Kleiner Feldberg (Hallberg et al., 1994), which is a low mountain of comparable height located about 200 km west of the summit site.

3.4. In-cloud mass production

A modification of the PNSD in the size range that undergoes cloud processing (diameters down to at least 60 nm according to Fig. 3) is noticeable for E III in Fig. 2, where the accumulation mode around $d_p = 160$ nm at the downwind site increases and shifts to larger diameters with respect to the PNSD measured at the upwind site. Such a change is not directly obvious for E I and E II where the same size range is located in the falling edge between Aitken and accumulation mode. Indeed, no increase in dry particle mass can be assigned when the mass concentration is derived from the PNSD in Fig. 2 using a specific weight of 1.8 $g\,cm^{-3}$. On the contrary, the mass concentration steadily decreased from the upwind along the summit to the downwind site for E I and E II by 19% and 10% or did not change at all for E III (Table 2). The amount of mass reductions at small changes of particle number can only be caused by losses of large accumulation mode particles that were mostly activated to cloud droplets. This strongly

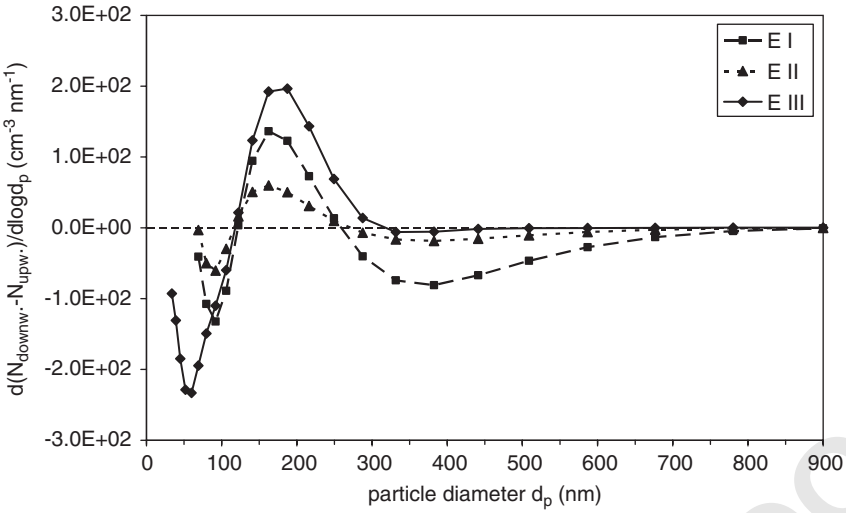

Fig. 4. Difference of average downwind to upwind dry particle size distribution for E I, EII and E III. Details are given in the text.

supports the occurrence of droplet deposition along the forest canopy as the dominating loss process. The particle number concentration of cloud processed particles (Table 2) that is obtained by integrating the product of the PNSD times the SF function decreased from the upwind to the downwind site by 11%, 3% and 0% for E I, E II and E III. According to cloud base height and cloud droplet size (cf. Table 1) most droplets are expected to be lost in E I and fewest droplets in E III, which is confirmed by the relative particle number and mass reductions given above. These losses were quite small, but still bias the examination of a particle mass increment due to cloud processes.

In order to estimate the limits of such a particle mass increase, the change in particle concentration as a function of particle size is derived from the difference of downwind to upwind PNSD, which is shown in Fig. 4 for the individual cloud events. Here, the downwind PNSD is scaled up above $d_p = 30$ nm according to the number concentration loss given above in order to account for the effect of droplet deposition. In principal, this single normalization factor may under or overestimate the impact of droplet deposition on the downwind PNSD for different particle size ranges.

In terms of number concentration, the reduction of particles below $d_p = 100$ nm seems to be obviously compensated by the particle gain in the diameter range between 100 and 300 nm similar for all events (Fig. 4). This implies the growth of particles from below to above $d_p = 100$ nm caused by in-cloud mass production which is rather independent of the shape of the initial PNSD and the scavenged fraction curve. The negative values above $d_p = 300$ nm for E I demonstrate that the normalization of the downwind PNSD is not sufficient to compensate the effect of droplet deposition for large particles in this cloud event, but for E II and E III the normalization worked well for the whole particle size range.

Integrating the difference PNSD from Fig. 4 up to about $d_p = 300$ nm, i.e. ignoring the larger size range that is affected by droplet deposition and high uncertainty due to low counting statistics, yields a particle mass enhancement of 0.14, 0.07 and 0.29 $\mu g\,m^{-3}$ for E I, E II and E III. The constraint that the particles number should be conserved during cloud processing (interpreted as particles that vanished below 100 nm are to 100% recovered in the mode above 100 nm) yields slight different in-cloud mass productions of 0.13, 0.05 and 0.38 $\mu g\,m^{-3}$ which represents the range of uncertainty (Table 3). From a simple geometrical calculation assuming spherical particles it can be inferred that the observed increase in mass should be detected as a change in size only up to $d_p = 250$ nm (E I, E II) and 290 nm (E III) as a consequence of a much smaller diameter change for larger particles and of the logarithmic decreasing DMPS size resolution. These calculated limits match the largest sizes where an increase was found in Fig. 4. Above the calculated size limits it cannot be decided whether in-cloud mass production did not occur, whether it is not resolved by the DMPS measurements or whether it is counter acted by outgassing of NH_3 and HNO_3 (Flynn et al., 2000). However, modifications in the same diameter range have been observed and theoretically predicted in similar cloud passage experiments (Bower et al., 1997; Bradbury et al., 1999). Because average PNSD were used to analyze the in-cloud mass production it is important to verify whether this was a permanent mechanism or appeared only

Table 3
Parameters derived for in-cloud mass production and cloud-associated particle formation from the evaluation of the particle number size distributions at the upwind, summit and downwind site

Parameter	E I	E II	E III
Absolute in-cloud mass production ($\mu g\,m^{-3}$)	0.13–0.14	0.05–0.07	0.29–0.38
Fraction of aerosol mass (%)	1	1	5
Mean mass production rates ($\mu g\,m^{-3}\,h^{-1}$)	0.56 (3% h^{-1})	—	1.16 (18% h^{-1})
Mean absolute ultra-fine particle production (cm^{-3})	—	228	310
Fraction of ultra-fine particle concentration (%)	—	1110	397
Fraction of total particle concentration (%)	—	12	10
Mean dry particle surface area ($\mu m^2\,cm^{-3}$)	727	305	365

temporarily. Fig. 5 shows contour plots of the PNSD versus time at the upwind and downwind site. It is obvious that the upwind and downwind PNSD did hardly change at all or altered simultaneously in the respective size range between $d_p = 50$ and 300 nm which indicates a rather constant mass production throughout the cloud events. This justifies the evaluation of the in-cloud mass production by means of average PNSD in order to increase the statistical significance.

3.4.1. Relation to aerosol chemical measurements and model predictions

The findings obtained from the PNSD are also qualitatively supported by aerosol mass and chemical component analysis of impactor measurements at the upwind and downwind site (Brüggemann et al., 2005) although a decrease of the total mass and chemical substances was found for the cloud events analogue to the DMPS results. However, normalizing upwind and downwind total aerosol mass yields a mass depletion on stage 1 ($d_p = 38-106$ nm, calculated for dry particle size and mobility diameter to be comparable to the DMPS measurements) and an increase on stage 2 ($d_p = 106-313$ nm). On impactor stage 2, SO_4^{2-}, NH_4^+ and organic carbon (OC) were found to be enriched during E I and E III with respect to the aerosol mass of this stage. A mass increment of 0.33 and 0.25 $\mu g\,m^{-3}$ is estimated for the sum of the three species with regard to the mass on stage 2, which is close to the results derived from the PNSD analysis. Simulations of the cloud events with a parcel model including detailed microphysics and complex multiphase chemistry (Tilgner et al., 2005b) show the same trend as the empirical DMPS results for E I and E II with predicted in-cloud mass productions of 0.28 and 0.55 $\mu g\,m^{-3}$ up to particle diameters $d_p = 400$ nm. These values are somewhat higher than the experimentally derived ones, potentially because the model calculations did not consider droplet deposition. The model results do not agree for E III, where similar mass increments of 0.55 $\mu g\,m^{-3}$ are predicted but above $d_p = 300$ nm. From the model simulations (Tilgner et al., 2005b) and the measured chemical aerosol information (Brüggemann et al., 2005), the main pathways for the observed in-cloud mass production are most likely liquid-phase SO_2 oxidation by H_2O_2 and O_3, uptake of NH_3 and HNO_3 with subsequent conversion to NH_4^+ and NO_3^-. Liquid-phase formation of OC cannot be ruled out from the impactor measurements, whereas it should be too small to be measured according to the model results.

3.4.2. Comparison with former studies

The absolute in-cloud mass productions below 0.5 $\mu g\,m^{-3}$ derived from the PNSD correspond to relative mass increments in the range from 1% (E I, E II) to 5% (E III) in relation to the upwind aerosol masses given in Table 2. This is much less than mass enhancements of more than 1 $\mu g\,m^{-3}$ observed at Great Dun Fell (Birmili et al., 1999b) that increased the upwind aerosol mass by more than 20%. This might be due to smaller in-cloud residence times or to lower concentrations of gaseous precursors that are able to produce aerosol mass by liquid-phase reactions. Using an in-cloud residence time estimated from the number concentration time shift of about 15 min, average mass production rates of 0.56 and 1.16 $\mu g\,m^{-3}\,h^{-1}$ (or 3 and 18% h^{-1}) are derived for E I and E III (Table 3). These values are already less than the sulphate in-cloud production rates of 3–5 $\mu g\,m^{-3}\,h^{-1}$ observed at Great Dun Fell (Laj et al., 1997), which can be consistently explained by the low average SO_2 (<0.8 ppb), H_2O_2 (<20 ppt) and cloud water pH (<4.8). Due to low pH, the uptake of NH_3 should be of similar importance for in-cloud mass production (Flynn et al., 2000).

3.5. Cloud associated particle production

An increase of particle number with $d_p < 10$ nm downwind cloud is obvious at the right edge of an ultra-fine particle mode at $d_p = 3$ nm in Fig. 2 during E

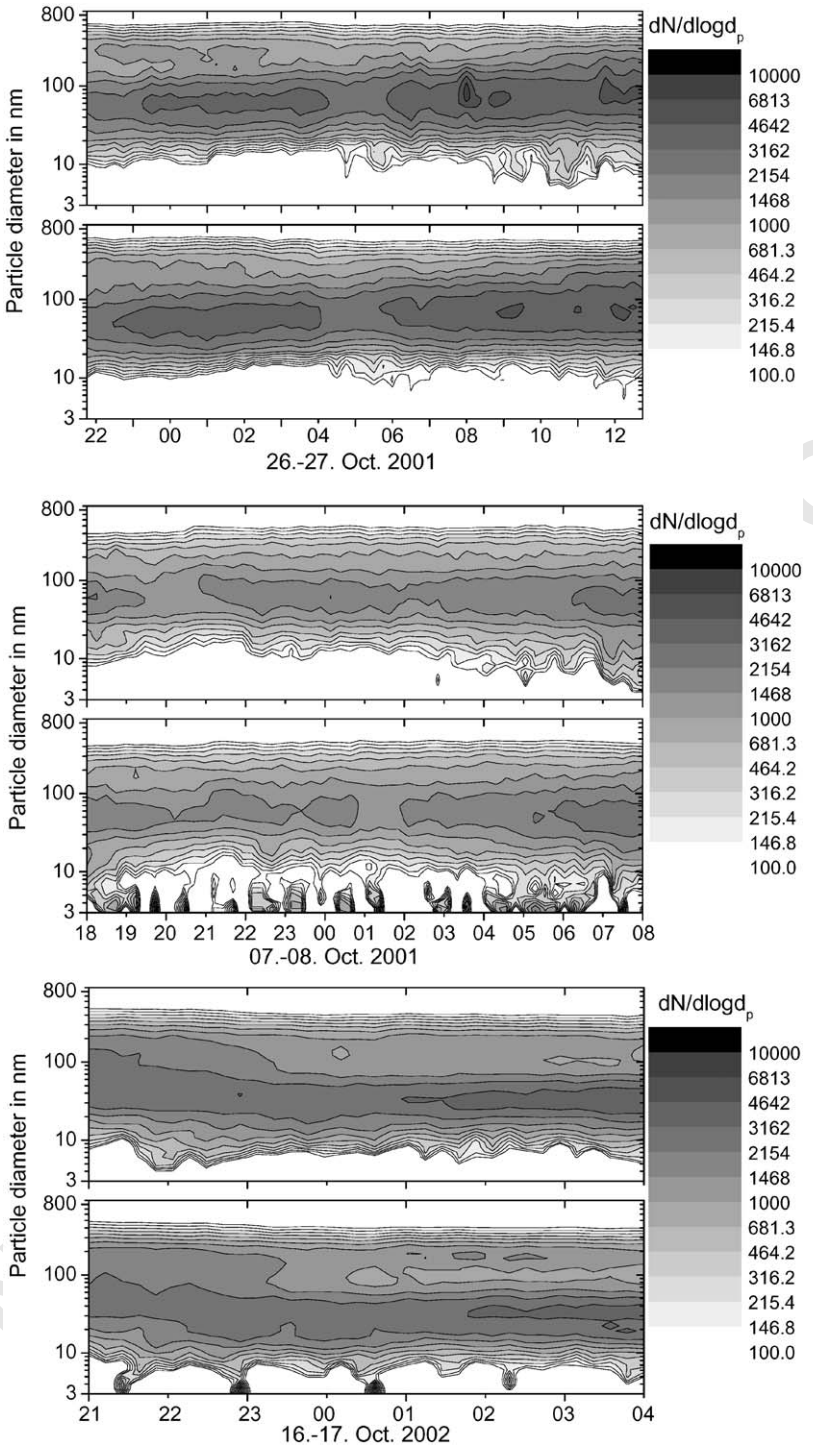

Fig. 5. Contour plots of the particle number size distributions versus time for E I (26–27.10.2001), EII (07–08.10.2001) and E III (16–17.10.2002).

II and E III but not observed for E I. Unfortunately, only a DMPS and not a TDMPS was deployed at the interstitial inlet inside cloud, i.e. there exists no information about the abundance of ultra-fine particles at the summit site. The ultra-fine modes extend to 7 nm (E II) and 5 nm (E III) which implies growth rates in the order of 1 nm min^{-1} taking into account the transit times of several minutes between summit and downwind site. In contrast to the in-cloud mass production, it is obvious from Fig. 5 that the particle production did not occur continuously but in shorter periods within the cloud events. These periods lasted between 15 min (mostly observed during two consecutive DMPS scans) and 2 h. Averaging and integrating the downwind PNSD of E II and E III where particle production was seen, yields an ultra-fine particle number concentration of 228 and 310 cm^{-3} for E II and E III (Table 3). This accounts for 12 and 10% of the total number concentration integrated over the PSND. The amount of ultra-fine particles increased by 1110% and 397%, respectively. As a reference case of no particle production, a difference of $-9\,cm^{-3}$ between upwind and downwind site for particles smaller than 10 nm was inferred for E I.

An increase of particle number below $d_p = 15$ nm was also observed by comparing upwind and downwind PNSD at Great Dun Fell interpreted as ultra-fine particle production in the outflow of the hill cap cloud. Wiedensohler et al. (1997) observed two particle nucleation events producing ultra-fine particles between $d_p = 5$ and 15 nm with a number concentration of about 950 and 140 cm^{-3} that amounted to 38% and 5% of the particle number concentration. Birmili et al. (1999b) measured an ultra-fine particle burst in the diameter range $3 < d_p < 8$ nm of up to 5000 cm^{-3} lasting 3 h that represented 70% of the particle number concentration. This nucleation event appeared at a low aerosol surface area of about 100 $\mu m^2\,cm^{-3}$ which reduces the chance of precursor gases to condense on pre-existing particles and thus facilitates new particle nucleation. Average dry particle surface areas during FEBUKO inferred from the PNSD assuming spherical particles were 727, 305 and 365 $\mu m^2\,cm^{-3}$ for E I, E II and E III. Thus, the lower ultra-fine particle production compared to Great Dun Fell is consistent with the expectation of a stronger condensation of outgassing substances on the larger pre-existing particle surface area which is a competition process to new particle generation. Especially the even larger surface area during E I most likely prevented a detectable nucleation of ultra-fine particles at all. Particle nucleation associated with clouds was mostly detected at cloud tops (Clarke et al., 1999; Hegg et al., 1990; Keil and Wendisch, 2001) where large amounts of OH formed in the region of maximum actinic radiation can efficiently oxidize SO_2 to H_2SO_4. The high RH in the vicinity of the cloud imply favourable conditions for the binary nucleation of H_2SO_4 and H_2O. At Great Dun Fell the new particle formation was observed at the dissipating downwind side of the clouds during night-time. Thus, particle production processes that require actinic radiation to initiate gas-phase oxidation by OH can be excluded. Instead, ternary nucleation processes of HCl, HNO_3 and NH_3 that are released from the evaporating droplets that may lead to high gas-phase concentrations of these substances on a limited volume in combination with high H_2O levels (Korhonen et al., 1999) in the vicinity of clouds were hypothesized for the particle production observed at Great Dun Fell (Birmili et al., 1999b; Wiedensohler et al., 1997). Although the measured ultra-fine particle concentrations cannot be reproduced by nucleation models at present, the same hypothesis can be adopted for the FEBUKO results in the Thüringer Wald. However, elevated local ion concentrations in the vicinity of evaporating droplets are conceivable as well, which could initiate ion-mediated particle nucleation (Yu and Turco, 2000). Since it is argued that dicarboxylic acids are semi-volatile (Limbeck et al., 2001) it can also be speculated that these organic substances are first driven into the gas phase at low droplet pH values during evaporation and then form new organic particles according to their gas/particle equilibrium (the abundance and cloud processing of particulate dicarboxylic acids is discussed by vanPinxteren et al. (2005)). Unfortunately, these hypotheses concerning the particle nucleation mechanism cannot be verified, because parameters like the ultra-fine particle chemical composition were not measured, were not measured with the required time resolution of the nucleation periods (e.g. submicron aerosol chemical composition) or did not show a significant time correlation with the occurrence of particle nucleation periods (e.g. meteorological parameters, precursor gases if measured).

4. Summary

By means of concentration and size distribution measurements of atmospheric particles carried out upwind, inside and downwind a hill cap cloud within the ground-based cloud passage experiment FEBUKO, the meteorologically predicted connected flow as well as a minor influence of entrainment and of local particle sources on the measured parameters could be confirmed. A small amount of large activated particles were lost which was most likely caused by droplet deposition leading to a total mass deficit inside and downwind cloud.

Nevertheless, the comparison of upwind and downwind dry particle size distributions yielded an in-cloud mass production between $d_p = 60$ and 300 nm for three favoured cloud events in the range of 0.05–0.38 $\mu g\,m^{-3}$. At larger particle sizes a further mass increase did not

occur or was not resolved by the measurements. Taking into account the air mass residence time inside cloud, average mass production rates of 0.56 and $1.16\,\mu g\,m^{-3}\,h^{-1}$ were derived. According to simultaneous impactor measurements and accompanying model simulations (Brüggemann et al., 2005; Tilgner et al., 2005b), the observed mass gain is mainly attributed to liquid-phase SO_2 oxidation and uptake of NH_3 and HNO_3 into the droplets but a non-volatile OC formation in the liquid phase might be possible as well.

During two of three cloud events where the pre-existing dry particle surface area was about $300\,\mu m^2\,cm^{-3}$, ultra-fine particle formation was observed in the outflow of the orographic cloud during nighttime with number concentrations up to $300\,cm^{-3}$. The non-appearance of ultra-fine particles at a more than twice as high particle surface area is consistent with the expectation that condensation of precursor gases on existing particles is a quenching process for new particle formation. In contrast to the rather permanent in-cloud mass production, the particle production did not occur continuously but during shorter periods of 15 min up to 2 h within the cloud events. Ternary nucleation of gaseous substances outgassing from the evaporating droplets at high RH is the most likely particle formation mechanism in the absence of solar radiation but also ion-mediated nucleation cannot be ruled out. However, the temporal behaviour of the particle production periods is not understood.

Acknowledgements

This study was funded by the Bundesministerium für Bildung und Forschung within the German atmospheric research program AFO2000 under the Grant FKZ 07ATF01. We like to acknowledge the great support by the Deutsche Wetterdienst and the Deutsche Umweltbundesamt. We thank Werner Sarwatka†, Hartmut Haudek, Andrea Haudek and Stephan Günnel for their help in the preparation and setup of the experimental equipment.

References

Alkezweeny, A.J., 1995. Field observations of in-cloud nucleation and the modification of atmospheric aerosol size distributions after cloud evaporation. Journal of Applied Meteorology 34 (12), 2649–2654.

Baumgardner, D., 1983. An analysis and comparison of five water droplet measuring instruments. Journal Applied Meteorology 22, 891–910.

Birmili, W., Stratmann, F., Wiedensohler, A., 1999a. Design of a DMA-based size spectrometer for a large particle size range and stable operation. Journal Aerosol Science 30 (4), 549–553.

Birmili, W., Yuskiewicz, B., Wiedensohler, A., Stratmann, F., Choularton, T.W., Bower, K.N., 1999b. Climate-relevant modification of the aerosol size distribution by processes associated with orographic clouds. Atmospheric Research 50, 241–263.

Bower, K.N., Choularton, T.W., 1993. Cloud processing of the cloud condensation nucleus spectrum and its climatological consequences. Quarterly Journal of Royal Meteorological Society 119, 655–679.

Bower, K.N., Choularton, T.W., Gallagher, M.W., Colvile, R.N., Wells, M., Beswick, K.M., Wiedensohler, A., Hansson, H.-C., Svenningsson, B., Swietlicki, E., Wendisch, M., Berner, A., Kruisz, C., Laj, P., Facchini, M.C., Fuzzi, S., Bizjak, M., Dollard, G., Jones, B., Acker, K., Wieprecht, W., Preiss, M., Sutton, M.A., Hargreaves, K.J., Storeton-West, R.L., Cape, J.N., Arends, B.G., 1997. Observations and modelling of the processing of aerosol by a hill cap cloud. Atmospheric Environment 31 (16), 2527–2543.

Bower, K.N., Choularton, T.W., Gallagher, M.W., Beswick, K.M., Flynn, M.J., Allen, A.G., Davison, B.M., James, J.D., Robertson, L., Harrison, R.M., Hewitt, C.N., Cape, J.N., McFadyen, G.G., Milford, C., Sutton, M.A., Martinsson, B.G., Frank, G., Swietlicki, E., Zhou, J., Berg, O.H., Mentes, B., Papaspiropoulos, G., Hansson, H.-C., Leck, C., Kulmala, M., Aalto, P., Väkevä, M., Berner, A., Bizjak, M., Fuzzi, S., Laj, P., Facchini, M.-C., Orsi, G., Ricci, L., Nielsen, M., Allan, B.J., Coe, H., McFiggans, G., Plane, J.M.C., Collett Jr., J.L., Moore, K.F., Sherman, D.E., 2000. ACE-2 HILLCLOUD. An overview of the ACE-2 ground-based cloud experiment. Tellus 52B, 750–778.

Bradbury, C., Bower, K.N., Choularton, T.W., Swietlicki, E., Birmili, W., Wiedensohler, A., Yuskiewicz, B., Berner, A., Dusek, U., Dore, C., McFayden, G.G., 1999. Modelling of aerosol modification resulting from passage through a hill cap cloud. Atmospheric Research 50, 185–204.

Brüggemann, E., Gnauk, T., Mertes, S., Acker, K., Auel, R., Wieprecht, W., Möller, D., Collett Jr., J.L., Chemnitzer, R., Rüd, C., Junek, R., Herrmann, H., 2005. Schmücke hill cap cloud and valley stations aerosol characterisation during FEBUKO (I): particle size distribution and main components. Atmospheric Environment (this issue).

Charlson, R.J., Schwartz, S.E., Hales, J.M., Cess, R.D., Coakley Jr., J.A., Hansen, J.E., Hofmann, D.J., 1992. Climate forcing by anthropogenic aerosols. Science 256, 423–430.

Clarke, A.D., Kapustin, V.N., Eisele, F.L., Weber, R.J., McMurry, P.H., 1999. Particle production near marine clouds: sulfuric acid and predictions from classical binary nucleation. Geophysical Research. Letter 26 (16), 2425–2428.

Colvile, R.N., Bower, K.N., Choularton, T.W., Gallagher, M.W., Wobrock, W., Hargreaves, K.J., Storeton-West, R.L., Cape, J.N., Jones, B., Wiedensohler, A., Hansson, H.-C., Wendisch, M., Acker, K., Wieprecht, W., Pahl, S., Winkler, P., Berner, A., Kruisz, C., 1997. Meteorology of the Great Dun Fell cloud experiment 1993. Atmospheric Environment 31 (16), 2407–2420.

Flynn, M.J., Bower, K.N., Choularton, T.W., Wobrock, W., Mäkelä, J.M., Martinsson, B., Frank, G., Hansson, H.-C., Karlsson, H., Laj, P., 2000. Modelling cloud processing of

aerosol during the ACE-2 HILLCLOUD experiment. Tellus 52B, 779–800.

Hallberg, A., Noone, K.J., Ogren, J.A., Svenningsson, I.B., Flossmann, A., Wiedensohler, A., Hansson, H.-C., Heintzenberg, J., Anderson, T., Arends, B., Maser, R., 1994. Phase partitioning of aerosol particles in clouds at Kleiner Feldberg. Journal Atmospheric Chemistry 19, 107–127.

Hegg, D.A., Radke, L.F., Hobbs, P.V., 1990. Particle production associated with marine clouds. Journal of Geophysical Research 95 (D9), 13917–13926.

Heinold, B., Tilgner, A., Jaeschke, W., Haunold, W., Knoth, O., Wolke, R., Herrmann, H., 2005. Meteorological characterisation of the FEBUKO hill cap cloud experiments, Part II: tracer experiments and flow characterisation with nested non-hydrostatic atmospheric models. Atmospheric Environment (this issue).

Herrmann, H., Wolke, R., Müller, K., Brüggemann, E., Gnauk, T., Barzaghi, P., Mertes, S., Lehmann, K., Massling, A., Birmili, W., Wiedensohler, A., Wieprecht, W., Acker, K., Jaeschke, W., Kramberger, H., Svrcina, B., Bächmann, K., Collett Jr., J.L., Galgon, D., Schwirn, K., Nowak, A., van Pinxteren, D., Plewka, A., Chemnitzer, R., Rüd, C., Hofmann, D., Tilgner, A., Diehl, K., Heinold, B., Hinneburg, D., Knoth, O., Sehili, A.M., Simmel, M., Wurzler, S., Mauersberger, G., Majdik, Z., Müller, F., 2005. FEBUKO and MODMEP: field measurements and modelling of aerosol and cloud multiphase processes. Atmospheric Environment (this issue).

Keil, A., Wendisch, M., 2001. Bursts of Aitken mode and ultrafine particles observed at the top of continental boundary layer clouds. Journal of Aerosol Science 32 (5), 649–660.

Korhonen, P., Kulmala, M., Viisanen, Y., 1997. A theoretical study of binary homogenous nucleation of water-ammonium chloride particles in the atmosphere. Journal of Aerosol Science 28 (6), 901–917.

Korhonen, P., Kulmala, M., Laaksonen, A., Viisanen, Y., McGraw, R., Seinfeld, J., 1999. Ternary nucleation of H_2SO_4, NH_3, and H_2O in the atmosphere. Journal of Geophysical Research 104 (D21), 26,349–26,353.

Kreidenweis, S.M., Walcek, C.J., Feingold, G., Gong, W., Jacobson, M.Z., Kim, C.-H., Liu, X., Penner, J.E., Nenes, A., Seinfeld, J.H., 2003. Modification of aerosol mass and size distribution due to aqueous-phase SO_2 oxidation in clouds: Comparison of several models. Journal of Geophysical Research 108 (D7), 4213 AAC 1-12.

Laj, P., Fuzzi, S., Facchini, M.C., Orsi, G., Berner, A., Kruisz, C., Wobrock, W., Beswick, K.M., Gallagher, M.W., Colvile, R.N., Choularton, T.W., Nason, P., Jones, B., 1997. Experimental evidence for in-cloud production of aerosol sulphate. Atmospheric Environment 31 (16), 2503–2514.

Leaitch, W.R., 1996. Observations pertaining to the effect of chemical transformation in cloud on the anthropogenic aerosol size distribution. Aerosol Science Technology 25, 157–173.

Lelieveld, J., Heintzenberg, J., 1992. Sulfate cooling effect on climate through in-cloud oxidation of anthropogenic SO_2. Science 258, 117–120.

Limbeck, A., Puxbaum, H., Otter, L., Scholes, M.C., 2001. Semivolatile behavior of dicarboxylic acids and other polar organic species at a rural background site (Nylsvley, RSA). Atmospheric Environment 35 (10), 1853–1862.

Mertes, S., Lehmann, K., Nowak, A., Massling, A., Wiedensohler, A., 2005. Link between aerosol hygroscopic growth and droplet activation observed for hill cap clouds at connected flow conditions during FEBUKO. Atmospheric Environment (this issue).

Ogren, J.A., Heintzenberg, J., Charlson, R.J., 1985. In-situ sampling of clouds with a droplet to aerosol converter. Geophysical Research Letter 12 (3), 121–124.

Schwarzenböck, A., Heintzenberg, J., Mertes, S., 2000. Incorporation of aerosol particles between 25 and 850 nanometers into cloud elements: measurement with a new complementary sampling system. Atmospheric Research 52 (4), 241–260.

Tilgner, A., Heinold, B., Nowak, A., Herrmann, H., 2005a. Meteorological characterisation of the FEBUKO hill cap cloud experiments, Part I: synoptic characterisation of measurement periods. Atmospheric Environment (this issue).

Tilgner, A., Majdik, Z., Simmel, M., Wolke, R., Herrmann, H., 2005b. SPACCIM simulations of multiphase chemistry occuring in the FEBUKO hill-capped cloud experiments. Atmospheric Environment (this issue).

vanPinxteren, D., Plewka, A., Hofmann, D., Müller, D., Kramberger, H., Svrcina, B., Bächmann, K., Jaeschke, W., Mertes, S., Collett Jr., J.L., Herrmann, H., 2005. Schmücke hill-capped cloud and valley stations aerosol chemical compostion during FEBUKO (II): organic compounds. Atmospheric Environment (this issue).

Wiedensohler, A., Hansson, H.-C., Orsini, D., Wendisch, M., Wagner, F., Bower, K.N., Choularton, T.W., Wells, M., Parkin, M., Acker, A., Wieprecht, W., Fachini, M.C., Lind, J.A., Fuzzi, S., Arends, B.G., Kulmala, M., 1997. Nighttime formation and occurrence of new particles associated with orographic clouds. Atmospheric Environment 31 (16), 2545–2559.

Wieprecht, W., Acker, K., Mertes, S., Collett Jr., J.L., Jaeschke, W., Brüggemann, E., Möller, D., Herrmann, H., 2005. Cloud physics and cloudwater sampler comparison during FEBUKO. Atmospheric Environment (this issue).

Yu, F., Turco, R.P., 2000. Ultra-fine aerosol formation via ion-mediated nucleation. Geophysical Research Letter 27 (6), 883–886.

Yuskiewicz, B.A., Stratmann, F., Birmili, W., Wiedensohler, A., Swietlicki, E., Berg, O., Zhou, J., 1999. The effects of in-cloud mass production on atmospheric light scatter. Atmospheric Research 50, 265–288.

3B2v8.06a/w (Dec 5 2003).51c XML:ver:5.0.1 AEA : 5767 Prod.Type:FTP pp.1–10(col.fig.:NIL) ED:S.Latha PAGN:vs SCAN:global

ARTICLE IN PRESS

Available online at www.sciencedirect.com

SCIENCE DIRECT®

ELSEVIER

Atmospheric Environment ▮ (▮▮▮▮) ▮▮▮–▮▮▮

ATMOSPHERIC ENVIRONMENT

www.elsevier.com/locate/atmosenv

Link between aerosol hygroscopic growth and droplet activation observed for hill-capped clouds at connected flow conditions during FEBUKO

S. Mertes*, K. Lehmann, A. Nowak, A. Massling, A. Wiedensohler

Leibniz-Institut für Troposphärenforschung, Permoserstr. 15, 04318 Leipzig, Germany

Abstract

Within the ground-based cloud passage experiment FEBUKO, which was carried out at the mountain ridge Thüringer Wald (Germany) during October 2001 and 2002, the dry number size distribution and hygroscopic growth of aerosol particles upwind cloud and the dry number size distributions of interstitial particles and cloud droplet residuals inside cloud were measured at connected flow conditions. The connected flow between the upwind and in-cloud summit site was meteorologically predicted and experimentally confirmed for three selected cloud events. For these events, it could be verified that entrainment and droplet deposition had only a minor influence on the evolution of the particle size distribution between the two sites. Hence, the size resolved soluble volume fraction of the cloud input aerosol particles determined from the hygroscopic growth measurements could be related to the particle activation inferred from the particle size distributions observed inside cloud. The shape and steepness of the scavenging fraction as a function of particle diameter was found to correlate with the increase of soluble volume fraction with size, which had implications for the droplet activation diameter of the cloud condensation nuclei (CCN) that ranged between 110 and 180 nm. The minimum soluble volume fraction ε_{min} that was required to serve as CCN was determined for three different dry diameters from the relation of the particle volume fraction and scavenging fraction. From the comparison with ε_{min} predictions from classical Köhler theory it is inferred that aerosol particles remained in the interstitial phase although they should have been activated. A discussion of different processes which have the general ability to explain this finding favoured the hypothesis of organic surface films retarding the uptake of water molecules.

Keywords: Particle soluble volume fraction; Cloud droplet residues; Interstitial particles; Droplet activation; Cloud condensation nuclei

1. Introduction

The number concentration of atmospheric particles that form clouds, the so-called cloud condensation nuclei (CCN), have been found to impact the number and size of cloud droplets (Leaitch et al., 1996; Vong and Covert, 1998). Consequently, they are able to affect the radiative properties of clouds (Twomey et al., 1984). In order to quantify this indirect aerosol forcing on climate (Charlson et al., 1992) it is indispensable to understand the activation of atmospheric aerosol particles to cloud droplets. At a given supersaturation and given dry particle diameter, the water soluble fraction of the aerosol particle is the key parameter that determines whether it will form a cloud droplet or not. Inorganic ions and especially non-seasalt sulphate were known to

*Corresponding author. Tel.: +49 341 235 2153; fax: +49 341 235 2361.

E-mail address: mertes@tropos.de (S. Mertes).

1352-2310/$ - see front matter © 2005 Published by Elsevier Ltd.
doi:10.1016/j.atmosenv.2005.02.010

be a dominant CCN component (Hegg et al., 1993) and in the last years it was suggested that organic aerosol particles might be a source of additional CCN (Novakov and Penner, 1993). In order to investigate the potential of atmospheric particles to serve as CCN in field experiments hygroscopic growth measurements, up to 90% relative humidity (RH) were carried out (Saxena et al., 1995) and were later on combined with particle activation measurements at controlled and constant supersaturation by means of CCN counters (Hämeri et al., 2001). The relation between particle hygroscopic growth and nucleation scavenging in real clouds was studied within ground-based cloud experiments at Kleiner Feldberg, Germany (Svenningsson et al., 1994) and Great Dun Fell (Svenningsson et al., 1997). The hygroscopicity of interstitial and cloud residual particles were compared by Svenningsson et al. (1994) concluding that more hygroscopic particles form droplets to a much greater extend than less hygroscopic particles. Furthermore, they concluded that the ability of the more hygroscopic particles to serve as CCN is especially essential for cloud formation at low peak supersaturations. Svenningsson et al. (1997) measured the particle hygroscopic growth downwind a hill cap cloud. Therefore they were not able to correlate the hygroscopicity of the cloud input aerosol to droplet formation. They found a considerable amount of hygroscopically inactive material added during particle growth from the Aitken to the accumulation mode. The material was suspected to be organic carbon but the mass increment could not be clearly assigned to cloud processes.

This work takes advantage of field measurements from the ground-based cloud experiment FEBUKO (field investigations of budgets and conversions of particle phase organics in tropospheric cloud processes), which was carried out at the low mountain ridge Thüringer Wald in central Germany to evaluate the relation between the hygroscopicity of the cloud aerosol particles entering a hill-capped cloud and the particle activation inside cloud. In refinement to the previous studies, results of interstitial and cloud residual particle size distributions and solubility of the aerosol particles (in terms of soluble volume fractions) located upwind cloud are considered.

2. Experimental

The field measurements were carried out at the Thüringer Wald in central Germany in October 2001 and 2002. The Thüringer Wald is a low mountain ridge which extends from south-east to north-west endways for about 60 km, so that at south-westerly winds the air masses are forced to cross the ridge. At sufficient moisture, supersaturation is reached below the summit caused by the lifting of the air parcels so that orographic clouds are formed. The in-cloud station Schmücke (937 m asl, named summit site in the following) is situated on a saddle of the ridge and the upwind station Goldlauter (605 m asl) is located in a valley at an air distance of about 3 km south-west from the summit site. All experimental activities and a detailed presentation of the topographic situation is summarised in Herrmann et al. (2005). Measurements were started and continued after cloud formation at south-westerly winds when (a) liquid water content was larger than 0.1 g m^{-3}, (b) wind direction was between 190° and 230°, (c) wind speed was in a range from 5 to 12 m s^{-1} at the summit site, (d) as long as upwind and downwind site remained underneath cloud base and (e) no rain was observed at all three measuring sites.

2.1. Measurements at the upwind site

At the upwind site the aerosol was sampled through an inlet facing the main wind direction 6 m above ground and dried below 30% RH. Thereafter, the sampled air was distributed to a differential mobility particle sizer (TDMPS, Birmili et al., 1999) and a hygroscopicity tandem differential mobility analyser (HTDMA, Liu et al., 1978) to measure the dry particle size distribution (22 nm $< d_p <$ 900 nm) and the particle hygroscopic growth (at 90% RH, for d_p = 50, 150 and 250 nm), respectively. Due to the dry sheath air, the relative humidity inside the DMPS system at the upwind site was around 10%. The size distribution measurements were carried with a time resolution of 15 min whereas the hygroscopic growth measurements of the three dry particle diameters were repeated every 40 min.

2.2. Measurements at the summit site

Inside a cloud counterflow virtual impactor (CVI, Ogren et al., 1985) and a complementary droplet segregating interstitial inlet (INT) were deployed to separately collect cloud droplets and interstitial particles at a operationally defined discrimination diameter of 5 μm (Schwarzenböck et al., 2000). The segregation of the interstitial phase (particles and gases) by the CVI is achieved by a counterflow effusing from the inlet tip, which allows only hydrometeors of sufficient inertia to enter the CVI system provided that the cloud air is accelerated to a velocity of more than 100 m s^{-1} at the CVI tip. Therefore the CVI inlet is installed in a small wind tunnel. The CVI wind tunnel and the interstitial inlet were installed outside of two separate windows that are located at the upright wall of the top floor of a research building. Both inlets faced the favoured south-west direction (215° which was close to the centre of the accepted wind direction range) at a height of 15 m, which was above the forest canopy. Upon sampling, the droplets remain airborne in the CVI system where they

are evaporated in a particle free and dry carrier air. The liquid water and other volatile compounds dissolved in the droplets are driven into the gas phase, whereas the non-volatile components remain as dry residual particles (RH < 10%). At the INT sampling system interstitial particles were dried to 50% RH. Downstream the INT and CVI, two DMPS systems measured the residual and interstitial dry particle number size distribution ($22\,nm < d_p < 900\,nm$) simultaneously. Inside both DMPS systems the dry sheath air reduced the relative humidity down to less than 10%. The time resolution of the dry particle number size distribution measurements at both inlets was 15 min. Prior to the field experiments, the DMPS systems were inter-compared yielding an agreement within 10% with regard to particle concentration per size bin. No relative shifts with regard to particle size were observed between the different DMPS systems. An overview about the inlets and the instrumentation at the two measurement sites used for this study is shown in Table 1.

3. Results

The best connected flow conditions from the upwind to the summit site were validated for three of 14 investigated cloud events by a synoptic and a flow modelling evaluation (Heinold et al., 2005; Tilgner et al., 2005). These golden FEBUKO cloud events (termed E I, E II and E III in the following) were chosen for the objective of this study. The fact that the in-cloud site is situated on a saddle at the lowest point in this region of the mountain ridge gives further confidence that the same aerosol population detected in the surface air upstream of the ridge is measured at the summit site. This assumption is much more unlikely when the in-cloud measurement site would be positioned at the highest locations of the mountain ridge. However the term connected flow conditions does not necessarily imply that exactly the same air parcel is passing the upwind and summit site. But it should indicate that the same air mass traversed both sites. Therefore, the physico-chemical properties of the aerosol particles measured upwind and inside cloud are representative for the cloud input aerosol, for the CCN and for the interstitial particles, respectively.

Event E I (2001: 26.10. 21:45–27.10. 12:45) and E III (2002: 16.10. 21:00–17:10. 04:00) were not temporally subdivided whereas event E II consists of two short periods (4 and 2 h) of undesirable and one very long period (17 h) of favourable meteorological conditions (Tilgner et al., 2005). Thus, the discussion of E II will be restricted to the long period only (2001: 07.10. 18:00–08.10. 11:15). During all three cloud events maritime air masses originating from the Atlantic Ocean that were affected by the western European continent prevailed at the measurement sites according to backward trajectories analysed by Tilgner et al. (2005). Only for E II the air mass arrived from the western Mediterranean Sea and travelled over southern France for a short time period between 01:00 and 05:00. The clouds observed at the summit site during all three events could be clearly identified as orographic but were temporarily mixed with advected stratus clouds at heights above the summit level (Tilgner et al., 2005).

3.1. Dry particle number size distributions at upwind and summit site

Mean number size distributions of total ambient aerosol particles upwind cloud and interstitial particles and cloud droplet residuals inside cloud in the diameter range of the DMPS measurements for the three selected cloud events are depicted in Fig. 1. The total particle number size distribution persisting at the summit site which is inferred from the sum of the interstitial and residual particle number size distribution is indicated in addition. The error bars added to the particle number size distributions measured at the summit site take into account the 10% relative DMPS deviations determined in the lab and the Poisson error which is only perceivable at low counting statistics. It is obvious in Fig. 1 that the upwind ambient aerosol particle number size distribution is quite well reproduced by the sum of the interstitial and residual particle number size distributions determined at the summit site in all cloud events. This observation supports on one hand the meteorological evaluation of a connected airflow be-

Table 1
Overview of microphysical aerosol particle measurements at the upwind and summit site

Measurement site	Inlet	Aerosol type	Instrument	Dry particle size range
Upwind	Wind facing inlet	Ambient	DMPS	$22\,nm < d_p < 900\,nm$
(Below cloud-base)			HTDMA	$d_p = 50, 150, 250\,nm$
Summit (in-cloud)	CVI	Droplet residuals	DMPS	$22\,nm < d_p < 900\,nm$
	INT	Interstitial	DMPS	$22\,nm < d_p < 900\,nm$

The DMPS measured dry particle number size distribution and the HTDMA determined the particle hygroscopicity.

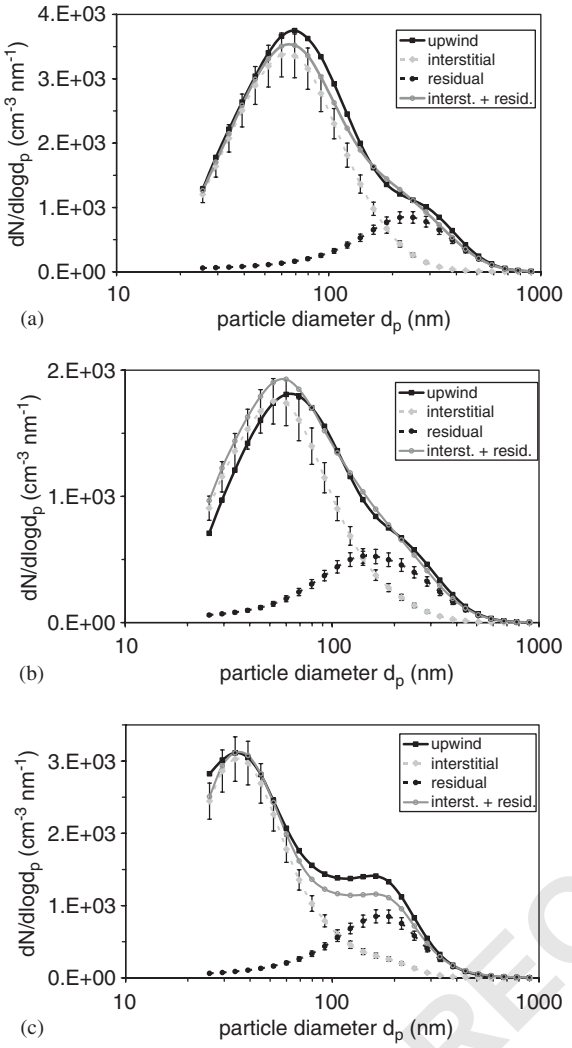

Fig. 1. Dry particle number size distributions determined upwind and inside cloud (interstitial, residual) averaged over the cloud events (a) E I, (b) E II, (c) E III. Furthermore, the total particle number size distribution at the summit site derived from the interstitial and residual particle number size distribution is shown.

tween the two sites and gives on the other hand a first impression of how the upwind aerosol population is partitioned into an activated and a non-activated fraction inside cloud. Furthermore, it implies that entrainment and droplet deposition had only a negligible influence on the total particle number budget up to $d_p = 900$ nm. In principle, entrainment which is defined as mixing of air from above into the cloud top can occur even for air flows across a hill. For hill-capped clouds the mixing from above should be mostly restricted to the upper cloud regions and the entrained, sub-saturated air, which might additionally contain a different aerosol population, is not mixed down to the hill surface until downwind of the summit. Different indicators to identify whether entrainment affects the surface measurements of a hill cloud experiment are proposed by Colvile et al. (1997). The mono-modal droplet number size distribution and a liquid water content (LWC) closely correlated with cloud base height (Wieprecht et al., 2005), identical ozone concentration time series at upwind and summit site (Brüggemann et al., 2005; Heinold et al., 2005) and a satisfactory particle number closure between both sites (Mertes et al., 2005) give evidence that entrained air did not substantially penetrate to the summit surface during all presented cloud events. From a detailed inter-comparison of the upwind, summit and downwind particle number size distributions, Mertes et al. (2005) found a very low impact of entrainment on the particle size distributions too, that nevertheless seemed to gradually increase from E I, E III and E II. Additionally, small losses of activated particles larger than $d_p = 300$ nm caused by droplet deposition were observed (Mertes et al., 2005). This particle loss process did not affect the subsequent discussion, because the hygroscopic growth measurements were restricted to dry particle sizes below $d_p = 300$ nm.

The shape of the dry particle number size distributions in E I and E II (Fig. 1a and b) looks very similar with a strong Aitken-mode and a less pronounced accumulation mode centred at $d_p = 70$ and 200 nm. Only the particle number is lower by roughly a factor of two during E II. For E III, the Aitken and accumulation mode are more separated and located at smaller particle diameters of $d_p = 30$ and 160 nm, respectively (Fig. 1c). The dry particle number size distributions measured in-cloud reveal that most Aitken mode particles remained in the interstitial phase whereas most accumulation mode particles served as CCN and are found as residual particles.

3.2. Droplet activation observed inside cloud

The number fraction of aerosol particles that undergo nucleation scavenging (scavenging fraction SF) as a function of particle size can be derived by the interstitial and residual dry particle number size distributions according to Eq. (1), where N_{res} and N_{int} denote residual and interstitial particles:

$$SF_{ri} = \frac{dN_{res}/d\log d_p}{dN_{res}/d\log d_p + dN_{int}/d\log d_p}. \quad (1)$$

With respect to the consideration of air flow connection between upwind and summit site the same parameter can be calculated from the upwind and interstitial dry particle number size distributions (Svenningsson et al., 1997) as shown below:

$$SF_{ui} = \frac{dN_{upwind}/d\log d_p - dN_{int}/d\log d_p}{dN_{upwind}/d\log d_p}. \quad (2)$$

The two different approaches are illustrated in Fig. 2 (this time with a linear x-scale up to 400 nm). It can be noticed that SF_{ui} determined from Eq. (2) is closely related to the particle phase partitioning observed in the cloud (Eq. (1)) which again signifies that the particles measured at the upwind site represent the cloud input aerosol.

The small deviations between the two different approaches might be partly caused by the 5 μm cut-off diameter and the non-ideal cut-off characteristics of CVI and INT when many droplets equal or smaller 5 μm were present. This primarily applies to the used CVI for which the collection efficiency increases from 0.1 to 0.9 within less than 2 μm whereas the collection efficiency of the INT designed as a classical inertial impactor is even steeper. Thus, the good agreement of Eq. (2) (that did not use CVI results) and Eq. (1) signifies that the scavenging fractions were not significantly influenced by the instrumentation. Very similar phase partitioning curves with respect to shape, steepness and diameter dependence were determined at Great Dun Fell by Martinsson et al. (1999) using the Droplet Aerosol Analyzer (DAA) technique which is not affected by sampling cut-off characteristics to separate droplets and interstitial particles.

In Fig. 2 SF did not reach a value of 1 for large particles but was always above 0.9. According to Noone et al. (1992) this denotes a low entrainment influence (largest for E II, lowest for E I), which is in agreement to the findings of Mertes et al. (2005) mentioned before. The simple S-shape of SF implies that the CCN are not strictly internally mixed and experienced a range of supersaturations (Noone et al., 1992). A complete externally mixed CCN population would contain different activation diameter thresholds resulting in a SF step function which was not found for one of the cloud events. For E I and E III it is obvious that the increase of SF_{ri} and SF_{ui} is rather steep but appeared at different particle size ranges whereas for E II both different scavenging fractions increase less sharp. A scavenging fraction > 0.1 was observed down to 60 nm during E II and E III and down to 100 nm during E I. Based on Eq. (1), a so-called droplet activation diameter $d_{p,50}$, which is defined for SF = 0.5, of about 180, 140 and 110 nm are inferred for E I, E II and E III. Hallberg et al. (1994) obtained similar shapes of the SF functions and similar $d_{p,50}$ from their measurements of interstitial and total aerosol particle size distributions at Kleiner Feldberg, which is a low mountain of comparable height located only about 200 km west of the Thüringer Wald.

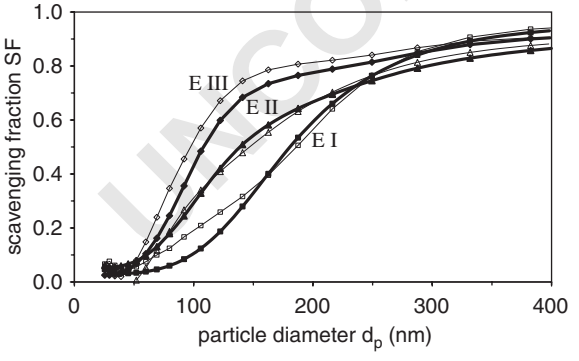

Fig. 2. Scavenging fractions SF as function of the dry particle diameter determined for the cloud events E I, E II and E III. Lines with thick and open symbols are derived from Eq. (1) and (2), respectively.

3.3. Soluble volume fraction of the aerosol particles upwind cloud

The hygroscopic growth of the cloud input aerosol particles was determined at the upwind site by HTDMA measurements at three different dry diameters at 90% RH. The dry sizes of d_p = 50, 150, and 250 nm refer to particle subsets that are hardly, partly, and mostly activated to cloud droplets along the SF curves in Fig. 2. The obtained growth factors, defined by the ratio of the wet to the dry particle radius and measured with an uncertainty of 5%, were translated into a soluble volume fraction ε using the hygroscopic growth of ammonium sulphate as a reference. Details of the HTDMA operating conditions and of the determination of ε are given in Lehmann et al. (2005). The derivation of ε is based on the simple assumption of a two-component aerosol consisting of a completely insoluble part and ammonium sulphate. Thus, an ε below 100% can also be derived for a single component particle that consists of a substance with a lower hygroscopic growth than ammonium sulphate. Nevertheless, the growth properties of such a particle should be similar to the assumed particle. Furthermore, Lehmann et al. (2005) found a good agreement of their method to the independent ε determination from chemical analysis of aerosol samples collected on impactor stages. The number distributions of the soluble volume fraction subdivided in discrete 10% solubility classes are illustrated as event averages in Fig. 3. It is obvious that the 50 nm particles possess a much less soluble volume fraction and show a different ε distribution than the two larger particle diameters. In E III, the 50 nm particles were even more hydrophobic than in E I and E II with a maximum number fraction of 32% for ε between 0% and 10% compared to a maximum number fraction (about 17%) at the class of 20–30% soluble volume fraction for E I and E II. Another distinction between E I and E II on one hand and E III on the other hand can be noticed for the 150 and 250 nm particles. During E III, these particles

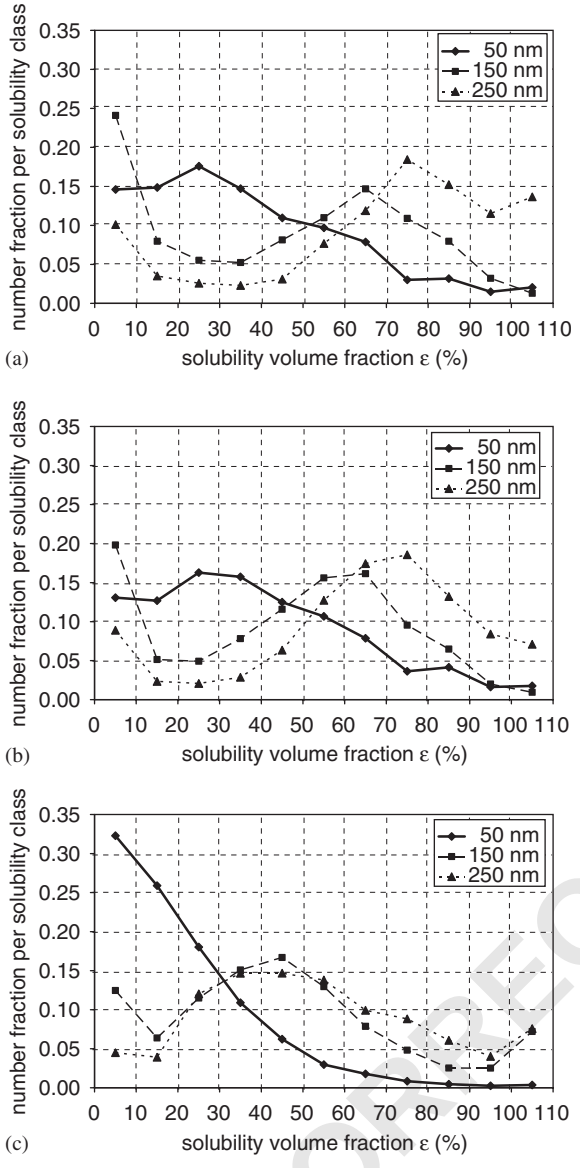

Fig. 3. Number distribution of the soluble volume fractions derived from HTDMA measurements of the cloud input aerosol at the upwind site averaged over the cloud events (a) E I, (b) E II, (c) E III.

contained nearly the same number fraction in each solubility class (maximum at ε between 40% and 50%) whereas in the 2001 events the ε distribution of the 250 nm particles is shifted to higher soluble volume fractions (maximum in the class of 70–80% soluble volume fraction) compared to the ε distribution of the 150 nm particles (maximum at 60–70% soluble volume fraction). These findings are corroborated by the measured dry size distributions indicating that for E III 150 and 250 nm particles belong to the accumulation mode whereas for the other two events the particles with a diameter of 150 nm are partly related to the Aitken mode (Fig. 1). The non-zero values for the solubility class >100% observed mainly for 250 nm particles reveal the slight existence of aerosol components growing larger than ammonium sulphate. Due to the marine origin of the air mass, this might be sodium chloride (growth factor of 2.35 at 90% RH and dry diameter of 250 nm compared to a growth factor of 1.72 for ammonium sulphate) coated by less hygroscopic material. However, ammonium nitrate particles (growth factor 1.82) would cause the same effect. A less and more hygroscopic mode for 150 and 250 nm particles are visible during all cloud events, which is similar to measured growth factor distributions at Kleiner Feldberg (Svenningsson et al., 1994). Moreover, it can be noted from Fig. 3 that the soluble volume fraction varies substantially within the two different hygroscopic modes, i.e. they represent a distribution of diverse hygroscopic properties and cannot be described by one ε value only.

3.4. Relation particle soluble volume fraction and droplet activation

By cumulating the number fractions of the ε classes from high to low soluble volume fractions, the particle number fractions above a specified ε limit is obtained. These values are plotted as a function of the dry particle size in Fig. 4 and interpolated by straight lines for a better lucidity, even though the behaviour in between the single data points might be different. The lowest curve, e.g., illustrates the change in number fraction from $d_p = 50$ to 250 nm of particles that contain a soluble volume fraction of more than 90%. For all events the number fraction of the different upper ε limits increases with particle size (at least for $\varepsilon > 40\%$). This enhancement is less steep than the scavenging fraction determined inside cloud (cf. Eq. (1)) which is additionally included in Fig. 4. The comparison of SF and the set of ε curves implies for E I and E III that larger particles needed a smaller soluble fraction to form cloud droplets, which is in qualitative agreement with Köhler theory and observations of Svenningsson et al. (1994, 1997). This relation is not strictly found for E II, which might be an indication, that the little stronger entrainment influence found for this cloud event already offsets the correlation which is observed for the other two events between upwind and summit site. Thus, the further interpretation will be restricted to E I and E III. The array of ε curves shows a convex and a concave curvature for event E I and E III which is obviously associated with the shape of SF (Fig. 4). Fig. 4 implies that a strong gain in the number fraction of the different ε limits promotes the steepness of the SF curve between $d_p = 50$ and 150 nm for E III and between $d_p = 150$ and 250 nm for E I leading to the significantly higher $d_{p,50}$ for

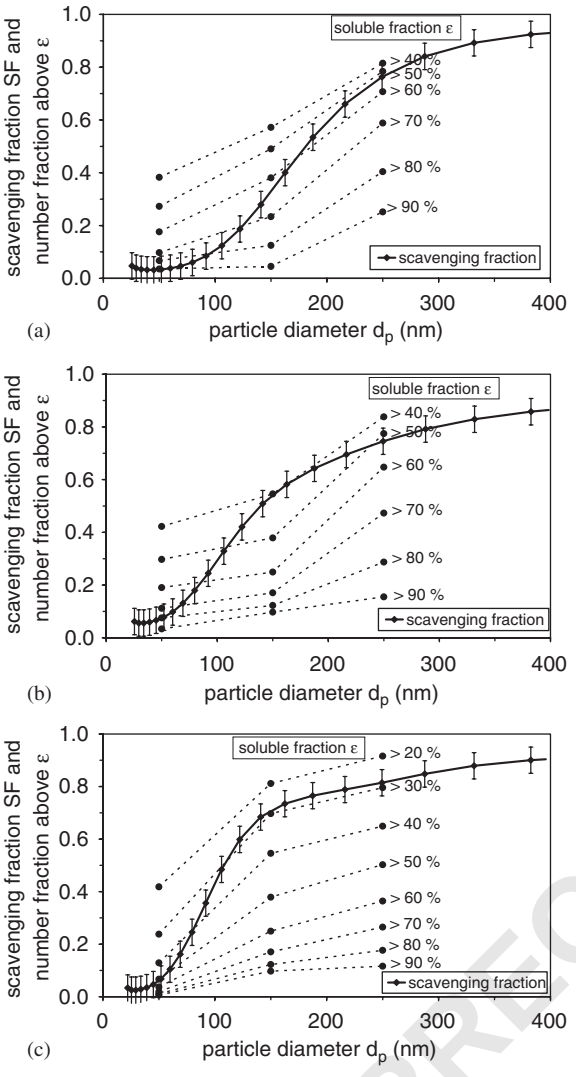

Fig. 4. Number fraction of aerosol particles above the given soluble volume fraction as a function of particle diameter determined at the upwind site for the cloud events (a) E I, (b) E II, (c) E III. SF obtained by Eq. (1) for the different cloud events are included. Error bars represent an uncertainty of SF of 0.05.

E I. Whenever the gain in ε as a function of particle diameter is small, the scavenging fraction is rather flat. The minimum soluble volume fraction ε_{min} that was required to act as CCN at a specified dry particle size can be extracted from the intersections of SF with the upper ε limits in Fig. 3. These ε_{min} values are given in Table 2 (including E II) with errors that are inferred from a SF uncertainty of 0.05 already indicated in Fig. 3. With regard to Fig. 2 it should be noticed that the more hygroscopic mode of 150 and 250 nm particles were entirely activated in all three cloud events but with the one exception of 150 nm particles in E I where only particles at the right "even more hygroscopic" edge of this mode could serve as CCN. The ε_{min} values for E I and E III are plotted in Fig. 5. ε_{min} curves calculated from the Köhler equation taking into account ammonium sulphate as soluble material (consistent with the HTDMA data processing) are added in Fig. 5 as a function of dry particle diameter for different maximum supersaturations S_{max}. From the comparison with the 50 nm particle results it can be concluded that S_{max} had to be about 0.55% and 0.4% for droplet activation during E III and E I. These values are consistent with cloud microphysical model calculations of the saturation profiles inside the orographic clouds formed during the respective cloud events conducted by Simmel et al. (2005). The data points for 150 and 250 nm do not follow the lines of constant peak supersaturation but decrease much less steep, i.e. particles in this size range remained interstitial although they should be activated due to their sufficient soluble volume fraction according to Köhler theory. This phenomena was already qualitatively observed in former ground-based cloud studies (Hallberg et al., 1998; Hallberg et al., 1994; Martinsson et al., 1999; Svenningsson et al., 1994). These studies discussed a variation of the maximum supersaturation, entrainment and different aerosol chemical properties for explanation. In order to reconcile the results for the particles with $d_p = 50$ and 250 nm in Fig. 5 with the classical Köhler theory, the peak supersaturation would need to vary from 0.40 to 0.06 for E I and from 0.55 to 0.08 for E III (for $d_p = 150$ nm, intermediate peak supersaturations of 0.10 and 0.16 would be derived from Fig. 5). This implies variations in S_{max} of at least a factor

Table 2
Minimum soluble volume fractions ε_{min} required for particles to serve as CCN inferred from the intersections of SF with the upper ε limits in Fig. 3

Dry particle diameter	E I (26.10–27.10.2001)	E II (07.10–08.10.2001)	E III (16.10–17.10.2002)
$d_p = 50$ nm	0.99 (+0.11,−0.14)	0.94 (+0.12,−0.14)	0.60 (+0.42,−0.15)
$d_p = 150$ nm	0.64 (+0.04,−0.04)	0.39 (+0.03,−0.03)	0.28 (+0.05,−0.03)
$d_p = 250$ nm	0.48 (+0.08,−0.18)	0.44 (+0.08,−0.10)	0.26 (+0.05,−0.04)

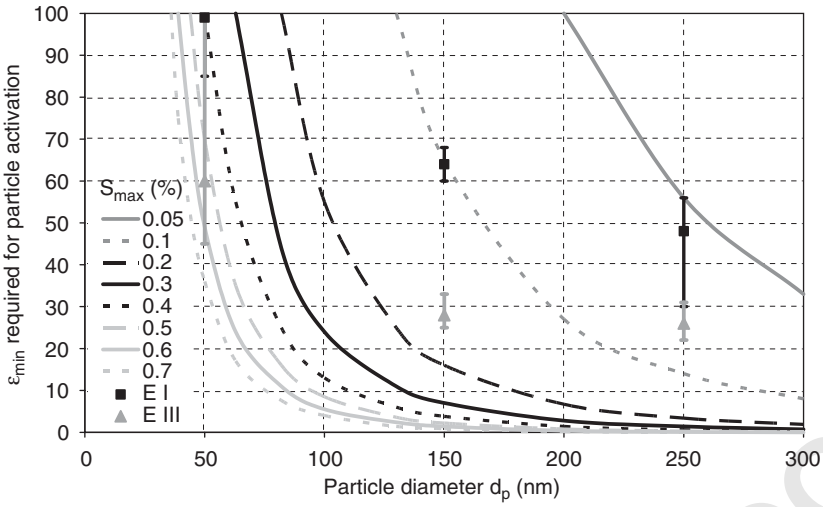

Fig. 5. ε_{min} derived from intersections of soluble volume fractions and SF in Fig. 4 for E I (squares) and E III (triangles) and ε_{min} required for particle activation at constant maximal supersaturation calculated by the Köhler equation using ammonium sulphate as soluble substance.

of 7. Since the measurements were only conducted in a very limited range of meteorological conditions (cf. Section 2) especially with regard to wind direction and wind speed it can be excluded that the updraft and thus S_{max} vary in the required range during the averaged time periods. The same conclusion was drawn by Hallberg et al. (1994) where a variation of the maximum supersaturation by a factor of 5 would have been required to explain the existence of interstitial particles with $d_p = 300$ nm. According to the detailed discussion in Sections 3.1 and 3.2, entrainment seems to be unlikely as well to explain the observed existence of the large interstitial particles. This is further supported by the fact that there is a significant difference in S_{max} inferred from $d_p = 150$ and 250 nm for E I and E III in Fig. 5. It is not conclusive that external influences like entrainment, variations in updraft velocities and mixing of air parcels travelling different paths uphill, would affect the 150 and 250 nm particles differently. The observed trend with particle size more likely implies that the existence of large interstitial particles is linked to their special particle chemical composition as it was also proposed in the study of Martinsson et al. (1999). According to Hallberg et al. (1998) particles with an organic surface layer that slow down the uptake of water and thus extend the time needed to grow beyond the particles critical diameter is a hypothesis that would consistently explain the experimental finding. Those particles (8% and 4% of all 250 nm particles, 25% and 6% of all 150 nm particles in E I and E III) might not be activated during the short time period of high supersaturation close to the cloud base. Subsequently, when the supersaturation decreased in the cloud their soluble volume fraction is insufficient to become activated or they formed droplets that do not grow beyond 5 μm, which was the operationally defined separation size between cloud droplets and interstitial particles. The time required to reach their equilibrium size inside a HTDMA, where they are exposed to a constant RH, is smaller than their residence time of about 6 s (Sjögren et al., 2004). Thus, the determination of the soluble volume fraction of these particles should not be biased by this effect and would be otherwise under- but never overestimated. CCNs containing substances with low solubility that go into solution above 90% RH would also cause only an underestimation of ε. Only a 5% fraction of film forming compounds to the total particle mass is sufficient to create complete monolayers (Feingold and Chuang, 2002). Simulations of Podzimek and Saad (1975) indicated that these layers break later for larger CCN, which is consistent with the different behaviour of 150 and 250 nm particles in Fig. 5. These condensation-inhibiting organic films do not need to consist of so-called surface active substances, i.e. they do not necessarily lead to a reduction of surface tension. Unfortunately no analysis method was employed to proof the existence of film forming organic compounds were existent during FEBUKO. However, organic layers have been already observed on marine aerosol particles (Tervahattu et al., 2002) in air masses originating from the Atlantic Ocean which is identical to this study. The existence of organic films on part of the aerosol particles would be in addition an explanation of the observed broadening of the droplet number size distribution (Simmel et al., 2005) according to model simulations by Feingold and Chuang (2002).

4. Summary

The meteorologically predicted connected flow conditions for three selected cloud events within the ground-based cloud passage experiment FEBUKO could be confirmed by simultaneous measurements of dry particle number size distribution carried out upwind and inside the existing hill-capped clouds. From the deduced scavenging fractions as functions of dry particle diameter no or only a minor influence of droplet deposition and entrainment (mixing of a different aerosol population) on the dry particle number size distributions is observed during the events which is in agreement to results of other FEBUKO investigations. Droplet activation diameters $d_{p,50}$ in a range between 110 and 180 nm were inferred from the calculated scavenging fractions.

Upwind cloud, hygroscopic growth factors at dry particle diameters $d_p = 50, 150, 250$ nm at 90% RH were determined and translated to classes of particle soluble volume fractions between 0% and 100%. In general larger particles contained higher soluble volume fractions ε but differences in the number distribution of ε between the cloud events were found. When referring the ε number distribution to the droplet activation observed in cloud during connected flow conditions a strong correlation between the increase of soluble volume fraction with size and the shape and steepness of the scavenging fraction as a function of particle diameter was observed in two of three cases. This close relationship affected the absolute value of the droplet activation diameter $d_{p,50}$.

From the comparison of particle soluble volume fraction and scavenging fraction the minimum soluble volume fraction ε_{min} that was required to act as CCN at a specified dry particle size was determined and compared to predictions of the Köhler equation. It was found, that aerosol particles remained interstitial although they should be activated according to Köhler theory due to their adequate soluble volume fraction. Because meteorological issues like entrainment, variations in peak supersaturation and different particle uphill trajectories are inconclusive to explain the observation, the existence of film-forming compounds on part of the cloud input particles are hypothesized. It is supposed that these particles did not form cloud droplets during the time period of high supersaturation close to cloud base because of condensation inhibiting organic surface layers that extend the time to grow beyond the critical diameter until regions of lower supersaturation are reached where they cannot be activated anymore.

Acknowledgement

This study was funded by the Bundesministerium für Bildung und Forschung within the German atmospheric research program AFO2000 under the grant FKZ 07ATF01. We like to acknowledge the great support by the Deutsche Wetterdienst and the Deutsche Umweltbundesamt. We thank Werner Sarwatka*, Hartmut Haudek, Andrea Haudek and Stephan Günnel for their help in the preparation and set-up of the experimental equipment and Diane Galgon and Katrin Schwirn for the inversion of the dry particle number size distributions.

References

Birmili, W., Stratmann, F., Wiedensohler, A., 1999. Design of a DMA-based size spectrometer for a large particle size range and stable operation. Journal of Aerosol Science 30 (4), 549–553.

Brüggemann, E., Gnauk, T., Mertes, S., Acker, K., Auel, R., Wieprecht, W., Möller, D., Collett Jr., J.L., Chemnitzer, R., Rüd, C., Junek, R., Herrmann, H., 2005. Schmücke hill-capped cloud and valley stations aerosol chemical composition during FEBUKO (I): Standard trace gases, main components, and metals. Atmospheric Environment this issue.

Charlson, R.J., Schwartz, S.E., Hales, J.M., Cess, R.D., Coakley Jr., J.A., Hansen, J.E., Hofmann, D.J., 1992. Climate forcing by anthropogenic aerosols. Science 256, 423–430.

Colvile, R.N., Bower, K.N., Choularton, T.W., Gallagher, M.W., Wobrock, W., Hargreaves, K.J., Storeton-West, R.L., Cape, J.N., Jones, B., Wiedensohler, A., Hansson, H.-C., Wendisch, M., Acker, K., Wieprecht, W., Pahl, S., Winkler, P., Berner, A., Kruisz, C., 1997. Meteorology of the Great Dun Fell cloud experiment 1993. Atmospheric Environment 31 (16), 2407–2420.

Feingold, G., Chuang, P.Y., 2002. Analysis of the influence of film-forming compounds on droplet growth: implications for cloud microphysical processes and climate. Journal of Atmospheric Science 59, 2006–2018.

Hallberg, A., Noone, K.J., Ogren, J.A., Svenningsson, I.B., Flossmann, A., Wiedensohler, A., Hansson, H.-C., Heintzenberg, J., Anderson, T., Arends, B., Maser, R., 1994. Phase partitioning of aerosol particles in clouds at Kleiner Feldberg. Journal of Atmospheric Chemistry 19, 107–127.

Hallberg, A., Noone, A., Ogren, J.A., 1998. Aerosol particles and clouds: which particles form cloud droplets? Tellus 50B, 59–75.

Hämeri, K., Väkevä, M., Aalto, P., Kulmala, M., Swietlicki, E., Zhou, J., Seidl, W., Becker, E., O'Dowd, C.D., 2001. Hygroscopic and CCN properties of aerosol particles in boreal forest. Tellus B—Chemical and Physical Meteorology 53, 359–379.

*Deceased.

Hegg, D.A., Ferek, R.J., Hobbs, P.V., 1993. Light scattering and cloud condensation nucleus activity of sulfate aerosol measured over the Northeast Atlantic Ocean. Journal of Geophysical Research 98 (D8), 14,887–14,894.

Heinold, B., Tilgner, A., Jaeschke, W., Knoth, O., Wolke, R., Herrmann, H., 2005. Meteorological characterisation of the FEBUKO hill capped cloud experiments, Part II: Tracer experiments and flow characterization of the FEBUKO measurement periods with nested non-hydrostatic atmospheric models. Atmospheric Environment this issue.

Herrmann, H., Wolke, R., Müller, K., Brüggemann, E., Gnauk, T., Mertes, S., Lehmann, K., Massling, A., Birmili, W., Wiedensohler, A., Wieprecht, W., Acker, K., Jaeschke, W., Kramberger, H., Svrcina, B., Bächmann, K., Collett Jr., J.L., Galgon, D., Schwirn, K., Nowak, A., vanPinxteren, D., Plewka, A., Chemnitzer, R., Rüd, C., Hofmann, D., Diehl, K., Hinneburg, D., Knoth, O., Sehili, A.M., Simmel, M., Mauersberger, G., Müller, F., 2005. FEBUKO and MODMEP: Field measurements and modelling of aerosol and cloud multiphase processes. Atmospheric Environment this issue.

Leaitch, W.R., Banic, C.M., Isaac, G.A., Couture, M.D., Liu, P.S.K., Gultepe, I., Li, S.-M., Kleinman, L., Daum, P.H., MacPherson, J.I., 1996. Physical and chemical observations in marine stratus during the 1993 North Atlantic Regional Experiment: factors controlling cloud droplet number concentrations. Journal of Geophysical Research 101 (D22), 29,123–29,135.

Lehmann, K., Massling, A., Tilgner, A., Mertes, S., Wiedensohler, A., 2005. Size-resolved soluble volume fractions of sub-micrometer particles in different air masses. Atmospheric Environment this issue.

Liu, B.Y.H., Pui, D.Y.H., Whitby, K.T., Kittelson, D.B., Kousaka, Y., L.McKenzie, R., 1978. The aerosol mobility chromatograph: a new detector for sulfuric acid aerosols. Atmospheric Environment 12, 99–104.

Martinsson, B., Frank, G., Cederfelt, S.-I., Swietlicki, E., Berg, O., Zhou, J., Bower, K.N., Bradbury, C., Birmili, W., Stratmann, F., Wendisch, M., Wiedensohler, A., Yuskiewicz, B., 1999. Droplet nucleation and growth in orographic clouds in relation to the aerosol population. Atmospheric Research 50, 289–315.

Mertes, S., Galgon, D., Schwirn, K., Nowak, A., Lehmann, K., Massling, A., Wiedensohler, A., Wieprecht, W., 2005. Evolution of particle concentration and size distribution observed upwind, inside and downwind hill clouds at connected flow conditions during FEBUKO. Atmospheric Environment this issue.

Noone, K.J., Ogren, J.A., Hallberg, A., Heintzenberg, J., Ström, J., Hansson, H.-C., Svenningsson, I.B., Wiedensohler, A., Fuzzi, S., Facchini, M.C., Arends, B.G., Berner, A., 1992. Changes in aerosol size- and phase distributions due to physical and chemical processes in fog. Tellus B 44, 489–504.

Novakov, T., Penner, J.E., 1993. Large contribution of organic aerosol to cloud-condensation-nuclei concentrations. Nature 365, 823–826.

Ogren, J.A., Heintzenberg, J., Charlson, R.J., 1985. In-situ sampling of clouds with a droplet to aerosol converter. Geophysical Research Letters 12 (3), 121–124.

Podzimek, J., Saad, A.N., 1975. Retardation of condensation nuclei growth by surfactant. Journal of Geophysical Research 80, 3386–3392.

Saxena, P., Hildemann, L.M., McMurry, P.H., Seinfeld, J.H., 1995. Organics alter hygroscopic behavior of atmospheric particles. Journal of Geophysical Research 100 (D9), 18,755–18,770.

Schwarzenböck, A., Heintzenberg, J., Mertes, S., 2000. Incorporation of aerosol particles between 25 and 850 nanometers into cloud elements: measurement with a new complementary sampling system. Atmospheric Research 52 (4), 241–260.

Simmel, M., Diehl, K., Wurzler, S., 2005. Numerical simulation of the microphysics of an orographic cloud: comparison with measurements and sensitivity studies. Atmospheric Environment this issue.

Sjögren, S., Weingartner, E., Baltensperger, U., Cubison, M., Topping, D., McFiggans, G., Coe, H., 2004. Hygroscopic growth and times of phase change for aerosol mixtures of inorganic salts and organic substances. European Aerosol Conference 2004, Budapest, pp. S497–S498.

Svenningsson, B., Hansson, H.-C., Wiedensohler, A., Noone, K.J., Ogren, J.A., Hallberg, A., Colvile, R., 1994. Hygroscopic growth of aerosol particles and its influence on nucleation scavenging in cloud: experimental results from Kleiner Feldberg. Journal of Atmospheric Chemistry 19, 129–151.

Svenningsson, B., Hansson, H.-C., Martinsson, B., Wiedensohler, A., Swietlicki, E., Cederfelt, S.-I., Wendisch, M., Bower, K.N., Choularton, T.W., Colvile, R.N., 1997. Cloud droplet nucleation scavenging in relation to the size and hygroscopic behaviour of aerosol particles. Atmospheric Environment 31 (16), 2463–2475.

Tervahattu, H., Hartonen, K., Kerminen, V.-M., Kupiainen, K., Aarnio, P., Koskentalo, T., Tuck, A.F., Vaida, V., 2002. New evidence of an organic layer on marine aerosols. Journal of Geophysical Research 107 (D7–D8) art. no. 4053.

Tilgner, A., Heinold, B., Nowak, A., Herrmann, H., 2005. Meteorological characterisation of the FEBUKO hill capped cloud experiments, Part I: Synoptic characterisation of measurement periods. Atmospheric Environment this issue.

Twomey, S.A., Piepgrass, M., Wolfe, T.L., 1984. An assessment of the impact of pollution on global cloud albedo. Tellus 36, 356–366.

Vong, R.J., Covert, D.S., 1998. Simultaneous observations of aerosol and cloud droplet size spectra in marine stratocumulus. Journal of Atmospheric Science 55 (12), 2180–2192.

Wieprecht, W., Mertes, S., Collett Jr., J.L., Acker, K., Brüggemann, E., Hofmann, D., Jaeschke, W., Herrmann, H., 2005. Cloud physics and cloudwater sampler comparison during FEBUKO. Atmospheric Environment this issue.

3B2v8.06a/w (Dec 5 2003).51c XML:ver:5.0.1 AEA : 5768 Prod.Type:FTP pp.1–10(col.fig.:NIL) ED:Sushma PAGN:vino SCAN:Geetha

ARTICLE IN PRESS

Available online at www.sciencedirect.com

SCIENCE DIRECT®

ELSEVIER

Atmospheric Environment ▮ (▮▮▮▮) ▮▮▮–▮▮▮

ATMOSPHERIC ENVIRONMENT

www.elsevier.com/locate/atmosenv

Size-resolved soluble volume fractions of submicrometer particles in air masses of different character

K. Lehmann*, A. Massling, A. Tilgner, S. Mertes, D. Galgon, A. Wiedensohler

Leibniz-Institute for Tropospheric Research, Permoserstr. 15, 04318 Leipzig, Germany

Abstract

As a contribution to the joint research project FEBUKO, hygroscopic properties of atmospheric Aitken and accumulation mode particles were measured in the Thueringer Wald, Germany, using a hygroscopicity-tandem differential mobility analyser (H-TDMA).

The hygroscopic growth of particles with initial dry diameters of $D_p = 50$, 150, and 250 nm at 90% relative humidity was used to calculate average distributions of the soluble volume fraction with respect to the hygroscopic growth of ammonium sulphate. The application of this parameterisation procedure was tested by analysing the dataset with respect to the dependence of the soluble volume fraction on particle size and air masses character. With increasing dry particle size, the fraction of particles containing high soluble volume fractions was found to increase. The number of accumulation mode particles in marine air masses passing the sampling site having a large soluble volume fraction was significantly higher than in air masses of more continental character. For particles with $D_p = 50$ nm, no air mass dependence of the soluble volume fraction was found. In marine air masses, particles with $D_p = 150$ and 250 nm are assumed to undergo similar evolution processes, whereas in continental air masses this seemed to be the case for particles with $D_p = 50$ nm and 150 nm.

Keywords: H-TDMA; Soluble volume fraction; Hygroscopicity; Air masses

1. Introduction

The impact of aerosol particles on the earth's radiation budget has been in the focus of atmospheric research for the last few years. Aerosol particles cause a direct climate effect by scattering and absorbing the solar radiation. Also, depending on their size and chemical composition, they can serve as nuclei for condensation and thus influence cloud formation processes (1992). An increase in aerosol number concentration, caused by e.g., anthropogenic emissions, leads to higher cloud droplet concentrations and smaller radii, yielding higher cloud albedo (Twomey, 1977) and increased cloud life times (Albrecht, 1989). The influence of aerosol particles on cloud formation, cloud physical properties, and lifetime is called the indirect climate effect.

The hygroscopic growth of particles, which describes the change of particle size as a function of relative humidity (RH), mainly depends on the chemical composition as well as on the particle size and is described by the Köhler equation (Pruppacher and Klett, 1997). A change of particle size as a function of ambient RH yields impacts on the particles' radiative properties. Also, the ability of particles to serve as CCN

*Corresponding author. Tel.: +49 341 235 2411; fax: +49 341 235 2361.

E-mail address: lehmann@tropos.de (K. Lehmann).

1352-2310/$ - see front matter © 2005 Elsevier Ltd. All rights reserved.
doi:10.1016/j.atmosenv.2005.02.011

strongly depends on the particles' size and hygroscopic growth. Thus, the hygroscopic growth of particles is important for the direct as well as for the indirect climate effect.

The hygroscopic growth of particles in the submicrometer size range can be measured using a hygroscopicity-tandem differential mobility analyser (H-TDMA) (Liu et al., 1978). The H-TDMA is capable of identifying the mixing state of particles of a certain size in terms of their chemical composition. An internal mixture exists when all particles consist of the same chemical composition and thus exhibit the same hygroscopic growth behaviour. In an externally mixed particle population, particle groups exist that contain different chemical constituents. Often, a non-hygroscopic and a more hygroscopic particle group can be found, consisting of particles with less and more soluble material, respectively.

At a given supersaturation, the probability of particles belonging to the more hygroscopic group to be activated is much higher than for the non-hygroscopic particles. The Kelvin effect, which describes the increase of saturation vapour pressure over a curved surface, favours the growth of larger particles. Schwarzenböck et al. (2000) presented measurements performed with a counterflow virtual impactor (CVI) that show the activation of Aitken mode particles even though an accumulation mode particle fraction remained in the interstitial phase. He suggested the existence of an externally mixed particle population to be a possible explanation for these findings. Svenningsson et al. (1994) found evidence that for the clouds at Kleiner Feldberg, Taunus, Germany, the more hygroscopic particles were more efficiently scavenged than less hygroscopic particles. Similar results were presented by Noone et al. (1992), who reported a stepwise activation of particles in the Po Valley fog experiment and explained these findings by the existence of particles groups with different hygroscopic behaviour. Thus, the knowledge of the mixing state of submicrometer aerosol particles is of great importance for cloud models.

The amount as well as the type of soluble material contained in the particle has a strong impact on the particle's hygroscopicity. Often a simplified chemistry considering only one soluble component is used in cloud parcel models. In the Köhler equations, which are used to parameterise the particle growth as a function of RH in such models, the soluble fraction ε is one of the crucial input parameters. Usually, bulk chemistry sampled with an impactor is analysed to derive size segregated information about the soluble mass fraction of a certain size range. The time resolution is in the order of several hours and the determination of the mixing state is not possible. Single aerosol mass spectrometer are capable of identifying the particle composition as well as the mixing state, but the calibration has uncertainties and detection efficiency is low for particles with $D_p < 200$ nm (Trimborn et al., 2000).

This paper presents a climatologic overview of the soluble volume fraction contained in aerosol particles in air masses of different character. A new parameterisation procedure is introduced which allows to obtain time- and size-resolved information of the soluble volume fraction together with the mixing state of a particle population by transferring the hygroscopic growth of particles as measured with the H-TDMA into a soluble volume fraction with respect to ammonium sulphate.

2. Experimental

The FEBUKO (Field Investigations of Budgets and Conversions of Particle Phase Organics in Tropospheric Cloud Processes) field campaigns were conducted in October and November 2001 and in October 2002 in the Thueringer Wald, Germany. A detailed overview of the experiment and conducted measurements is given by Herrmann et al. (2005). The dataset presented in this paper includes 65 days of measurements.

The field site is situated in a valley 400 m northwesterly of the small village Goldlauter (605 m asl) and can be described as a continental site influenced by regional anthropogenic sources such as car traffic and coal combustion. The aerosol was sampled through an inlet facing the main wind direction at 6 m above ground and led into an air-conditioned container. The aerosol was then dried to a RH below 30% and conducted into the different measurement systems described below.

2.1. Instrumentation

The hygroscopic growth of aerosol particles was determined using a H-TDMA. The H-TDMA measures the change of size that particles experience when they are exposed to a defined RH by means of two differential mobility analysers (DMA). The hygroscopic growth factor (gf) is defined as the ratio of the humidified particle diameter to the dry particle diameter. As a first step, the polydisperse aerosol (ambient RH) is dried to a RH < 10% and passed through a first DMA, where particles of a certain mobility are selected. In order to exceed their deliquescence RH, the quasi-monodisperse particles are then humidified to a RH of about 90% using of a commercial humidifier. Thereafter, the aerosol particles are exposed to the desired RH by means of the RH-controlled sheath air of the second DMA. This DMA is operated as a mobility size spectrometer and measures the size distribution of the grown particles at the adjusted RH. By dividing each of the size bins of the size distribution with the dry particle diameter one obtains the growth factor distribution.

For the FEBUKO field campaign, the first DMA was operated at particle diameters of 50, 150, and 250 nm and particles were humidified to 30, 55, 75, and 90% RH. The measurement of a hygroscopic growth distribution for one particle size at a selected RH took approximately 12 min. For the presented study, only the hygroscopic growth at 90% RH was analysed. The RH was measured by means of capacitive sensors in the sample, sheath and excess air lines of the second DMA. The uncertainties of the humidity sensors are in the order of 2% for RHs around 90%. Especially at high RHs, where the hygroscopic growth curve of most atmospheric aerosol particles is steep, this uncertainty yields a large effect on the growth factor. Moreover, the measurements are very sensitive to a temperature gradient that can arise over the length of the DMA due to unstable temperature conditions in the laboratory container. In order to assign each scan at 90% RH to the actual RH inside the DMA, the hygroscopic growth of pure sodium chloride (NaCl) particles was measured several times each day. The hygroscopic behaviour of NaCl was measured with the H-TDMA at stable temperature under laboratory conditions, allowing to assign the growth factor of the NaCl particles to a certain RH. NaCl was chosen as calibration substance rather than ammonium sulphate because of its steep growth behaviour at the considered RH-range, making the attribution between growth factor and RH more distinct.

It was found that the average RH in the second DMA was 91.5% during the campaign in 2001 and 90.1% in 2002.

Particle number size distributions were measured using a differential mobility particle sizer (DMPS) (Birmili et al., 1999) operated at 10% RH.

2.2. Data quality

After the measurements, the data was checked for stability of flows, temperatures and humidities. All hygroscopic growth distributions were excluded for which

- flow fluctuations occurred that were larger than 2% of the target flow value,
- the temperature gradient in the second DMA exceeded 0.5 K,
- the excess air humidity varied by more than 2% RH or the sheath air humidity or the aerosol humidity varied by more than 0.5%,[1] and
- the number of particles for the chosen size was too low to obtain statistically significant information about their hygroscopic behaviour.

In general, about 75% of the data remains for further analysis. The exclusion of data for technical reasons (flow and humidity fluctuations, temperature gradient in the DMA) did not depend on meteorological conditions. The criteria accounting for counting statistics applied for about 5% of the hygroscopic growth distributions of particles with $D_p = 50$ nm in continental and $D_p = 250$ nm in marine air masses. During the first 2 weeks of the campaign in 2002, the temperature in the laboratory container was unstable, leading to large vertical temperature gradients over the H-TDMA, and thus high uncertainties in growth factors. Therefore, only 50% of the data measured in 2002 was used for the analysis.

2.3. Data processing

2.3.1. Modal versus sectional approach

Often, the humidified distributions measured in the second DMA show a modal behaviour, with a non-hygroscopic mode close to a growth factor of 1, a less hygroscopic mode with gfs between 1.1 and 1.3, and a so-called more hygroscopic mode with gfs between 1.3 and 1.8 at 90% RH, depending on the chemical composition and size of the particles. In marine air masses, a fourth mode can sometimes be observed, that contains particles exhibiting gfs close to that of pure sea salt (Berg et al., 1998; Massling et al., 2003; Svenningsson et al., 1992). This modal growth behaviour implies that particles of one size are externally mixed with respect to their chemical composition. These hygroscopic properties suggest a parameterisation of the grown size distributions by the application of a Gaussian fit to each of the growth modes, and defining the mean diameter of the Gaussian as the growth factor of this mode.

The model of a modal growth behaviour does not always apply. Sometimes the particle population exhibits a rather continuous growth distribution not allowing a distinction between the different particle groups. This was found to be the case for the data measured at the FEBUKO field campaign, especially for particles with $D_p = 50$ nm. For this reason, a sectional parameterisation was chosen rather than the modal one, having the advantage of being suitable for all data, because it does not require the particle mixture to comply with a modal growth model.

[1]The criteria for the excess air humidity is less strict compared to that of the sheath air and aerosol humidity because the excess air humidity is a function of the sheath and aerosol air humidity, the flow rates and the temperature gradient in the second DMA and is thus subject to larger fluctuations than the sheath air humidity.

2.3.2. Calculation of the soluble volume fraction

The growth factor of an internally mixed particle can be calculated using Eq. (1) (Pitchford and McMurry, 1994):

$$gf^3_{particle} = 1 + \varepsilon \cdot gf^3_{soluble} - \varepsilon. \quad (1)$$

Thus, the measured growth factor of an atmospheric particle and the knowledge of the hygroscopic growth of the soluble constituent allow an estimate of the soluble volume fraction ε contained in the particle:

$$\varepsilon = \frac{gf^3_{particle} - 1}{gf^3_{soluble} - 1}. \quad (2)$$

In literature, ammonium sulphate is often used to estimate ε in Eq. (2) (Svenningsson et al., 1997; Swietlicki et al., 1999; Zhou et al., 2002). Many cloud parcel models consider only one soluble compound, and because of its atmospheric relevance, ammonium sulphate is often used as the single salt component.

For these reasons, the soluble volume fraction with respect to ammonium sulphate was calculated in this study and its dependency of dry particle size and air mass type was analysed. The hygroscopic growth of pure ammonium sulphate as experimentally determined by Tang and Munkelwitz (1994) and corrected for droplet curvature effects by applying a Kelvin term calculated according to Brechtel and Kreidenweis (2000) was used in Eq. (2). Fig. 1 shows a sketch of the parameterisation procedure.

Fluctuations of the RH in the H-TDMA system described above can mask changes in the hygroscopic growth and thus the soluble volume fraction. For instance, at a nominal RH of 90%, the actual RH derived using the NaCl calibration was found to vary from 88% to 93%, depending on the stability of temperature in the container. To achieve a higher accuracy, the reference growth was recalculated for each hygroscopic growth distribution at the RH determined by the NaCl growth measurements (Section 2.1).

Moreover, the Kelvin effect, which describes the increase of saturation vapour pressure over a curved surface, influences the hygroscopic growth of particles, especially for particles with $D_p < 100$ nm. It causes a 50 nm particle consisting of pure ammonium sulphate to grow by a factor of 1.65 at 90% RH, whereas a 250 nm particle of the same chemical composition grows at the same RH by a factor of 1.72. In Eq. (2), the hygroscopic growth of the atmospheric particle is related to the hygroscopic growth of a pure ammonium sulphate particle of the same wet size. Thus, we account for the Kelvin effect and the soluble volume fractions of particles with different sizes can be compared directly.

2.3.3. Chemical analysis

In order to verify the use of ammonium sulphate, samples of a five-stage Berner impactor operated at the

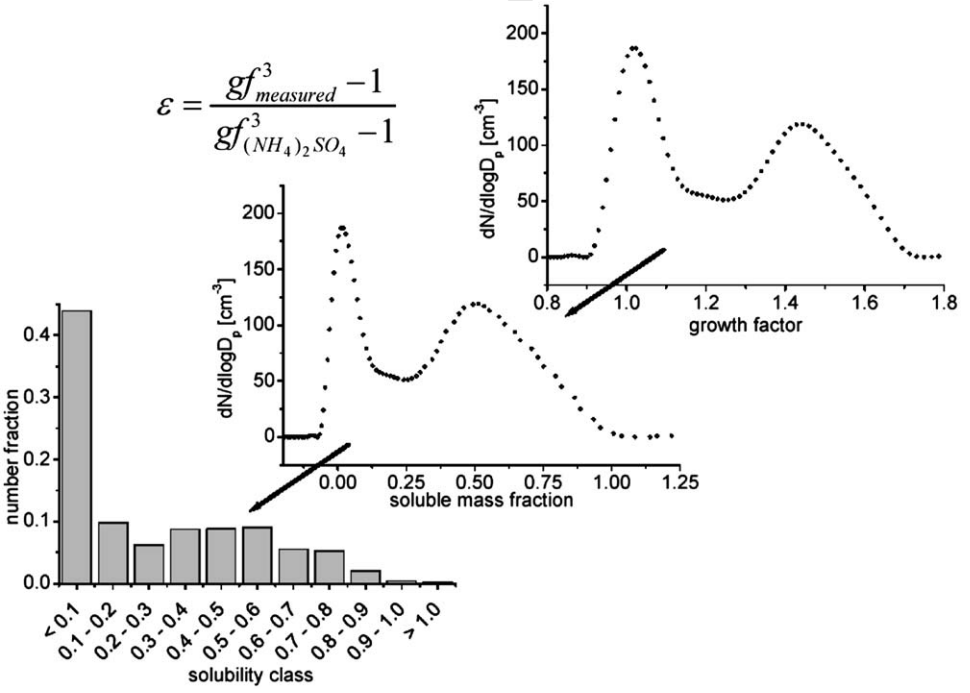

Fig. 1. Sketch of the parameterisation procedure: hygroscopic growth distributions are transferred into soluble volume fraction distributions and counted into evenly spaced soluble fraction classes.

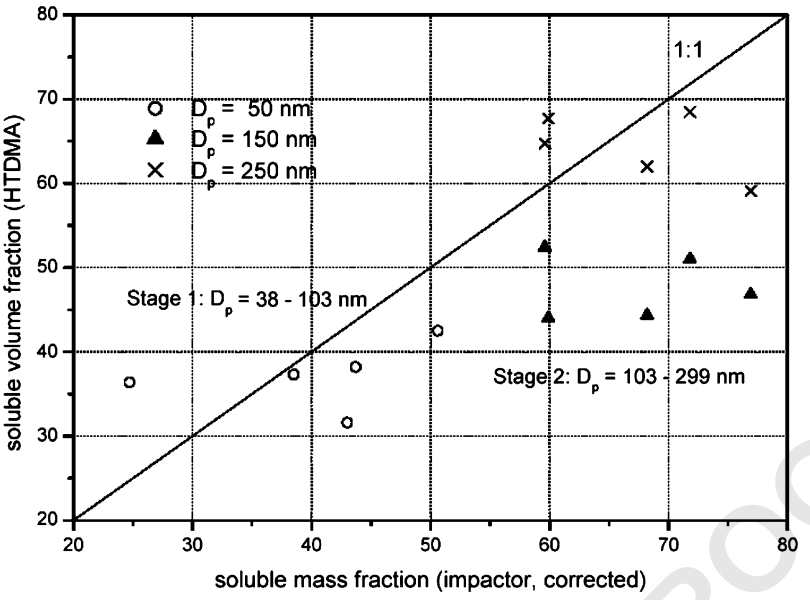

Fig. 2. Comparison of the chemically derived soluble mass fractions (impactor stage 1 and 2) and the soluble volume fractions with respect to ammonium sulphate for particles with $D_p = 50, 150$, and 250 nm calculated using Eq. (2).

sampling site at 60% RH were analysed to determine chemical size distributions and subsequently the soluble material to be used in Eq. (2).

When relating impactor and H-TDMA results, the different size definitions and operating conditions need to be considered.[2] Impactor stage 1 can be assumed to represent particles with $D_p = 50$, whereas particles with $D_p = 150$ and 250 nm are better characterised by impactor stage 2. However, it must be kept in mind that the size resolution of the H-TDMA is much greater than the one of the impactor. The mixing state within on impactor stage can thus vary significantly.

The impactor analysis yielded ammonium sulphate to be the main inorganic constituent of the particles in the second impactor stage. In the first impactor stage the fraction of water-soluble organics is in the same order as the inorganic ions. Nevertheless, ammonium sulphate was used as reference, but the high fraction of water-soluble compounds needs to be considered when interpreting the results for particles with $D_p = 50$ nm. The possible effects of this assumption will be discussed in the following. Cruz and Pandis (1998) analysed the activation of ammonium sulphate particles coated with glutaric acid, a soluble dicarboxylic acid, and showed that Köhler theory that treats the interaction of the organic and inorganic masses as additive can be used to predict their behaviour. Using the presented method, mixed particles of this type will have a similar effect as inorganic species other than ammonium sulphate, which would cause an offset to the calculated soluble volume fraction, but the variability as a function of air mass change should become apparent as well. Svenningsson, (1997) reported, that the error in ε is small, as long as the major ions contained in the particles are ammonium, sulphate, hydrogen or nitrate in a neutral solution. Little is known about the hygroscopic behaviour of water-soluble organic substances other than dicarboxylic acid.

The identification of all organic and inorganic water-active substances and the knowledge of their hygroscopic behaviour would enable a closure of the chemical and physical determination of the soluble volume fraction contained in atmospheric particles. This is not possible, and in the following it will be shown that the calculation of the soluble volume fraction with respect to ammonium sulphate is a useful approximation.

To validate the normalisation to ammonium sulphate, a mean soluble volume fraction was calculated by transferring hygroscopic growth distributions into soluble volume fraction distributions. The first moment of the distribution was then compared to soluble mass fractions derived by chemical analysis of impactor samples, which is described in detail in Tilgner et al. (2005). It should be noticed that the soluble mass fraction and the soluble volume fraction are connected by a factor of proportionality, which is the ratio of densities of the soluble material and the total particle.

Fig. 2 shows the soluble volume fractions of the particle sizes analysed with the H-TDMA versus the soluble mass fractions for 5 time periods when the

[2]The Berner impactor separates particles with respect to their aerodynamic size at 60% RH.

impactor and the H-TDMA were operated simultaneously. Although the statistical significance of the correlation is low, there is a good agreement of the chemical and the physical approach, indicating that the presented method to be reasonable. For impactor stage 2, the soluble volume fractions of 250 nm particles are closer to the 1:1 line than the 150 nm particles, which can be explained by the higher mass fraction they contribute to that stage.

3. Air mass classification

In order to assign a type to the prevailing air mass at the experimental site, synoptic weather maps of the Institute for Meteorology of the University of Berlin were used. On daily basis, the air masses over Europe in 850 h Pa are classified with respect to their source region and type. From climatologic point of view, the air mass type is the result of the energy and material impact of the surface on the air mass. Air mass type is perceptible due to typically graded values of the heat content, the amount of water vapour and characteristic aerosol properties (Geb, 1981).

Using this tool as well as backward trajectories calculated by means of the Hybrid Single Particle Lagrangian Integrated Trajectory model (HYSPLIT) provided by the National Oceanic and Atmospheric Administration (NOAA) (Draxier and Hess, 1998), the air mass character was classified as either marine or continental, or a mixture of both, which is often found over Europe. Also, when backward trajectory analysis and synoptic maps yielded different results and an unambiguous classification was not possible, the character was named "mixed type". Of the time, 62% was classified as with a marine character, 15% with a continental and 23% with a mixed character. It should be kept in mind that a marine air mass resides at least 400 km over land surface before it reaches the experimental site, and is therefore modified compared to pure marine air masses. Also, due to the location in central Europe, it can be expected that the aerosol of all air mass types will be to some degree anthropogenic influenced when reaching the measurement site.

4. Results and discussion

All hygroscopic growth distributions were transformed into evenly spaced classes of soluble volume fractions with respect to ammonium sulphate. Thereafter, average distributions were calculated for each of the three particle diameters representative for the time periods with marine, continental and mixed-type character. The results are presented in the following section. In the following, the soluble volume fraction is used as a synonym for soluble volume fraction with respect to ammonium sulphate.

4.1. Distribution of soluble particle volume fractions in dependence on dry particle diameter

Fig. 3 shows the distribution of the soluble volume fraction for particles with $D_p = 50$, 150, and 250 nm in air masses of different types. Error bars denote the statistical standard deviation of the mean.

About 40% of particles with $D_p = 50$ nm consist of less than 25% soluble material (Fig. 3a). This finding is independent of air mass history. The number fraction decreases with increasing soluble volume fraction, and only 5% of particles with this diameter contain a soluble volume fraction >0.75. For particles with $D_p = 50$ nm, an influence of the prevailing air mass is not visible. Here, the anthropogenic influence predominates. This may be expected since removal processes such as coagulation and below clouds scavenging are efficient for particles in this size range (Seinfeld and Pandis, 1998). The fraction of particles that consist mainly of insoluble material is probably locally emitted by sources near the sampling site or was incorporated into the air mass during the transport over inhabited land surface. This assumption is supported by the fact that coal combustion was the main mechanism used for heat generation in the village Goldlauter, which is located 400 m upwind the main wind direction. The fraction of particles taking up water as if containing more than 50% soluble material might have formed by the condensation of vapours with low volatility on small insoluble particles such as soot or on particles that are formed by nucleation. It should again be mentioned that the chemical analysis of the first impactor stage, which is representative for particles with $D_p = 50$ nm, revealed high mass fractions of water-soluble organic compounds. The derived soluble volume fractions with respect to ammonium sulphate is used to analyse an air mass dependence, but a conclusion regarding the behaviour of this particle size at RHs $>90\%$ should be drawn with care (refer to Section 2.3.3).

The distribution of the soluble volume fraction changes for the two particle sizes belonging to the accumulation mode (Fig. 3a and c). In marine air masses, about 55% of particles with $D_p = 150$ nm contain more soluble than insoluble material, whereas in continental air masses this was found for only 34% of all particles. For particles with $D_p = 250$ nm, the fraction of particles with high soluble volume fractions has further increased in all air masses. In the air masses characterised as most continentally influenced, particles of all four classes exist and are almost equally distributed with fractions between 20% and 30% in each class. In marine air masses, almost half of the particles take up water as if composed of more than

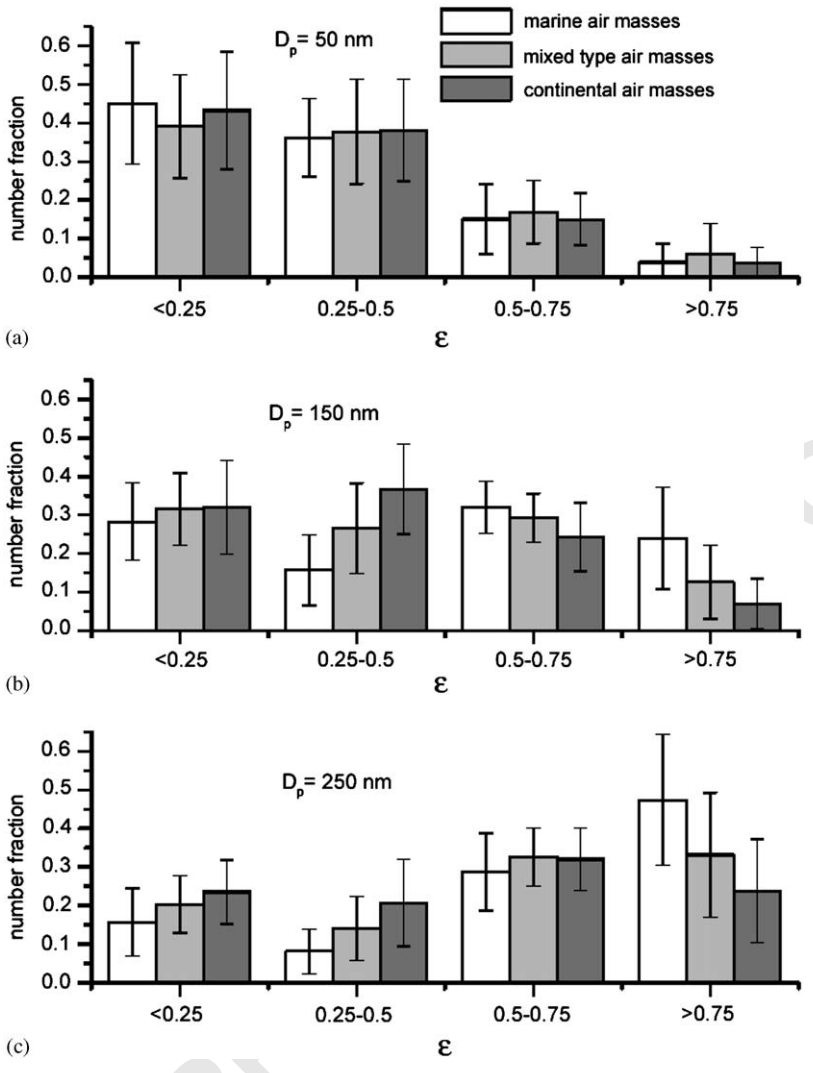

Fig. 3. Distribution of the soluble volume fraction as calculated using Eq. (2) of particles with (a) $D_p = 50$, (b) 150, and (c) 250 nm for air masses with marine, continental and mixed type character.

75% soluble material. Particles of air masses with mixed type character show properties between those of marine and continental character. The fraction of accumulation mode particles consisting mainly of insoluble material can be explained by anthropogenic sources as well as by coagulation of smaller particles with low soluble volume fractions.

It can be seen that the influence of the air mass character increases with increasing particle diameter, at least for the analysed size range. This agrees with the findings of Birmili et al. (2001), who reports that the continental influence that is also present for air masses with marine character, is more pronounced for Aitken than for accumulation mode particles.

4.2. Accumulated distribution of the soluble volume fraction in dependence on air mass character

Fig. 4a–c shows the accumulated number fraction as a function of the soluble volume fraction, divided in 11 evenly spaced classes, for different air mass characters and particle sizes. The similarity in the progression of the curves indicates similar formation and ageing processes for the three different particle sizes in dependence on air mass type. In all three air mass types, the accumulated particles number fraction with a soluble volume fraction above a certain limit increases with particle diameter. This is caused by the longer lifetime and thus higher probability of accumulation mode particles to have experienced ageing processes. Most of these processes, for example the gas-to-particle conver-

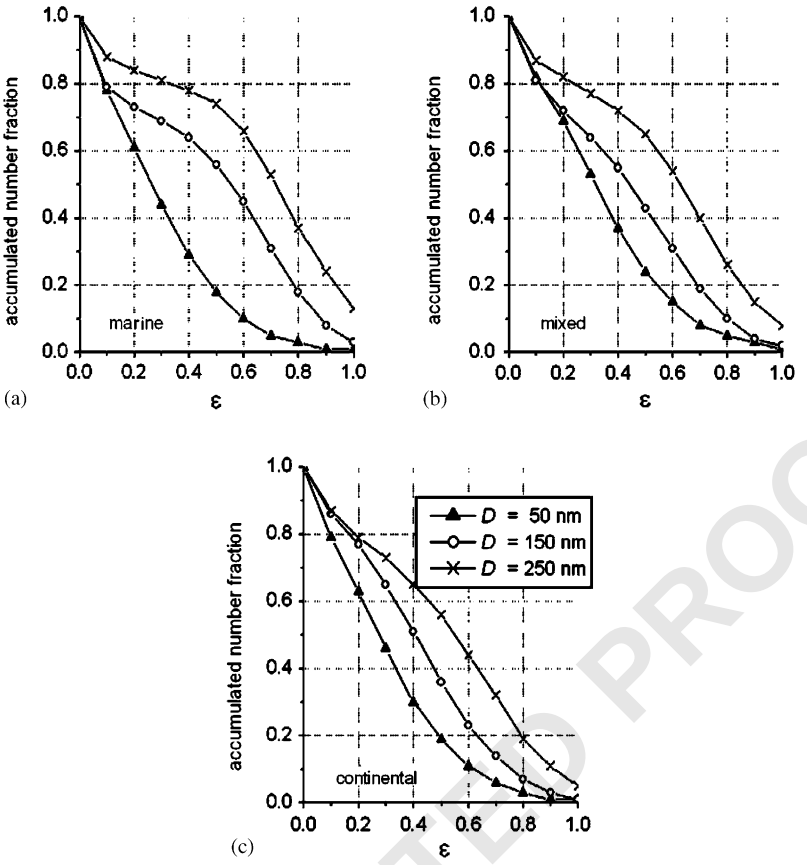

Fig. 4. Cumulative distributions of the soluble volume fraction as calculated using Eq. (2) as a function of particle size in air masses of (a) marine, (b) mixed, and (c) continental type.

sion of SO_2, NO_x and NH_3 as well as the oxidation of S(IV) to S(VI) in clouds (Bower and Choularton, 1993; Hegg et al., 1996) lead to an addition of soluble material.

The behaviour of particles with $D_p = 150$ nm indicates that the relationship in marine air masses is closer to particles with $D_p = 250$ nm than to particles with $D_p = 50$ nm (Fig. 4a). This finding is supported by the particle number size distribution representative for marine air masses at the measurement site as shown in Fig. 5, which reveals a bimodal shape typical for marine air masses. Particles with $D_p = 150$ and 250 nm both belong to the accumulation mode. One of the major particle sources over the ocean is sea salt, having its maximum emission rate in the coarse particle mode size range, but depending on the wind speed also accumulation and Aitken mode particles can be formed. Through the addition of sulphate by either cloud processing or condensation the growth of these particles is reduced compared to that of pure sea salt within a few hours (Swietlicki et al., 2000), and particles of the Aitken mode grow fast to accumulation mode size. The existence of particles that grow like pure ammonium sulphate and larger ($D_p = 250$ nm in Fig. 4a) supports this conclusion. We hypothesize that the large number of Aitken mode particles apparent in the particle number size distribution is the result of local anthropogenic emissions.

In continental air masses (Fig. 4a), the progression is reversed, i.e. particles with $D_p = 150$ show a closer relation to particles with $D_p = 50$ nm than to particles with $D_p = 250$ nm. This distinction cannot be seen in the particle size distribution typical for continental air masses at the measurement site (Fig. 5), which shows a broad mode peaking at 100 nm. In these air masses, only the particles with $D_p = 250$ nm might be large enough to be involved in cloud cycles and reach high particle number fractions with high soluble volume fraction.

5. Summary

Atmospheric particles are often externally mixed with regard to their hygroscopic behaviour. The fact that there are particle groups of one size containing different amounts of soluble material yields consequences for the activation of particles to cloud droplets. Using a simple growth model, H-TDMA measurements performed at

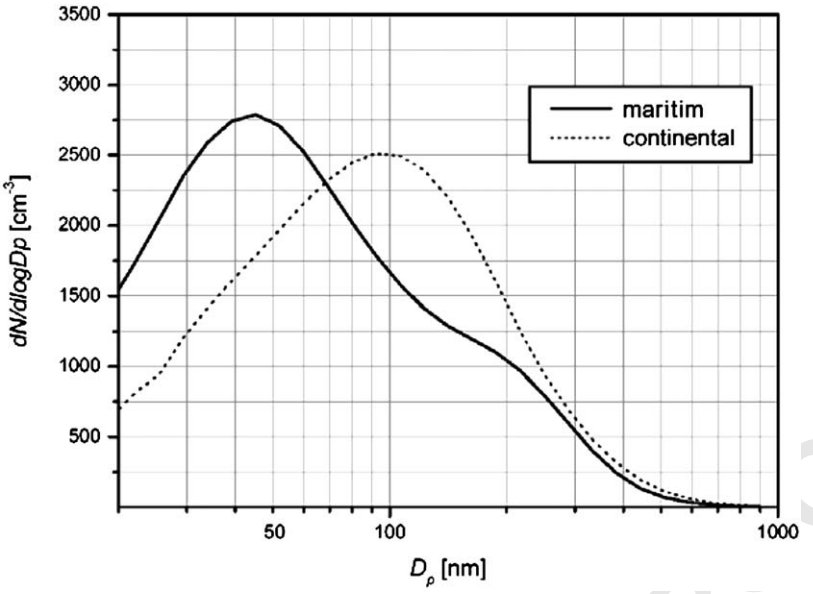

Fig. 5. Particle size distribution representative for marine (solid line) and continental (dotted line) air masses at the measurements site. Distributions are averages over the same periods that were used for the H-TDMA analysis.

90% RH for particles with $D_p = 50$, 150 and 250 nm were used to calculate soluble volume fractions with respect to ammonium sulphate and the associated particle number fractions. The dataset was analysed for characteristic distributions of the soluble volume fraction in air masses of different characters (marine, continental and mixed type).

It was found that on average almost half of the particles with $D_p = 50$ nm takes up water as if they contain less than 25% soluble material, and only a small number fraction (20%) takes up water as if consisting mainly of soluble material ($\varepsilon > 50\%$). For particles with $D_p = 150$ nm, the fraction of mainly insoluble particles decreases whereas the fraction of particles that contain more soluble than insoluble material increases. The highest soluble volume fractions can be found for particles with $D_p = 250$ nm.

For particles with $D_p = 50$ nm, no impact of the character of the prevailing air mass was found. For the two particle sizes belonging to the accumulation mode ($D_p = 150$ and 250 nm), a distinct air mass dependence was found, with the highest soluble volume fractions occurring in marine air masses. The cumulative distributions of the soluble volume fractions allow a deduction of similar formation and ageing for particles of different sizes. In marine air masses, the cumulative distribution of the soluble volume fraction of particles with $D_p = 150$ and 250 nm is similar, suggesting that particles of these sizes might have been involved in cloud cycles or experienced similar gas-to-particle conversion, whereas particles with $D_p = 50$ nm show a different behaviour. On the contrary, in air masses of continental character, particles with $D_p = 50$ and 150 nm seem to undergo similar formation and ageing processes, and it is hypothesized that in these air masses only larger particles were involved in cloud processing.

6. Uncited reference

Charlson et al., 1992.

Acknowledgements

The authors like to thank F. Brechtel and for providing his growth model.

This work was supported by the "Bundesministerium für Bildung, Wissenschaft, Forschung und Technik" (BMBF) within the atmospheric research program AFO 2000, project number 07ATF01. Also the authors are very thankful to the two anonymous reviewers for their valuable suggestion and comments.

References

Albrecht, B.A., 1989. Aerosols, cloud microphysics, and fractional cloudiness. Science 245, 1227–1230.

Berg, O.H., Swietlicki, E., Krejci, R., 1998. Hygroscopic growth of aerosol particles in the marine boundary layer over the Pacific and Southern Oceans during the First Aerosol Characterization Experiment (ACE 1). Journal of Geophysical Research 103 (D13), 16535–16545.

Birmili, W., Stratmann, F., Wiedensohler, A., 1999. Design of a DMA-based size spectrometer for a large particle size range and stable operation. Journal of Aerosol Science 30 (4), 549–553.

Birmili, W., Wiedensohler, A., Heintzenberg, J., Lehmann, K., 2001. Atmospheric particle number size distribution in Central Europe: statistical relations to air masses and meteorology. Journal of Geophysical Research 106 (D23), 32005–32018.

Bower, K.N., Choularton, T.W., 1993. Cloud processing of the cloud condensation nucleus spectrum and its climatological consequences. Quarterly Journal of the Royal Meteorological Society 119, 655–679.

Brechtel, F.J., Kreidenweis, S.M., 2000. Predicting particle critical supersaturation from hygroscopic growth measurements in the humidified TDMA. Part I: theory and sensitivity studies. Journal of the Atmospheric Sciences 57 (12), 1854–1871.

Charlson, R.J., Schwartz, S.E., Hales, J.M., Cess, R.D., Coakley Jr., J.A., Hansen, J.E., Hofmann, D.J., 1992. Climate forcing by anthropogenic aerosols. Science 256, 423–430.

Cruz, C.N., Pandis, S.N., 1998. The effect of organic coatings on the cloud condensation nuclei activation of inorganic atmospheric aerosol. Journal of Geophysical Research 103 (D11), 13111–13123.

Draxier, R.R., Hess, G.D., 1998. An overview of the HYSPLIT_4 modelling system for trajectories, dispersion and deposition. Australian Meteorological Magazine 47 (4), 295–308.

Geb, M., 1981. Klimatologische Grundlagen der Luftmassenbestimmung in Mitteleuropa. Beilage zur Berliner Wetterkarte des Instituts für Meteorologie der Freien Universität Berlin.

Hegg, D.A., Majeed, R., Yuen, P.F., Baker, M.B., Larson, T.V., 1996. The impacts of SO_2 oxidation in cloud drops and in haze particles on aerosol light scattering and CCN activity. Geophysical Research Letters 23 (19), 2613–2616.

Herrmann, H., Wolke, R., Müller, K., Brüggemann, E., Gnauk, T., Barzaghi, P., Mertes, S., Lehmann, K., Massling, A., Birmili, W., Wiedensohler, A., Wieprecht, W., Acker, K., Jaeschke, W., Kramberger, H., Syrcina, B., Bächmann, K., Collett Jr., J.L., Galgon, D., Schwirn, K., Nowak, A., van Pinxteren, D., Plewka, A., Chemnitzer, R., Rüd, C., Hofmann, D., Tilgner, A., Diehl, K., Heinold, B., Hinneburg, D., Knoth, O., Sehili, A.M., Simmel, M., Wurzler, S., Mauersberger, G., Majdik, Z., Müller, F., 2005. FEBUKO and MODMEP: field measurements and modelling of aerosol and cloud multiphase processes, Atmospheric Environment, this issue.

Liu, B.Y.H., Pui, D.Y.H., Whitby, K.T., Kittelson, D.B., Kousaka, Y., L.McKenzie, R., 1978. The aerosol mobility chromatograph: a new detector for sulfuric acid aerosols. Atmospheric Environment 12, 99–104.

Massling, A., Wiedensohler, A., Busch, B., Neusüß, C., Quinn, P., Bates, T., Covert, D., 2003. Hygroscopic properties of different aerosol types over the Atlantic and Indian Oceans. Atmospheric Chemistry and Physics 3, 1377–1397.

Noone, K.J., Ogren, J.A., Hallberg, A., Heintzenberg, J., Ström, J., Hansson, H.-C., Svenningsson, I.B., Wiedensohler, A., Fuzzi, S., Facchini, M.C., Arends, B.G., Berner, A., 1992. Changes in aerosol size- and phase distributions due to physical and chemical processes in fog. Tellus 44B, 489–504.

Pruppacher, H.R., Klett, J.D., 1997. Microphysics of Clouds and Precipitation. Kluwer Academic Publishers, Dordrecht/Boston/London 945pp.

Schwarzenböck, A., Heintzenberg, J., Mertes, S., 2000. Incorporation of aerosol particles between 25 and 850 nanometers into cloud elements: measurement with a new complementary sampling system. Atmospheric Research 52 (4), 241–260.

Seinfeld, J.H., Pandis, S.N., 1998. Atmospheric Chemistry and Physics. Wiley, New York, NY 1326pp.

Svenningsson, B., 1997. Hygroscopic growth of atmospheric aerosol particles and its relation to nucleation scavenging in cloud. Ph.D. Thesis, University of Lund, Lund, 22pp.

Svenningsson, B., Hansson, H.-C., Wiedensohler, A., Noone, K.J., Ogren, J.A., Hallberg, A., Colvile, R., 1994. Hygroscopic growth of aerosol particles and its influence on nucleation scavenging in cloud: experimental results from Kleiner Feldberg, 129pp.

Svenningsson, I.B., Hansson, H.-C., Wiedensohler, A., Ogren, J.A., Noone, K.J., Hallberg, A., 1992. Hygroscopic growth of aerosol particles in the Po Valley. Tellus 44B, 556–569.

Svenningsson, B., Hansson, H.-C., Martinsson, B., Wiedensohler, A., Swietlicki, E., Cederfelt, S.-I., Wendisch, M., Bower, K.N., Choularton, T.W., Colvile, R.N., 1997. Cloud droplet nucleation scavenging in relation to the size and hygroscopic behaviour of aerosol particles. Atmospheric Environment 31 (16), 2463–2475.

Swietlicki, E., Zhou, J., Berg, O.H., Martinsson, B.G., Frank, G., Cederfelt, S.-I., Dusek, U., Berner, A., Birmili, W., Wiedensohler, A., Yuskiewicz, B., Bower, K.N., 1999. A closure study of sub-micrometer aerosol particle hygroscopic behaviour. Atmospheric Research 50, 205–240.

Swietlicki, E., Zhou, J., Covert, D.S., Hämeri, K., Busch, B., Väkevä, M., Dusek, U., Berg, O.H., Wiedensohler, A., Aalto, P., Mäkelä, J., Martinsson, B.G., Papaspiropoulos, G., Mentes, B., Frank, G., Stratmann, F., 2000. Hygroscopic properties of aerosol particles in the north-eastern Atlantic during ACE-2. Tellus 52B, 201–227.

Tang, I.N., Munkelwitz, H.R., 1994. Water activities, densities and refractive indices of aqueous sulfates and sodium nitrate droplets of atmospheric importance. Journal of Geophysical Research 99 (D9), 18801–18808.

Tilgner, A., Majdik, Z., Simmel, M., Wolke, R., Herrmann, H., 2005. SPACCIM: simulations of the multiphase chemistry occurring in the FEBUKO hill cap cloud experiments, Atmospheric Environment, this issue.

Trimborn, A., Hinz, K.-P., Spengler, B., 2000. Online analysis of atmospheric particles with a transportable laser mass spectrometer. Aerosol Science and Technology 33 (1–2), 191–201.

Twomey, S., 1977. The influence of pollution on the shortwave albedo of clouds. Journal of the Atmospheric Sciences 34, 1149–1152.

Zhou, J., Swietlicki, E., Hansson, H.C., Artaxo, P., 2002. Submicrometer aerosol particle size distribution and hygroscopic growth measured in the Amazon rain forest during the wet season. Journal of Geophysical Research 107 (D20), 8055.

3B2v8.06a/w (Dec 5 2003).51c XML:ver:5.0.1 AEA : 5769 Prod.Type:FTP pp.1–12(col.fig.:NIL) ED:MangalaK. PAGN:NS SCAN:Global

ARTICLE IN PRESS

Available online at www.sciencedirect.com

SCIENCE DIRECT®

ELSEVIER

Atmospheric Environment ▮ (▮▮▮▮) ▮▮▮–▮▮▮

ATMOSPHERIC ENVIRONMENT

www.elsevier.com/locate/atmosenv

Cloud physics and cloud water sampler comparison during FEBUKO

W. Wieprecht[a,*], K. Acker[a], S. Mertes[b], J. Collett Jr.[c], W. Jaeschke[d], E. Brüggemann[b], D. Möller[a], H. Herrmann[b]

[a]*Brandenburgische Technische Universität Cottbus (BTU), Lehrstuhl für Luftchemie und Luftreinhaltung, Volmer Str. 13, 12489 Berlin, Germany*

[b]*Leibniz-Institut für Troposphärenforschung (IfT), Permoserstr. 15, 04318 Leipzig, Germany*

[c]*Colorado State University, Atmospheric Science Department, Fort Collins, CO 80523, USA*

[d]*Universität Frankfurt, Zentrum für Umweltforschung (ZUF), Georg Voigt Str. 14, 60325 Frankfurt, Germany*

Abstract

Optical methods for counting and sizing cloud droplets and a wide range of cloud water sampling methods were used to characterize the atmospheric liquid phase during the FEBUKO cloud experiments. Results near cloud base as well as more than 300 m inside the hill cap clouds are presented, reflecting their inhomogeneous nature. The cloud droplet number varies from 50 to 1000 cm^{-3} and drop sizes between 1 and 20 μm diameter are most frequent. Variations in the liquid water content (LWC) and in the total ion content (TIC) are much smaller when the measurement position is deeper in the cloud. Near cloud base variability in updraft strength and, near cloud top, entrainment processes (droplet evaporation by mixing with drier air, aerosol and gas scavenging) disturb the adiabatic conditions and produce large variations in LWC and chemical composition. Six different active cloud water collectors and impactors were running side by side; they differ in the principle of sampling, in the throughput of cloudy air per unit time and in the calculated 50% cutoff diameter, which influence also their sampling efficiency. Two of them are designed to collect cloud water in two droplet size fractions. Three cloud events were selected by the FEBUKO team for detailed cloud physical and chemical analyses because they serve best the modelling demands concerning connected flow between the upwind, summit and downwind sites for process studies. Frequency distributions of the LWC and, also of the cloud base height are given as statistical parameters for both FEBUKO experiments.

Keywords: Cloud water sampling; Liquid water content; Cloud base height; Droplet size distribution; Cloud chemistry

1. Introduction

Ground-based cloud experiments were performed in autumn 2001 and 2002 at a mountain ridge in the Thuringian Forest (Germany) to study the airflow over hills, the cloud microphysics, and air and cloud chemistry. Air approaching the ridge is forced to rise, cools by adiabatic expansion, and forms low clouds in the boundary layer. During south-westerly winds, the air is characterized at an upwind site before it enters the cloud, in the cloud at the summit and at a downwind site after cloud processing. Details about the investigations conducted are given in Herrmann et al. (2005).

*Corresponding author.
E-mail address: wie@btu-lc.fta-berlin.de (W. Wieprecht).

1352-2310/$ - see front matter © 2005 Elsevier Ltd. All rights reserved.
doi:10.1016/j.atmosenv.2005.02.012

Typically 50–1000 cloud droplets are found per cm^3 air together with about 200–3000 non-activated particles in *cumulus* or *stratus* clouds at a given supersaturation (Arends, 1996). Droplet number is highest at cloud base. Above cloud base existing droplets take up available supersaturated water vapor produced by the updraft leading to an increase in liquid water content (LWC) and droplet diameter with height above cloud base (Pruppacher and Klett, 1978). It is known from many field measurements (Junkermann et al., 1994; Wieprecht et al., 1995; Möller et al., 1996) and expected under wet adiabatic conditions, that the LWC of a low cloud increases almost linearly with the height above cloud base, reaching a maximum at about 80–90% of the cloud thickness. Variations in LWC and in cloud water composition are much smaller if the measurement position is located well inside the cloud. Near cloud base variability in updraft strength and, near cloud top, entrainment processes (droplet evaporation by mixing with drier air, aerosol and gas scavenging) disturb the adiabatic conditions and produce large variations in LWC and chemical composition. Studies conducted over the last two decades have clearly demonstrated the important role clouds and fogs serve as processors of inorganic fine aerosol particles, contributing both to production of new particle mass and particle removal. Different cloud droplet collectors for research purposes have been developed during the last decade in order to sample fog or cloud water droplets (Daube et al., 1987; Fuzzi et al., 1997; Schell, 1997a; Moore et al., 2002; Straub and Collett, 2002). In addition to samplers that collect cloud droplets as liquid water samples there exists another technique, using a counterflow virtual impactor (CVI) (Ogren et al., 1985) where the individual sampled droplets are evaporated and the released cloud droplet residuals analyzed. Various cloud water samplers were tested in several field campaigns (Schell et al., 1997b; Herckes et al., 2002; Laj et al., 1998; Mertes et al., 2001) and some intercomparison campaigns have been carried out under different fog and cloud conditions (e.g., Schell et al., 1992). Sampling characteristics of some cloud water collectors have been determined in the laboratory (Straub and Collett, 2002) and wind tunnel experiments (Schwarzenböck and Heintzenberg, 2000). During planning for the FEBUKO field experiments, it became clear that different participants had needs which could not fulfilled by a single type of cloud water sampler.

Some of these needs included

- a very well characterized cloud water sampler (cutoff calculated and tested in wind tunnel, cloud chamber and field experiments),
- cloud water sampling in two or more droplet size fractions,
- simultaneous sampling of cloud water and interstitial aerosol,
- large volume of cloud water for the analysis of trace organic species,
- half hour time resolution to permit comparison between cloud water composition and aerosol composition measured by a steamjet chamber,
- short time between cloud water sampling and analysis of reactive compounds (e.g., peroxides, nitrite),
- special CVI inlets for microphysical and chemical characterization of cloud droplet residual particles.

The decision was made to use cloud and fog water samplers of different designs to adequately address the identified requirements. This paper is intended to demonstrate the benefits of, and address issues of comparability resulting from, this multi-sampler approach.

2. Experimental

Cloud water sampling was carried out during the field campaigns on a tower platform approximately 20 m above ground at the summit site (S). The meteorological sensors and the sensors (see below) measuring LWC, effective droplet diameter and, droplet size distribution were also located on this platform. The tower was constructed of aluminum scaffolding in order to permit an undisturbed airflow around the samplers and instruments. Cloud LWC was measured every 10 s using a forward-scattering particulate volume monitor (model PVM100) for droplet diameters from 3 to 45 μm (Gerber, 1991). Cloud drop size and number distributions were measured at the same frequency using a forward-scattering spectrometer probe (Particle Measurement Systems FSSP-100) equipped for ground-based operation. This laser-based light scattering instrument measures droplet number in 16 different size bins. From the drop distribution, the total volume of liquid water can be calculated.

At a distance of about 20 m from the tower but at the same height above ground, the inlets of two CVI and an additional PVM100 were mounted at a window and on a roof platform of the weather service building, respectively. The analyzers and sampling units connected downstream of the CVI (see below and Mertes et al., 2005) were deployed inside for protection from the weather. Additional information, including cloud base altitude (derived from ceilometer data), cloud coverage (obtained from NOAA satellite data) and backward trajectories (NOAA) for air mass history, are available for data analysis. At the upwind study site (U) a Vaisala CTK25 laser ceilometer (resolution in time 15 s, in space 30 m) was operated for continuous determination of

cloud base height by backscattering of a vertically directed laser beam.

Discrete periods of several hours, which meet the right experimental conditions, were selected as cloud monitoring events. Criteria to initiate measurements included cloud occurrence only at the summit site with LWC > 100 mg m^{-3} for more then 15 min, connected airflow at the three sites (south-westerly winds) and temperature > 1 °C without rain at all sites. Generally, a sampling time of 2 h was utilized in order to sample enough cloud water for the planned chemical analyses. For some special needs a shorter sample time of $\frac{1}{2}$ h was used in 2001. The amount of collected cloud water was determined by weight (most cloud collectors) or by using Ly alpha measurements of evaporated cloud water (for the CVI, see Mertes et al., 2005). Chemical analysis of collected samples was completed by various FEBUKO participants. For details see other FEBUKO-related papers in this special issue (Gnauk et al., 2005; Müller et al., 2005; Brüggemann et al., 2005; van Pinxteren et al., 2005).

The various cloud water collectors used in the study are briefly described below.

2.1. CASCC2_4:Caltech Active Strand Cloudwater Collector Version 2

The design of this sampler is described by Demoz et al. (1996). The CASCC2 is a compact version of the original CASCC which in turn was based on a similar collector developed by Daube et al. (1987). Air containing cloud droplets is drawn by a fan through the CASCC2 where the droplets are collected by inertial impaction on six rows of 508 μm diameter Teflon strands. The size cut (droplet diameter collected with 50% efficiency) was estimated to be approximately 3.5 μm. The collector design was adopted by IfT with a 220 V frequency controlled fan used to generate a stable airflow of 348 m^3 h^{-1}. Four CASCC2 samplers were mounted side by side in order to collect a larger cloud water volume for analysis of trace organic compounds.

2.2. SAJ-16: Set of Active round Jet collectors—16 samplers)

The sampling head of this fog impactor has 16 single-jet collectors arranged in a circle. A single collector consists of a round nozzle for the formation of a jet and a collection disc and funnel assembly underneath the nossel. This collector has been described in some detail by Berner (1988). All single-jet collectors were connected to a common exhaust tube, equipped with a throttle for limiting the flow to the desired amount, and with a tap for measuring the pressure ahead of the throttle. Assuming uniform flow conditions for individual jets, the cut diameter of the collector has been calculated as $D_{p,50} = 4.5$ μm. This sampler was used primarily for H_2O_2 analysis in the cloud water.

2.3. SSI: Single-Stage slit jet Impactor

The low-volume SSI sampler consists of two parallel slit jets, air is drawn through the impactor with a total sample volume of 120 m^3 h^{-1} using a vacuum pump. The airflow was tested and set before and after each FEBUKO campaign. The calculated 50% cutoff diameter for cloud droplets is 5 μm (Winkler, 1992). The cloud water collected by this sampler was used for analysis of inorganic anions and cations, water-soluble organic compounds (WSOC), organic peroxides (see Valverde-Canossa et al., 2005), and for measurements of pH and conductivity.

2.4. TSCI:Two Stage Cloud water Impactor

The TSCI cloud water sampler operates on the principle of internal impaction on plane surfaces, used widely in aerosol particle sampling, as reported by Marple and Willeke (1976). The TSCI consists of three vertical slit impactor stages. The first stage collects larger droplets, followed by two identical stages in parallel to collect smaller droplets. The 50% cutoff diameter in the first stage was fixed at 12 μm and the second stages at 4 μm. The airflow through the sampler was 180 m^3 h^{-1}. The sampler was equipped with an isokinetic inlet (Schell et al., 1997a, b) and a wind vane to keep the inlet directed into the wind.

2.5. Sf-CASCC:Size-Fractionating Caltech Active Strand Cloud water Collector

The size-fractionating Caltech Active Strand Cloud water Collector collects cloud drops in two size ranges (Demoz et al., 1996). The first stage (referred to as the fractionating inlet) consists of a bank of four rows, each containing eight 12.7 mm diameter Teflon rods. Each row is offset from the one in front of it so that rods are not shadowed by those in the previous row. Mounted downstream of the inlet is the second stage, which contains a bank of six rows each containing 102 Teflon strands (508 μm diameter) spaced 2.3 mm apart (center to center). By removing the large drops from the air stream in the fractionating inlet (modelled 50% size cut of ~16 μm), a second sample of cloud water comprised of smaller cloud drops is collected on the second stage (50% size cut of 4 μm). Consequently, the operator can simultaneously collect independent large and small drop size fractions from the sampled cloud. Cloud water sampled by this high-volume two-stage sampler was analyzed for inorganic cations and anions and several different WSOC.

2.6. CVI: Counterflow Virtual Impactor

A CVI was deployed to collect cloud droplets in the size range between 5 and 50 μm (Schwarzenböck et al., 2000). By means of a counterflow directed out of the inlet (opposite to the sampling direction) interstitial particles and gases are pre-segregated. Upon collection, cloud drops are evaporated in a dry and particle-free carrier stream of air releasing all dissolved, volatile substances into the gas phase and non-volatile components as residual particles. Downstream of the CVI and an interstitial inlet, two particle counters (TSI-3010) and two differential mobility particle sizers measured the residual and interstitial particle concentrations ($D_p > 12$ nm) and dry size distributions (22 nm < d-p < 900 nm). Filter units and cartridges were combined to sample material for chemical analysis. More details about the CVI systems used in this study are given in Mertes et al. (2005).

3. Results and discussion

3.1. Liquid water content and cloud base height

Based on the LWC measurements made at Mt. the Schmücke tower (957 m above sea level (a.s.l.)) between 02 October and 05 November 2001, the mean value of cloud LWC was determined to be 221 ± 130 mg m^{-3}. The mean LWC of clouds intercepting this site between 22 September and 31 October 2002 was 187 ± 121 mg m^{-3}. These 10-min averages varied between 10 and 670 mg m^{-3}. The summit was in cloud 40% of the study time in 2001 and 51% in 2002. Fig. 1 shows frequency distributions of LWC for both FEBUKO experimental periods. Knowledge of the distance between the sampling position and cloud base is essential for any physico-chemical interpretation of cloud data. Ceilometer measurements from a point 352 m below the Schmücke tower were made continuously. It was found, that about 65% of all low clouds (clouds observed up to 2500 m a.s.l.) had their cloud base below the Mt. Schmücke tower (957 m a.s.l.). As can be seen from Fig. 2, Mt Schmücke tower was often (25–35% of the time) 250–300 m deep in the cloud and in about 20–25% of the cases near the cloud base. Unfortunately, there are no observations of cloud top height. In an undisturbed (stratus) cloud, the condensation conditions inside the cloud are strongly correlated with decreases in temperature above the cloud base altitude.

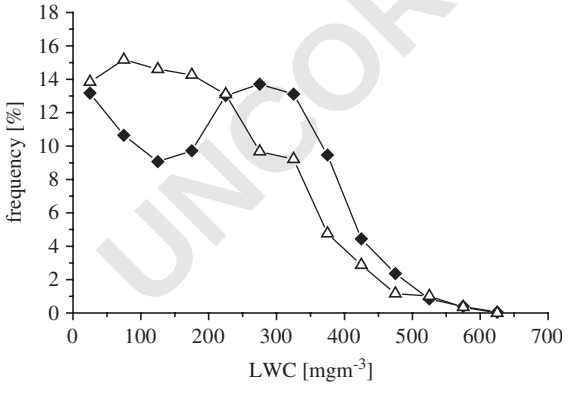

Fig. 1. Frequency distribution of liquid water content of low clouds observed at Mt. Schmücke during the two FEBUKO experiments: 02 October–05 November 2001 (solid line with closed diamonds) and 22 September–31 October 2002 (solid line with open triangels).

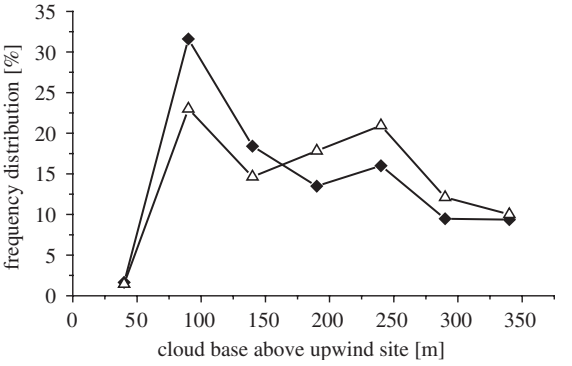

Fig. 2. Frequency distribution of the cloud base if Mt. Schmücke (tower) is in cloud for the two FEBUKO experiments: 02 October–05 November 2001 (solid line with closed diamonds) and 22 September–31 October 2002 (solid line with open triangels). The vertical distance between measurement platform at Mt. Schmücke and ceilometer position is 352 m.

3.2. Selected cloud events

Three out of 14 cloud events observed during the two measurement campaigns were selected for detailed cloud physical and chemical analyses and modelling activities (using synoptic parameters, airflow analysis, and meteorological, chemical and physical data): 26/27 October 2001 22:00–13:00, called E I; 07/08 October 2001 19:00–08:00, called E II; 16/17 October 2002 21:00–04:00, called E III. These events featured connected flow between the study sites with continuous advection of air masses of maritime origin from the south-west. During long distance transport over Western Europe the aerosol should be altered and become more continental (e.g., Tilgner et al., 2005; Heinold et al., 2005). Air masses during these selected episodes featured low to medium pollution levels. On average concentrations of SO_2 below 1 ppb and of NO_2 below 10 ppb were observed.

Time series of LWC, its distribution between two different droplet size ranges (4–12 μm and 12–32 μm),

and the altitude of the cloud base above the upwind site are presented for two events in Figs. 3a (E I) and 3b (E III). Cloud drop number distributions for these events are given in Figs. 4a and b.

Mt. Schmücke summit was already in cloud when intensive measurements started at 22:00 UTC on 26 October 2001 (E I). At 00:00 UTC about the summit is approximately 150–200 m above cloud base and the two droplet size ranges are comparable contributors to total cloud LWC (see Fig. 3a). Later, the base of the stratus descends. At approximately 03:00 UTC a summit LWC of 500 mg m^{-3} was measured and, at this position 300 m deep in the cloud, most of the water was found in the drops larger than 12 μm. The droplet size distribution of E I given in Fig. 4a reveals a droplet number reduction

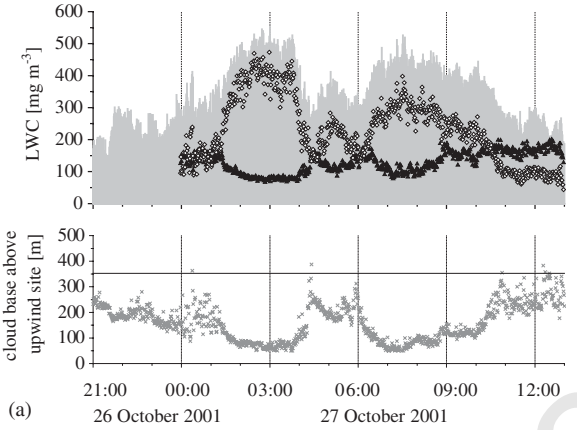

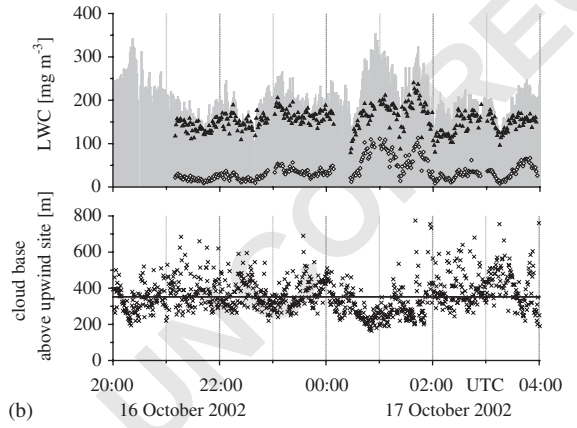

Fig. 3. Relationship between liquid water content of cloud, droplet size distribution and the position inside the cloud. Upper diagram: LWC for all droplets (gray area, PVM100), for the droplet fraction 4–12 μm (closed triangles, FSSP100) and the droplet fraction 12–32 μm (open diamonds, FSSP100). Lower diagram: height of the cloud base above the upwind site (605 m a.s.l.). The solid line presents the level of measurement platform at Mt. Schmücke tower (957 m a.s.l.): (a) cloud event E I; (b) cloud event E III.

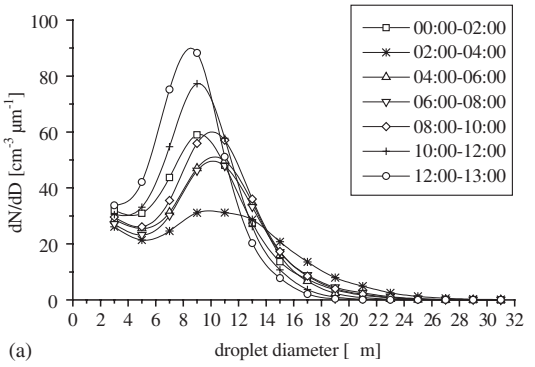

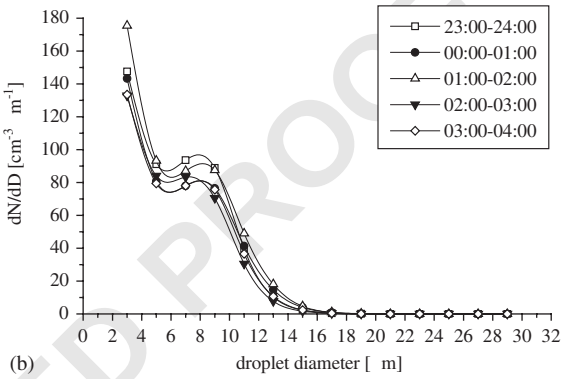

Fig. 4. Cloud droplet number distribution during two sampling periods: (a) 26/27 October 2001 (E I); (b) 16/17 October 2002 (E III).

and a shift of the droplet volume to bigger droplets in the sampling period 02:00–04:00 UTC. The increase in LWC per meter of height is about 2 mg m^{-3}. Colvile et al. (1997) expected similar values during adiabatic changes in the temperature of air parcels flowing over the hill. During the whole event E I a strong correlation between LWC and height above cloud base was observed ($r = 0.78$). At 13:00 UTC, after several hours of cloud lifting, the Mt. Schmücke tower was located near cloud base. The observed decrease in LWC is connected with a shift of the droplet size distribution to smaller drops after 10:00 UTC (Fig. 4a).

Cloud physical properties during event E III (Fig. 3b) were significantly different than observed in E I. A much lower LWC is related to a much smaller vertical distance between our sampling position and cloud base, averaging only 50–100 m during the measurement period. Very little correlation between LWC and height above cloud base was found ($r = 0.08$) during this event. Reasons for the little correlation may be among others the principle of cloud base detection (overflow over complex orographic terrain) and the cloud base structure during E III (very inhomogeneous concerning

droplet number density). Reflections of the laser beam often from more than 100 m inside cloud (above the sampling position) were registered. Any time delay caused by the horizontal distance between both measurements (3 km) was already corrected in the data. Near cloud base, mixing with unsaturated air cannot be excluded. Little liquid water was found in droplets larger than 12 μm and, cloud drops with diameter $D > 15$ μm were rarely observed. Throughout E III the droplet number distribution was relatively stable, as indicated by Fig. 4b. As expected near cloud base, mainly small cloud droplets were observed with a broad maximum in the size range 4–10 μm.

Cloud event E II can be divided into three sampling periods (Müller et al., 2005) including times near cloud base and other times higher inside the cloud. This event is not discussed here in detail.

As already mentioned, cloud droplets were sampled by CVI and evaporated to permit drop residue characterization. Agreement between the FSSP drop number concentration and the CVI residual particle concentration was found during all three focus episodes (E I–E III) indicating that on average one evaporated droplet released one residual particle.The number of interstitial (non-activated) particles (< 5 μm) inside cloud was also determined (Mertes et al., 2005).

3.2. Cloud water sampling at the summit

All cloud water samplers as well as the instruments for the measurement of LWC, cloud droplet size and number concentrations were concentrated side by side on the measurement platform at summit. One important feature of cloud water samplers is their sampling efficiency. The efficiency ε can be defined as the ratio of sampled water volume to the *real* cloud water volume in air, i.e., $\varepsilon = 1$ if the sampler collects *all* cloud droplets in a given air volume. There are some difficulties in estimating the efficiency. First, no sampler can collect all cloud droplets by several methods and secondly, each sampler has different characteristic (which even depends from atmospheric conditions, namely wind speed) in the droplet-size resolved sampling efficiency. It follows that each sampler must have always $\varepsilon < 1$. This is not a problem in characterising the chemical composition of clouds when the sampling efficiency is only weakly dependent from droplet size, which, however, cannot be presumed. Consequently, by using the total cloud water based on integrated measurement methods (LWC) the sampler efficiency cannot be calculated theoretically (not even taking into account data quality objectives) but only approached. In comparing different samplers in this experiment, we calculated ε as the relation between the predicted cloud water volume and the real sampled cloud water. The predicted cloud water volume was calculated for these samplers by

$$V_{\text{pred}} = \overline{\text{LWC}} V_{\text{air}} \Delta t, \quad (1)$$

where $\overline{\text{LWC}}$ is the cloud droplet water volume (calculated from FSSP measurements) integrated over the droplet spectra starting at sampler D_{50} cutoff, V_{air} airflow through the cloud water sampler and Δt sampling time. Sampler using the impaction of the cloud droplets at a plane plate with a defined droplet velocity have a sharp D_{50} cutoff, normally calculated for cloud droplets at 4 or 5 μm diameter. Two active strand collectors (CASCC2_4, sf-CASCC) used the principle of cloud drop impaction on cylinders (rods and strings). These samplers offer very high air sampling rates at low pressure drop, but do not feature sharp collection efficiency curves. Use of Eq. (1) for these samples will result in an overestimation of the predicted cloud water sample volume. Therefore, the cloud water volumes collected with the two-stage sf-CASCC were compared with those expected from the collector's performance characteristics and the observed drop size distributions. Collector performance characteristics for the first stage of the sf-CASCC were based on a computational fluid dynamics simulation (FLUENT) of the air and droplet flow through the collector. The collection performance of the second stage was based on the treatment by Demoz et al. (1996).

Observed and predicted cloud water sampling volumes of three high-volume and one low-volume cloud water sampler are presented in Fig. 5 for all events E I–E III. Measurements were made with the sf-CASCC only in 2002. Total sf-CASCC sample volumes (large + small drop fractions) have been used for the presentation in Fig. 5. As discussed above, there are systematic and random deviations from the "theoretical" efficiency (1:1 line). Closest to the 1:1 line lies the low-volume SSI. This sampler was tested in a wind tunnel and well characterized in many field campaigns. The sampling efficiency of the string collectors appears to decrease (Fig. 5) when there is a shift to bigger droplets and higher LWC. This

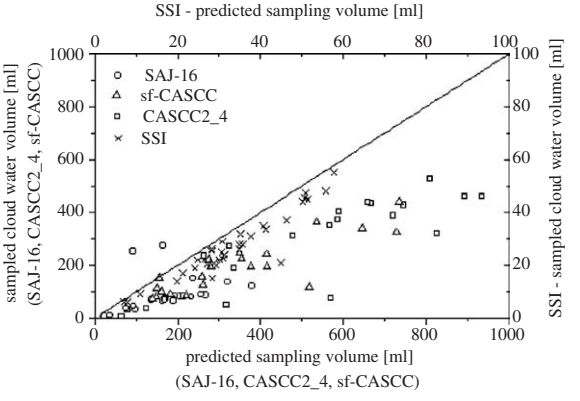

Fig. 5. Sampling efficiencies of low- and high-volume cloud water samplers during E I–E III.

may reflect loss of droplets off the collection strands and/or losses to interior collector walls, a phenomenon observed previously in large drop fogs.

The sampling efficiency for the two stages of the size fractionating samplers is presented in Fig. 6. Close to the 1:1 line is the sf-CASCC collector's first stage (17–32 μm). Actual collected volumes for the second stage, however, consistently fall below the "theoretical" line. This pattern also has been observed at other locations and appears to reflect inter-stage droplet losses during collector operation (Demos et al. 1996). In the TSCI-first stage (12–32 μm) the sampling efficiency as defined above was on average 56% (45–70%). The cloud water sampling efficiency was higher in the TSCI-second stage (4–12 μm) averaging 76% (58–96%). The biggest differences between predicted and collected cloud water volume were observed during E III in both stages of the TSCI and in the second stage (4–17 μm) of the sf-CASCC collector. This event was characterized by the dominant occurrence of small droplets and large variations in LWC due to sampling near the cloud base. CVI sampling efficiencies were calculated on event basis. During the three main events the CVI 2 sampling efficiency has shown no variations with 70% and somewhat lower (about 55%) for CVI 1 (see Table 1).

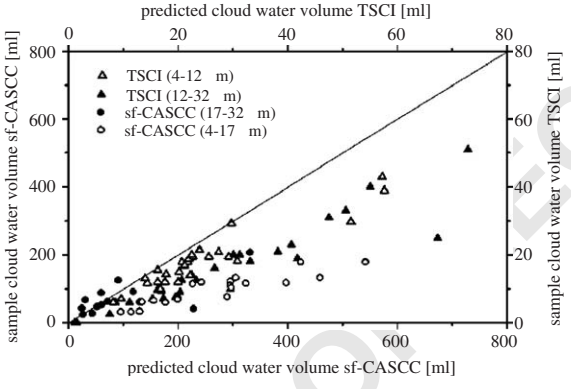

Fig. 6. Sampling efficiencies of the two size fractionating cloud water samplers.

Cloud water sampling performed by high- and low-volume samplers at Mt. Schmücke showed different sampling efficiencies from sampler to sampler and, in some cases from event to event. As already mentioned, the reasons for the variation of the sampling efficiencies are several. High wind speeds (gusts) near 10 m s^{-1} produced an environment where cloud drop sampling was often non-isokinetic. Differences in sampler design certainly influence sampler efficiency. Observed sampling of efficiencies near 50% and higher were judged adequate since sufficient water was collected for all planned analytical processes. Important is a representative sampling over the whole droplet spectra or the selected droplet fraction. Chemical cloud water composition results are described below using observations from the low-volume SSI and the high-volume CASCC2_4 collectors, the TSCI two-stage impactor and the CVI.

3.3. Cloud water ionic composition

Aerosols comprised of water-soluble compounds are often efficient cloud condensation nuclei (CCN). However, each particle may have a different chemical composition and hence, hygroscopicity. Inorganic salt particles, for example NaCl, NH_4NO_3, and $(NH_4)_2SO_4$, are often quite effective CCN (e-g., Lohmann et al., 2004). The role of organic compounds as CCN is more uncertain. However, organic compounds with oxygenated functional groups, such carboxylic and dicarboxylic acids, that contribute to their water solubility may also act as CCN. This confirm results from the Schmücke experiment (van Pinxteren et al., 2005; Müller et al., 2005; Wolke et al., 2005) The main factors controlling the cloud droplet number concentrations and hence the effective radius of the droplets are the chemical size distribution of the aerosol and the updraft speed at cloud base (Bower et al., 1997).

The ion concentrations of a cloud water sample are influenced by the cloud LWC. For intercomparisons at different sampling locations and times, therefore, it is important to account for dilution due to changing LWC. This can be done by multiplying the aqueous solute

Table 1
Cloud water samplers used at the summit site during the FEBUKO experiment

Sampler ID	Operator	Airflow (m^3 h^{-1})	Sampling efficiency (%)	Sampling direction
CASCC2_4	IfT	1392	56±17, $n = 56$	Horizontal
SAJ-16	ZUF	400	51±37, $n = 53$	Vertical
SSI	BTU	120	79±11, $n = 92$	Horizontal
TSCI	BTU	180	66±13, $n = 45$	Horizontal
sf-CASCC	Collett Jr./IfT	1140	45±11, $n = 21$	Horizontal
CVI-1	IfT	6	53±11, $n = 22$	Horizontal
CVI-2	IfT	6	64±17, $n = 21$	Horizontal

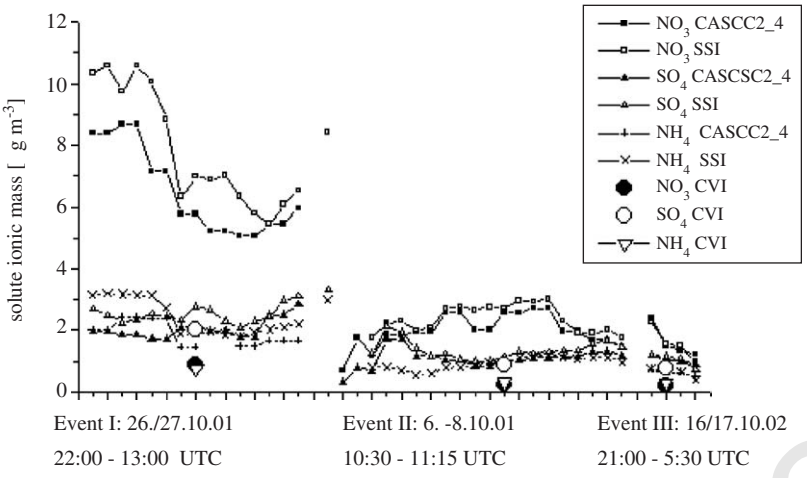

Fig. 7. Comparison of solute ionic mass in the cloud water collected by the low-volume samplers SSI and CVI and the high-volume sampler CASCC2_4.

concentration by LWC to obtain the amount of solute present in cloud drops per unit volume of air:

$$m_{isol} = c_{isample} \times \overline{LWC}, \quad (2)$$

where m_{isol} is the solute mass of compound i (i.e. μg) in cloud per m^3 air, $c_{isample}$ the aqueous concentration of compound i (i.e. $mg\,l^{-1}$) in cloud water, and $\overline{LWC}$ is the LWC averaged over the sampling time.

Temporal variations of the concentrations of NO_3^-, SO_4^{2-}, and NH_4^+ observed during cloud events E I–III are shown in Fig. 7, where results for two different samplers are given. Comparing the three events, solute masses in "E I" are nearly a factor of 2–3 above those in "E II" and "E III". Differences in meteorology and air composition between these events are discussed by Brüggemann et al. (2005). A systematic small difference in the ion concentrations was found between samples collected by the SSI low-volume jet impactor and the high-volume CASCC2_4 string collector; the solute ionic mass in cloud water sampled by the SSI was on average about 8–15% higher than in CASCC2_4 samples. The sulfate content of the cloud droplets sampled with the CVI agree well with the solute sulfate in the cloud water samples; not surprisingly, the nitrate and ammonium concentrations in cloud drop residuals were about ten times lower compared to the cloud water samples, likely reflecting evaporative losses of these more volatile constituents during drop evaporation in the CVI (Mertes et al., 2005).

The cloud water collected by the both SSI and CASCC2_4 samplers was also analyzed for WSOC. Analyses were completed by the BTU central laboratory (SSI samples) and the IfT-laboratory (CASCC2_4 samples). Results for events E I and E II are presented in Fig. 8, the data agree well. Further discussion of WSOC data is given in Brüggemann et al. (2005). The

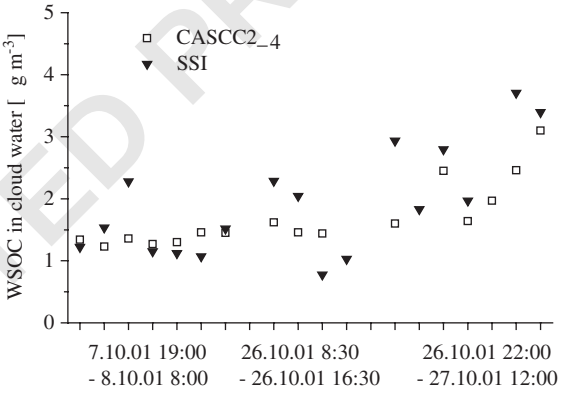

Fig. 8. Mass of water soluble organic carbon (WSOC) in the cloud water sampled by the string collector CASCC2_4 and the droplet impactor SSI during E I and E II.

WSOC content in the cloud water was in the same range as the solute concentrations of the SO_4^{2-} and NH_4^+, indicating the potential importance of these clouds in the processing of organic matter in the atmosphere (see also among others Feng and Möller, 2004; Mészáros, 1999; Novakov and Penner, 1993).

The time available for the droplets to grow is important for the size dependence of solute concentrations. Size resolved cloud water sampling was made during events "E I" and "E III". Data from the Two-Stage Cloud water Impactor (TSCI) are presented here (see Figs. 9a and b and 10a and b). During both events nitrate was the dominant inorganic anion, followed by sulfate and ammonium. During E I the solute ionic mass per m^3 air was a factor 2–4 higher in the big droplets

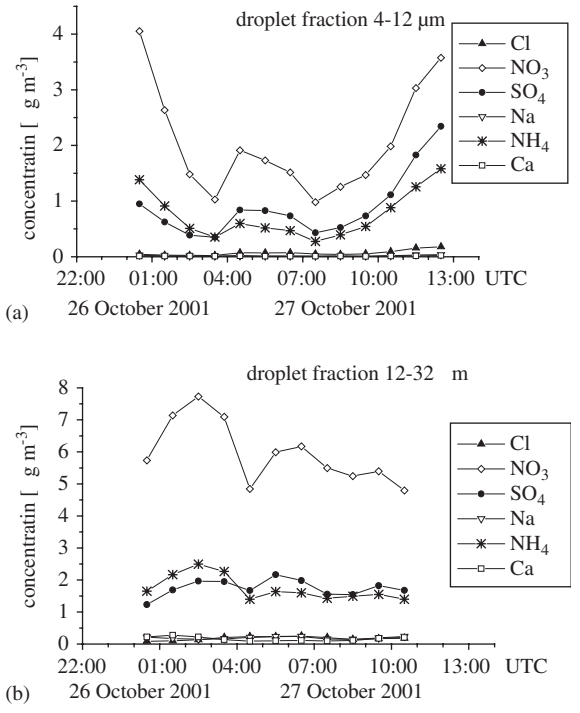

Fig. 9. Ionic composition of event E I: (a) in the small droplet fraction of the TSSI; (b) in the fraction of big droplets of the TSSI.

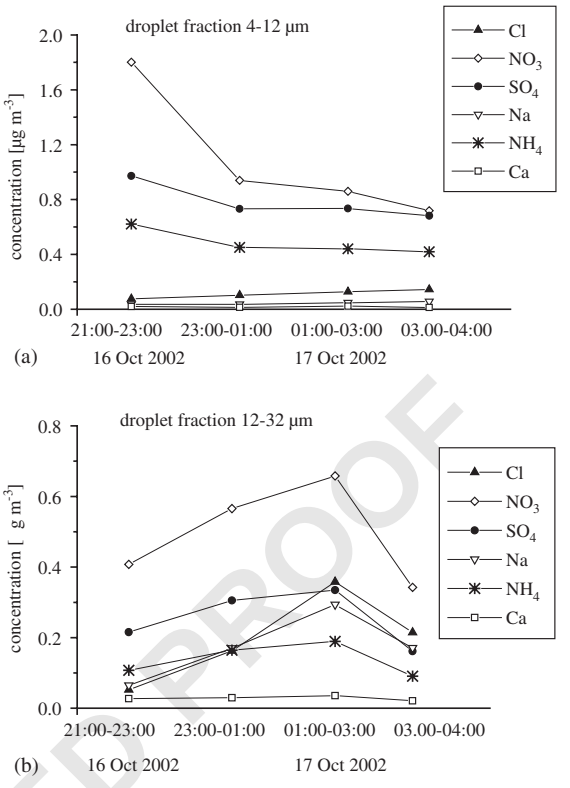

Fig. 10. Ionic composition of event E III: (a) in the fraction of small droplets of TSSI; (b) in the fraction of big droplets of the TSSI.

(12–32 µm) compared to the small ones (Figs. 9a and b). This could be an indication that the cloud droplets were formed by orographic lifting of the air at Mt. Schmücke. The observed time series are very similar for the main inorganic ions and follow changes in LWC and droplet spectra (Section 3.1, Figs. 3a and 4a). Concentration changes observed between 03:00 and 05:00 UTC may be caused also by changes in the particle number concentration observed simultaneously at the upwind site (Mertes et al., 2005) and changes in height above cloud base (see Fig. 3a). Sodium and chloride were observed in both size ranges at low concentration, indicating the loss of sea salt dominance in the air mass during cross-continent transport.

During "E III" cloud droplets were collected all the time near cloud base and concentrations of all main ions (esp. sulfate, nitrate and ammonium) are about three times larger in the small droplet fraction (Figs. 10a and b). With no significant changes of the droplet spectra (Fig. 4b) and of particle number concentration below cloud or of interstitial particles in the cloud (Mertes et al., 2005), no significant changes resulted in the chemical composition of both drop size fractions (Fig. 10b). The observed drop size-partitioning of sodium and chloride (indicating the marine influence of the air mass) suggest that (larger) sea salt aerosol particles served as activation sites for larger droplets than observed for (smaller) ammonium sulfate or ammonium nitrate particles.

4. Summary

For the first time at Mt. Schmücke in the Thuringian Forest (Germany), measurements of cloud liquid water content and cloud base height were made simultaneously. About two-thirds all low clouds (up to a height of 2000 m above ground at the upwind site) observed in October 2001 and October 2002 had their cloud base below Mt. Schmücke summit. The station was in cloud nearly half of both experimental periods. Summit LWC in these clouds averaged approximately 200 mg m^{-3}.

The observations done at this site confirm the increase in liquid water content with the height above cloud base. During event E I a high correlation between LWC and height above cloud base was found ($r = 0.78$), these LWC measurements were made often 300 m deep in the cloud. Throughout E III the Mt. Schmücke summit was near cloud base, only 50 to 100 m deep in cloud.

Conditions for adiabatic condensation are probably disturbed this close to cloud base by processes like droplet evaporation by mixing with drier air, and aerosol and gas scavenging. The drop size spectrum was very stable in this event, mainly droplets between 2 and 10 μm diameter were observed. Differences in sampling position within the cloud between these two events provide a nice contrast for planned numerical simulations of cloud development and pollutant processing. Several cloud water collectors were in use during the field campaign. Cloud collectors sampling efficiencies ranged from 45% to 79% when averaged over all cloud events of the FEBUKO campaigns. A good agreement between the high-volume strand collectors and the low-volume cloud droplet impactors was found in the LWC range between 100 and 350 mg m^{-3}. At higher liquid water contents with higher number of bigger droplets, the sampling efficiency of the strand collectors decreased. On average, a difference of approximately 10% was observed between measured cloud water chemical compositions from these two collector types.

The chemical composition of cloud droplets varies as a function of size because of the inhomogeneous chemical composition of the cloud condensation nuclei (CCN) on which the droplets grow and the sampling height above cloud base. Size-resolved ionic cloud water composition in two cloud drop classes ($4\,\mu m < D < 12\,\mu m$ and $D > 12\,\mu m$ diameter) are presented for sample times near cloud base (E III) and deep inside cloud (E I).

Uncited references

Acker et al., 2002; Acker et al., 2003; Pruppacher and Jaenicke, 1995.

Acknowledgements

We would like to thank our colleagues from Institute for Tropospheric Research Leipzig, Zentrum für Umweltforschung Universität Frankfurt, Technical University Darmstadt as well as Deutscher Wetterdienst (station Schmücke) and Umweltbundesamt (station Schmücke) for excellent co-operation in the field measurements and the two reviewers for their careful revision of the manuscript. This work was supported by the German BMBF (07ATF01; 07ATF40) and by the US National Science Foundation (ATM-9980540 and ATM-0222607).

References

Acker, K., Mertes, S., Möller, D., Wieprecht, W., Auel, R., Kalaß, D., 2002. Case study of cloud physical and chemical processes in low clouds at Mt. Brocken. Atmospheric Research 64, 41–51.

Acker, K., Wieprecht, W., Möller, D., 2003. Chemical and physical characterisation of low clouds: results from the ground based cloud experiment FEBUKO. Archives of industrial hygiene and toxicology 54, 231–238.

Arends, B.G., 1996. Aerosol and cloud microphysics, measurements and interpretations. Dissertation. University Utrecht, Netherlands.

Berner, A., 1988. The collection of fog droplets by a jet impaction stage. Science of the Total Environment 73, 217–228.

Bower, K.N., Choularton, T.W., Gallagher, M.W., Colvile, R.N., Wells, M., Beswick, K.M., Wiedensohler, A., Hansson, H.-C., Svenningsson, B., Swietlicki, E., Wendisch, M., Berner, A., Kruisz, C., Laj, P., Facchini, M.C., Fuzzi, S., Bizjak, M., Dollard, G., Jones, B., Acker, K., Wieprecht, W., Preiss, M., Sutton, M.A., Hargreaves, K.J., Storeton-West, R.L., Cape, J.N., Arends, B.G., 1997. Observations and modelling of the processing of aerosol by a hill cap cloud. Atmospheric Environment 31, 2527–2543.

Brüggemann, E., Gnauk, T., Mertes, S., Acker, K., Auel, R., Wieprecht, W., Möller, D., Collett Jr., J.L., Chemnitzer, R., Rüd, C., Junek, R., Herrmann, H., 2005. Schmücke hill cap cloud and valley stations aerosol characterisation during FEBUKO (I): particle size distribution and main components. Atmospheric Environment, this issue.

Colvile, R.N., Bower, K.N., Choularton, T.W., Gallagher, M.W., Beswick, K.M., Arends, B.G., Kos, G.P.A., Wobrock, W., Schell, D., Hargreaves, K.J., Storeton-West, R.L., Cape, J.N., Jones, B.M.R., Wiedensohler, A., Hansson, H.-C., Wendisch, M., Acker, K., Wieprecht, W., Pahl, S., Winkler, P., Berner, A., Kruisz, C., Gieray, R., 1997. Meteorology of the Great Dun Fell Cloud Experiment 1993. Atmospheric Environment 31, 2407–2420.

Demoz, B., Collett Jr., J.L., Daube Jr., B.C., 1996. On the Caltech active strand cloudwater collectors. Atmospheric Research 41, 47–62.

Daube Jr., B., Kimball, K.D., Lamar, P.A., Weathers, K.C., 1987. Two new ground-level cloud water sampler designs which reduce rain contamination. Atmospheric Environment 21 (4), 893–900.

Feng, J., Möller, D., 2004. Characterization of water-soluble macromolecular substances in cloud water. Journal Atmospheric Chemistry 48, 217–233.

Fuzzi, S., Orsi, G., Bonforte, G., Zardini, B., Franchini, P.L., 1997. An automated fog water collector suitable for deposition networks: design, operation and field tests. Water Air Soil Pollution 93, 383–394.

Gerber, H., 1991. Direct measurement of suspended particulate volume concentrations and far-infrared extinction coefficient with a laser diffraction instrument. Applied Optics 33, 4824–4831.

Gnauk, T., Brüggemann, E., Müller, K., Chemnitzer, R., Rüd, C., Galgon, D., Wiedensohler, A., Acker, K., Auel, R., Wieprecht, W., Möller, D., Jaeschke, W., Herrmann, H., 2005. Aerosol characterisation at the FEBUKO upwind

station Goldlauter (I): particle mass, main ionic components, OC/EC, and mass closure. Atmospheric Environment, this issue.

Herckes, P., Hannigan, M.P., Trenary, L., Lee, T., Collett Jr., J.L., 2002. The organic composition of radiation fogs in Davis (California). Atmospheric Research 64, 99–108.

Heinold, B., Tilgner, A., Jaeschke, W., Haunold, W., Knoth, O., Wolke, R., Herrmann, H., 2005. Meteorological characterisation of the FEBUKO hill cap cloud experiments, part II: tracer experiments and flow characterisation with nested non-hydrostatic atmospheric models. Atmospheric Environment, this issue.

Herrmann, H., Wolke, R., Müller, K., Brüggemann, E., Gnauk, T., Barzaghi, P., Mertes, S., Lehmann, K., Massling, A., Birmili, W., Wiedensohler, A., Wieprecht, W., Acker, K., Jaeschke, W., Kramberger, H., Syrcina, B., Bächmann, K., Collett Jr., J.L., Galgon, D., Schwirn, K., Nowak, A., van Pinxteren, D., Plewka, A., Chemnitzer, R., Rüd, C., Hofmann, D., Tilgner, A., Diehl, K., Heinold, B., Hinneburg, D., Knoth, O., Sehili, A.M., Simmel, M. Wurzler, S., Mauersberger, G., Majdik, Z., Müller, F., 2005. FEBUKO and MODMEP: field measurements and modelling of aerosol and cloud multiphase processes. Atmospheric Environment, this issue.

Junkermann, W., Dietrich, J., Wolf, P., Wieprecht, W., Slemr, J., Kolthoff, G., Niessner, R., 1994. Investigation of the vertical distribution of trace components in the lower troposphere using a cable car. In: Borrell, M., Borrell, P., Cvitas, T., Seiler, W. (Eds.), Proceedings of the EUROTRAC Symposium '94, Transport and Transformation of Pollutants in the Troposphere. SPB Academic Publishing, Den Haag, 1156–1161.

Laj, P., Fuzzi, S., Lazzari, A., Ricci, L., Orsi, G., Berner, A., Schell, D., Günther, A., Wendisch, M., Wobrock, W., Frank, G., Martinsson, B., Hillamo, R., 1998. The size-dependent chemical composition of fog drops. Contributions to Atmospheric Physics 71, 115–130.

Lohmann, U., Broekhuizen, K., Leaitch, R., Shantz, N., Abbat, J., 2004. How efficient is cloud droplet formation of organic aerosols. Geophysical Research Letters 31, L05108.

Marple, V.A., Willeke, K., 1976. Impactor design. Atmospheric Environment 10, 10–15.

Mertes, S., Schwarzenböck, A., Laj, P., Wobrock, W., Pichon, J.M., Orsi, G., Heintzenberg, J., 2001. Changes of cloud microphysical properties during the transition from supercooled to mixed-phase conditions during CIME. Atmospheric Research 58 (4), 267–294.

Mertes, S., Galgon, D., Schwirn, K., Nowak, A., Lehmann, K., Massling, A., Wiedensohler, A., Wieprecht, W., 2005. Evolution of particle concentration and size distribution observed upwind, inside and downwind hill clouds at connected flow conditions during FEBUKO. Atmosheric Environment, this issue.

Mészáros, E., 1999. New results of the chemical composition of aerosol particles in the atmosphere. Are cloud condensation nuclei produced by the biosphere? Idöjaras 103, 85–91.

Möller, D., Acker, K., Wieprecht, W., 1996. A relationship between liquid water content and chemical composition in clouds. Atmospheric Research 41, 321–335.

Moore, K.F., Sherman, D.E., Reilly, J.E., Collett Jr., J.L., 2002. Development of a multi-stage cloud water collector: 1. Design and field performance evaluation. Atmospheric Environment 36, 31–44.

Müller, K., van Pinxteren, D., Plewka, A., Svrcina, B., Kramberger, H., Hofmann, D., Bächmann, K., Herrmann, H., 2005. Aerosol characterisation at the FEBUKO upwind station Goldlauter (II): detailed organic chemical characterisation. Atmospheric Environment, this issue.

Novakov, T., Penner, J.E., 1993. Large contribution of organic aerosols to cloud-condensation-nuclei concentrations. Nature 365, 823–826.

Ogren, J.A., Heintzenberg, J., Charlson, R.J., 1985. In-situ sampling of clouds with a droplet to aerosol converter. Geophysical Research Letters 12 (3), 121–124.

Pruppacher, H.R., Jaenicke, R., 1995. The processing of water vapour and aerosols by atmospheric clouds, a global estimate. Atmospheric Research 38, 283–295.

Pruppacher, H.R., Klett., J.D., 1978. Microphysics of Clouds and Precipitation. Reidel Publishing Company, Dortrecht, Boston, London.

Schell, D., Georgii, H.-W., Maser, R., Jaeschke, W., Arends, B.G., Kos, G.P.A., Winkler, P., Schneider, T., Berner, A., Kruisz, C., 1992. Intercomparison of fog water samplers. Tellus 44B (5), 612–631.

Schell, D., Maser, R., Wobrock, W., Jaeschke, W., Georgii, H.W., Kos, G.P.A., Arends, B.G., Beswick, K.M., Bower, K.N., Gallagher, M.W., 1997a. A two-stage impactor for fog droplet collection: design and performance. Atmospheric Environment 31 (16), 2671–2679.

Schell, D., Wobrock, W., Maser, R., Preiss, M., Jaeschke, W., Georgii, H.W., Gallagher, M.W., Bower, K.N., Beswick, K.M., Pahl, S., Facchini, M.C., Fuzzi, S., Wiedensohler, A., Hansson, H.-C., Wendisch, M., 1997b. The size-dependent chemical composition of cloud droplets. Atmospheric Environment 31 (16), 2561–2576.

Schwarzenböck, A., Heintzenberg, J., 2000. Cut size minimization and cloud element break-up in a ground-based CVI. Journal of Aerosol Science 31 (4), 477–489.

Schwarzenböck, A., Heintzenberg, J., Mertes, S., 2000. Incorporation of aerosol particles between 25 and 850 nanometers into cloud elements: Measurement with a new complementary sampling system. Atmospheric Research 52 (4), 241–260.

Straub, D.J., Collett Jr., J.L., 2002. Development of a multistage cloud water collector: 2. Numerical and experimental calibration. Atmospheric Environment 36, 45–56.

Tilgner, A., Heinold, B., Nowak, A., Herrmann, H., 2005. Meteorological characterisation of the FEBUKO hill cap cloud experiments, part I: synoptic characterisation of measurement periods. Atmospheric Environment, this issue.

Valverde-Canossa, J., Wieprecht, W., Acker, K., Moortgat, G.K., 2005. H_2O_2 and organic peroxide measurements in an orographic cloud: the FEBUKO experiment. Atmospheric Environment, this issue.

van Pinxteren, D., Plewka, A., Hofmann, D., Müller, K., Kramberger, H., Svrcina, B., Bächmann, K., Jaeschke, W., Mertes, S., Collett Jr., J.L., Herrmann, H., 2005. Schmücke hill cap cloud and valley stations aerosol chemical composition during FEBUKO (II): organic compounds. Atmospheric Environment, this issue.

Wieprecht, W., Möller, D., Acker, K., Naumann, S., 1995. Influence of cloud physical parameters on chemical compo-

sition of clouds. In: Power, H., et al. (Eds.), Air Pollution III, vol. 2: Air Pollution Engineering and Management. Computational Mech. Publ., Southampton, UK, pp. 199–205.

Winkler, P., 1992. Design and calibration of a fog water collector. Instruments and observing methods. WMO/TD-No. 462, 17–21.

Wolke, R., Sehili, A.M., Simmel, M., Knoth, O., Tilgner, A., Herrmann, H., 2005. SPACCIM: a parcel model with detailed microphysics and complex multiphase chemistry. Atmospheric Environment, this issue.

3B2v8.06a/w (Dec 5 2003).51c XML:ver:5.0.1 AEA : 5770 Prod.Type:FTP pp.1–13(col.fig.:NIL) ED:JojiG. PAGN:VG SCAN:– – –

ARTICLE IN PRESS

Available online at www.sciencedirect.com

SCIENCE DIRECT®

ELSEVIER

Atmospheric Environment ▮ (▮▮▮▮) ▮▮▮–▮▮▮

ATMOSPHERIC ENVIRONMENT

www.elsevier.com/locate/atmosenv

Schmücke hill cap cloud and valley stations aerosol characterisation during FEBUKO (I): Particle size distribution, mass, and main components

E. Brüggemann[a,*], T. Gnauk[a], S. Mertes[a], K. Acker[b], R. Auel[b], W. Wieprecht[b], D. Möller[b], J.L. Collett Jr.[c], H. Chang[c], D. Galgon[a], R. Chemnitzer[a], C. Rüd[a], R. Junek[d], W. Wiedensohler[a], H. Herrmann[a]

[a]*Leibniz-Institut für Troposphärenforschung e.V., Permoserstr. 15, D-04318 Leipzig, Germany*
[b]*Brandenburgisch-Technische Universität, Abt. Luftchemie, Vollmerstr. 13, D-12489 Berlin, Germany*
[c]*Department of Atmospheric Science, Colorado State University, Ft. Collins, CO 80523, USA*
[d]*Umweltbundesamt, Messstelle Schmücke, D-98559 Gehlberg, Germany*

Abstract

Hill cap cloud field experiments were performed during autumn 2001 and 2002 in the Thüringer Wald (Germany). Gas phase trace compounds were determined at an upwind, summit, and downwind sites and major particulate components at an upwind and downwind site. Cloud water and total cloud components (drop residuals and interstitial particles) were determined at a summit site. Three events were fulfilling the criteria for the best conditions defined by during a connected flow upwind–summit–downwind sites and further detailed analysis was performed on these events. Cloud water components were compared with particle concentration at upwind and downwind site. The concentrations of non-volatile components in cloud water were found to be in good agreement with corresponding particle phase concentrations at the upwind site. Downwind site particulate component concentrations of non-volatile compounds were lower than in cloud water indicating loss processes during transport such as deposition. The concentrations of volatile components were found to be higher in cloud water than in the particle phase concentrations at up- and downwind site samples probably due to a loss from impactor sampling technique as well as a transport loss. Indications for changes of aerosol composition by cloud processes were found from a limited number of cases. Elevated sulphate and ammonium concentrations from upwind to downwind site in the smallest particle size range ($PM_{0.05–0.14}$) were found during event I (20% and 17%) and event III (70% and 150%), respectively. In the particle size range of $PM_{0.14–0.42}$ an increase of OC by about 20% for event I was observed. Considering the relative contributions of components to the single size range mass (avoiding physical sink processes), comparatively higher increases for sulphate, nitrate, ammonium, OC, and EC could be observed. Indications of an increase of aerosol mass can be derived in some cases from the aerosol number and volume size distributions. Results from a complex multiphase model (SPACCIM) are consistent showing an increase in concentrations of some compounds for some cases.

Keywords: Size-segregated particle characterisation; Cloud water; Major ions; OCEC; Metals

*Corresponding author. Tel.: +49 341 235 2535; fax: +49 341 235 2325.
E-mail address: erika@tropos.de (E. Brüggemann).

1352-2310/$ - see front matter © 2005 Published by Elsevier Ltd.
doi:10.1016/j.atmosenv.2005.02.013

1. Introduction

The chemical and physical characterisation of trace gases and aerosol before, during, and after a cloud passage is important to understand the cloud chemistry and the interaction between gases, aerosol, and cloud droplets. Most of such characterisation studies in the past focused mainly on inorganic components and only a small number of organic species (e.g. MSA, formic and acetic acid) were included. On the other hand, the knowledge of organic components is necessary for the development of better physico-chemical multiphase models.

During the last decades, a number of cloud investigations have been carried out to characterise mainly cloud water. In Europe, investigations of cloud water were carried out for different parameters and processes, e.g. in Germany—Brocken (Plessow et al., 2001; Acker et al., 2002), Switzerland—Jungfraujoch (Oberholzer et al., 1992; Baltensperger et al., 1998), Austria—Sonnblick (Kasper et al., 1998, Hitzenberger et al., 2000), England—Holme Moss (Dore et al., 2001), France—Puy de Dome (Voisin and Legrand, 2000).

The FEBUKO research cluster (Field investigations of budgets and conversions of particle phase organics in tropospheric cloud processes) within the German Atmospheric Research Programme AFO2000 (www.afo-2000.de) intends to improve the understanding of tropospheric multiphase processes and especially the interaction of aerosols and clouds with an emphasis on organic particle constituents. Therefore, a hill cap cloud experiment was carried out in order to investigate the changes of major particulate inorganic components and a wide spectrum of organic species.

2. Experimental setup

A set of meteorological parameters, trace gas components, cloud parameters and particle characteristics were determined at the two valley measurement sites (upwind site U, 605 m asl and downwind site D, 732 m asl) and at the summit site S, (937 m asl). The following meteorological conditions had to be met for the measurements: wind direction 210–250°, wind speed 5–12 $m\,s^{-1}$, $LWC > 0.1\,g\,m^{-3}$, and no precipitation. Trace gas concentrations (SO_2, NO_x, O_3) are available for E I (event I), E II (event II), and E III (event III) CO concentrations are only available for E III (see Table I, Electronic Supplemental Material, ESM). An overview of the FEBUKO experimental design is given by Herrmann et al. (2005).

The collection of particles for chemical characterisation using filter samplers and impactors was carried out at the valley stations (U and D), where an equal set of particle samplers was used (BERNER impactor—BI) (50% cut-offs: stage 1: 0.05–0.014, stage 2: 0.14–0.42, stage 3: 0.42–1.2, stage 4: 1.2–3.5, stage 5: 3.5–10 μm aerodynamic diameter) and High Volume Andersen filter sampler—HVA (PM_{10}). BERNER impactor samples were collected at 60% RH using a relative humidity conditioner. Only at site U, the Steamjet technique (Acker et al., 2003) with online ion chromatography—StJ) was used. A Twin Differential Mobility Particle Sizer (T-DMPS) within the particle size range of 3–900 nm was used to measure the number size distribution (NSD) of particles at U and D sites (Birmili et al., 1999).

On top of a 20 m research tower different active cloud water collectors operated at the summit site: four single stage samplers CASCC2_4 (Caltech Active Strand Cloud Water Collector in 2001 and 2002, see Demoz et al., 1996) from the Colorado State University (addressed CW-IfT), a Single Stage slit jet Impactor (SSI, Winkler, 1992) from the Brandenburgisch-Technische Universität Cottbus (in 2001 and 2002), (CW-BTU), and a size fractionating sampler sf-CASCC (Demoz et al., 1996) from the Colorado State University, (called CW-CSU), used only in 2002 for the determination of ionic components, water-soluble carbon and metals. A detailed description of collectors is given in Wieprecht et al. (2005). The interstitial aerosol (I) and the cloud droplet residues (R) were collected by means of a counterflow virtual impactor (CVI) and an inlet for interstitial particles (INT) as well (Schwarzenböck et al., 2000).

Particle mass concentrations were gravimetrically determined using a Mettler-Toledo micro-balance UMT2 after 48 h conditioning of the samples at 20 °C and 50% RH. The ionic components Na^+, NH_4^+, K^+, Mg^{2+}, Ca^{2+} of particles were analysed using ion chromatography (Metrohm), Cl^-, NO_3^-, SO_4^{2-} using capillary electrophoresis (Spectrophoresis), (Neusüß et al., 2000a, b) as well as from the StJ samples with online analysis using IC (Dionex) (Brüggemann and Rolle, 1998; Acker et al., 2003). The particulate organic carbon (OC) and elemental carbon (EC) concentration were determined by a two step thermographic method (C-mat 5500, Ströhlein) (Plewka et al., 2004). From HVA samples the metals (Fe, Cu, Mn, Zn) were analysed by atomic absorption spectrometry (Perkin Elmer) (Chemnitzer, 2002; Rüd, 2003). The components in cloud water were determined using the same analytical methods as the particle components. For the water-soluble OC a Shimadzu TOC-V CPH analyser was used. Total organic carbon (TOC) was separated in dissolved organic carbon (DOC) and particulate organic carbon (POC) by filtration of the liquid samples (0.45 μm pore size).

The successful participation in international ring analysis by WMO-EPA each year since 1991 (http://marble.asrc.cestm.albany.edu/qasac/) ensures the high

quality of the ion analysis. The International Round Robin Test Carbon Shoot of Stage I (Schmid et al., 2001) and Stage II (Puxbaum, TU Vienna, unpublished) served as quality assurance for the used OCEC method.

Analytical uncertainties were determined in different concentration ranges by replicate analysis of ionic and carbonaceous components. The repeatability (95% confidence level) was found to be about 15% for nitrate, sulphate, and ammonium and about 20% for OCEC for stages 1 and 5 and about 5% and 10% for stages 2–4.

3. Results and discussion

In both campaigns a total set of 14 events was identified for intensive measurements (Herrmann et al., 2005). Among these 14 events connected flow conditions were fulfilled during three events (E)—E I: 26 October 22:00–27 October 13:00 UTC (2001), E II: Part 1: 06 October 10:30–14:15 UTC (2001), Part 2: 07 October 13:15–15:15 UTC (2001), Part 3: 07 October 18:00–08 October 11:15 UTC (2001), and E III: 16 October 21:00–17 October 4:10 (2002). A connected flow condition was demonstrated by a profound meteorological analysis including all information available (e.g. data of synoptic and local scale meteorological conditions, satellite data, trace gas concentrations) (Tilgner et al., 2005a; Heinold et al., 2005). These periods were selected for further discussion. Additionally, tracer experiments before and during the campaigns were carried out to investigate the real flow conditions.

In all events a particle mass concentration loss from site U to D was observed (Fig. 4). The losses (in total about 30% to 40%) were due to physical sink processes during transport or sampling losses. The estimation of entrainment for the three events discussed in Herrmann et al. (2005) reveals that no significant entrainment occurred. The particle sampling techniques may cause errors, e.g. flow (bounce-off in impactor, volatilisation and/or adsorption in filter) and/or temperature and pressure effects (change of gas to particle equilibrium) (Gnauk et al., 2005). BI particle sampling was performed under controlled relative humidity (60% RH) in order to maintain size cuts independent of the changing ambient RH and to minimise bounce-off effects (Neusüß et al., 2000a). These effects were investigated, e.g. in the INTERCOMP 2000 campaign (e.g. Müller et al., 2004; Hitzenberger et al., 2004).

Physical loss processes influence the particulate trace components and are able to mask results of chemical cloud processing. The use of percentage of the size range particle mass seems to be the better way to find out cloud effects avoiding the influence of physical losses. Therefore, the mass fraction values are included in the following discussion.

3.1. Cloud water

Cloud water samples were taken in 1 and 2 h intervals at summit site by bulk sampler (CW-IfT and CW-BTU). In Fig. 1 the cloud water time series of liquid water content (LWC, measured by a PVM100, see Wieprecht et al., 2005), nitrate, sulphate, ammonium (CW-BTU sampler), as well as DOC, POC, and pH value (CW-IfT sampler) are shown. All values for the cloud water components (including chloride, sodium, potassium, magnesium, calcium, and metals) are listed in Table III and pH and LWC values in Table IV (ESM).

The variability and the level of the LWC in E I was higher than in E II and III. Measurements of LWC in droplets of 4–12 and 12–32 μm diameters as well as the cloud base height (Wieprecht et al., 2005) showed that the sampling site S was located alternating in cloud and at cloud base during E I. The LWC in E I decreased simultaneously with the increase of cloud base height. The change of cloud base height was possibly caused by mixing of another air mass (frontal process) between 4 and 6 UTC (Tilgner et al., 2005a).

The pH values range between 4.0 and 5.0 (E I), 4.3 and 5.1 (E II), as well as 4.1 and 4.6 (E III). The LWC was found to be on average 334 ± 77, 230 ± 50, and $196 \pm 19\,\mathrm{mg\ m^{-3}}$ for E I, II, and III, respectively. In E I the initial increase of LWC was associated with a decrease of acidity from 50 to $10\,\mu\mathrm{eq\,l^{-1}}$ of $[H^+]$, corresponding to pH 4.3 and 5.0, respectively. This was followed by an increase up to $100\,\mu\mathrm{eq\,l^{-1}}$ (pH 4.0) and a drop of the LWC by about 30%. Simultaneously, a decrease of the nitrate concentration by about 50% was observed.

Cloud water TOC was separated to DOC and POC by filtration with syringe filters of 0.45 μm pore size. TOC in cloud water was found to be 80–95% of DOC. The time resolved cloud water samples show higher variations (TOC = 2–3.7 $\mu\mathrm{g\,m^{-3}}$) during E I compared to E II (1.3–1.7 $\mu\mathrm{g\,m^{-3}}$) and E III (1–1.4 $\mu\mathrm{g\,m^{-3}}$). In E I an increase of DOC by nearly 100% was observed during the most acidic period of cloud water (pH about 4). It is difficult to compare the carbonaceous concentrations with other hill cap cloud experiments performed in Europe during the last 15 years (Kleiner Feldberg Cloud Experiment 1990; Great Dun Fell Experiment 1993 and 1995; ACE-2 HILLCLOUD Experiment 1997) because the past studies focussed on the ionic composition and OCEC data are not available. Other cloud investigations addressing carbonaceous material indicate similar levels to this study: e.g. 1.4–3.3 $\mu\mathrm{g\,m^{-3}}$ OC and 0.04–0.36 $\mu\mathrm{g\,m^{-3}}$ EC in the liquid phase were found at the Mount Brocken (Harz, Germany) in 1998 (Acker et al., 2002); 0.31–3.65 $\mu\mathrm{g\,ml^{-1}}$ Black Carbon (BC) in 1996 and 0.55–3.0 $\mu\mathrm{g\,ml^{-1}}$ BC in 1997 were detected at the Mount Sonnblick (Alps, Austria) (Hitzenberger et al., 2000). Polluted samples like Po Valley fog water showed

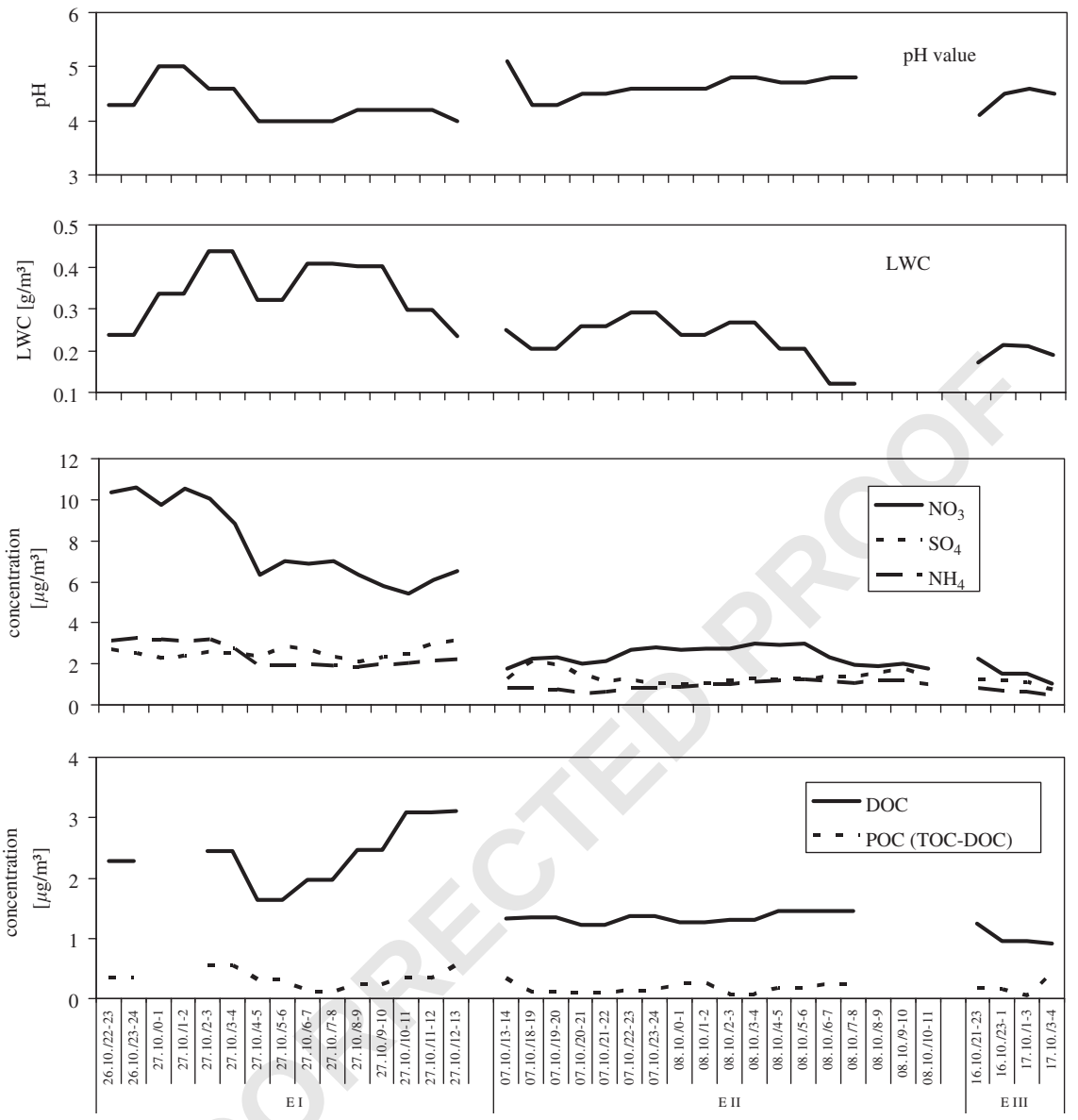

Fig. 1. Time series of pH value, LWC, nitrate, sulphate, ammonium, and DOC in cloud water for events I, II, and III at S site (E I: Part 1: interval not considered due to data gap).

WSOC air concentrations of 3.0–14.3 µg m^{-3} (Facchini et al., 1999).

The mean concentrations of water-soluble metals were of the following order Zn (36, 26, 56 ng m^{-3}) > Fe (17, 18, 10 ng m^{-3}) > Cu (3, 2, 1 ng m^{-3}) ≈ Mn (2, 1, 2 ng m^{-3}) for all three events. In E II and III no significant changes of metal concentrations were found besides analytical variations. In contrast, the Fe concentration in E I was found to be increased probably due to the observed decrease of the pH value in cloud water. It is known that the solubility of different Fe species increases with decreasing pH in the range of 5–4 (Finnlayson-Pitts and Pitts Jr., 2000).

Little information is available on CW trace element concentrations. In a study at Mt. Brocken (Germany) a number of trace metals was investigated (Plessow et al., 2001, and references therein). The ranges of total metal contents were found to be 21–3950 (Fe), 0.8–60 (Mn), 0.42–60.6 (Cu), and 2.5–421 (Zn) ng m^{-3}. In the Great Dun Fell Experiment (Sedlak et al., 1997) average total Fe and Cu concentrations in CW were 27 and

0.24 ng m^{-3}. The CW concentrations determined in this study are found to be in the same range.

3.2. Comparison of cloud water with upwind and downwind site particulate chemical composition

The ionic components and OCEC of droplet residues (R) and interstitial particles (I) in the cloud were determined. Additionally, in E III (campaign 2002) a two stage sampler (CW-CSU) was used and the results are presented as volume-weighted total values. Particles were measured as size-segregated (BI) and PM_{10} (HVA) at the upwind (Gnauk et al., 2005) and downwind site. Additionally, at the site U the Steamjet technique was used for anion determination (avoiding sampling losses of volatile components).

In Fig. 2 results are shown for average concentrations of nitrate, sulphate, and ammonium (about 90% of the total ionic concentration), OCEC, and metals. All impactor stages were summed up forming PM_{10} in order to compare this concentration with those of the HVA, StJ, cloud water components, R and I of clouds. All measured particulate concentrations of the upwind and downwind sites are listed in Tables II and IV (ESM).

Component concentrations in cloud water sampled by different collectors roughly agree for all events. Time series from cloud water components are given in Table III (ESM). Further comparisons between the different cloud water samplers are discussed in Wieprecht et al. (2005).

The sulphate concentration of R corresponds to the concentration of other CW collectors. However, nitrate and ammonium concentrations are smaller. By evaporation of the droplet water the R were released and thereby a fraction of volatile components can be lost. In all three events only 10% of CW nitrate and 30–50% of CW ammonium were found in R. In E I and II a similar concentration of OC for both in CW and R were found, but in E III a considerably higher content (about 80% more) in R, probably due to contamination, was observed. The ionic components were dissolved in CW droplets (more than 90% in E I and II). In E III a considerable part of ionic components was found in the interstitial phase: 40%, 30%, and 30% for nitrate, sulphate, and ammonium, respectively. This means that in comparison to e.g. E I a larger part of small particles was present as non-activated interstitial particles. This is consistent with the finding of the dry particle size distribution inside cloud which showed a shift of a mean diameter to smaller particles (see Mertes et al., 2005). The comparison of OCEC contents in R and I particles shows that in all events the OC/EC ratio was higher in R (R: 3.12, 2.40, 8.14; I: 1.54, 1.72, 1.91 for E I, II, and III, respectively). This means that particles acting as cloud condensation nuclei (CCN) contain more OC and non-activated particles contain more EC in agreement with Gieray et al., 1997.

The CW chemical composition depends on the particulate composition of the activating CCN from the upwind site, the uptake of gaseous components and, finally, components produced by in-cloud reactions. In Table 1 the component fractions of the U and D site particulate samples are related to cloud water concentrations. For the non-volatile components, sulphate (all events) and EC (E I and E III) show approximately the same concentrations in particles at the upwind site as in clouds. The particulate EC deviation in E II is caused possibly by contamination. For the volatile components, nitrate, ammonium, and OC show different behaviour. The particulate nitrate concentration determined by Steamjet technique added with the gas phase concentration of HONO and HNO_3 reaches the nitrate concentration of CW, by the HVA sampler about 60–75%, and by the BI only about 25–40%. Ammonium from the HVA samples was in good agreement with CW, but only 50–90% of CW concentrations were found from BI samples. The particulate OC amounted to 40–90% of CW-TOC.

The concentrations of component determined at the downwind site were found to be lower than that of the upwind site for BI. This also concerns non-volatile components like sulphate and therefore additional physical sink processes can be assumed. The HVA samples from U and D sites show the same concentrations as from CW except nitrate which exhibits smaller values. The HVA collects under 'natural' conditions and can adsorb gaseous components in contrast to the BI which is conditioned to 60% RH producing additional losses by heating of the sample air stream. The expected overestimation of sulphate by HVA in comparison to BI can be seen in event III (difference about 0.3 μg m^{-3}) at the U site, whereas in E I and E II this effect could not be observed. No explanation can be given for these differences at this moment. The measured SO_2 concentrations of about 0.5 ppb are sufficient to produce the excess sulphate of HVA during sampling at the D site of 0.37, 0.70, and 0.35 μg m^{-3} in E I, II, III, respectively.

Despite all drawbacks mentioned impactors are the only instruments for size-segregated particle sampling and analysis of components especially in the size range $D_p < 1$ μm. Losses caused by sampling technique (BI) are the same at U and D sites and were corrected accordingly using the data from other particle samplers for model initialisation.

Particulate metals can be dissolved in cloud droplets. Metals solved in CW can catalyse chemical reactions and contribute to the radical formation and interconversion in atmospheric liquid phase systems (see Herrmann et al., 2005). The water-soluble metals (Fe, Cu, Mn, and Zn) were determined in particles (PM_{10} by

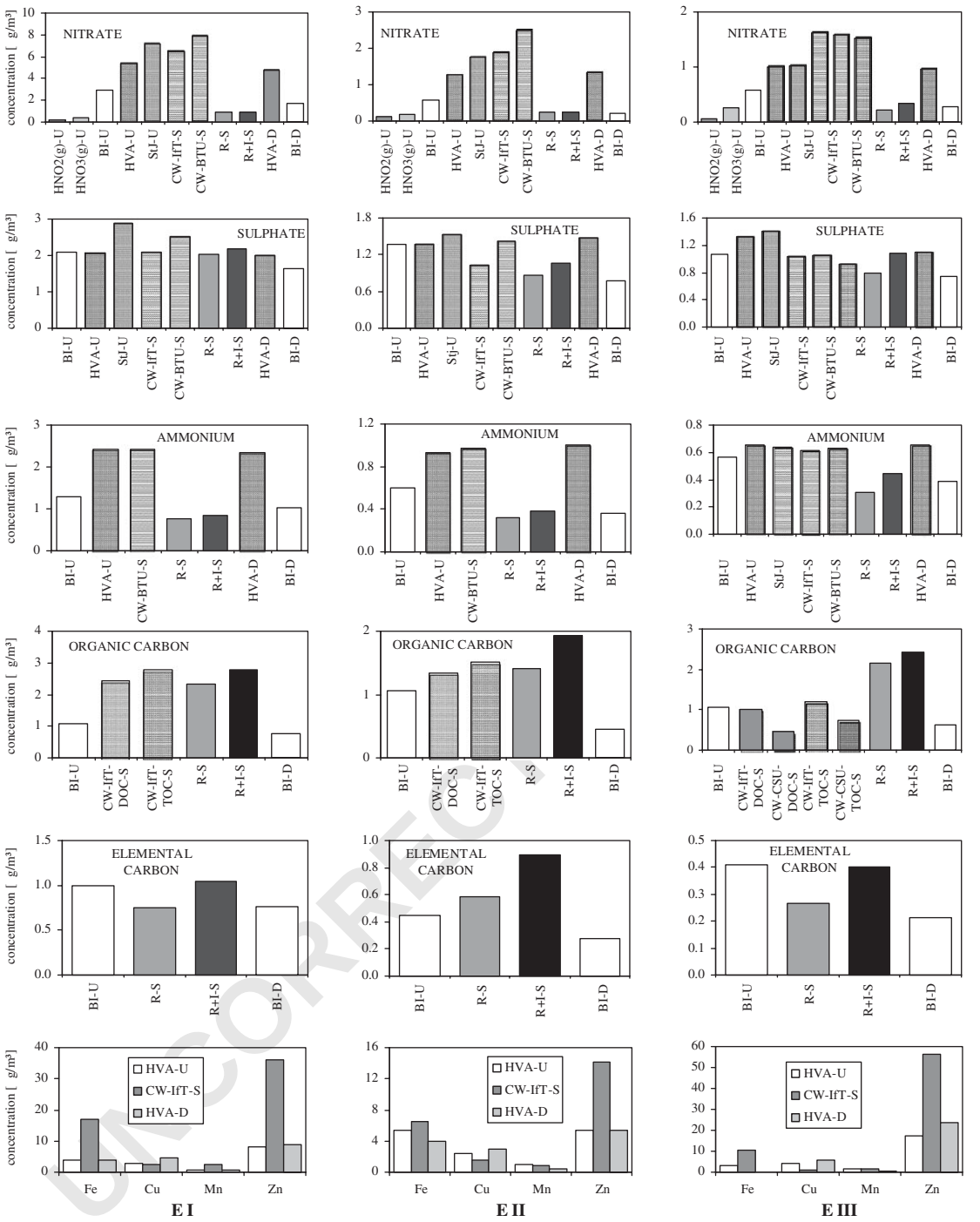

Fig. 2. Comparison of total (PM_{10}) particulate (at U and D sites) with cloud water components (at S site), TOC = DOC + POC (BI: BERNER impactor, HVA: high volume Andersen filter sampler, CW-IfT: CASCC2_4, CW-BTU: Single Stage slit jet Impactor, CW-CSU: sf-CASCC, R: residual particles, I: interstitial particles). Note that the scales are different.

HVA filter collector) before and after the cloud passage and in CW samples (CW-IfT).

The particle phase concentrations of Fe, Cu, and Mn were rather similar in the all three events. Zn showed the highest concentrations especially in E III. The particle

Table 1
Components fractions of upwind and downwind site particulate samples referred to cloud water concentrations

Event	Component	Upwind			Summit	Downwind	
		BI particle (%)	HVA particle (%)	StJ particle (%)	cloud water (%)	BI particle (%)	HVA particle (%)
E I	SO_4^{2-}	≈	≈	≈	100	70	≈
	NO_3^-	40	75	≈	100	25	65
	NH_4^+	50	≈		100	40	≈
	OC/TOC	40			100	30	
	EC	≈			100*	70	
E II	SO_4^{2-}	≈	≈	≈	100	60	≈
	NO_3^-	25	60	≈	100	10	60
	NH_4^+	60	≈		100	40	≈
	OC/TOC	70			100	30	
	EC	50			100*	30	
E III	SO_4^{2-}	≈	≈	≈	100	70	≈
	NO_3^-	40	60	≈	100	20	60
	NH_4^+	90	≈		100	60	≈
	OC/TOC	90			100	50	
	EC	100			100*	50	

≈: Roughly equal amounts; *: sum of residual and interstitial particulate EC; OC/TOC: particulate OC, cloud water TOC.

concentrations for Fe, Cu, Mn, and Zn were between 3 and 5, 2.5 and 6, 0.5 and 1.5, and 5 and 24 ng m^{-3}, respectively. The comparison between summit (cloud water) and upwind sites (particle phase) results in different findings: At the U site the water-soluble particle phase concentrations of Fe were about 20%, 80%, and 30% of the concentrations in cloud water, about 85%, 60%, and 20% for Cu, and about 20%, 40%, and 30% for Zn for E I, E II, and E II, respectively. Mn concentration in particles for EI shows about 30% of CW concentration but the concentrations are similar in E II and E III. The dissolution mechanisms of the metals from particles often include complexation with organic ligands. For iron dissolution it is well known that complexation with organics (mainly oxalate) is responsible for the concentration of dissolved iron in atmospheric droplets (see, e.g. Pehkonen et al., 1993; Faust and Zepp, 1993). Also the pH-value and the photo-chemistry contribute to the solubility of the metals (e.g. Deutsch et al., 2001).

The comparison of the water-soluble metal concentration in particles before and after the cloud passage results in the following: an increase in Cu concentration (about 30% on average) was observed at the U site in all events. This could be caused by automobile traffic (Sedlak et al., 1997) from a road near the D site. The concentrations of Fe and Mn in E I remained the same, but their concentrations dropped by 30% (E I) and 100% (E II) for Fe and 20% (E I) and 30% (E II) for Mn; the Zn concentration were stable in E I and E II, and 25% increase was observed in E III after the cloud.

3.3. Changes in particle size distribution and composition

3.3.1. Particle size distribution

NSD was measured continuously in the size range from 3 to 900 nm at upwind and downwind sites. Possible aerosol transformation processes can be found using this NSD with a time resolution of 15 min. Furthermore, the NSD observed at the U site can be used as input parameters for models determining cloud formation and processing. The NSD can be also used to calculate the volume size distribution (VSD) assuming spherical particles. The VSD can provide information if there was an increase in aerosol particle volume or mass during a certain period of time.

To make the NSDs comparable at sites up- and downwind of the orographic cloud, the NSDs taken at the U site are normalised to the peak maximum in the Aitken mode of the NSDs measured at the D site. This procedure can be done if the Aitken mode is not affected by passing the hill. As the Aitken mode is neither influenced by cloud activation nor by diffusion scavenging in the cloud, this assumption is valid. Since the differences between the two size distributions were within 10% (less than the uncertainty range of both instruments together), the corrections made for the NSDs of the D site were small and reasonable. In terms of the VSDs, these normalisations are important to discuss chemical cloud processing with a subsequent increase in aerosol mass.

During event I (Fig. 3), the average NSD at the D site decreased in accumulation mode compared to the U site.

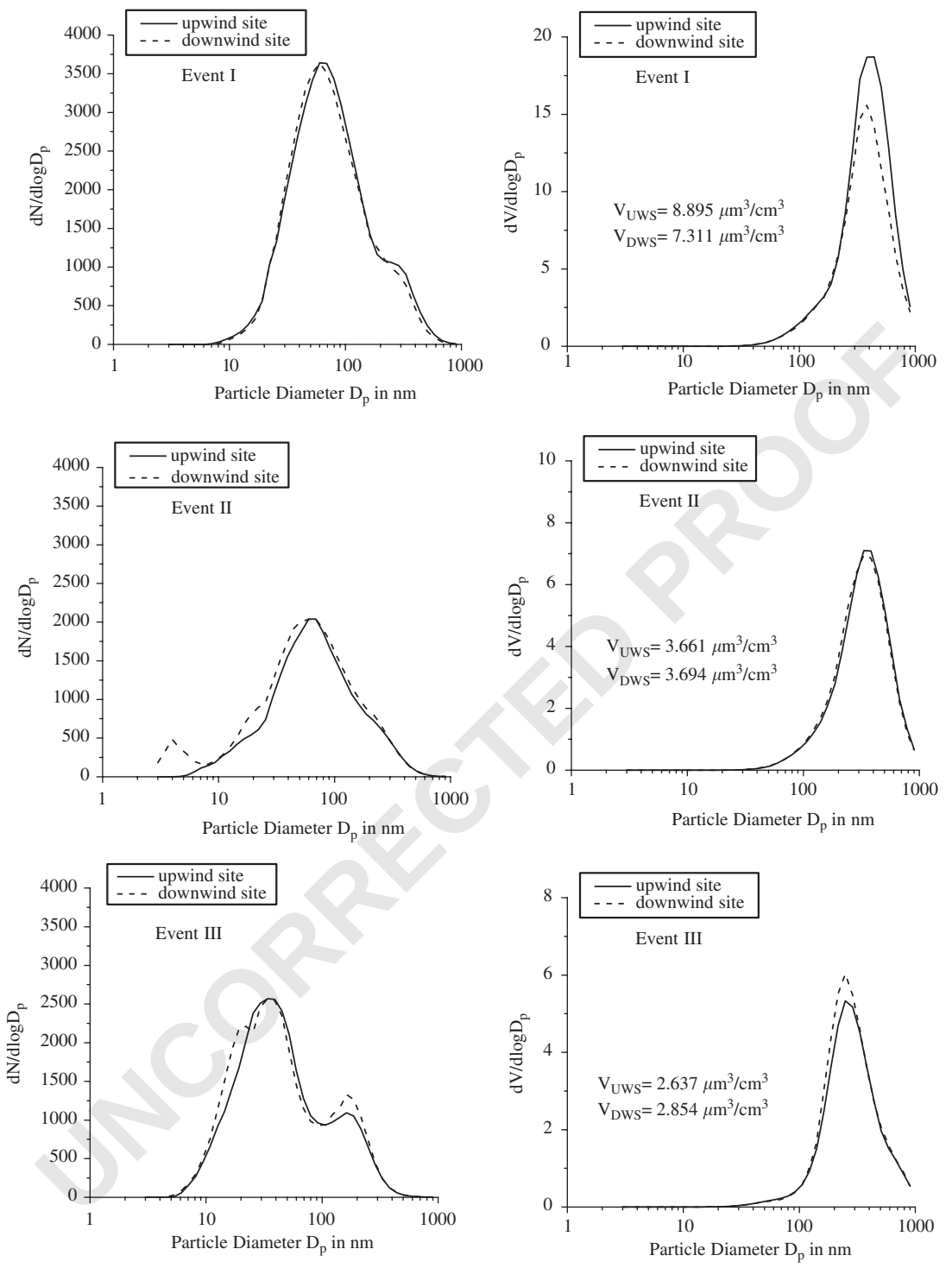

Fig. 3. Number and volume size distribution for events I, II, and III at U and D sites. Note that the scales are different.

Therefore, the VSD at the D site shows a significant decrease by approximately 15% in the accumulation mode range. The loss hints to deposition of droplets and particles during the transport to the D site.

The average NSD at the D site during event II (Fig. 3) shows some deviation at the smaller particle sizes. The nucleation mode particles below 10 nm are within the uncertainty range of the Poisson statistic, while the deviation around 20 nm is due to a poor overlap of the both mobility size spectrometers. The VSD (Fig. 3), however, is almost identical indicating no significant increase in aerosol mass.

During event III (Fig. 3), clear indications of an increase in aerosol volume due to cloud processing are visible from the NSDs and VSDs. The accumulation mode NSDs and VSDs are clearly lifted to higher concentrations. Different chemical components in $PM_{0.05-0.014}$ range show a clear increase in fraction, but observed increases in higher size ranges were found to be $<50\%$. In contrast to former hill cap cloud experiments, a significant change in NSDs and VSDs can be noticed here for the average distributions for the whole experiment durations. Clearly, a volume increase can be noticed which is ascribed to chemical mass production given in Tilgner et al. (2005b). Further details of the increase in aerosol volume or mass are outlined in Mertes et al. (2005). The deviation in the NSD around 20 nm is again due to a poor overlap of the mobility spectrometers at the D site.

3.3.2. *Size-segregated chemical particle composition*

In order to find changes in the chemical particulate composition caused by possible cloud processing the different size ranges were compared between U and D sites. To avoid the physical loss processes from U to D site the fraction of mass at respective impactor stage was also considered.

The size-segregated concentrations and the fraction of mass, nitrate, sulphate, ammonium, OC, and EC of particles are shown in Fig. 4. All data are listed in Tables II and V (ESM) for both the U and D sites.

The comparison shows that the mass concentration of particles for all size classes is always smaller at the D than the U site. For E I the decreases in mass concentrations in the five size classes amount to between 25% and 50% (from stages 2 to 5) and 75% (stage 1), for E II from 20% to 35%, and for E III about 45% (from stages 2 to 5) and 60% (stage 1). Considering the fraction of stage mass to the total mass concentration no significant difference between U and D sites can be observed except for the smallest particles of E I and III.

The concentration of the particle components is generally decreased at the D site. Nevertheless, in the smallest size range ($PM_{0.05-0.14}$) with nanogramme concentrations increases of sulphate and ammonium in E I and E III and nitrate in E III were observed. This represents about 20% (E I) and 70% (E III) for sulphate, about 17% (E I) and 150% (E III) for ammonium. The remaining ionic components rose about 150% in E I. It should be noted that an increase below 20% is in the analytical error range. In the Great Dun Fell Experiment (1993), a sulphate production by cloud processing on the particles in the range from 0.2 to 1.1 μm and a simultaneous ammonium increase were observed (Laj et al., 1997). Ammonium increase could be a consequence of the neutralisation of the formed sulphuric and/or nitric acid by gaseous ammonia.

Increases in sulphate, nitrate, and ammonium concentrations found in this experiment were in part found from a result of SPACCIM model calculations (Spectral Aerosol Cloud Chemistry Interaction Model—Tilgner et al., 2005b). Coincidence of increasing trends is marked by an asterisk (*). Differences between experiment and modelling are discussed in Tilgner et al. (2005a, b).

Considering the fraction of stage mass (avoiding the physical loss processes) the same cases of increases were found in the $PM_{0.05-0.14}$ (see Fig. 4). Sulphate shows 5-fold (E I* and E III*), ammonium 4-fold (E I) and 6-fold (E III*), and nitrate 6-fold (E III*) increase. More increases in stage mass fraction were observed: about 3-fold in stage 1* (E I) and 1.5- and 2-fold in stage 1* and 5 for nitrate, in E II, respectively, to about 1.5-, 2-, and 1.5-fold in stage 4, 5, and 5* for sulphate in E I, E II, and E III, respectively, to about 1.5-fold in stage 5* for ammonium in E II. Minor changes ($<$ 1.5-fold) were not considered and attributed to analytical variation.

In E I a significant increase of OC concentration by 20% in stage 2 was observed, the OC fraction of particle stage mass rose by 1.5-fold. Furthermore, an increase of OC in stage 1 by about 3-fold (E I) and 1.5-fold (E III) as well as for EC to about 2-fold (E I and E III) was observed. The increase of OC could be attributed to secondary organic aerosol (SOA) formation from organic precursor substances processed in cloud droplets. SOA formation was found to be stronger in clear sky episodes than in cloudy events, but Strader et al. (1999) also found that under conditions of reduced photochemical activity a third to a half of the maximum SOA quantities was produced. On the other hand, the simultaneous increase of OC and EC in stage 1 in E I and E III hints at a more local contamination.

The fraction of the stage mass is related to the weighed mass. Although the standard deviation of weighing was about 1%, possible random error could have influenced the accuracy especially within the range around 10 μg mass mainly appearing in stage 1.

4. Summary

Size-segregated particle and cloud water measurements were performed during a hill cap cloud experi-

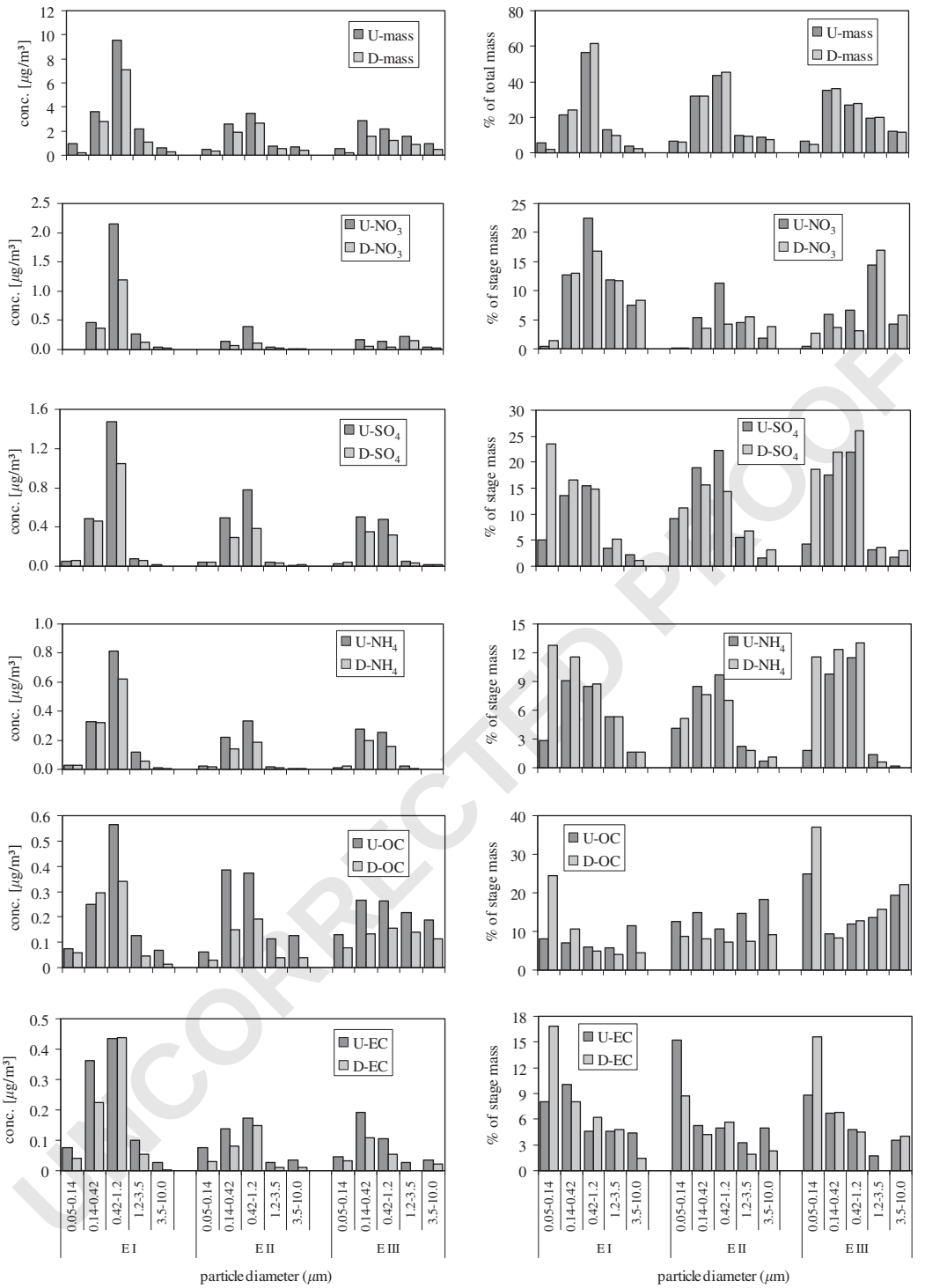

Fig. 4. Size-segregated mass, nitrate, sulphate, ammonium, OC, and EC concentration and part of total (for mass) and stage mass concentration for events I, II, and III at U and D sites.

ment in autumn 2001 and 2002. Cloud and particulate components were measured by different sampling techniques. Additionally, trace gas mixing ratios and meteorological parameters were measured. Three out of 14 events fulfilling the connected flow between the sites were discussed.

Particle mass concentration losses were observed from upwind to downwind sites (in total about 30–40%) caused by physical sink processes. In addition to the changes in concentration, the changes of mass parts of the components were considered.

During event I LWC, pH, and nitrate decreases and an OC increase in cloud water were found. During events II and III only minor variations were observed.

The concentrations of ionic components and TOC sampled by different collectors roughly agree for the three events. Non-volatile species (in E I, II, III for sulphate and in E I, III for EC) were found to be in agreement in cloud water and particulate component concentration at upwind site, whereas volatile components (nitrate, ammonium, and OC) in general were lower at the U site due to losses by some of the collecting techniques applied. Losses found between cloud water and particle concentration at the D site are additionally caused by deposition and dilution during transport. For Fe and Zn higher concentrations in cloud water (more acidic) were measured than in aqueous particle extracts. Particulate Cu was higher after the cloud passage probably due to local traffic emissions from the road nearby.

Concentration increases occur only in the smallest range (0.05–0.14 μm) representing for sulphate about 20% (E I) and 70% (E III), ammonium about 17% (E I) and 150% (E III as well as for OC in the 0.14–0.42 μm range about 20% (E I). Considering the fraction of stage mass the same components were increased and some others too. In several cases consistency between experimental and modelled results could be found. The observed mass increases are possibly related to acid formation (sulphuric and nitric acid) and neutralisation (ammonia) processes as well as SOA formation.

Uncited references

Cadle and Mulawa, 1990; Lehmann et al., 2005.

Acknowledgements

This work was supported financially by the German BMBF (AFO2000, project 07ATF01). For the support at the field and laboratory work we thank H. Bachmann, B. Gerlach, S. Haferkorn, N. Heim, A. Kappe, E. Neumann, K. Pielok, and A. Thomas.

References

Acker, K., Mertes, S., Möller, D., Wieprecht, W., Auel, R., Kalaß, D., 2002. Case study of cloud physical and chemical processes in low clouds at Mt. Brocken. Atmospheric Research 64, 41–51.

Acker, K., Wieprecht, W., Möller, D., 2003. Distribution of reactive nitrogen compounds between atmospheric gas and aerosol phase. In: ten Brink, H., Baltensberger, U. (Eds.), Composition and Size Evolution of the Secondary Aerosol. EUROTRAC-2 subproject AEROSOL Final Report, GSF Munich, pp. 197–203.

Baltensperger, U., Schwikowski, M., Jost, D.T., Nyeki, S., Gäggeler, H.W., Poulida, O., 1998. Scavenging of atmospheric constituents in mixed phase clouds at the high-alpine site Jungfraujoch, Part I: basic concept and aerosol scavenging by clouds. Atmospheric Environment 32, 3975–3983.

Birmili, W., Stratmann, F., Wiedensohler, A., 1999. Design of a DMA-based size spectrometer for a large particle size range and stable operation. Journal of Aerosol Science 30, 549–553.

Brüggemann, E., Rolle, W., 1998. Changes of some components of precipitation in East Germany after the unification. Water, Air, and Soil Pollution 107, 1–23.

Cadle, S.H., Mulawa, P.A., 1990. Atmospheric carbonaceous species measurement methods comparison study: general motors results. Aerosol Science and Technology 12, 128–141.

Chemnitzer, R., 2002. Bestimmung von Metallen in troposphärischen Partikeln und Wolkentröpfchen mittels Atom-Absorptionsspektrometrie. Diplomarbeit Technische Universität Bergakademie Freiberg.

Demoz, B.B., Collett Jr., J.L., Daube Jr., B.C., 1996. On the caltech active strand cloudwater collectors. Atmospheric Research 41, 47–62.

Deutsch, F., Hoffmann, P., Ortner, H.M., 2001. Field experimental investigations on the Fe(II)- and Fe(III) content in cloud water samples. Journal of Atmospheric Chemistry 40, 87–105.

Dore, A.J., Choularton, T.W., Inglis, D.W.F., 2001. Monitoring studies of precipitation and cap cloud chemistry at Holme Moss in the Southern Pennines. Water, Air, and Soil Pollution: Focus 1, 381–390.

Electronic supplemental material: (http://projects.tropos.de:8088/afo2000g3/FEBUKO-dateien/font!.html/).

Facchini, M.C., Fuzzi, S., Zappoli, S., Andracchio, A., Gelencser, A., Kiss, G., Krivacsy, Z., Meszaros, E., Hansson, H.-C., Alsberg, T., Zebühr, Y., 1999. Partitioning of the organic aerosol component between fog droplets and interstitial air. Journal of Geophysical Research 104, 26,821–26,832.

Faust, B.C., Zepp, R.G., 1993. Photochemistry of aqueous iron(III)-polycarboxylate complexes: roles in the chemistry of atmospheric and surface water. Environmental Science and Technology 27, 2517–2522.

Finnlayson- Pitts, B.J., Pitts Jr., J.N., 2000. Chemistry of the Upper and Lower Atmosphere. Academic Press, San Diego, USA Chapter 8, p. 310.

Gieray, R., Wieser, P., Engelhardt, T., Swietlicki, E., Hansson, H.-C., Mentes, B., Orsini, D., Martinsson, B., Svennings-

son, B., Noone, K.J., Heintzenberg, J., 1997. Phase partitioning of aerosol constituents in cloud based on single-particle and bulk analysis. Atmospheric Environment 31, 2491–2502.

Gnauk, T., Brüggemann, E., Müller, K., Chemnitzer, R., Rüd, C., Galgon, D., Nowak, A., Wiedensohler, A., Acker, K., Auel, R., Wieprecht, W., Möller, D., Jaeschke, W., Herrmann, H., 2005. Aerosol characterisation at the FEBUKO upwind station Goldlauter (I): particle mass, main ionic components, OC/EC, and mass closure. Atmospheric Environment (this issue).

Heinold, B., Tilgner, A., Jaeschke, W., Haunold, W., Knoth, O., Wolke, R., Herrmann, H., 2005. Meteorological characterisation of the FEBUKO hill cap cloud experiments, Part II: tracer experiments and flow characterisation with nested non-hydrostatic atmospheric models. Atmospheric Environment (this issue).

Herrmann, H., Wolke, R., Müller, K., Brüggemann, E., Gnauk, T., Barzaghi, P., Mertes, S., Lehmann, K., Massling, Birmili, W.A., Wiedensohler, A., Wieprecht, W., Acker, K., Jaeschke, W., Kramberger, H., Svrcina, B., Bächmann, K., Collett Jr., J.L., Galgon, D., Schwirn, K., Nowak, A., vanPinxteren, A., Plewka, A., Chemnitzer, R., Rüd, C., Hofmann, D., Tilgner, A., Diehl, K., Heinold, B., Hinneburg, D., Knoth, O., Sehili, A.M., Simmel, M., Wurzler, S., Mauersberger, G., Majdik, Z., Müller, F., 2005. FEBUKO and MODMEP: field measurements and modelling of aerosol and cloud multiphase processes. Atmospheric Environment (this issue).

Hitzenberger, R., Berner, A., Kromp, R., Kasper-Giebl, A., Limbeck, A., Tscherwnka, W., Puxbaum, H., 2000. Black carbon and other species at a high-elevation European site (Mount Sonnblick, 3106 m, Austria): concentrations and scavenging efficiencies. Journal of Geophysical Research 105, 637–645.

Hitzenberger, R., Berner, A., Galambos, Z., Maenhaut, W., Cafmeyer, J., Schwarz, J., Mueller, K., Spindler, Wieprecht, W., Acker, K., Hillamo, R., Mäkelä, T., 2004. Intercomparison of methods to measure the mass concentration of the atmospheric aerosol during INTERCOMP 2000—influence of instrumentation and size cuts. Atmospheric Environment 38, 6467–6476.

Kasper, A., Puxbaum, H., Brantner, B., Paleczek, S., 1998. Scavenging efficiency of lead and sulfate in supercooled clouds at Sonnblick, 3106 m a.s.l., Austria. Atmospheric Environment 32, 3967–3974.

Laj, P., Fuzzi, S., Facchini, M.C., Orsi, G., Berner, A., Kruisz, C., Wobrock, W., Hallberg, A., Bower, K.N., Gallagher, M.W., Beswick, K.M., Colvile, R.N., Choularton, T.W., Nason, P., Jones, B., 1997. Experimental evidence for in-cloud production of aerosol sulphate. Atmospheric Environment 31, 2503–2514.

Lehmann, K., Massling, A., Tilgner, A., Mertes, S., Galgon, D., Wiedensohler, A., 2005. Size-resolved soluble volume fractions of submicrometer particles in air masses of different character. Atmospheric Environment (this issue).

Mertes, S., Galgon, D., Schwirn, K., Nowak, A., Lehmann, K., Massling, A., Wiedensohler, A., Wieprecht, W., 2005. Evolution of particle concentration and size distribution observed upwind, inside and downwind hill cap clouds at connected flow conditions during FEBUKO. Atmospheric Environment (this issue).

Müller, K., Spindler, G., Maenhaut, W., Hitzenberger, R., Wieprecht, W., Baltensperger, U., ten Brink, H., 2004. INTERCOMP 2000, a campaign to assess the comparability of methods in use in Europe for measuring aerosol composition. Atmospheric Environment 38, 6459–6466.

Neusüß, C., Pelzing, M., Plewka, A., Herrmann, H., 2000a. A new analytical approach for size-resolved speciation of organic compounds in atmospheric aerosol particles: methods and first results. Journal of Geophysical Research 105, 4513–4527.

Neusüß, C., Weise, D., Birmili, W., Wex, H., Wiedensohler, A., Covert, D.S., 2000b. Size-segregated chemical, gravimetric, and number distribution-derived mass closure of the aerosol in Sagres, Portugal during ACE-2. Tellus 52B, 169–184.

Oberholzer, B., Collett Jr., J.L., Staehelin, J., Waldvogel, A., 1992. In-cloud scavenging of gases and aerosols at a mountain site in Central Switzerland. Journal of Atmospheric Chemistry 14, 61–71.

Pehkonen, S.O., Siefert, R., Erel, Y., Webb, S., Hoffmann, M.R., 1993. Photoreduction of iron oxyhydroxides in the presence of important atmospheric organic compounds. Environmental Science and Technology 27, 2056–2062.

Plessow, K., Acker, K., Heinrichs, H., Möller, D., 2001. Time study of trace elements and major ions during two cloud events at the Mt. Brocken. Atmospheric Environment 35, 367–378.

Plewka, A., Gnauk, T., Brüggemann, E., Neusüß, C., Herrmann, H., 2004. Size-resolved aerosol characterisation for a polluted episode at the IfT research station Melpitz in Autumn 1997. Journal of Atmospheric Chemistry 48, 131–156.

Rüd, C., 2003. Bestimmung von Metallen in Aerosolpartikeln und Wolkenwasser mittels Atom-Absorptionsspektrometrie. Diplomarbeit Universität Leipzig.

Sedlak, D.L., Hoigné, J., David, M.M., Colvile, R.N., Seyffer, E., Acker, K., Wieprecht, W., Lind, J.A., Fuzzi, S., 1997. The cloud water chemistry of iron and copper at Great Dun Fell, UK. Atmospheric Environment 31, 2515–2526.

Schmid, H., Laskus, L., Abraham, H.J., Baltensperger, U., Lavanchy, V., Bizjak, M., Burba, P., Cachier, H., Crow, D., Chow, J., Gnauk, T., Even, A., ten Brink, H.M., Giesen, K.-P., Hitzenberger, R., Hueglin, C., Maenhaut, W., Pio, C., Carvalho, A., Putaud, J.-P., Toom-Sauntry, D., Puxbaum, H., 2001. Results of the "carbon conference" international aerosol carbon round robin test stage I. Atmospheric Environment 35, 2111–2121.

Schwarzenböck, A., Heintzenberg, J., Mertes, S., 2000. Incorporation of aerosol particles between 25 and 850 nanometers into cloud elements: measurement with a new complementary sampling system. Atmospheric Research 54, 241–260.

Strader, R., Lurmann, F., Pandis, S.N., 1999. Evaluation of secondary organic aerosol formation in winter. Atmospheric Environment 33, 4849–4863.

Tilgner, A., Heinold, B., Nowak, A., Herrmann, H., 2005a. Meteorological characterisation of the FEBUKO hill cap cloud experiments, Part I: synoptic characterisation of measurement periods. Atmospheric Environment (this issue).

Tilgner, A., Majdik, Z., Sehili, A.M., Simmel, M., Wolke, R., Herrmann, H., 2005b. SPACCIM: simulations of the multiphase chemistry occurring in the FEBUKO hill cap cloud experiments. Atmospheric Environment (this issue).

Voisin, D., Legrand, M., 2000. Scavenging of acidic gases (HCOOH, CH_3COOH, HNO_3, HCl, and SO_2) and ammonia in mixed liquid–solid water clouds at the Puy de Dome mountain (France). Journal of Geophysical Research 105, 6817–6835.

Wieprecht, W., Acker, K., Mertes, S., Collett Jr., J.L., Jaeschke, W., Brüggemann, E., Möller, D., Herrmann, H., 2005. Cloud physics and cloud water sampler comparison during FEBUKO. Atmospheric Environment 0 (this issue).

3B2v8.06a/w (Dec 5 2003).51c XML:ver:5.0.1 AEA : 5771 Prod.Type:FTP pp.1–16(col.fig.:NIL) ED:AnilaM. PAGN:Uday SCAN:Global

ARTICLE IN PRESS

Available online at www.sciencedirect.com

SCIENCE DIRECT®

ELSEVIER

Atmospheric Environment ▮ (▮▮▮▮) ▮▮▮–▮▮▮

ATMOSPHERIC ENVIRONMENT

www.elsevier.com/locate/atmosenv

Schmücke hill cap cloud and valley stations aerosol characterisation during FEBUKO (II): Organic compounds

D. van Pinxteren[a], A. Plewka[a], D. Hofmann[a,1], K. Müller[a], H. Kramberger[b,2], B. Svrcina[b], K. Bächmann[b], W. Jaescke[c], S. Mertes[a], J.L. Collett Jr.[d], H. Herrmann[a,*]

[a]*Leibniz-Institut für Troposphärenforschung, Permoserstr. 15, 04318 Leipzig, Germany*
[b]*Technische Universität Darmstadt, Institut für Anorganische Chemie, Petersenstraße 18, 64287 Darmstadt, Germany*
[c]*Universität Frankfurt, Zentrum für Umweltforschung, Georg-Voigt-Straße 14, 60325 Frankfurt, Germany*
[d]*Colorado State University, Departement of Atmospheric Science, Fort Collins, CO 80523, USA*

Abstract

An extensive speciation of organic compounds was conducted during the FEBUKO cloud experiments in autumn 2001 and 2002. Three measurement sites were chosen at the Schmücke mountain in the Thüringer Wald region, Germany, which allowed to characterise air masses chemically before, during, and after their passage of a hill cap cloud. Concentrations of 33 organic carbonyl compounds, 5 monocarboxylic acids (MCAs), and 10 dicarboxylic acids (DCAs) are reported for different atmospheric phases at the three sites. Some of them were determined for the first time in cloud water. The concentration levels of the compounds were usually low, consistent with the rural sampling region. The identified fraction of dissolved organic carbon in the cloud water was 17.3%, 14.7%, and 10.1%, on average, for three independent cloud events. For the gas phase compounds the phase partitioning between liquid phase and interstitial gas phase inside the cloud was determined and compared to the theoretically expected values considering thermodynamic equilibrium conditions (Henry's law). For relatively polar organic carbonyl compounds (with a high Henry constant and a high effective water solubility), the ratio of measured to calculated liquid phase fractions was close to 1 (0.6–3.4). For the more hydrophobic compounds, however, a significant liquid phase supersaturation with respect to the gas phase concentrations was observed (ratios of 45–912). For the MCAs, only small deviations from Henry's law were determined, comparable to the ones of the polar carbonyl compounds. The scavenging efficiency of the particulate DCAs inside of the cloud was close to 100%. Concentrations of both particulate and gas phase organic compounds were usually lower at the downwind site than at the upwind site. This was most likely due to physical sink processes during the passage of the air parcel over the forested Schmücke mountain.

Keywords: Cloud water chemistry; Organic carbonyl compounds; Organic acids; Phase partitioning; Aerosol processing

1. Introduction

Clouds play a very important role in atmospheric chemistry, because they strongly affect the chemical composition of the troposphere. Aqueous cloud droplets

*Corresponding author. Tel.: +49 341 235 2446; fax: +49 341 235 2325.
E-mail address: herrmann@tropos.de (H. Herrmann).
[1]Now at Universität Leipzig, Germany.
[2]Now at Deutsche Amphibolin-Werke, Ober-Ramstadt, Germany.

1352-2310/$ - see front matter © 2005 Elsevier Ltd. All rights reserved.
doi:10.1016/j.atmosenv.2005.02.014

provide an efficient medium for liquid phase reactions of chemical constituents, which result from the activation of cloud condensation nuclei and the scavenging of gaseous species. In order to reveal possible effects of clouds on the multiphase chemistry of the atmosphere, a number of ground-based cloud experiments have been conducted during the past few decades. Extensive field campaigns have been performed at Kleiner Feldberg, Germany, in 1990 (Fuzzi, 1994), at Great Dun Fell, England, in 1993 (Fuzzi, 1997) and 1995 (Gallagher, 1999), and in Tenerife, Spain, in 1997 (Bower et al., 2000). In terms of chemical measurements all of them focus on the inorganic speciation of aerosol particles and cloud water and include only few contributions to the multiphase chemistry of organic compounds (formic and acetic acid: Winiwarter et al., 1994; phenols and nitrophenols: Lüttke and Levsen, 1997). Therefore, during the FEBUKO cloud experiments (field investigations of budgets and conversions of particle phase organics in tropospheric cloud processes), strong emphasis was placed on a more detailed characterisation of the organic fraction of the cloud input aerosol (both particle and gas phase), cloud water, interstitial aerosol phases (particle and gas), and the residual aerosol phases after evaporation of the cloud. Detailed information about the idea and the experimental setup of FEBUKO is given by Herrmann et al. (2005). Briefly, a detailed physical and chemical characterisation of air masses at three sites in front of, inside, and after a hill cap cloud took place. The experiment was conducted in autumn 2001 and 2002 at the Schmücke mountain in the Thüringer Wald, Germany. The measurements at the valley stations gave information about physical and chemical properties of the aerosol particles entering (upwind site) and leaving (downwind site) the hill cap cloud. The measurements inside the cloud revealed the physical and chemical properties of both cloud droplets and interstitial aerosol particles. Additionally, gas phase species were determined at all three sites. A total of 14 cloud events occurred during the campaigns. Three of them were found to fulfil best the strict conditions for a good comparison of all the three measurement sites (see Tilgner et al., 2005a; Heinold et al., 2005). These three events are: E I: 26 October–27 October 2001 22:00–13:00; E II: Part 1: 06 October 2001 10:30–14:15, Part 2: 07 October 2001 13:15–15:15, Part 3: 07 October–08 October 2001 18:00–11:15; and E III: 16 October–17 October 2002 17:00–04:10 (time always in coordinated universal time, UTC). The results of the field measurements of different organic trace compounds in the gas phase, aerosol particles, and cloud water are presented in this contribution.

2. Experimental

Herrmann et al. (2005) give an overview of the instruments used in the FEBUKO campaigns to determine meteorological, physical and chemical parameters of the different atmospheric phases. Sampling and analysis of organic aerosol constituents during FEBUKO is described by Müller et al. (2005) and hence only shortly summarised here.

2.1. Sampling

At the upwind and downwind sites different instruments were used for the sampling of the gas and particle phase. Five-stage Berner impactors with 50% aerodynamic cut-off diameters of 0.05, 0.14, 0.42, 1.2, 3.5 and 10 μm were used for the size-resolved collection of particulate short-chain dicarboxylic acids (DCAs). The relative humidity (RH) of the sampling air was regulated to $60 \pm 5\%$ by heated inlet tubes. Time-resolved (2 h interval) samples of the integral gas and particulate phase were taken with scrubbers for the determination of short-chain MCAs and DCAs. The scrubbers were custom made, similar to the design of Cofer et al. (1985). Water was used as absorber medium and every device was carefully tested and validated before the start of the campaign (Kramberger, 2003). For the sampling of gas phase organic carbonyl compounds two types of adsorption cartridges were used. One type consisted of glass tubes packed with 2,4-dinitrophenylhydrazine (DNPH) as derivatisation reagent on Silicagel 60 (125–200 μm, Merck). A second type consisted of sep-Pak tC18 tubes (Waters), which were coated with pentafluorobenzylhydroxylamine (PFBHA). For ozone removal potassium iodide scrubbers were used.

At the summit different cloud water samplers were used (Wieprecht et al., 2005). The concentrations of organic species given in this work refer to the Caltech Active Strand Cloud water Collector 2 (CASCC2, Demoz et al., 1996). Aliquots of the cloud water samples were taken immediately after collection and stored frozen until analysis. The sampling interval was usually 2 h. A system of counterflow virtual impactor (CVI) and interstitial inlet (INT) separated cloud droplets and interstitial aerosol (Mertes et al., 2005). Interstitial particles were collected on Teflon filters (37 mm, 0.45 μm, Schleicher & Schuell TE 36). Interstitial gas phase carbonyl compounds were sampled with the DNPH cartridges as used at the valley stations. Cloud droplets entering the CVI were evaporated in a dry air stream and the non-volatile residual particles were collected on Teflon filters. Organic carbonyl compounds were released to the gas phase during the evaporation of the droplets and trapped on cartridges. This sampling strategy directly results in cloud water loadings (CWLs) with the dimension (liquid phase) mass per volume air.

2.2. Analysis of organic carbonyl compounds

The analysis of organic carbonyl compounds in the cloud water was performed by derivatisation with PFBHA in combination with gas chromatography (GC). The frozen cloud water was melted and 30 µl of a 15 gl^{-1} PFBHA solution were added to 1 ml of cloud water. The mixture was kept in the dark at room temperature for 48 h to ensure a complete derivatisation reaction. Afterwards the solution was extracted with 1 ml hexane. The extract was washed with 0.1 moll^{-1} HCl-solution and then 5–25 µl of the extract were analysed by a GC method as described by Müller et al. (2005). The cartridges which sampled carbonyl compounds after the CVI and INT were extracted with acetonitrile and analysed by High Performance Liquid Chromatography (HPLC) as described by Müller et al. (2005). While a few carbonyl compounds were detected by both the GC and the HPLC methods, the majority of the compounds could only be determined by one of the methods.

2.3. Analysis of pinonaldehyde and pinic acid

For the analysis of pinonaldehyde and pinic acid from cloud water the acidified cloud water samples (pH 2 with concentrated sulphuric acid) were extracted for 5 h with methyl *t*-butyl ether by application of a light phase rotary perforator. After drying with $CaSO_4$ and filtration of the extract, GC-MS analysis was performed as described by Müller et al. (2005). The recovery of the sample preparation was tested to be 98 ± 27% (mean ± one standard deviation) for pinonaldehyde and 70 ± 34% for pinic acid. Pinic acid concentrations given in this work are corrected for the analyte losses during sample preparation.

2.4. Analysis of organic acids

The analysis of DCAs from the cloud water samples was performed at two different institutes. One group applied capillary electrophoresis (CE) with indirect UV detection after filtration of the cloud water with syringe filters. The method is described by Neusüß et al. (2000), and is referred to as procedure A for DCA determination throughout this work. The second group also applied CE, but with different parameters. An optimised version of the system described by Mainka et al. (1997) was applied. A reduction of sample volume by evaporating water in a gentle nitrogen gas flow prior to analysis allowed for sufficiently low detection limits. This sample preparation together with the CE method is referred to as procedure B for determination of DCAs throughout this work. Sometimes, the different procedures gave different concentrations for the same analyte and sample. On average, oxalate determined with procedure A was 138 ± 45% (± one standard deviation) of oxalate determined with procedure B. Malonate, which was usually much closer to the analytical detection limits, showed a deviation of 207 ± 53%. C4- and C5-diacids cannot be directly compared, because procedure A quantifies these compounds together with their branched isomers, and procedure B does not. Other DCAs were determined by only one of the two procedures. For the discussion of the data we only compared results obtained by the same analytical procedure. As the time-resolved DCA concentrations at the valley stations were determined by prodedure B (Müller et al., 2005), we calculated the summit recoveries with the corresponding cloud water data (see Section 3.3). Monocarboxylic acids (MCAs) were determined together with the DCAs by procedure B. The interstitial filter samples were cut into pieces and extracted with deionised water prior to the analysis of DCAs by procedure A.

3. Results and discussion

The combination of a large variety of sampling systems and analytical methods at three sites yielded an extensive set of organic compound concentrations during three independent cloud events. Among the quantified compounds are 33 aldehydes and ketones, 5 MCAs, and 10 DCAs, many of them found both at the summit and valley sites. Due to space limitations, not all data can be directly presented. Therefore, we selected some of the more abundant species of each compound class for further discussion. The complete data set, however, is provided in detailed tables of the electronic supplementary material (ESM), which can be accessed freely at http://projects.tropos.de:8088/afo2000g3/FEBUKO_dateien/febuko.html. A part of the data serve as a valuable tool for the initialisation and validation of a coupled multiphase chemistry and microphysics model (Tilgner et al., 2005b).

The concentrations of organic compounds determined in bulk cloud water and CVI samples (evaporated droplets) are summarised in Table 1. Both solute concentrations in µmoll^{-1} and CWLs in ngm^{-3} are given. The CWL was calculated as the product of the aqueous phase concentration and the liquid water content (LWC) of the cloud. It allows one to compare the summit concentrations with the corresponding upwind site and downwind site concentrations. Also, it was suggested to use CWLs instead of solute concentrations to characterise the degree of pollution in cloudy environments (Elbert et al., 2000).

ARTICLE IN PRESS
AEA : 5771

Table 1
Concentrations of organic compounds in the FEBUKO cloud water during E I–E III

Compound	Event I		Event II		Event III		Event I		Event II		Event III	
	Range ($\mu mol\,l^{-1}$)	Mean ($\mu mol\,l^{-1}$)	Range ($\mu mol\,l^{-1}$)	Mean ($\mu mol\,l^{-1}$)	Range ($\mu mol\,l^{-1}$)	Mean ($\mu mol\,l^{-1}$)	Range ($ng\,m^{-3}$)	Mean ($ng\,m^{-3}$)	Range ($ng\,m^{-3}$)	Mean ($ng\,m^{-3}$)	Range ($ng\,m^{-3}$)	Mean ($ng\,m^{-3}$)
Saturated carbonyl compounds												
Formaldehyde[a]	1.6–4.8	3.4	0.10–3.6	2.0	1.0–1.4	1.2	22.4–58.8	33.7	0.7–20.0	11.0	6.1–7.9	7.0
Formaldehyde[b]	3.5–7.0	5.9	2.9–3.7	3.5	2.4–2.4	2.4	31.4–84.8	63.8	18.1–29.8	26.0	13.9–13.9	13.9
Acetaldehyde[a]	0.2–1.0	0.6	0.08–0.4	0.2	0.2–1.2	0.5	4.8–10.8	7.7	0.7–4.4	2.1	2.1–9.0	4.3
Acetaldehyde[b]	0.5–1.6	1.0	1.3–1.8	1.5	0.9–0.9	0.9	11.0–18.1	14.2	13.9–21.2	16.3	8.1–8.1	8.1
Propionaldehyde[a]	0.1–0.4	0.2	0.04–0.3	0.1	0.07–0.14	0.09	2.8–6.4	4.0	0.6–2.1	1.2	0.8–1.4	1.0
Butyraldehyde[b]	<DL	<DL	0.6–0.9	0.8	<DL	<DL	<DL	<DL	12.2–16.9	14.0	<DL	<DL
Valeraldehyde[b]	<DL–0.3	0.2	<DL	<DL	<DL	<DL	<DL–7.9	7.3	<DL	<DL	<DL	<DL
Isovaleraldehyde[b]	0.7–1.1	0.9	0.5–0.9	0.6	<DL	<DL	18.3–38.4	27.3	10.3–18.9	13.1	<DL	<DL
Hexanal[b]	<DL	<DL	<DL	<DL	0.4–0.4	0.4	<DL	<DL	<DL	<DL	7.1–7.1	7.1
Heptanal[b]	<DL–0.3	0.3	<DL	<DL	0.6–0.6	0.6	<DL–10.1	10.1	<DL	<DL	13.6–13.6	13.6
Octanal[a]	<DL–0.1	0.1	<DL–0.1	0.1	0.2–0.2	0.2	<DL–6.6	5.7	<DL–5.0	5.0	4.8–4.8	4.8
Acetone[a]	NA	NA	NA	NA	0.4–0.8	0.5	NA	NA	NA	NA	4.9–7.7	5.9
Acetone[b]	0.8–1.5	1.2	3.5–3.8	3.6	1.5–1.5	1.5	16.2–29.0	23.4	45.5–57.9	52.0	17.6–17.6	17.6
Methyl ethyl ketone[a]	0.05–0.11	0.07	0.03–0.1	0.1	0.06–1.0	0.3	1.2–2.3	1.7	0.6–1.3	0.9	0.9–12.1	4.4
Hydroxy carbonyl compounds[a]												
Glycolaldehyde	2.5–4.9	3.6	0.4–1.9	1.0	0.2–0.4	0.3	43.2–95.8	71.5	5.0–18.6	11.0	2.8–4.5	3.4
Hydroxyacetone	0.4–0.7	0.6	0.07–0.3	0.2	0.1–0.2	0.2	7.7–16.7	13.4	0.6–4.5	2.6	2.1–2.9	2.4
3-Hydroxy-2-butanone	0.1–0.2	0.2	0.03–0.1	0.08	0.07–0.1	0.09	2.4–6.6	4.6	0.5–2.0	1.3	1.4–1.8	1.5
4-Hydroxy-2-butanone	NA	NA	NA	NA	0.08–0.1	0.09	NA	NA	NA	NA	1.3–1.6	1.5
Dicarbonyl compounds[a]												
Glyoxal	1.9–6.0	3.9	1.3–11.3	3.8	0.8–1.2	0.9	51.9–88.5	70.9	18.7–87.1	35.4	8.4–12.3	10.6
Methylglyoxal	0.70–2.5	1.8	0.5–3.3	1.2	0.4–0.6	0.5	24.0–55.8	41.3	10.2–22.1	13.8	5.4–8.8	7.0
Diacetyl	0.2–0.5	0.3	0.1–0.4	0.2	0.06–0.12	0.08	5.8–10.8	7.9	1.7–4.3	2.9	1.1–1.8	1.4
Other carbonyl compounds												
Methacrolein[a]	<DL–0.04	0.02	<DL–0.09	0.04	0.01–0.01	0.01	<DL–0.8	0.5	<DL–0.4	0.2	0.1–0.1	0.1
Methyl vinyl ketone[a]	0.06–0.2	0.10	0.02–0.1	0.1	0.04–0.05	0.05	1.3–3.1	2.2	0.4–1.2	0.8	0.6–0.7	0.6

Benzaldehyde[b]	0.6–4.7	3.6	0.3–0.4	0.4	<DL	<DL	20.4–225.8	139.6	5.9–12.1	10.1	<DL	<DL
Trans-hexenal[b]	0.2–0.6	0.3	0.3–3.7	2.0	<DL	<DL	3.6–21.7	10.9	5.0–86.0	48.7	<DL	<DL
Pinonaldehyde[a]	0.3–0.7	0.5	0.1–0.5	0.3	0.6–0.8	0.7	15.0–42.3	25.0	4.5–21.1	13.9	22.0–24.0	23.1
Pinonaldehyde[b]	<DL–0.4	0.3	0.8–1.1	0.9	<DL	<DL	<DL–31.3	17.2	35.2–44.0	37.6	<DL	<DL
Carboxylic acids												
Formic acid	4.9–10.0	7.0	9.2–39.1	16.2	6.8–10.4	8.3	74.0–126.0	109.1	113.5–217.9	150.3	65.4–82.4	73.7
Acetic acid	1.6–4.4	3.0	8.2–41.4	15.5	2.0–5.3	3.0	38.9–78.3	59.9	129.1–300.8	182.5	25.2–54.3	34.0
Propionic acid	<DL–0.3	0.3	<DL–0.9	0.5	<DL–0.3	0.2	<DL–7.0	6.0	<DL–9.1	7.5	<DL–3.3	3.0
Butyric acid	<DL–0.5	0.3	<DL–0.8	0.4	<DL–0.2	0.2	<DL–13.1	8.0	<DL–8.5	7.0	<DL–3.3	3.3
Lactic acid	NA	NA	NA	NA	0.5–1.1	0.8	NA	NA	NA	NA	8.9–17.8	14.7
Dicarboxylic acids[c]												
Oxalic acid	1.5–3.3	2.1	1.2–5.8	2.1	1.5–1.9	1.7	38.8–87.2	66.6	26.0–63.1	37.7	26.0–36.0	29.7
Malonic acid	0.2–0.7	0.4	0.2–0.9	0.4	0.2–0.5	0.3	7.7–22.9	13.3	4.9–11.2	7.9	3.9–8.8	5.8
Succinic acid	<DL–0.4	0.3	<DL–0.5	0.5	0.2–0.5	0.3	<DL–19.5	12.5	<DL–6.9	6.9	3.8–9.6	5.9
Glutaric acid	<DL	<DL	<DL	<DL	<DL–0.1	0.1	<DL	<DL	<DL	<DL	<DL–2.3	2.3
Azelaic acid	<DL–0.2	0.2	<DL–0.3	0.3	0.4–0.7	0.5	<DL–11.2	11.2	<DL–6.4	6.4	13.9–22.0	17.6
Other dicarboxylic acids												
Tartronic acid[d]	<DL—0.1	0.1	<DL–0.1	0.1	<DL	<DL	<DL–5.7	5.7	<DL–1.9	1.9	<DL	<DL
Malic acid[d]	0.1–0.3	0.2	0.1–0.4	0.2	0.2–0.3	0.2	4.7–10.4	6.6	4.8–8.0	6.3	4.8–7.4	5.8
Tartaric acid[d]	<DL–0.2	0.2	<DL–0.2	0.2	<DL	n.d	4.6–7.7	6.2	3.5–4.6	4.0	<DL	<DL
Maleic acid[d]	0.2–0.4	0.3	<DL–0.2	0.1	0.05–0.1	0.1	6.6–14.2	10.8	2.1–5.4	4.0	1.1–1.8	1.4
Pinic acid	0.003–0.05	0.03	0.03–0.10	0.06	0.03–0.11	0.06	0.2–2.5	1.7	1.5–3.8	2.8	1.1–3.9	2.2

<DL: concentration below analytical detection limit, NA: sample not available for analysis. Solute concentrations are given in $\mu mol\,l^{-1}$ and cloud water loadings in $ng\,m^{-3}$.

[a]Determined from bulk cloud water.

[b]Determined from evaporated droplets after CVI, see text.

[c]Prodecure A, see text.

[d]Procedure B, see text.

3.1. Organic carbonyl compounds

While in the air samples at the valley sites a comprehensive spectrum of carbonyl compounds was present (Müller et al., 2005), in the cloud water only the more polar ones were frequently found. Glyoxal was usually the most abundant carbonyl compound in the cloud water samples, followed by formaldehyde, glycolaldehyde, and methylglyoxal (Table 1). From the CVI samples, formaldehyde was the most abundant compound, followed by benzaldehyde (only E I), acetone, and acetaldehyde. Some discrepancies exist between compounds which were determined from both liquid cloud water samples and evaporated droplets (formaldehyde, acetone, acetaldehyde, pinonaldehyde). The CVI samples usually show higher concentrations, which might be due to the completely different sampling strategies. In the CVI the compounds are immediately trapped on cartridges as soon as they evaporate from the cloud droplets. The bulk cloud water is accumulated over 2 h in the sampling bottles. One could speculate that liquid phase reactions might occur during that time which may lead to a negative artefact for the bulk samples. It has to be noted that the average values given in Table 1 are sometimes determined from different numbers of samples. They are therefore not always directly comparable. A more detailed view on the data can be obtained from Tables I–V (ESM). Only sparse data for cloud water concentrations of carbonyls is available from literature. In Table 2 literature data for conditions similar to FEBUKO (rural or remote clouds) is summarised. While the concentrations of acetaldehyde, propionaldehyde, glyoxal and methylglyoxal measured during FEBUKO were similar to the literature values, the formaldehyde concentrations were usually lower or at the lower end of the reported data. Both for acetone and benzaldehyde (only during E I), significantly higher concentrations than the reported ones were found. However, the available data set is very sparse for these compounds. Cloud water concentrations of all the other carbonyl compounds given in Table 1 are to our knowledge reported for the first time in this work.

In a first approach to evaluate the data we compared the concentrations at the three sampling sites by calculating the percentage recoveries of the upwind site concentrations for the summit and the downwind site. In Fig. 1 the results are shown for some compounds during E I. For formaldehyde, acetaldehyde, acetone, and methyl ethyl ketone, cloud water and interstitial concentrations were added to give a total system concentration at the summit. For glyoxal and glycolaldehyde no interstitial data are available, so the summit recovery refers only to the liquid phase fraction of these compounds. An increase of upwind site concentrations during the morning hours of the event can be noted for all presented aldehydes. The ketones acetone and methyl ethyl ketone, in contrast, show roughly the same concentrations during night and day. Interestingly, the elevated morning concentrations of formaldehyde and acetaldehyde at the upwind site were not found at the downwind site. The concentrations here stay roughly at the nighttime level, which leads to the decreasing recoveries in Fig. 1. For glyoxal and glycolaldehyde, the downwind recoveries stay close to 100% during the morning. This might indicate chemical sinks for the former two aldehydes during the passage of the cloud. In a few cases the summit recoveries for formaldehyde and glyoxyl were cleary above 100%. The travelling time of an air parcel is roughly 10–15 min from the upwind site to the summit and an equal time from the summit to the downwind site. Regarding the 2 h time resolution of the measurements we do not expect the very high revovery values to be caused by the time delay between the two sites. The reasons for these phenomena unfortunately remain unclear at the present stage of investigations.

In order to obtain information about the phase partitioning of the carbonyl compounds in the cloud, the liquid phase fraction $X_{\mathrm{calculated}}$ predicted by Henry's law was calculated following an approach of Seinfeld and Pandis (1998):

$$X_{\mathrm{calculated}} = \frac{HRT\,\mathrm{LWC} \times 10^{-6}}{1 + HRT\,\mathrm{LWC} \times 10^{-6}}, \quad (1)$$

where H is the Henry constant at the mean temperature during the sampling interval in $\mathrm{M\,atm^{-1}}$, R is the universal gas constant equal to $0.08205\,\mathrm{atm\,l\,mol^{-1}\,K^{-1}}$, T is the mean temperature during the sampling interval in K, and LWC is the mean liquid water content of the cloud during the sampling interval in $\mathrm{g\,m^{-3}}$. The factor 10^{-6} is a result of the units used in Eq. (1). For comparison with the measurements, X_{measured} was calculated by

$$X_{\mathrm{measured}} = \frac{\mathrm{CWL}}{\mathrm{CWL} + c_{\mathrm{int}}}, \quad (2)$$

where CWL is the cloud water loading in $\mathrm{\mu g\,m^{-3}}$ and c_{int} is the interstitial gas phase concentration in $\mathrm{\mu g\,m^{-3}}$. For compounds where c_{int} is not available we assumed a closed system between the upwind site and the Schmücke summit, where the following relation holds:

$$\mathrm{CWL} + c_{\mathrm{int}} = c_{\mathrm{upw}}, \quad (3)$$

where c_{upw} is the upwind site gas phase concentration in $\mathrm{\mu g\,m^{-3}}$.

The Henry constants, the thermodynamic data and other data used for the calculations, such as temperature, LWC and pH of the cloud water, are given in Tables VI–VII (ESM). In Fig. 2 the results are shown for some carbonyl compounds during the three events (if data are available). The solid lines are regression curves. Due to the substantial scattering of the measured data points, the correlation coefficients R^2 are usually poor,

Table 2
Literature data of organic compounds in cloud water, min–max (mean), all concentrations in $\mu mol\,l^{-1}$

Location	Compounds							Reference
	Formaldehyde	Acetaldehyde	Propionaldehyde	Glyoxal	Methylglyoxal	Acetone	Benzaldehyde	
Organic carbonyl compounds								
Pinnacles, USA	<0.1–21.9[a]			<0.15–12.4	<0.3–9.4			Munger et al. (1995)
Sequoia Nat. Park, USA[b]	7.8–14.1	0.2–2.8		4.4–13.1	0.9–2.5			Collett et al. (1990)
Puy de Dôme, France	7.37–10.51	0.56–0.83	0.26–0.28			0.11–0.15		Houdier et al. (2000)
Vosges, France	(6.6)	(0.39)						Levsen et al. (1993)
Sonnblick, Austria				0.07–0.11			0.008–0.016	Limbeck and Puxbaum(2000)
St. Barbara Channel, USA[c]	3.0–32							Munger et al. (1989)
United States[d]	4.9–36.1[a]							Rao and Collett (1995)

	Formic acid	Acetic acid	Propionic acid	Lactic acid	
Monocarboxylic acids					
Sequoia Nat. Park, USA[b]	18.2–30.2	1.9–4.0			Collett et al. (1990)
Lower Kaweah, CA, USA	19.6–106.7	8.5–72.8			Collett et al. (1989)
Whiteface Mountain, USA	14.0–40.0	5.1–15.0			Khwaja et al. (1995)
Pinnacles, USA	ca. 4–ca. 25	ca. 2–ca. 11			Keene et al. (1995)
St. Barbara Channel, USA[c]	16.0–103.0	3.0–173.0			Munger et al. (1989)
Off California coast, USA	0.7–5.7	<DL–11.1			Hegg et al. (2002)
Rax, Austria	1.3–34.3 (13.3)	4.0–37.8 (15.5)			Löflund et al. (2002)
Puy de Dôme, France	0.8–69.8 (9.7)	0.6–47.8 (8.2)	<DL–8.1 (0.7)	0.2–5.7 (1.4)	Marinoni et al. (2004)

	Oxalic acid	Malonic acid	Succinic acid	Glutaric acid	Azelaic acid	Tartaric acid	Maleic acid	
Dicarboxylic acids								
Whiteface Mountain, USA	<DL–19.0	<DL–15.0						Khwaja et al. (1995)
Off California coast, USA	0.3–4.3	0.3–2.4	<DL–1.4	0.01–0.81				Hegg et al. (2002)
Sonnblick, Austria	0.5–3.0	0.1–0.9	0.3–1.3	0.05–0.17	0.02–0.03			Limbeck and Puxbaum(2000)
Rax, Austria	0.7–12.7 (4.2)	0.4–2.9 (1.9)	0.7–2.5 (1.3)					Löflund et al. (2002)
Puy de Dôme, France	0.1–17.0 (1.8)	<DL–3.9 (0.9)	0.1–4.0 (1.1)	0.1–2.6 (0.6)		<DL–0.8 (0.1)	<DL–1.6 (0.3)	Marinoni et al. (2004)

[a]Fine droplet fraction.
[b]Two different sites: Lower Kaweah, Moro Rock.
[c]Four different sites: Casitas Pass, Venture, Laguna Peak, Laguna Road.
[d]Four different sites: Mt. Mitchell, NC; La Jolla Peak, CA; Angora Peak, OR; Whiteface Mountain, NY.

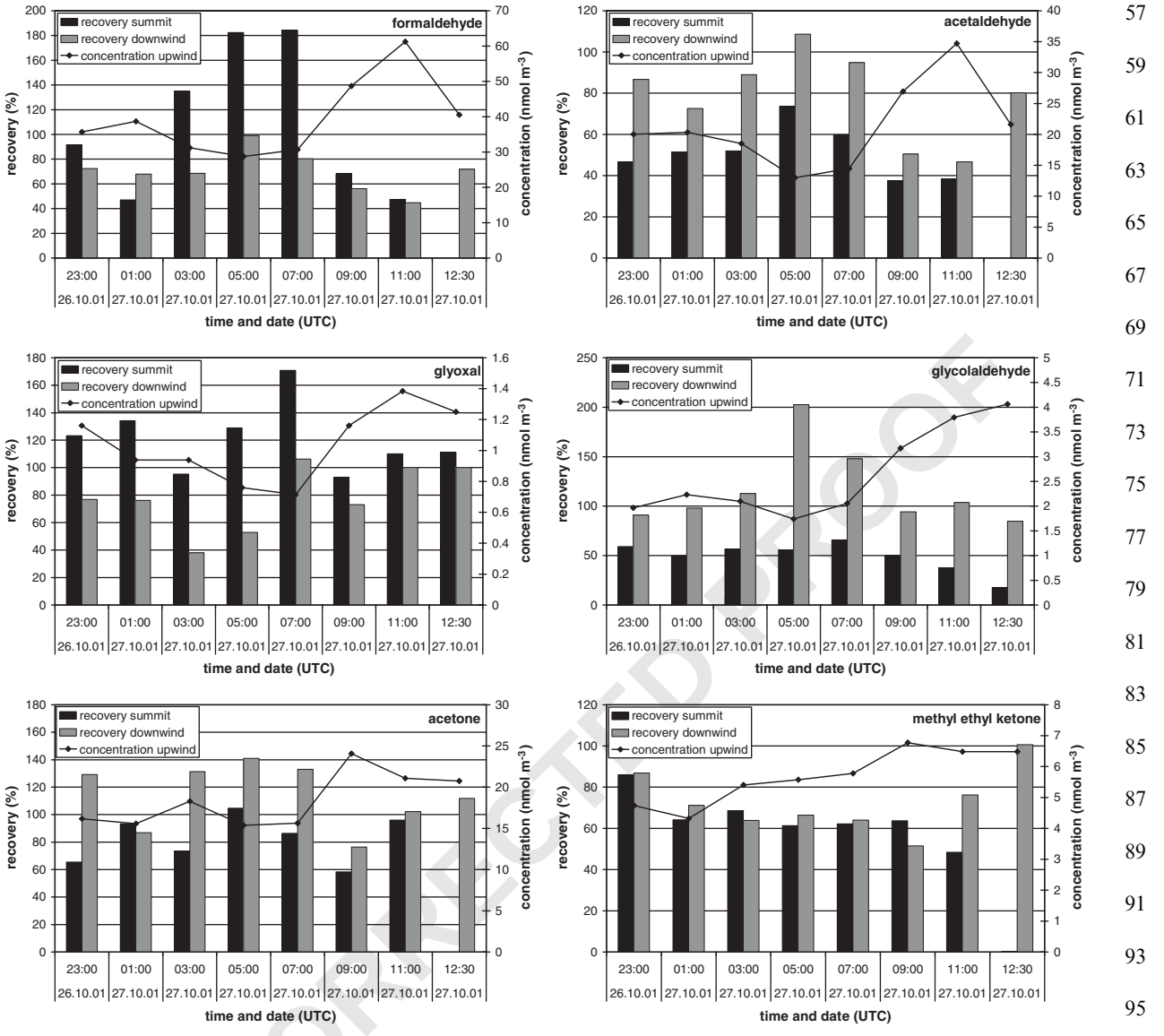

Fig. 1. Upwind site concentrations and recoveries of summit and downwind site for some carbonyl compounds during event I. Missing bar means sample not available. See text for details.

but the lines are useful in conceiving the information of the plots. Interestingly, for most of the compounds (including the ones not shown in Fig. 1) $X_{measured}$ was much higher than $X_{calculated}$. Notable exceptions are the relatively polar compounds formaldehyde and glycolaldehyde, which showed measured liquid phase fractions equal to or lower than the calculated ones. Due to the different concentrations of formaldehyde and acetaldehyde from bulk cloud water and CVI sample analysis, we plotted both values in combination with the interstitial data. Except for formaldehyde during E II, the qualitative conclusion from the comparison is the same. Our results for formaldehyde are different to the ones reported by Munger et al. (1995) and Facchini et al. (1992). These authors found a considerable supersaturation of the liquid phase with respect to the gas phase concentrations for one cloud event at Pinnacles, USA, and fog water measurements in the Po Valley, Italy.

To obtain a general conclusion from our observations, we calculated the ratio $R = X_{measured}/X_{calculated}$ for each data point in Fig. 2 and averaged the ratios over the three cloud events. The same was done for other compounds not shown in Fig. 2. Plotting this average ratio as a function of the Henry constant (at a mean

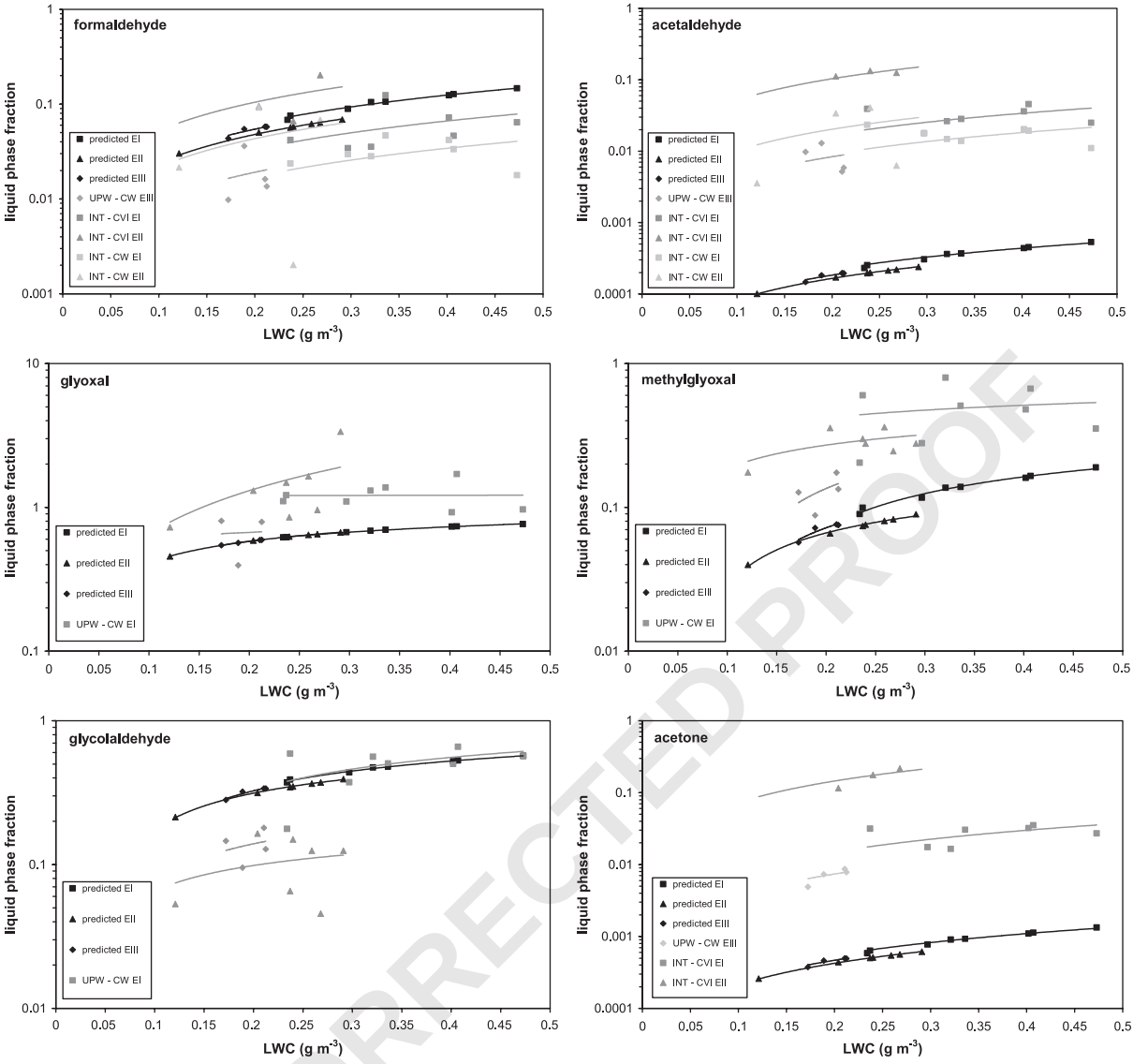

Fig. 2. Calculated (Henry's law) and measured liquid phase fractions of organic carbonyl compounds. Lines are linear or logarithmic regressions. UPW = upwind site concentration, CVI = CVI cloud water concentration, CW = bulk cloud water concentration.

temperature of 281 K) reveals an interesting result (Fig. 3). For carbonyl compounds with low effective water solubilities (small Henry constants) the measured liquid phase fractions are up to three orders of magnitude higher than the calculated fractions assuming thermodynamic equilibrium conditions ($45 < R < 912$). With increasing Henry constants this liquid phase excess factor decreases to values close to 1 for highly soluble compounds ($0.6 < R < 3.4$). Similar observations were reported for different hydrophobic compounds such as certain pesticides, PAHs, PCBs, and alkanes in atmospheric aqueous phases (Valsaraj et al., 1993, and references therein). Consistent with our results for carbonyl compounds, pronounced aqueous phase supersaturation was found for compounds with low water solubility. Early investigations suggested the association of hydrophobic compounds with dissolved or colloidal organic matter as an explanation for these observations (Glotfelty et al., 1987). More recent discussions stressed onthe importance of adsorption of organic species to the air–water interface (Valsaraj et al., 1993; Djikaev and Tabazadeh, 2003). Apart from physical processes, in the case of organic carbonyl compounds, chemical production may also potentially attribute to the reported findings. Especially for compounds with relatively low solute concentrations (due to a small Henry constant),

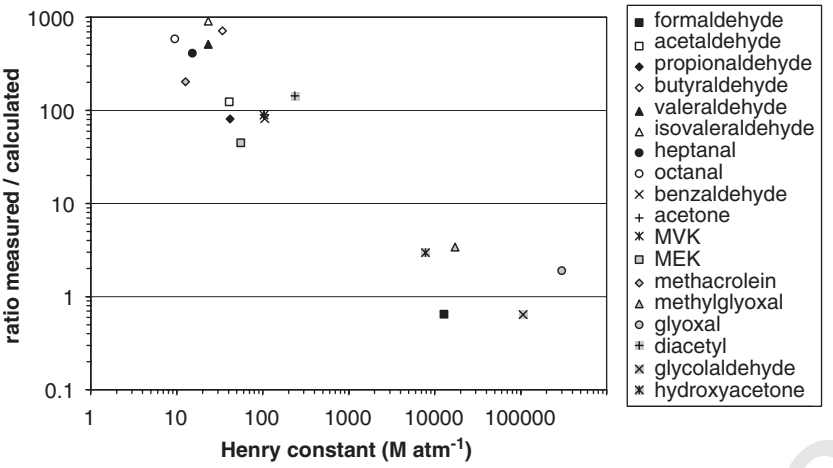

Fig. 3. Average liquid phase fraction ratio (measured/calculated) as a function of the Henry constant for all determined organic carbonyl compounds during E I–E III. Details see text.

small production rates from higher concentrated precursors might readily lead to a high aqueous phase supersaturation. A combination of both physical and chemical effects might be possible too.

3.2. Monocarboxylic acids

Concentration ranges and average values for MCAs in the cloud water samples are shown in Table 1. The complete set of concentrations can be found in Tables VIII–X (ESM). The solute concentrations of formic acid compare best with data from Rax, Austria, and Puy de Dôme, France (Löflund et al., 2002; Marinoni et al., 2004). The same applies to acetic acid during E II, whereas during E I and E III the concentrations were considerably lower and in the range of the values reported for some California clouds by Collett et al. (1990). A time-resolved comparison of the mixing ratios at the upwind station with the summit and downwind station is given in Fig. 4 for the two most abundant acids during E I. The values for the summit and downwind site are given as relative recoveries of the upwind site mixing ratios. As the interstitial concentrations at the summit were not measured, the recovery at this site refers only to the liquid phase fraction of the total budget. This leads to the relatively low values. The recoveries at the downwind station are much higher for all analytes and events. Average values are $75\pm12\%$ ($\pm$ one standard deviation), $77\pm10\%$ and $98\pm10\%$ for formate during E I, E II, and E III, respectively, and $99\pm12\%$, $93\pm10\%$, and $119\pm15\%$ for acetate. These findings reflect the general behaviour of short chain MCAs, which partition in a cloud between the aqueous droplet phase and the interstitial gas phase. After the evaporation of the cloud the volatile acids are released back to the gas phase. Reasons for lower mixing ratios at the downwind station compared to the upwind station (recoveries $<100\%$) may lie in physical sink processes during the passage of the air parcel over the forested Schmücke mountain. Entrainment of cleaner air masses and droplet deposition due to gravitational settling or interception on trees could account for the observed losses of analyte mass. As described in Brüggemann et al. (2005), the total particle mass also shows some loss on the way from the upwind to the downwind site. Interestingly, acetate shows higher downwind recoveries than formate, with values close to or even higher 100%. Given the assumption of physical sink processes, this finding might indicate sources of acetic acid on the air parcel trajectory. Photochemical reactions in the cloud, such as oxidation of acetaldehyde to acetic acid may potentially account for additional mass in the acetate budget. Also, primary sources of acetic acid must be kept in mind. Microbiological activity in autumnal vegetation biomass is known to be a significant source of acetic acid (Kesselmeier et al., 1998) and may lead to the described results. The idea of analyte losses due to wet deposition could, however, also explain the observations qualitatively. The scavenged fraction of acetic acid in the cloud is usually lower than the scavenged fraction of formic acid (Fig. 4), which leads to relatively higher aqueous phase concentrations of formate and, thereby, to a relatively higher risk of losses due to gravitational settling of droplets or cloud water interception on trees.

A similar approach as described for carbonyl compounds was taken to investigate the phase partitioning of the MCAs in the cloud, using the upwind site concentrations and Eqs. (1)–(3). The pH effects on the solubility of carboxylic acids were considered by calculating the effective Henry constant H^*:

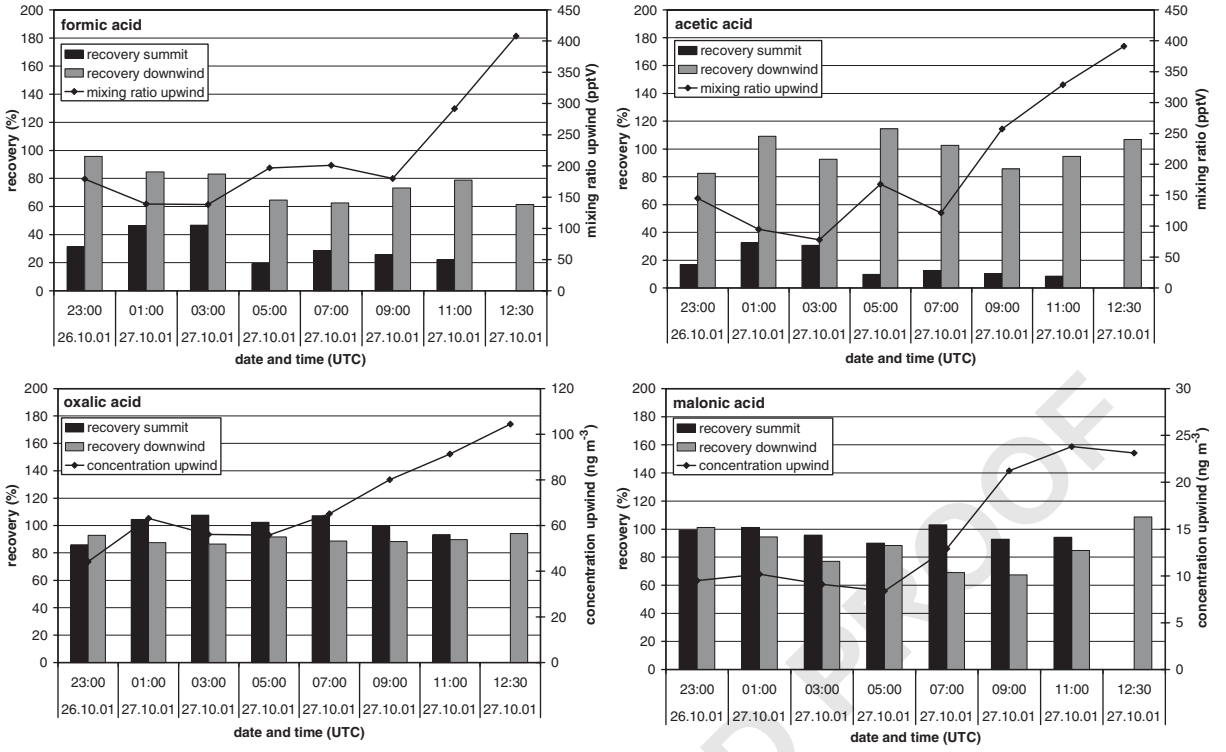

Fig. 4. Upwind site concentrations and recoveries of summit and downwind site for some mono- and dicarboxylic acids during event I. Missing bar means sample not available. See text for details.

$$H^* = H\left(1 + \frac{K_a}{[H^+]}\right), \quad (4)$$

where K_a is the dissociation constant and $[H^+]$ the concentration of H^+ ions in mol l^{-1}, derived from the measured pH value of the cloud water samples. H^* was used instead of H in Eq. (1) to calculate the theoretical liquid phase fraction. The timelines of $X_{calculated}$ and $X_{measured}$ for formic and acetic are given in Fig. 5A. A slight subsaturation of the liquid phase with respect to thermodynamic equilibrium concentrations can be recognised in many cases for formic acid and in some samples for acetic acid and butyric acid (not shown). A liquid phase supersaturation was observed during E II and in the first sample of E III for acetic acid. The data for propionic acid are sparse due to many concentrations below the analytical detection limit, but generally the calculated and measured liquid phase fractions agreed very well (not shown). Deviations up to two orders of magnitude from Henry's law equilibrium were reported for formic and acetic acid as a function of the fog or cloud water pH (Winiwarter et al., 1994). The range of ratios R obtained in this work for the MCAs (Fig. 5B) agrees quite well with the range presented by Winiwarter et al. for pH 4–5. Theoretical considerations showed that mixing of droplets in thermodynamic equilibrium with the surrounding gas phase may result in a supersaturated bulk sample (Pandis and Seinfeld, 1991). A high variability of the cloud's LWC during the sampling interval may in contrast produce samples which are subsaturated with respect to the gas phase concentrations (Winiwarter et al., 1992). These effects, together with the uncertainty of both the experimental and thermodynamic data, are likely to account for the relatively small deviations from Henry's law for formic and acetic acid during FEBUKO.

3.3. Dicarboxylic acids

In Table 1 the ranges and averages of the DCA concentrations in the bulk cloud water are given. More details for all the sampling sites can be found in Tables XI–XV (ESM). While oxalic acid compares roughly to the literature data given in Table 2, the longer chain diacids usually show values in the lower reported range. The concentrations of azelaic acid are higher by a factor of 10 than those found at the Sonnblick Observatory (Limbeck and Puxbaum, 2000). Especially during E III unexpectedly high concentrations of azelaic acid were also found on the particle samples at the upwind and downwind site (Tables XI and XIV, ESM). Kawamura et al. (1996) found similar results during long-time

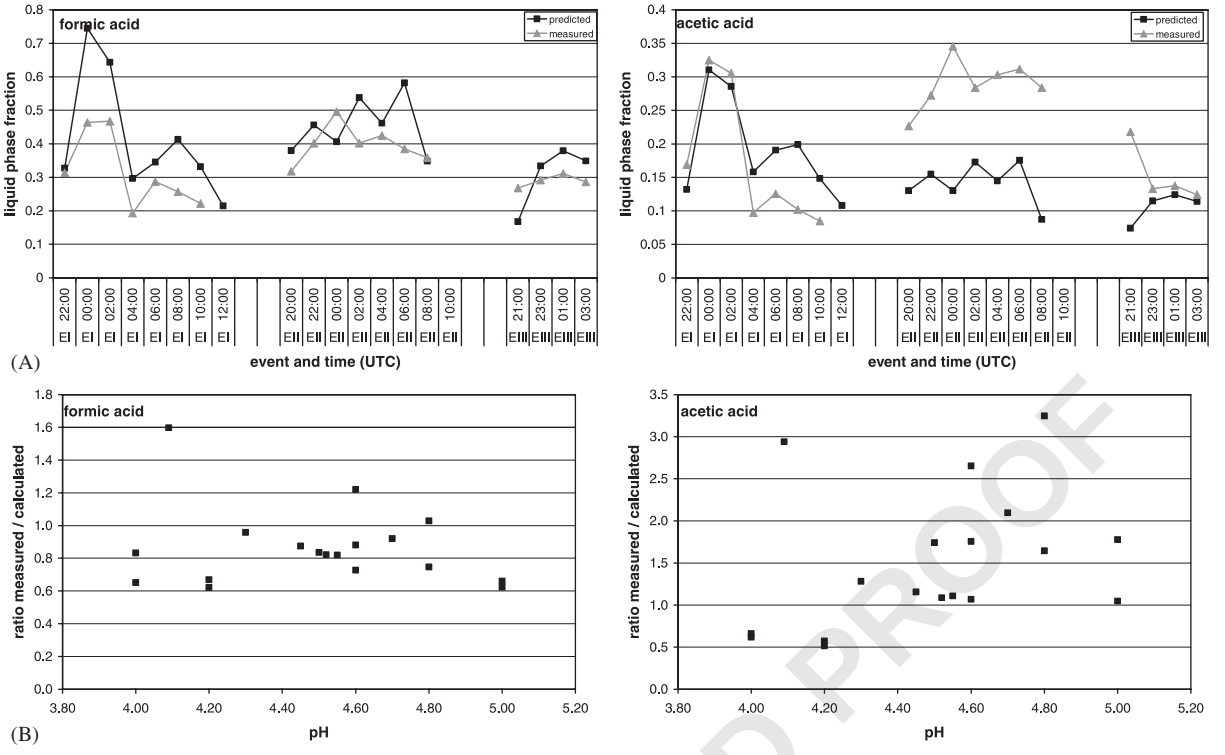

Fig. 5. (A) Calculated (Henry's law) and measured liquid phase fractions of MCAs (details see text) B) ratio of measured and calculated liquid phase fraction as a function of cloud water pH.

measurements of azelaic acid in remote areas and there is some evidence that seasonally specific precursor substances are emitted by trees during the autumnal stage of vegetation.

At the valley stations both impactors and scrubbers were used to determine the concentrations of particulate DCAs. A comparison of the two different sampling devices is done for the upwind site in Müller et al. (2005) and reveals indications for possible sampling artefacts. Even so, we believe that a comparison of data sets obtained by the same sampling device is suitable to acquire information about the behaviour of the diacids during cloud passage.

In Fig. 4 the upwind concentrations and the recoveries at the summit and downwind site are shown for oxalic and malonic acid during E I. The recoveries were usually very close to 100% in the liquid cloud phase and slightly but significantly lower at the downwind site. DCAs were virtually completely located on aerosol particles during FEBUKO (Müller et al., 2005). Thus, their transition into the aqueous phase is due only to nucleation scavenging and it is irreversible under the conditions of cloud formation. The summit recoveries found here are consistent with the data from the Sonnblick observatory (Austria), where in-cloud scavenging efficiencies of 0.89–0.98 were calculated for C1–C4 DCAs (Limbeck and Puxbaum, 2000). In an attempt to calculate the scavenging efficiency of oxalic acid directly, we determined its interstitial concentrations from the INT filters. For E I a concentration of 5 ng m^{-3} was found which translates to 7% of the total oxalic acid budget (mean CWL + interstitial concentration). This is consistent with the close to 100% recoveries and the data of Limbeck and Puxbaum (2000). The interstitial oxalic acid mass results from particles which were too small to be activated into cloud droplets. The 50% activation diameter (geometric) during E I was calculated to be 180 nm (Mertes et al., 2005). From the size-resolved impactor measurements at the upwind station (Table XII, ESM) we calculated that 5% of oxalic acid mass was present in particles with aerodynamic diameters from 50 to 140 nm. Considering the somewhat larger activation diameter this is in good agreement with the above given value of 7% interstitial oxalic acid mass.

In addition to the time-resolved determination of DCAs we obtained information about their size distribution from impactor samples. As for the scrubber concentrations, the impactor data also show lower concentrations of the diacids at the downwind site compared to the upwind site. All concentration data of the impactor samples are given in Tables XII and XIV (ESM). The recoveries for oxalate, malonate, succinate

and malate at the downwind site are calculated on the basis of this data. They lie in the range of 70–83%, 55–63%, and 34–64% for E I, E II, and E III, respectively. The concentrations of other diacids are often below the analytical detection limit for some of the impactor stages, which may lead to biased recovery data. This effect accounts also for the 34% value (succinic acid, E III), where three out of five impactor stages did not show detectable concentrations at the downwind site. Possible reasons for the low recoveries are the physical sink processes discussed above. Following this idea we calculated relative mass fractions of the compounds as $f_{x,i} = m_{x,i}/\mathrm{PM}_i$, where $m_{x,i}$ is the mass of compound x on the impactor stage i in ng, PM_i is the mass of particulate matter on the impactor stage i in μg and $f_{x,i}$ is the resulting mass fraction of compound x on the stage i in ng μg^{-1}. Note that PM refers to the humid mass of the particles at 60% RH (due to the conditioning of the impactor substrates before weighing, Gnauk et al., 2005). The results of these calculations are given in Fig. 6 for the four most abundant diacids. In most instances the mass fractions at the downwind site are close to the ones of the upwind site, indicating a similar relative composition of the particles with respect to DCAs. For some cases though there seems to be a trend of decreased mass fractions in smaller particles and increased fractions in larger particles. This trend is most pronounced for malonic acid during E II and, to different extents, also for oxalic acid during E II and for malonic acid during E III. A slight increase of the mass fractions of oxalic and malonic acids can be observed for coarse mode particles during E I, but without a decrease in the smaller size fraction. The greatly higher fractions for stage 1 particles during E I are due to an unusually lower particle mass for this impaction substrate, which may possibly be caused by a weighing error (Gnauk et al., 2005). An interpretation of these findings is difficult, because the differences are not always significant (mostly within the analytical error) and a difference in the relative mass fractions may be due to altered concentrations of the respective compound on the particles; or it may be due to altered concentrations of other particle constituents. Yet, the data give some hints that chemical transformations of atmospheric particles may have occurred during the cloud passage.

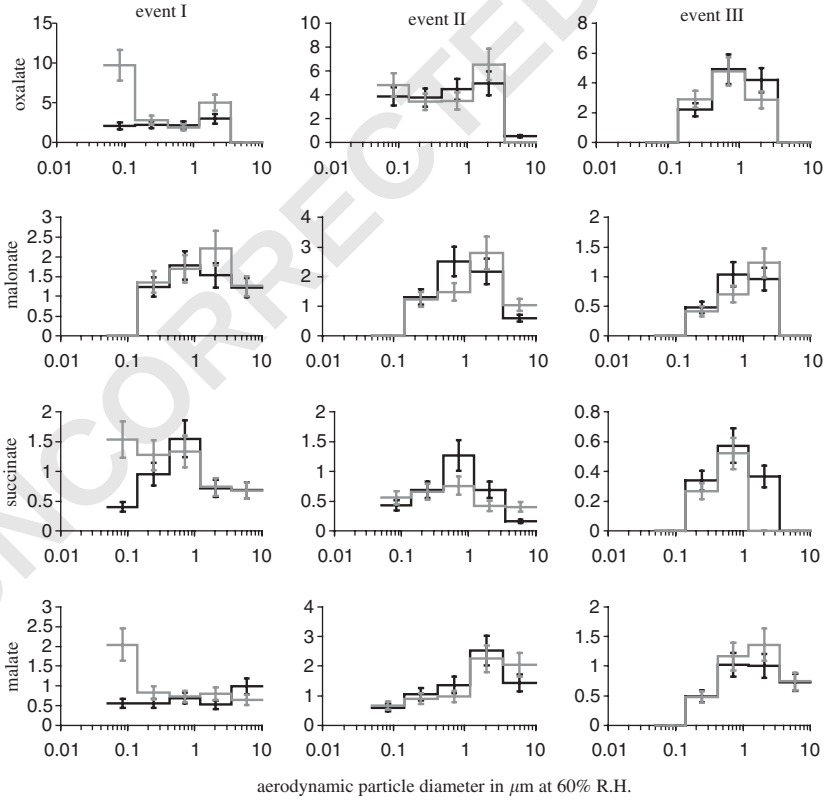

Fig. 6. Mass fractions (in ng μg^{-1} per impactor stage) of the most abundant dicarboxylic acids, black line for upwind station, grey line for downwind station, error bars represent propagated analytical errors.

3.4. Contribution to DOC

The carbon fraction of all determined compounds together accounted for 10.6–21.8% (average 17.3%) of the DOC mass in the cloud water during E I (DOC data reported by Brüggemann et al., 2005). For E II and E III the average values are 14.7% and 10.1%, respectively. With 13.4% on average, the organic carbonyl compounds constituted the largest identified fraction during E I. For E II and E III their contribution decreased to 5.5% and 4.1%, respectively. MCAs contributed 2.4%, 8.0%, and 3.3% (on average) to the DOC during E I, E II, and E III, respectively. DCAs always showed the lowest values (1.5%, 1.3%, 2.6% for E I–E III, respectively). Facchini et al. (1999) reported contributions to DOC between 2.6% and 31.1% with an average of 8.8% for a similarly extensive speciation of fog water constituents in the Po Valley, Italy. For Central California radiation fogs the contribution of several short-chain MCAs and DCAs and formaldehyde to the total organic carbon (TOC) was found to be 22% on average (Ervens et al., 2003). In cloud water at Mt. Rax, Austria, Löflund et al. (2002) determined an average value of 11% for the same compound classes to the DOC. Marinoni et al. (2004) state that in cloud water collected at the Puy de Dôme, France, a variety of 13 MCAs and DCAs contributed from 18% to 71% (36% on average) to the DOC. From the data presented, however, it seems that the concentrations were not normalised to carbon mass. Recalculating the appropriately converted average concentration data of Marinoni et al. gives a contribution of 11.1% to the DOC, which is more consistent with the above-cited values. Leaving the data for the highly impacted California fogs aside, the comparison shows that the identified fraction of the cloud water DOC was as high or even higher in this work than in previous studies.

4. Summary

The concentrations of a large number of organic compounds were determined in different atmospheric phases before, during, and after their passage through a hill cap cloud. Carbonyl compounds, MCAs, and DCAs were discussed with respect to their behaviour during three independent cloud events. While DCAs were incorporated into the cloud by nucleation scavenging with high efficiencies, the scavenging of the gaseous compounds was much less efficient. For the monocarboxylic acids a rough agreement with Henry's law behaviour was observed. Some carbonyl compounds revealed high liquid phase excess factors, depending on their effective water solubility. The downwind site concentrations were lower than the upwind site concentrations for most of the compounds. In the cloud water, a high fraction of the DOC could be identified by applying a variety of analytical techniques.

Acknowledgements

This work was supported by the Bundesministerium für Bildung und Forschung atmospheric research program (AFO 2000) within the FEBUKO project under contract 07ATF01.

References

Bower, B.K.N., Choularton, T.W., Gallagher, M.W., Beswick, K.M., Flynn, M.J., Allen, A.G., Davison, B.M., James, J.D., Robertson, L., Harrison, R.M., Hewitt, C.N., Cape, J.N., McFadyen, G.G., Milford, C., Sutton, M.A., Martinsson, B.G., Frank, G., Swietlicki, E., Zhou, J., Berg, O.H., Mentes, B., Papaspiropoulos, G., Hansson, H.C., Leck, C., Kulmala, M., Aalto, P., Vakeva, M., Berner, A., Bizjak, M., Fuzzi, S., Laj, P., Facchini, M.C., Orsi, G., Ricci, L., Nielsen, M., Allan, B.J., Coe, H., McFiggans, G., Plane, J.M.C., Collett Jr., J.L., Moore, K.F., Sherman, D.E., 2000. ACE-2 HILLCLOUD. An overview of the ACE-2 ground-based cloud experiment. Teljlus 52B (2), 750–778.

Brüggemann, E., Gnauk, T., Mertes, S., Acker, K., Auel, R., Wieprecht, W., Möller, D., Collett Jr., J.L., Chemnitzer, R., Rüd, C., Junek, R., Herrmann, H., 2005. Schmücke hill cap cloud and valley stations aerosol characterisation during FEBUKO (I): particle size distribution and main components. Atmospheric Environment (this issue).

Cofer, W.R., Collins, V.G., Talbot, R.W., 1985. Improved aqueous scrubber for collection of soluble atmospheric trace gases. Environmental Science and Technology 19 (6), 557–560.

Collett Jr., J.L., Daube, B., Munger, J.W., Hoffmann, M.R., 1989. Cloud water chemistry in Sequoia National Park. Atmospheric Environment 23 (5), 999–1007.

Collett Jr., J.L., Daube, B.C., Gunz, D., Hoffmann, M.R., 1990. Intensive studies of Sierra Nevada cloud water chemistry and its relationship to precursor aerosol and gas concentrations. Atmospheric Environment. Part A, General Topics 24 (7), 1741–1757.

Demoz, B.B., Collett Jr., J.L., Daube, B.C., 1996. On the Caltech active strand cloudwater Collectors. Atmospheric Research 41 (1), 47–62.

Djikaev, Y.S., Tabazadeh, A., 2003. Effect of adsorption on the uptake of organic trace gas by cloud droplets. Journal of Geophysical Research—Atmospheres 108 (D22).

Elbert, W., Hoffmann, M.R., Kramer, M., Schmitt, G., Andreae, M.O., 2000. Control of solute concentrations in cloud and fog water by liquid water content. Atmospheric Environment 34 (7), 1109–1122.

Ervens, B., Herckes, P., Feingold, G., Lee, T., Collett Jr., J.L., Kreidenweis, S.M., 2003. On the drop-size dependence of organic acid and formaldehyde concentrations in fog. Journal of Atmospheric Chemistry 46 (3), 239–269.

Facchini, M.C., Fuzzi, S., Lind, J.A., Fierlingeroberlinninger, H., Kalina, M., Puxbaum, H., Winiwarter, W., Arends, B.G., Wobrock, W., Jaeschke, W., Berner, A., Kruisz, C., 1992. Phase-partitioning and chemical-reactions of low-molecular-weight organic-compounds in fog. Tellus 44B (5), 533–544.

Facchini, M.C., Fuzzi, S., Zappoli, S., Andracchio, A., Gelencser, A., Kiss, G., Krivacsy, Z., Meszaros, E., Hansson, H.C., Alsberg, T., Zebuhr, Y., 1999. Partitioning of the organic aerosol component between fog droplets and interstitial air. Journal of Geophysical Research—Atmospheres 104 (D21), 26,821–26,832.

Fuzzi, S. (Ed.), 1994. The Kleiner Feldberg cloud experiment 1990 (special issue). Journal of Atmospheric Chemistry 19(1–2).

Fuzzi, S. (Ed.), 1997. The Great Dun Fell cloud experiment 1993 (special issue). Atmospheric Environment 31(16).

Gallagher, M.W. (Ed.), 1999. The Great Dun Fell experiment 1995 (special issue). Atmospheric Research 50(3–4).

Glotfelty, D.E., Seiber, J.N., Liljedahl, L.A., 1987. Pesticides in fog. Nature 325 (6105), 602–605.

Gnauk, T., Brüggemann, E., Müller, K., Chemnitzer, R., Rüd, C., Galgon, D., Wiedensohler, A., Acker, K., Auel, R., Wieprecht, W., Möller, D., Jaeschke, W., Herrmann, H., 2005. Aerosol characterisation at the FEBUKO upwind station Goldlauter (I): particle mass, main ionic components, OC/EC, and mass closure. Atmospheric Environment (this issue).

Hegg, D.A., Gao, S., Jonsson, H., 2002. Measurements of selected dicarboxylic acids in marine cloud water. Atmospheric Research 62 (1–2), 1–10.

Heinold, B., Tilgner, A., Jaeschke, W., Haunold, W., Knoth, O., Wolke, R., Herrmann, H., 2005. Meteorological characterisation of the FEBUKO hill cap cloud experiments, Part II: tracer experiments and flow characterisation with nested non-hydrostatic atmospheric models. Atmospheric Environment (this issue).

Herrmann, H., Wolke, R., Müller, K., Brüggemann, E., Gnauk, T., Barzaghi, P., Mertes, S., Lehmann, K., Massling, A., Birmili, W., Wiedensohler, A., Wieprecht, W., Acker, K., Jaeschke, W., Kramberger, H., Syrcina, B., Bächmann, K., Collett Jr., J.L., Galgon, D., Schwirn, K., Nowak, A., van Pinxteren, D., Plewka, A., Chemnitzer, R., Rüd, C., Hofmann, D., Tilgner, A., Diehl, K., Heinold, B., Hinneburg, D., Knoth, O., Sehili, A.M., Simmel, M., Wurzler, S., Mauersberger, G., Majdik, Z., Müller, F., 2005. FEBUKO and MODMEP: Field measurements and modelling of aerosol and cloud multiphase processes. Atmospheric Environment (this issue).

Houdier, S., Perrier, S., Defrancq, E., Legrand, M., 2000. A new fluorescent probe for sensitive detection of carbonyl compounds: sensitivity improvement and application to environmental water samples. Analytica Chimica Acta 412 (1–2), 221–233.

Kawamura, K., Kasukabe, H., Barrie, L.A., 1996. Source and reaction pathways of dicarboxylic acids, ketoacids and dicarbonyls in arctic aerosols: one year of observations. Atmospheric Environment 30 (10–11), 1709–1722.

Keene, W.C., Mosher, B.W., Jacob, D.J., Munger, J.W., Talbot, R.W., Artz, R.S., Maben, J.R., Daube, B.C., Galloway, J.N., 1995. Carboxylic acids in clouds at a high-elevation forested site in central Virginia. Journal of Geophysical Research—Atmospheres 100 (D5), 9345–9357.

Kesselmeier, J., Bode, K., Gerlach, C., Jork, E.M., 1998. Exchange of atmospheric formic and acetic acids with trees and crop plants under controlled chamber and purified air conditions. Atmospheric Environment 32 (10), 1765–1775.

Khwaja, H.A., Brudnoy, S., Husain, L., 1995. Chemical characterization of three summer cloud episodes at Whiteface Mountain. Chemosphere 31 (5), 3357–3381.

Kramberger, H., 2003. Carbonsäuren und Dicarbonsäuren in atmosphärischen Mehrphasenprozessen. Dissertation Thesis, Technische Universität Darmstadt, Darmstadt.

Levsen, K., Behnert, S., Mussmann, P., Raabe, M., Priess, B., 1993. Organic compounds in cloud and rain water. International Journal of Environmental Analytical Chemistry 52 (1–4), 87–97.

Limbeck, A., Puxbaum, H., 2000. Dependence of in-cloud scavenging of polar organic aerosol compounds on the water solubility. Journal of Geophysical Research—Atmospheres 105 (D15), 19,857–19,867.

Löflund, M., Kasper-Giebl, A., Schuster, B., Giebl, H., Hitzenberger, R., Puxbaum, H., 2002. Formic, acetic, oxalic, malonic and succinic acid concentrations and their contribution to organic carbon in cloud water. Atmospheric Environment 36 (9), 1553–1558.

Lüttke, J., Levsen, K., 1997. Phase partitioning of phenol and nitrophenols in clouds. Atmospheric Environment 31 (16), 2649–2655.

Mainka, A., Ebert, P., Kibler, M., Prokop, T., Tenberken, B., Bachmann, K., 1997. Development of new methods for the analysis of carboxylic acids and carbonyl compounds in size classified raindrops by CE for application in modelling atmospheric processes. Chromatographia 45, 158–162.

Marinoni, A., Laj, P., Sellegri, K., Mailhot, G., 2004. Cloud chemistry at the Puy de Dome: variability and relationships with environmental factors. Atmospheric Chemistry and Physics 4, 715–728.

Mertes, S., Lehmann, K., Nowak, A., Massling, A., Wiedensohler, A., 2005. Link between aerosol hygroscopic growth and droplet activation observed for hill cap clouds at connected flow conditions during FEBUKO. Atmospheric Environment (this issue).

Müller, K., van Pinxteren, D., Plewka, A., Svrcina, B., Kramberger, H., Hofmann, D., Bächmann, K., Herrmann, H., 2005. Aerosol characterisation at the FEBUKO upwind station Goldlauter (II): detailed organic chemical characterisation. Atmospheric Environment (this issue).

Munger, J.W., Collett, J.L., Daube, B.C., Hoffmann, M.R., 1989. Carboxylic acids and carbonyl compounds in southern California clouds and fogs. Tellus 41B (3), 230–242.

Munger, J.W., Jacob, D.J., Daube, B.C., Horowitz, L.W., Keene, W.C., Heikes, B.G., 1995. Formaldehyde, glyoxal, and methylglyoxal in air and cloud water at a rural mountain site in Central Virginia. Journal of Geophysical Research—Atmospheres 100 (D5), 9325–9333.

Neusüß, C., Pelzing, M., Plewka, A., Herrmann, H., 2000. A new analytical approach for size-resolved speciation of organic compounds in atmospheric aerosol particles: methods and first results. Journal of Geophysical Research—Atmospheres 105 (D4), 4513–4527.

Pandis, S.N., Seinfeld, J.H., 1991. Should bulk cloud water or fog water samples obey Henry's Law? Journal of Geophysical Research—Atmospheres 96 (D6), 10,791–10,798.

Rao, X., Collett Jr., J.L., 1995. Behavior of S(IV) and formaldehyde in a chemically heterogeneous cloud. Environmental Science and Technology 29 (4), 1023–1031.

Seinfeld, J.H., Pandis, S.N., 1998. Atmospheric Chemistry and Physics: From Air Pollution to Climate Change. Wiley, New York.

Tilgner, A., Heinold, B., Nowak, A., Herrmann, H., 2005a. Meteorological characterisation of the FEBUKO hill cap cloud experiments, Part I: synoptic characterisation of measurement periods. Atmospheric Environment (this issue).

Tilgner, A., Majdik, Z., Sehili, A.M., Simmel, M., Wolke, R., Herrmann, H., 2005b. SPACCIM: simulations of the multiphase chemistry occurring in the FEBUKO hill cap cloud experiments. Atmospheric Environment (this issue).

Valsaraj, K.T., Thoma, G.J., Reible, D.D., Thibodeaux, L.J., 1993. On the enrichment of hydrophobic organic compounds in fog droplets. Atmospheric Environment 27A (2), 203–210.

Wieprecht, W., Acker, K., Mertes, S., Collett Jr., J.L., Jaeschke, W., Brüggemann, E., Möller, D., Herrmann, H., 2005. Cloud physics and cloud water sampler comparison during FEBUKO. Atmospheric Environment (this issue).

Winiwarter, W., Brantner, B., Puxbaum, H., 1992. Should bulk cloud water or fog water samples obey Henry's law—comment. Journal of Geophysical Research—Atmospheres 97 (D5), 6075–6078.

Winiwarter, W., Fierlinger, H., Puxbaum, H., Facchini, M.C., Arends, B.G., Fuzzi, S., Schell, D., Kaminski, U., Pahl, S., Schneider, T., Berner, A., Solly, I., Kruisz, C., 1994. Henry's law and the behavior of weak acids and bases in fog and cloud. Journal of Atmospheric Chemistry 19 (1–2), 173–188.

3B2v8.06a/w (Dec 5 2003).51c XML:ver:5.0.1 AEA : 5772 Prod.Type:COM pp.1–10(col.fig.:2–5) ED:MangalaK. PAGN:dini SCAN:Global

ARTICLE IN PRESS

Available online at www.sciencedirect.com

SCIENCE DIRECT®

ELSEVIER

Atmospheric Environment ▮ (▮▮▮▮) ▮▮▮–▮▮▮

ATMOSPHERIC ENVIRONMENT

www.elsevier.com/locate/atmosenv

Non-dissipative cloud transport in Eulerian grid models by the volume-of-fluid (VOF) method

Detlef Hinneburg*, Oswald Knoth

Institute for Tropospheric Research, Permoserstr. 15, 04318 Leipzig, Germany

Abstract

The formation of clouds is coupled to the vapour saturation condition. Cloud modelling is therefore dramatically disturbed by dilution processes, which are induced by recurrent interpolations on the fixed (Eulerian) grid. The numerical diffusion gives rise to degeneration and premature disappearance of the modelled clouds. The difficulties increase, if sectional mass representation in the drop microphysics and aerosol chemistry is considered. To tackle this problem, stringently defined and tracked phase boundaries are required.

The numerical diffusion of clouds can be totally suppressed by the volume-of-fluid (VOF) method, which is applied here in connection with an atmospheric model. The cloud phase is distinguished by prognosing the partial cloud volume in all grid cells near the cloud boundary. Adopting elementary geometrical forms for the intracellular cloud volume and simple diagnostic rules of their alignment, the standard transport fluxes can be used in the new equation. Separate variables for the cloud and environmental phase complete the transport scheme.

The VOF method and its realisation are described in detail. Advection, condensation, evaporation, and turbulent diffusion are considered within the VOF framework. The variation of the grid resolution and turbulence conditions for a rising thermal leads to striking arguments in favour of the VOF method, resulting in higher intensity, lifting, and lifetime as well as clear boundaries of the simulated clouds (even for low grid resolution).

Keywords: Cloud model; Cloud volume; Diffusion; Entrainment

1. Introduction

New developments in cloud microphysics and chemistry are directed towards a sectional mass representation of the cloud drops and aerosol particles (see this issue, e.g., Wolke et al., 2005). They reflect the real cloud–aerosol–gas interactions, the tracking of individual particles, and the variability of their composition. Since it is of crucial importance, whether the phase-specific processes take place within the cloud or outside, the cloud boundary needs to be clearly defined and tracked. Interface tracking and separate treatment of the phases not only support the individual multi-phase processes but also allow for long-term processes and undisturbed phase transport.

Most atmospheric models use Eulerian grid systems and finite-differencing techniques, although the numerical defects originating from gradient levelling during the transport through fixed grids are long anticipated facts. The so-called numerical diffusion leads to diluted distributions, separately for each variable (temperature, vapour and water content) and independently on the grid resolution, so that inconsistent phases and phase changes are produced near the cloud boundary. The

*Corresponding author. Fax: +49 341 2352139.
E-mail address: hinnebur@tropos.de (D. Hinneburg).

1352-2310/$ - see front matter © 2005 Elsevier Ltd. All rights reserved.
doi:10.1016/j.atmosenv.2005.02.027

transport process thus implies the permanent and unrealistic decrease of the cloud intensity and extent as well as the premature disappearance.

Recent publications address the subject of numerically induced cloud diffusion with enhanced effort (e.g., Grabowski, 1989; Stevens et al., 1996). Some of the methods proposed are the extended semi-Lagrangian integration (Pellerin et al., 1995), explicit interface tracking (Unverdi and Tryggvason, 1992), and volume tracking with diagnostic interface reconstruction known as volume-of-fluid (VOF). The VOF method originally applied to fluids with free surfaces (Hirt and Nichols, 1981), was also used in detailed investigations of the advection–condensation problem (Margolin et al., 1997; Kao et al., 2000). The present study utilises this method due to the total elimination of numerical diffusion, the natural approach and matching with existing models. Moreover, the VOF method is extended to include the turbulent diffusion process.

The atmospheric model used for the VOF application is presented in Section 2. Details of the VOF method and its realisation in the advection, diffusion, and diagnostic cloud boundary reconstruction are described in Section 3. The influence of the grid resolution and diffusion conditions with VOF switched on or off is examined in Section 4 for a rising thermal. Section 5 summarises the unique improvements, which qualify the VOF method for future applications with complex cloud–aerosol physics–chemistry models.

2. Atmospheric Model

The All-Scale Atmospheric Model (ASAM) used to test the VOF method is prognostic, non-hydrostatic, anelastic, and includes advection, turbulent diffusion, wall friction, Coriolis force, geostrophic pressure, condensation/evaporation, and buoyancy due to local temperature/vapour/condensate deviations. The model is suitable for 1…3-dimensional applications on all scales between the micro and global scale.

The turbulence concept is based on the standard k-ε model with first-order closure (Launder and Spalding, 1974). The diffusion coefficients are derived from the prognosed turbulent kinetic energy and dissipation. The respective equations account for shear and buoyant production of turbulent kinetic energy. Logarithmic wall functions are used for the wall-parallel momentum. The continuity equation is satisfied by diagnostic pressure and flux corrections via Poisson's equation, solved by conjugate gradient methods with multi-grid techniques as pre-conditioner (Schlünzen et al., 2003).

The model equations are solved on an Arakawa-C grid with z-coordinate system in parallelised structure. The orography and possible obstacles are realised by partially or completely filled grid cells with defined surfaces. The terms attain simplest form because of the rectangular Cartesian system and finite-volume differencing, where additional items are required only for spherical coordinates. The upwind biased advection scheme is of third order (Hundsdorfer et al., 1995). The time integration utilises a third-order Runge–Kutta–Rosenbrock procedure including implicitly the linear dependences between the variables on the right-hand side of the equations (Lanser et al., 2001).

The equations for the cloud variables $\chi = \{q^{\mathrm{v}}, q^{\mathrm{l}}, \theta\}$ consisting of the mixing ratios of vapour/liquid water and the potential temperature consider advection, diffusion, and cloud processes (phase conversion)

$$\partial(\rho\chi)/\partial t = \mathrm{ADV}(\chi) + \mathrm{DIFF}(\chi) + \mathrm{CLOUD}(\chi), \quad (1)$$

with

$$\mathrm{ADV}(\chi) = -\nabla(\rho\, \boldsymbol{v}\, \chi), \quad (2)$$

$$\mathrm{DIFF}(\chi) = \nabla(\rho\, D\, \nabla\, \chi) \quad (3)$$

$$\mathrm{CLOUD(c)} = \rho r C^{\chi} \mathrm{Min}(q^{\mathrm{vs}} - q^{\mathrm{v}}, q^{\mathrm{l}}), \quad (4)$$

where ρ denotes the density, $\boldsymbol{v}$ the velocity vector, D the diffusion coefficient, r the evaporation/condensation rate (here $r = 1\,\mathrm{s}^{-1}$), q^{vs} . the saturation value of q^{v}, $C\chi = \{1, -1, -c^{\theta}\}$ with c^{θ} defining the potential temperature loss per mixing ratio of vapourised water. The advection term is cited in standard form, whereas the diffusion term implies simplified sub-grid scale fluxes. The cloud term describes condensation and evaporation by relaxed degradation of excess vapour or liquid water, respectively (Schultz, 1995). The amount of phase conversion is independent on the time step due to the sophisticated time integration method (see above).

3. Volume-of-fluid (VOF) method

3.1. General characteristics

The VOF method improves the advection process of two-phase flows in Eulerian grid systems by separate treatment of the phases (cloud, environment). The standard transport fluxes are reinterpreted by a phase-specific volumetric approach (Margolin et al., 1997; Kao et al., 2000). The scheme acts as a by-pass in the model integration cycle and is confined to the cloud-constituting variables in two-phase grid cells. The following aspects characterise the VOF method (Fig. 1a):

(1) *Advection of the cloud-volume:* The geometrical information, to what extent the cloud migrates through the grid, is obtained from a prognostic equation for the cloud volume fractions in the grid cells (new variable). The algorithm performs the geometrical transport of the cloud volume for given

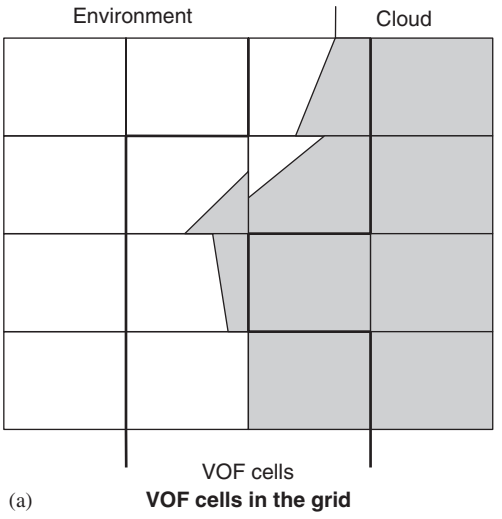

Fig. 1. The VOF method: (a) Cloud boundary and VOF cells in the model grid. (b) Interface geometry (Section 3.2) and advection process (Section 3.3) in a two-phase cell.

interface geometry.

(2) *Interface geometry:* A diagnostic reconstruction of the cloud boundary is required in dependence on the actual cloud volume distribution, which is the only prognosed geometrical information in VOF.

(3) *Advection of the phase-specific cloud variables:* As regards the changing properties of the phases, the operators of the governing Eq. (1) have to be applied separately to the phases. Double-defined (phase-specific) cloud variables, at least in grid cells cut by the cloud boundary, are therefore provided.

The presentation of the VOF method differs on many points from the general and abstract descriptions of Margolin et al. (1997) and Kao et al. (2000). The formalism refers to the concrete model equations, focused on the more practical and geometrical aspects and simplified by operator-splitting. Variable density, the diffusion problem and the design of the realised 3D interface reconstruction are included in the frame of anelastic approach. Moreover, the adjustment between VOF and standard model routines is explicitly addressed.

The demonstration of the VOF method starts with the new variables. The relative phase volume V_{phase} is defined as the mass ratio of the respective phase = {cloud, environment} in a grid cell:

$$V_{\text{phase}} = M_{\text{phase}}/M,$$

with

$$V_{\text{cl}} + V_{\text{env}} = 1, \tag{5}$$

where M_{phase} is the mass fraction of the given phase and M the total mass in the grid cell. Different phases are described by separate cloud variables χ_{phase}, and mean grid cell values are generated by volume weighted averaging:

$$\chi = \sum_{\text{phase}} V_{\text{phase}}\chi_{\text{phase}}. \tag{6}$$

The phase variables χ_{phase} are subjected to the VOF scheme, whereas the total values of χ applies to all processes and grid cells outside the VOF framework (e.g., buoyancy).

In order to derive the VOF-specific governing equations, Eqs. (1) and (6) are combined, noticing the separate operator scopes for different phases:

$$\begin{aligned}\partial(\rho V_{\text{phase}}\chi_{\text{phase}})/\partial t = {} & \text{ADV}(V_{\text{phase}}\chi_{\text{phase}}) \\ & + \text{DIFF}(V_{\text{phase}}\chi_{\text{phase}}) \\ & + \text{CLOUD}(V_{\text{phase}}\chi_{\text{phase}}).\end{aligned} \tag{7}$$

Indicating $\chi_{\text{phase}} = 1$ in these equations, the additional 'continuity' equations for the phase volumes are found.

$$\begin{aligned}\partial(\rho V_{\text{phase}})/\partial t = {} & \text{ADV}(V_{\text{phase}}) + \text{DIFF}(V_{\text{phase}}) \\ & + \text{CLOUD}(V_{\text{phase}}).\end{aligned} \tag{8}$$

This equation needs to be solved for one phase only (e.g., cloud volume) because of the phase partitioning in Eq. (5). The volume flow of the individual phases is controlled by Eq. (8), while the associated changes of the cloud variables are given by Eq. (7). The geometrical construction of the cloud volume fractions is described in Section 3.2, whereas the changes by advection and diffusion processes via Eq. (8) are treated in Sections 3.3 and 3.4, respectively. The phase conversion process and the solution of Eq. (7) follow in Section 3.5.

3.2. Cloud interface reconstruction

The VOF method manages the volumetric flow of separate phases for given interface geometry, however, it generates a new phase volume distribution rather than

the interface location. To remedy this gap, the interface is reconstructed after each time step by means of a diagnostic estimation of the actual cloud phase distribution. Central principle for the geometrical configuration of a cloud volume fraction within a grid cell is a maximal contact with the neighbouring cloud phase and a planar boundary against the environment (Fig. 1b). Several schemes were elaborated (Pilliod and Puckett, 1997) which differ in the geometrical interface shape, the number of involved neighbour cells, etc. Here, the interface reconstruction passes the following two steps.

(1) *Interface direction:* The normal n of the interface plane in the considered cell (3-dimensional (3D) indices ijk) is identified as the opposite direction from the centre of the cell to the local cloud centroid. The inspection sphere for the centroid determination should encompass the cells (indices ijk) behind the faces (7-stencil) and for improved quality all immediate neighbours on the faces, edges and corners (3^3-stencil). In this study, the inspected cells are extended by a further ring of cells (5^3-stencil). The cloud centroid is calculated from the index-difference vectors weighted by the respective cloud volumes

$$n(ijk) = -\sum_{ijk} V_{\mathrm{cl}}(ijk)\frac{(i-i, j-j, k-k)}{|(i-i, j-j, k-k)|}, \tag{9}$$

where $(\ldots)$ and $|\ldots|$ denote a vector and its absolute value, respectively; $\boldsymbol{n}$ is un-normalised.

(2) *Interface position*: Once the interface direction is determined, the plane is positioned such that the cell volume fraction underneath equals the given cloud volume of the cell. The found distance d of the plane from the cell centre completes the interface specification

$$d = f_1(V; \boldsymbol{n}, V_{\mathrm{cl}}), \tag{10}$$

where V is the cell volume. The symbolic function f_1 describes the dependence of the position of a plane (cutting the cuboid V) on its direction $\boldsymbol{n}$ and the enclosed cloud volume V_{cl}. The problem is well-defined but complicated because of non-linear dependences (Scardovelli and Zaleski, 2000; compare also Eq. (16) below).

3.3. Cloud volume advection

The cloud volume satisfies Eq. (8) with the advection term analogous to Eq. (2)

$$\mathrm{ADV}(V_{\mathrm{cl}}) = -\nabla(\rho \boldsymbol{v} V_{\mathrm{cl}}). \tag{11}$$

Although the equation implies formal similarity of V_{cl} with homogeneously distributed specific mixing ratios, the geometrically discrete feature of V_{cl} has to be considered appropriately. Henceforth, the outline focuses to 1D transport in a rectangular grid (for 3D transport see last paragraph). Finite-volume discretisation of Eq. (11) results in the following approximation:

$$\mathrm{ADV}(V_{\mathrm{cl}}) = -[(\rho v\, V_{\mathrm{cl}} F)^{\mathrm{faceR}} - (\rho\, v\, V_{\mathrm{cl}} F)^{\mathrm{faceL}}]/V, \tag{12}$$

where v is the velocity component and F the area of the cell face (Right/Left). Since the transported quantity V_{cl} is agglomerated in the cells, its interpolation to the cell face is impossible; only the transporting flux is defined on the face

$$(\rho\, v\, V_{\mathrm{cl}} F)^{\mathrm{face}} = (\rho\, v F)^{\mathrm{face}}(V_{\mathrm{cl}})^{\mathrm{face}}, \quad \text{with indefinite}(V_{\mathrm{cl}})^{\mathrm{face}}. \tag{13}$$

The way out of the incompatibility in Eq. (13) is found by the reinterpretation of both factors after explicit time integration by the step Δt. Then, the flux factor converts to a finite mass portion transported through the face out of the upwind cell, and the second factor simply means a fraction of V_{cl} carried along. If the mass flux is related to the cell mass M, it can be interpreted as a cuboid, while the multiplication with V_{cl} in Eq. (13) transforms to an intersection (overlapping) between the cuboid of the total volume transport and the geometrical form of the cloud volume (Fig. 1b):

$$(\rho\, \underline{v}\, V_{\mathrm{cl}} F)^{\mathrm{face}} \Delta t = M(V_{\mathrm{trans}} \cap V_{\mathrm{cl}}), \tag{14}$$

$$\text{with} \quad V_{\mathrm{trans}} = (\rho\, \underline{v}\, F \Delta t)^{\mathrm{face}}/M, \quad \text{limitation}: \ 0 \leqslant V_{\mathrm{trans}} \leqslant 1, \tag{15}$$

$$V_{\mathrm{trans}} \cap V_{\mathrm{cl}} = f_2(F\, \underline{v}\, \Delta t;\ \boldsymbol{n}, d), \tag{16}$$

where v denotes the absolute value of v, V_{trans} symbolises the cuboid of the transported total volume $Fv\Delta t$ projected into the upwind cell; M, V_{cl}, $\boldsymbol{n}$, d refer to the upwind cell.

The overlap function f_2 represents the inverse function of f_1 in Eq. (10) and depends on the geometrical specifications of both volume participants. The location and extent of the cuboid V_{trans} is provided by the flux term ($Fv\Delta t$), while the sloped cut cuboid V_{cl} is specified by the interface plane ($\boldsymbol{n}$,d). The mathematic-geometrical calculations consist in successive sloped and grid-parallel cuttings of cuboids and are case-dependent because of arbitrary conjunction of flux and interface directions (Scardovelli and Zaleski, 2000). The functions f_1 and f_2 can be substantially simplified by the restriction to grid-parallel interface orientation. The maximum vector component of $\boldsymbol{n}$ has then to be selected as the permitted direction. This additional option of the model, though inducing stronger artificial lapse of the cloud boundary, leads to comparable simulation results.

The described procedure remains valid for 3D transport, when the individual velocity components are treated separately and in succession (operator splitting; see Pilliod and Puckett, 1997). The problems arising from temporary violations of the flux balance in the split-steps ($V_{\mathrm{cl}} + V_{\mathrm{env}} \neq 1$) are solved by additional

processing of the non-cloud volume V_{env} by Eq. (8). The mass flux divergences are then accounted for by applying intermediate values of $M = \rho V(V_{cl} + V_{env})$. After each split-step a new interface reconstruction is applied. The splitting procedure is made second-order accurate by alternating the sweep directions and averaging them within each time step.

3.4. Cloud volume diffusion

The VOF method was developed to prevent the numerical diffusion, and by most applications even the real (turbulent) diffusion is excluded or, if at all, treated outside of the VOF scheme and with diminished coefficients (Kao et al., 2000). In fact, turbulent diffusion sweeps off the achievements of VOF so long as it is regarded as a complete homogenisation. However, there has to be drawn a distinction between turbulent and molecular diffusion according to experimental findings and theoretical concepts in the context of cloud entrainment (Paluch and Baumgardner, 1989; Grabowski, 1993; Krüger et al., 1997). Aircraft penetration through clouds yielded the following results: Original (undiluted) cloud material is uniformly distributed over large scales, whereas completely mixed (diluted) cloud properties are highly non-uniform and exist only on small scales. The conclusion was drawn, that

(a) turbulent diffusion is by no means the direct source of phase mixing and change;
(b) turbulent diffusion produces bulk entrainment and coarse (non-homogeneous) 'mixing' with stirred interface structure and the coexistence of different phases;
(c) molecular diffusion solely and finally produces phase homogeneity with one resulting (diluted) phase.

Accordingly, the diffusion process in the foregoing model equations is realised by two terms which are responsible for turbulent diffusion and molecular mixing

$$\mathrm{DIFF} = \mathrm{TURB} + \mathrm{MOL} \tag{17}$$

both defined by Eq. (3), with separate coefficients D_{turb} and D_{mol}, respectively. Most atmospheric models beyond the VOF framework consider turbulent diffusion as the dominant process which is immediately followed by condensation/evaporation due to homogeneous mixing in the region involved. However, special developments are addressed to the disassembly of the diffusion cascade between the eddy and the Kolmogorov scale (e.g., Broadwell and Breidenthal, 1982; Krüger et al., 1997), providing for a retardation of the fine-scale (molecular) homogenisation. In the following, the VOF framework is opened to include the diffusion processes adequately.

(1) *Turbulent diffusion* with coefficients $D_{turb} \gg D_{mol}$ results from dynamic heterogeneities on the grid scale with the corresponding interchange of volume parcels. Phase changes are not directly associated with turbulence. If different phases are included in the volume exchange, only deformation and enlargement of the interface is produced (coarse mixing). This turbulent volume diffusion is described by using the standard diffusion term (3) in the cloud volume Eq. (8):

$$\mathrm{TURB}(V_{cl}) = \nabla(\rho\, D_{turb} \nabla V_{cl}), \tag{18}$$

assuming quasi-steady (diffusive) distribution of V_{cl} in the concerned region. The turbulent cloud volume diffusion acts as a loss-free dispersion of the cloud phase, resulting in a zone of two-phase grid cells without mixing or dilution of the cloud and environmental properties. The interaction between the phases is instead represented by the molecular diffusion, which operates on a small scale within all two-phase grid cells.

(2) *Molecular diffusion* with coefficients D_{mol} of the magnitude $10^{-5}\,\mathrm{m^2\,s^{-1}}$ for atmospheric conditions (Rogers, 1976) is based on the molecular mobility and mean free path length. It is responsible for homogeneous phase mixing across the interface with a final uniform phase in a very narrow zone. The corresponding loss of cloud volume is also deduced from Eq. (3), considering the case of two neighbouring grid cells with opposite phases ($V_{cl} = 0$ or 1, respectively)

$$\mathrm{MOL}(V_{cl}) = -\rho D_{mol}/\Delta x^2. \tag{19}$$

The efficiency of molecular mixing deopends not only on its coefficient D_{mol}, but exceedingly on the effective interface area. This area (as related to the cell volume) increases with time, enforced by the local turbulence. The mixing process of the different phases requires therefore the application of variable effective molecular diffusion coefficients $D_{mol}(\mathrm{eff.})$ in Eqs. (19) and (22) below:

$$D_{mol}(\mathrm{eff.}) = S(t) D_{mol}, \quad 1 \leqslant S(t) < \infty, \tag{20}$$

where $S(t)$ is a monotonic forcing function with strong dependences on time, location, and turbulence conditions. This subject is not investigated here (see e.g., Broadwell and Breidenthal, 1982; Krüger et al., 1997); however, the direction of including diffusion in the VOF framework was given, and some test examples are analysed in Section 4.3.

3.5. Treatment of cloud variables

3.5.1. Decoupled equations for cloud variables

The determination of the cloud variables by Eq. (7) would require an online coupled solution with the volume Eq. (8) in the VOF cells (e.g., Margolin et al.,

1997). Since the model ASAM utilises sophisticated implicit numerical transport schemes (Section 2) spanning three grid cells and therefore excluding a strictly defined gateway to the VOF cells, the way of adjustments is persued. Consequently, the volume controlled balancing of the transport fluxes in the two-phase cells (i.e., Eq. (7)) is replaced by the standard flux balancing for individual phases:

$$\partial(\rho\chi_{\text{phase}})/\partial t = \text{ADV}(\chi_{\text{phase}}) + \text{TURB}(\chi_{\text{phase}}) + \text{MOL}(\chi_{\text{phase}}) + \text{CLOUD}(\chi_{\text{phase}}). \quad (21)$$

This equation formally corresponds to the standard model Eq. (1), however, it is restricted to a specified phase in the VOF cells, and boundary conditions are necessary at the outer edge of the VOF cells as well as at the cloud-environment interface (Section 3.5.3).

The terms for advection, turbulent diffusion, and cloud processes in the VOF cells are treated conventionally by phase-specific use of the appropriate Eqs. (2)–(4), whereas the molecular mixing term MOL as the unique interaction (conversion) between the phases requires response to the cloud volume loss by Eq. (19). The equivalent change of the phase variables is assigned to the non-cloud phase

$$\begin{aligned}\text{MOL}(\chi_{\text{env}}) &= -\text{MOL}(V_{\text{cl}})(\chi_{\text{cl}} - \chi_{\text{env}}) \\ &= \rho D_{\text{mol}}(\chi_{\text{cl}} - \chi_{\text{env}})/\Delta x^2, \;\; \text{MOL}(\chi_{\text{cl}}) \\ &= 0 \end{aligned} \quad (22)$$

with effective molecular diffusion coefficients in the sense of Eq. (20).

3.5.2. Phase conversion adjustment

Generally, the cloud processes are acting in the cloud phase with corresponding effects on the cloud variables. Only those events that alter the phase state (cloud → environment or vice versa) belong to the term CLOUD(V_{phase}) in the cloud volume Eq. (8). They arise, when liquid water vanishs completely or emerges for the first time (in a given phase volume fraction). It is customary in cloud modelling, that this phase conversion is treated by a diagnostic analysis of the provisional solutions for the cloud variables. Thus, the prognostic volume term CLOUD(V_{phase}) is eliminated and traditional phase conversion adjustment is performed. For example, when liquid water is disappeared in the cloud fraction of a grid cell, then this fraction is appended to the non-cloud part of the cell, including the corresponding properties.

$$\begin{aligned}\text{q}^{\text{l}}_{\text{cl}} = 0, \quad \text{then} \quad & (V_{\text{env}}\,\chi_{\text{env}} + V_{\text{cl}}\,\chi_{\text{cl}})/(V_{\text{env}} + V_{\text{cl}}) \to \chi_{\text{env}}, \\ & (V_{\text{env}} + V_{\text{cl}}) \to V_{\text{env}}, \\ & V_{\text{cl}} \to 0. \end{aligned} \quad (23)$$

3.5.3. Flux balance adjustment

The relative independence of the numerical procedures between inside and outside of the VOF cells (Section 3.5.1) implicates additional adjustment for the VOF solution of Eq. (21) in the VOF cells. The non-VOF solution of Eq. (1) can be used as a benchmark, if any impact of the cloud boundary on the solution outside of the VOF cells is excluded. For this purpose, the set of VOF cells (Fig. 1a) is widened by the immediate monophase neighbour cells, so that absolute reliability of the non-VOF solution is provided outside of the VOF cells (even if Eq. (1) is solved in the whole domain). The VOF variables χ_{phase} can be bounded on the outer edge of the VOF cells by the non-VOF values and on the cloud boundary by zero gradient.

The universal flux balance of the non-VOF solution for the conservative quantities serves then to adjust the delimited VOF solution. The total of vapour and liquid water in the VOF cells must be equal for the non-VOF and the VOF solution (based on Eq. (6)). The actual ratio b between both values is used to correct the VOF variables, thereby excluding the vapour content of the cloud phase (q^{v}_{cl}) because of fixed amounts (saturation).

$$b = q(\text{non} - \text{VOF})/q(\text{VOF}), \quad (24)$$

$$\text{with} \quad q(\text{non} - \text{VOF}) = \sum_{\text{VOF-cells}} \{q^{\text{v}}(\text{non} - \text{VOF}) + q^{\text{l}}(\text{non} - \text{VOF}) - V_{\text{cl}} q^{\text{v}}_{\text{cl}}\}, \quad (25)$$

$$q(\text{VOF}) = \sum_{\text{VOF-cells}} \{q^{\text{v}}(\text{VOF}) + q^{\text{l}}(\text{VOF}) - V_{\text{cl}} q^{\text{v}}_{\text{cl}}\}, \quad (26)$$

where $q^{\text{v,l}}$(non-VOF) is determined by the standard Eq. (1) and $q^{\text{v,l}}$(VOF) by the VOF scheme. The correction factor b is applied to the phase-specific variables $q^{\text{v}}_{\text{env}}$, $q^{\text{l}}_{\text{env}}$, and q^{l}_{cl} before updating via Eq. (6). Temperature balancing by means of total heat comparison is not followed up here, since the phase conversion heat is expected to dominate the flux discrepancies.

4. Results

4.1. Details of simulations

The sensibility of the VOF method against the grid resolution and diffusion coefficients is examined for a rising thermal in a stably stratified atmosphere with potential temperature slope of 3.7 K km^{-1} and constant vapour saturation of 20%. The 2D thermal is initialised as a temperature-adapted, vapour-saturated, and minimal liquid–water charged (1×10^{-3} g kg^{-1}) bubble of the radius 80 m, surrounded by an 80 m thick shell with linear transition to the environmental humidity. In distinction to similar studies (Grabowski and Clark, 1991; Margolin et al., 1997), the concerned grid cells

were divided in 100×100 sub-cells to get exact cell averages from the sub-cell specifications and to minimise the numerical boundary instabilities. The bubble centre is positioned at a height of 160 m in the model region (width: 640 m, height: 800 m). A uniform mesh size of 5, 10, or 20 m is applied, ensuring comparable grid positions for the bubble centre (on grid node) and the edge.

Variable integration time steps amount to about 1 s. Due to third-order time integration methods, the degree of phase conversion by Eq. (4) is independent on the time step and grid resolution (Section 2). In no case the supersaturation did exceed the value 1×10^{-3} which is insignificant as compared to the achieved relative liquid water mixing ratios (q^{l}/q^{vs}) of larger than 1×10^{-2}. The reference simulations for studying the effects of activated VOF with varied spatial resolutions (Section 4.2) and diffusion coefficients (Section 4.3) are thus defined. The VOF method had been verified for the case of inactive cloud processes and constant density in a rotating wind field (preserved cloud volume and shape).

Driven by the buoyant forces, the bubble rises, condensates and warms up increasingly, while evolving vortices cause deformation and whirling. In the case of inactivated diffusion ($D = 0$), there is no way for the cloud phase to disappear, unless it falls below the condensation level. The reference simulation without VOF illustrates, however, that the traditionally simulated thermal is disrupting and disappearing at a progressive rate even above this level (Fig. 2). Numerical diffusion appears as the only source of these shortcomings.

4.2. Influence of grid resolution on VOF

Considering advective transport only, simulations were executed with and without VOF for different spatial grid resolutions (5, 10, 20 m). The cloud state after 560 s turns out to be underdeveloped for the traditional (non-VOF) simulations and, in contrast, intensively evolved for the VOF simulations (Fig. 3). Furthermore, the non-VOF results strongly depend on the grid resolution and even at highest resolution there remains a drastic discrepancy to the VOF simulations: numerical diffusion cannot ultimately be overcome by an increased spatial resolution. On the other hand, the VOF method yields total independence on the spatial resolution because of the volumetric balancing of the cloud and environmental phases, and no need of extensive high-resolved simulations arises.

In the VOF frame, extremely coarse grid resolutions can lead to more compactness and symmetry of the cloud as seen for 20 m grid spacing; however, the amount of liquid water and the intensity of the cloud evolution remain rather unaffected (Fig. 4). It is noticed in this context, that crude initialisation (Section 4.1) or shifting of the initialised bubble centre from the grid node to a mesh centre can result in altered cloud shapes and boundary instabilities also in non-VOF applications (Grabowski and Clark, 1991). Fig. 4 depicts the differences in the cloud evolution between traditional and VOF treatment on the basis of the total liquid water content in the domain. The traditional cloud evolution is unable to follow the VOF-controlled evolution and breaks down the earlier, the coarser the grid (dashed and dotted lines) and the dryer the surrounding sphere (Tradit. 0) is chosen.

4.3. Influence of diffusion on VOF

The examination of turbulent diffusion and molecular phase mixing (homogenisation) requires the specification of the corresponding coefficients (Section 3.4). For this study with a grid resolution of 5 m, four constant turbulence coefficients (D_{turb} between 0 and $10\,m^2\,s^{-1}$) and two fixed forcing factors for the turbulence-forced homogeneous mixing ($S = 1$ or 500) were chosen.

Fig. 5 shows for various turbulence conditions (4 rows), that after 10 min the cloud is disappeared (columns 1 and 2), unless advection and diffusion are both subjected to the VOF treatment (columns 3 and 4). Column 3 represents the case of a 500-fold enhanced effective phase mixing, whereas in column 4 the phase mixing is set to the minimal value. The apparent similarity between these cases signifies certain insensitivity of the VOF application against moderate phase mixing conditions and cloud ages, respectively.

The case of vanishing turbulence was discussed in Section 4.2. As soon as turbulence is present, its traditional treatment (identity between cloud deformation and phase homogenisation) leads to undelayed phase dissolution (column 2 in Fig. 5), whereas the VOF

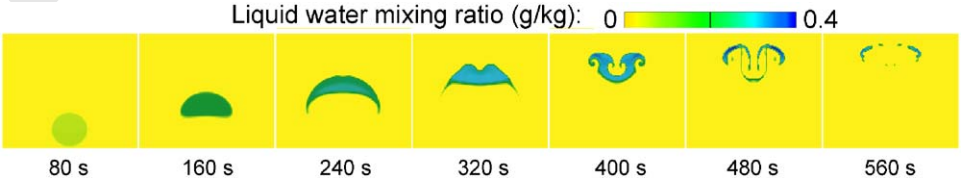

Fig. 2. Evolution of a rising thermal by the non-VOF (traditional) method without diffusion (cell width 5 m). Selected region: 640 m (width), 120 m … 660 m (height).

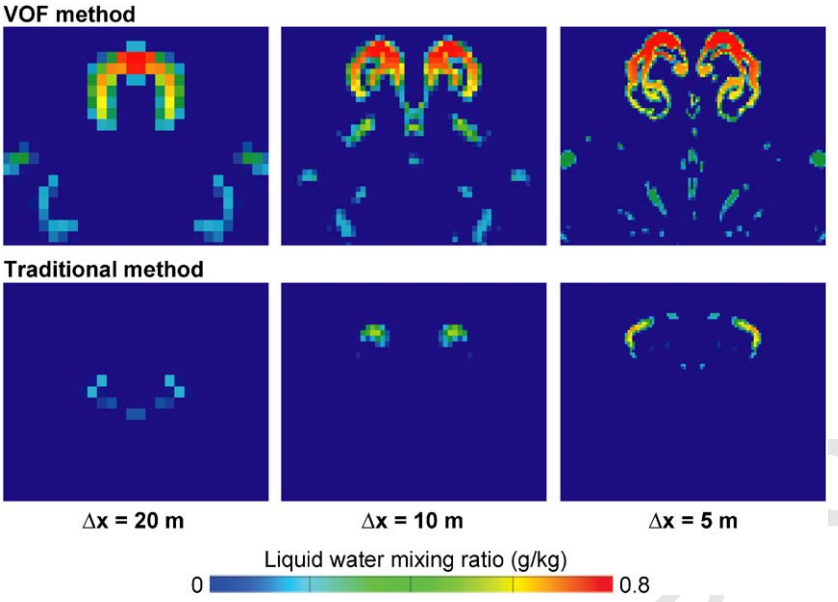

Fig. 3. Cloud after 560 s for different spatial resolutions by the VOF and non-VOF (traditional) method, without diffusion. Selected region: 520 m (width), 220 m … 660 m (height).

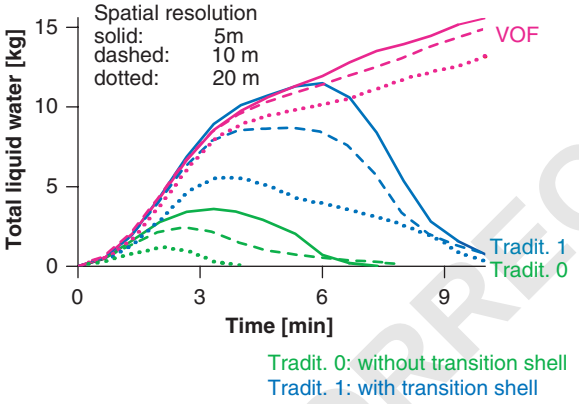

Fig. 4. Development of the total liquid water mass for different grid resolutions by the VOF and non-VOF (traditional) method, without diffusion. Initialisation without (Tradit. 0) or with (Tradit. 1, VOF) transition shell (Section 4.1).

approach enables the cloud to evolve, until the increasing homogeneous mixing prevails over turbulent deformation. The moment and region of total mixing depends on the actual situation and it is impossible here to give quantitative information. The conclusion is drawn that the VOF method contributes to longer lifetimes of the simulated clouds or cloud fractions, at least for weak turbulence. In face of the unfinished implementation of VOF in the diffusion problem (Section 3.4), the results indicate, that turbulent diffusion does by far not nullify the advantages of the VOF-controlled advection (loss-free transport).

5. Conclusions

The volume-of-fluid (VOF) method represents a very effective and forceful supplement for atmospheric grid models in describing clouds and their boundaries without numerical dissipation and loss. The following advantages compared to traditional (non-VOF) treatment can be quoted:

(1) advection process for the cloud phase without numerical loss or diffusion;
(2) turbulent diffusion with moderate cloud loss and dissipation;
(3) regained evaporation heat by prevention of numerically induced phase changes;
(4) numerically unhindered development of cloud intensity, extent, lifetime, and long-term processes;
(5) independence on the grid resolution, thus supporting low resolution and run-time;
(6) particular benefit for small clouds or cloud fragments (in relation to the grid width);
(7) phase-specific operation of the cloud processes.

Although acting with doubled cloud variables (in two-phase cells) and additional mathemathic-geometrical procedures, the VOF method enters into the basic

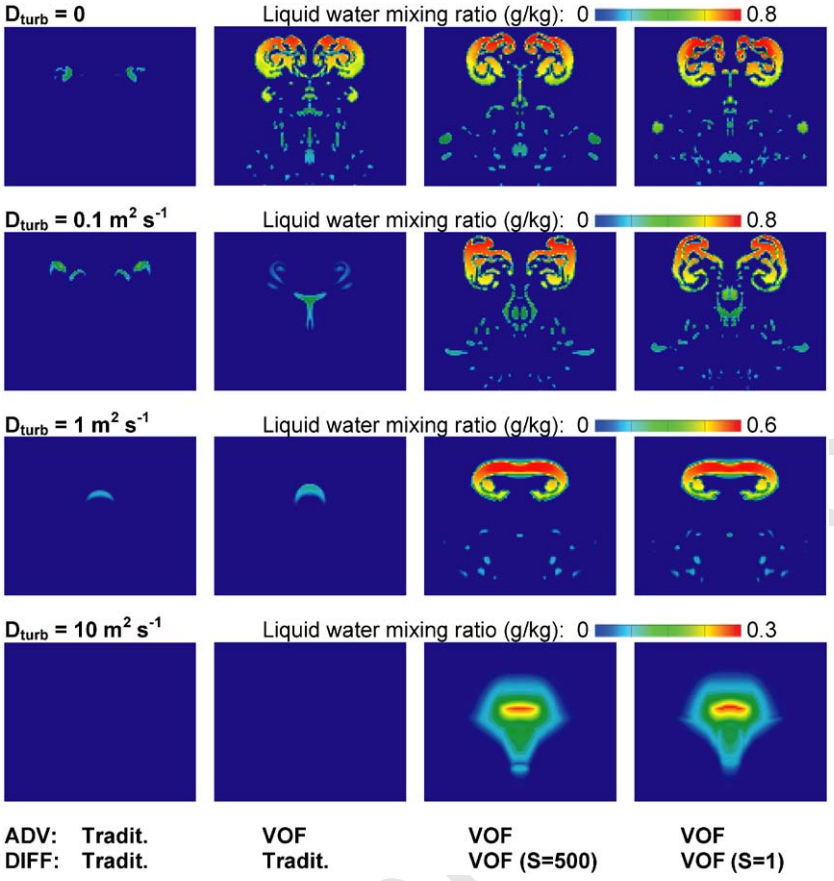

Fig. 5. Cloud after 600 s for different turbulence conditions (rows) and degrees of VOF application (columns). Selected region: 520 m (width), 220 m … 660 m (height).

atmospheric model only by updating the cell-averaged cloud variables in the limited set of VOF cells. There is no impact on the standard model procedures, and the additional numerical expense is marginal as compared to an increase of the overall grid resolution. The VOF method enables a model to dispense with high grid resolutions and thus provides for solid results at low resolution and run-time. Noticeable turbulence needs to be examined more detailed than by the present work. In a future step, the model is to be combined with an advanced cloud parcel model (Knoth, 2005; Wolke et al., 2005).

Acknowledgements

This work was supported by the Federal Ministry of Education and Research (Germany) in the frame of the German Program on Atmospheric Research (AFO 2000).

References

Broadwell, J.E., Breidenthal, R.E., 1982. A simple model of mixing and chemical reaction in a turbulent shear layer. Journal of Fluid Mechanics 125, 397–410.

Grabowski, W.W., 1989. Numerical experiments on the dynamics of the cloud-environment interface: Small cumulus in a shear-free environment. Journal of the Atmospheric Sciences 46, 3513–3541.

Grabowski, W.W., 1993. Cumulus entrainment, fine-scale mixing, and buoyancy reversal. Quarterly Journal of the Royal Meteorological Society 119, 935–956.

Grabowski, W.W., Clark, T.L., 1991. Cloud-environment interface instability: Rising thermal calculations in two spatial dimensions. Journal of the Atmospheric Sciences 48, 527–546.

Hirt, C.W., Nichols, B.D., 1981. Volume of fluid (VOF) method for the dynamics of free boundaries. Journal of Computational Physics 39, 201–225.

Hundsdorfer, W., Koren, B., vanLoon, M., Verwer, J.G., 1995. A positive finite-difference advection scheme. Journal of Computational Physics 117, 35–46.

Kao, C.-Y.J., Hang, Y.H., Reisner, J.M., Smith, W.S., 2000. Test of the volume-of-fluid method on simulations of marine boundary layer clouds. Monthly Weather Review 128, 1960–1970.

Knoth, O., 2005. A parcel model for the combined treatment of microphysical and multiphase chemical processes. Atmospheric Environment, this issue.

Krüger, S.K., Su, C.-W., McMurtry, P.A., 1997. Modeling entrainment and finescale mixing in Cumulus clouds. Journal of the Atmospheric Sciences 54, 2697–2712.

Lanser, D., Blom, J.G., Verwer, J.G., 2001. Time integration of the shallow water equations in spherical geometry. Journal of Computational Physics 171, 373–393.

Launder, B.E., Spalding, D.B., 1974. The numerical computation of turbulent flows. Computer Methods in Applied Mechanics and Engineering 3, 269–289.

Margolin, L., Reisner, J.M., Smolarkiewicz, P.K., 1997. Application of the volume-of-fluid method to the advection-condensation problem. Monthly Weather Review 125, 2265–2273.

Paluch, I.R., Baumgardner, D.G., 1989. Entrainment and finescale mixing in a continental convective cloud. Journal of Atmospheric Science 46, 261–278.

Pellerin, P., Laprise, R., Zawadzki, I., 1995. The performance of a semi-Lagrangian transport scheme for advection-condensation problem. Monthly Weather Review 123, 3318–3330.

Pilliod, J. E., Puckett, E. G., 1997. Second-order accurate volume-of-fluid algorithms for tracking material interfaces. Lawrence Berkeley National Laboratory, Technical Report LBNL-40744, 47pp.

Rogers, R. R., 1976. A short course in cloud physics. International Series in Natural Philosophy, first edition, vol. 84. Pergamon Press, Oxford.

Scardovelli, R., Zaleski, S., 2000. Analytical relations connecting linear interfaces and volume fractions in rectangular grids. Journal of Computational Physics 164, 228–237.

Schlünzen, K.H., Hinneburg, D., Knoth, O., Lambrecht, M., Leitl, B., López, S., Lüpkes, C., Panskus, H., Renner, E., Schatzmann, M., Schoenemeyer, T., Trepte, S., Wolke, R., 2003. Flow and transport in the obstacle layer: first results of the micro-scale model MITRAS. Journal of Atmospheric Chemistry 44, 113–130.

Schultz, P., 1995. An explicit cloud physics parameterization for operational numerical weather prediction. Monthly Weather Review 123, 3331–3343.

Stevens, B., Walko, R.L., Cotton, W.R., Feingold, G., 1996. The spurious production of cloud-edge supersaturations by Eulerian models. Monthly Weather Review 124, 1034–1041.

Unverdi, S.O., Tryggvason, G., 1992. A front-tracking method for viscous, incompressible, multi-fluid flows. Journal of Computational Physics 100, 25–37.

Wolke, R., Sehili, A. M., Simmel, M., Knoth, O., Tilgner, A., Hermann, H., 2005. SPACCIM: a parcel model with detailed microphysics and complex multiphase chemistry. Atmospheric Environment, this issue.

3B2v8.06a/w (Dec 5 2003).51c XML:ver:5.0.1 AEA : 5773 Prod.Type:FTP pp.1–10(col.fig.:figs1–8) ED:MangalaK. PAGN:lmn SCAN:global

ARTICLE IN PRESS

Available online at www.sciencedirect.com

SCIENCE DIRECT®

ELSEVIER

Atmospheric Environment ▮ (▮▮▮▮) ▮▮▮–▮▮▮

ATMOSPHERIC ENVIRONMENT

www.elsevier.com/locate/atmosenv

A parcel model for the combined treatment of microphysical and multiphase chemical processes

Oswald Knoth

Institut für Troposphärenforschung, D-04318 Leipzig, Permoserstrasse 15, Germany

Abstract

The accurate and efficient description of aerosol microphysical and chemical processes is required for the assessment of radiative and chemical effects of natural and anthropogenic atmospheric aerosols. The combined modeling of microphysical and chemical processes in the gas and aqueous phase such as meteorological changes, transformation of chemical species in the gas and liquid phase and the transfer of species from one phase to the other is required. Since the aforementioned processes proceed on similar time scales the usual time splitting schemes which perform process by process in a sequential order are not appropriate. In contrast to other approaches where a microphysical and a cloud chemistry model are coupled, the new approach treats both processes in a unified way both from the modeling and numerical point of view. It is argued that this new model type is better suited for incorporation in multidimensional atmospheric and transport models. Essential parts of the model are outlined. The differential equations are discretized in mass space by a discontinuous Galerkin method and integrated after that in time by an implicit–explicit time integration scheme. Numerous simulations are performed to show the reliability of the new approach. The Eulerian fixed grid approach is compared with a 2000 bin moving simulation to demonstrate the merits and demerits of a fixed grid.

Keywords: Aerosols; Growth equation; Aqueous phase chemistry; Mathematical model

1. Introduction

The accurate and efficient description of aerosol microphysical and chemical processes is required for the assessment of radiative and chemical effects of natural and anthropogenic atmospheric aerosols. The combined modeling of microphysical and chemical processes in the gas and aqueous phase such as meteorological changes, transformation of chemical species in the gas and liquid phase and the transfer of species from one phase to the other is required. Since the aforementioned processes proceed on similar time scales the usual time splitting schemes which perform process by process in a sequential order are not appropriate. Essential parts of the model are outlined and an implicit time integration method is proposed for the model simulation. In contrast to the SPACCIM model (Wolke et al., 2005) where a microphysical and a cloud chemistry model are coupled, the new approach treats both processes in a unified way both from the modeling and numerical point of view. It is believed that this new model type is better suited for incorporation in multi-dimensional atmospheric and transport models.

Our numerical approach to solve a part of the multicomponent general dynamics equation coupled with aqueous phase chemistry is based on a sectional approach. For each, section number and mass properties are used to track aerosol growth, evaporation, and

1352-2310/$ - see front matter © 2005 Elsevier Ltd. All rights reserved.
doi:10.1016/j.atmosenv.2005.02.037

chemical transformations. Aerosol particles are separated into the section by their total mass including water. A common mass grid is obtained by doubling each mass section and starts with particles in the range of 5 nm. From a mathematical point of view the discretization scheme belongs to the class of discontinuous Galerkin methods which are very popular to solve advection-type equations with discontinuities.

Interactions between cloud dynamics, microphysics and chemistry occur on different temporal and spatial scales and affect the cloud droplet number concentration (CDNC) in sometimes highly nonlinear ways. Chemical factors which can have an influence on the CDNC are among other highly soluble trace gases, slightly soluble solute, and surface tension depression due to organic compounds. Aqueous-phase chemical processing of aerosol that has participated as cloud condensation nuclei can lead to a bimodal size distribution with an increased dry mass after the cloud evaporates which can influence the CNDC of a further cloud cycle. There is a large interest in the influence of soluble trace gases in the atmosphere on the number of activated particles. In Laaksonen et al. (1998) a modified Köhler equation is presented which includes the effect of soluble gases and slightly soluble aerosol substances. It is argued that highly soluble gases, such as HNO_3 or HCl, can add solute and depress vapor pressure early in the droplet growth. For instance an enhanced nitric acid concentration can significantly increase the number of activated particles. Furthermore, slightly soluble gases, such as SO_2, can also contribute to the solute throughout the growth phase. In the current model these effects are modeled explicitly and also the dynamic aspects of the simultaneous mass flux of different gaseous species including water are taken into account. However, the description of the individual mass fluxes does not rely on the multicomponent condensation theory (Mattila et al., 1997), and for trace gases apart from water vapor the mass flux is described by the simplified approach of Schwartz (1986). Furthermore, effects due to highly concentrated particles which leads to activity coefficients different from one are neglected.

In the literature, there have been several attempts to numerically simulate cloud microphysical and chemical processes inside one model. In most cases, however, the processes are not covered with the same rigorousness. A very sophisticated model is described by Jacobson (2003) where the different processes are integrated in time by operator splitting. Modeling description for each process and an adapted unconditional time-integration scheme are presented together and often interleave. There is no hint in the paper of how the time steps of the different processes have to be chosen. In contrast, the presented approach differentiates between modeling a process and choosing later on a time-integration method for the whole model which avoids operator splitting. Furthermore, only the mass distribution is prognosed.

A model without aqueous-phase chemistry but similar to our one is given by Russel and Seinfeld (1998). To avoid the problem of merging the dry aerosol mass in different activated sections water condensation is calculated using a moving sectional approach. It should be noted that this special treatment of the water also avoids the numerical problems for the advection of the water mass in the fixed grid. The idea can easily be incorporated as an option in our implemented code. However, outside a box model application, a fixed section for all constituents may be preferable. The feedback of the condensed material to a changing water vapor saturation pressure is not mentioned in the paper.

The remainder of the paper is organized as follows. In Section 2 the numerical solution algorithm is presented. We start with the unimodal case and describe then the necessary extension for a multicomponent aerosol. Section 3 is devoted to test examples of different complexity. At first, a simple three component system containing water and soluble and non-soluble material is discussed with respect to the magnitude of the Raoult term to the numerical behavior of the proposed algorithm. The other two examples are from two model comparison exercises described in Sehili et al. (2005) and Kreidenweis et al. (2003). Some conclusions are given in Section 4.

2. Numerical solution of the condensation advection equation

2.1. The unimodal case

The aerosol particle distribution is described by a part of the general dynamics equation (GDE)

$$\frac{\partial n(m,t)}{\partial t} + \frac{\partial}{\partial m}[I(m,t)n(m,t)] = 0, \tag{1}$$

where m is the mass of the particle, $n(m,t)$ is the size distribution density function at time t, such that $n(m,t)\,\mathrm{d}m$ is the number concentration of particles in the mass interval $[m, m+\mathrm{d}m]$. $I(m,t)$ is the rate of change of total mass of a particle, $\mathrm{d}m/\mathrm{d}t$, due to condensation, evaporation and chemical transformations. Eq. (1) represents an advection-type equation for which a lot of different numerical solution methods exists, [e.g. Nguyen and Dabdub (2002), Sandu and Borden (2003), von Salzen and Schlünzen (1999), Dhaniyala and Wexler (1996)]. Here, we will concentrate on discontinuous Galerkin methods (DGM) which has been successfully applied to different kinds of nonlinear hyperbolic equations. A good introduction to the subject is given by Cockburn (1988). Without referring to DGM Tzivion et al. (1987) proposed a solution method for the

GDE which conserves the total number of concentrations in case of the pure condensation equation, the total mass concentration in case of the pure coagulation equation. A method which also conserves these two moments is described in a paper by Chen and Lamb (1992). The DGM is described first for Eq. (1) and is then generalized to the multicomponent case. To discretize in mass space, we proceed as follows. The mass space $[\underline{m}, \bar{m}]$ is partitioned in N intervals $D_k = (m_{k-1}, m_k)$, $k = 1, \ldots, N$. We seek an approximation $n_h(m,t)$ to $n(m,t)$ which coincides inside in each interval D_k with a prescribed function $n_k(m, P_k, t)$ with two degrees of freedom P_k. In order to determine the approximate solution we multiply Eq. (1) by smooth test functions v and integrate over the interval D_k, and get, after a simple integration by parts,

$$\int_{D_k} \frac{\partial n(m,t)}{\partial t} v(m)\,\mathrm{d}m - \int_{D_k} I(m,t)n(m,t)\frac{\partial v(m)}{\partial m}\,\mathrm{d}m + I(m_k,t)n(m_k,t)v(m_k^-) - I(m_{k-1},t)n(m_{k-1},t)v(m_{k-1}^+) = 0,$$

where $v(m_k^-)$ is the left-sided value of v at the point m_k and analogous for $v(m_{k-1}^+)$. Next, we replace the exact solution $n(m,t)$ by the approximate solution $n_k(m, P_k, t)$ and the smooth test functions v by the functions $v_0(m) = 1$ and $v_1(m) = m$. Since the function n_h is discontinuous at m_k the "flux" $f(n(m_k,t)) = I(m_k,t)n(m_k,t)$ has to be replaced by a numerical "flux" that depends on the two values of n_h at the point m_k, that is by the function

$$h(n)_k(t) = h(n_k(m_k^-, P_k, t), n_{k+1}(m_k^+, P_{k+1}, t)),$$

that will be suitably chosen later.

With the definition

$$N_k(t) = \int_{D_k} n_k(m, P_k, t)\,\mathrm{d}m$$

and

$$M_k(t) = \int_{D_k} n_k(m, P_k, t)\,\mathrm{d}m$$

the approximate solution given by the discontinuous Galerkin mass space discretization is defined as the solution of the following system of ordinary differential equations:

$$\frac{\partial N_k(t)}{\partial t} + h(n)_k(t) - h(n)_{k-1}(t) = 0,$$

$$\frac{\partial M_k(t)}{\partial t} + h(n)_k(t)m_k - h(n)_{k-1}(t)m_{k-1} = \int_{D_k} I(m,t)n_k(m, P_k, t)\,\mathrm{d}m. \quad (2)$$

The integral

$$\int_{D_k} I(m,t)n_k(m, P_k, t)\,\mathrm{d}m \quad (3)$$

is approximated by $N_k I(M_k/N_k, t)$ which is a second-order approximation to the integral above. It remains to specify the computation of the 'flux' function $h(n)_k(t)$. A Godunov-type flux function is applied with

$$h(n)_k(t) = \begin{cases} I(m_k,t)n_k(m_k, P_k, t) & \text{if } I(m_k,t) > 0, \\ I(m_k,t)n_{k+1}(m_k, P_{k+1}, t) & \text{if } I(m_k,t) <= 0. \end{cases} \quad (4)$$

For the evaluation of the flux function the ansatz function has to be computed in the endpoints of the interval D_k. To construct a continuous function $n_k(m, P_k)$ inside each interval D_k we make the ansatz

$$n_k(m, A_k, b_k) = A_k\left(\frac{m}{m_{k-1}}\right)^{b_k}.$$

The free parameters A_k and b_k are determined for an arbitrary interval D_k from the conditions

$$N_k = \int_{D_k} n_k(m, A_k, b_k)\,\mathrm{d}m$$

and

$$M_k = \int_{D_k} n_k(m, A_k, b_k)m\,\mathrm{d}m.$$

Without referencing to the index k and with the notation $D = [m_L, m_U]$ the nonlinear equations

$$N = \begin{cases} Am_L \ln\left(\frac{m_U}{m_L}\right) & \text{if } b = -1, \\ \frac{Am_L}{b+1}\left(\left(\frac{m_U}{m_L}\right)^{b+1} - 1\right) & \text{otherwise} \end{cases}$$

and

$$M = \begin{cases} Am_L^2 \ln\left(\frac{n_U}{x_L}\right) & \text{if } b = -2, \\ \frac{Am_L^2}{b+2}\left(\left(\frac{m_U}{m_L}\right)^{b+2} - 1\right) & \text{otherwise} \end{cases}$$

are obtained. In the cases $b \neq -1$ and -2 the parameter b is the unique solution of the nonlinear equation

$$\psi(b) = \frac{(p^{b+2} - 1)/(b+2)}{(p^{b+1} - 1)/(b+1)} = \frac{M}{Nm_L},$$

where $p = m_U/m_L$. The function ψ is differentiable in the argument b and convex–concave with an inflection point in $b = 0$. Therefore Newton's method converges globally starting from $b = 0$.

2.2. Condensational growth for multicomponent systems

For a multicomponent system, we make the assumption that particles of the same mass m have the same composition with partial masses $m^l(m,t)$, $l = 1, \ldots, L$. This implies

$$m = \sum_{l=1}^{L} m^l(m,t)$$

and

$$I(m^1,\ldots,m^L) = \frac{\mathrm{d}m}{\mathrm{d}t} = \sum_{l=1}^{L} \frac{\mathrm{d}m^l}{\mathrm{d}t} = \sum_{i=1}^{L} I_l(m^1,\ldots,m^L).$$

The condensational growth takes the form

$$\frac{\partial n(m,t)}{\partial t} = -\frac{\partial}{\partial m}[I(m^1,\ldots,m^L)n(m,t)].$$

Instead of the second test function m the partial mass functions $m^l(m,t)$ are used. Integration over the interval D_k

$$\int_{D_k} \frac{\partial n(m,t)}{\partial t} m^l(m,t)\,\mathrm{d}m = -\int_{D_k} \frac{\partial}{\partial m}[I(m^1,\ldots,m^L)n] \times m^l(m,t)\,\mathrm{d}m$$

and partial integration

$$\int_{D_k} \frac{\partial}{\partial t}[n(m,t)m^l(m,t)]\,\mathrm{d}m = -[I(m^1,\ldots,m^L)n(m,t)m^l(m,t)]_{m_{k-1}}^{m_k} + \int_{D_k}\left[I(m^1,\ldots,m^L)\frac{\partial m^l(m,t)}{\partial m} + \frac{\partial m^l(m,t)}{\partial t}\right] \times n(m,t)\,\mathrm{d}m,$$

$$\int_{D_k} \frac{\partial}{\partial t}[n(m,t)m^l(m,t)]\,\mathrm{d}m = -[I(m^1,\ldots,m^L)n(m,t)m^l(m,t)]_{m_{k-1}}^{m_k} + \int_{D_k} n(m,t)I_l(m^1,\ldots,m^L)\,\mathrm{d}m.$$

With the definition

$$M_k^l(t) = \int_{D_k} n_k(m,P_k,t)m^l(m,t)\,\mathrm{d}m$$

we get

$$\frac{\partial M_k^l(t)}{\partial t} = -[I(m^1,\ldots,m^L)n(m,t)m^l(m,t)]_{m_{k-1}}^{m_k} + N_k I_l(M_k^1/N_k,\ldots,M_k^L/N_k), \quad (5)$$

where the last integral is approximated similar to integral (3). Finally, the advective part of Eq. (5) has to be discretized. As a first approach we use

$$h(n)_k(t)m_k^l = \begin{cases} I(m_k,t)n_k(m_k,P_k,t) \times m_k\dfrac{M_k^l}{M_k} & \text{if } I(m_k,t) > 0, \\ I(m_k,t)n_{k+1}(mk,P_{k+1},t) \times m_k\dfrac{M_{k+1}^l}{M_{k+1}} & \text{if } I(m_k,t) <= 0. \end{cases} \quad (6)$$

A more sophisticated approach relies on a further interpolation of the cell values of the mixing ratio $\xi_k^l = M_k^l/M_k$ to the cell interfaces by a third-order-biased upwind formula together with the Van Leer limiter. See Hundsdorfer et al. (1995) for a comprehensive survey. Depending on the sign of the rate change at a cell interface two upwind cell values and one downwind cell value are used in the interpolation. The rate change $I(m,t)$ is interpolated linearly from the two values $I(M_k^1/N_k,\ldots,M_k^L/N_k)$ and $I(M_{k+1}^1/N_{k+1},\ldots,M_{k+1}^L/N_{k+1})$. The time integration of the semidiscretized system will be described later on after the specification of the rate change functions I_l for a coupled microphysics chemistry model.

2.3. The microphysics chemistry model

In the model we assume that the particles are internally mixed and composed by water and other soluble and non-soluble chemical species. The masses of these substances for an individual particle are denoted by m_W, m_S^l, $l = 1,\ldots,L_S$ and $m_U^{l'}$, $l' = 1,\ldots,L_U$ respectively, their molar masses by M_W, M_S^l and $M_U^{l'}$. The condensation/evaporation of water vapor is described after Pruppacher and Klett (1997) by

$$I_W = \frac{\mathrm{d}m_W}{\mathrm{d}t} = Gr(S - S_{eq})$$

where r is the radius of the particle, S the supersaturation and S_{eq} equilibrium supersaturation. The kinetic factor G is given by

$$G = \frac{1}{R_v T/e_{s,w}D^* + (L_v/R_v T - 1)L_v/K^* T}$$

with L_v the latent heat of condensation, $e_{s,w}$ the saturation vapor pressure, D^* the modified diffusion coefficient for water vapor in air, K^* the modified thermal conductivity of air.

$$D^* = \left[\frac{1}{\alpha_C r}\sqrt{\frac{2\pi}{R_v T}} + \frac{r}{D(r+\Delta_v)}\right]^{-1}$$

with

$$D = 4.0122\ 10^{-5}\,\frac{T^{1.94}}{p}$$

and

$$K^* = \left[\frac{1}{\alpha_T C_p \rho_{Air} r}\sqrt{\frac{2\pi}{R_{Dry} T}} + \frac{r}{D(r+\Delta_T)}\right]^{-1}$$

with

$$K = 418.5\ 10^{-5}(5.69 + 0.017(T - 273.15)).$$

The equilibrium supersaturation S_{eq} is modeled using Köhler theory by

$$S_{eq} = \frac{m_W/M_W}{\sum_l m_S^l/M_S^l} \exp\left[\frac{2\sigma}{R_v T \rho_W r}\right]$$

with R_v gas constant for water vapor, ρ_W density of water. The sum $\sum_l m_S^l/M_S^l$ goes through all soluble species including water. The surface tension σ depends only from temperature T

$$\sigma = 0.2358(1 - T/647.069)^{1.256} \times (1 - 0.625(1 - T/647.069))$$

where T is measured in Kelvin.

The transfer of other gaseous species than water vapor follows the kinetic formulation of mass transfer defined in Schwartz (1986)

$$I_H(m_S, m_W) = k_t\left(\frac{m_W}{\rho_W} C_G - \frac{m_S}{M_S}\frac{1}{k_H R T}\right)$$

with

$$k_t = \left[\frac{r^2}{3D_g} + \frac{4r}{3v\alpha}\right]^{-1},$$

where D_g is the gaseous diffusion coefficient, $v = \sqrt{8R_B T/(\pi M_S)}$ is the mean quadratic speed of the corresponding gaseous species (R_B Boltzmann constant) and α the accommodation coefficient of the species. Besides the mass transfer from the gas phase to the particle phase and vice versa the rate change $I_l(m,t)$ of the individual species in the particle phase also includes the chemical transformation between these species. Because these transformations conserve the total mass of the particle they do not contribute to the overall rate change $I(m,t)$. For a typical second-order reaction with the reaction partners A and B the contribution of this reaction rate change to I_A is

$$-kM_A m_W \frac{m_A}{M_A m_W}\frac{m_B}{M_B m_W}.$$

The model is completed with a gas phase mechanism and is embedded in an adiabatic dry parcel meteorological model. The phase transfer results to a reverse change in the concentration of the corresponding gas phase species including water vapor whereby the exchange with the particles in every interval has to be taken into account.

2.4. Time integration of the coupled model

For the integration in time we start from the discretized equations (2) and (5), whereas Eq. (2) is a pure advection equation the discretized equations for the partial masses are of advection-reaction type. Since the global rate change I is very sensitive to small changes in the composition of the particles due to the Raoult term in the change rate of water an additional relaxation equation for the rate change is introduced

$$\frac{dI_k^\varepsilon}{dt} = 1/\varepsilon(I_k(m,t) - I_k^\varepsilon), \tag{7}$$

and I_k re replaced by I_k^ε in the advective part of Eqs. (2) and (5). For the limit $\varepsilon \to 0$ the original equations are recovered. To this relaxed equation an implicit–explicit time-integration scheme is applied where the advective part is integrated with an explicit integration method and the reactive and the relaxation part with an implicit one. Here we present the simplest one which is a combination of the forward and backward Euler method. For this purpose the relaxed equations are represented in the form

$$\frac{dy}{dt} = F_E(y,t) + F_I(y,t), \tag{8}$$

where F_E denotes the part in the equations which will be integrated explicitly and F_I the implicitly integrated one. A new approximation in time $u^{n+1} \approx y(t_n + \Delta t_n)$ are computed from a given time approximation $u^n \approx y(t_n)$ from the nonlinear equation

$$u^{n+1} - u^n = \Delta t(F_E(u^n, t_n) + F_I(u^{n+1}, t + \Delta t_n)).$$

To determine u^{n+1} a simplified Newton method is used with a fixed number of iterations. Simplified means that the necessary Jacobian matrix is held fixed during the iteration so the matrix is computed only once for each integration step. For the solution of the linear system in the Newton method the special structure of the Jacobian matrix is exploited in a two fold way. At first, note that this matrix has a block structure where the blocks correspond to each of the mass intervals and the last one to the gas phase and the other meteorological unknowns. Furthermore, each of the blocks represent a sparse matrix by itself. A detailed solution algorithm for this special type of linear equations is outlined in Wolke and Knoth (2002). The main advantage of the algorithm is that the computational costs only increase linearly with number of grid cells.

This method belongs to the class of implicit–explicit Runge–Kutta methods which are discussed for instance in Ascher et al. (1995). The choice of the time step is regulated by an automatic error control and time step restriction due to a CFL condition.

3. Model applications

For all Eulerian simulations (fixed grid approach) presented a grid with 66 sections are used in mass space with mass doubling after each bin. The first mass point corresponds to particles with a radius of 1 nm. For comparison purposes part of the simulations are also carried out with the same model in a moving framework. To do this the advective part F_E is set equal to zero in Eq. (8). Runs are performed with two 2000 bins which are logarithmically distributed within the fixed grid

width. This solution is also referenced as the exact solution. To compare the results, the output is transformed back to the fixed grid by inserting each moving bin according to its mean mass in the fixed grid cells. The adiabatic parcel model is applied to two different meteorological scenarios. A detailed description is given in the electronic supplementary material of Sehili et al. (2005). The first scenario is inspired by Kreidenweis et al. (2003) and simulates an air parcel lifted up adiabatically at $0.5\,m\,s^{-1}$ from 98 m below cloud base up to 1200 m. The simulation time is 2596 s with the cloud base being reached at 196 s. The second scenario simulates an orographic cloud which occurs three times due to the underlying orography. The aerosol is therefore processed by three cloud events. Each cycle includes three phases, ascent, horizontal flow in the cloud and descent. The initial relative humidity is 95% and it is assumed that the amount of water which is contained in the particles is in equilibrium with this vapor pressure and that all soluble material is completely solved. Both meteorological scenarios are then combined with different dry aerosol distributions and aqueous- and gas-phase chemical mechanisms. All results which are discussed afterwards refer to simulations within the fixed grid (Eulerian) approach.

In the actual implementation the adaptive time step selection is done by Richardson extrapolation where the implicit–explicit method is applied for a given time step and then again twice for the time step halved. The two solutions obtained are then involved in the new time step selection. Furthermore, the time step is restricted by the CFL number and a prescribed maximal time step. The number of Newton iteration is fixed during the whole time integration period and is set to 5. The mass mixing ratios at the cell interfaces are determined by the three-point interpolation method with limiting.

3.1. A simple three component example without chemistry

In the first example (SIMPLE), the dry aerosol is composed by a soluble and a non-soluble component which are mixed at a ratio of 1:1 and have the same mass. The molar mass of the soluble component is assumed to be 1, 10, or 100, which reduces the number of solved moles. For the meteorology scenario 2 is used. Let us start the discussion of the computational results for the base case with a molar mass of 10. Fig. 1 shows the number distribution at the middle of the three summits in comparison to the exact solution which should be the same for the three events and the number of activated (particles with a diameter larger than 1 μm) particles during the whole simulation period. Due to the numerical diffusion and the finite resolution the number of activated particles decreases from summit to summit. For the same reasons, a bimodal structure of the number distribution appears after the first evaporation cycle for the base case and a molar mass 100, whereas the exact solution agrees with the initial distribution. In Fig. 2 the number distribution at the valley level is plotted for the three cases. The bimodal structure is more pronounced after the further evaporation events but are similar to the first one which means that essentially only this "new" mode is activated during the next cloud passages. For the smaller amount of soluble moles the bimodal structure is yet more visible which is the result of a smaller number of activated particles and therefore larger droplets. These droplets contain more dry mass than particles in the initial dry distribution. In addition the "new" mode benefits more from the water available in the system. A decreasing number of soluble molecules leads also to an increased number of time steps (cf. Fig. 3) which is mainly caused by smaller CFL-numbers. In Fig. 4 the CFL-number is plotted together with the number distribution at time point 780 s for the base case and molar mass 100. The CFL-number is small in the region which separates the non-activated and activated

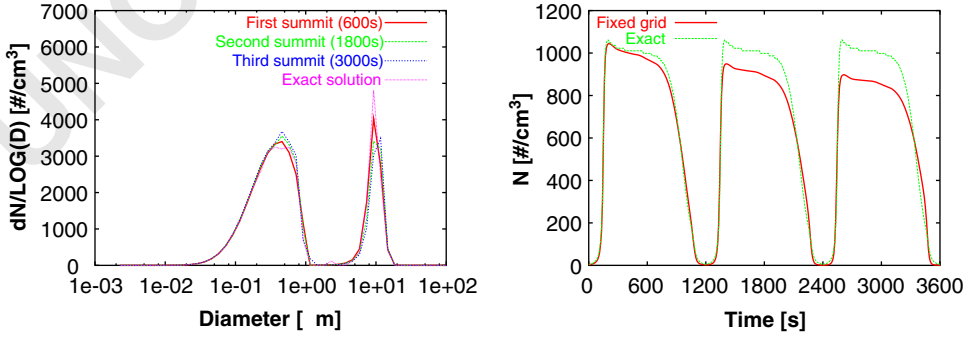

Fig. 1. Number distribution for the example SIMPLE for the base case on the three summits and the exact solution (left); number of activated particles (right).

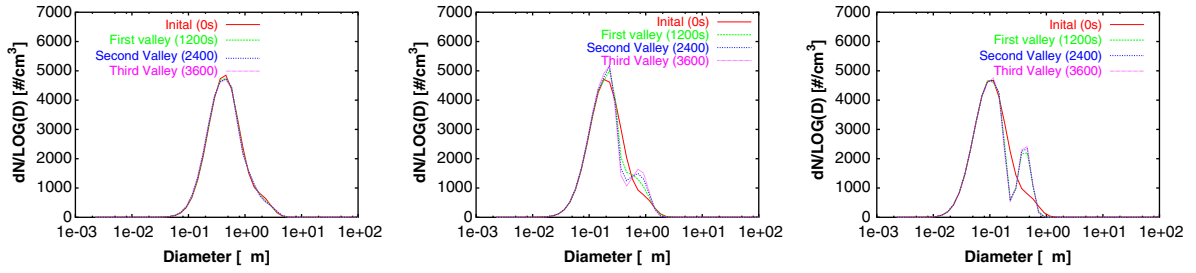

Fig. 2. Number distribution for the example SIMPLE for the base case on the four valley levels with increasing molar mass from left to right.

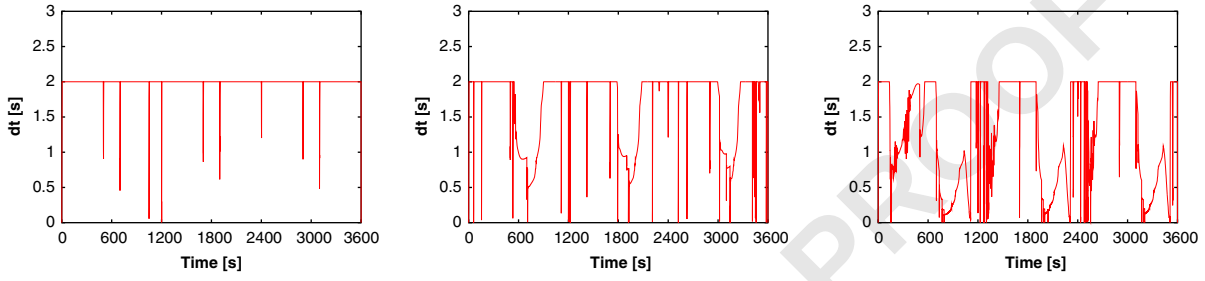

Fig. 3. Time steps taken during the time integration with increasing molar mass from left to right.

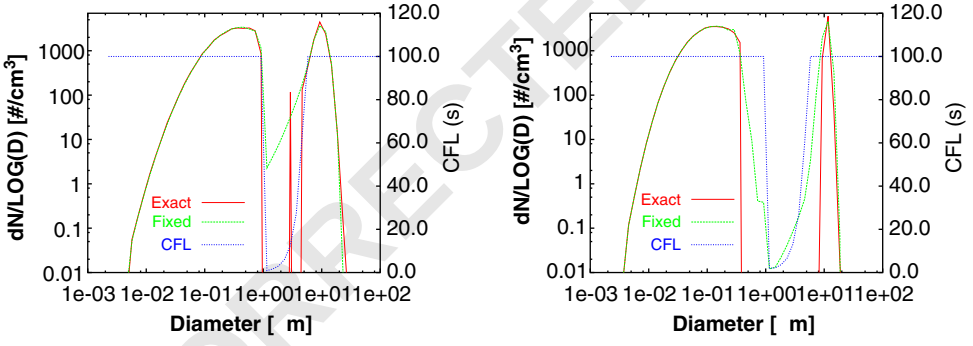

Fig. 4. Number distribution and CFL-number at 780 s for the base case (left) and molar mass 100 (right).

particles and where in the exact solution no or only a few number of particles are present. These particles are very unstable and fall back after activation in a non-activated state. For the fixed grid approach there are always some evaporating particles whose total mass falls into this region. This small amount of particles unfortunately determines the feasible maximal time step. It is also observed (not shown) that the amount of soluble mass in these particles is smaller than in the largest non-activated ones which also increases the differences between vapor and surface vapor pressure. This artifact is only caused by the proposed numerical method and deserves more research in the future. A remedy to the problem may be an artificial delay of the evaporation.

3.2. *Microphysics coupled with aqueous phase chemical mechanism CAPRAM*

For the same meteorological conditions and the same initial number distribution the simulation is repeated for a realistic multicomponent aerosol and the aqueous chemistry mechanism CAPRAM 2.3. The aqueous-phase chemistry mechanism CAPRAM 2.3 (Chemical Aqueous Phase RAdical Mechanism) (Herrmann et al., 2000) contains an explicit description of aqueous-phase chemical transformation of tropospheric constituent initiated by primary radicals and secondary radical anions such as OH, NO_3, SO_4^-, Cl_2^-, Br_2^- or CO_3^-. In addition, a module of halogen activation is also

included. Apart from that, CAPRAM 2.3 considers organic compounds up to two carbon atoms. Starting from the alcohols, methanol and ethanol, the aldehydes and acids are produced. The gas phase in CAPRAM 2.3 is RACM and is described in Stockwell et al. (1997). The mechanism is available in electronic form under "http://projects.tropos.de:8088/capram/". The additional uptake of constituents from the gas phase leads already for the exact solution to a bimodal structure of the number distribution. Another new feature is that the non-activated particles are shifted to the left from valley to valley. Due to the uptake of trace gases and chemical conversion in the gas phase there is a change in vapor pressure of soluble trace gases which leads to a redistribution of soluble volatile material from smaller to larger particles. This solution is compared to the fixed grid solution with and without chemistry in Figs. 5 and 6 in the consecutive valleys. The appearance of a bimodal structure as already mentioned in the discussion of the previous example due to the logarithmically grid coarsening is also seen in the comparison of the three cases. It is evident that the numerical influence on this mode splitting is more dominant versus the enhancement of mass by gas uptake and subsequent aqueous-phase chemical transformations. Concerning the redistribution of volatile mass between particles we should mention that the modeling of the small particles do not account for the activity of a solute due to the interactions between ions (Knipping and Dabdub, 2002). The incorporation of the activity can increase the effective Henry's constant which on its part lowers the surface vapor pressure and is therefore opposite to the described effect.

3.3. The cloud chemistry comparison example

The last application of the model is an example from the aerosol parcel model component of the Fifth International Cloud Modeling Workshop, (Kreidenweis et al., 2003). Dissolved constituents in cloud water result from the scavenging of a specified lognormal dry aerosol size distribution and dissolution of gases, and concentrations are modified by the oxidation of SO_2 by H_2O_2 and O_3. The chemical composition of cloud water is simulated for an air parcel lifted adiabatically at $0.5\,m\,s^{-1}$ starting from a height slightly below cloud base. The simulation time is 2596 s with the cloud base being reached at 196 s. The initial ammonium and sulfate concentrations of the dry aerosol represent a slightly acidic ammonium bisulfate. The initial ammonia gas concentration is not in equilibrium with this aerosol composition. For more details cf. Kreidenweis et al. (2003). The obtained results fit well in the range of results presented for the different models in the paper. The number of activated particles is $320\,cm^{-3}$ for the exact solution and $324\,cm^{-3}$ for the fixed grid solution

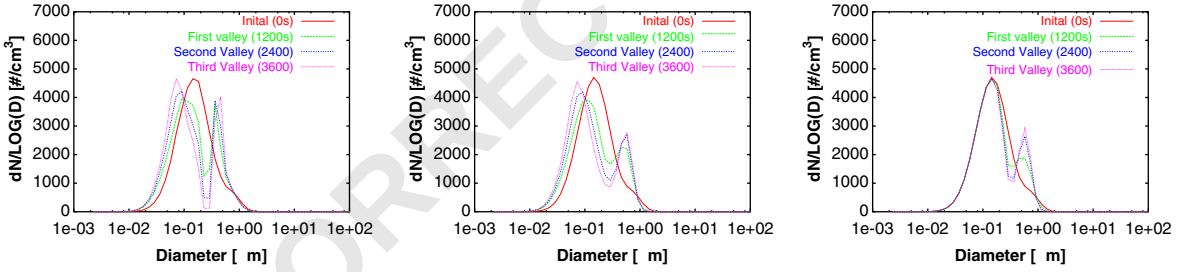

Fig. 5. Number distribution for the example CAPRAM with chemistry, exact (left), fixed (middle), and without chemistry with a fixed grid (right).

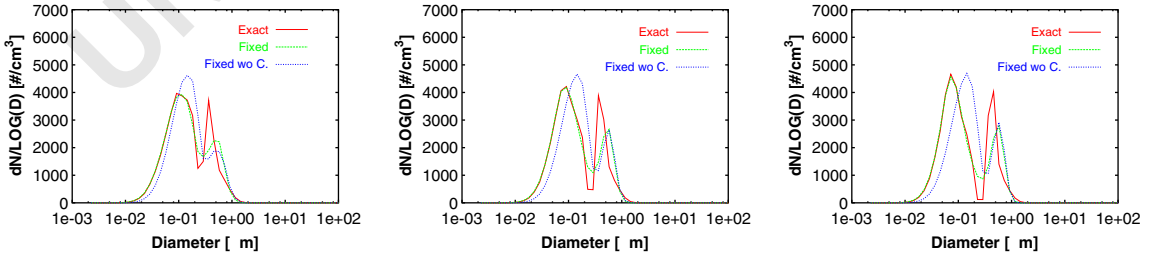

Fig. 6. Comparison of the number distribution in the consecutive valleys for the example CAPRAM for the cases exact and fixed grid with chemistry and fixed grid without chemistry, 1200 s (left), 2400 s (middle), 3600 s (right).

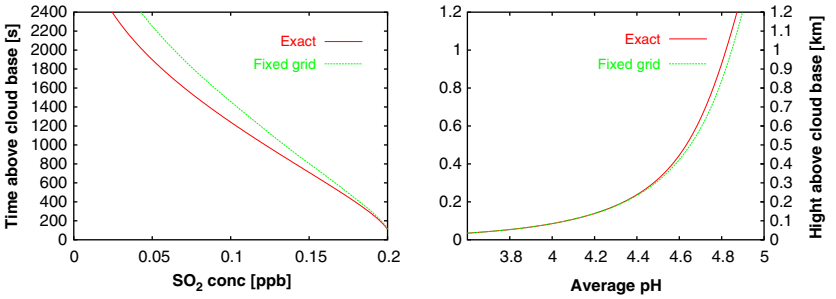

Fig. 7. Vertical variation of SO_2 (left) and average cloud water pH (right).

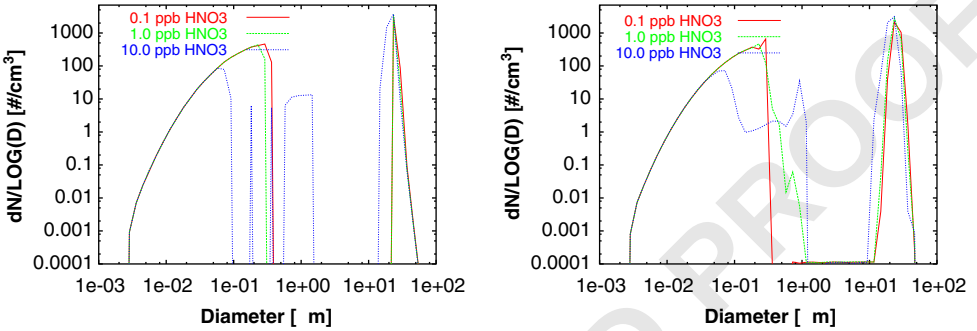

Fig. 8. Number distribution at the end of the simulation for the three different initial concentrations of HNO_3, exact simulation (left), fixed grid simulation (right).

where the variation in the participating models is from 275 to 358 cm^{-3}. In Fig. 7 (left) the uptake of SO_2 is shown for the exact and the fixed grid solution where more SO_2 is consumed in the moving bin approach. The curve presented here for 2000 moving bins is also reproduced for 25 bins spanning the same range. The reason for this difference is the high sensitivity of the sulfate production in the aqueous phase from the existing pH value. The average pH value is 4.87 for the exact case and 4.9 for the fixed grid case. A comparison of the number distribution at the end of the simulation show that the activated part in the fixed grid is broader and shifted to the right compared to the exact solution. Larger droplets are more diluted, and therefore the increase in the pH value. See also the discussion in Kreidenweis et al. (2003).

Finally, the effect of an increased initial concentration of nitric acid (HNO_3) on the number of activated particles is presented. This exercise is not a part of the comparison example. For a detailed study concerning the influence of nitric acid compare the paper by Xue and Feingold (2004). In addition to the above base case with an initial concentration of HNO_3 of 0.1 ppb runs with a concentration of 1 and 10 ppb are carried out where all other conditions are remain unchanged. As expected the number of activated particles are increased from 324 to 366 cm^{-3} and finally 532 cm^{-3}. In Fig. 8 number concentration at the end of the simulation is plotted for the three initial concentrations of nitric acid. The activated part is broadened and shifted to the left with increasing initial concentrations. Note that for an initial concentration of 10 ppb there is a third mode of evaporating particles which is present both in the exact solution and the fixed grid one. A part of this intermediate mode belongs in our definition to the activated particle spectrum. In contrast, a 10 fold increase of the SO_2 gas-phase concentration has no influence on the number of activated droplets.

4. Conclusion

A combined microphysical and aqueous-phase chemistry model has developed in order to explain a variety of microphysical and atmospheric chemistry problems and their interaction. The proposed numerical scheme handles all processes in a coupled manner and allows to simulate the activation and processing of aerosols of different chemical compositions. The simulation system is very flexible with respect to the aerosol composition and the use of the gas- and aqueous-phase chemical mechanisms and the grid structure. If coagulation is not

important it can be run in a moving and fixed grid mode. In the model, number and mass concentration are prognosed and conserved unless there are no particles produced by nucleation or mass is transferred to or from the particles. The model is open to incorporate more sophisticated rate changes like the inclusion of the surface tension depending on the chemical composition and the consideration of activity coefficients both for the transfer of water vapor and other trace gases. The aqueous-phase chemical mechanism allows furthermore the description of low soluble material in the particle whose solubility depends on the acidity and composition of the particle. The proposed examples indicate that the model and the proposed numerical method are reliable and that a fixed grid approach compares very well with a high resolution moving grid solution. Numerical artefacts which are inherent to the fixed grid approach are discussed and should be in mind when discussing more complex applications.

References

Ascher, U., Ruuth, S., Wetton, B., 1995. Implicit–explicit methods for time-dependent PDE's. SIAM Journal of Numerical Analysis 32, 797–823.

Chen, J.-P., Lamb, D., 1992. Simulation of cloud microphysical and chemical processes using a multicomponent framework. Part I: Description of the microphysical model. Journal of the Atmospheric Sciences 51, 2613–2630.

Cockburn, B., 1988. An introduction to the discontinuous Galerkin method for convection-dominated problems. In: Quarteroni, A. (Ed.), Advanced Numerical Approximation of Non-linear Hyperbolic Equations. Springer, Berlin, pp. 151–268.

Dhaniyala, S., Wexler, A.S., 1996. Numerical schemes to model condensation and evaporation of aerosols. Atmospheric Environment 30, 919–928.

Herrmann, H., Ervens, B., Jacobi, H.-W., Wolke, R., Nowacki, P., Zellner, R., 2000. CAPRAM2.3: a chemical aqueous phase radical mechanism for tropospheric chemistry. Journal of Atmospheric Chemistry 36, 231–284.

Hundsdorfer, W., Koren, B., van Loon, M., Verwer, J.G., 1995. A positive finite-difference advection scheme. Journal of Computational Physics 117, 35–46.

Jacobson, M.Z., 2003. Development of mixed-phase clouds from multiple aerosol size distributions and the effect of the clouds on aerosol removal. Journal of Geophysical Research 108 (D8), 4245.

Knipping, E.M., Dabdub, D., 2002. Modeling Cl_2 formation from aqueous NaCl particles: evidence for interfacial reactions and importance of Cl_2 decomposition in alkaline solution. Journal of Geophysical Research 107 (D18), 4360.

Kreidenweis, S.M., Walcek, C.J., Feingold, G., Gong, W., Jacobson, M.Z., Kim, C.-H., Liu, X., Penner, J.E., Nenes, A., Seinfeld, J.H., 2003. Modification of aerosol mass and size distribution due to aqueous-phase SO_2 oxidation in clouds: comparison of several models. Journal of Geophysical Research 108 (D7), 4213.

Laaksonen, A., Korhonen, P., Kulmala, M., Charlson, R.J., 1998. Modification of the Köhler equation to include soluble trace gases and slightly soluble substances. Journal of the Atmospheric Sciences 55, 853–862.

Mattila, T., Kulmala, M., Vesala, T., 1997. On the condensational growth of a multicomponent droplet. Journal of Aerosol Science 28, 553–564.

Nguyen, K., Dabdub, D., 2002. Semi-Lagrangian flux scheme for the solution of the aerosol condensation/evaporation equation. Aerosol Science and Technology 36, 407–418.

Pruppacher, H.R., Klett, J.D., 1997. Microphysics of Clouds and Precipitation. Kluwer Academic Publishers, Dordrecht.

Russel, L.M., Seinfeld, J.H., 1998. Size- and composition-resolved externally mixed aerosol model. Aerosol Science and Technology 28, 403–416.

Sandu, A., Borden, C., 2003. A framework for the numerical treatment of aerosol dynamics. Applied Numerical Mathematics 45, 475–497.

Schwartz, S., 1986. Mass transport considerations pertinent to aqueous phase reactions of gases in liquid water clouds. In: Jaeschke, W. (Ed.), NATO ASI Series, vol. G6. Chemistry of Multiphase Atmospheric Systems. Springer, Berlin, pp. 415–471.

Sehili, A.M., Wolke, R., Knoth, O., Simmel, M., Tilgner, A., Herrmann, H., 2005. Comparison of different model approaches for the simulation of multiphase processes. Atmospheric Environment, this issue.

Stockwell, W.R., Kirchner, F., Kuhn, M., Seefeld, S., 1997. A new mechanism for regional atmospheric chemistry modelling. Journal of Geophysical Research 102 (D22), 25847–25879.

Tzivion, S., Feingold, G., Levin, Z., 1987. An efficient numerical solution to the stochastic-collection equation. Journal of the Atmospheric Sciences 44, 3139–3149.

von Salzen, K., Schlünzen, K.H., 1999. A prognostic physico-chemical model of secondary and marine inorganic multicomponent aerosols. Part I. Model description. Atmospheric Environment 33, 567–576.

Wolke, R., Knoth, O., 2002. Time-integration of multiphase chemistry in size-resolved cloud models. Applied Numerical Mathematics 42, 473–487.

Wolke, R., Sehili, A.M., Simmel, M., Knoth, O., Tilgner, A., Herrmann, H., 2005. SPACCIM: a parcel model with detailed microphysics and complex multiphase chemistry. Atmospheric Environment, this issue.

Xue, H., Feingold, G., 2004. A modeling study of the effect of nitric acid on cloud properties. Journal of Geophysical Research 109, D18204.

3B2v8.06a/w (Dec 5 2003).51c XML:ver:5.0.1 AEA : 5774 Prod.Type:FTP pp.1–10(col.fig.:NIL) ED:AnilaM. PAGN:CSR SCAN:Global

ARTICLE IN PRESS

Available online at www.sciencedirect.com

SCIENCE DIRECT®

ELSEVIER

Atmospheric Environment ▮ (▮▮▮▮) ▮▮▮–▮▮▮

ATMOSPHERIC ENVIRONMENT

www.elsevier.com/locate/atmosenv

ISSA (iterative screening and structure analysis)—a new reduction method and its application to the tropospheric cloud chemical mechanism RACM/CAPRAM2.4

G. Mauersberger*

Fakultät für Umweltwissenschaften und Verfahrenstechnik, Brandenburgische Technische Universität Cottbus, Postfach 101344, D-03013 Cottbus, Germany

Abstract

An automated reduction method ISSA (iterative screening and structure analysis) has been developed. It is aimed at the analysis of complex atmospheric chemical multiphase mechanisms and produces reduced mechanisms for specifiable application purposes. Cyclic and non-cyclic reactions identified by a structure analysis are separately evaluated. The normalized valuation coefficients are calculated in a box model framework by using time-averaged reaction rates. Starting with a set of target species, important reactions and species are selected together in an iteration procedure. So, only one threshold value fixed for all box model scenarios is necessary. For every scenario a specific reduced mechanism is obtained. The sum of reactions and species included in the specific reduced mechanisms generates then the ISSA-reduced mechanism. All reactants in the reduced mechanism are included in the verification procedure where the concentrations simulated with the full and the reduced mechanism are compared. The maximum relative deviation of daily maxima was found to be a suitable deviation measure for atmospheric trace species concentrations.

An application of the ISSA method to the large cloud chemical mechanism RACM/CAPRAM2.4 resulted in reduction rates of 55% for reactions (46% gas phase, 60% liquid phase), 23% for species, and 23% for phase transfers. The deviation between full and reduced mechanism averaged over all scenarios and reactants was 2.5%. The liquid-phase part of this application was compared with a condensed version of the CAPARAM2.4 mechanism developed simultaneously with the full version. It was found that these two reduced versions of CAPRAM2.4 differ significantly. Whereas the condensed version achieves good verification results only for the target species, the ISSA-reduced version reproduce very well the complete full mechanism results and should be useful for future large-scale models, which will include both detailed microphysics and complex (reduced) multiphase chemistry.

Keywords: Modelling; Automatic mechanism reduction; Multiphase photochemistry; Deviation measure; Cloud-chemical box model

1. Introduction

In contrast to technical applications, the input of chemical reactive substances to the atmosphere is determined by all emission types and therefore not a controlled process. The number of atmospheric trace species considered in regional chemistry-transport models increases continuously, the reaction mechanisms used in these models become more and more complex. The current model generation is usually limited to pure gas-phase chemistry. Nevertheless, most part of present-day

*Corresponding author.
E-mail address: mau@tu-cottbus.de.

1352-2310/$ - see front matter © 2005 Published by Elsevier Ltd.
doi:10.1016/j.atmosenv.2005.02.015

computation costs is already caused by the chemical code, which is therefore restricting all further model developments. In order to counteract this trend, mechanism reduction techniques mostly developed to simplify complex combustion mechanisms are increasingly used in the chemistry of polluted troposphere.

Mechanism reduction methods can be divided into two groups: either with or without reformulation of the original mechanism. The first category comprises the species lumping technique where species with similar reactivity are manually (Stockwell et al., 1997) or automatically (Fish, 2000) lumped together into a single variable and the timescale analysis where the quasi-steady-state approximation (QSSA) is applied (Hesstvedt et al., 1978; Neophytou et al., 2004). The mechanisms are reduced by these methods but an identification of redundant reactions or species is not included.

As well as decreasing the computation costs, the reduction methods in the second category provide important information for mechanism development. This paper focuses on such methods in the second category that select not only redundant reactions but also redundant species. This condition is satisfied by the well-established sensitivity analysis applied by Turányi (1990a), Tomlin et al. (1992), Heard et al. (1998) and Carslaw et al. (1999) as a semiautomatic technique that combines sensitivity analysis and QSSA in the method package KINAL (Turányi, 1990b). The sensitivity analysis selects important species in an iteration procedure using elements of the Jacobian. Redundant reactions are identified via principal component analysis of the rate sensitivity matrix. Here, three threshold values are required. Notably, the determination of a threshold value for the species selection is difficult (Turányi, 1990a). Suitable values differ from application to application and vary during the iteration procedure. Additionally, a rate of net production analysis is carried out to eliminate redundant fast reversible reactions.

In contrast to sensitivity analysis, the iterative screening and structure analysis (ISSA) method proposed in this paper is mathematically simple and can be automatically performed. Important species and important reactions are selected together; only one fixed threshold value for normalised valuation coefficients is necessary. A chemical degradation mechanism of dimethoxymethane (Geiger and Becker, 1999) was used to compare the KINAL method package with the ISSA method. It was found that ISSA produces better reduction results for this example; the ISSA-reduced mechanism combines both higher reduction rates and lower deviations between full and reduced mechanism results than the KINAL-reduced mechanism (Mauersberger and Geiger, 1999).

2. The reduction method ISSA

The classical screening analysis has the drawback that a different threshold value has to be found for each species and that the application of this method requires considerable human effort in case of larger mechanisms (Turányi, 1990a). All species in the original mechanism are supposed to be equally important, and, therefore, species cannot be eliminated even if they are insignificant. In contrast, the newly developed ISSA method is automated and requires only one threshold value. It is aimed at the analysis of complex atmospheric chemical multiphase mechanisms and produces reduced mechanisms for specifiable application purposes. Redundant species as well as redundant reactions are identified. The ISSA method combines four method elements described in the following sections where the chemical initial mechanism is assumed to be formally given by the index set S of species and the index set R of reactions.

2.1. Structure analysis

Reaction cycles that join a high mass circulation with a low net effect for the mass balance of species involved are typical for atmospheric chemical mechanisms. They dominate the sink and source balances and disguise the contributions of real sink and source reactions. To avoid the requirement of different threshold values for species with and without reaction cycles, the first step in ISSA is a structure analysis of mechanism that separates cyclic and non-cyclic reactions. A symbolic pathway

$$A_1 \rightarrow A_2 \rightarrow \cdots \rightarrow A_m \rightarrow A_1 \qquad (1)$$

is designated as reaction cycle if every step in Eq. (1) is performed by at least one reaction in the system.

The set of all reactions participating in pathway (1) is denoted as cyclic set $\mathrm{CS}(A_1, \ldots, A_m)$ of length $m+1$. ISSA has been qualified to identify all cyclic sets until length five. But since most reactions in atmospheric chemistry have more than one reactant and more than one product, not all cyclic sets are desired. For example, the CAPRAM2.4 reactions

$$\mathrm{ClNO_2 + Br^- \rightarrow BrCl + NO_2^-},$$
$$\mathrm{BrNO_2 + Br^- \rightarrow Br_2 + NO_2^-},$$
$$\mathrm{NO_2^- + Br_2^- \rightarrow 2Br^- + NO_2},$$

constitute the cyclic set $\mathrm{CS(Br^-, NO_2^-)}$ which is undesirable since $\mathrm{Br^-}$ and $\mathrm{NO_2^-}$ do not contain a common chemical element. To avoid such artificial cycles, species families are defined (e.g. all sulphur-containing compounds) and only reaction cycles within these families are identified. The determination of species families has the additional aim to limit the number of cyclic sets. A strategy for best selection of families will be discussed in Section 3.3. The identified cyclic sets are denoted

uniformly as $R_1, \ldots, R_n$. Then

$$R_0 = \mathbf{C}\left(\bigcup_{k=1}^{n} R_k\right)$$

is the non-cyclic remainder of reactions in R ($\mathbf{C}$M designate the complement of set M).

2.2. Improved screening analysis

The reduction procedure is performed within the framework of box-model simulation. Therefore, time development of concentrations is governed by the continuity equation

$$\frac{\mathrm{d}c_i}{\mathrm{d}t} = p_i(\boldsymbol{c},t) - l_i(\boldsymbol{c},t) + e_i(t), \tag{2}$$

where p and l are chemical production and loss terms, respectively. The term $\boldsymbol{e}$ contains all additional volume sinks and sources included in the box model especially emission rates.

The chemical mass balance term can be expressed as

$$p_i(\boldsymbol{c},t) - l_i(\boldsymbol{c},t) = \sum_{j\in R} v_{ij} r_j(\boldsymbol{c},t), \tag{3}$$

where v_{ij} is the stoichiometric number of species i in reaction j, and r_j is the reaction rate for reaction j. Extended stoichiometric numbers

$$v^{+}_{ijk} = \begin{cases} v_{ij} \text{ for } v_{ij} > 0 \text{ and } j \in R_k, \\ 0 \text{ for } v_{ij} \leqslant 0 \text{ or } j \notin R_k, \end{cases}$$

$$v^{-}_{ijk} = \begin{cases} -v_{ij} \text{ for } v_{ij} < 0 \text{ and } j \in R_k, \\ 0 \text{ for } v_{ij} \geqslant 0 \text{ or } j \notin R_k, \end{cases} \tag{4}$$

are defined to separate sinks and sources as well as reactions in sets R_k, $k = 0, \ldots, n$. Then, chemical production and loss terms can be written as

$$p_i(\boldsymbol{c},t) = \sum_{k=0}^{n}\sum_{j\in R} v^{+}_{ijk} r_j(\boldsymbol{c},t), \quad l_i(\boldsymbol{c},t) = \sum_{k=0}^{n}\sum_{j\in R} v^{-}_{ijk} r_j(\boldsymbol{c},t). \tag{5}$$

Definition (4) is used to formulate the normalised valuation coefficients of the ISSA method

$$f^k_{ij} = \frac{v^{+}_{ijk}\bar{r}_j}{\sum_{j\in R} v^{+}_{ijk}\bar{r}_j}, \quad g^k_{ij} = \frac{v^{-}_{ijk}\bar{r}_j}{\sum_{j\in R} v^{-}_{ijk}\bar{r}_j}. \tag{6}$$

The time-averaged rate of reaction j during simulation time, $\bar{r}_j$, is calculated simultaneously with the solution of Eq. (2). The coefficients defined in Eq. (6) are relative measures. For example, f^k_{ij} gives the relative importance of reaction j as source of species i in comparison with other i-sources in reaction group R_k. It was found that the use of time-averaged reaction rates results in significantly higher reduction rates than the established way of analysis in discrete time points due to the fundamental difference between daytime and nighttime chemistry in atmospheric chemical mechanisms.

2.3. Iteration procedure

The iteration procedure enables the reduction of species and the elimination of complete branches of the reaction system. The following steps are carried out starting with a given set of target species.

(a) For the actual group of important species (index set S_{imp}) the valuation coefficients f^k_{ij}, g^k_{ij} are calculated. At the start S_{imp} contains the target species only.

(b) The maximum member groups of redundant reactions (index sets F_{ik}, G_{ik}) with the property

$$\sum_{j\in F_{ik}} f^k_{ij} < \mathrm{eps}, \quad \sum_{j\in G_{ik}} g^k_{ij} < \mathrm{eps}$$

are determined. Especially reactions with $f^k_{ij} = 0, g^k_{ij} = 0$ are always part of F_{ik} and G_{ik}, respectively. The threshold value eps with $0 \leqslant \mathrm{eps} \leqslant 1$ controls the reduction intensity.

(c) The important reactions (index set R_{imp}) of important species in S_{imp} are calculated by

$$R_{\mathrm{imp}} = \bigcup_{i\in S_{\mathrm{imp}}} \bigcup_{k=0}^{n} (\mathbf{C}F_{ik} \cup \mathbf{C}G_{ik}).$$

(d) The reactants of R_{imp} (species i with $v_{ij} < 0$ for $j \in R_{\mathrm{imp}}$) form the new set of important species S^*_{imp} with $S^*_{\mathrm{imp}} \supseteq S_{\mathrm{imp}}$. If $S^*_{\mathrm{imp}} \supset S_{\mathrm{imp}}$ then the iteration goes on with $S_{\mathrm{imp}} = S^*_{\mathrm{imp}}$ in step (a). In the other case the iteration is finished; S_{imp} and R_{imp} contain the important species and reactions of the reduced mechanism.

Note that the valuation coefficients in Eq. (6) and consequently also the reduced mechanisms resulting from the iteration procedure depend additionally on the respective scenario used for box model simulation.

2.4. Generalisation and verification

Supposing n_{s} different scenarios are used to calculate the valuation coefficients and to perform the iteration procedure then n_{s} specific reduced mechanisms ($S_{\mathrm{imp},i}$, $R_{\mathrm{imp},i}$) are obtained. The (general) reduced mechanism that should be valid for all emission situations represented by the n_{s} scenarios is generated by summing

$$R_{\mathrm{imp}} = \bigcup_{i=1}^{n_{\mathrm{s}}} R_{\mathrm{imp},i}, \quad S_{\mathrm{imp}} = \bigcup_{i=1}^{n_{\mathrm{s}}} S_{\mathrm{imp},i}. \tag{7}$$

The last procedure is the verification of the reduced mechanism. For all species in S_{imp} and for all scenarios the species concentrations calculated with the full and

with the reduced mechanism are compared. The quality of verification depends strongly on the choice of deviation measure. Heard et al. (1998) use simultaneously the standard deviation measures maxdev (maximum percentage error), meandev (mean percentage error), and devmax (percentage error in concentration maximum) to compare full and reduced mechanisms. Only the O_3 concentration is employed for verification but especially in box models the variation of $[O_3]$ is relatively small.

A suitable deviation measure for use in the ISSA method has to give relevant deviation information for all types of concentration evolutions. Nighttime concentrations of short-lived intermediates such as $O(^1D)$ produced only by photochemical reactions are practically zero, their values in the model can be strongly influenced by numerical treatment. A relative deviation at night is irrelevant; thus, maxdev and meandev are inappropriate. The SO_2 concentration decreases continuously during most cloud events. In this case all deviations in $[SO_2]$ maximum are zero since the maximum is the initial value. Therefore, devmax is also not suitable and was modified to provide the maximum relative deviation of daily maxima

$$\text{devmax2} = \max_i(|\text{dev}(t_i)|),$$

$$\text{dev}(t) = \frac{c(t) - \tilde{c}(t)}{\max(c(t), \tilde{c}(t))}, \tag{8}$$

where $c(t)$ and $\tilde{c}(t)$ are concentrations of the same species simulated with the full and the reduced mechanism, respectively, and t_i, $i = 1, \ldots, n_d$, are the points of time when $c(t)$ has the daily maximum. The transient time is assumed to be the first 30 min of the simulation interval. This time period is additionally excluded from the calculation of t_i to prevent the first day being dominated by the initial value. Note that |dev| is restricted to 1; a value >0.9 means that c and $\tilde{c}$ differ more than by a factor of 10.

3. Application to the cloud chemical mechanism RACM/CAPRAM2.4

The ISSA method description given in Section 2 is of general nature. Specific features of multiphase mechanism reduction will be discussed below.

3.1. The cloud chemical box model

In a cloud chemical box model the development of species concentrations in the gas and liquid phase are governed by the continuity Eq. (2). The chemical mass balance terms (3) are completed by phase transfer terms for all soluble gases. The approach proposed by Schwartz (1986) is used to formulate these terms.[1] Hence, the droplets are assumed to be spherical and well mixed; only gas-phase and interfacial mass transport effects are taken into account. This phase-transfer approximation can formally be written as first-order reversible reaction

$$A_g \underset{k^-}{\overset{k^+}{\rightleftharpoons}} A_l, \tag{9}$$

where A_g denotes the gaseous state and A_l the physical dissolved state of a soluble gas A.

It is important that the ISSA reduction method includes the phase transfer. Otherwise the iteration procedure in Section 2.3 would not be able to cross the phase boundary. If reaction (9) is a priori declared as important, then it would be excluded from the reduction. So, the ISSA method uses the following procedure. Only the net effect during simulation time is taken into account. Assuming that the time-averaged net rate $\bar{r}_{net}$ of reaction (9) is positive, that is, the phase flux is mainly directed into the liquid phase and is a source of A_l and a sink of A_g. If $\bar{r}_{net}$ is smaller than the largest time-averaged rate of all non-reversible source reactions of A_l and smaller than the largest time-averaged rate of all non-reversible sink reactions of A_g, then $\bar{r}_{net}$ is included in the calculation of valuation coefficients and in the iteration procedure. In the other case, reaction (9) is excluded from the reduction process and considered as important.

The application presented here consists of the gas-phase mechanism RACM (Stockwell et al., 1997) and the liquid-phase mechanism CAPRAM2.4 (Ervens et al., 2003) coupled by the phase transfers. A revised CAPRAM2.4 version from 09/2004 has been used; the actual version is available on the website: http://www.projects.tropos.de:8088/capram (hereafter referred to as CAPRAM homepage). Table 1 shows the numbers of species and reactions of this combination. The 54 reversible liquid-phase reactions are dissolved as forward and back reaction by the pre-processor that generates the program code for mass balance terms (3). Exceptions will be discussed in the next subsection. However, these reactions are included in the ISSA reduction procedure with their time-averaged net rate as the phase transfer discussed above.

3.2. Explicit and implicit modelling

There are 30 electrolytic dissociation reactions among the 54 reversible reactions of CAPRAM2.4. These reactions play a special role in cloud-chemistry modelling. Their forward and back reactions are very fast, i.e.

[1] Accommodation coefficients, Henry's Law constants, and gas-phase diffusion coefficients necessary to calculate the phase transfer terms are listed in Herrmann et al. (2000).

Table 1
Number of reactions and species in the cloud chemical mechanism RACM/CAPRAM2.4

	Reactions		Species		Phase transfer
	Non-reverse	Reversible	Gas phase	Liquid phase	
RACM	237	—	77	—	—
CAPRAM2.4	328	54	9[a]	137	34
Total	619		223		34

[a]Soluble gases necessary for CAPRAM2.4 but not contained in RACM.

the characteristic time to achieve equilibrium is short compared with competing processes. In many cases, only the equilibrium constants are available but not the rate coefficients of forward and back reactions. There are two ways, given here as explicit and implicit modelling, to solve this problem. In the first case, the electrolytic dissociation reactions are treated as the other reversible reactions; a uniform artificial rate coefficient for all unknown back reactions is fixed. The simulation results of Herrmann et al. (2000) and Ervens et al. (2003) are based on this explicit method (Wolke et al., 2000).

In contrast, the implicit modelling assumes that the electrolytic dissociation reactions keep their equilibrium because of short characteristic times. Then, the mass balance is necessary only for the concentration sum of species involved. For example, if the reactions[2]

$$aSO_2 \rightleftharpoons H^+ + HSO_3^-,$$
$$HSO_3^- \rightleftharpoons H^+ + SO_3^{2-},$$

are in equilibrium then the concentrations $[aSO_2]$, $[HSO_3^-]$, and $[SO_3^{2-}]$ can be expressed in the form $f \cdot [S(IV)]$ where the factors f are rational functions of $[H^+]$ only and S(IV) denotes the total dissolved sulphur in oxidation state 4, that is,

$$[S(IV)] = [aSO_2] + [HSO_3^-] + [SO_3^{2-}],$$

$[aSO_2]$, $[HSO_3^-]$, and $[SO_3^{2-}]$ are replaced by [S(IV)] in differential equations system (2). So, the number of equations in Eq. (2) and the number of prognostic variables are reduced by the number n_e of dissociation equilibria. Note that [S(IV)] is invariant against $[H^+]$ changes in contrast to the concentrations that it replaces. The remaining H^+ concentration is obtained from the electroneutrality equation, which becomes an algebraic equation of degree n_e+1 in $[H^+]$ by replacements.

Both methods have been implemented in the ISSA box model. The only disadvantage of the implicit modelling is that the pre-processing is much more complex. This study found that the results of explicit and implicit modelling agree very well. Box model simulations resulted in devmax2 values $<1\%$ for the concentrations of all species in the RACM/CAPRAM2 mechanism and several scenarios.

The implicit modelling already represents a mechanism reduction. It is comparable with the QSSA method except that there is a special role of H^+ in aqueous-phase chemistry. However, since QSSA and implicit modelling require a reformulation of the original mechanism they are not of interest as reduction methods in this paper. But it was found that implicit modelling is important for the ISSA reduction. The application of the ISSA method produce significantly larger reduction rates in the implicit box model than in the explicit one, despite the fact that in the first case the electrolytic dissociation reactions are not incorporated in the balance terms (3) and are subsequently excluded from the reduction procedure. For example, the reduction rate for reactions is in the implicit case 8% higher (4.9% gas phase, 9.9% liquid phase) than in the explicit case. The probable reason is that the introduction of sum variables results in more sink and source reactions for some key species. Hence, implicit modelling is recommended for future application of ISSA method to aqueous-phase mechanisms. In the following sections, only ISSA reduction results produced by implicit modelling will be presented.

3.3. Reduction results

Three scenarios for cloud-chemical box models; urban, remote, and marine (see Herrmann et al. (2000) and CAPRAM homepage), commonly used in the project MODMEP (Wolke and Herrmann, 2005) were applied to perform the ISSA method. The scenarios comprise initial values for both phases, emission rates, photolysis rate functions, droplet size (a monodisperse distribution is assumed), liquid water content, and other physical parameters. The simulation time period was 1 day. The target species were HO, NO, NO_2, NO_3, O_3, aH_2O_2, aHO, aNO_3, aSO_2, and H^+. This choice was taken from Ervens et al. (2003) in order to make the ISSA-reduced mechanism comparable with an existing condensed version of CAPRAM2.4 (see Section 4). It was found that the families (HO, HO_2, H_2O_2), (NO,

[2]For a soluble gas such as SO_2, the dissolved state $SO_2 \cdot H_2O$ in the aqueous phase is denoted as aSO_2 in this paper.

Table 2
Reduction rates [%] for specific and general reduced mechanisms of RACM/CAPRAM2.4

Reduced mechanisms	Reactions			Species	Phase transfer
	Gas	Liquid	Total		
Mech_urban	53.2	67.8	62.2	29.6	32.4
Mech_remote	53.6	66.0	61.2	29.6	35.3
Mech_marine	69.6	67.5	68.3	38.6	41.2
Mech_general	46.0	60.2	54.8	23.3	23.5

NO_2), (aCO_2, H_2CO_3), and (Fe^{2+}, Fe^{III}), where Fe^{III} denotes a sum variable of Fe^{3+}, $Fe(OH)^{2+}$, and $Fe(OH)_2^+$, are sufficient to provide a structure (see Section 2.1) that results in a successful reduction of RACM/CAPRAM2.4 mechanism. More structure reduces the reduction rate; less structure causes poor verification results. The threshold value eps = 0.11 was fixed for all input scenarios. It was determined as the eps maximum with devmax2 $\leqslant$ 3% for all target species and all scenarios.

The reduction rates achieved by the ISSA method are presented in Table 2. The specific reduced mechanisms, which are intermediates of the reduction procedure, have reduction rates for reactions between 61% and 68% and for species between 29% and 38%. After generalisation step (7), the reduction rates of the (general) ISSA-reduced mechanism are still 54.8% for reactions and 23.3% for species. With the exception of the specific reduced mechanism for the marine scenario, the reduction rates for liquid-phase reactions are significantly larger than those for gas-phase reactions.

The set of reactions in the reduced mechanism is generated as a sum of the sets of reactions in the specific reduced mechanisms (Eq. (7)). In the case of three input scenarios, this sum can be separated into seven disjunct parts. Three of these consist of reactions that are identified as important for only one scenario, a further three contain reactions that are important for only two scenarios, and the last part is the kernel which contains reactions that are important for all scenarios. Table 3 shows the distribution of reactions in the reduced mechanism over these parts. The largest part (57%, both phases) is the kernel; thus, the scenarios are not too specific. On the other hand, every scenario provides a specific contribution, that is, no scenario is covered by the others. As expected, the scenarios marine and urban have the largest difference; their common contribution outside the kernel is the smallest. So, this analysis of ISSA reduction results can assess the independence and representation of scenarios.

The final procedure step is the verification of the reduced mechanism. It was carried out with the same scenarios that were used for the reduction calculation.

Table 3
Contribution of input scenarios to the reduced cloud chemical mechanism RACM/CAPRAM2.4 via specific reduced mechanisms

Reaction sets	Number of important reactions		
	Gas phase	Liquid phase	Both phases
Urban only	11	13	24
Remote only	10	5	15
Marine only	2	9	11
(Urban and remote) only	35	10	45
(Remote and marine) only	5	15	20
(Marine and urban) only	5	0	5
Urban and remote and marine	60	100	160
Urban or remote or marine	128	152	280

Table 4
Deviations devmax2 [%] of target species between full and reduced cloud chemical mechanism RACM/CAPRAM2.4

Target species	Scenarios		
	Urban	Remote	Marine
HO	0.6	1.0	0.1
NO	0.3	1.1	0.2
NO_2	0.3	1.1	0.2
NO_3	0.6	0.4	0.1
O_3	0.2	0.1	0.0
aH_2O_2	0.7	0.4	0.1
aHO	2.9	1.0	1.3
aNO_3	2.8	0.5	0.0
aSO_2	0.6	1.0	0.1
H^+	0.2	0.3	0.1
Average	0.9	0.7	0.2

Table 4 lists the deviations of target species. It can be seen that the target concentrations simulated with the full and the reduced RACM/CAPRAM2.4 mechanism are in excellent agreement. The maximum and average

Table 5
Number of reactions in different CAPRAM2.4 versions (columns 2–4) and number of identical reactions in the condensed and ISSA-reduced versions (column 5) for different reaction classes

Reaction classes	CAPRAM2.4			Identical reactions
	Full	Condensed	ISSA-reduced	
HO_x and TMI chemistry	70	27	35	24
Nitrogen chemistry	35	16	10	7
Sulphur chemistry	56	18	17	11
Organic chemistry	113	38	34	22
Halogen chemistry	33	15	15	9
Carbonate chemistry	21	0	0	0
Reversible reactions	54	37	40	33
Phase transfer	34	33	26	25
Total	416	184	177	131

TMI: transition metal ions.

deviation measure devmax2 over all scenarios and target species are 2.9% (aHO, scenario urban) and 0.6%, respectively. The average deviation over all scenarios and reduced mechanism reactants is 2.5%.

4. Comparison of ISSA reduction results with the condensed version of CAPRAM2.4

A condensed version of CAPRAM2.4 was developed simultaneously with the CAPRAM2.4 mechanism by Ervens et al. (2003) (see the CAPRAM homepage for the actual version). Three different methods, which were based on box model simulation results made with the same scenarios used in this paper, were combined to select the condensed version. Also the same set of target species was given. A considerable manual effort was necessary and the CAPRAM development experience was involved in the reduction procedure. Hence, the condensed version of CAPRAM2.4 can be considered as an expert reduction.

In Section 3 the results of an ISSA-reduced cloud chemical mechanism RACM/CAPRAM2.4 have been presented. In this section, the aim is a comparison with the condensed version of CAPRAM2.4, which is an aqueous-phase mechanism only. In order to achieve a correct result, only the CAPRAM2.4 part of the ISSA-reduced mechanism was used. Both the condensed version and the ISSA-reduced version of CAPRAM2.4 were combined with the full RACM mechanism.[3]

Table 5 shows the numbers of reactions in the condensed and the ISSA-reduced version, which seem to be very similar. For reactions including phase transfer reduction rates of 55.8% (condensed) and 57.4% (ISSA-reduced) were achieved. However, the analysis of the agreement in different reaction classes (classification according to Herrmann et al., 2000) gives the opposite result. Only the carbonate chemistry was identically reduced. The largest differences were found in the nitrogen chemistry (44% agreement, ratio of identical reactions to the maximum of reactions in the condensed and the ISSA-reduced versions), in the comprehensive organic chemistry (58% agreement), in the halogen chemistry (60% agreement), and in the sulphur chemistry (61% agreement). The whole mechanisms have an agreement of 71%. There are two possible consequences: the large difference between these two mechanisms consists of further unidentified redundant reactions or their simulation results have to differ significantly.

Table 6 lists the deviations of target species concentrations between applications of full and reduced CAPRAM2.4 versions. For both reduced mechanisms relatively little deviations were found. The maximum and average deviation over all scenarios and target species are 5.8% (aHO, scenario marine) and 1.9% for the condensed version and 2.3% (aHO, scenario urban) and 0.4% for the ISSA-reduced version, respectively. The ISSA deviations are significantly smaller, but the agreement of the condensed version is also excellent (average deviation $<2\%$) for the urban and the remote case and good (average deviation $<2.5\%$) for the marine case. However, only if all species are considered the fundamental difference between the condensed and the ISSA-reduced version occurs.

The average deviation measure devmax2 over all scenarios and all reactants is 10.9% for the condensed version and 1.2% for the ISSA-reduced version. The average over all scenarios and all liquid-phase reactants is 15.6% for the condensed version and 2.1% for the ISSA-reduced version. Thirteen reactants of the con-

[3]The ISSA-reduced version of CAPRAM2.4 is available in parser readable ASCII format on the website: The ISSA-reduced version of CAPRAM2.4 is available in parser readable ASCII format on the website: http://www.projects.tropos.de:8088/afo2000g3/FEBUKO_dateien/febuko.html.

densed version have a deviation between 90% and 100% for at least one scenario, that is, they differ in orders of magnitude according to the definition (8) of devmax2. The largest deviation of all reactants in the case of ISSA-reduced version is 13.1%, that is, all species concentrations have during all scenarios the same order of magnitude as in the case of full version.

There is obviously an elemental difference in the role of target species. The development of the condensed version was aimed to achieve a good agreement with the full version of CAPRAM2.4 for the target species only. In contrast, the ISSA method uses the target species to start the iteration procedure. Otherwise, all species identified during iteration procedure as important are treated in the same way as the target species; thus, the ISSA-reduced version is consistently good.

Figs. 1–4 show concentration and deviation (dev, Eq. (8)) time-profiles to illustrate the comparison of condensed and ISSA-reduced CAPRAM2.4 mechanisms. Three target species and one non-target species have been selected to demonstrate the possible effects of deviation measure devmax2. In the urban scenario, H_2O_2 is exhausted during the first half of simulation time period due to a large initial value of SO_2 concentration and subsequently large sulphate production rate. Therefore, $[H_2O_2]$ is very small at night and |dev| increases to about 18% for the condensed version (Fig. 1). But devmax2 defined by Eq. (8) takes the value of dev at time $t = 15$ h (4.0% for condensed version and 1.7% for ISSA-reduced version, see Table 6) when concentration maximum of the first day is achieved. In contrast, $[aNO_3]$ has the maximum at midnight, and thus devmax2 is 3.5% (condensed version) and 1.9% (ISSA-reduced version) though the functions dev increase after midnight especially in the case of the condensed version (Fig. 2). The aHO radical has the largest deviation of all target species (Table 6, marine scenario, condensed version). Here, the daily maxima correspond to the |dev| maxima (Fig. 3). Therefore, devmax2 is calculated at time $t = 12.5$ h (1.3%, ISSA-reduced version) and $t = 36$ h (5.8%, condensed version), respectively.

As mentioned previously, the main differences between the condensed and the ISSA-reduced version occur for non-target species. This is shown in Fig. 4 using the example PAN, which denotes in RACM a lumped species representing different peroxyacyl nitrates (PANs). In the marine scenario, the very low concentration level of PAN is overestimated up to 2.3 times by the condensed version (Fig. 4). However, dev is smaller than 60% and devmax2 is 44% (the value of dev at $t = 16.8$ h) according to Eq. (8). Due to the scale of Fig. 3 the PAN

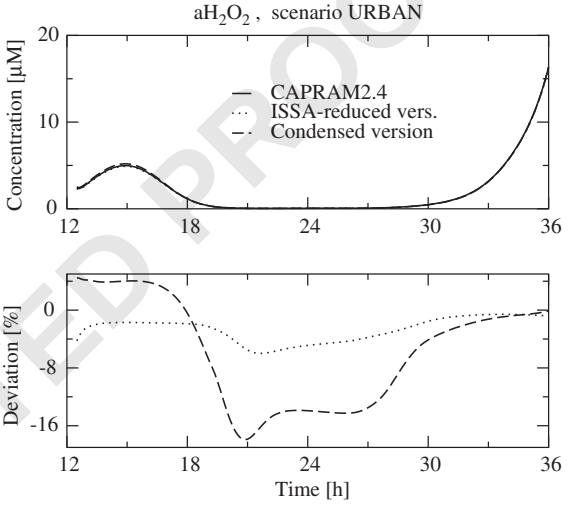

Fig. 1. Comparison between full CAPRAM2.4 mechanism and reduced versions: simulated concentrations of target species aH_2O_2 and percentage deviations.

Table 6
Deviations devmax2 [%] of target species between full and reduced CAPRAM2.4 versions

Target species	Urban		Remote		Marine	
	CV	ISSA	CV	ISSA	CV	ISSA
HO	0.9	0.2	0.7	0.3	1.0	0.1
NO	2.2	0.0	1.4	0.1	3.6	0.3
NO_2	0.9	0.1	0.9	0.0	4.4	0.0
NO_3	0.4	0.0	0.3	0.0	3.9	0.0
O_3	0.3	0.0	0.3	0.0	0.0	0.0
aH_2O_2	4.0	1.7	3.7	0.2	0.5	0.1
aHO	2.5	2.3	1.0	0.8	5.8	1.3
aNO_3	3.5	1.9	1.6	0.1	3.4	0.1
aSO_2	3.5	0.6	3.1	0.7	0.1	0.2
H^+	0.8	0.1	0.4	0.7	1.7	0.2
Average	1.9	0.7	1.3	0.3	2.4	0.2

CV: condensed version; ISSA: ISSA-reduced version.

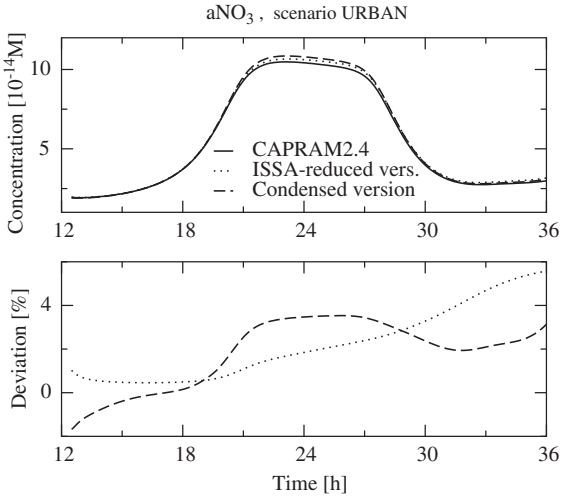

Fig. 2. Comparison between full CAPRAM2.4 mechanism and reduced versions: simulated concentrations of target species aNO_3 and percentage deviations.

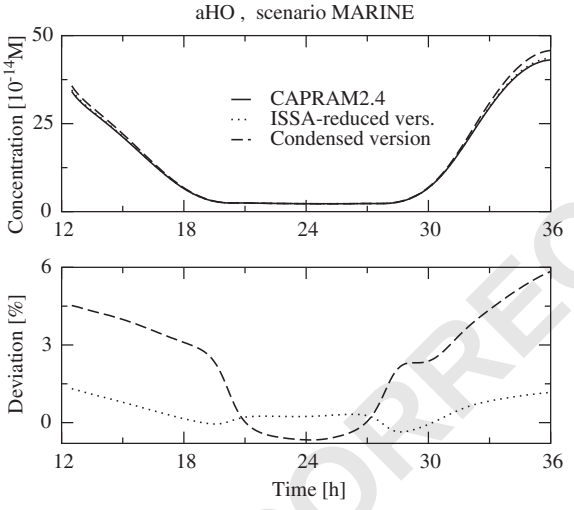

Fig. 3. Comparison between full CAPRAM2.4 mechanism and reduced versions: simulated concentrations of target species aHO and percentage deviations.

deviation for the ISSA-reduced version is nearly invisible; the measure devmax2 is 1.1% in this case.

The PAN mass balance is simple compared with the species in Figs. 1–3, a short explanation for the deviation is possible. PANs are considered as insoluble in the RACM/CAPRAM2.4 mechanism but the precursors and decomposition products, $RC(O)O_2$ (peroxyacyl radicals; ACO3 in RACM notation) are soluble. The liquid-phase pathway from ACO3 to peroxyacetic acid (PAA in RACM notation) and the PAA phase transfer

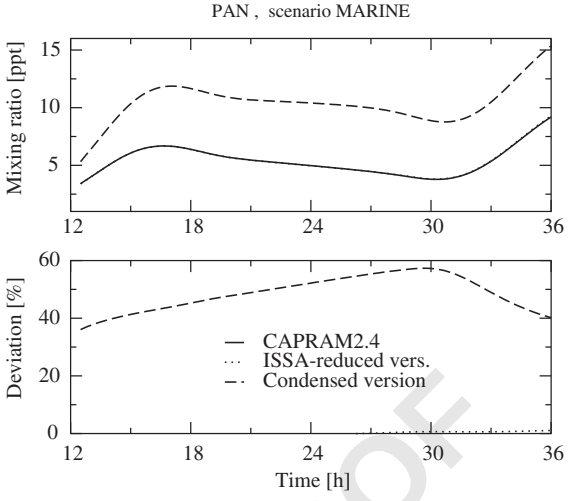

Fig. 4. Comparison between full CAPRAM2.4 mechanism and reduced versions: simulated concentrations of non-target species PAN and percentage deviations.

are deleted in the condensed CAPRAM2.4 mechanism. Thus, PAN and ACO3 are overestimated, PAA is extremely underestimated by the condensed version (devmax2 = 94% in the marine case).

5. Conclusions

A new systematic reduction method, applicable to homogeneous reaction systems as well as to complex multiphase mechanisms, has been developed. The reduction of complex mechanisms such as cloud chemical mechanisms should be useful for future large-scale models, which will include both detailed microphysics and complex (reduced) multiphase chemistry. It has been found that implicit modelling of cloud chemical mechanisms results in better ISSA reduction results than explicit modelling. Although the reasons are currently not full understood, implicit modelling is recommended for future application of ISSA method to aqueous-phase mechanisms. The determination of specific reduced mechanisms can be controlled by the selection of appropriate input scenarios. On the other hand, ISSA has the self-adjusting ability that the analysis of ISSA results can be used to assess the independence and representation of the input scenarios.

The ISSA application to the cloud chemical mechanism RACM/CAPRAM2.4 achieved large reduction rates where reduction rates for gas-phase reactions are significantly smaller than those for liquid-phase reactions. The special role of the target species in the ISSA method is restricted to starting the iteration procedure. Otherwise, all species identified during iteration proce-

dure as important are treated in the same way as the target species. Thus, the ISSA-reduced mechanisms are consistently good; results from the full and the reduced mechanism agree very well for all species in the reduced mechanism. In contrast, the condensed version of CAPRAM2.4 developed simultaneously with the full version as an expert reduction obtains a good agreement only for the target species.

Acknowledgements

This work was supported by the BMBF in the framework of AFO2000-project MODMEP under Grant 07ATF40.

References

Carslaw, N., Jacobs, P.J., Pilling, M.J., 1999. Modeling OH, HO_2, and RO_2 radicals in the marine boundary layer, 2. Mechanism reduction and uncertainty analysis. Journal of Geophysical Research 104, 30257–30273.

Ervens, B., George, C., Williams, J.E., Buxton, G.V., Salmon, G.A., Bydder, M., Wilkinson, F., Dentener, F., Mirabel, P., Wolke, R., Herrmann, H., 2003. CAPRAM 2.4 (MODAC mechanism): an extended and condensed tropospheric aqueous phase mechanism and its application. Journal of Geophysical Research 108, 4426.

Fish, D.J., 2000. The automatic generation of reduced mechanisms for tropospheric chemistry modelling. Atmospheric Environment 34, 1563–1574.

Geiger, H., Becker, K.H., 1999. Degradation mechanisms of dimethoxymethane and dimethoxyethane in the presence of NO_x. Atmospheric Environment 33, 2883–2891.

Heard, A.C., Pilling, M.J., Tomlin, A.S., 1998. Mechanism reduction techniques applied to tropospheric chemistry. Atmospheric Environment 32, 1059–1073.

Herrmann, H., Ervens, B., Jacobi, H.-W., Wolke, R., Nowacki, P., Zellner, R., 2000. CAPRAM2.3: a chemical aqueous phase radical mechanism for tropospheric chemistry. Journal of Atmospheric Chemistry 36, 231–284.

Hesstvedt, E., Hov, O., Isaacsen, I., 1978. Quasi-steady-state-approximation in air pollution modelling: comparison of two numerical schemes for oxidant prediction. International Journal of Chemical Kinetics 10, 971–994.

Mauersberger, G., Geiger, H., 1999. Iterative screening analysis—a new reduction method for atmospheric chemical mechanisms. In: Vogt, R. (Ed.), Proceedings of EC/EUROTRAC-2 Workshop, Aachen, pp. 339–342.

Neophytou, M.K., Goussis, D.A., van Loonb, M., Mastorakos, E., 2004. Reduced chemical mechanisms for atmospheric pollution using computational singular perturbation analysis. Atmospheric Environment 38, 3661–3673.

Schwartz, S., 1986. Mass transport considerations pertinent to aqueous phase reactions of gases in liquid-water clouds. In: Jaeschke, W. (Ed.), Chemistry of Multiphase Atmospheric Systems, NATO ASI Series, vol. 6. Springer, Berlin, pp. 415–471.

Stockwell, W.R., Kirchner, F., Kuhn, M., 1997. A new mechanism for regional atmospheric chemistry modeling. Journal of Geophysical Research 102, 25847–25879.

Tomlin, A.S., Pilling, M.J., Turányi, T., Merklin, J.H., Brimdley, J., 1992. Mechanism reduction for the oscillatory oxidation of hydrogen: sensitivity and quasi-steady-state analysis. Combustion and Flame 91, 107–130.

Turányi, T., 1990a. Reduction of large reaction mechanisms. New Journal of Chemistry 14, 795–803.

Turányi, T., 1990b. KINAL: a program package for kinetic analysis of complex reaction mechanisms. Computers & Chemistry 14, 253–254.

Wolke, R., Knoth, O., Herrmann, H., 2000. Numerical treatment of aqueous phase chemistry in atmospheric chemistry transport modelling. In: Gryning, S.E., Schiermeier, F.A. (Eds.), Air Pollution Modeling and Its Application XIV. Kluwer Academic/Plenum Publishers, New York, pp. 399–407.

Wolke, R., Herrmann, H., 2005. Introduction to FEBUKO and MODMEP. Atmospheric Environment this issue.

3B2v8.06a/w (Dec 5 2003).51c XML:ver:5.0.1 AEA : 5775 Prod.Type:FTPFTP pp.1–13(col.fig.:NIL) ED:MangalaK.mangalak PAGN:hashmath SCAN:global

ARTICLE IN PRESS

Available online at www.sciencedirect.com

SCIENCE DIRECT®

ELSEVIER

Atmospheric Environment ▮ (▮▮▮▮) ▮▮▮–▮▮▮

ATMOSPHERIC ENVIRONMENT

www.elsevier.com/locate/atmosenv

Towards a more detailed description of tropospheric aqueous phase organic chemistry: CAPRAM 3.0

H. Herrmann[a,*], A. Tilgner[a], P. Barzaghi[a], Z. Majdik[a], S. Gligorovski[a], L. Poulain[b], A. Monod[b]

[a]*Leibniz Institut für Troposphärenforschung, e.V., Permoserstraße 15, 04318 Leipzig, Germany*
[b]*Laboratoire de Chimie et Environnement, Université de Provence, Place Victor Hugo 3, Marseille cedex 3, France*

Abstract

CAPRAM 3.0 is the latest development of the chemical aqueous phase radical mechanism (CAPRAM) series which is incorporating CAPRAM 2.4 (Ervens et al., 2003a, Journal of Geophysical Research—Atmospheres 108) and a new extended reaction mechanism for atmospherically relevant hydrocarbons containing more than two and up to six carbon atoms. The chemistry of organics containing three and four carbon atoms is now described in detail. Almost 400 new reactions are now implemented considering the chemistry of organic compounds containing different functional groups, i.e. alcohols, carbonyl compounds, mono- and dicarboxylic acids, polyfunctional compounds as well as some esters and one heterocyclic compound.

The aqueous chemistry has been coupled to the gas phase mechanism RACM (regional atmospheric chemistry modeling) (Stockwell et al., 1997, Journal of Geophysical Research—Atmpspheres 102, 25847–25879), and phase exchange is treated using the resistance model of Schwartz (1986. In: Jaeschke, W. (Ed.), Chemistry of Multiphase Atmospheric Systems, NATO ASI Series, Springer, Berlin, pp. 415–471). The CAPRAM remote scenario which was chosen as the standard scenario showed that the introduction of the higher organic chemistry has a relevant influence on the standard subsystems. The diurnal peak concentration of OH radical in the droplets decreases with about 40% and the reactions of OH with hydrocarbons containing 3 or 4 carbon atoms account for about 10% out of the total sinks of OH in the droplets. A slightly stronger acidification of the aqueous phase in comparison to CAPRAM 2.4 is observed.

The simulations for the standard scenario showed that there is an increase of organic mass within the droplets where the organic compounds containing 4 carbon atoms represent the 67.5% of the total mass, whereas in the urban and in the marine scenario the contribution of two carbon atom compounds is dominating.

The formation and accumulation of substituted mono- and dicarboxylic acids such as tartaric, mesoxalic and acetic acid in the aqueous phase are also observed.

Keywords: Modeling; Multiphase chemistry; VOC oxidation; Box model

1. Introduction

Tropospheric aqueous phase chemical processes which not only restrict cloud chemical conversions but

*Corresponding author. Tel.: +49 341 235 2446; fax: +49 341 235 2325.
E-mail address: herrmann@tropos.de (H. Herrmann).

1352-2310/$ - see front matter © 2005 Published by Elsevier Ltd.
doi:10.1016/j.atmosenv.2005.02.016

also include deliquescent particle chemistry might have profound effects in atmospheric chemistry. Such effects include establishing aqueous phase parts in the oxidation of volatile organic compounds (VOCs) of both biogenic and anthropogenic origin, an influence on the oxidation capability of the gas phase by changing radical budgets, release of reaction products both inorganic and organic to the gas phase and, last but not least, mass production for the aerosol phase which in turn might influence physical particle properties. For further details and referencing, a condensed overview on tropospheric aqueous phase model developments has been recently published (Herrmann, 2003). Up to now, only few studies have attempted to characterise the conversions of higher organics within the tropospheric aqueous phase and (Herrmann et al., 2003; Ervens et al., 2003a) it should be noted that the clear description and documentation of the applied chemical mechanism in full detail is a prerequisite for such modelling studies.

It has been shown that in-cloud sulphur oxidation may extensively contribute to aerosol mass (Zhang et al., 1999). However, the importance of sulphur oxidation is critically dependent on gas phase SO_2 concentration. Therefore, it is expected that especially under remote conditions, when the gas phase SO_2 concentration decreases considerably compared to a more polluted urban case, particulate mass increase due to in-cloud production of organics might play a role. Aqueous phase chemistry might contribute to such mass production as it has been shown that aqueous phase reactions might represent a possible source for oxalic acid (Ervens et al., 2003a; Warneck, 2003) which is an ubiquitous particle phase constituent.

In the following, a brief description of the reaction scheme of CAPRAM 3.0 is presented. The first model results for the standard scenario (remote scenario) are shown and possible atmospheric implication are discussed. For specific details regarding the schemes as well as comments, extensions and supporting material can also be found at http://projects.tropos.de:8088/capram/ and in the electronic supplementary material (ESM) of this study.

2. Model description

2.1. Details of the box model, emissions and depositions, gas phase chemistry and uptake processes

The simulations were carried out in a zero-dimensional box model considering a permanent cloud with a size-segregated droplet spectrum containing a number of twenty size bins with a radius between 1 and 64 μm. The total LWC of $3 \times 10^{-7}\,\mathrm{vol_{aq}\,vol_g^{-1}}$ is lognormal distributed over the 1–64 μm size range. Previous modelling studies showed that a further increase of the number of different size bins leads to a considerably stiffer system but just has a minor influence (<6%) on the simulation results in the respective size range. For the runs time constant microphysical values were considered, for temperature and pressure the following values were assumed: $T = 298\,\mathrm{K}$; $p = 1\,\mathrm{atm}$. The simulations were carried out at the latitude of 51 °N on the 21st of June.

Three different scenarios were considered in this work, namely remote (standard), urban and marine. The initial concentrations for the gas phase and aqueous phase species have been adopted from Ervens et al. (2003a).

For the simulations, dry emissions and depositions are considered throughout the simulation time. These parameters remained unchanged against the modelling with CAPRAM2.4, hence the reader is referred to Ervens et al. (2003a) for further details.

For the simulations the regional atmospheric chemical mechanism (RACM) (Stockwell et al., 1997) was employed. Again, the application of RACM for the description of the gas phase chemistry has been performed earlier and the reader is referred to Ervens et al. (2003) and Stockwell et al. (1997) and references therein.

A delumping of some RACM group compounds had to be implemented in the mechanism in the form of equilibrium reactions between the group compound and the standalone species. Table 1 gives the percentage of the contribution of the stand alone species to the RACM group compounds. The percentages are calculated after the emission data by (Middleton et al., 1990).

Uptake processes of soluble species are included in the mechanism following the approach by Schwartz (1986), see Ervens et al. (2003a). In CAPRAM 3.0 the phase

Table 1
Percentage of the contribution of organics implemented in CAPRAM 3.0 to the RACM lumped species

Compound	RACM group compound	Percent out of group compound
Acetaldehyde	Ald	49%
Propionaldehyde	Ald	2%
Butyraldehyde	Ald	2%
Acetic acid	Ora2	60%
Propanoic acid	Ora2	0%
Butyric acid	Ora2	0%
1-Propanol	Hc5	0.07%
2-Propanol	Hc5	19%
1-Butanol	Hc5	0.4%
2-Butanol	Hc5	0.3%
Acetone	Ket	51%
2-Butanone	Ket	27%
Methyl isobutyl ketone	Ket	7%
Ethylene glycol	Hc8	0.52%

transfer of the following organics was implemented in addition to those compounds already treated in CAPRAM2.4: 1-propanol; 2-propanol; 1-butanol; 2-butanol; propionaldehyde; butyraldehyde; propanoic acid; butyric acid; methylglyoxal; acetone; methyl ethyl ketone (MEK); hydroxy acetone; 1,4-dioxo butene; methyl isobutyl ketone (MIBK); ethyl formate; *N* methyl pyrrolidin-2-one and ethylene glycol (Table I, ESM).

2.2. Aqueous reaction scheme in CAPRAM 3.0

2.2.1. General considerations

CAPRAM 3.0 is the latest development of the CAPRAM series where particular emphasis is given to the aqueous phase chemistry of organic compounds. In the current model the chemistry of organic compounds is extended to better describe C_3 and C_4 chemistry. Moreover, some compounds with more than 4 carbon atoms are also treated. The oxidation pathways of 34 chemical species (5 alcohols, 10 carbonyl compounds, 13 mono- and dicarboxylic acids, 1 ester, 4 polyfunctional compounds and 1 heterocyclic compound) were included and critically reviewed (Table I, ESM). The kinetic data from the recent review of Herrmann (2003) and very recent data originating from the European project MOST (http://most.univ-lyon1.fr) were adopted throughout the mechanisms. However, a significant number of rate constants are still missing in the literature; therefore, available correlations (Herrmann and Zellner, 1998; Herrmann, 2003; Ervens et al., 2003b; Gligorovski and Herrmann, 2004) for the estimation of H-abstraction reaction rate constants were used to fill the gaps whenever it was needed. For the accuracy of the applied published correlations the reader is referred to the above original and overview literature.

In CAPRAM 3.0 the oxidation consecutive reactions are initiated by the reaction of OH and NO_3. In both cases an H-abstraction reaction at the weakest carbon–hydrogen bond is suggested to occur (Herrmann, 2003; Herrmann and Zellner, 1998 and references therein), viz.

$$R-H + X\cdot \rightarrow R\cdot + HX \qquad (X\cdot = OH,\ NO_3). \qquad \text{(R-1)}$$

The resulting alkyl radicals are known to react with oxygen at rates which are close to diffusion control (von Sonntag, 1987). Thus, in line with former versions of CAPRAM, the rate constant for the oxygen addition is estimated to be $k = 2 \times 10^9\,l\,mol^{-1}\,s^{-1}$ throughout the mechanistic scheme.

The fate of peroxyl radicals in aqueous solution has been studied before to considerable extent. Generally, four possible pathways can be identified. In some cases, the contribution of a single pathway can be estimated and/or the relative abundance of the different products can be determined (see von Sonntag, 1987; von Sonntag and Schuchmann, 1997 for reviews).

α-hydroxy-alkylperoxy radicals might decay by eliminating HO_2/O_2^-, in unimolecular reactions (see Bothe et al., 1978 for a review). If no literature values for the decomposition of the peroxyl radical were available a value of k (HO_2-elimination) $= 1000\,s^{-1}$ was applied throughout the mechanism taking into account that the rate constant for the elimination increases with carbon number of the substrate.

2.2.2. C_2 chemistry

Further revisions and updates have been made to the organic chemistry of C_2 compounds which has been used in CAPRAM 2.4 (Table I, ESM). Even if the mechanism contained a detailed description of the chemistry of organic compound up to 2 carbon atoms, the oxidation of compounds such as glycolaldehyde ($HOCH_2CHO$) and glycolic acid ($HOCH_2COOH$) was not included. In the new version of the mechanism presented here, the aqueous phase oxidation sequences of ethylene glycol (CH_2OHCH_2OH), glycolaldehyde and glycolic acid are now added. These reactions complete the C_2 chemistry of CAPRAM 2.4.

The atmospheric aqueous phase oxidation of acetic acid is leading the formation of the corresponding peroxy radicals. These are known to react readily in aqueous phase with O_2^-/HO_2 (Bielski et al., 1985) leading to the formation of hydroperoxy acetic acid ($HOOCH_2COOH$) and the chemistry of this latter compound is also included now.

2.2.3. C_3 chemistry

The C_3 chemistry represents an important part of the processes introduced with CAPRAM 3.0. Oxidation pathways of atmospheric constituents such as acetone (CH_3COCH_3), methylglyoxal (CH_3COCHO) and hydroxyacetone (CH_3COCH_2OH) have been implemented. Moreover, the oxidation schemes of 1-propanol, 2-propanol, propionaldehyde and propanoic acid are now being considered. However, their contribution to the conversion of VOCs in the aqueous phase is expected to be of minor importance due to their low concentrations.

The aqueous phase conversion of acetone driven by OH radicals might potentially contribute to the production of hydoxyacetone and methylglyoxal which are rapidly converted through the reaction with OH in pyruvic acid ($CH_3COCOOH$). Within the oxidation chain of these C3-compounds, important couplings to gas phase chemistry exist described by phase transfer of acetone and methylglyoxal. Together with the phase transfer description of glyoxal a link to consider the fate of ring cleavage products which are formed in the gas phase oxidations of aromatics. This approach is also extended to C_4-compound where 2-butene-1,4-dial is also considered now (Scheme I, ESM).

In the reaction scheme, a loss process for pyruvic acid via the reactions of OH and NO_3 to form the oxopyruvic

acid (CHOCOCOOH) is now included (Scheme I, ESM). The latter is then oxidised to mesoxalic acid which represents an ending species which is hence accumulating during the simulation.

In fact, the only sink reaction for mesoxalic acid (HOOCCOCOOH) is the decarboxylation process which is expected to proceed very slowly compared to the simulation time. Decarboxylation of carboxylic acids is generally thermodynamically favourable but kinetically unfavourable, yet it is generally a very slow reaction. β-ketoacids are exceptions to this generalisation because they have a low energy path for decarboxylation through the enol form of the product ketone. The conversion of β-ketoacids to their anions makes decarboxylation more difficult because the immediate product must be the enolate and not the enol. Hence, the decarboxylation processes are proceeding very slow and the unimolecular decay was assumed equal to 10^{-5} and $10^{-6}\,s^{-1}$ for the undissociate form and its anion throughout the mechanism, respectively, as observed for the acetoacetic acid and its anion (Guthrie and Jordan, 1972). Great care should be taken when decarboxylation reactions are implemented in reaction schemes, not to overestimate their importance.

As shown in several studies dicarboxylic acid are ubiquitous in tropospheric particles (see Neususs et al., 2000, 2002; Narukawa et al., 2002; Plewka et al., 2004; Simoneit et al., 2004). Hence, in CAPRAM 3.0 the oxidation of malonic acid ($HOOCCH_2COOH$) and its oxidation product tartronic acid (HOOCCHOHCOOH), initiated in the aqueous phase by the reaction with OH and NO_3, is implemented and leads to the formation of mesoxalic acid which in this case also represents the end product of the reaction chain (Scheme I, ESM).

2.2.4. C_4 chemistry

Succinic acid is among the most abundant dicarboxylic acids usually identified in tropospheric particles. Hence, in CAPRAM 3.0, a complete scheme of the oxidation for the dicarboxylic acids containing 4 carbon atoms such as succinic and malic acid is included (Scheme I, ESM).

The oxidative conversion of those acids leads to the accumulation of polyfunctional acids within the aqueous phase. The latter are also reacting in the aqueous phase and enter the chemistry of the carboxylic acids containing 3 carbon atoms through the slow decarboxylation process. A possible contribution to the formation of polyfunctional C_4-acids mass is expected from the conversion of 2-buten-1,4-dial which links to gas phase aromatics oxidation. A complete oxidation scheme is included in CAPRAM 3.0 (Scheme I, ESM).

Moreover, the oxidation pathway of butyraldehyde is also considered. The oxidation product is butyric acid which is further converted in two substituted monocarboxylic acids, 2-oxobutyric and 2-hydroxybutyric acid. These compounds represent end products in the current model and are accumulating throughout the simulation.

2.2.5. MOST compounds

There is considerable interest on the atmospheric chemistry of oxygenated organic compounds which are used as solvents and fuel additives, especially, for those compounds which are intended to substitute the traditional solvents. Compounds such as 2,3-butadione, ethyl formate, MEK and MIBK might be released to the troposphere following their technical application. These compounds themselves or their respective oxidation products might play a role in the tropospheric aqueous phase in a close interplay with their respective gas phase chemistry. MEK and MIBK are well-recognised potential ozone producers (Jenkin et al., 2002). In fact, these oxygenated compounds have some degree of solubility in water and are generally less volatile than traditional solvents (Wypych, 2001) thus undergo phase transfer and react in the aqueous phase. Therefore, detailed oxidation schemes for ethyl formate, MEK and MIBK have been developed in the MOST project and are now included in CAPRAM 3.0 (Table I and Scheme I, ESM). In this context, the oxidation pathway of a heterocyclic compounds is considered for the first time in an aqueous phase tropospheric model. On the basis of a recent aqueous phase study (Friesen et al., 1999) and results on *N*-methylpyrrolidin-2-one (NMP) gas phase oxidation obtained in the MOST project, a reaction mechanism for the oxidation of NMP is presented. Also in this case, the oxidation is initiated by the reaction with OH and NO_3 and proceeds further through different pathways as shown in the reaction mechanism overview (Scheme I, ESM).

3. Model results

3.1. Standard subsystems

In the following, the effect of the introduction of the higher organics chemistry on standard subsystems such as inorganic radicals (OH, NO_3), ozone, pH, sulphur (IV) oxidation and TMI is discussed. A comparison of the results obtained with CAPRAM 2.4 and CAPRAM 3.0 for the standard scenario (remote) is also performed. For sake of clarity, it must be said that the observed variations discussed in this section cannot be addressed always to a different contribution of a single reaction in the two models but as a result of small distinct effects which might lead to noticeable overall changes in diurnal profiles. In the current model CAPRAM 3.0 the number of the reactive species, their uptakes and equilibrium reactions is increased remarkably with

respect to CAPRAM 2.4. Thus, it becomes more difficult and complex to identify a unique cause to the differences modelled in system such as sulphur (IV) oxidation and, especially, pH.

3.1.1. Inorganic radicals

A comparison of the results obtained with CAPRAM 2.4 and CAPRAM 3.0 shows that, in the case of OH radical, the two different model versions predict initial maximal diurnal concentrations and fluxes (Fig. 2) which are in general agreement as can be seen from the diurnal profiles for the remote scenario (Fig. 1) and the sink/source plot (Fig. 2). However, an important effect of a better described aqueous phase organic chemistry can be observed. In the 96 h simulations, the diurnal peak concentration of OH radical in the droplets decreases by about 40% indicating that even in weakly polluted environments such as the remote standard scenario a sensible effect of the dissolved organic compounds is to be expected.

In Fig. 2 sinks and sources for OH radical modelled with CAPRAM 2.4 and 3.0 are presented. As shown in the detailed sink analysis for OH radical at noon marked differences do appear. While in CAPRAM 2.4 the most important sinks of OH were established by the reactions of OH with formaldehyde (49%), formate (32%) and H_2O_2 (10%), in CAPRAM 3.0 the reactions of OH with formaldehyde and formate represent the major sinks with contributions of 29% and 16%, respectively. However, their contributions become smaller and the reactions of OH with higher organics do significantly contribute. In particular, the reactions of OH with glyoxylate (8.3%), ethylene glycol (6.5%), hydrated glycolaldehyde (6.5%) and glycolate/glycolic acid (9.2%) are newly identified sinks. Furthermore, it can be noted that the reactions of OH with organic compounds containing 3 or 4 carbon atoms account for about 10% of the total sinks of OH in the droplets.

No significant difference exists between the results obtained with the two models for the sources of OH radicals in the aqueous phase is shown in Fig. 2. In both

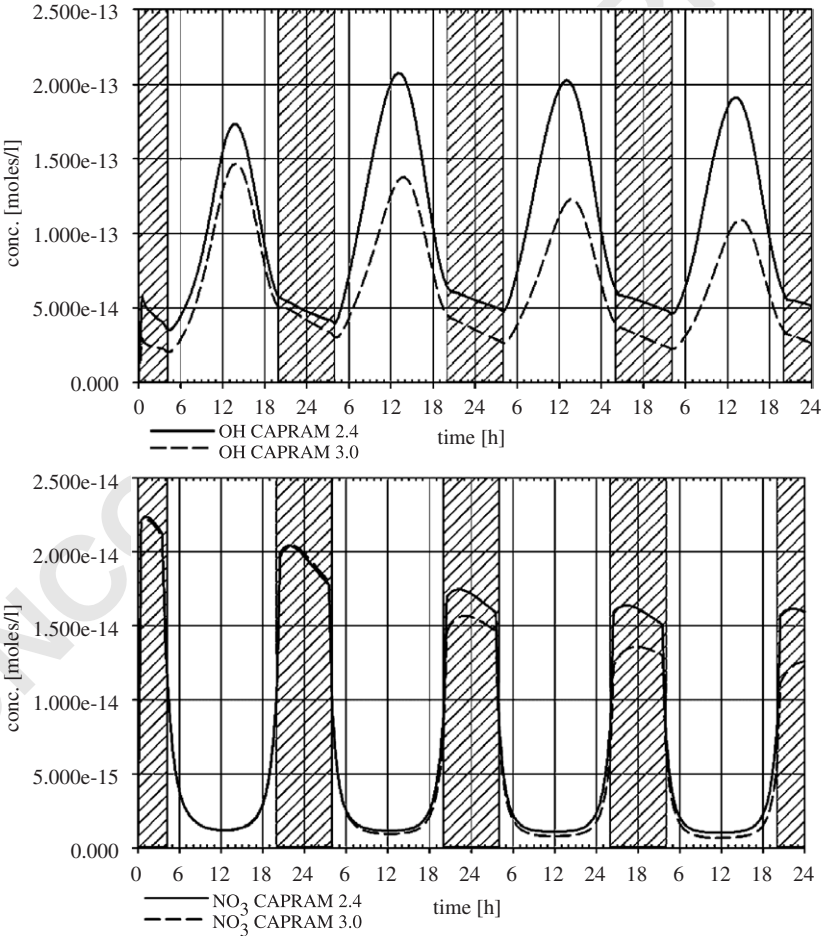

Fig. 1. Aqueous phase concentrations of OH and NO_3 obtained with CAPRAM 2.4 and 3.0 for the remote scenario.

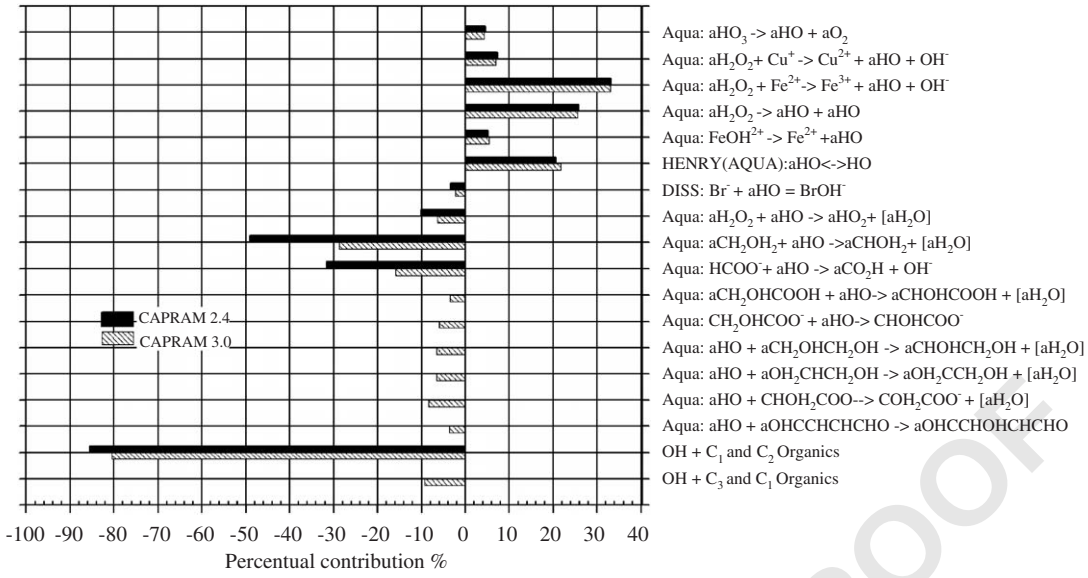

Fig. 2. Comparison of the relative contributions (%) of sinks and sources of OH between CAPRAM 2.4 and CAPRAM 3.0 in the aqueous phase for the standard scenario (remote). Total fluxes: 4.55×10^{-9} mol l^{-1} s^{-1} in CAPRAM 2.4 and 4.58×10^{-9} mol l^{-1} s^{-1} in CAPRAM 3.0.

cases the most important sources are (i) the Fenton reaction between Fe^{2+} and H_2O_2 accounting for about 33%, (ii) the photolytic decomposition of H_2O_2 with a contribution of about 25.8% in case of CAPRAM 2.4 and 25.5% in case of CAPRAM 3.0 and (iii) uptake of OH radical into the droplets accounts for 20.6% in case of CAPRAM 2.4 and 21.6% in case of CAPRAM 3.0 out of the total source of OH in the droplets.

In the case of the nitrate radical (Fig. 1), the simulations with both mechanisms CAPRAM 2.4 and CAPRAM 3.0 are leading to similar NO_3 levels at the beginning. At later simulation times, however, it becomes evident that in the presence of extended organic chemistry the NO_3 concentration decreases compared to CAPRAM 2.4. At the end of the of simulation time (96 h) the NO_3 concentration reaches a concentration about 30% smaller compared to CAPRAM 2.4. In both cases, at midnight the almost exclusive source of NO_3 in the droplets is its uptake from the gas phase accounting for almost 100% out of the total sources. The reactions with halides (Cl^- and Br^-, 93% and 5%, respectively, in CAPRAM 2.4; 81% and 4.5% in CAPRAM 3.0) are the major sinks for NO_3 in the aqueous phase. In the remote scenario the observed differences in the sinks are attributed to the reactions with substituted carboxylic acids and their anions such as oxopyruvic acid (5.8%), glycolate (4.6%) and hydroxypyruvic acid (1.6%) which represent an alternative oxidation pathway for higher organics under nighttime conditions. Moreover, the aqueous phase conversion of NO_3 radicals through its reactions with organic compounds might have an indirect influence on the pH due to the formation of HNO_3.

3.1.2. Non-radical oxidants: peroxides and ozone

As can be seen in Fig. 3a, the chemistry of the higher organics has no apparent effect on the concentration levels of H_2O_2 in the aqueous phase in the two different versions of the model. In fact the newly implemented reactions can only partially influence the levels of H_2O_2 which is produced in very low concentrations through peroxy radical recombination reactions including HO_2 recombination.

The influence of aqueous droplets on the gas phase concentration of ozone is still controversial. The results obtained with CAPRAM 3.0 show a small decrease of the gas phase concentration of ozone (Fig. 3b) as observed in the former study (Ervens et al., 2003a). Moreover, this decrease becomes more important by the end of the simulation with a difference of about 8% in the peak concentrations.

Ozone undergoes phase transfer into the droplets being an almost exclusive source of O_3 in the droplets. At noon, uptake O_3 concentration fluxes of about 9.5×10^{-6} and 8.9×10^{-6} mol l^{-1} h^{-1} were modelled in case of CAPRAM 2.4 and CAPRAM 3.0, respectively. In the droplets, in case of CAPRAM 2.4, ozone reaches concentration levels (in average about

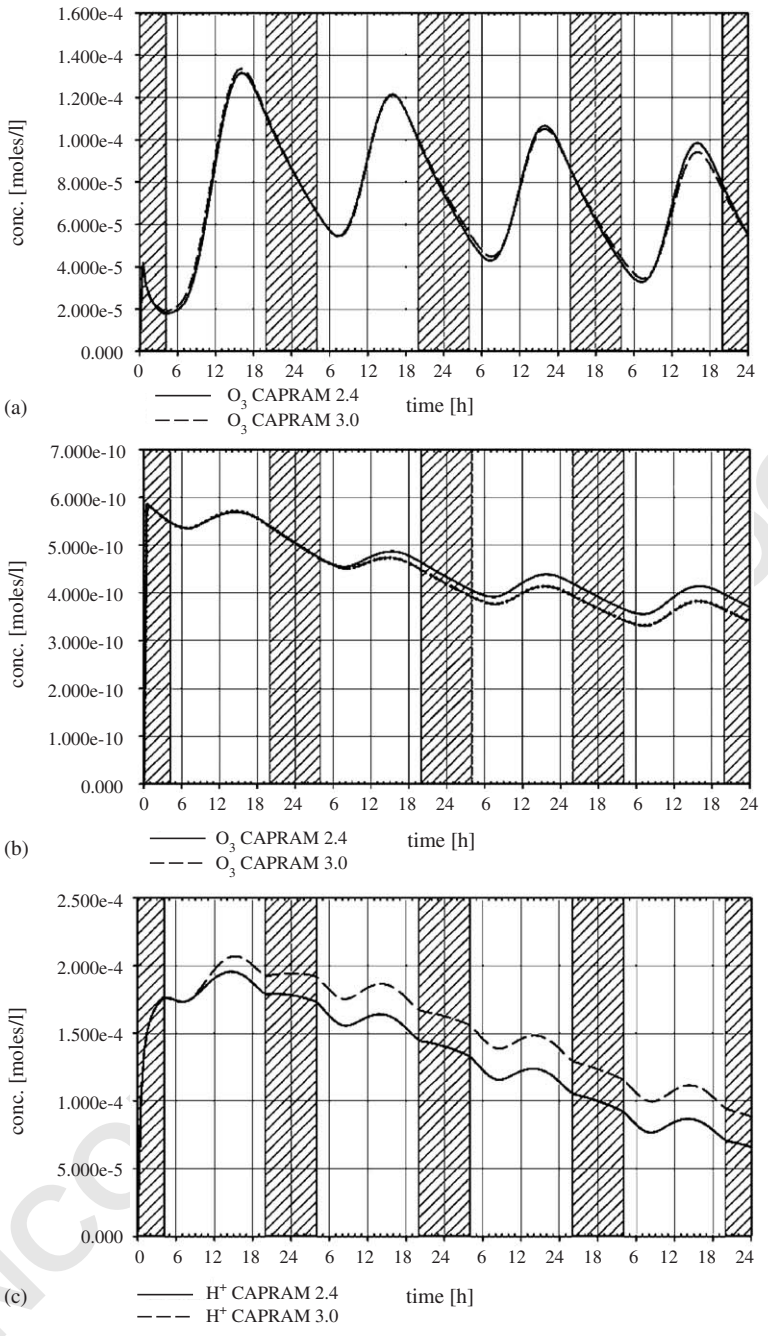

Fig. 3. Evolution of (a) H_2O_2, (b) ozone and (c) pH over the simulation time with CAPRAM 2.4 and 3.0 for the remote scenario.

1.44×10^{-11} mol l^{-1}) smaller compared to CAPRAM 3.0. The most important sinks for ozone in the aqueous phase are the reactions between O_3 and O_2^-, Fe^{2+} and Cu^+ with no appreciable differences in the percentage of the contributions between CAPRAM 2.4 and CAPRAM 3.0. Thus, the differences observed in the gas phase concentrations can be ascribed to gas phase processes mainly due to lower production rates.

3.1.3. pH

The evolution of the pH value over the total simulation time of four days is shown in Fig. 3c. In

CAPRAM 3.0 the diurnal profile of pH is similar to the one obtained with CAPRAM 2.4, however, reaching somewhat smaller values. At the end of the simulation the pH reaches a minimum value of about 4.05 in case of CAPRAM 3.0 and 4.18 in case of CAPRAM 2.4. The main formation pathways of H^+ are the reactions between HO_2 and Cu^{2+}, and HSO_3^- with H_2O_2 and they are sensible to the equilibrium reactions (E1–E2):

$$HO_2 \rightleftarrows O_2^- + H^+, \quad \text{(E1)}$$

$$Fe^{3+} + H_2O \rightleftarrows Fe(OH)^{2+} + H^+, \quad \text{(E2)}$$

$$HNO_3 \rightleftarrows NO_3^- + H^+, \quad \text{(E3)}$$

$$SO_2 + H_2O \rightleftarrows HSO_3^- + H^+, \quad \text{(E4)}$$

$$HCOOH \rightleftarrows HCOO^- + H^+. \quad \text{(E5)}$$

At noon, the reaction between HO_2 and Cu^{2+} is the most important source accounting for about 36.6% and 41.1% out of the total sources for H^+ in case of CAPRAM 2.4 and CAPRAM 3.0, respectively. The equilibrium reactions (E1–E5) have a contribution to the total sources of about 20.7%, 14.5%, 8.1%, 5.9%, and 5.4% in case of CAPRAM 2.4 and 15.5%, 14.8%, 9.0%, 6.2% and 2.9% in case of CAPRAM 3.0. The predominant loss of H^+ is due to neutralisation with OH^-. Other neutralisation reactions have only little contributions. At this level of analysis, there is no direct evidence that the contributions of the single dissociations of the organic acid formed during the simulation significantly contribute to the final pH. However, the formation of HNO_3 in H-abstraction reaction of NO_3 is surely contributing to the acidity budget via (E3).

3.1.4. S(IV) oxidation

Several pathways exist in which S(IV) species are oxidised to S(VI). Under the remote scenario conditions, the most important conversions are identical in both mechanisms, i.e. CAPRAM 2.4 and CAPRAM 3.0. The predominant source of S(VI) is the reaction between HSO_3^- and H_2O_2 accounting for about 95.4% and 96.0%, respectively, out of the total sources. S(VI) in the droplets is produced by the reaction between HSO_3^- and HNO_4 having a contribution of about 3.8% and 3.3% to the total sources in case of CAPRAM 2.4 and CAPRAM 3.0, respectively. The direct uptake of H_2SO_4 in the droplets is not significant (0.4%). However, in the presence of higher organics the total S(VI) production rate increases from a value of about $4.4 \times 10^{-5}\,mol\,l^{-1}\,h^{-1}$ to about $5.4 \times 10^{-5}\,mol\,l^{-1}\,h^{-1}$ at noon.

The total S(VI) sink rate reaches considerably smaller values that the S(VI) production rate indicating a net sulphate production. At noon, the total sink rate reaches a value of about $2.0 \times 10^{-8}\,mol\,l^{-1}\,m^{-3}\,h^{-1}$ and $1.5 \times 10^{-8}\,mol\,l^{-1}\,h^{-1}$ in case of CAPRAM 2.4 and CAPRAM 3.0, respectively.

3.1.5. TMIs

The implementation of an extended organic chemistry resulted in no significant differences in the chemistry of TMIs. However, the comparisons were performed for the remote scenario where low concentrations of TMIs occur. As observed in a previous study (Ervens et al., 2003a), the influence of TMIs will be most important for the urban scenario due to the higher TMI concentration levels. However, the results obtained with CAPRAM 3.0 shows a general agreement with the ones obtained with CAPRAM 2.4.

3.2. Organic chemistry

The revision of the C_1–C_2 chemistry in CAPRAM 2.4 and the extension of the model to the chemistry of organic compounds containing mainly 3 and 4 carbon atoms delivered significant effects on the standard subsystems and the results presented in following section might be used to better interpret the oxidation processes involving the tropospheric aqueous phase and its possible influence on the budgets of organic species in the tropospheric aqueous phase, which is of relevance not only for cloud chemistry but also for mass production of particles which are processed sequentially in the air mass history of a given tropospheric air parcel.

In the first part of the following section, an overview of the results of oxidation processes initiated by radical reactions in the aqueous phase is given. A comparison of the different contributions on the rates of formation of the different classes of compounds is discussed for all three different scenarios (remote, urban and marine) and the atmospheric implications are discussed. Moreover, two distinct oxidations pathways of the key species ethylene glycol (C_2) and acetone (C_3) are analysed in detail.

3.2.1. Classification

Observing the diurnal behaviours in the simulations for the three different scenarios under the assumption of continuous cloud chemistry, the stable organic species considered in the current model can be divided into three main classes (Table II, ESM): (i) species that are increasing and accumulating throughout the simulation with no strong daily variation, (ii) species with a strongly diurnal variation neither accumulating nor decreasing significantly and (iii) species that have an increase in the concentration only at the beginning of the simulation and then decrease throughout the experiment. The first class of compounds comprises either species having a significant flux from the gas phase into the aqueous phase which dominates over the aqueous phase production terms, as for acetone, MEK and MIBK (Figs. I–III

in the ESM). Moreover, this first class of compounds includes species that are terminal oxidation products with no strong sinks implemented in the current model. Important examples are mesoxalic acid, tartaric acid and polyfunctional butyric acids (Figs. IV–VI in ESM).

In the second class those species are found which have a high aqueous phase reactivity with respect to OH radical. In the remote scenario, the aldehydes like propionaldehyde, butyraldehyde and 2-buten-1,4-dial (Figs. VII–IX in ESM) all belong to this group. Although in highly polluted conditions (urban scenario) where the source fluxes, both in the aqueous and the gas phase, are dominating over the aqueous phase conversion aldehydes such as glycolaldehyde, propionaldehyde and butyraldehyde change their diurnal behaviour and move to the first class (Table I, EMS).

Finally, the third compound class includes organic compounds: (i) which are initialised in the gas phase only at the start of the simulation such as NMP (Fig. X; ESM) or (ii) compounds where their precursors are consumed during the experiment and never replaced. That is the case for *N*-methylsuccinimide, Tartronic and Oxalacetic acids (Figs. XI–XIII in ESM).

3.2.2. Production rates

In the standard remote scenario, the carboxylic acids containing 4 carbon atoms show the highest mass production rates among all organic compounds considered in CAPRAM 3.0. As can be seen in Table 2, the aqueous phase conversion of succinic acid and 2-buten-1,4-dial leads to the formation of substituted mono- and dicarboxylic acids that contribute about 67% to the total mass production. In Table 3 the compounds are

Table 2
Contribution per classes of organic compounds (C_2, C_3, C_4 and $C>4$) to the total mass production

Compounds	Remote		Urban		Marine	
	Rate ($\mu g\,m^{-3}\,h^{-1}$)	%	Rate ($\mu g\,m^{-3}\,h^{-1}$)	%	Rate ($\mu g\,m^{-3}\,h^{-1}$)	%
C_1	5.98×10^{-6}	0.05	2.76×10^{-2}	4.17	5.40×10^{-5}	1.13
C_2	1.58×10^{-3}	14.44	5.25×10^{-1}	79.30	4.71×10^{-3}	98.73
C_3	2.01×10^{-3}	18.34	1.18×10^{-3}	0.18	3.60×10^{-6}	0.08
C_4	7.34×10^{-3}	67.15	1.08×10^{-1}	16.35	2.05×10^{-6}	0.04
$C>4$	1.92×10^{-6}	0.02	3.87×10^{-6}	0.00	9.53×10^{-7}	0.02

Table 3
Production rates of organic compounds for the three different scenarios with CAPRAM 3.0

Remote		Urban		Marine	
Compound	Rate ($\mu g\,m^{-3}\,h^{-1}$)	Compound	Rate ($\mu g\,m^{-3}\,h^{-1}$)	Compound	Rate ($\mu g\,m^{-3}\,h^{-1}$)
Tartaric acid	4.49×10^{-3}	Ethylene glycol	1.86×10^{-1}	Acetic acid hydroperoxide	2.75×10^{-3}
2-Hydroxy 3-oxosuccinic acid	1.77×10^{-3}	Glycolaldehyde	1.86×10^{-1}	Acetic acid	1.79×10^{-3}
Mesoxalic acid	1.76×10^{-3}	Glycolic acid	1.13×10^{-1}	Glyoxylic acid	1.10×10^{-4}
Acetic acid	1.07×10^{-3}	2,3-Dihydroxy-4-oxo butyraldehyde	3.54×10^{-2}	Glycolic acid	6.80×10^{-5}
2,3-Dihydroxy 4-oxobutyric acid	3.95×10^{-4}	2-Hydroxy-3,4-dioxo butyraldehyde	3.48×10^{-2}	Formaldehyde	4.68×10^{-5}
2-Hydroxy 3,4-dioxobutyric acid	3.16×10^{-4}	Glyoxylic acid	2.75×10^{-2}	Methylhydroperoxide	7.20×10^{-6}
Glyoxylic acid	2.47×10^{-4}	Formaldehyde	2.34×10^{-2}	Mesoxalate	2.81×10^{-6}
2,3-Dihydroxy 4-oxobutyraldehyde	1.77×10^{-4}	2-Hydroxy-3,4-dioxo butyric acid	1.58×10^{-2}	Peroxy acetic acid	2.04×10^{-6}
2-Hydroxy 3,4-dioxobutyraldehyde	1.74×10^{-4}	2,3-Dihydroxy-4-oxo butyric acid	1.58×10^{-2}	Acetone	6.96×10^{-7}
Acetic acid hydroperoxide	1.37×10^{-4}	Acetic acid	8.93×10^{-3}	2,3-Dioxoisohexane	6.84×10^{-7}

reported which show the largest mass production rates within the aqueous phase. As can be seen, tartaric acid and 2-hydroxy-3-oxo-succinic acid appear to be produced efficiently in the aqueous phase in the remote scenario. In CAPRAM 3.0, only very slow loss reactions are implemented (Table I, ESM), thus the accumulation might be artificial.

At the current stage of model development, mesoxalic acid represents the C_3 compound which is most efficiently produced in the aqueous phase being also the connecting point of the different oxidation pathways and having only one loss reaction currently implemented in the model (Scheme I and Table I in ESM). Thus, an overestimation of its concentration in the aqueous phase in comparison to field measurements may be expected.

Acetic acid and glyoxylic acid showed high rates of production in the aqueous phase among the organic compounds containing two carbon atoms.

A different picture is obtained in the polluted and the marine cases where production fluxes of organic species are dominated by the organic compounds containing two carbon atoms with a contribution of about 80% and 99%, respectively. These observed patterns can be explained, in the urban case, mainly with the uptake processes which dominate the aqueous phase production as observed for ethylene glycol and glycolaldehyde. Quite different to that, in the marine scenario the main reason is that, part of the reactive species (“HC8”) which are not occurring in the gas phase and therefore, the important precursors for the C_3 and C_4 chemistry are missing. In the marine scenario hydroperoxy acetic acid and acetic acid represent the most important produced species. It should be noted that significant differences in the production fluxes exist which are due to the different emission rates applied for the different scenarios.

3.2.3. Oxidation of ethylene glycol

According to recent modelling studies, the aqueous phase oxidation of glyoxal is regarded as a very important process because only the pathways involved in the formation of oxalate in the aqueous phase (Ervens et al., 2003a; Warneck, 2003) where the only source is the uptake from the gas phase. Glyoxal is present in its hydrated form in solution which is then oxidised to form glyoxylic acid which is the precursor for the formation of oxalate. Due to the completion and update of organic chemistry in CAPRAM 3.0 this process becomes now less important for oxalate formation because the oxidation of ethylene glycol is implemented. Phase transfer of ethylene glycol into the aqueous phase opens a new way of formation of oxalic acid through glycolaldehyde which is further oxidised to glycolic acid and finally to glyoxylic acid that is the direct precursor of oxalic acid. At noon after 36 h of simulations, the modelled concentrations for glyoxal were 2.46×10^{-7} M in CAPRAM 2.4 and 2.59×10^{-7} M in CAPRAM 3.0, the concentration of glycolic acid is now three orders of magnitude higher compared to CAPRAM 2.4 and it reaches a value of 3.86×10^{-6} which is almost hundred times higher than the modelled concentration of glyoxal. As can be seen in Fig. 4, no significant differences are observed in the diurnal behaviours of glyoxal, whereas a different trend in the concentrations of glyoxylic acid is modelled with the two different versions of CAPRAM. In CAPRAM 2.4, a high-initial concentration of glyoxylic acid was obtained followed by a rapid decrease in the early stage of simulation. Afterwards a small increase in the concentration was observed. In the current model, glyoxylic acid is formed at the start of simulation in lower concentrations compared to CAPRAM 2.4; however, a constant increase is now obtained due to the contribution of the oxidation of ethylene glycol.

The model predicts that 80% of the production fluxes of glyoxylic acid are due to the unimolecular decomposition of the peroxyl radical originating from the sequential reactions of OH and O_2 with glycolic acid and its anion. Hence, the contribution of glyoxal is now only 20% at noon in the remote scenario.

However, an increase in the net production and relative accumulation of oxalate in the aqueous phase is not observed even if the concentration of the glyoxylic acid is slightly increased compared to the one modelled with CAPRAM 2.4. This result can be explained with a more efficient removal of oxalic acid due to the newly implemented kinetic data for its reaction with OH radical.

3.2.4. Oxidation of acetone

The aqueous phase oxidation of acetone represents another interesting system because it demonstrates that aqueous phase processes might contribute significantly to the formation of reactive intermediates, such as hydroxyl acetone and methylglyoxal, directly in solution. Although the oxidation of 2-propanol is now implemented and its oxidation leads to the formation of acetone, the uptake from the gas phase represents the most important source of acetone in solution which accumulates throughout the simulation reaching an ending concentration of about 2.6×10^{-8} M in the remote scenario. The OH-driven oxidation of acetone leads to the formation of hydroxyl acetone and methylglyoxal which represent an important precursor of pyruvic acid and its oxidation products. With the current oxidation scheme it has been modelled that the contribution of the oxidation of acetone to the formation of methylglyoxal, which was coming only from the gas phase in CAPRAM 2.4, is increasing constantly during the experiment and after 36 h it represents 40% of the production flux. The oxidation of methylglyoxal

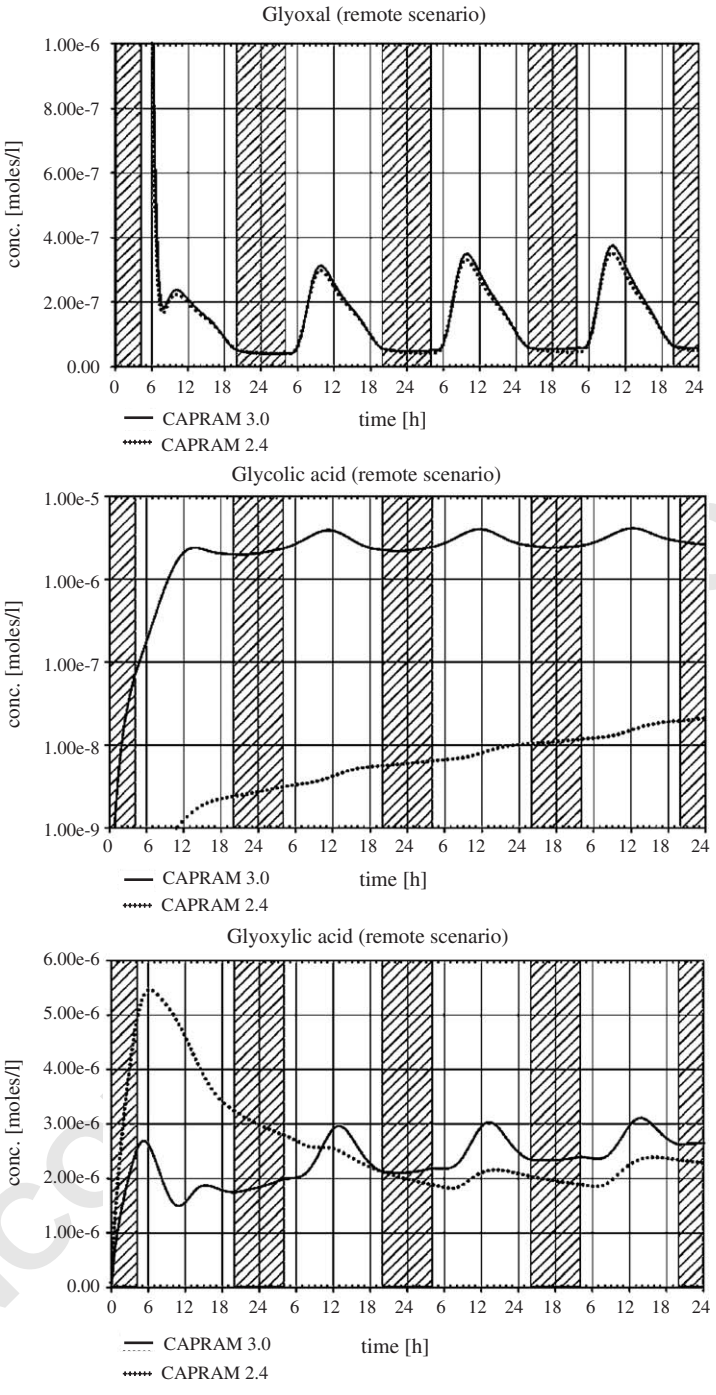

Fig. 4. Comparison of the aqueous phase concentrations of glyoxal, glycolic and glyoxylic acid obtained with CAPRAM 2.4 and 3.0 for the remote scenario.

in its hydrated form represents the exclusive source of pyruvic acid in the current model.

4. Conclusions and summary

The present study analysed the effect of the implementation of a more complete aqueous phase organic

chemistry on current tropospheric model which is addressed as CAPRAM 3.0. The results obtained with this latest version of CAPRAM shows a variety of effects of the organic compounds and their oxidation pathways on atmospheric subsystems. In particular, a marked decrease on the concentration levels of important radicals such as OH and NO_3 has been modelled for the standard scenario (remote). Moreover, this work showed that the oxidation, both in the gas phase and in the aqueous phase, of aldehydes and ketone lead to the formation of mono- and dicarboxylic which accumulate in the aqueous phase. Among those, the carboxylic acids containing 3 carbon atoms represent the major contributions to the organic mass production. Furthermore, it was shown for the remote scenario that not only the gas phase conversion but also the aqueous phase conversions might contribute to the formation of important atmospheric species such as methylglyoxal in the particle phase.

5. Uncited references

Barth et al., 2003; Saxena and Hildemann, 1996.

Acknowledgements

This study was carried out within the MODMEP project of the AFO2000 program of the BMBF under contract No. 07ATF40. Support of this study by the EC within the project "Multiphase chemistry of Oxygenated Species in the Troposphere (MOST)" under contract No. EVK2-CT-2001-00114 is also gratefully acknowledged.

References

Barth, M.C., Sillman, S., Hudman, R., Jacobson, M.Z., Kim, C.H., Monod, A., Liang, J., 2003. Summary of the cloud chemistry modeling intercomparison: photochemical box model simulation. Journal of Geophysical Research—Atmospheres 108.

Bielski, B.H.J., Cabelli, D.E., Arudi, R.L., Ross, A.B., 1985. Reactivity of HO_2/O_2^- radicals in aqueous-solution. Journal of Physical and Chemical Reference Data 14 (4), 1041–1100.

Bothe, E., Schuchmann, M.N., Schultefrohlinde, D., Vonsonntag, C., 1978. HO_2 elimination from alpha-hydroxyalkylperoxyl radicals in aqueous-solution. Photochemistry and Photobiology 28 (4–5), 639–644.

Ervens, B., George, C., Williams, J.E., Buxton, G.V., Salmon, G.A., Bydder, M., Wilkinson, F., Dentener, F., Mirabel, P., Wolke, R., Herrmann, H., 2003a. CAPRAM 2.4. (MODAC mechanism): an extended and condensed tropospheric aqueous phase mechanism and its application. Journal of Geophysical Research—Atmospheres 108.

Ervens, B., Gligorovski, S., Herrmann, H., 2003b. Temperature-dependent rate constants for hydroxyl radical reactions with organic compounds in aqueous solutions. Physical Chemistry Chemical Physics 5 (9), 1811–1824.

Friesen, D.A., Headley, J.V., Langford, C.H., 1999. The photooxidative degradation of N-methylpyrrolidinone in the presence of Cs3PW12O40 and TiO_2 colloid photocatalysts. Environmental Science and Technology 33 (18), 3193–3198.

Gligorovski, S., Herrmann, H., 2004. Kinetics of reactions of OH with organic carbonyl compounds in aqueous solution. Physical Chemistry Chemical Physics 6 (16), 4118–4126.

Guthrie, J.P., Jordan, F., 1972. Amine-catalyzed decarboxylation of acetoacetic acid—rate constant for decarboxylation of beta-imino acid. Journal of the American Chemical Society 94 (26), 9136–9141.

Herrmann, H., 2003. Kinetics of aqueous phase reactions relevant for atmospheric chemistry. Chemical Reviews 103 (12), 4691–4716.

Herrmann, H., Zellner, R., 1998. Reactions of NO_3^- radicals in aqueous solution. In: Alfassi, Z.B. (Ed.), N-Centered Radicals. Wiley, New York, pp. 291–343.

Herrmann, H., Majdik, Z., Ervens, B., Weise, D., 2003. Halogen production from aqueous tropospheric particles. Chemosphere 52, 485–502.

Jenkin, M.E., Saunders, S.M., Derwent, R.G., Pilling, M.J., 2002. Development of a reduced speciated VOC degradation mechanism for use in ozone models. Atmospheric Environment 36, 4725–4734.

Middleton, P., Stockwell, W.R., Carter, W.P.L., 1990. Aggregation and analysis of volatile organic-compound emissions for regional modeling. Atmospheric Environment Part A—General Topics 24, 1107–1133.

Narukawa, M., Kawamura, K., Li, S.-M., Bottenheim, J.W., 2002. Dicarboxylic acids in the Arctic aerosols and snowpacks collected during ALERT 2000 Atmospheric Environment 36, 2491–2499.

Neususs, C., Pelzing, M., Plewka, A., Herrmann, H., 2000. A new analytical approach for size-resolved speciation of organic compounds in atmospheric aerosol particles: methods and first results. Journal of Geophysical Research—Atmospheres 105 (D4), 4513–4527.

Neususs, C., Gnauk, T., Plewka, A., Herrmann, H., Quinn, P.K., 2002. Carbonaceous aerosol over the Indian Ocean: OC/EC fractions and selected specifications from size-segregated onboard samples. Journal of Geophysical Research—Atmospheres 107 (D19).

Plewka, A., Gnauk, T., Bruggemann, E., Neususs, C., Herrmann, H., 2004. Size-resolved aerosol characterization for a polluted episode at the IfT research station Melpitz in autumn 1997. Journal of Atmospheric Chemistry 48 (2), 131–156.

Saxena, P., Hildemann, L.M., 1996. Water-soluble organics in atmospheric particles: a critical review of the literature and application of thermodynamics to identify candidate compounds. Journal of Atmospheric Chemistry 24, 57–109.

Schwartz, S., 1986. Mass transport considerations pertinent to aqueous phase reactions of gases in liquid water clouds. In: Jaeschke, W. (Ed.), Chemistry of Multiphase Atmospheric Systems, NATO ASI Series. Springer, Berlin, pp. 415–471.

Simoneit, B.R.T., Kobayashi, M., Mochida, M., Kawamura, K., Lee, M., Lim, H.J., Turpin, B.J., Komazaki, Y., 2004. Composition and major sources of organic compounds of aerosol particulate matter sampled during the ACE-Asia campaign. Journal of Geophysical Research—Atmospheres 109 (D19).

Stockwell, W.R., Kirchner, F., Kuhn, M., Seefeld, S., 1997. A new mechanism for regional atmospheric chemistry modeling. Journal of Geophysical Research—Atmospheres 102, 25847–25879.

von Sonntag, C., 1987. The chemical Basis of Radiation Biology. Taylor and Francis, London.

Warneck, P., 2003. In-cloud chemistry opens pathway to the formation of oxalic acid in the marine atmosphere. Atmospheric Environment 37 (17), 2423–2427.

Wypych, G., 2001. Handbook of Solvents, first ed. Chem. Tech. Publishing, Toronto.

Zhang, Y.P., Kreidenweis, S.M., Feingold, G., 1999. Stratocumulus processing of gases and cloud condensation nuclei 2. Chemistry sensitivity analysis. Journal of Geophysical Research—Atmospheres 104, 16061–16080.

3B2v8.06a/w (Dec 5 2003).51c XML:ver:5.0.1 AEA : 5776 Prod.Type:FTP pp.1–9(col.fig.:NIL) ED:MangalaK. PAGN:Mamatha SCAN:Global

ARTICLE IN PRESS

Available online at www.sciencedirect.com

SCIENCE DIRECT®

ELSEVIER

Atmospheric Environment ▮ (▮▮▮▮) ▮▮▮–▮▮▮

ATMOSPHERIC ENVIRONMENT

www.elsevier.com/locate/atmosenv

Numerical simulation of the microphysics of an orographic cloud: Comparison with measurements and sensitivity studies

Martin Simmel*, Karoline Diehl[1], Sabine Wurzler[2]

Leibniz Institute for Tropospheric Research, Permoserstraße 15, 04318 Leipzig, Germany

Abstract

The formation and evolution of orographic clouds are modeled using a parcel model with sectional microphysics based on the Linear Discrete Method and a size-dependent representation of the soluble particle fraction. The model results are compared to observations from three periods of the field experimental campaigns FEBUKO 2001 and 2002 covering about 150 single cases. Processing of aerosol is sensitive to cloud droplet number and size. Therefore, droplet nucleation is emphasized. Sensitivity studies concerning the soluble particle fraction ε, the water accommodation coefficient α_C, and model dynamics were carried out. The size-dependent representation of ε turned out to be very important for a correct nucleation description whereas a shift of the soluble fraction by ± 0.1 induces much smaller effects. Decreasing α_C and increasing vertical velocity both lead to enhanced droplet formation due to higher supersaturations reached. This effect often occurred for the same parameter configuration. Entrainment was shown to be important to reach better agreement between the calculated and the observed data, reducing the liquid water contents below the respective adiabatic values and leading to a broadening of drop size distributions including an increase of small droplets.

Keywords: Spectral cloud model; Condensation; Nucleation; Cloud microphysics; Drop growth

1. Introduction

Over the continents clouds are often influenced by the underlying orography. A special subtype are orographic clouds which are often non-precipitating. Therefore, the effects of the multiphase chemistry taking place within the clouds can be studied during cloud lifetime and after cloud evaporation when modified aerosol particle (AP) size distributions with altered chemical compositions are released inducing changed radiation and condensation properties (e.g., Wurzler et al., 2000; Feingold and Kreidenweis, 2002). Thus, orographic clouds are of special interest for the scientific community. In contrast to other cloud types ground-based in situ measurements can be made within orographic clouds. This allows one to carefully characterize the cloud properties over longer time periods compared to, e.g., aircraft measurements. Field experiments at Kleiner Feldberg (Wobrock et al., 1994) and Great Dun Fell (Choularton et al., 1997; Bower et al., 1999) were undertaken to study orographic clouds acting as chemical flow-through reactors. Additionally, measurements of the AP size distribution upwind of the cloud were used to study the process of droplet nucleation which highly depends on (a) the

*Corresponding author. Tel.: +49 341 235 2176; fax: +49 341 235 2139.

E-mail address: simmel@tropos.de (M. Simmel).

[1]Present address: Institut für Physik der Atmosphäre, Universität Mainz, Becherweg 21, 55099 Mainz, Germany.

[2]Present address: North Rhine-Westphalia State Environment Agency, PO Box 102363, 45023 Essen, Germany.

1352-2310/$ - see front matter © 2005 Elsevier Ltd. All rights reserved.
doi:10.1016/j.atmosenv.2005.02.017

aerosol properties (e.g., size, number, chemical composition) and (b) the atmospheric dynamics and thermodynamics (e.g., humidity, vertical velocity, turbulence), see Colvile et al. (1994), Hallberg et al. (1997), and Martinsson et al. (1999). Each of these contributions presents model calculations including sensitivity studies for one selected case.

In contrast to the previous studies the present model simulations as well as the corresponding sensitivity studies cover the whole time span of selected measurement periods (about 150 cases in total). This gives a good impression of the variability of the considered quantities and, therefore, the findings should be more representative than those obtained for a single case. The model results are based on and compared to data from the field campaigns FEBUKO 2001 and 2002 (Müller et al., 2004). The microphysical properties of the cloud and their appropriate numerical description are crucial for the calculation of the multiphase chemistry due to the different behavior of interstitial particles and activated droplets with respect to gas uptake and liquid phase reactions. If an AP does not become a drop it will leave the cloud rather unchanged compared to the changes the residuals of evaporated droplets experience. Therefore, formation of cloud droplets (nucleation) and their further development are emphasized in the present work. The multiphase chemistry processes (gas uptake, liquid phase reactions) potentially leading to changes in the AP spectra are treated in Wolke et al. (2004), Tilgner et al. (2004a,b), and Sehili et al. (2004).

2. Model and data

The present study is based on data from the field experimental campaigns FEBUKO 2001 and 2002 (Müller et al., 2004). In both campaigns, measurements were carried out at three stations: U—upwind station (Goldlauter, 605 m asl), cloud free; S—summit (Schmücke, 937 m asl) inside the orographic cloud; D—downwind station (Gehlberg, 732 m), cloud free. Due to the focus on cloud formation, the present work is restricted to the two stations U and S which are located 2.7 km away from each other.

Tilgner et al. (2004a,b) and Heinold et al. (2004) identified three measurement periods when the summit was in-cloud and the flow between the three stations was connected. Those are referred to as events E I (26./27.10.2001), E II (07./08.10.2001), and E III (16./17.10.2002), respectively. The connected flow justifies the use of an adiabatic air parcel model starting at U to simulate the formation and development of the orographic cloud observed at the summit S. Additionally, entrainment as described by Pruppacher and Klett (1997) can be taken into account. Please note that an air parcel model cannot assess atmospheric mixing processes in their full complexity. The model includes one-dimensional sectional microphysics with an iterative calculation of the saturation ratio (Simmel and Wurzler, 2004). As microphysical processes the model considers growth/shrinking of AP by water vapor diffusion as well as nucleation and growth/evaporation of drops, impaction of AP and collision–coalescence of drops. The predicted model fields include liquid water mass, soluble and total particulate mass as well as particle number within each size bin. This implies a radius-dependent representation of the soluble aerosol fraction ε. Details about the model are given in Simmel et al. (2002) and Simmel and Wurzler (2004).

For the initialization of the model, meteorological data at U (e.g., temperature, pressure, humidity) and aerosol properties (size distributions, soluble content ε) were used as measured during FEBUKO (Gnauk et al., 2004). The parcel is driven by the wind (constant value at U, measured value at S) flowing over the orography and thereby lifting the parcel. Modeled liquid water contents (LWC), drop numbers, and drop size distributions at S are compared to the observed values (Wieprecht et al., 2004). Model runs were carried out for successive 15 min periods (corresponding to the time needed for one scan of the AP size distribution in the field experiment) covering the total event duration. Measurements with higher time resolution were averaged, ε represents the average for each event. Transport from U to S needs about 12–15 min for the standard case depending on measured wind speed at S. The complete initial data sets are listed in the electronic supplementary material (ESM).[3]

3. Results and discussion

In a first part, model results using a standard model setup are compared to the FEBUKO 2001 and 2002 observations. Secondly, the model is tested for sensitivity with regard to various dynamical and microphysical parameters. In contrast to previous studies (e.g., Hallberg et al., 1997; Martinsson et al., 1999), model calculations are not limited to one selected case but cover the whole time span and parameter range of the three events E I, E II, and E III. As could be expected, all cases studied had in common that impaction of AP and collision–coalescence of drops were negligible due to the small drop sizes and short residence times of the droplets within the cloud.

[3] http://projects.tropos.de:8088/afo2000g3/FEBUKO_dateien/febuko.html

3.1. Comparison with observations

Fig. 1 shows LWC and drop numbers for the standard model configuration (see Table 1) compared to the observed values for E I, E II, and E III, respectively. In the model, the two parameters are anti-correlated. This is due to orography which becomes steeper towards the mountain top. Therefore, a smaller LWC representing a higher cloud base is connected with stronger updrafts and higher supersaturation leading to enhanced drop numbers. In the observations, this connection is rather clear for most of E I and partly for E II and E III. This corresponds to the findings of Arends et al. (1994) at Kleiner Feldberg (1990) where higher drop numbers were observed when the cloud base was high. Generally, as in most other observations (e.g., Pruppacher and Klett, 1997) the measured LWC is below the adiabatic value which is calculated by the model. The good model representation of the observed time-dependent structures of both, LWC and drop numbers, supports the assumption of connected flow conditions. The time lag of the S data compared to U data caused by the transport time is not taken into account since transport time mostly is below the time resolution of the averaged data.

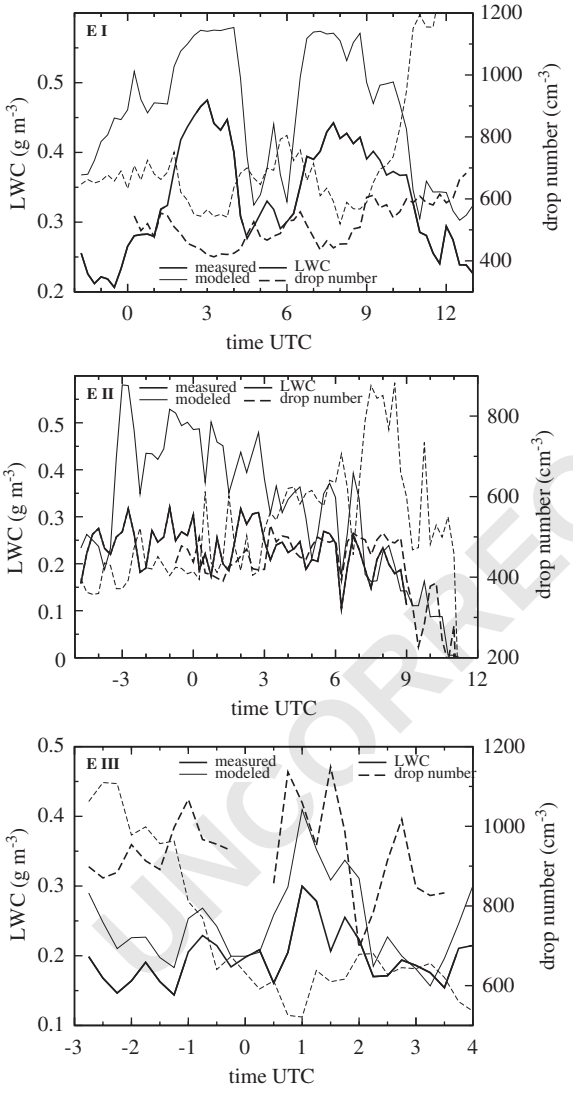

Fig. 1. Time series of liquid water content (full lines) and drop number (dashed lines) at S for the standard model runs (thin lines) of E I (top), E II (middle), and E III (bottom) compared to the respective measurements (thick lines).

For E I, the model overestimates both LWC and drop number (Fig. 1, top panel) with a rather constant offset. However, the time-dependent structure is reproduced very well, except for drop number in the last 3 h of the event. This large overestimation is due to a rise in total AP (and, therefore, potential cloud condensation nuclei, CCN) number combined with strong updrafts due to the high cloud base.

In the first half of E II the observed LWC is far below its adiabatic value, whereas in the second half the differences are much smaller (Fig. 1, middle panel). Like in E I the low LWC in the last 5 h of the event leads to rather high drop numbers in the model.

E III provides the highest observed drop numbers (about 1000 cm^{-3}). In contrast to E I and E II drop number is underestimated by the model (Fig. 1, bottom panel) for most of the event. LWC is closest to its adiabatic value.

3.2. Model sensitivities

The influence of soluble particle fraction ε, water accommodation coefficient α_C and transport time are investigated (see Table 1):

- ε was derived from size-resolved chemistry measurements ranging from 0.25 (E I) to almost 0.5 (E III) for the smallest particles to 0.6–0.8 for the potential CCN (standard case). These values are shifted by a constant offset of ± 0.1 (cases EPS+, EPS−). The average value of the soluble particle fraction was about 0.7 (case EPS_AVE). For exact numbers see ESM, Table 1.
- α_C describes how efficient a water vapor molecule sticks to the surface of the particle it is colliding with. For the standard case $\alpha_C = 1$ is used (Morita et al., 2004; Vieceli et al., 2004) which means that each colliding water molecule is transferred to the particle surface. However, values ranging from about 0.01–1 can be found in the literature (e.g., see reviews in Pruppacher and Klett, 1997; Li et al., 2001). Therefore, a sensitivity study with $\alpha_C = 0.042$ as it was used in Kreidenweis et al. (2003) based on data of Shaw

and Lamb (1999) was carried out (case ALPHA).

- For the investigation of dynamics influence on cloud microphysics wind speed at U is doubled (case FAST) leading to shorter transport times (about 8–11 min compared to 12–15 min in the standard case) and higher updraft velocities.

Table 1
Parameter configurations for the investigation of the model sensitivities

Case	Wind speed	ε	α_C
Standard	$2\,ms^{-1}$	Size-resolved	1
EPS+	$2\,ms^{-1}$	Size-res. +0.1	1
EPS−	$2\,ms^{-1}$	Size-res.−0.1	1
EPS_AVE	$2\,ms^{-1}$	Average	1
ALPHA	$2\,ms^{-1}$	Size-resolved	0.042
FAST	$4\,ms^{-1}$	Size-resolved	1

ε is the soluble fraction of the particulate mass and α_C is the water accommodation coefficient.

Fig. 2 shows the percentage difference in drop number of the various sensitivity cases compared to the respective standard cases for E I, E II, and E III.

On the left side effects of the change of the soluble particle fraction ε on drop numbers is shown. Generally, higher ε values (full lines) result in higher drop numbers inducing lower maximum super-saturations (not shown) and vice versa. On average, the effects of variations in ε by ± 0.1 on drop number are about 5–10%, reaching 15–25% occasionally. Deviations are highest for E II (Fig. 2, left). For some cases, no significant differences are found.

If the size-dependent ε is replaced by the respective average value (EPS_AVE, dot-dashed lines) drop numbers increase by about 10% on average. This is in agreement with the findings of Eichel et al. (1996). A

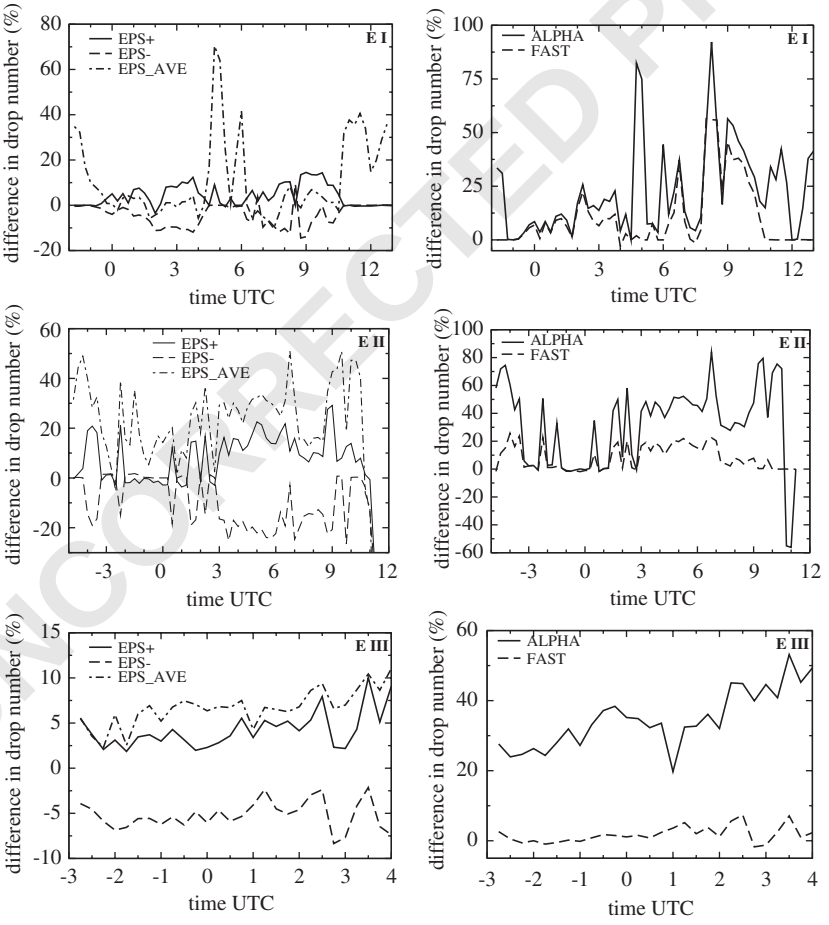

Fig. 2. Time series of drop number sensitivities vs. changes in soluble fraction ε (left), transport time and water accommodation coefficient α_C (right) for E I (top), E II (middle), and E III (bottom). Note the different y-axis scales.

much stronger increase can be seen for the cases with low LWC (high cloud base) where drop number is overestimated by 30–70%. This is due to the activation of small AP with a significantly increased value for ε compared to the size-resolved cases (E I and E II). Obviously, E III is influenced much less, which can be explained by the smaller difference (<0.2) between the average ε and the ε of the smallest AP in E III compared to E I (>0.4) and E II (>0.3).

Compared to $\alpha_C = 1$ the use of a small α_C exerts a stronger limitation on phase transfer of the water vapor molecules. This induces higher supersaturations which enable activation of smaller AP being present in rather high numbers. Therefore, drop numbers increase by more than 20–30% on average and up to 50–100% (Fig. 2, right, full lines) occasionally. These findings are in agreement with those of, e.g., Hallberg et al. (1997).

As expected, a faster transport (Fig. 2, right, dashed lines) from U to the S leads to higher drop numbers due to higher supersaturations reached. For E I and E II the deviations to the standard case average about 10% but like in the ALPHA cases they are highly variable and can reach up to 50% and more. E III seems to be rather insensitive to those changes.

One can observe that the effects of a small α_C and a faster transport often occur at the same time for the same parameter configurations. This arises from the fact that both effects lead to a rise of maximum supersaturation resulting in enhanced droplet activation if the proper AP are present. Obviously, the change in maximum supersaturation caused by a small α_C value is higher than that caused by the altered transport time in the cases presented here. Generally, the sensitivity studies show that changes of each of the parameters investigated can have highly different implications for the drop number depending on the specific set of initial conditions.

3.3. Entrainment

According to Colvile et al. (1997) indications for entrainment are that LWC is much lower than adiabatic and that broad or multimodal droplet number size distributions occur (see below). This is fulfilled for all events considered. As was shown above the LWC in E II deviates most from the adiabatic value, but also LWC in the events E I and E III are lower than adiabatic (see Fig. 1). Therefore, the model runs using the standard configuration are repeated but now with entrainment. A variation of the entrainment strength is realized by changing the parcel size: a smaller parcel is more influenced by entrainment than a larger one. Three different parcel sizes R_p are applied: 500 m (strong entrainment), 1000 m (moderate), and 2000 m (weak). Additionally, entrainment depends on the absolute velocity $|v|$ of the parcel. The entrainment mixes out activated drops and mixes in AP which are represented by the drop residuals to ensure particulate mass conservation as it was observed. The detrainment of a drop quantity Q (liquid water mass, soluble and total particulate mass, particle number) in size bin J is determined according to Pruppacher and Klett (1997):

$$\frac{dQ_J}{dt} = \frac{0.6|v|}{R_p} Q_J. \quad (1)$$

Without the mixing in of the (larger) AP roughly half of the particulate mass would be lost depending on the size of the air parcel. Interstitial AP are supposed not to be affected by entrainment. This is based on the assumption that the AP distribution is the same within the parcel and outside and that water vapor uptake/release is fast for small AP.

Fig. 3 (left) shows the LWC for the model runs with entrainment for all events compared to the respective standard cases and the measurements. For E II moderate to strong entrainment reproduces the LWC observations best whereas for E I and E III weak to moderate entrainment is sufficient for most of the event time. In this approach drop numbers are hardly influenced by entrainment, especially for E II and E III (Fig. 3, right). Only in E I significant (positive) deviations from the standard run are observed for the entrainment cases. This is due to the increasing vertical velocity towards the mountain top S causing rather high supersaturations and, therefore, activating the entrained larger AP replacing the drops that were mixed out.

3.4. Selected drop size distributions

Typically, the drop number size distributions measured by Wieprecht et al. (2004) are rather broad. The smallest droplets observed (2–6 μm) can be reproduced well only when entrainment is taken into account. Entrainment strength highly influences the number of this droplet fraction and agreement is best for the values where LWC is reproduced best as well.

The drop size distributions of the events show rather different features. In E I (Fig. 4, top panel) only a moderate number of the smallest droplets was observed supporting the assumption of weak entrainment. A more or less distinct maximum occurs around 10 μm which is overestimated by the model. The bimodal distribution at 7:15 UTC (left) and less pronounced at 10:00 UTC (right) for the standard case (which occurs more often throughout E I) is caused by in cloud nucleation of drops rather close to the summit S. Generally, E II shows a similar behavior (Fig. 4, middle panel). The number of the smallest droplets corresponds to a stronger entrainment (like the LWC above). The maximum is shifted to smaller sizes (<10 μm) and again it is overestimated by the model. In contrast, E III has very high numbers of the smallest droplet fraction and

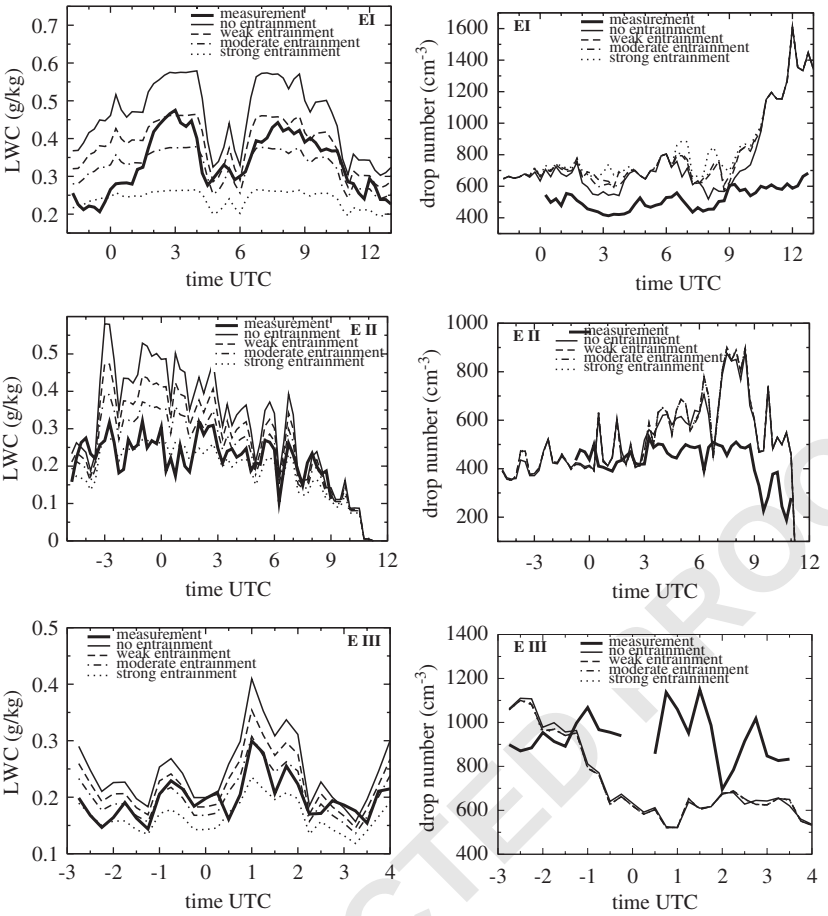

Fig. 3. Time series of LWC (left) and drop number (right) at S for model runs using entrainment (dashed, dot-dashed, and dotted lines) compared to the respective standard runs (thin full lines) and measurements (thick full lines) of E I (top), E II (middle), and E III (bottom).

the maximum around 10 μm is much less pronounced (Fig. 4, bottom panel). In the model, such high numbers only could be reproduced with very strong entrainment, which would be contrary to the findings deduced from the LWC results above. Fig. 5 shows the initial dry AP size distributions measured in U for the same cases as in Fig. 4. It is striking that the distributions of E III are significantly shifted to smaller sizes. This could be the reason for the observed high number of small droplets that must have been activated just before reaching the summit.

At the large end of the spectrum with drop sizes above 20 μm (E I) and 15 μm (E II, E III) more drops are observed than modeled. Estimations of drop growth velocity show that drops could not grow that large when they were activated near the cloud base described by the model. Therefore, these larger drops must have a different history and have to be mixed in from above which could not be included in the model due to missing data.

The present results are consistent with the findings of Hallberg et al. (1997) stating that models often overestimate cloud droplet number and calculate size distributions narrower than those observed.

4. Conclusions

The formation and evolution of an orographic cloud was modeled based on thermodynamic data as well as AP size distributions and solubility. Model results were compared to observations from the field experimental campaigns FEBUKO 2001 and 2002 for three events covering about 150 single cases. The general features could be reproduced by the model.

Sensitivity studies showed that the choice of the water accommodation coefficient α_C highly influences drop

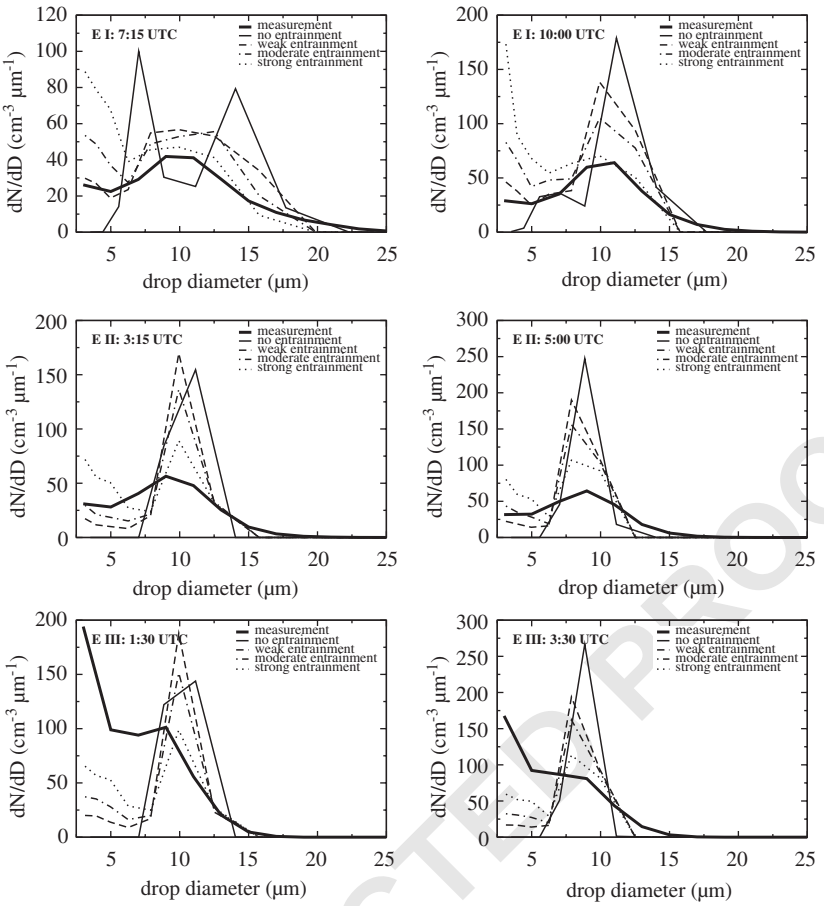

Fig. 4. Selected drop size distributions for model runs using entrainment (dashed, dot-dashed, and dotted lines) compared to the respective standard runs (thin full lines) and measurements (thick full lines) of E I (top; left: 7:15 UTC, right: 10:00 UTC), E II (middle; left: 3:15 UTC, right: 5:00 UTC), and E III (bottom; left: 1:30 UTC, right: 3:15 UTC).

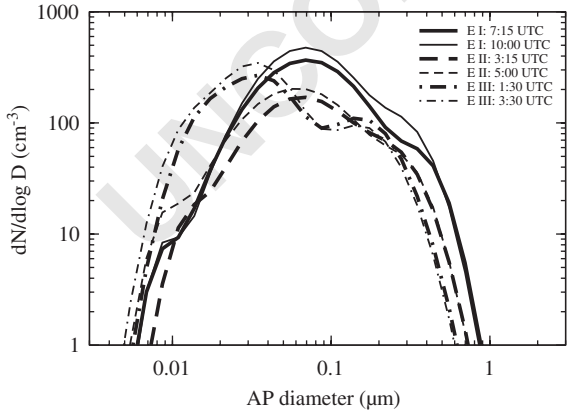

Fig. 5. Initial dry AP distributions for the model runs shown in Fig. 4 as measured at U.

number depending on the specific conditions. Further field and laboratory experiments would be an asset to narrow the rather broad range of α_C found in the literature and thereupon the related uncertainties in cloud modeling. A faster transport acts in a similar way as a lower α_C: super-saturation is enhanced, smaller AP are nucleated and, therefore, drop number increases. A constant deviation in the soluble fraction ε of ± 0.1 leads to comparatively small but relatively stable differences. Much higher deviations were obtained when the size-dependent ε was replaced by an average value for the whole spectrum. This is due to the overestimation of ε of the small AP when the average value is used (increase by up to 0.4 compared to the standard case). The effect is a strong enhancement in drop number for those cases with high supersaturations. For each of the parameters investigated deviations from the standard cases highly

depend on the specific conditions and vary throughout the event. The present study underlines the importance of a size-resolved implementation of ε for the correct description of the droplet nucleation.

Entrainment was shown to be an important process influencing both LWC and drop size distribution. It leads to a decrease in LWC, size distribution broadening, and increase in small droplets with diameters of 2–6 μm. Surprisingly, the simple entrainment parametrization used resulted in a rather consistent picture with different entrainment strengths being appropriate for the events.

Generally, the model is able to reproduce and explain the observed microphysical features. Due to the small droplet sizes and the short cloud lifetime in the cases presented here, coalescence and impaction scavenging are not able to alter the AP distribution, which means that multiphase processes should be responsible for the observed changes of the AP spectra. Therefore, coupling with chemistry models is done (Wolke, et al., 2004; Tilgner et al. 2004a,b; Sehili, et al., 2004). This allows the description of the cloud processing of AP by multiphase processes and the interaction of cloud microphysics and multiphase chemistry.

Acknowledgements

This work was supported by the German Ministry of Education and Research (BMBF) in the framework of AFO 2000 (project MODMEP, 07ATF40). Use of data from the field experimental campaigns FEBUKO 2001 and 2002 is gratefully acknowledged.

References

Arends, B.G., Kos, G.P.A., Maser, R., Schell, D., Wobrock, W., Winkler, P., Ogren, J.A., Noone, K.J., Hallberg, A., Svenningsson, I.B., Wiedensohler, A., Hansson, H.-C., Berner, A., Solly, I., Kruisz, C., 1994. Microphysics of clouds at Kleiner Feldberg. Journal of Atmospheric Chemistry 19, 59–86.

Bower, K.N., Choularton, T.W., Gallagher, M.W., Colvile, R.N., Beswick, K.M., Inglis, D.W.F., Bradbury, C., Martinsson, B.G., Swietlicki, E., Berg, O.H., Cederfelt, S.I., Frank, G., Zhou, J., Cape, J.N., Sutton, M.A., McFadyen, G.G., Milford, C., Birmili, W., Yuskiewicz, B.A., Wiedensohler, A., Stratmann, F., Wendisch, M., Berner, A., Ctyroky, P., Galambos, Z., Mesfin, S.H., Dusek, U., Dore, C.J., Lee, D.S., Pepler, S.A., Bizjak, M., Divjak, B., 1999. The great dun fell experiment 1995: an overview. Atmospheric Research 50, 151–184.

Choularton, T.W., Colvile, R.N., Bower, K.N., Gallagher, M.W., Wells, M., Beswick, K.M., Arends, B.G., Mols, J.J., Kos, G.P.A., Fuzzi, S., Lind, J.A., Orsi, G., Facchini, M.C., Laj, P., Gieray, R., Wieser, P., Engelhardt, T., Berner, A., Kruisz, C., Möller, D., Acker, K., Wieprecht, W., Luttke, J., Levsen, K., Bizjak, M., Hans-son, H.C., Cederfelt, S.I., Frank, G., Mentes, B., Martinsson, B., Orsini, D., Svenningsson, B., Swietlicki, E., Wledensohler, A., Noone, K.J., Pahl, S., Winkler, P., Seyffer, E., Helas, G., Jaeschke, W., Georgii, H.W., Wobrock, W., Preiss, M., Maser, R., Schell, D., Dollard, G., Jones, B., Davies, T., Sedlak, D.L., David, M.M., Wendisch, M., Cape, J.N., Hargreaves, K.J., Sutton, M.A., StoretonWest, R.L., Fowler, D., Hallberg, A., Harrison, R.M., Peak, J.D., 1997. The great dun fell cloud experiment 1993: An overview. Atmospheric Environment 31, 2393–2405.

Colvile, R.N., Sander, R., Choularton, T.W., Bower, K.N., Inglis, D.W.F., Wobrock, W., Schell, D., Svenningsson, I.B., Wiedensohler, A., Hansson, H.-C., Hallberg, A., Ogren, J.A., Noone, K.J., Facchini, M.C., Fuzzi, S., Orsi, G., Arends, B.G., Winiwarter, W., Schneider, T., Berner, A., 1994. Computer modelling of clouds at Kleiner Feldberg. Journal of Atmospheric Chemistry 19, 189–230.

Colvile, R.N., Bower, K.N., Choularton, T.W., Gallagher, M.W., Beswick, K.M., Arends, B.G., Kos, G.P.A., Wobrock, W., Schell, D., Hargreaves, K.J., StoretonWest, R.L., Cape, J.N., Jones, B.M.R., Wiedensohler, A., Hansson, H.C., Wendisch, M., Acker, K., Wieprecht, W., Pahl, S., Winkler, P., Berner, A., Kruisz, C., Gieray, R., 1997. Observations and modelling of the processing of aerosol by a hill cap cloud. Atmospheric Environment 31, 2407–2420.

Eichel, C., Krämer, M., Schütz, L., Wurzler, S., 1996. The water-soluble fraction of atmospheric aerosol particles and its influence on cloud microphysics. Journal of Geophysical Research 101 (D23), 29499–29510.

Feingold, G., Kreidenweis, S.M., 2002. Cloud processing of aerosol as modeled by a large eddy simulation with coupled microphysics and aqueous chemistry. Journal of Geophysical Research 107 (D27), 4687.

Gnauk, T., Brüggemann, E., Müller, K., Jaeschke, W., Chemnitzer, R., Rüd, C., Galgon, D., Nowak, A., Acker, K., Auel, R., Wieprecht, W., Möller, D., Wiedensohler, A., Herrmann, H., 2004. Aerosol characterisation at the FEBUKO upwind station goldlauter (I): Trace gases, particle masses, main components, metals and dry size distributions. Atmospheric Environment, this issue.

Hallberg, A., Wobrock, W., Flossmann, A.I., Bower, K.N., Noone, K.J., Wiedensohler, A., Hansson, H.-C., Wendisch, M., Berner, A., Kruisz, C., Laj, P., Facchini, M.C., Fuzzi, S., Arends, B.G., 1997. Microphysics of clouds: model vs measurements. Atmospheric Environment 31, 2453–2462.

Heinold, B., Tilgner, A., Jaeschke, W., Knoth, O., Herrmann, H., 2004. Meteorological characterisation of the FEBUKO hill capped cloud experiments, Part II: Tracer experiments and flow characterization of the FEBUKO measurement periods with nested non-hydrostatic atmospheric models. Atmospheric Environment, this issue.

Kreidenweis, S.M., Walcek, C.J., Feingold, G., Gong, W., Jacobson, M.Z., Kim, C.-H., Liu, X., Penner, J.E., Nenes, A., Seinfeld, J.H., 2003. Modification of aerosol mass and size distribution due to aqueous-phase SO_2 oxidation in clouds: Comparison of several models. Journal of Geophysical Research 108 (D7), 4213.

Li, Y.Q., Davidovits, P., Shi, Q., Jayne, J.T., Kolb, C.E., Worsnop, D.R., 2001. Mass and thermal accommodation coefficients of $H_2O(g)$ on liquid water as a function of temperature. Journal of Physical Chemistry A 105, 10627–10634.

Martinsson, B.G., Frank, G., Cederfelt, S.-I., Swietlicki, E., Berg, O.H., Zhou, J., Bower, K.N., Bradbury, C., Birmili, W., Stratmann, F., Wendisch, M., Wiedensohler, A., Yuskiewicz, B.A., 1999. Droplet nucleation and growth in orographic clouds in relation to the aerosol population. Atmospheric Research 50, 289–315.

Morita, A., Sugiyama, M., Kameda, H., Koda, S., Hanson, D.R., 2004. Mass accommodation coefficient of water: Molecular dynamics simulation and revised analysis of droplet train/flow reactor experiment. Journal of Physical Chemistry B 108, 9111–9120.

Müller, K., Brüggemann, E., Gnauk, T., Mertes, S., Lehmann, K., Massling, A., Wiedensohler, A., Wieprecht, W., Acker, K., Jaeschke, W., Kramberger, H., Svrcina, B., Bächmann, K., Galgon, D., Nowak, A., vanPinxteren, D., Plewka, A., Rüd, C., Hofmann, D., Herrmann, H., 2004. FEBUKO experiment design and measurements. Atmospheric Environment, this issue.

Pruppacher, H.R., Klett, J.D., 1997. Microphysics of clouds and precipitation. Kluwer Academic Publisher, Dordrecht.

Sehili, A., Müller, F., Wolke, R., Knoth, O., Simmel, M., Tilgner, A., Herrmann, H., 2004. Comparison of different model approaches for the simulation of multiphase processes. Atmospheric Environment, this issue.

Shaw, R.A., Lamb, D., 1999. Experimental determination of the thermal accommodation and condensation coefficients of water. Journal of Chemical Physics 111, 10659–10663.

Simmel, M., Wurzler, S., 2004. Condensation and nucleation in sectional cloud microphysical models based on the Linear Discrete Method. Atmospheric Research, submitted for publication.

Simmel, M., Trautmann, T., Tetzlaff, G., 2002. Numerical solution of the stochastic collection equation—Comparisons of the Linear Discrete Method with other methods. Atmospheric Research 61, 135–148.

Tilgner, A., Heinold, B., Nowak, A., Herrmann, H., 2004a. Meteorological characterisation of the FEBUKO hill capped cloud experiments, Part I: Synoptic characterisation of measurement periods. Atmospheric Environment, this issue.

Tilgner, A., Majdik, Z., Simmel, M., Wolke, R., Herrmann, H.M., 2004b. SPACCIM simulations of multiphase chemistry occurring in the FEBUKO hill-capped cloud experiments. Atmospheric Environment, this issue.

Vieceli, J., Roeselova, M., Tobias, D.J., 2004. Accommodation coefficients for water vapor at the air/water interface. Chemical Physics Letters 393, 249–255.

Wieprecht, W., Mertes, S., Acker, J.L.C. Jr., Brüggemann, E., Hofmann, D., Jaeschke, W., Herrmann, H., 2004. Cloud physics and cloudwater sampler comparison during FEBUKO. Atmospheric Environment, this issue.

Wobrock, W., Schell, D., Maser, R., Jaeschke, W., Georgii, H.-W., Wieprecht, W., Arends, B.G., Möls, J.J., Kos, G.P.A., Fuzzi, S., Facchini, M.C., Orsi, G., Berner, A., Solly, I., Kruisz, C., Svenningsson, I.B., Wiedensohler, A., Hansson, H.-C., Ogren, J.A., Noone, K.J., Hallberg, A., Pahl, S., Schneider, T., Winkler, P., Wini-warter, W., colvile, R.N., Choularton, T.W., Flossmann, A.I., Borrmann, S., 1994. The Kleiner Feldberg Cloud Experiment 1990: An Overview. Journal of Atmospheric Chemistry 19, 3–36.

Wolke, R., Sehili, A., Knoth, O., Simmel, M., Majdik, Z., Tilgner, A., Herrmann, H., 2004. SPACCIM: A parcel model with detailed microphysics and complex multiphase chemistry. Atmospheric Environment, this issue.

Wurzler, S., Reisin, T.G., Levin, Z., 2000. Modification of mineral dust particles by cloud processing and subsequent effects on drop size distributions. Journal of Geophysical Research 105 (D4), 4501–4512.

3B2v8.06a/w (Dec 5 2003).51c XML:ver:5.0.1 AEA : 5777 Prod.Type:FTP pp.1–14(col.fig.:3–9) ED:Asha PAGN:VG SCAN:Global

ARTICLE IN PRESS

Available online at www.sciencedirect.com

SCIENCE DIRECT®

ELSEVIER

Atmospheric Environment ▮ (▮▮▮▮) ▮▮▮–▮▮▮

ATMOSPHERIC ENVIRONMENT

www.elsevier.com/locate/atmosenv

SPACCIM: A parcel model with detailed microphysics and complex multiphase chemistry

R. Wolke*, A.M. Sehili, M. Simmel, O. Knoth, A. Tilgner, H. Herrmann

Leibniz Institute for Tropospheric Research, Permoserstr. 15, 04318 Leipzig, Germany

Abstract

Multiphase processes, such as the uptake of gases by clouds or the production of gas phase halogens from particulate halides are of increasing importance for the understanding of the tropospheric system. Mass transfer and chemical reactions modify the concentrations of stable compounds and oxidants in either phase. The parcel model SPACCIM is presented which combines a complex multiphase chemical model with a detailed microphysical model. For this purpose, a new coupling scheme is implemented. The description of both components is given for a fine-resolved particle/drop spectrum. The SPACCIM approach allows the coupling of multiphase chemical models with microphysical codes of various types. An efficient numerical solution of such systems is only possible utilizing the special structure. An implicit time-integration scheme with an adapted sparse solver for the linear systems is applied. Its numerical efficiency and robustness is analyzed for two scenarios and versions of different complexity of the multiphase chemistry mechanism CAPRAM. The sensitivity of simulation results against variations in the particle/droplet size resolution, the coupling time step and numerical control parameters is discussed. Guidelines for an "optimal" choice of control parameters are derived from this sensitivity study. The coupling scheme operation is always robust and reliable. Model simulations are compared with several measurements from the FEBUKO field campaign. Simulated and measured results show a reasonable agreement.

Keywords: Air pollution modeling; Multiphase chemistry; Chemical kinetics; Stiff ODE solution; Implicit integration schemes; Sparse linear solver

1. Introduction

Multiphase processes are appreciated to be of increasing importance in the comprehension of atmospheric processes. On one hand, they directly influence the life cycles of trace constituents and facilitate conversions of these trace constituents, which are not possible or very inefficient in the pure gas phase. On the other hand, they influence cloud formation and the radiation budget of the atmosphere. Several model studies have indicated that considering the liquid phase as a sink for trace gases fundamentally modifies the chemistry in the gas phase (Lelieveld and Crutzen, 1991; Kreidenweis et al., 2003; Barth et al., 2003). Many recently, available models focus either on complex multiphase chemistry only in a few aggregated drop classes (Audiffren et al., 1998; Herrmann et al., 2000; Djouad et al., 2002; Ervens et al., 2002), or detailed microphysics for strongly simplified chemical mechanisms (Liu and Seidl, 1998; Bott, 1999; Fahey and Pandis, 2001). To better understand the interaction, effects and evolution of the different physico-chemical processes taking place in the atmosphere their modeling requires a

*Corresponding author. Tel.: +49 341 235 2860.
E-mail address: wolke@tropos.de (R. Wolke).

1352-2310/$ - see front matter © 2005 Elsevier Ltd. All rights reserved.
doi:10.1016/j.atmosenv.2005.02.038

detailed description of all transformations with equal rigor. Efforts made in the past to develop sophisticated cloud models with complex multiphase chemistry allows more detailed studies on the interaction between microphysical and chemical multiphase processes (Leriche et al., 2003; Ervens et al., 2004b). In the coupled model of Leriche et al. (2000, 2001), the natural variability of cloud droplets is parameterized in a quasi-spectral form. Ervens et al. (2004a, b) use a model with moving droplet radii with ten different fractions combined with complex inorganic and organic chemistry. Chemical conversions within cloud drops are essentially determined by the mass transfer between gas and liquid phases. Numerical studies show that these phase transitions must be described dynamically (Audiffren et al., 1998; Chaumerliac et al., 2000; Djouad et al., 2003). Furthermore, the phase interchange depends strongly on the phase surface area (Fahey and Pandis, 2001; Kreidenweis et al., 2003). Therefore, a highly resolved drop spectrum should be considered for an appropriate description.

The air parcel model SPACCIM (spectral aerosol cloud chemistry interaction model) is developed for the description of cloud processes by coupling complex multiphase chemistry and detailed microphysics. The description of both process groups is given for a size-resolved particle/drop spectrum. The droplets are subdivided into several classes. This discretization of the droplet spectrum into classes is based on droplet size. Additionally, the amount of scavenged material inside the drops can be taken into account depending on the used microphysical approach. All meteorological parameters needed by the multiphase chemistry are taken from the microphysical model. For this purpose, a new coupling scheme between microphysical and multiphase chemical models is implemented. This approach allows the coupling of the complex multiphase chemistry model with microphysical codes of different types (Sehili et al., 2005a). The coupling scheme provides time-interpolated values of the meteorological parameters (temperature, water vapor, liquid water content) and time-averaged mass fluxes between different droplet classes caused by microphysical processes, e.g., condensation, coagulation and breakup. Changes of the chemical aerosol composition by gas scavenging and chemical reactions feed back on the microphysical processes, e.g., water condensation growth rates via changes in surface tension and the Raoult term. The movement of the air parcel can follow a predefined trajectory. Entrainment and detrainment processes are included in a parameterized form (Sehili et al., 2005b). The model allows a detailed description of the transformation of gases and particles shortly before cloud formation, during the cloud lifetime and shortly after cloud evaporation.

The model equations resulting from multiphase chemical systems are nonlinear, highly coupled and extremely stiff. Multiphase systems are in general much stiffer than pure gas phase systems (Djouad et al., 2002). Explicit time integration methods are not suitable for an efficient integration of very stiff systems (Sandu et al., 1997a, b), since stability requirements can be maintained for very short time steps only. Therefore, implicit methods for treating multiphase processes have been investigated (Jacobson, 2002; Fahey and Pandis, 2001; Djouad et al., 2002). In our approach (Wolke et al., 2001; Wolke and Knoth, 2002), the aqueous phase and gas phase chemistry, the mass transfer between the different droplet classes, among droplets of the same class and with the gas phase are integrated in an implicit and coupled manner by a higher order backward differential formula (BDF) method. For this part, a modification of the code LSODE (Hindmarsh, 1983) with special linear system solvers is used. These direct sparse techniques exploit the special block structure of the corresponding Jacobians. Furthermore, we utilize an approximate matrix factorization which decouples multiphase chemistry and microphysical exchange processes of liquid water at the linear algebra level. The sparse Jacobians are generated explicitly and stored in a sparse form.

The present paper focuses on the coupling scheme between multiphase chemistry and microphysics, the applied numerical techniques and the sensitivity of the coupled model against changes in microphysics as well as the used control parameters. The numerical efficiency and robustness are investigated for a rising parcel test scenario (Kreidenweis et al., 2003; Sehili et al., 2005a) and one scenario derived from FEBUKO[1] data (Herrmann et al., 2005a; Tilgner et al., 2005). An inorganic chemical scheme and four CAPRAM versions (Herrmann et al., 2000; Ervens et al., 2002; Herrmann et al., 2005b) of different complexity are used. The model simulations are compared with several measurements of the FEBUKO field campaign. Finally, we emphasize that this paper is not aimed at a discussion of the different chemical schemes and the FEBUKO results. Tilgner et al. (2005) apply the SPACCIM model for the chemical interpretation of the FEBUKO field campaign whereas Simmel et al. (2005) discuss the related microphysics. A comparison of SPACCIM simulations driven by four different microphysical models is given in Sehili et al. (2005a).

2. Model formulation

In the real atmosphere, multiphase chemistry is in close interaction with microphysical cloud processes. These essential interchange effects have to be taken into

[1]http://projects.tropos.de:8088/afo2000g/FEBUKO_dateien/febuko.html.

consideration also for the development of numerical techniques. As a first step, we focus on the treatment of the multiphase chemistry for a size-resolved particle/droplet spectrum in a box model (e.g., one "grid cell" of an Eulerian grid model). The particles/droplets are segregated into M classes. This discretization is based on droplet size and, possibly, on the amount of scavenged material inside the drops. We assume that the size distribution and all other meteorological parameters are given by a microphysical cloud model. In each of the M droplet classes, N_A aqueous phase species are considered. Some of these aqueous phase species interact with the corresponding gas phase species. Note that the number of species in the gas phase N_G is not necessarily the same as the number of aqueous species which occur in each droplet classes.

In a box model the multiphase chemical processes can be described by the following mass balance equations:

$$\frac{\mathrm{d}c_{l^*}^{\mathrm{G}}}{\mathrm{d}t} = R_{l^*}^{\mathrm{G}}(t, c_1^{\mathrm{G}}, \ldots, c_{N_{\mathrm{G}}}^{\mathrm{G}}) - \kappa_l \sum_k L_k k_t^{kl}\left[c_{l^*}^{\mathrm{G}} - \frac{m_l^k}{H_l}\right] + \mu[c_{l^*}^{\mathrm{G}} - c^{\mathrm{G}_{ent}}], \tag{1}$$

$$\frac{\mathrm{d}(c_l^k)}{\mathrm{d}t} = L^k R_l^{\mathrm{A}}(t, m_1^k, \ldots, m_{N_{\mathrm{A}}}^k) + \kappa_l L_k k_t^{kl}\left[c_{l^*}^{\mathrm{G}} - \frac{m_l^k}{H_l}\right] + T(c_l^1, \ldots, c_l^M) + \mu[c_l^k - c_l^{k_{ent}}], \quad l^* = 1, \ldots, N_{\mathrm{G}}; \quad l = 1, \ldots, N_{\mathrm{A}}; \quad k = 1, \ldots, M, \tag{2}$$

where L_k denotes the volume fraction $[V_k/V_{\mathrm{box}}]$ of the kth droplet class inside the box volume. The vectors c^k, $k = 1, \ldots, M$, are the mass concentrations related to air volume of all aqueous phase species in the kth class. The corresponding aqueous phase concentrations in the kth droplet class are given by $m^k = c^k/L_k$. The vector c^{G} stands for the gas phase concentrations. All concentrations are defined in moles per cubic meters. The chemical reaction terms are denoted by R^{G} and R^{A}. The second terms on the right-hand sides describe the interchange between the gas and aqueous phases. It will be referred to as Henry term in the following. The indicator κ is equal to 1 if the species is soluble. In other cases, κ is equal to 0, and the Henry term will be dropped in both equations. The term T in Eq. (2) stands for the mass transfer between different particle/droplet classes by microphysical exchange processes of liquid water (e.g., by condensation, coagulation and breakup). The time-dependent natural and anthropogenic emissions as well as dry and wet deposition are parameterized in the last terms of the right-hand sides using the time-dependent entrainment/detrainment rate μ. Additionally in a parcel model, variations in the air density should be considered. These density changes influence especially the gas phase chemistry and the mass transfer. To simplify the model formulation, density variations are neglected in (1,2).

The interchange between the gas and liquid phases is specified according to the Schwartz approach (Schwartz, 1986). The value H_l denotes the real dimensionless Henry's law coefficient for the lth species. The mass transfer coefficient

$$k_t^{kl} = \left(\frac{r_k^2}{3D_{\mathrm{g}}} + \frac{4r_k}{3v\alpha_l}\right)^{-1} \tag{3}$$

depends on the droplet radius r_k, the gas diffusion coefficient D_{g}, the molecular speed v and the mass accommodation coefficient α_l of the lth species. For the mass transfer and the aqueous phase chemistry, well-diluted droplets are assumed. In fact, the assumption of an ideal solution is not valid especially for non-activated particles and small droplets. The non-ideal behavior can be parameterized by activity coefficients.

In Fig. 1, the mass fluxes T caused by microphysical exchange processes are described. These liquid water fluxes transport the corresponding fractions of all included aqueous phase species into other classes. When two particles coagulate, for instance, they transfer their masses to the resulting particle class. Assuming an internally mixed aerosol in each class, the input and mixing in this class happens instantly. In the ODE system (1,2), the species within one class are coupled through the chemical reaction system. Furthermore, two types of coupling between different droplet classes can be identified. First, the aqueous phase species within different classes interact directly by the exchange term T. Additionally, they are indirectly coupled via the gas phase by the phase interchange described by the Henry term. The chemistry in the aqueous phase differs from the gas phase chemistry by the occurrence of fast dissociation equilibria. In our approach, these fast dissociations are considered as forward and backward reactions. In contrast to Djouad et al. (2002), the lumping of species is avoided. Most of the dissociations

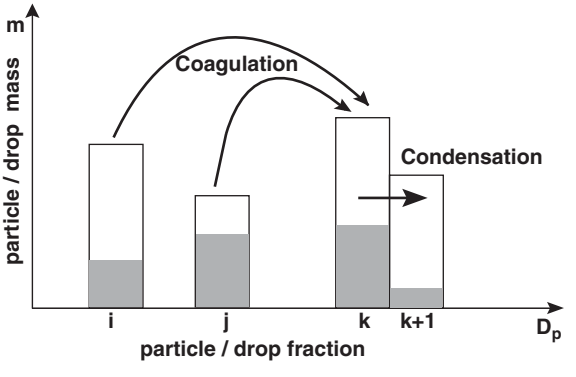

Fig. 1. Schematic representation of mass transport among several sections due to physical processes. The dark part represents the mass fraction of one selected species in the corresponding section.

include H^+ or OH^- ions. Therefore, the behavior of the system depends very strongly on the underlying pH value. In contrast to other authors (Chaumerliac et al., 2000), the pH value is not prescribed a priori. The H^+ concentration as part of the chemical system is computed for each droplet class dynamically.

3. Coupling scheme

The mass fluxes T and all meteorological parameters needed by the multiphase chemistry are taken from the microphysical model. For this purpose, a new coupling scheme between microphysical and multiphase chemical models is implemented as described schematically in Fig. 2. The coupling scheme provides time-interpolated values of the meteorological variables (temperature, water vapor, liquid water content) and generates time-averaged mass fluxes T over the coupling time interval. The changes in the chemical aerosol composition by gas scavenging and the chemical reactions feed back on the microphysical processes (e.g., water condensation growth rates via changes in surface tension and the Raoult term). Therefore, the modified chemical composition of the particle/drop spectrum has to be taken into account by the microphysical model. This feedback is also considered in the coupling scheme, see Fig. 2.

The two models run separately and exchange information only every coupling time step. Each of the two models uses its own time step control. This approach allows the coupling of a complex multiphase chemistry model with microphysical codes of different types. The exchange of information is organized over well-defined interfaces. The size bin discretization of the multiphase chemistry is taken from the microphysical model. However, the use of coarser resolutions in the multiphase chemistry computations is possible by averaging the meteorological variables. The mass fluxes of the matrix T are summarized. In the feedback case, the chemical composition of the coarser size bin calculated in multiphase chemistry is transferred to all corresponding microphysical bins. In the framework of SPACCIM simulations, two adiabatic air parcel models with detailed microphysics and interactions between aerosol particles and drops are employed: one with traditional one-dimensional treatment of the microphysics (water mass only) and one with a two-component treatment of the microphysics (water and aerosol mass) (Simmel and Wurzler, 2004). The latter allows drops of the same size to have different aerosol mass contents and, therefore, different gas scavenging properties (Sehili et al., 2005a).

In the following, only the one-dimensional version is considered. The prognostic microphysical variables for each bin are water mass, total and soluble particulate mass as well as particle number. The model considers the following processes: growth/shrinking and impaction of aerosol particles as well as nucleation, condensation/evaporation and coalescence of droplets. The activation of droplets is explicitly described. One important feature of the model is the description of the water phase transfer feedback on water vapor and air temperature (latent heat release) which is done in an iterative way to avoid overestimation of supersaturation (and, therefore, nucleation) especially at the cloud base. The model accounts for the fact that larger aerosol particles do not have enough time to reach their equilibrium size at high relative humidities near 100% due to the faster changing environment. A moving bin version of the traditional one-dimensional microphysical model is also coupled, motivated by the predominance of condensation/evaporation processes in some case studies (Simmel and Wurzler, 2004). In the moving bin representation, an initial size distribution based on a fixed grid discretization evolves with bins growing by condensation and decreasing by evaporation independently of each other. This approach is more accurate than a fixed bin discretization when only condensation/evaporation is considered. In this case, the number concentration of

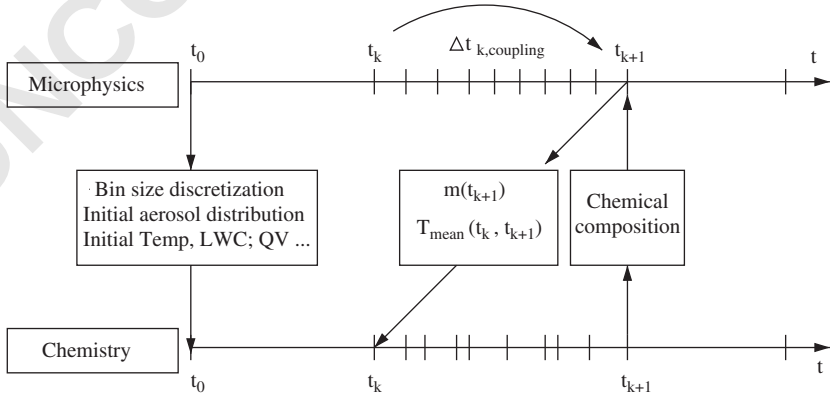

Fig. 2. Schematic representation of the coupling strategy.

Table 1
Characteristics of the used chemical mechanisms

Mechanism	Number of species			Number of reactions					Reference
	Total	Gas	Aqua	Total	Gas	Henry	Disso	Aqua	
INORGANIC	100	80	20	259	237	8	10	4	Sehili et al. (2005a)
CAPRAM2.3	162	82	80	508	237	34	27	210	Herrmann et al. (2000)
CAPRAM2.4	220	83	137	653	237	34	54	328	Ervens et al. (2003)
CAPRAM2.4RED	194	83	111	421	237	33	37	114	Ervens et al. (2003)
CAPRAM3.0	492	99	389	1087	261	51	88	687	Herrmann et al. (2005b)

particles in a size bin does not change. The treatment of coagulation/breakup is possible, but difficult to implement (Jacobson, 1999).

4. Multiphase chemical processes

In our implementation, the chemical reaction systems (gas and aqueous phases, phase transfer according to Schwartz) are given in ASCII data files. The syntax to describe the system is very easy and allows large flexibility (Wolke and Knoth, 2002; Sehili et al., 2005a). Changes within the chemical mechanism or the replacement of the whole chemistry can be performed in a simple and comprehensive way. For the task of reading and interpreting the chemical data, a preprocessor was developed. It provides SPACCIM with all data structures required for the computation of the chemical terms R as well as the corresponding Jacobians.

For the tests a more simple inorganic reaction mechanism (Sehili et al., 2005a) and four versions of the chemical aqueous phase radical mechanism (CAPRAM)[2] are used (Herrmann et al., 2000; Ervens et al., 2002; Herrmann et al., 2005b). The CAPRAM mechanisms contain a complex implementation of aqueous phase inorganic as well as organic chemistry including organic species with up to mainly four carbon atoms in version 3.0. The gas phase chemistry of all mechanisms is based on the RACM mechanism (Stockwell et al., 1997). Typical characteristics of the mechanisms are given in Table 1.

5. Numerical method

System (1,2) of ordinary differential equations (ODE) is integrated in an implicit and coupled manner by a higher order BDF method. For this part a modification of the code LSODE (Hindmarsh, 1983) with special linear system solvers is used. The time step and order control is the same as in the original LSODE code. The main task in an implicit method is the approximate solution of linear systems of the form

$$(I - \beta \Delta t J)\Delta c = b, \tag{4}$$

which involves the Jacobian J of the right-hand side of the ODE system. I is the identity matrix. Δt stands for the time step size and β denotes a parameter which depends on the order of the BDF method. For an efficient solution of system (4) the properties of the Jacobian (e.g., sparsity, block structure, different types of coupling) have to be utilized. The solution of linear systems during the integration of system (1,2) is only practicable by applying sparse techniques. In atmospheric gas phase chemistry, the sparse linear system (4) can be solved by linear Gauss–Seidel iterations (Knoth and Wolke, 1995). Unfortunately, for aqueous chemistry mechanisms the Gauss–Seidel iteration converges only slowly or even fails (Wolke and Knoth, 2000).

The Jacobian structure of the right-hand side of the multiphase system (1,2) is given in Fig. 3. The blue blocks in the diagonal are the Jacobians of the gas phase and aqueous phase reaction terms, respectively. In our example, the upper left block stems from the gas phase. The other two diagonal blocks coming from the aqueous phase chemistry have the same sparse structure. The green left and upper boundary blocks represent the phase interchange according to Schwartz (1986). The orange diagonal matrices include the coupling terms resulting from the mass transfer between the droplet classes. In the implementation, the sparse block matrices are generated explicitly and stored in a sparse form. The sparse factorization is stored and performed only when the Jacobian J has to be recalculated. By utilizing an approximate matrix factorization (AMF), the splitting between the multiphase chemistry part and the part from microphysical exchange processes is performed at the linear algebra level (Wolke and Knoth, 2000). The idea is to approximate the matrix $(I - \beta \Delta t\, J)$ by

[2] http://projects.tropos.de:8088/capram.

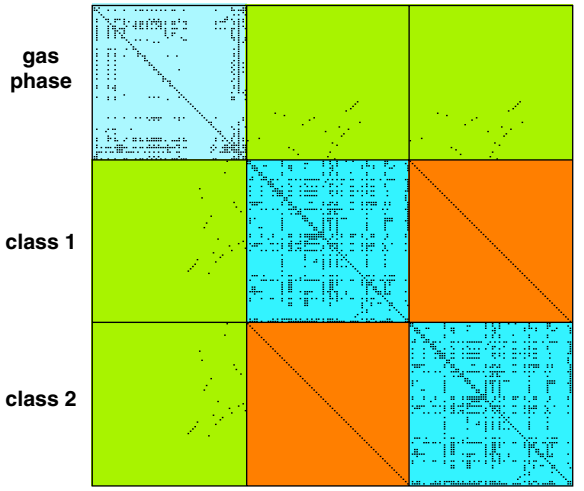

Fig. 3. Sparse structure of Jacobian for CAPRAM2.3 and two droplet classes.

$$(I-\beta\Delta tJ)\approx(I-\beta\Delta tJ^{\mathrm{P}})(I-\beta\Delta tJ^{\mathrm{C}})$$
$$=(I-\beta\Delta tJ)+\beta^2\Delta t^2J^{\mathrm{P}}J^{\mathrm{C}}, \quad (5)$$

where $J=J^{\mathrm{P}}+J^{\mathrm{C}}$. The matrix J^{P} includes the mass transfer between the droplet classes and J^{C} denotes the Jacobian from the multiphase chemistry as well as the phase interchange. Then the linear system (4) can be solved by two sequential linear system solutions:

$$(I-\beta\Delta tJ^{\mathrm{P}})b^*=b, \quad (6)$$

$$(I-\beta\Delta tJ^{\mathrm{C}})\Delta c=b^*. \quad (7)$$

For a linear liquid water transfer term T, the linear system (6) is resolved into N_{A} non-coupled M-dimensional subsystems. These linear subsystems are solved by a full LU decomposition without pivoting. The coefficient matrix is the same for all subsystems. Consequently, only one LU decomposition is required. Note that the decoupling into the N_{A} subsystems is also valid for a nonlinear term T. But the coefficient matrix can be dependent on the considered species in this case. The sparse linear system (7) is solved by a sparse LU decomposition with diagonal pivoting. An optimal order of the pivot elements to avoid fill-in is determined by a diagonal Meis–Markowitz strategy, e.g., Sandu et al. (1996). To improve this usual strategy two additional requirements are introduced:

1. All gas phase species which occur in Henry terms are placed at the end of the pivot order.
2. In the modified strategy, the vector $\mathbf{c}_l \in R^M$ of the lth aqueous phase concentration is understood as a "supernode". If one of these species is picked up as pivot element the whole submatrix is treated as the pivot. After the reordering all species of the vector appear one after another in the order.

Additionally, a Schur complement implementation for the solution of system (7) is investigated in Wolke and Knoth (2002).

Two alternative matrix approximations

$$(I-\beta\Delta tJ)\approx(I-\beta\Delta tJ^{\mathrm{C}})(I-\beta\Delta tJ^{\mathrm{P}})$$
$$=(I-\beta\Delta tJ)+\beta^2\Delta t^2J^{\mathrm{C}}J^{\mathrm{P}}, \quad (8)$$

$$(I-\beta\Delta tJ)\approx(I-\beta\Delta tJ^{\mathrm{C}})$$
$$=(I-\beta\Delta tJ)+\beta\Delta tJ^{\mathrm{P}} \quad (9)$$

are tested in addition to Eq. (5). This is inspired by the discussion of the influence of the splitting sequence and the quality of the Jacobian approximation on the accuracy, e.g., in Verwer and Sportisse (1998) and Wolke and Knoth (2000). In approach (9), $J^{\mathrm{P}}\approx 0$ and only the sparse system from the multiphase chemistry has to be solved. In Appendix A of the electronic supplementary material (ESM),[3] the approximation error of approaches (5) and (8) is analyzed.

6. Robustness, sensitivity and numerical efficiency

6.1. Test scenarios

Simulations for two different scenarios are carried out. Note that a short description of both cases is given in the ESM footnote 3, Appendix B. To confirm the conclusions, further relevant results are also presented in the ESM, Appendix C. The RISING AEROSOL1 scenario is defined in Sehili et al. (2005a). It was inspired by Kreidenweis et al. (2003) and simulates an air parcel lifted adiabatically at 0.5 m s^{-1} from 98 m below cloud base up to 1200 m above cloud base. The initial dry aerosol number size distribution consists of two lognormal modes, covering the Aitken and the accumulation size range. The air parcel start location is 45°N and 600 m altitude for summer solstice at 9.00 AM. In-cloud gas phase photolysis rates are decreased using a factor 0.5 due to cloud droplet scattering. The second scenario simulates an orographic cloud. The meteorological and initial data are derived from the collected ones during event EI of the FEBUKO experiment (Herrmann et al., 2005a). The detailed data set of the used FEBUKO scenario is given in Tilgner et al. (2005). In both test cases, the initial aerosol composition is prescribed independently from the used mechanism. All species not participating in the corresponding reaction scheme are considered as "passive", non-reactive tracers. They affect the pH value and are part of the

[3] http://projects.tropos.de:8088/afo2000g3/FEBUKO_dateien/febuko.html.

total mass. The initial pH value is determined through the charge balance equation for the initial aerosol and is then computed dynamically throughout the whole simulation time.

6.2. Model setup

The discussion of the chemical issues is beyond the focus of this paper. We refer to Sehili et al. (2005a) and Tilgner et al. (2005). The main task here is to investigate some features and parameter setups of SPACCIM from a numerical point of view. This sensitivity study is performed in order to determine "optimal" control parameters without significant loss of accuracy. Due to the availability of measurements, most of the results presented here concern the FEBUKO case. Options and parameters being subject to assessment are the used mechanism, the coupling time step Δt_{cpl}, feedback from microphysics to chemistry, the number of bins NUMFRAC, the solver relative tolerance RTOL and the applied AMF. Furthermore, coarser size bin resolutions in the multiphase chemistry to reduce the computational costs are investigated. In this approach, RESCHEM bins of the microphysical grid are summarized for the chemistry calculations. The FEBUKO default run is carried out with CAPRAM 2.4 RED, without feedback, NUMFRAC = 66 bins, RESCHEM = 1, a coupling time step $\Delta t_{\mathrm{cpl}} = 10$ s, RTOL $= 10^{-5}$ and approximation (9) with Meis–Markowitz LU decomposition strategy. The RISING default run uses CAPRAM 2.3, RTOL $= 10^{-3}$, AMF (8) and otherwise the same parameters. The changes are motivated by preliminary simulations. In the moving bin runs, $J^{\mathrm{P}} = 0$ and, therefore, approximation (9) is applied.

In the following, the time series plots of aqueous phase variables show summarized masses and averaged concentrations over the whole spectrum. aORA1 represents the sum of formic acid and formate. aORA2 stands for the sum of acetic acid and acetate. All mass concentrations in the tables are given in moles per cubic meters. The numerical effort is characterized by the number of required time integration steps stp, right-hand side evaluations fcn and the CPU time. All runs are carried out on a four-processor IBM pSerie workstation with 8 GByte memory.

6.3. Microphysical processes

As the parcel ascends, the air becomes supersaturated and aerosols whose radii exceed the critical ones are considered to be "activated" and continue to grow according to the Koehler equation. During the FEBUKO scenario, the air parcel reaches Schmuecke summit after 710 s, then evaporation proceeds until the final parcel location. In RISING the top of the cloud is reached after 2596 s simulation time.

Fig. 4 shows the explicit description of the activation process for the two versions of SPACCIM. In the moving bin discretization, no remapping to the original fixed grid is considered and bins evolve independently from each other. Therefore, spectral variables are plotted using points which are not connected with lines. Between the activated and non-activated part of the spectrum, the microphysical properties cannot be resolved. However, the smaller gap for the fixed bin approach seems to be mainly caused by numerical diffusion. Furthermore, the number distribution of the activated droplets remains within a narrow size range around 10 μm and agrees well with the fixed bin representation. The same remarks can be made for the spectrum of the liquid water content (LWC). The total LWC is a key value in model simulations dealing with complex multiphase reacting systems including phase uptake. Fig. 5 (left) illustrates the correlation between simulated total LWC and total non-water mass (NWM) during FEBUKO caused by uptake processes. A punctual comparison with measured LWC on mount Schmuecke shows that about 25% more LWC is simulated. On the other hand, simulated and measured

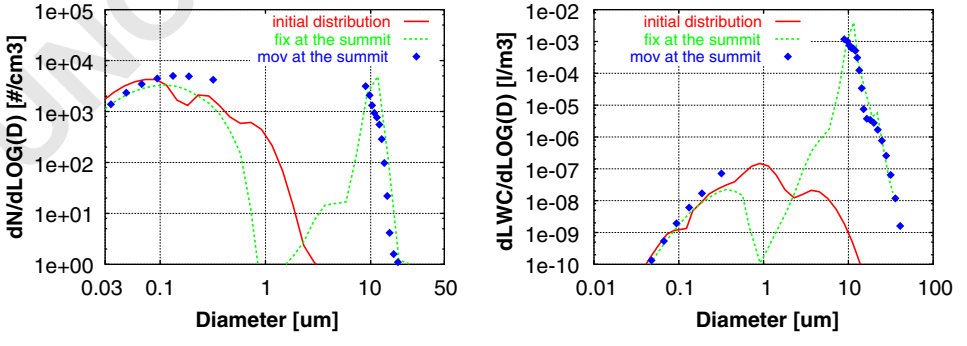

Fig. 4. Number size distribution (left) and LWC spectrum (right) at Schmuecke summit for the FEBUKO simulation applying CAPRAM2.4RED. Comparison is shown between the fixed bin and moving bin approaches.

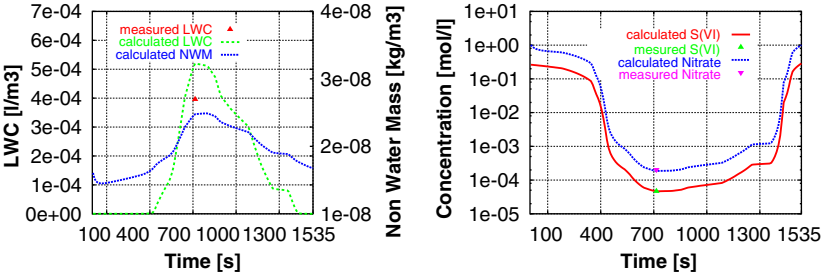

Fig. 5. Comparison of simulated and measured LWC, non-water mass, S(VI) and nitrate during FEBUKO at Schmuecke. Simulation are with SPACCIM–FIX using CAPRAM2.4RED mechanism.

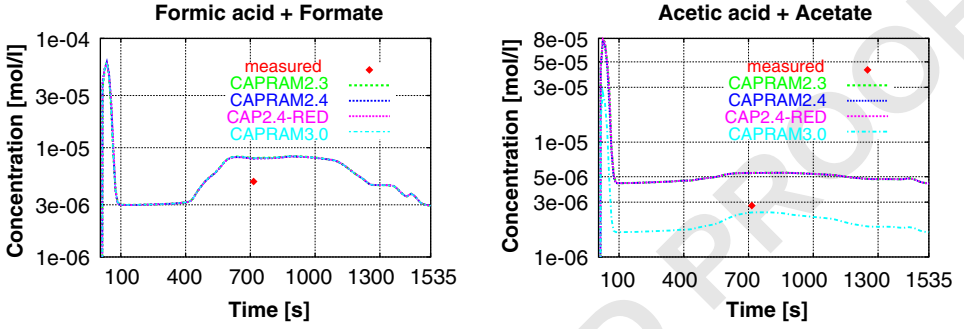

Fig. 6. Comparison of simulated and measured aORA1 (formic acid + formate) and aORA2 (acetic acid + acetate) during FEBUKO at Schmuecke. Simulations with SPACCIM–FIX for four different versions of CAPRAM are plotted.

Table 2
Sensitivity of SPACCIM–FIX to different reacting mechanisms during the FEBUKO scenario

Mechanism	S(VI)	NO_3^-	aORA1	aORA2	pH	stp	Fcn	CPU (s)
CAPRAM2.3	2.414e-8	9.690e-8	3.650e-9	2.621e-9	4.238	8079	13885	861
CAPRAM2.4	2.417e-8	9.690e-8	3.651e-9	2.618e-9	4.237	8138	14098	1659
CAPRAM2.4RED	2.415e-8	9.690e-8	3.653e-9	2.618e-9	4.238	8336	14308	1412
CAPRAM3.0	2.417e-8	9.691e-8	3.666e-9	1.166e-9	4.242	7744	13182	4105
INORGANIC	2.373e-8	9.493e-8	—	—	4.301	7037	12155	245

molalities of S(VI) and nitrate on mount Schmuecke are in good agreement (Fig. 5,right).

6.4. Simulations for chemical mechanisms of different complexity

The use of CAPRAM3.0 (where much more organic compounds and reacting pathways are considered) leads to a better agreement between measured and simulated molalities of some organic species, e.g., aORA2 at mount Schmuecke as shown in Fig. 6(right) and Table 2. For other organic species, no significant differences between the mechanisms are observed (Fig. 6, left). Moving to sulfur chemistry (Fig. C.1, ESM), SPACCIM–FIX simulates less SO_2 uptake when using the INORGANIC mechanism. Runs with the other mechanisms remain comparable whereas the good agreement between CAPRAM2.4 and CAPRAM3.0 is remarkable. Results with SPACCIM–FIX for S(VI) show that INORGANIC and CAPRAM2.3 mechanisms have a similar behavior before activation. Deviations compared to the other mechanisms can be explained by a different equilibrium constant in the Schwartz approach. The initial sharp decrease in S(VI) predicted by the three newer versions of CAPRAM is caused by the imbalance of initial particulate S(VI) and the gas phase applying the modified equilibrium constant. Therefore, S(VI) is released as H_2SO_4 from

the particle to the gas phase. Using INORGANIC, less S(VI) is taken up in the particle phase after activation due to the omission of the aqueous phase dissociation pathways of organic acids such as formic acid and, additionally for CAPRAM2.4 or higher versions, dicarbonylic acids such as oxalic acid. These dissociations influence strongly the pH and, consequently, the S(VI) chemistry. The flexibility of SPACCIM concerning the use of various mechanisms offers the possibility to analyze pathways of selected species.

Tables 2 and 3 summarize the mass concentrations of selected aqueous phase species, the pH values and the computational effort simulated by SPACCIM–FIX and SPACCIM–MOV. The numbers of steps stp and function evaluations fcn are comparable for all mechanisms. However, the CPU times are strongly related to the complexity of the mechanisms. Besides the dimension of the system and the number of reactions, the types of reaction rates has a large influence on the computing time. For instance, the calculation of a large number of Arrhenius-type reaction constants can consume more CPU time than the efficient solution of the sparse linear systems, SPACCIM–MOV runs much faster since neither a remapping to original grid nor the computation of microphysical fluxes are required. The resulting deviations from SPACCIM–FIX are small (Table 3). Hence, SPACCIM–MOV constitutes a reliable alternative when only condensation/evaporation are involved.

6.5. Feedback of multiphase chemical on microphysical processes

The Raoult term in the condensation rate is calculated using osmotic coefficient according to Pruppacher and Klett (1997). The microphysical model considers initially ammonium bisulfate aerosol. As described in the coupling scheme, SPACCIM allows the feedback of chemical particle composition onto microphysics. For that, the original Raoult term in the condensation rate calculation is replaced by the sum of the molar ratios (mol_{sol}/mol_w) of all soluble aqueous phase species

$$\mathrm{Raoult}^k_{\mathrm{chem}} = \sum_i^{N_{\mathrm{aqua}}} \mathrm{mol}^k_{\mathrm{sol}_i}/\mathrm{mol}^k_{\mathrm{w}}.$$

The quantities $\mathrm{mol}^k_{\mathrm{sol}_i}$ of soluble material are given by the chemistry and kept constant in the microphysical calculations over the coupling time interval. The molar water fraction $\mathrm{mol}^k_{\mathrm{w}}$ is taken directly from the microphysics.

When the feedback of chemistry onto microphysics is considered more particles are activated in the fixed bin case (Fig. 7). That means that droplets competing for the

Table 3
Sensitivity of SPACCIM–MOV to different reacting mechanisms during the FEBUKO scenario

Mechanism	S(VI)	NO_3^-	aORA1	aORA2	pH	stp	fcn	CPU (s)
CAPRAM2.3	2.383e-8	9.859e-8	4.134e-9	2.806e-9	4.195	3515	6295	77
CAPRAM2.4	2.386e-8	9.860e-8	4.126e-9	2.797e-9	4.193	3619	6456	134
CAPRAM2.4RED	2.384e-8	9.860e-8	4.129e-9	2.799e-9	4.193	3984	6931	97
CAPRAM3.0	2.386e-8	9.861e-8	4.168e-9	1.269e-9	4.199	3204	5732	271
INORGANIC	2.343e-8	9.662e-8	—	—	4.26	2915	5232	25

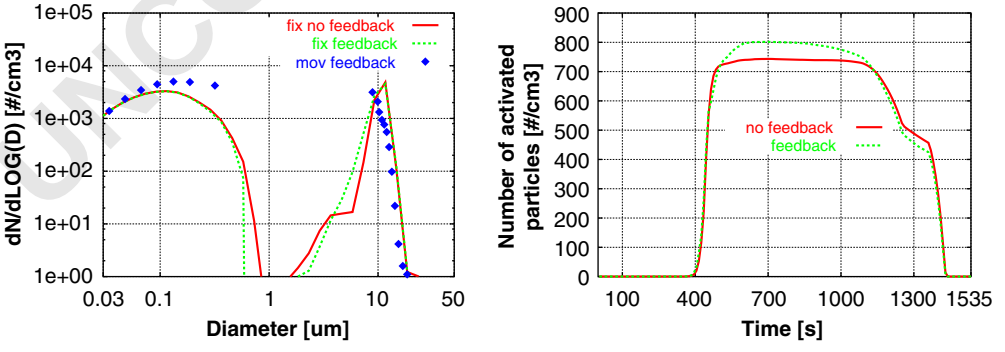

Fig. 7. Number size distribution (left) and total number of activated particles (right) at Schmuecke summit for the FEBUKO simulation applying CAPRAM2.4RED. Comparison is shown between the moving and fixed bin approaches with and without feedback of microphysics to chemistry.

same available humidity are smaller in size. When evaporation becomes significant, particles smaller in size evaporate faster. Therefore, the two curves in Fig. 7 (right) evolve almost identically during the evaporation phase. Moreover, a spectral analysis of the number distribution at the summit confirms this observation (Fig. 7, left). In the feedback run, the non-activated part of the spectrum shrinks towards smaller sizes. One explanation could be that the more realistic Raoult term delivered by chemistry reduces the critical supersaturation. Furthermore, more particles are being activated due to the lower critical radius. These additional smaller particles are activated and grow into droplets. No significant influence of the feedback on microphysics is observed for the moving bin version. The main reason may be that the Raoult term is calculated from the soluble fraction of the initial aerosol composition. For the "non-activated" particles, the ratio between soluble and total mass is only slightly changed by the gas uptake. For the "activated" particles, the Raoult term is dominated by the large water fraction. As seen in Fig. 8 for HNO_3 and nitrate, the effect of the feedback on the species evolution is also not substantial. We refer to Sehili et al. (2005a) for a further discussion of the differences between the moving and fixed bin approach.

6.6. Coupling time step and its control

The coupling strategy is based on a definition of a coupling time step Δt_{cpl} along which the two models communicate. Δt_{cpl} is a key control parameter of SPACCIM. It has an influence on chemistry, numerics and also on microphysics when considering feedback. A first and precautionary attempt to choose Δt_{cpl} is to take a small one. But this implies more numerical costs in the time integration of multiphase chemistry due to the larger number of restarts which are expensive for higher order implicit solvers. In contrary, using a large Δt_{cpl} increases the risk to not resolve critical time points like the start of the activation. Furthermore, the differences between the interpolated meteorological variables and their real values can adulterate also species chemical evolution. The benefit in the computational effort is bought by a lower accuracy in the simulated species concentrations (Tables 4 and 5). For the FEBUKO scenario, a coupling time step of 10 s appears to be reasonable and gives satisfactory results. SPACCIM allows also a dynamical control of Δt_{cpl} during the runs. This control is closely related to changes in LWC. During periods with large local variations of the LWC, Δt_{cpl} is reduced. If the changes in LWC are small then

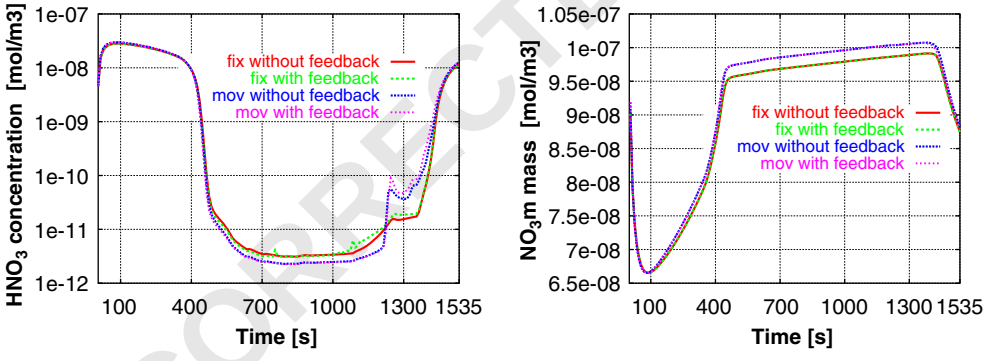

Fig. 8. Simulation of HNO_3 and NO_3^- evolution of the FEBUKO scenario by applying CAPRAM2.4RED. Comparison is shown between the fixed and the moving bin approaches with and without feedback.

Table 4
Sensitivity of SPACCIM–FIX to different coupling time steps during the rising scenario

Δt_{cpl}	S(VI)	NO_3^-	aORA1	AORA2	pH	stp	fcn	CPU (s)
5	3.423e-8	1.152e-7	7.081e-9	7.188^e-9	4.472	4747	6458	400
10	3.426e-8	1.152e-7	7.078e-9	7.193^e-9	4.473	4447	6035	410
20	3.432e-8	1.152e-7	7.069e-9	7.204^e-9	4.477	3875	5456	344
30	3.435e-8	1.152e-7	7.065e-9	7.211^e-9	4.479	3631	5142	341
40	3.442e-8	1.152e-7	7.054e-9	7.224e-9	4.484	3275	4596	528
Controlled	3.429e-8	1.152e-7	7.072e-9	7.201e-9	4.476	3446	4726	334

Table 5
Sensitivity of SPACCIM–MOV to different coupling time steps during the RISING scenario

Δt_{cpl}	S(VI)	NO_3^-	aORA1	AORA2	pH	stp	fcn	CPU (s)
5	3.502e-8	1.150e-7	7.185e-9	7.371e-9	4.459	2233	2743	63
10	3.406e-8	1.150e-7	7.185e-9	7.365e-9	4.460	1686	2231	59
20	3.399e-8	1.138e-7	7.173e-9	7.320e-9	4.470	1557	2097	51
30	3.405e-8	1.150e-7	7.191e-9	7.372e-9	4.459	1304	1757	47
40	3.405e-8	1.150e-7	7.191e-9	7.372e-9	4.459	1266	1750	108
Controlled	3.413e-8	1.149e-7	7.190e-9	7.375e-9	4.460	1578	1985	58

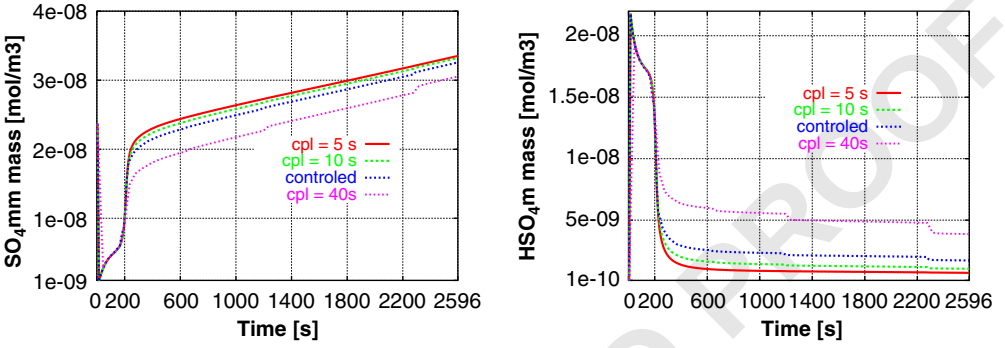

Fig. 9. SPACCIM–FIX simulations of the RISING scenario applying CAPRAM2.3: Sensitivity of SO_4^{2-} and HSO_4^- mass concentrations against variations of the coupling time step.

Δt_{cpl} can be increased. Additionally, critical points along the parcel trajectory (e.g., start of activation, summits and other turning points) are located and taken into account for the control. The results in Tables 4, 5 and Fig. 9 for RISING illustrate the benefit of such dynamic strategy. However, our experiences for the FEBUKO runs shows that such strategy does not always bring noticeable gain. In general, simulations of multiphase processes for air parcels forced by synoptic events over a long period need the optimization of the control parameters. A dynamic choice of Δt_{cpl} is a promising issue in this context.

6.7. Size resolution of multiphase chemical model

The dimension of the ODE system (1,2) depends on the size resolution of the spectrum. Usually, the multiphase chemistry uses the discretization of the spectrum specified by the microphysical model. Coarser resolutions RESCHEM for multiphase chemistry calculations reduce the dimension of the system and, consequently, the numerical costs. Obviously, the accuracy suffer in this case. Especially, the lower resolution of the spectrum part where activation takes place influences mainly the chemistry. Simulations with RESCHEM = 2 and 4 are carried out. The use of RESCHEM = 2 is a good compromise between the loss of accuracy and the numerical gain (Tables 6 and C.1, ESM). Furthermore, it is observed that the loss of accuracy using SPACCIM–FIX increases gradually with RESCHEM in the same tendency (increase or decrease). For SPACCIM–MOV, the loss of accuracy with RESCHEM = 4 evolves in an opposite way to RESCHEM = 2. A finer size resolution in microphysics as well as in multiphase chemistry improves the accuracy of chemical species concentrations (Table 6 and C.1, ESM). As expected, the effect of NUMFRAC is contrary to RESCHEM. Using NUMFRAC = 264 does not lead to a noticeable difference in species concentrations compared to NUMFRAC = 132. The numerical cost of a finer size resolution is evidently much higher. The default setup with NUMFRAC = 66 represents a good compromise between the chemical and numerical aspects.

6.8. Optimal choice of numerical control parameters

The time step control of the BDF solver requires the definition of a relative error tolerance. Stronger relative tolerances imply smaller time steps and, hence, higher numerical costs. But the risk of a solver failure is minimized in this case. When the solver fails, an expensive restart using sharper tolerances has to be

Table 6
Sensitivity of SPACCIM–FIX to different chemistry resolution and different bin size resolution during the FEBUKO scenario

Resolution	S(VI)	NO_3^-	aORA1	aORA2	pH	stp	fcn	CPU (s)
DEFAULT	2.414e-8	9.688e-8	3.643e-9	2.612e-9	4.237	8336	14308	1412
RESCHEM = 2	2.435e-8	1.001e-7	3.494[e]-9	2.567e-9	4.185	6641	11475	335
RESCHEM = 4	2.477e-8	1.005e-7	3.427[e]-9	2.547e-9	4.154	6050	10395	311
NUMFRAC = 132	2.385e-8	9.634e-8	3.769e-9	2.655e-9	4.254	10310	17218	10472
NUMFRAC = 264	2.382e-8	9.619e-8	3.925e-9	2.714e-9	4.250	9949	16511	27008

Table 7
Numerical efficiency of SPACCIM for different relative tolerances and the FEBUKO scenario

Relative tolerance	SPACCIM–FIX			SPACCIM–MOV		
	Stp	fcn	CPU	stp	fcn	CPU (s)
RTOL = 1.E − 7	17024	26742	1948	8776	14203	120
RTOL = 1.E − 6	11902	19500	1731	6117	10322	132
RTOL = 1.E − 5	8336	14308	1412	3984	6931	97
RTOL = 1.E − 4	6010	10598	1351	2463	4188	65
RTOL = 1.E − 3	3939	6913	1301	81694	2860	69

Table 8
Numerical efficiency of SPACCIM for different solver variants during FEBUKO and RISING scenarios

Model	AMF	LU strategy	FEBUKO			RISING		
			stp	fcn	CPU (s)	stp	fcn	CPU (s)
SPACCIM–FIX	(8)	Meis–Markowitz	9161	15997	1714	4447	6035	410
	(5)	Meis–Markowitz	9423	18563	1968	10491	43122	2050
	(9)	Meis–Markowitz	8336	14308	1412	5404	9961	610
	(8)	Schur complement	9138	15978	1723	4378	6061	403
	(5)	Schur complement	9345	18431	1867	10440	42543	2112
	(9)	Schur complement	8546	14467	1675	5388	9992	625
SPACCIM–MOV	(9)	Meis–Markowitz	3984	6931	97	1686	2231	59
	(9)	Schur complement	4134	7120	128	4131	5859	130

performed. A compromise is reached when those two sides of the problem are taken into account. Thus, every simulated scenario needs its specific tolerance to reach "optimal" performance. In the case of FEBUKO simulations (Table 7), the convergence of the solver is ensured with $RTOL = 10^{-3}$ for both versions. No influence on the solution accuracy between sharper and weaker tolerances is observed.

From a numerical point of view, the direct sparse Meis–Markowitz and Schur complement solvers discussed in Wolke and Knoth (2002) for time-constant microphysics remain comparable for more realistic coupled simulations (Table 8). Furthermore, the choice of AMF can become important under some microphysical conditions. The deviations between the numerical efficiencies of AMF (5), (8) and (9) become substantial during the "monotone" RISING scenario. Approximation (9) is comparable to Eq. (8). As shown in Table 8, less function evaluations fcn and, therefore, less CPU time are needed for approach (8) in comparison to Eq. (5). Here the transport matrix J^P is mostly lower bidiagonal due to the presence of condensation mainly. One explanation for the benefit of Eq. (8) could be that the predicted vector of aqueous chemical species c is firstly updated through the solution of the sparse multiphase chemistry system (7) and then

passed to the transport part (6). The vector c given by Eq. (7) is only slightly modified by Eq. (6) and remains closer to the solution of original system (4). Surprisingly, the approximation (9) is the most efficient one for the FEBUKO simulations which needs further investigations.

7. Summary

The size-resolved parcel model SPACCIM with detailed microphysics and complex multiphase chemistry is presented. The performance of the model is discussed for simulations of realistic scenarios like event EI of the FEBUKO field campaign. The simple chemical mechanism INORGANIC which contains only inorganic aqueous phase chemistry and very complex mechanisms of the CAPRAM family are involved in this study. A high flexibility is offered concerning the use of the reacting systems. Local events like FEBUKO can be analyzed by using SPACCIM. The comparison between simulated and measured results shows a reasonable agreement. The sensitivity study indicates that the coupling scheme is robust and reliable. The setup of the control parameters afford to find an "optimal" adjustment depending on the considered application. The SPACCIM approach allows the coupling of a complex multiphase chemistry model with microphysical codes of various types. In addition to the one-dimensional discretization of the particle spectrum used in the present paper, a microphysical model with a two-component treatment of the microphysics (water and aerosol mass) is implemented into SPACCIM (Sehili et al., 2005a).

Acknowledgements

This research is supported by the BMBF (AFO2000 atmospheric research program, Project no. 07ATF40).

References

Audiffren, N., Renard, M., Buisson, E., Chaumerliac, N., 1998. Deviation from the Henry's law equilibrium during cloud events: a numerical approach of the mass transfer between phases and its specific numerical effects. Atmospheric Research 49, 139–161.

Barth, M.C., Sillman, R., Hudman, R., Jacobson, M.Z., Kim, C.H., Monod, A., Liang, J., 2003. Summary of the cloud chemistry modeling intercomparison: photochemical box model simulation. Journal of Geophysical Research 108 (D7).

Bott, A., 1999. A numerical model of the cloud-topped planetary boundary layer: chemistry in marine stratus and the effects on aerosol particles. Atmospheric Environment 33, 1921–1936.

Chaumerliac, N., Leriche, M., Audiffren, N., 2000. Modeling of scavenging processes in clouds: some remaining questions about the partitioning of gases among gas and liquid phases. Atmospheric Research 53, 29–43.

Djouad, R., Sportisse, B., Audiffren, N., 2002. Numerical simulation of aqueous-phase atmospheric models: use of non-autonomous Rosenbrock method. Atmospheric Environment 36, 873–879.

Djouad, R., Michelangeli, D.V., Gong, W., 2003. Numerical solution for atmospheric multiphase models: testing the validity of equilibrium assumptions. Journal of Geophysical Research 108 (D19), 4602–4614.

Ervens, B., George, C., Williams, J.E., Buxton, G.V., Salmon, G.A., Bydder, M., Wilkinson, F., Dentener, F., Mirabel, P., Wolke, R., Herrmann, H., 2002. CAPRAM2.4 (MODAC mechanism): an extended and condensed tropospheric aqueous phase mechanism and its application. Journal of Geophysical Research 108 (D14), 4426.

Ervens, B., Feingold, G., Frost, G.J., Kreidenweis, S.M., 2004a. A modeling study of aqueous production of dicarboxylic acids: 1. Chemical pathways and speciated organic mass production. Journal of Geophysical Research 109, D15205.

Ervens, B., Feingold, G., Clegg, S.L., Kreidenweis, S.M., 2004b. A modeling study of aqueous production of dicarboxylic acids: 2. Implications for cloud microphysics. Journal of Geophysical Research 109, D15206.

Fahey, K.M., Pandis, S.N., 2001. Optimizing model performance: variable size resolution in cloud chemistry modeling. Atmospheric Environment 35, 4471–4478.

Herrmann, H., Ervens, B., Jacobi, H.-W., Wolke, R., Nowacki, P., Zellner, R., 2000. CAPRAM2.3: a chemical aqueous phase radical mechanism for tropospheric chemistry. Journal of Atmospheric Chemistry 36, 231–284.

Herrmann, H., Wolke, R., Müller, K., Brüggemann, E., Gnauk, T., Barzaghi, P., Mertes, S., Lehmann, K., Massling, A., Birmili, W., Wiedensohler, A., Wieprecht, W., Acker, K., Jaeschke, W., Kramberger, H., Syrcina, B., Bächmann, K., Collett, J.L., Jr., Galgon, D., Schwirn, K., Nowak, A., van Pinxteren, D., Plewka, A., Chemnitzer, R., Rüd, C, Hofmann, D., Tilgner, A., Diehl, K., Heinold, B., Hinneburg, D., Knoth, O., Sehili, A.M., Simmel, M., Wurzler, S., Mauersberger, G., Majdik, Z., Müller, F., 2005a. FEBUKO and MODMEP: field measurements and modelling of aerosol and cloud multiphase processes. Atmospheric Environment, this issue.

Herrmann, H., Tilgner, A., Barzaghi, P., Majdik, Z., Gligorovski, S., Poulain, L., Monod, A., 2005b. Towards a more detailed description of tropospheric aqueous phase organic chemistry: CAPRAM 3.0. Atmospheric Environment, this issue.

Hindmarsh, A.C., 1983. Scientific Computing Chapter ODEPACK: A Systematized Collection of ODE Solvers. North-Holland, Amsterdam, pp. 55–74.

Jacobson, M.Z., 1999. Fundamentals of Atmospheric Modeling. Cambridge University Press, Cambridge, New York, Oakleigh.

Jacobson, M.Z., 2002. Analysis of aerosol interactions with numerical techniques for solving coagulation, nucleation, condensation, and reversible chemistry among multiple size

distributions. Journal of Geophysical Research 107 (D19), 4366.

Knoth, O., Wolke, R., 1995. Numerical methods for the solution of large kinetic systems. Applied Numerical Mathematics 18, 211–221.

Kreidenweis, S.M., Walcek, C.J., Feingold, G., Gong, W., Jacobson, M.Z., Kim, C., Liu, X., Penner, J.E., Nenes, A., Seinfeld, J.H., 2003. Modification of aerosol mass and size distribution due to aqueous phase SO_2 oxidation in clouds: comparisons of several models. Journal of Geophysical Research 108 (D7), 4213.

Lelieveld, J., Crutzen, P.J., 1991. The role of clouds in tropospheric photochemistry. Journal of Atmospheric Chemistry 12, 229–267.

Leriche, M., Voisin, D., Chaumerliac, N., Monod, A., Aumont, B., 2000. A model for tropospheric multiphase chemistry: application to one cloudy event during the CIME experiment. Atmospheric Environment 34 (29/30), 5015–5036.

Leriche, M., Chaumerliac, N., Monod, A., 2001. Coupling quasi-spectral microphysics with multiphase chemistry: a case study of a polluted air mass at the top of the Puy de Dome mountain (France). Atmospheric Environment 35, 5411–5423.

Leriche, M., Deguillaume, L., Chaumerliac, N., 2003. Modeling study of strong acids formation and partitioning in a polluted cloud during wintertime. Journal of Geophysical Research 108 (D14), 4433.

Liu, X., Seidl, W., 1998. Modelling study of cloud droplet nucleation and in-cloud sulfate production during the Sanitation of the Atmosphere (SANA) 2 campaign. Journal of Geophysical Research 103 (D13), 16,145–16,158.

Pruppacher, H.R., Klett, J.D., 1997. Microphysics of Clouds and Precipitation. Kluwer, Dordrecht.

Sandu, A., Potra, F.A., Charmichael, G.R., Damian, V., 1996. Efficient implementation of fully implicit methods for atmospheric chemical kinetics. Journal of Computational Physics 129, 101–110.

Sandu, A., Verwer, J.G., Van Loon, M., Charmichael, G.R., Potra, F.A., Dabdub, D., Seinfeld, J.H., 1997a. Benchmarking stiff ODE solvers for atmospheric chemistry problems I: implicit versus explicit. Atmospheric Environment 31, 3151–3166.

Sandu, A., Verwer, J.G., Van Loon, M., Spee, E.J., Charmichael, G.R., Potra, F.A., 1997b. Benchmarking stiff ODE solvers for atmospheric chemistry problems II: Rosenbrock solvers. Atmospheric Environment 31, 3151–3166.

Schwartz, S.E., 1986. Mass transport considerations pertinent to aqueous phase reactions of gases in liquid water clouds. Chemistry of Multiphase Atmospheric Systems, NATO ASI Series, vol. G6. Springer, Berlin, pp. 415–471.

Sehili, A.-M., Wolke, R., Knoth, O., Simmel, M., Tilgner, A., Herrmann, H., 2005a. Comparison of different model approaches for the simulation of multiphase processes. Atmospheric Environment, this issue.

Sehili, A.-M., Wolke, R., Helmert, J., Simmel, M., Schröder, W., Renner, E., 2005b. Cloud chemistry modeling: Parcel and 3D simulations. In: Borrego, C., Norman, A.L. (Eds.), Air Pollution Modeling and Its Application XVII, Kluwer Academic Publishers, New York, in press.

Simmel, M., Wurzler, S., 2004. Condensation and nucleation in sectional cloud microphysical models based on the linear discrete method. Atmospheric Research, submitted for publication.

Simmel, M., Diehl, K., Wurzler, S., 2005. Numerical simulation of the microphysics of an orographic cloud: comparison with measurements and sensitivity studies. Atmospheric Environment, this issue.

Stockwell, W.R., Kirchner, F., Kuhn, M., Seefeld, S., 1997. A new mechanism for regional atmospheric chemistry modeling. Journal of Geophysical Research 102 (D22), 25,847–25,879.

Tilgner, A., Majdik, Z., Sehili, A.M., Simmel, M., Wolke, R., Herrmann, H., 2005. SPACCIM: simulations of the multiphase chemistry occurring in the FEBUKO hill cap cloud experiments. Atmospheric Environment, this issue.

Verwer, J.G., Sportisse, B., 1998. A note on operator splitting in a stiff linear case. CWI Report MAS-R9830 Centre for Mathematics and Computer Science, Amsterdam.

Wolke, R., Knoth, O., 2000. Implicit–explicit Runge–Kutta methods applied to atmospheric chemistry-transport modelling. Environmental Modelling and Software 15, 711–719.

Wolke, R., Knoth, O., 2002. Time-integration of multiphase chemistry in size-resolved cloud models. Applied Numerical Mathematics 42, 473–487.

Wolke, R., Knoth, O., Herrmann, H., 2001. Numerical treatment of aqueous phase chemistry in atmospheric chemistry transport modelling. Air Pollution Modeling and Its Application XIV. Kluwer Academic Plenum Publishers, New York, pp. 399–407.

3B2v8.06a/w (Dec 5 2003).51c XML:ver:5.0.1 AEA : 5778 Prod.Type:COM pp.1–13(col.fig.:1–7) ED:MangalaK. PAGN:padmini SCAN:v4soft

ARTICLE IN PRESS

Available online at www.sciencedirect.com

SCIENCE DIRECT®

ELSEVIER

Atmospheric Environment ▮ (▮▮▮▮) ▮▮▮–▮▮▮

ATMOSPHERIC ENVIRONMENT

www.elsevier.com/locate/atmosenv

SPACCIM: simulations of the multiphase chemistry occurring in the FEBUKO hill cap cloud experiments

A. Tilgner, Z. Majdik, A.M. Sehili, M. Simmel, R. Wolke, H. Herrmann*

Leibniz-Institut für Troposphärenforschung, Permoserstr. 15, D-04303 Leipzig 04318, Germany

Abstract

The parcel model SPACCIM is applied to investigate the effect of multiphase cloud processing of tropospheric aerosol particles and trace gases resulting from a passage through an orographic cloud at Mt. Schmücke (Germany) during the joint research project FEBUKO. The applied model combines a complex microphysical and a detailed multiphase chemistry model with about 261 gas-phase and 776 aqueous-phase reactions. The chemical multiphase model incorporates a detailed description of the inorganic and organic multiphase chemistry based on time-dependent size-resolved aerosol/cloud spectra. The data measured at the upwind site provided the basis for the chemical and physical model initialisation under real environmental conditions. The simulation results were compared to experimental cloud water composition data at Schmücke summit site as well as gas and aerosol measurements at downwind site in order to interpret the experimental data and to evaluate the model results. To this end, a detailed analysis of the chemical multiphase system was performed including source and sinks studies with special emphasis on aqueous-phase oxidants and S(IV) to S(VI) conversion. A central objective of the study has been to assess in-cloud oxidations of organic compounds and results for important C2 and C3 oxidation subsystems are presented. This modelling study shows that the observed multiphase chemistry is strongly affected by dynamic microphysical processes. Furthermore, a significant cloud condensation nuclei (CCN) modification with sizes up to about 400 nm, mass productions up to about 0.7 $\mu g\,m^{-3}$ and acidification caused by cloud processing was identified in the model in agreement with the experimental findings. However, for organic compounds with low solubilities the cloud water measurements show considerably higher concentrations than expected from both (i) their Henry solubilities and (ii) the complex multiphase modelling as performed by the model.

Keywords: Spectral model; Microphysics; Multiphase chemistry; Aerosol cloud processing

0. Introduction

Clouds may potentially alter the chemical composition of the troposphere on a global scale (Ravishankara, 1997) and, among other effects, contribute to aerosol processing which is of particular interest in current atmospheric research due to the influence on climate forcing (Charlson et al., 1992) as well as atmospheric composition change. The understanding of physico-chemical in-cloud modification of aerosol properties is currently limited because of the high complexity of the atmospheric multiphase system. Particle composition and spectra can be influenced by physical in-cloud processes such as collision-coalescence but also by

*Corresponding author. Tel.: +49 341 235 2446; fax: +49 341 235 2325.
E-mail address: herrmann@tropos.de (H. Herrmann).

1352-2310/$ - see front matter © 2005 Elsevier Ltd. All rights reserved.
doi:10.1016/j.atmosenv.2005.02.028

chemical processes like gas-phase uptake of soluble gases and subsequent aqueous-phase reactions. Therefore, a model which will be used to study the aerosol processing during a cloud passage has to include a detailed description of the microphysical (Pruppacher and Klett, 1997) and chemical multiphase processes (Jaeschke, 1986). In order to improve the system understanding of complex cloud processing processes, a number of ground-based cloud passage experiments have been performed during the last decades e.g. at Kleiner Feldberg, Germany, in 1990 (Fuzzi, 1994), at Great Dun Fell, UK, in 1993 (Fuzzi (1997) and 1995 (Gallagher, 1999), and in Tenerife, Spain, in 1997 (Bower et al., 2000). In particular, the results of associated cloud passage modelling studies (Sander et al., 1995; Colvile et al., 1994; Bower et al., 1997; Bradbury et al., 1999; Flynn et al., 2000) including comparisons of model results with observations have considerably contributed to the current state of knowledge.

The present model study is based on the work of the joint research projects FEBUKO (field investigation of budgets and conversions of particle phase organics in tropospheric cloud processes) and MODMEP (modelling of tropospheric multiphase processes: tools and chemical mechanisms) and is focused on the physicochemical modification of the multiphase system (gas|aerosol|cloud). The ground-based cloud passage experiment FEBUKO was performed on and around the Mt. Schmücke (937 m asl), Thüringer Wald, Germany, in October 2001 and 2002, see Herrmann et al. (2005a) for details.

1. Model description

The air parcel model SPACCIM (Wolke et al., 2005) was developed for the description of cloud processes combining a complex multiphase chemistry with detailed microphysics. The description of both separate processes is performed for a highly size-resolved particle and droplet spectrum. The model allows a detailed description of the processing of gases and deliquescent particles before the cloud formation, under cloud conditions and after cloud evaporation. All microphysical parameters required by the multiphase chemistry model are taken over from the microphysical model. The adiabatic air parcel model contains a detailed description of microphysical processes of deliquescent aerosol particles and droplets, see Simmel et al. (2005). The physical initial conditions for the cloud simulations were taken mainly from measurements at upwind site during the field campaign of the joint research project FEBUKO. The orographic profile of the mountain joining the three measurement sites was integrated into the model and combined with measured horizontal wind velocities. Both together allow calculating a height- and time-dependent vertical velocity along the trajectory and leading to a complex evolution of water vapour saturation ratio. Analyses of several indicators suggest (Herrmann et al., 2005a) that the effects of air entrainment were not dominating in the three events which were chosen for detailed analysis. Therefore, entrainment was neglected within this present ground-based study. Also, emissions and depositions of chemical compounds which can be optionally implemented in the parcel model were switched off due to the relatively small travelling time for the case studies. Finally, it should be noted that only the moving section version of the SPACCIM model was used within the present modelling study. A description and discussion of the different SPACCIM versions with regard to the 'moving' or 'fixed' bin treatment of size resolution are given in Wolke et al. (2005).

In SPACCIM the complex aqueous-phase mechanism CAPRAM 3.0, see Herrmann et al. (2005b) for details, was coupled to the gas-phase mechanism RACM (Stockwell et al., 1997). The uptake processes of soluble species are included in the mechanism following the approach by Schwartz (1986) considering Henry solubility, gas-phase diffusion and mass accommodation coefficients. CAPRAM 3.0 contains a complex implementation of aqueous-phase inorganic as well as organic chemistry including organic species with up to mainly four carbon atoms. Therefore, the model was suited for the analysis and interpretation of the complex FEBUKO field experiment data. In comparison to other cloud passage models mentioned above, which were used in ground-based cloud experiments, the SPACCIM model incorporates a much more detailed and up-to-date description of the multiphase daytime and nighttime chemistry. In contrast to the other models, the used multiphase mechanism includes also an explicit treatment of the HO_x-chemistry in the aqueous phase. Furthermore, in SPACCIM the chemistry of deliquescent aerosol particles is considered as well.

2. Model initialisation

The model initialisation with experimental data was one of the most important links between the field campaign FEBUKO and the associated modelling project MODMEP as well as an indispensable precondition for a successful actualisation of the comparison between observations and model results. Derived from a detailed meteorological characterisation and flow investigations given in Tilgner et al. (2005) and Heinold et al. (2005) three periods (E I: 26/27-10-2001; E II: 07/08-10-2001; E III: 16/17-10-2002) were chosen from the FEBUKO field campaign as appropriate cloud events for subsequent modelling studies. Based on the compar-

ison of the microphysical measurements (droplet number concentration, effective diameter and LWC) at summit site and the results of microphysical modelling (Simmel et al., 2005) adequate simulation times (EI: 09:00 UTC; EII: 02:00 UTC, EIII: 01:00 UTC)) were selected for the realisation of the SPACCIM modelling runs. The model was initialised with physical and chemical data based mainly on the measurements of the upwind site. The data considered are presented and discussed by Gnauk et al. (2005) and Müller et al. (2005). The detailed description of the chemical and physical model initialisation including the associated initialisation material is available in the electronic supplementary material (ESM) to this manuscript as well as at the FEBUKO webpage (http://projects.tropos.de:8088/afo2000g3/FEBUKO_dateien/febuko.html).

3. Results and discussion

3.1. Microphysical conditions and pH

The results of the microphysical model including a comparison with measured data at the summit are discussed in detail by Simmel et al. (2005). Therefore, this subsection is focused just on the temporal behaviour of microphysical parameters as well as the evolution of the particle/droplet spectra which are important for the understanding of the aerosol processing occurring during a passage through an orographic hill capped cloud. Due to manuscript size restrictions the detailed treatment of the microphysical conditions and the pH is placed in the ESM.

3.2. Oxidants

3.2.1. Radical oxidants

The most important radical oxidants in the tropospheric multiphase system are OH, HO_2 and the NO_3. In Fig. 1 plots of gas- and aqueous-phase radical concentrations vs. travelling time are presented for the three treated cloud events. According to the simulation times, E II and E III are characterized by full night conditions so that the OH concentrations in the gas phase are only in the range of about $1–4 \times 10^{+4}$ molecules cm^{-3} before cloud formation. On the other hand, the NO_3 radical concentration reaches values with about $2 \times 10^{+7}$ molecules cm^{-3} in the night regime. In contrast to E II and E III, the cloud event E I shows a more mixed radical regime of typical day and night conditions with NO_3 radical gas-phase concentrations which are up to about five times lower than in the full night regime. However, also this event appears to be mainly characterised by a nighttime chemistry regime because of the early time of 09:00 UTC and the low available actinic radiation due to the occurrence of high clouds shielding the experimental sites.

As can be seen from Fig. 1, gas-phase concentrations of the radicals become significantly reduced when the hill-capped cloud forms. In the case of OH, the decrease of the gas-phase concentration of about 44% (E I) in the cloud is mainly caused by the efficient uptake of the precursor HO_2 into the cloud and not by the direct phase transfer into the droplets (Lelieveld and Crutzen, 1990). The relative reductions of the gas-phase concentrations as well as the phase partitioning coefficients for each event are given in Table IV in the ESM. One remarkable fact is that the differences between cloud-free and in-cloud conditions are strongly dissimilar for the different events. The decrease of OH is more

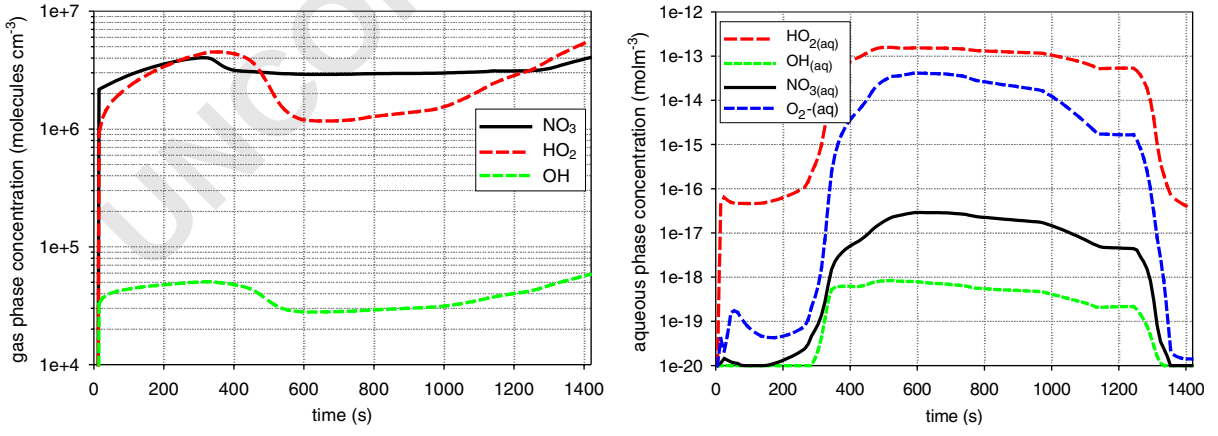

Fig. 1. Gas- and aqueous-phase concentration of the radicals OH, HO_2 ($/O_2^-$) and NO_3 as function of the travelling time for the cloud event E I.

significant for the mixed regime E I due to the uptake of photochemically formed HO_2 and hence the suppression of its gas-phase reaction with NO in comparison to E II and E III. The cloud effect on OH is much less distinct in the pure night cases E II and E III indicating that other sources for OH are operative here under nighttime conditions. Because of the nature of the experimental site widely surrounded by coniferous forests, the ozonolysis of biogenic VOC and especially terpenes might act as an active nighttime OH production pathway during these events. Other results obtained in the FEBUKO campaigns on the characterisation of organic peroxides (Valverde-Canossa et al., 2005) appear to support an active terpene oxidation chemistry during the measurement periods. Compared to OH, the NO_3 gas-phase concentration in the cloud decreases are more significant with about 61% and 49% in the full night regimes for E II and E III, respectively. (cp. Table IV in the ESM)

As can be seen from Fig. 1, the aqueous-phase concentrations of the highly soluble HO_2/O_2^- predominantly follow the LWC but the concentration level differs much more from the other radicals in the aqueous phase. Compared to the relatively low concentrations of OH and NO_3 in the aqueous phase, HO_2 and the corresponding anion O_2^- reaches concentrations at the summit of about 2.0×10^{-13}, 1.2×10^{-13} as well as 7.9×10^{-14} mol m^{-3} in the case of E I, E II and E III, respectively. These levels are very small for the hydroperoxyl radical which is generally regarded as the most abundant tropospheric aqueous-phase radical the concentration level of which was reported to be in the order of 3×10^{-12} to 3×10^{-13} mol m^{-3} in box model calculations (Herrmann et al., 2005a, b). The strong reduction in the HO_2 aqueous-phase concentration is caused by a predominant transitional metal ion (TMI) nighttime chemistry in all three events.

3.2.2. Non-radical oxidants

3.2.2.1. Hydrogen peroxide and organic hydroperoxides. In Fig. 2 the H_2O_2 and CH_3OOH multiphase concentrations vs. travelling time are plotted for the cloud event E I. As can be seen, the gas-phase concentrations decrease with the cloud formation and the resulting phase transfer. Both concentration profiles follow the LWC and partly show a notable decrease between the upwind and downwind site of about 52% ($5 \times 10^{+8}$ molecules cm^{-3}) and 0.25% ($6 \times 10^{+7}$ molecules cm^{-3}) for H_2O_2 and CH_3OOH, respectively. At the summit site about 87% of the initialized H_2O_2 is transferred into the aqueous phase. The relative change of the concentration is smaller for the other events due to the higher initial H_2O_2 concentration, shorter in-cloud times as well as an increasing competition by means of other chemical pathways (cp. Fig. 5 in the ESM). The total decrease in the H_2O_2 concentration during the cloud passage is caused predominantly by the sulphur oxidation process which is discussed in Section 3.3. The source for the H_2O_2 in the aqueous phase is mainly the transfer from the gas phase but also chemical processes such as the oxidation of copper [Cu(I)] by HO_2/O_2^- contribute with up to 10% as source for H_2O_2 in the aqueous phase. Because of the high solubility, the aqueous-phase H_2O_2 concentration profile is comparatively unaffected by chemical sinks and shows an inverse course compared to the gas-phase concentration. As can be seen from Fig. 2, the predicted H_2O_2 cloud water concentration of 1.1×10^{-9} mol m^{-3} is about two times higher than the measured value of 4.4×10^{-10} mol m^{-3} (Brüggemann et al. 2005; Valverde-Canossa et al., 2005). The difference between these two values can be explained by the fact that the initial gas-phase values were estimated. A more detailed treatment of the measured and modelled values including all cloud events can be found in Section 4 and Valverde-Canossa et al. (2005), respectively. At this

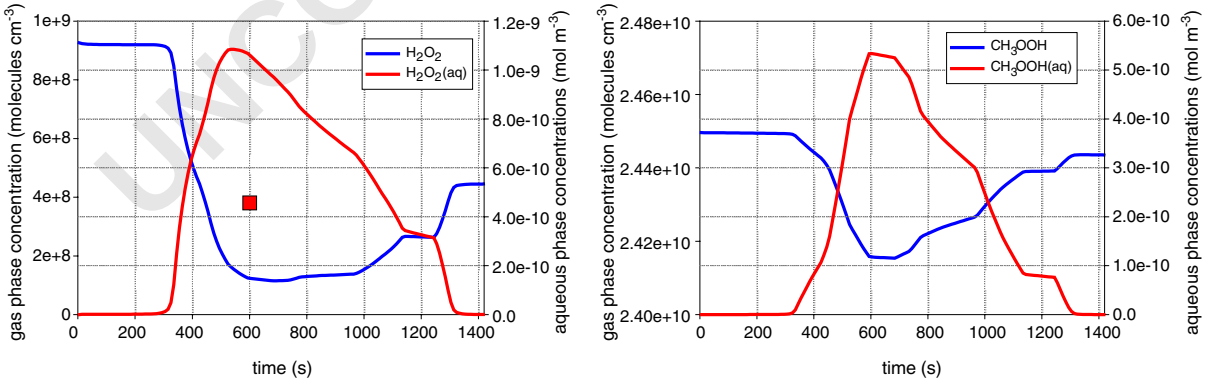

Fig. 2. Gas- and aqueous-phase concentration of the peroxides H_2O_2 (left) and CH_3OOH (right) as function of the travelling time for the cloud event E I. The red quadrate in the left figure shows the measured H_2O_2 cloud water concentration at summit site.

point, it has to be noted that the used cloud water sampler CASCC2 (cp. Wieprecht et al., 2005) collects only droplets larger than 3.5 μm. Therefore, just size bins within this sampling interval are integrated for the comparison between modelled and measured cloud water concentrations.

3.2.2.2. Ozone. In comparison to the other oxidants, no direct effect on the gas-phase ozone concentration can be recognised in the case of FEBUKO clouds. Due to the acidity of the CCN and, subsequently, the cloud droplets (cp. Table III in the ESM), as well as the in-cloud times of about 600 s, the main oxidation pathways are not efficient enough to significantly consume ozone (cp. Liang and Jacob, 1997). The decreases of the gas-phase level are lower than 1% (cp. Table IV in the ESM). As a consequence of this fact, ozone is suited for the application as a predominantly inert tracer for flow analyses of a cloud passage field experiment (cp. Heinold et al., 2005).

3.3. Sulphur chemistry

The in-cloud oxidation of S(IV) to S(VI) significantly contributes to the acidification and the physico-chemical processing of aerosols (Bower et al., 1997). According to the FEBUKO environmental conditions, see Gnauk et al. (2005), the conversion of S(IV) is not solely dominated by the oxidants H_2O_2 and O_3 due to their low mixing ratios. Apparently, the reaction of peroxynitric acid (HNO_4) with HSO_3^- is of importance under low H_2O_2 nighttime conditions within acidic clouds as has been discussed at the level of box model calculations before (Ervens et al., 2003). In polluted environments the primary source for S(IV) in the aqueous phase is the uptake of SO_2. The mixing ratios of SO_2 at the upwind site were generally lower than 2 ppb (cp. Gnauk et al., 2005). After cloud formation, the SO_2 is transferred into the cloud droplets and the dissolved S(IV) is oxidised to S(VI). Fig. 3 plots the S(VI) species as a function of the travelling time for the event E I (for E II and E III in the ESM). As can be seen from the plots, the aqueous-phase concentrations are characterised by a continuous change between the individual S(VI) species due to the changing pH and the varying LWC. In the case of E I, S(VI) is primarily present as HSO_4^- in the deliquescent aerosol particles and as SO_4^{2-} in cloud droplets. As can be seen from the plot, the total S(VI) increases shortly after cloud formation due to the efficient oxidation of S(IV). In contrast to the cloud droplets, in the deliquescent particles the efficiency of the S(IV) oxidation is reduced because of the insignificant uptake of SO_2 in the more acidic particles as well as the fact that predominantly most of the S(IV) is existent in the relatively chemical inert species hydroxy methanesulfonate (HMS). The multiphase S(VI) mass increases by 0.16 μg m^{-3} (7.3%), 0.08 μg m^{-3} (5.9%) and 0.06 μg m^{-3} (6.3%) during the cloud passage in the case of E I, E II and E III, respectively. The diagnosis of production rates at the summit shows that the main oxidation pathways strongly differ between the cloud events. For the more acidic cloud events of E I and E III, H_2O_2 is the main oxidant with contributions of about 58% and 76% to the total S(IV) production. Due to the generally higher pH in the case of E II, the main source of S(VI) in the aqueous phase with a production contribution of about 62% is due to the reaction of bisulphite/sulphite with O_3. The contribution of the oxidant HNO_4 differs between 4%, 15% and as well as 30%, for the cloud event E II, E III and E I, respectively. Besides the differences between the cloud events, significant variation of the source rates and relative contributions of each oxidant over the particle/droplet spectra is also observed. In Fig. 4, the production rates and the

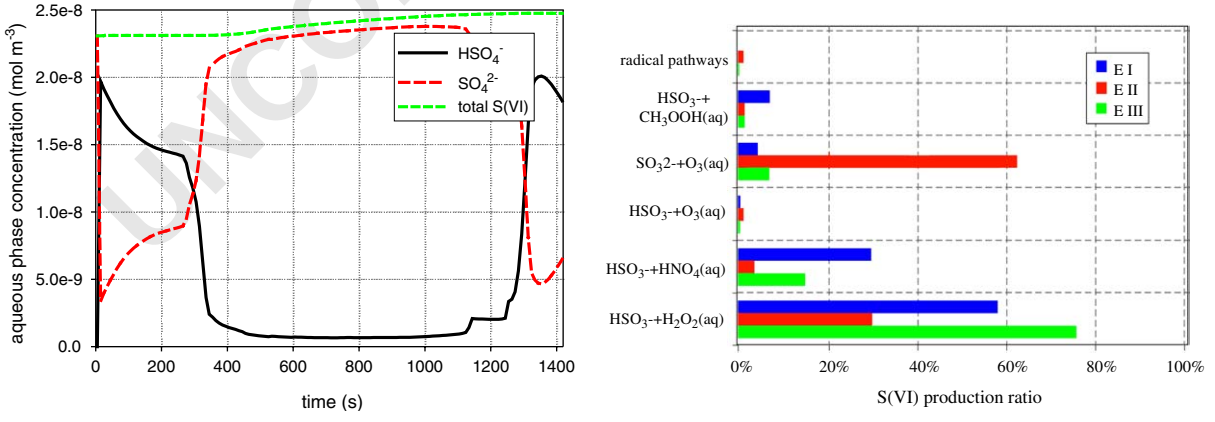

Fig. 3. S(VI) species and total S(VI) as function of the travelling time (left) for the cloud event E I and production ratios of the main S(VI) sources at summit for the three treated cloud events (right).

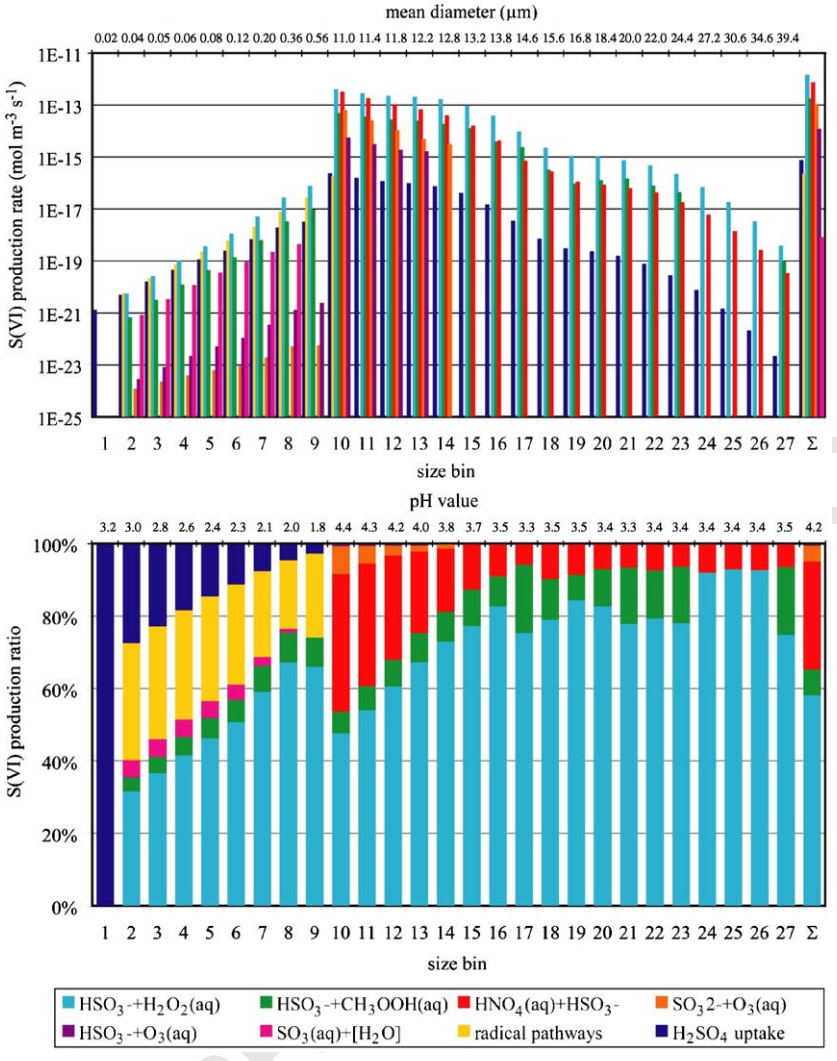

Fig. 4. Production rates (above) and production ratios (below) of the main S(VI) source reactions in each size bin with the according mean diameter and pH, respectively, for the cloud event E I at summit. The symbol Σ represents the total rate and ratio.

corresponding production ratios of all size bins at summit are plotted for the cloud event E I. The production rates are four orders of magnitude higher than those in the small deliquescent interstitial aerosol particles (size bins 1–9 in Fig. 4). The distribution of rates shows a pattern which reproduces more or less the LWC evolution. Furthermore, the chemical differences are caused by the dissimilar pH values in each bin. An interesting fact to be noticed in Fig. 4 is that, besides H_2O_2, the radical oxidation pathways significantly contribute to the S(VI) source rates in interstitial particles. All these facts demonstrate the relevance of the size-resolved models because of the pH-dependent process oxidation description.

3.4. Nitrogen chemistry

Additional to the sulphur oxidation, the formation of nitrate and ammonium are the most important mass production processes in the aqueous phase. The phase transfer of gaseous ammonia into acid particles/droplets and the following ammonium formation is an unspectacular chemical process but important for the accurate description of the pH. Furthermore, the mass productions from this process of about 0.4, 0.3 and 0.1 $\mu g\,m^{-3}$ for E I, E II and E III, respectively, are crucial for the evaluation of the aerosol processing. In Fig. 5, plots of the aqueous-phase nitrate, nitric acid in both phases and the total N(V) concentration vs. travelling time are

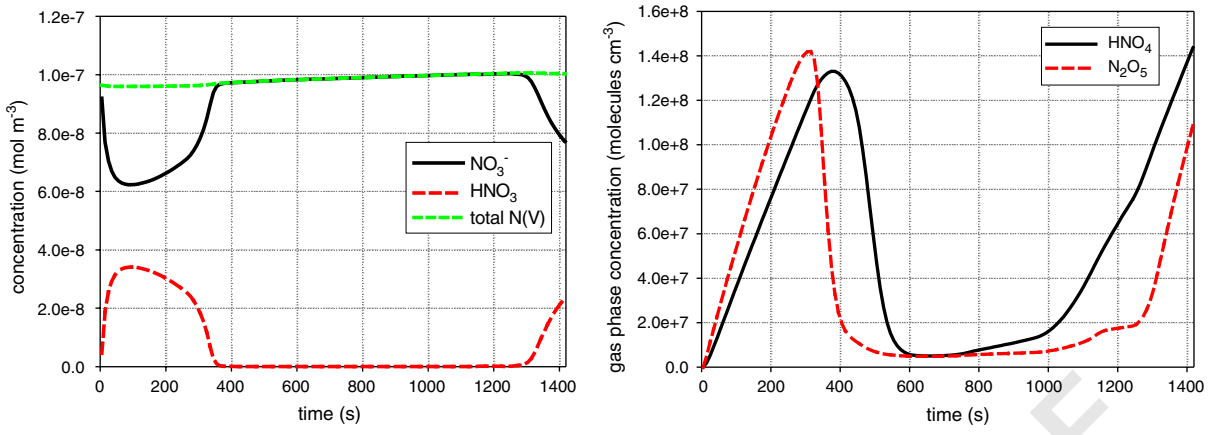

Fig. 5. Concentration of HNO_3 and NO_3^- as function of the travelling time (left) and gas-phase concentrations of N_2O_5 and HNO_4 as function of the travelling time (right) for the cloud event E1.

shown for the cloud event E I. Particularly during the first 100 s, the phase partitioning is controlled by the above-mentioned transient effects which were driven by the pH value and the LWC, respectively. The equilibrium between gas and aqueous phase follows LWC and pH, and leads to an outgassing at the beginning and end of the passage. The release of HNO_3 from several size bins finally leads to a small repartitioning, i.e. the outgassed HNO_3 is redistributed over the size spectrum from more acidic to less acidic bins. As can be seen from the plot, within the main droplet activation period of less than 50 s, all gaseous HNO_3 is transferred into the aqueous phase. During the cloud life sequence a steady increase of the total N(V) can be observed. Finally, the system concentration of N(V) is increased by about 4% (4×10^{-9} mol m^{-3}). The production of NO_3^- results mainly from the direct uptake of HNO_3, the hydrolysis of the transferred N_2O_5 as well as the reaction of solute HNO_4 with HSO_3^- (cp. Fig. 5). The recognisable delayed uptake between N_2O_5 and HNO_4, see Fig. 5, is caused by the different uptake sensitivity of their corresponding precursors NO_3 and HO_2, respectively. At summit N_2O_5 and HNO_4 contribute with about 75% and 19%, respectively, to the mass production rate of about 3.9×10^{-12} mol m^{-3} s^{-1}. The direct uptake process contributes approximately only 5% to the N(V) increase under in-cloud conditions and the radical pathways only 1%. Compared to cloud event E I, E II shows similar trend including a total N(V) system production of about 5.6% and a particle mass increase of about 0.3 μg m^{-3} (16%). In the case of E III, the multiphase N(V) concentration and the N (V) particle mass increase by about 5% and 76% (0.5 μg m^{-3}) predominantly due to the uptake of gas-phase HNO_3. The spectral mass productions for all treated events are discussed in detail within a following section.

3.5. Organic chemistry

Because of the limited cloud passage duration and the low or not available actinic radiation during the events the radical oxidation of organic compounds is generally quite restricted. Therefore, this subsection is focused just on the phase partitioning and multiphase chemistry of selected C2 and C3 carbonyls as well as important monocarboxylic acids. A more detailed analysis of the organic chemistry using CAPRAM 3.0 is given in Herrmann et al. (2005b).

In Fig. 6, plots of the multiphase concentrations (gas- and aqueous-phase concentrations) of glyoxal and methylglyoxal are shown. Glyoxal is initialised by its measured mixing ratios of about 26, 9 and 4 ppt for the event E I, E II and E III, respectively. According to its Henry solubility constant of 1.4 M atm^{-1} and its subsequent hydration, glyoxal is effectively transferred into the aqueous phase and then mainly exists in its hydrated form. At the summit, a decrease of the gas-phase concentrations of about 72%, 56% and 18% for E I, E II and E III, respectively, was observed. A notable fact is that the hydrated glyoxal and methylglyoxal concentrations reach the maximum in the aqueous phase not at the summit at the highest LWC level but rather about 100 s later due to the duration of the hydration process. This behaviour can be observed also for other hydrated carbonyls such as formaldehyde. Furthermore, not all of the dissolved glyoxal is transferred back to gas phase during the cloud evaporation. In the case of E I, about 19% of the glyoxal multiphase concentration is present in deliquescent aerosol particles. The multiphase concentration of glyoxal decreases during the cloud passage by $1.7 \times 10^{+7}$ (3%), $0.6 \times 10^{+7}$ (3%) and $0.1 \times 10^{+7}$ (1%) molecules cm^{-3} for E I, E II and E III, respectively. The significant decrease for E I is

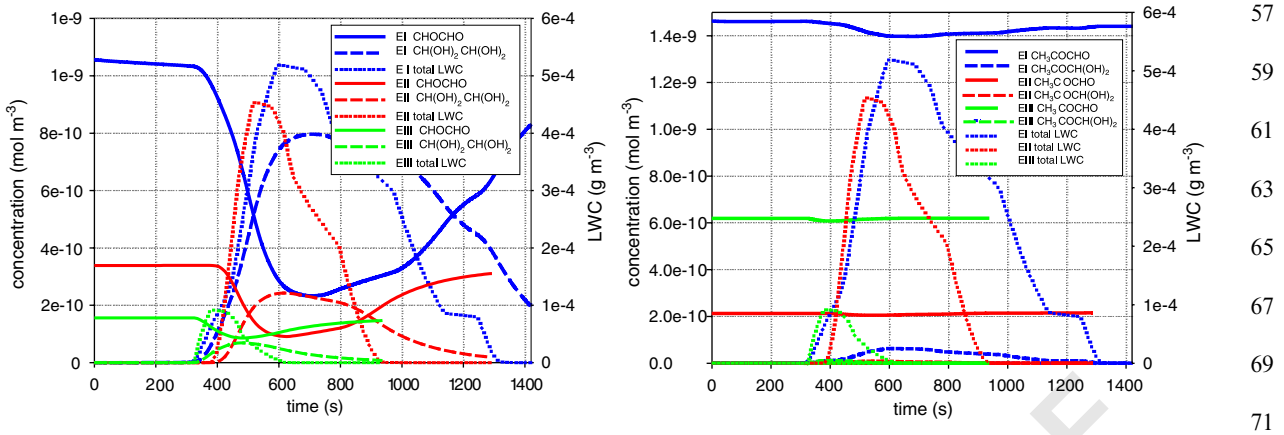

Fig. 6. Gas- (solid lines) and aqueous- (unhydrated: dotted lines; hydrated: dashed lines) phase concentrations of Glyoxal (left) and methyl glyoxal (right) for the three treated cloud events E I (blue lines), E II (green lines) and E III (red lines).

caused by the effective gas- and aqueous-phase degradation processes. For the night events E II and EIII, just the aqueous-phase radical reactions lead to the decreasing multiphase glyoxal concentration. The main aqueous radical oxidants under cloud conditions at summit are the SO_5^- radical with about 87%, 98% and 80% contribution to glyoxal degradation and the OH radical with about 12%, 2% and 20% for E I, E II and E III, respectively. The degradation path by aqueous OH radical is limited due to the low radical concentrations in the gas phase. The total degradation rates at the summit differ between 7.2×10^{-15}, 3.2×10^{-14} and 2.5×10^{-15} mol m^{-3} s^{-1} for E I, E II and E III, respectively. Whereas, the glyoxal degradation in the acidic S(IV) limited deliquescent particles at the downwind site is determined by the OH and SO_4^- radical reaction with rates which are only about one order of magnitude lower than the maximum OH degradation rate in cloud droplets. This fact and the characteristic lifetime of aerosol particles implicate that the glyoxal degradation process in deliquescent particles can also contribute to the atmospheric mass production of oxalic acid besides the established in-cloud production.

In comparison to glyoxal, methylglyoxal shows a lower degree of hydration efficiency and hence remains mainly in the gas phase e.g. to about 96% (E I) of the overall budget. Furthermore, the system concentrations of methylglyoxal behave different in the three treated cases. Only for the mixed regime of E I considering more effective gas-phase sinks, a concentration reduction of about 1.5% can be observed; whereas the totally dark regimes show a slight increase of the multiphase concentration of about 1.3% and 0.1% for E II and E III, respectively.

In accordance to the CAPRAM 3.0 process studies (Herrmann et al., 2005b), monocarboxylic acids are also produced under our low oxidant conditions. Contrary to the hydrated carbonyls the concentration of the well-soluble monocarboxylic acids like formic and acetic acid follow only the LWC. The multiphase concentration of formic acid is increased after the cloud passage with about 0.9%, 0.8% and 0.4% for E I, E II and E III, respectively. The only significant production pathway for formic acid in the aqueous phase is the oxidation of formaldehyde with source rates of about 1.6×10^{-14}, 6.2×10^{-15} and 1.1×10^{-14} mol m^{-3} s^{-1} for the three events. Contrary to this finding, the production of acetic acid which is increased after the cloud passage with approximately 0.6%, 1.1% and 1.3% for E I, E II and E III, respectively, is not dominated by the direct aqueous oxidation of acetaldehyde. The concentration increase is almost solely caused by the aqueous oxidation pathway of the acetylperoxy radical which is efficiently transferred into the cloud droplets. In comparison to formic acid, the corresponding acetic acid production rates at the summit of about 5.0×10^{-14}, 1.9×10^{-13} and 1.3×10^{-13} mol m^{-3} s^{-1} for E I, E II and E III, respectively, are partly more than one order of magnitude higher. The limitation of the direct aqueous acetaldehyde oxidation pathway is caused mainly by its insignificant modelled aqueous-phase concentration. A discussion of the limited aqueous-phase budget of higher carbonyls predicted by the model and the discrepancies compared to observations is given in the last section.

3.6. Mass production by aerosol cloud processing

A key question in aerosol processing studies is how physico-chemical multiphase processes affect and change the particle size spectrum and hence particle mass. Thus, this section is treating spectral mass changes resulting from the previously discussed in-cloud oxidation and repartitioning processes. In Fig. 7, the total dry particle/droplet mass (condensed non-water mass) is

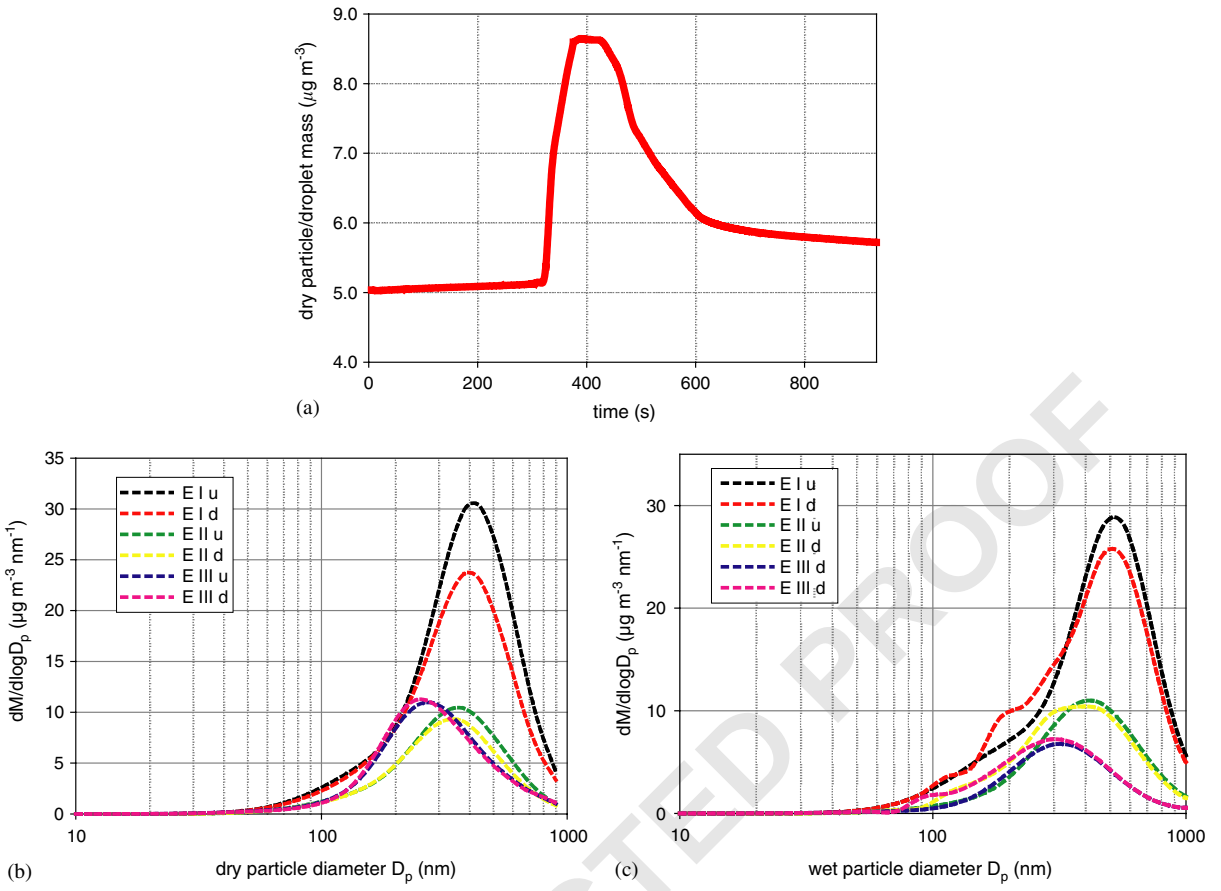

Fig. 7. Total dry condensed non-water mass as function of the travelling time for E III (a) as well as (b) measured (average of all measured size distribution of the event) and (c) calculated spectral distribution of the dry particle mass at the two valley stations (u: upwind, d: downwind) for the all treated cloud events.

plotted as a function of the travelling time for the cloud event E III (E I and E II in the ESM), and the spectral dry mass distribution at the two valley stations for all events are also shown. The dry mass increases slightly before and extensively during the cloud formation as well as decreases with the cloud evaporation due to the uptake of soluble gas-phase species followed by back-transfer of such species upon cloud water evaporation. At the end of the simulation the total mass has increased by $0.7\,\mu g\,m^{-3}$ or 14% for event EIII. The comparison between the valley stations spectrum shows that the mass increase is limited to a size interval between the activation diameter (E I: ~180 nm, E II: ~120 nm, E III: ~90 nm) and about 400 nm. This tendency can be found also for the other cloud events. For E I and E II, distinct outgassing effects predominantly by NO_3^- additionally lead to a repartitioning within the spectrum. In the case of E I and E II, especially size bins with the initial chemical composition of the third impactor stage are characterised by a temporal outgassing and a resulting repartitioning. Therefore, the interval of the mass productions is slightly narrower in this case compared to E III.

The comparison of the mean observed volume spectra, see Brüggemann et al. (2005) and Mertes et al. (2005a, b), and the modelled processed spectra shows a good agreement. In particular, the spectral changes in the case of E III are well reproduced. Furthermore, the modelled mass increases in the above-mentioned size interval and the slight shift towards smaller diameters are relatively well concordant with the results of measurements. Because of depositions currently not being considered, the model cannot reproduce the observed mass decrease for E I. Due to the presence of smaller droplets, lower LWC values and shorter cloud interaction times, no significant deposition effects are observed for E II and E III. Hence, the model results are in better agreement with the observations for these two events than for event E I.

In addition to the spectral mass modification, the contribution ratios of different mass production pathways are of major interest. The analysis of main oxidation pathways described above show significant variations among the three events. However, the analyses indicate that under the existing environmental conditions the mass increase is mainly due to nitrogen chemistry with e.g. about 84% for E II and, to a smaller extent, due to the conversion of S(IV) to S(VI) contributing with approximately 16% in E II to mass increase. Due to dissimilar environmental conditions and regimes, this result is somewhat different to former hill-capped cloud model studies (cp. Bradbury et al., 1999) within which the mass increase was mainly based on the S(IV) oxidation.

4. Comparison between measurements and model results

According to the in-cloud measurements at summit and the measurements at downwind site under cloud-free conditions this section is treating first the measured values at the summit in comparison to the modelled values. In the case of the cloud water measurements, only the simulation results of size bins larger than the cut-off diameter are considered. Secondly, in the subsequent comparison of the downwind site results, the modelled particle concentrations are integrated likewise according to the cut-off sizes of the used Berner impactor. The modelled and measured data for the three treated cloud events are summarized in several tables which are obtainable in the ESM (Table V–X). Four suited representations and the corresponding values are combined and shown in scatter plots (Figs. 8–11) only for the cloud event E III in the paper. The corresponding plots for E I and E II are obtainable in the ESM. Due to manuscript size restrictions only selected aspects are treated here.

4.1. Summit

In Fig. 8, a comparison between the measured and calculated cloud water concentrations of E III is presented. As can be seen from the plot, in general both data sets correlate relatively well. In particular, the best congruencies are observed in the case of compounds with high concentrations as well as low measurement uncertainties such as nitrate with relative difference of just about 5%. In addition to compounds mainly originating from particles, also substances being transferred from the gas phase like H_2O_2 and organic monocarboxylic acids are in a good agreement with the measurements. Larger discrepancies between the measurements and simulation results exist for the higher carbonyls. Thereby, the gas-phase concentrations do not differ much between model and observations (cp. Fig. 9)

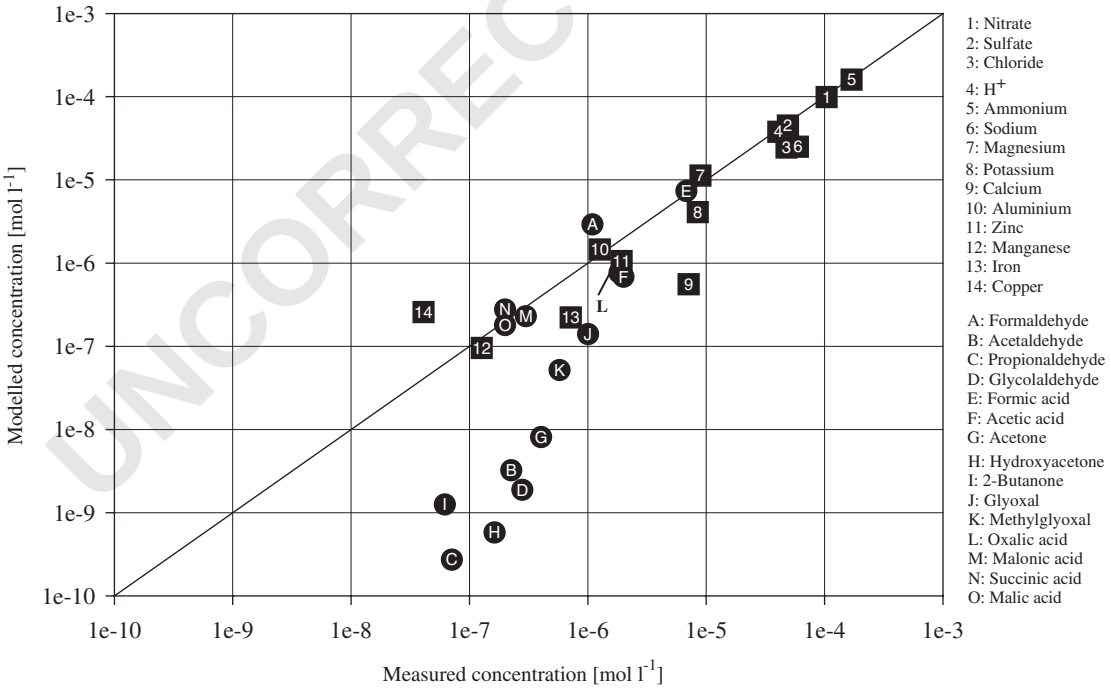

Fig. 8. Comparison between the measured and modelled cloud water concentrations (moll^{-1}) at summit for the cloud event E III.

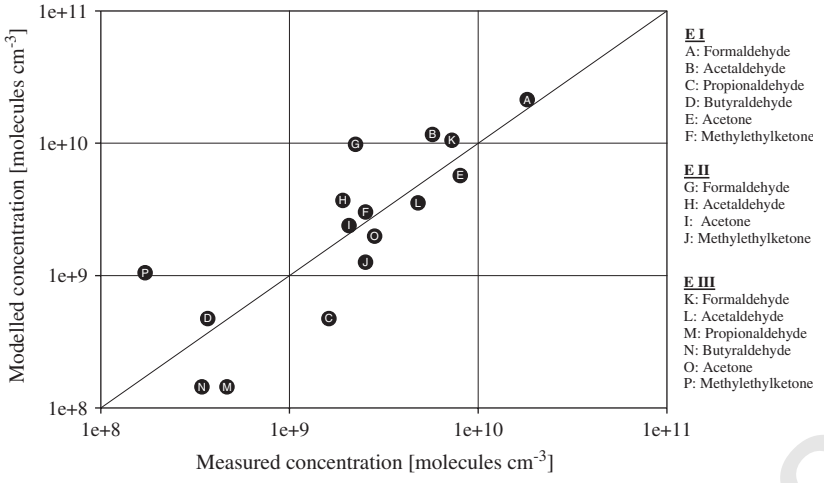

Fig. 9. Comparison between the measured and modelled gas-phase carbonyl concentrations (molecules cm^{-3}) at the summit for all treated cloud events.

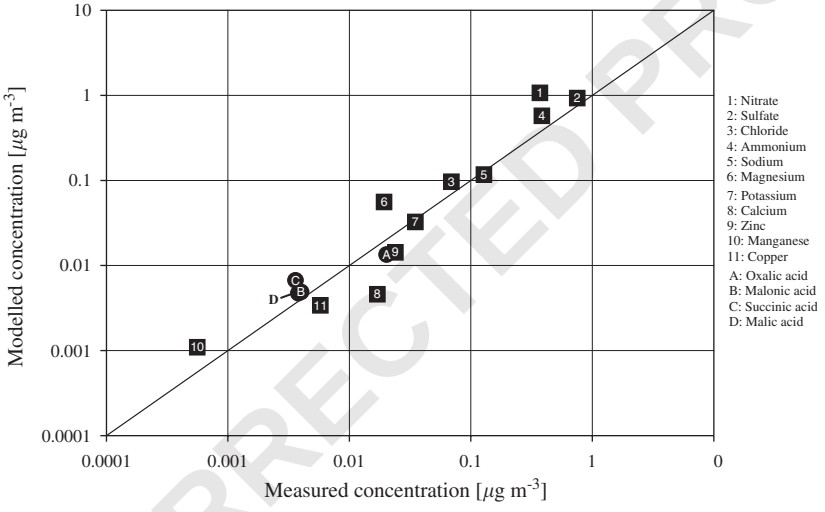

Fig. 10. Comparison between the measured and modelled particulate matter concentrations (μg m^{-3}) at downwind site for the cloud event E III.

but the cloud water concentrations of the model are partly more than two orders of magnitude lower than the measured ones. The measured concentrations of the carbonyls are significantly dissimilar from the value which can be derived from Henry solubility calculations, see van Pinxteren et al. (2005). The model is not able to explain these high cloud water concentrations. The only exception is formaldehyde with slightly higher modelled cloud water concentrations. The difference between model and measurements is predominantly increased for carbonyls with small Henry constants. Other previous field measurements showed similar observation also for other hydrophobic organic compounds such as pesticides (Glotfelty et al., 1987), PAHs, PCBs and alkanes in the aqueous phase (see Valsaraj et al., 1993). Possible explanations for these findings discussed in the literature are the adsorption of organic carbonyls on cloud droplet surfaces (Valsaraj et al., 1993) as well as chemical productions from higher concentrated and soluble carbonyl precursors. For a more detailed treatment of this interesting topic including investigations to the relationship between low effective water solubilities and the extent of measured deviations the reader is referred to van Pinxteren et al. (2005).

4.2. Downwind site

In Figs. 10 and 11, the measured and modelled particle as well as gas-phase concentrations are plotted. The scatter plots do not reveal significant deviations for

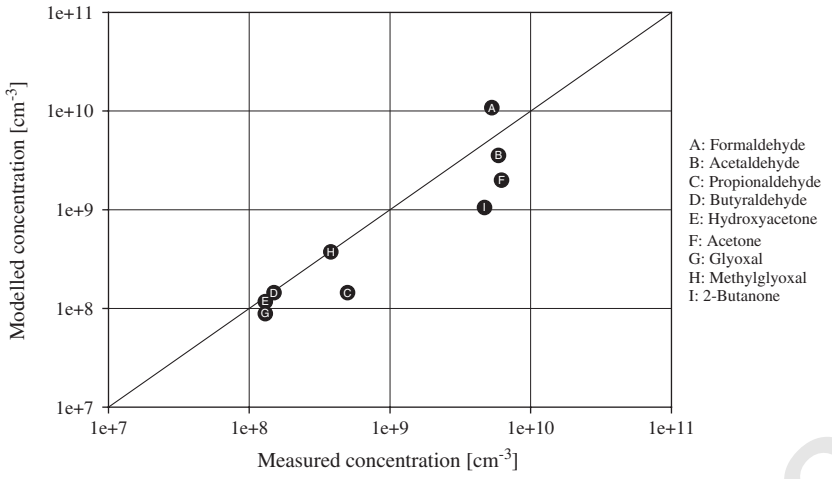

Fig. 11. Comparison between the measured and modelled gas-phase concentrations (molecules cm^{-3}) of organic compounds at downwind site for the cloud event E III.

all the three treated cloud events. The results of the measurements such as the mass increase predominantly within the second impactor stage and the corresponding concentrations are well reproduced by the model. Additional to the comparison of the datasets, some other information can be derived directly from the results in the tables such as the complexation of the TMIs in cloud droplets as well as deliquescent particles.

Recapitulating, the applied model reproduces well the measured data at both sites and is therefore an adequate tool for the interpretation of measurements as well as the analysis of the tropospheric multiphase processing. However, for organic compounds with low solubilities the cloud water measurements show considerably higher concentrations as expected from both (i) their Henry solubilities and (ii) the complex multiphase modelling as performed here.

Acknowledgements

This study was supported by the Bundesministerium für Bildung und Forschung (Project FKZ 07ATF01 and FKZ 07ATF40). We thank the Umweltbundesamt (UBA), the Deutscher Wetterdienst (DWD, Offenbach) and all the colleagues that participated in the FEBUKO/MODMEP project for the good cooperation and support.

References

Bower, B.K.N., Choularton, T.W., Gallagher, M.W., Beswick, K.M., Flynn, M.J., Allen, A.G., Davison, B.M., James, J.D., Robertson, L., Harrison, R.M., Hewitt, C.N., Cape, J.N., McFadyen, G.G., Milford, C., Sutton, M.A., Martinsson, B.G., Frank, G., Swietlicki, E., Zhou, J., Berg, O.H., Mentes, B., Papaspiropoulos, G., Hansson, H.C., Leck, C., Kulmala, M., Aalto, P., Vakeva, M., Berner, A., Bizjak, M., Fuzzi, S., Laj, P., Facchini, M.C., Orsi, G., Ricci, L., Nielsen, M., Allan, B.J., Coe, H., McFiggans, G., Plane, J.M.C., Collett, J.L., Moore, K.F., Sherman, D.E., 2000. ACE-2 HILLCLOUD. An overview of the ACE-2 ground-based cloud experiment. Tellus 52B, 750–778.

Bower, K.N., Choularton, T.W., Gallagher, M.W., Colvile, R.N., Wells, M., Beswick, K.M., Wiedensohler, A., Hansson, H.-C., Svenningsson, B., Swietlicki, E., Wendisch, M., Berner, A., Kruisz, C., Laj, P., Facchini, M.C., Fuzzi, S., Bizjak, M., Dollard, G., Jones, B., Acker, K., Wieprecht, W., Preiss, M., Sutton, M.A., Hargreaves, K.J., Storeton-West, R.L., Cape, J.N., Arends, B.G., 1997. Observation and modelling of the processing of aerosol by a hill cap cloud. Atmospheric Environment 31, 2527–2543.

Bradbury, C., Bower, K.N., Choularton, T.W., Swietlicki, E., Birmili, W., Wiedensohler, A., Yuskiewicz, B., Berner, A., Dusek, U., Dore, C., Mcfadyen, G.G., 1999. Modeling of aerosol modification resulting from passage through a hill cap cloud. Atmospheric Research 50, 185–204.

Brüggemann, E., Gnauk, T., Mertes, S., Acker, K., Auel, R., Wieprecht, W., Möller, D., Collett Jr., J.L., Chemnitzer, R., Rüd, C., Junek, R., Herrmann, H., 2005. Schmücke hill cap cloud and valley stations aerosol characterisation during FEBUKO (I): particle size distribution and main components. Atmospheric Environment, this issue.

Charlson, R.J., Schwartz, S.E., Hales, J.M., Cess, R.D., Coakley Jr., J.A., Hansen, J.E., Hofmann, D.J., 1992. Climate forcing by anthropogenic aerosols. Science 256, 423–430.

Colvile, R.N., Sander, R., Choularton, T.W., Bower, K.N., Inglis, D.W.F., Wobrock, W., Schell, D., Svenningsson, I.B., Wiedensohler, A., Hansson, H-C., Hallberg, A., Ogren, J.A., Noone, K.J., Facchini, M.C., Fuzzi, S., Orst, G., Arends, B.G., Winiwater, W., Schneider, T., Berner, A.,

1994. Computer modelling of clouds at Kleiner Feldberg. Journal of Atmospheric Chemistry 19, 189–229.

Ervens, B., George, C., Willams, J., Buxton, G., Salmon, G., Bydder, M., Wilkinson, F., Dentener, F., Mirabel, P., Herrmann, H., 2003. CAPRAM 2.4 (MODAC mechanism): an extended and condensed tropospheric aqueous phase mechanism and its application. Journal of Geophysical Research 108 (D14), 4426.

Flynn, M.J., Bower, K.N., Choularton, T.W., Wobrock, W., Mäkelä, J.M., Martinsson, B.G., Frank, G., Hansson, H.C., Karlsson, H., Laj, P., 2000. Modelling cloud processing of aerosol during the ACE-2 HILLCLOUD experiment. Tellus 52B, 779–800.

Fuzzi, S. (Ed.), 1994. The Kleiner Feldberg cloud experiment 1990 (special issue). Journal of Atmospheric Chemistry 19(1–2).

Fuzzi, S. (Ed.), 1997. The Great Dun Fell cloud experiment 1993 (special issue). Atmospheric Environment 31(16).

Gallagher, M.W. (Ed.), 1999. The Great Dun Fell experiment 1995 (special issue). Atmospheric Research 50 (3-4).

Glotfelty, D.E., Seiber, J.N., Liljedahl, L.A., 1987. Pesticides in fog. Nature 325 (6105), 602–605.

Gnauk, T., Brüggemann, E., Müller, K., Chemnitzer, R., Rüd, C., Galgon, D., Wiedensohler, A., Acker, K., Auel, R., Wieprecht, W., Möller, D., Jaeschke, W., Herrmann, H., 2005. Aerosol characterisation at the FEBUKO upwind station Goldlauter (I): particle mass, main ionic components, OC/EC, and mass closure. Atmospheric Environment, this issue.

Heinold, B., Tilgner, A., Jaeschke, W., Haunold, W., Knoth, O., Wolke, R., Herrmann, H., 2005. Meteorological characterisation of the FEBUKO hill cap cloud experiments, Part II: tracer experiments and flow characterisation with nested non-hydrostatic atmospheric models. Atmospheric Environment, this issue.

Herrmann, H., Wolke, R., Müller, K., Brüggemann, E., Gnauk, T., Barzaghi, P., Mertes, S., Lehmann, K., Massling, A., Birmili, W., Wiedensohler, A., Wieprecht, W., Acker, K., Jaeschke, W., Kramberger, H., Syrcina, B., Bächmann, K., Collett Jr., J.L., Galgon, D., Schwirn, K., Nowak, A., van Pinxteren, D., Plewka, A., Chemnitzer, R., Rüd, C., Hofmann, D., Tilgner, A., Diehl, K., Heinold, B., Hinneburg, D., Knoth, O., Sehili, A.M., Simmel, M. Wurzler, S., Mauersberger, G., Majdik, Z., Müller, F., 2005a. FEBUKO and MODMEP: field measurements and modelling of aerosol and cloud multiphase processes. Atmospheric Environment, this issue.

Herrmann, H., Tilgner, A., Barzaghi, P., Majdik, Z., Gligorovski, S., Poulain, L., Monod, A., 2005b. Towards a more detailed description of tropospheric aqueous phase organic chemistry: CAPRAM 3.0. Atmospheric Environment, this issue.

Jaeschke, W., 1986. Chemistry of Multiphase Atmospheric Systems. NATO ASI Series, vol. 6. Springer, Berlin.

Lelieveld, J., Crutzen, P.J., 1990. Influences of cloud photochemical processes on tropospheric ozone. Nature 343, 227–232.

Liang, J., Jacob, D.J., 1997. Effect of aqueous phase cloud chemistry on tropospheric ozone. Journal of Geophysical Research 102 (D5), 5993–6001.

Mertes, S., Galgon, D., Schwirn, K., Nowak, A., Lehmann, K., Massling, A., Wiedensohler, A., Wieprecht, W., 2005a. Evolution of particle concentration and size distribution observed upwind, inside and downwind hill cap clouds at connected flow conditions during FEBUKO. Atmospheric Environment, this issue.

Mertes, S., Lehmann, K., Nowak, A., Massling, A., Wiedensohler, A., 2005b. Link between aerosol hygroscopic growth and droplet activation observed for hill cap clouds at connected flow conditions during FEBUKO. Atmospheric Environment, this issue.

Müller, K., van Pinxteren, D., Plewka, A., Svrcina, B., Kramberger, H., Hofmann, D., Bächmann, K., Herrmann, H., 2005. Aerosol characterisation at the FEBUKO upwind station Goldlauter (II): detailed organic chemical characterisation. Atmospheric Environment, this issue.

Pruppacher, H.R., Klett, J.D., 1997. Microphysics of Cloud and Precipitation, second ed. Kluwer Academic Publishers, Dordrecht.

Ravishankara, A., 1997. Heterogeneous and multiphase chemistry in the troposphere. Science 276, 1058–1065.

Sander, R., Lelieveld, J., Crutzen, P., 1995. Modelling of nighttime nitrogen and sulfur chemistry in size resolved droplets of an orographic cloud. Journal of Atmospheric Chemistry 20, 89–116.

Simmel, M., Diehl, K., Wurzler, S., 2005. Numerical simulation of the microphysics of an orographic cloud: Comparison with measurements and sensitivity studies. Atmospheric Environment, this issue.

Stockwell, W., Kirchner, F., Kuhn, M., 1997. A new mechanism for regional atmospheric chemistry modeling. Journal of Geophysical Research 102 (D22), 25847–25879.

Tilgner, A., Heinold, B., Nowak, A., Herrmann, H., 2005. Meteorological characterisation of the FEBUKO hill cap cloud experiments, Part I: synoptic characterisation of measurement periods. Atmospheric Environment, this issue.

Valsaraj, K.T., Thoma, G.J., Reible, D.D., Thibodeaux, L.J., 1993. On the enrichment of hydrophobic organic compounds in fog droplets. Atmospheric Environment 27A (2), 203–210.

Valverde-Canossa, J., Wieprecht, W., Acker, K., Moortgat, G.K., 2005. H_2O_2 and organic peroxide measurements in an orographic cloud: the FEBUKO experiment. Atmospheric Environment, this issue.

van Pinxteren, D., Plewka, A., Hofmann, D., Müller, K., Kramberger, H., Svrcina, B., Bächmann, K., Jaeschke, W., Mertes, S., Collett Jr., J.L., Herrmann, H., 2005. Schmücke hill cap cloud and valley stations aerosol chemical composition during FEBUKO (II): organic compounds. Atmospheric Environment, this issue.

Wieprecht, W., Acker, K., Mertes, S., Collett Jr., J.L., Jaeschke, W., Brüggemann, E., Möller, D., Herrmann, H., 2005. Cloud physics and cloud water sampler comparison during FEBUKO. Atmospheric Environment, this issue.

Wolke, R., Sehili, A.M., Simmel, M., Knoth, O., Tilgner, A., Herrmann, H., 2005. SPACCIM: a parcel model with detailed microphysics and complex multiphase chemistry. Atmospheric Environment, this issue.

3B2v8.06a/w (Dec 5 2003).51c XML:ver:5.0.1 AEA : 5779 Prod.Type:FTP pp.1–15(col.fig.:1–13) ED:MangalaK. PAGN:Vino SCAN:Global

ARTICLE IN PRESS

Available online at www.sciencedirect.com

SCIENCE DIRECT®

ELSEVIER

Atmospheric Environment ▮ (▮▮▮▮) ▮▮▮–▮▮▮

ATMOSPHERIC ENVIRONMENT

www.elsevier.com/locate/atmosenv

Comparison of different model approaches for the simulation of multiphase processes

A.M. Sehili, R. Wolke*, O. Knoth, M. Simmel, A. Tilgner, H. Herrmann

Leibniz Institute for Tropospheric Research, Permoserstr. 15, 04318 Leipzig, Germany

Abstract

Cloud-chemistry models are developed intensively with increasing complexity, leading to new knowledge and offering new possibilities to understand the physico-chemical processes taking place in the atmosphere. Intercomparing such detailed models is the way to test the robustness and reliability of their parameterizations and numerical schemes. The present study involves newly developed parcel models treating microphysics and chemistry with equal rigor. The description of both kinds of processes is given for a size-resolved particle/droplet spectrum. Three different types of models are compared. In the SPACCIM approach, one- and two-dimensional particle/drop microphysical schemes are used in a time-splitting setup between chemistry and microphysics. The GALERKIN model employs a one-dimensional scheme in a fully coupled setup. For each of the three types, "fixed bin" and "moving bin" approaches are implemented. A comparison between "fixed" and "moving bin" approaches makes sense only for scenarios without coagulation and breakup. The paper focuses on the effects of different microphysical and numerical approaches on the multiphase chemistry. The resulting changes in the particle/droplet composition feed back on cloud microphysics. Substantiated conclusions can only be derived if these effects are studied for a wide range of cases. Thus, the simulations are performed for three chemical reaction mechanisms of different complexity and four scenarios derived from field measurements. The interaction between numerical schemes, microphysics and multiphase chemistry is discussed. Mostly, the results of the participating models agree in an appreciable way. Observable differences are noticed between the "moving bin" approach and models using fixed grids for the discretization of the particle/droplet spectrum. Furthermore, the initial aerosol composition influences the fate of chemical species as well as the behavior of the numerical solver in a substantial way.

Keywords: Air pollution modeling; Multiphase chemistry; Microphysics; Cloud processing; Time integration schemes; Model comparison

1. Introduction

Within atmospheric clouds, gaseous, aqueous, and solid species interact with each other in chemical and physical ways. These multiphase processes affect the global radiation field via modified scattering and absorption properties of the atmospheric system which in turn influences photolysis rates and the transport of chemical species. Modeling such complex physico-chemical processes demands the use of appropriate approaches and numerical techniques which differ from one single model to another. Literature addressing intercomparison of cloud chemistry models is not abundant and focuses only on some special issues. Jacobson (2002) presents some numerical techniques to

*Corresponding author. Tel.: +49 341 235 2860.
E-mail address: wolke@tropos.de (R. Wolke).

1352-2310/$ - see front matter © 2005 Elsevier Ltd. All rights reserved.
doi:10.1016/j.atmosenv.2005.02.039

solve the size- and time-dependent aerosol processes including dissolution and reversible chemistry. In Roelofs (1993) and Kreidenweis et al. (2003) simplified reacting mechanism and idealized meteorological conditions are used with a focus on bulk and size-resolved approaches. Some studies concerned with a more detailed reacting mechanism assume a prescribed microphysics (Sandu et al., 1996; Chaumerliac et al., 2000; Djouad et al., 2002; Barth et al., 2003). Furthermore, the phase interchange depends strongly on the phase surface area (Kreidenweis et al., 2003). For an appropriate description a highly resolved drop spectrum has to be considered.

The aim of the present intercomparison is to figure out the effect of different microphysical approaches and numerical schemes on cloud chemistry and, at last, on changes in particle composition and size distribution by microphysical processes. Moreover, these changes feed back on cloud microphysics. From the numerical point of view, the participating models differ in the manner of coupling between microphysics and multiphase chemistry, the discretization of the particle/droplet spectrum and the time integration schemes (see Section 2). Two principal approaches for coupling microphysics and multiphase chemistry are considered. In the "fully coupled" approach (Knoth, 2005), the model equations for the microphysical variables (temperature, water vapor, liquid water content) as well as for all chemical species are considered as one system which is integrated in a coupled manner by an implicit–explicit time integration scheme. Therefore, the splitting error between microphysics and multiphase is avoided. In the SPACCIM approach (Wolke et al., 2005), a multiphase chemistry model is coupled with a microphysical one. The two codes run separately as far as possible and exchange all information needed. This approach allows the coupling of a complex multiphase chemistry model with microphysical codes of various types. In this study, the multiphase chemistry is coupled to three microphysical models which use different discretization techniques of the particle/droplet spectrum.

In principle, the numerical behavior and/or the influence of microphysics on chemistry can change considerably for different chemical mechanisms, aerosol compositions or meteorological situations. Therefore, significant conclusions are only arrived at from simulations over a wide range of input data. Against this background, the behavior of the compared parcel models is discussed for three mechanisms of different complexity and two initial aerosol compositions. Two meteorological cases were studied. The first one is taken from Kreidenweis et al. (2003) representing a rising air parcel with a constant vertical velocity, traveling through a cloud. Inspired by the FEBUKO experiment (Herrmann et al., 2005), the second case describes an air parcel undergoing a cycle of hill cap clouds.

2. Theoretical background and the participating models

Generally, the chemical multiphase processes are described by the mass balance equations of the species in a size-resolved droplet spectrum. Formally, these can be written as a system of ordinary differential equations (ODE)

$$\dot{c} = f_{\mathrm{chem}}(t, c; m) + f_{\mathrm{henry}}(t, c; m) + f_{\mathrm{mphys}}(t, c; m), \qquad (1)$$

where c denotes the vector of mass concentrations related to air volume of the gas phase species and the aqueous species in each particle/droplet fraction. The vector m represents the time-dependent microphysical variables which have to be provided simultaneously. The term f_{chem} stands for the chemical reactions in gas and aqueous phase. Note that the liquid phase chemistry is always performed for ideal solutions. In fact, this assumption is not valid especially for non-activated particles and small droplets. However, activity coefficients are not taken into account in this study. The gas-liquid mass transfer term f_{henry} is parameterized by the approach of Schwartz (1986) assuming well mixed droplets. The term f_{mphys} stands for mass fluxes between different size bins caused by microphysical processes (condensation/evaporation, coagulation/breakup).

In this paper, we will not discuss the uncertainities associated with bulk and size-resolved approaches. That has been done in many intercomparison studies and the effects are close to be understood (Roelofs, 1993). All the considered models are size-resolved ones allowing alternatively a "fixed bin" or "moving bin" discretization of the particle/droplet spectrum. In the "fixed bin" approach, the spectrum is discretized in a fixed grid according to the droplet diameter. Usually the grid size increases in a logarithmic scale. This grid is fixed over the whole simulation time and, therefore, particle sizes have to be remapped to the original grid. The changes in the droplet distribution caused by microphysical processes are described by mass and number fluxes between the corresponding size bins. Neglecting coagulation in the "moving bin" representation, an initial size distribution based on a fixed grid discretization evolves with bins growing independently from each other and no fluxes are generated. This implies $f_{\mathrm{mphys}} = 0$ in Eq. (1). Of course, such a comparison between the two approaches is possible only for condensation and evaporation. Preliminary setup simulations show that coagulation and breakup can be neglected in our test scenarios.

The ODE system (1) resulting from multiphase chemical systems is nonlinear, highly coupled and extremely stiff. Because explicit ODE solvers require numerous short time steps in order to maintain stability, only implicit schemes can integrate these systems in an effective way (Sandu et al., 1997). In the participating models, system (1) is integrated in a coupled and implicit

manner. Special linear system solvers are applied for the solution of the linear systems, usually the expensive part of implicit methods. These direct sparse techniques exploit the special structure (sparsity, block structure, different types of coupling) of the corresponding Jacobians (Wolke and Knoth, 2002).

In the following, we discuss the main differences between the participating models. Table 1 summarizes some numerical features of the codes.

2.1. The SPACCIM approach

In the SPACCIM approach (Wolke et al., 2005), a multiphase chemistry model is directly coupled with a microphysical model. The two models run separately and exchange information only every coupling time step Δt_{cpl}. Each of the two models uses its own time step control. The coupling scheme provides time-interpolated values of the microphysical variables (temperature, water vapor, liquid water content) and generates time-averaged mass fluxes f_{mphys} over the coupling time interval. Changes of the chemical aerosol composition by gas scavenging and chemical reactions feed back on the water condensation growth rates via the Raoult term. The influence of resulting changes in the particulate mass of each bin is not considered in this study. The exchange of information is organized via well-defined interfaces. The size bin discretization for the multiphase chemistry is taken from microphysics. For the reduction of the computational costs, the use of coarser resolutions in the multiphase chemistry computations is possible by averaging the microphysical variables (Wolke et al., 2005). The implicit time integration of Eq. (1) is performed by a high-order BDF scheme. For this part, a modified version of the popular code LSODE (Hindmarsh, 1983) with an entire replacement of the linear algebra part is used. As mentioned before, the included direct sparse solver exploits the special structure of the related Jacobian (Wolke and Knoth, 2002). In the coupling scheme, the choice of an appropriate coupling time step has to be a compromise between a small splitting error and a low number of restarts which are expensive for higher order implicit solvers. In this paper, the multiphase chemistry is coupled with different microphysical models (Simmel and Wurzler, 2004).

2.1.1. One-dimensional particle distribution (SPACCIM1D)

This microphysical model is based on the discretization in mass space of the one component general dynamic equation (Gelbard and Seinfeld, 1980) using the linear discrete method (LDM). In this sectional approach, the number distribution is represented by a piecewise linear function over a prescribed number of size bins in the water mass space. Additionally, the soluble part in each bin is explicitly described for the calculation of the Raoult term (Simmel et al., 2002, 2005). The growth rate in the condensation/evaporation process and droplet activation are based on Köhler theory. Droplets are considered to be well diluted. In the present study, 66 bins and a sizing factor of 2 are applied. The range of the spectrum reaches from approximately 1 nm up to 5 mm. The model can operate in a "moving bin" as well as in a "fixed bin" mode. In the first case, the spectrum is obtained by discretizing the non-water mass of the particles. In this way, the "moving bin" discretization does not depend on the initial humidity. In the "fixed bin" case, the particle/droplet spectrum is discretized according to the water mass considered in equilibrium with the initial relative humidity. Note that droplets having the same size contain the same amount of aerosol.

2.1.2. Two-dimensional particle distribution (SPACCIM2D)

In this approach, the particles are classified according to their water mass and total aerosol mass on a two dimensional fixed grid which is comparable with the approach of Bott (2000). The discretization of the particle mass and water mass spectrum is similar to the 1D model. However, a finer resolution with a sizing factor $\sqrt{2}$ is used for the particle mass discretization. Similarly to the 1D model, the soluble part of the total particle mass is explicitly treated in the 2D spectrum. The condensation process changes the particle properties on the water mass axis only but not on the aerosol mass axis. Therefore, the shift of water mass and particle number is calculated similar to the 1D approach by an extended LDM (Simmel and Wurzler, 2004). Addition-

Table 1
Numerical aspects of the compared models

Models	Solver	Time step	Number of bins	Discretization scheme
SPACCIM1D	BDF	Controlled	66	LDM
SPACCIM2D	BDF	Controlled	66×90	LDM-2D
GALERKIN	Implicit Euler	Controlled	66	DGM

LDM: Linear discrete method. DGM: Discrete Galerkin method. BDF: Backward differentiation formula.

ally, the LDM is also applied to determine the shift of the soluble mass fraction in each size bin. Thus, droplets having the same size can show a different hygroscopic behavior (see Fig. 3). For the multiphase chemistry, several bins of the 2D grid are collected. In the first approach denoted as "moving bin" version, a projection of particle mass on the aerosol grid is performed. That means, all bins with the same aerosol mass are summarized. In the so-called "fixed bin" version, all particles with the same water mass are collected for chemistry. In this approach, the particle compositions of various bins are mixed for the chemistry calculations. This may be one reason for appreciable discrepancies of this approach from the other ones in our simulations. Furthermore, SPACCIM2D does not have to assume an internally mixed aerosol. However, a fair evaluation is only possible by the implementation of the more expensive and complicated 2D discretization also for the multiphase chemistry which will be tackled in the future.

2.2. Fully coupled GALERKIN approach

In this approach (referred to as GALERKIN), the model equations for the microphysical variables m (temperature, water vapor, liquid water content) as well as the system (1) for all chemical species are considered as one system which is integrated in a coupled manner (Knoth, 2005). Therefore, no splitting error between microphysics and multiphase chemistry occurs. The model is based on the discretization in mass space of the multicomponent general dynamic equation using the discontinuous Galerkin method (DGM) with a different formulation for the free parameters of the sectional distribution (Knoth, 2005). The DGM is a space discretization method for non-linear hyperbolic equations (Hirsch, 1992). Again, Köhler theory is used to determine the growth rate and droplet activation. Well diluted droplets are considered. A "fixed bin" and "moving bin" version of the model are implemented. The time integration in this fully coupled model is based on an implicit–explicit scheme. In the "fixed bin" case, the advective part caused by condensation and evaporation is integrated by an explicit Euler scheme. All other terms including the multiphase chemistry are treated by an implicit first order BDF method. The time step control is performed by a Richardson extrapolation scheme. Similar to the SPACCIM code, the linear solvers exploit the special sparse structure of the system. Our simulations reveal clearly that this fully coupled method combined with a DGM discretization technique works stable and keeps competitive to the SPACCIM approach.

3. Conditions of the intercomparison

Simulations for two different meteorological scenarios and two initial aerosol compositions were carried out. Note that a detailed description of both scenarios and the complete initial data sets are listed in the electronic supplementary material (ESM)[1]. In all runs, the air parcel is located at 45° N and starts at 600 m altitude for summer solstice at 9.00 AM (UTC). The RISING scenario inspired by Kreidenweis et al. (2003) simulates an air parcel lifted adiabatically at $0.5\,m\,s^{-1}$ from 98 m below cloud base up to 1200 m above cloud base. The air parcel in the WAVE scenario undergoes three cycles of hill cap clouds. It starts at 600 m altitude, rises adiabatically for 500 s until it reaches the altitude of 1000 m and a horizontal distance of 1000 m (an implicit $2\,m\,s^{-1}$ horizontal velocity is assumed), stays at the same altitude for 200 s, then descends for 500 s to recover its initial altitude. This cycle is repeated three times for an overall traveling time of 1 h. Descriptions of both scenarios are available in the ESM, Appendix A.4. The gas phase initial concentrations are the same for both scenarios (Table A.1, ESM). They correspond to the data collected during the FEBUKO experiment in the Thuringian forest in Germany (Herrmann et al., 2005; Tilgner et al., 2005). The initial dry aerosol number size distribution consists of two lognormal modes, covering the Aitken and the accumulation size range (Table A.2, ESM). Those data are inspired by the collected ones during EI of the FEBUKO experiment.

Two different initial aerosol compositions with the same number and mass distribution are considered for RISING and WAVE. AEROSOL1 is characterized by a high soluble part and has a uniform composition for all particles over the whole spectrum as specified in the second mode in Table A.3 (ESM). AEROSOL2 is given as an external mixture of two modes with different particle compositions (see Table A.3, ESM). The particles of the first mode are less hygroscopic. During the initialization of the microphysical models with a one-dimensional spectrum, an internally mixed aerosol is generated also for AEROSOL2. But in contrast to AEROSOL1, the composition depends on the particle size. For SPACCIM2D, the explicit mixture can be directly taken into account. It should be stressed that the initial aerosol composition is prescribed independently from the used chemical mechanism. All species not participating in the corresponding reaction scheme are considered as "passive", non-reactive tracers. They affect the pH value and are part of the total mass. The initial pH value is determined through the charge balance equation for the initial aerosol and is then computed dynamically throughout the whole simulation time.

[1] http://projects.tropos.de:8088/afo2000g3/FEBUKO_dateien/febuko.html

Table 2
Characteristics of the used chemical mechanisms

Mechanism	Number of species			Number of reactions					
	Total	Gas	Aqua	Total	Gas	Henry	Disso	Aqua	Reference
INORG	100	80	20	259	237	8	10	4	ESM, Appendix B.I
BARTH	122	80	42	284	237	14	6	27	Barth et al. (2003)
CAPRAM2.3	162	82	80	508	237	34	27	210	Herrmann et al. (2000)

The focus of this study is to find out the effect of different microphysical and numerical approaches on multiphase processes for various cloud exposure events. These investigations are performed for three multiphase mechanisms of different complexity using the same gas phase mechanism RACM (Stockwell et al., 1997). All in-cloud photolysis rates of RACM are decreased by a factor 0.5 due to cloud droplet scattering. The first considered multiphase mechanism is the rather complex CAPRAM2.3 (Herrmann et al., 2000). The sulfate dedicated mechanism INORG is extracted from CAPRAM2.3 by neglecting all organic reactions. The sulfur free mechanism BARTH (Barth et al., 2003) is slightly modified for this comparison. Table 2 summarizes the characteristics of the considered multiphase reaction schemes. A more detailed description of the three mechanisms is given in the ESM, Appendix B.

It should be stressed that all models involved in the present study treat the chemical reactions terms and the phase transfer in the same way. In all implementations, the reaction system (gas and aqueous phases, phase transfer according to Schwartz) is read from an ASCII data file. Afterwards all data structures required for the computation of the chemical terms and the corresponding Jacobians are generated. This approach allows a large flexibility in the choice of the chemical reacting mechanism.

4. Results

This intercomparison study should allow us at first to figure out the effect of different microphysical approaches on multiphase chemical processes, to compare the numerical schemes of involved models and to investigate the influence of the initial aerosol composition on the fate of some important chemical species like sulfate, nitrate or sulfuric dioxide for different kinds of cloud exposure. Due to space limitation, it is not possible to discuss all results. A selection is made for the most interesting and appropriate issues from our point of view. Comparison between models aims mainly to figure out differences and not to make an evaluation. In the following, time series figures describe averaged values over the whole spectrum. In the "moving bin" representation, the droplet radius corresponds to the average mass of one particle in each bin.

4.1. Microphysical aspects

Under the same meteorological conditions, the different microphysical models were expected to behave similarly. Fig. 1 shows the evolution of total liquid water content and supersaturation ratio of the parcel in RISING and WAVE. The liquid water content evolves linearly above cloud base during RISING and follows the orographic cycle in WAVE. As the parcel ascends the air becomes supersaturated and aerosol particles whose radii exceed the critical ones are considered "activated" and continue growing. Activation takes place at cloud base after nearly 200 s ascension in RISING and 150 s in WAVE. During the last, evaporation occurs down-hill allowing a processing of aerosol particles. As expected, no relevant differences have been noted between the models. The models contain an explicit size dependent description of the microphysical processes responsible for aerosol activation and droplet growth by condensation. The total particle number concentration is constant during all scenarios and cases when no entrainment, no deposition and no secondary particle formation from the gas phase are considered. Fig. 2 illustrates the time evolution of the number concentrations of particles having radii larger than 1 μm during RISING. The two variants of SPACCIM1D remain comparable for both cases. This is in good agreement with GALERKIN-MOV for both AEROSOL1 and AEROSOL2. In the GALERKIN simulations around 200 cm^{-3} particles more activate with the "moving bin" version in comparison with the "fixed bin" version. This discrepancy is caused by the used advection scheme in GALERKIN-FIX (Knoth, 2005). SPACCIM2D versions which involve an additional resolution of the particulate mass simulate less activated particles in the order of 650 cm^{-3} in AEROSOL1. During AEROSOL2, the "moving bin" version shows a step-wise activation behavior. Fig. 3(right) shows the effect of the external mixing of two modes with different hygroscopicity on activation (AEROSOL2).

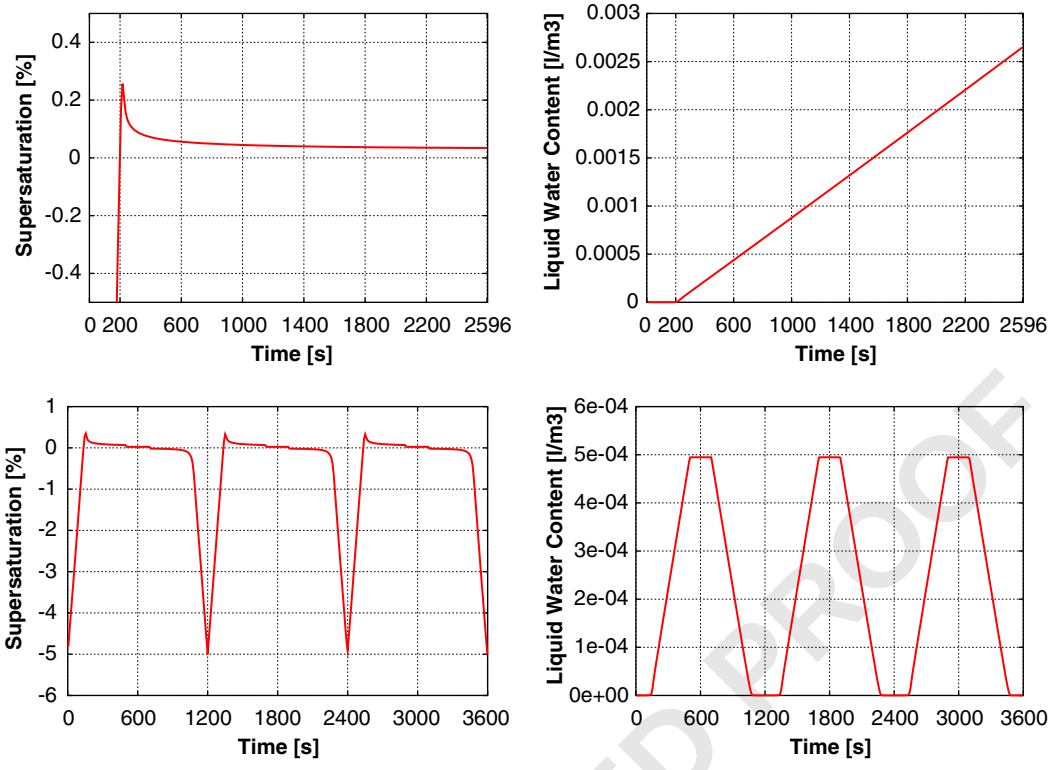

Fig. 1. Supersaturation (left) and LWC (right) during RISING (top) and WAVE (bottom).

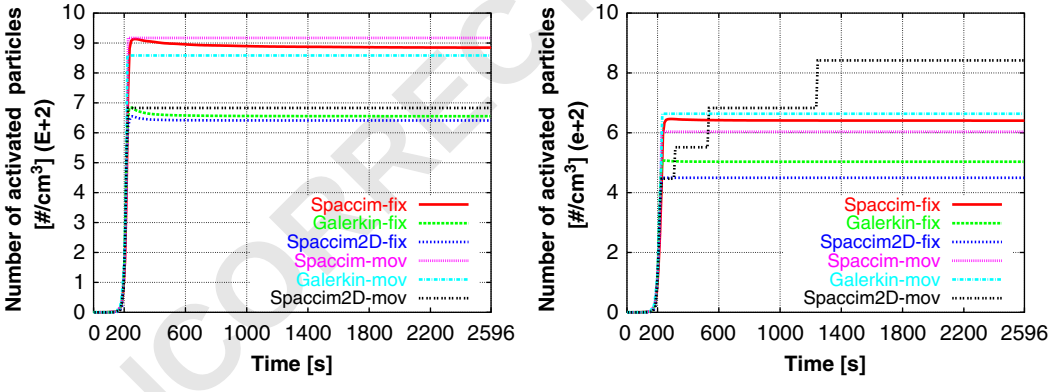

Fig. 2. Number concentration of "activated" droplets ($R > 1\,\mu m$) during RISING: AEROSOL1 (left); AEROSOL2 (right).

In Fig. 4(left) the number distribution of SPACCIM1D-FIX and SPACCIM1D-MOV are compared for RISING. Such plots are problematic and require a regridding of the moving bin approach. Usually the size represented by a moving bin is compressed by condensation which leads to a higher number of bins with smaller sizes especially for the activated part of the spectrum. Therefore, the particle numbers of the kth "moving bin" is scaled by the "compressing" factor $\log(d_0^{k+1}/d_0^{k-1})/\log(d^{k+1}/d^{k-1})$, where d_0^k and d^k denote the starting and the current mean diameter of the kth bin. The good agreement between the "fixed" and "moving bin" approach for the non-activated spectrum is a hint that this scaling is appropriate. Fig. 5(left) shows the development of the number distribution for SPACCIM1D-FIX and the WAVE AEROSOL1 scenario. Note that the parcel is located in the center of the plateau after 600 s as well as 3000 s. At the end of the cycles, the two

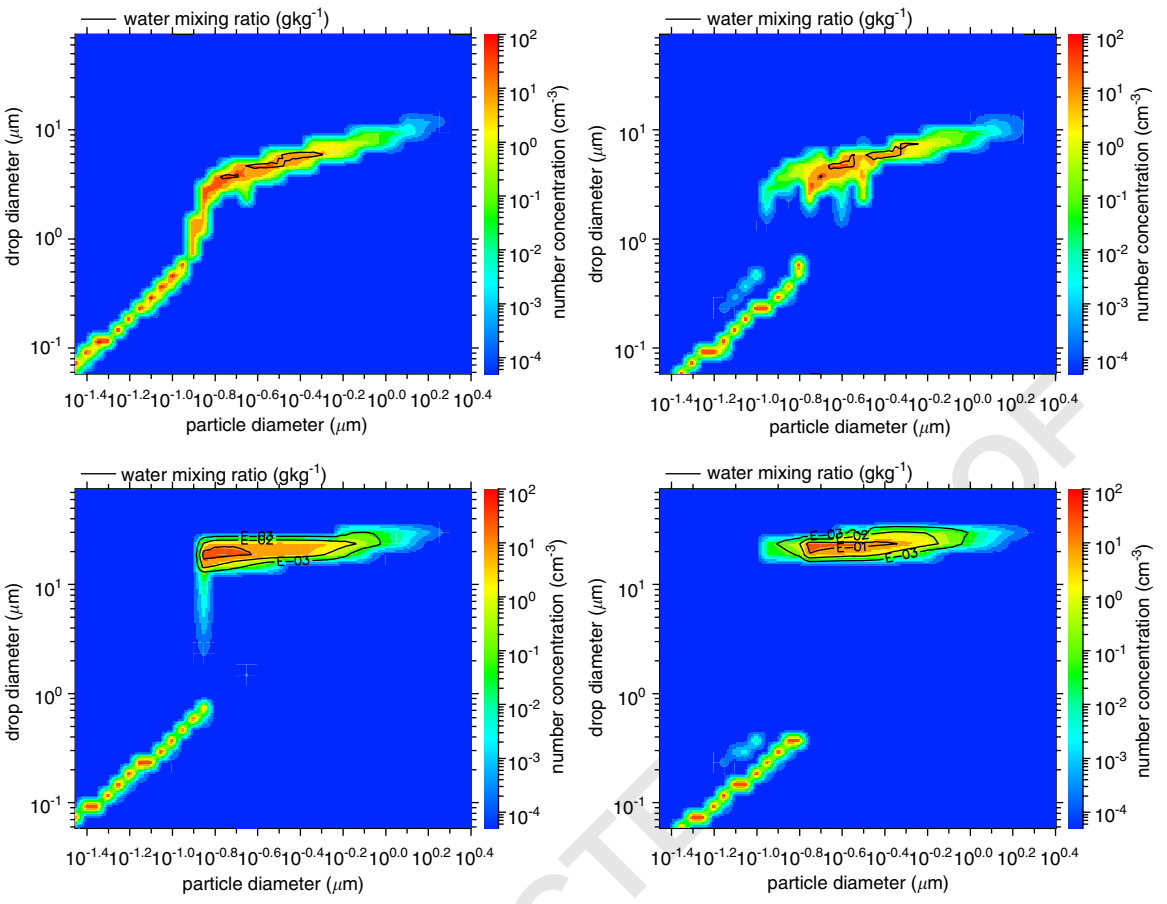

Fig. 3. 2D number size distribution RISING with SPACCIM2D-FIX: 26 m above cloud base (top) and at cloud top (bottom) for AEROSOL1 (left) and AEROSOL2 (right).

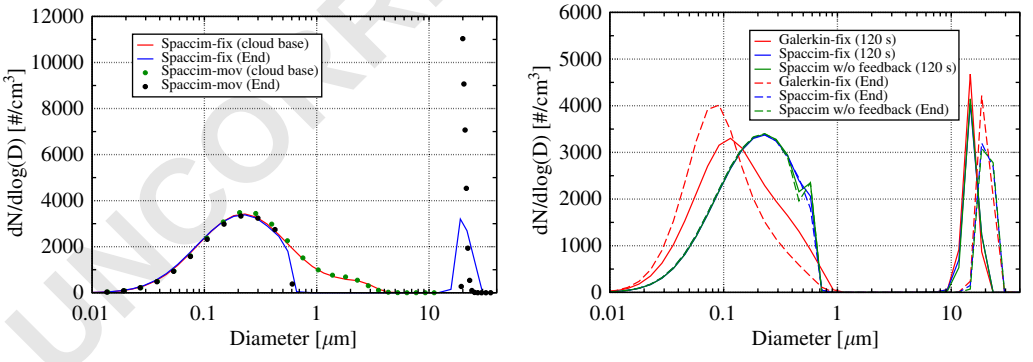

Fig. 4. Number size distribution during RISING AEROSOL1 case and CAPRAM2.3: with SPACCIM1D-FIX and SPACCIM1D-MOV (scaled according to the fraction size) at two different points of the trajectory (left); comparison between GALERKIN-FIX, SPACCIM1D-FIX and SPACCIM2D-FIX (without feedback) at two positions of the air parcel (right).

initial modes are more pronounced which is due to numerical diffusion.

A comparison between SPACCIM1D-FIX and GALERKIN-FIX for both scenarios is presented in Figs. 4(right) and 5(right). Additionally, a SPACCIM1D-FIX run without feedback is plotted. For both scenarios, feedback is insignificant. The main reason may be that the Raoult term is calculated from the soluble fraction of the initial

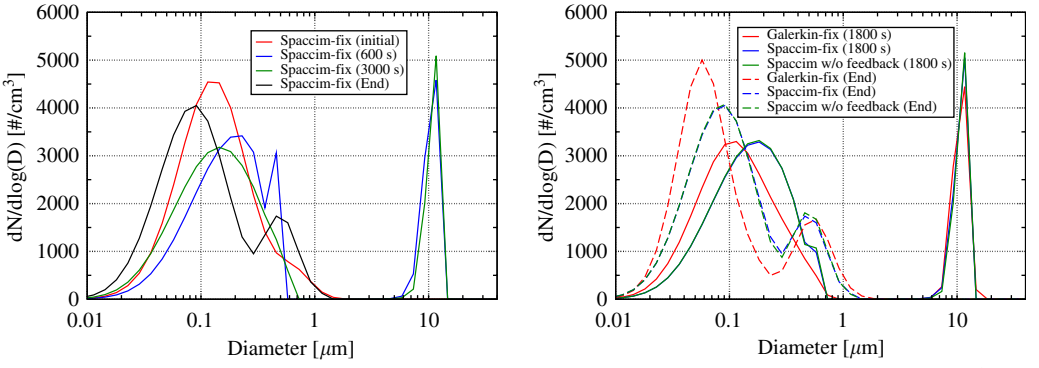

Fig. 5. Number size distribution during WAVE AEROSOL1 case and CAPRAM2.3: with SPACCIM1D-FIX at two different points of the trajectory (left); comparison between GALERKIN-FIX, SPACCIM1D-FIX and SPACCIM1D-FIX (without feedback) at two positions of the air parcel (right).

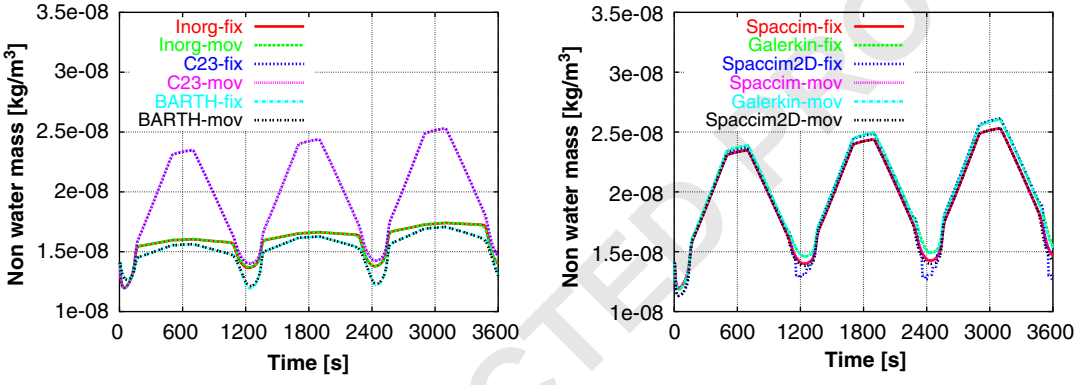

Fig. 6. Time evolution of non-water mass during WAVE AEROSOL1 case: with SPACCIM1D for the three involved mechanisms (left); with the six models using CAPRAM2.3 (right).

aerosol composition. For the "non-activated" particles, the ratio between soluble and total mass is only slightly changed by the gas uptake. For the "activated" particles, the Raoult term is dominated by the large water fraction. For scenarios with higher gas scavenging or/and heterogeneous particle compositions, appreciable differences are observed (Wolke et al., 2005). The differences between SPACCIM1D-FIX and GALERKIN-FIX result from the different numerical schemes. An additional reason for this effect in GALERKIN, where gas uptake modifies directly the total mass in each bin, may be the redistribution of total mass from smaller to larger particles by phase transfer. Fig. 6 illustrates the evolution of non-water mass (NWM) during WAVE AEROSOL1. The order of complexity of the mechanism plays an important role here (left). The reacting systems INORG and BARTH where several pathways are omitted simulate 35% less uptake from the gas phase compared to CAPRAM2.3. The increase of NWM over the simulation period is mainly caused by the nitrate production (Fig. 12). Using CAPRAM2.3 for different models yields no significant differences regarding NWM (Fig. 6(right)).

4.2. Chemical aspects

Several species (SO_2, HNO_3, SO_4^{2-}, HSO_4^-, NO_3^-, H^+) are chosen to figure out the deviations between the participating models. The BARTH mechanism is excluded from the sulfur chemistry discussion. The averaged values in Tables 3, 4, 6 and 7 are calculated without taking into account the values given by SPACCIM2D-FIX. Those last were singular and deviated in some cases largely from the ones given by the other participating models. As mentioned before, the coupling with chemistry in the case of SPACCIM2D-FIX is done in "1D way". Aerosol mass is collected over the dry mass spectrum for every droplet class (projection on y-axis in Fig. 3). The remapping on the fixed droplet grid of the so collected dry mass induces a different hygroscopic behavior that is not comparable with the other models.

SPACCIM2D-MOV is rather comparable in this 1D projection (on *x*-axis in Fig. 3) to SPACCIM1D-MOV and, therefore, remains close to other models.

4.2.1. Sulfur chemistry

The in-cloud sulfate production from SO_2 oxidation takes place mainly in the activated part of the spectrum. During RISING, the vertical profile of sulfate production shows that the sulfate is formed mostly (70–85% depending on the models and mechanisms used) within 150 m above cloud base and that at the end of the simulation, 20–45% of SO_2 is oxidized. The "moving bin" models tend to predict more SO_2 uptake from the gas phase as shown in Fig. 7 and Tables 3 and 4. This deviation takes place all over the time beyond the start of activation and begins to be significant from nearly 300 m above cloud base in AEROSOL1 and 200 m in AEROSOL2. The previous discrepancy can be explained by a different spectral distribution of the activated particles. A presence of more small activated droplets in the "fixed bin" approach due to the "remapping" can decrease the pH value and thus weakens the uptake process. In the "moving" representation, bins grow independently from each other without microphysical fluxes. Deviation is increasing with droplet size. Apart from that, SO_2 uptake depends on the acidity of droplets. To investigate this phenomenon, additional simulations with higher pH values were performed and showed a better agreement between the "fixed" and "moving" approaches. In addition, simulations using weaker updraft velocities allowing a slower dilution process through water condensation which by turn also means higher pH values showed likewise a better agreement. The above considerations are relevant for both mechanisms involving sulfur. As shown in Fig. 7 there is more SO_2 uptake for CAPRAM2.3, where other pathways compete for reacting with aqueous SO_2.

The gas phase species uptake and production are also sensitive to initial aerosol mixture. A lower soluble fraction like in AEROSOL2 restricts the activation of particles in comparison to AEROSOL1 (Fig. 2). As a result, less droplets compete for the same available water vapor and, consequently, grow to bigger sizes with higher pH values which leads to more SO_2 uptake. The GALERKIN models tend to take up less SO_2 while preserving the difference noted between the "fixed" and "moving bin"

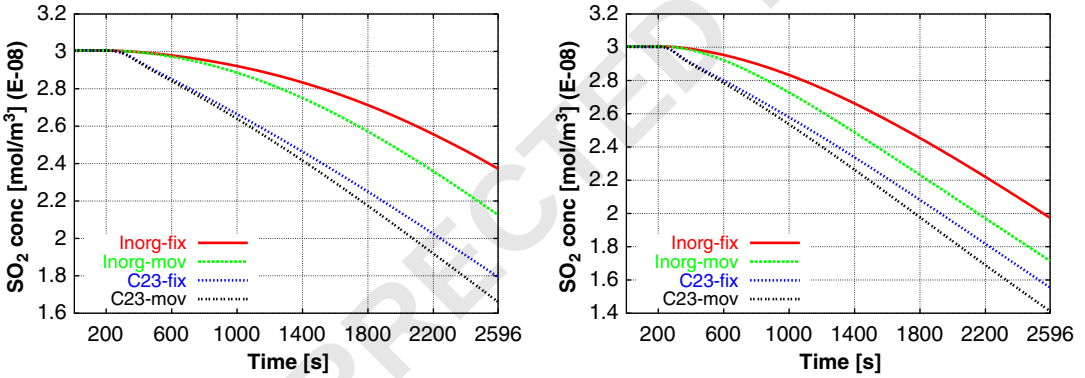

Fig. 7. Time evolution of SO_2 concentration during RISING simulation with the SPACCIM1D model using INORG and CAPRAM2.3 mechanisms: AEROSOL1 (left); AEROSOL2 (right).

Table 3
Relative deviation of selected gas phase species to the average concentration for the involved models in % during RISING AEROSOL1

Mechanism	SO_2		HNO_3			OH		
	Inorg	C23	Inorg	C23	Barth	Inorg	C23	Barth
AVERAGE	2.272e−8	1.739e−8	1.104e−11	1.951e−12	3.302e−12	5.162e−12	7.231e−13	1.472e−12
SPACCIM1D-FIX	+4.4	+3.1	−11.6	−22.4	−18.3	0.0	−5.1	−2.9
SPACCIM1D-MOV	−6.4	−4.5	−15.2	−23.2	−26.9	0.0	−7.5	−12.8
GALERKIN-FIX	+7.4	+5.1	+22.7	+40.4	+49.1	0.0	+9.8	+17.5
GALERKIN-MOV	−0.6	+0.2	+4.0	+10.0	+2.3	0.0	+2.2	+1.4
SPACCIM2D-MOV	−4.7	−3.7	+0.1	−4.8	−6.0	0.0	+0.6	−2.9
SPACCIM2D FIX	−33.4	−33.4	+115.6	−20.7	−47.8	+0.3	+51.8	−18.2

Average concentrations are in mol m^{-3}.

Table 4
Relative deviation of selected gas phase species to the average concentration for the involved models in % during RISING AEROSOL2

Mechanism	SO_2		HNO_3			OH		
	Inorg	C23	Inorg	C23	Barth	Inorg	C23	Barth
AVERAGE	1.909e−8	1.528e−8	1.293e−11	2.117e−12	3.972e−12	5.169e−12	7.832e−13	1.490e−12
SPACCIM1D-FIX	+3.3	+1.7	−6.9	−12.3	−17.0	0.0	−4.3	−4.9
SPACCIM1D-MOV	−10.2	−7.5	−9.2	−15.7	−23.5	0.0	−5.5	−10.9
GALERKIN-FIX	+13.3	+9.0	+18.2	+33.9	+23.9	0.0	+8.2	+16.1
GALERKIN-MOV	−0.7	+0.5	0.0	+1.1	+23.9	0.0	+0.3	+0.2
SPACCIM2D-MOV	−5.5	−3.4	−1.9	−6.8	−7.3	0.0	+1.3	−0.2
SPACCIM2D FIX	−20.3	−23.1	+100.6	+596.7	+318.6	+0.1	+49.6	−3.7

Average concentrations are in mol m^{-3}.

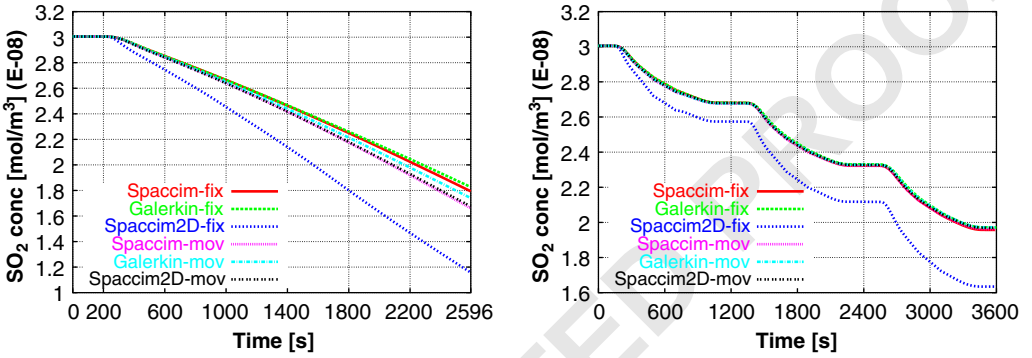

Fig. 8. SO_2 concentration of the participating models using CAPRAM2.3 mechanism: RISING AEROSOL1 (left); WAVE AEROSOL1 (right).

approach (Fig. 8). During WAVE, SO_2 undergoes a continuous uptake to the aqueous phase and its concentration decreases to the end of the cycles. The differences observed above between the mechanisms and the initial aerosol mixing for RISING are also valid during WAVE although the dynamics are different. The results for SO_2 are close for both scenarios except the SPACCIM2D-FIX one. Tables 3 and 4 summarize the final concentrations of some gas phase species during RISING for both cases AEROSOL1 and AEROSOL2.

The SO_2 analysis for RISING constitutes a basis to discuss differences between the models and the effect of different initial aerosol compositions. As mentioned above, SO_4^{2-} and HSO_4^- are the products of SO_2 oxidation in clouds. Fig. 9(top-left) illustrates the anti-correlation existing between HSO_4^- and SO_4^{2-} due to dissociation. The equilibrium is reached rapidly during the start period. Between this time and the start of activation, SO_4^{2-} increases strongly accompanied by a moderate decrease in HSO_4^-. After the activation, this scheme is inverted. The differences noted previously for SO_2 are clearly reflected on SO_4^{2-}. HSO_4^- does not experience a significant difference. As expected, the models simulate more SO_4^{2-} where more SO_2 uptake is found. Obviously, the lower sulfate fraction of AEROSOL2 leads to a faster SO_2 uptake (Fig. 9, top-right). The total sulfur concentration for both cases is conserved. WAVE allows to stress the effect of the hill cap cycles on the SO_4^{2-} and HSO_4^- evolution. As plotted in Fig. 9(bottom), a cyclic behavior of SO_4^{2-} and HSO_4^- is observed. The minimum (maximum) SO_4^{2-} concentrations in the valleys (on the hills) decreases (increases) from cycle to cycle. Among the models, SPACCIM1D-FIX delivers lower SO_4^{2-} and, consequently, higher HSO_4^- concentrations. SPACCIM2D-FIX deviates again observably.

4.2.2. pH value

While a huge number of aqueous reactions depends on the acidity of the droplets, the variation of pH during any cloud exposure plays a substantial role. Cloud water pH starts with a low value determined by the charge balance and the initial aerosol composition. Then pH increases rapidly due to dilution as illustrated in Fig. 10. During RISING, the four versions of SPACCIM are in good agreement. The two GALERKIN models deliver at the end of the simulation a higher pH value as resumed in Table 5. For all models, the average cloud water pH over the hills during WAVE decreases with the cycles (Fig. 10). The

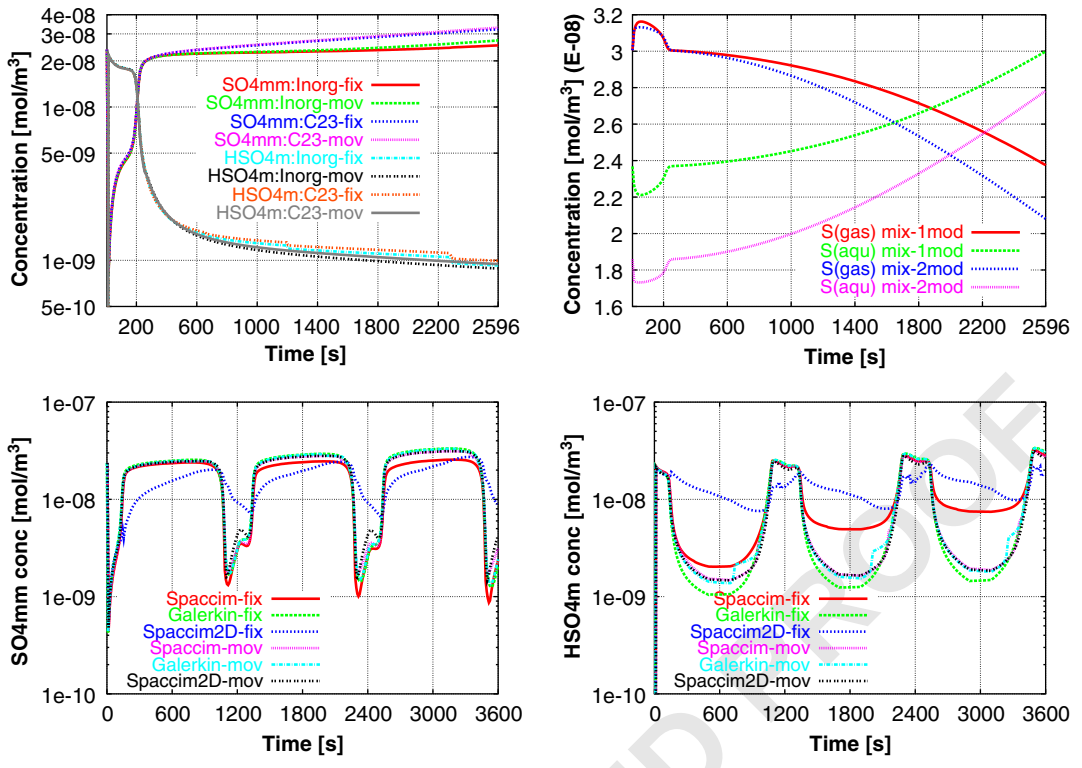

Fig. 9. Evolution of SO_4^{2-} and HSO_4^- concentrations during RISING simulation with SPACCIM1D using INORG and CAPRAM2.3 mechanisms (top-left). Comparison of total sulfur processing in the gas and aqueous phase between AEROSOL1 and AEROSOL2 using the INORG mechanism (top-right). SO_4^{2-} and HSO_4^- evolution during the WAVE AEROSOL1 simulation with the participating models using CAPRAM2.3 mechanism (bottom).

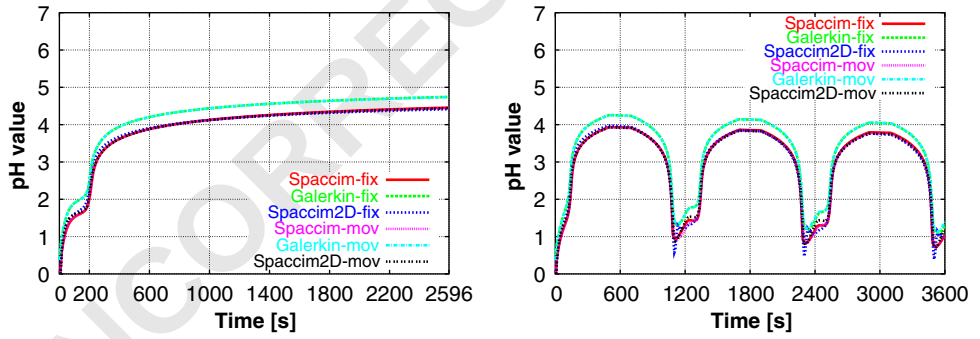

Fig. 10. Mean cloud water pH (averaged over all bins) using CAPRAM2.3 mechanism according to models involved in the study: RISING AEROSOL1 (left); WAVE AEROSOL1 (right).

same behavior is observed for the particles during the valley phases. This confirms the acidification of cloud condensation nuclei by cloud processing. Furthermore, pH changes lead to differences in cloud chemistry and gas uptake from cycle to cycle.

4.2.3. Nitrogen chemistry

Only WAVE results presented in Figs. 11–11 are discussed due to its clearness. The gas phase HNO_3 concentrations increases during the start period to realize the equilibrium with the particle phase. After the activation it is taken up rapidly almost completely. During the two following hill cap passages, HNO_3 experiences the same fate with differences between the

Table 5
Average cloud water pH values

Models	AEROSOL1			AEROSOL2		
	INORG	CAPRAM23	BARTH	INORG	CAPRAM23	BARTH
SPACCIM1D-FIX	4.51	4.45	4.40	4.67	4.58	4.54
SPACCIM1D-MOV	4.49	4.44	4.40	4.62	4.56	4.54
GALERKIN-FIX	4.82	4.74	4.68	4.97	4.86	4.81
GALERKIN-MOV	4.80	4.73	4.68	4.92	4.85	4.81
SPACCIM2D-MOV	4.49	4.44	4.40	4.62	4.55	4.53
SPACCIM2D-FIX	4.47	4.41	4.41	4.61	4.52	4.53

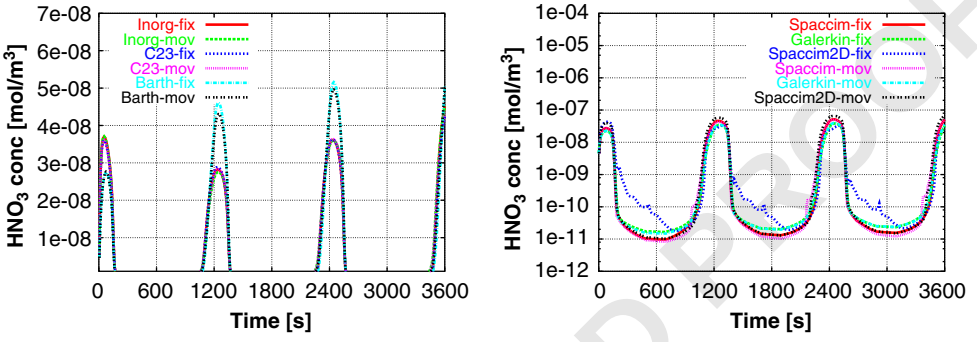

Fig. 11. Time evolution of HNO_3 concentration during the WAVE AEROSOL1 simulation: with SPACCIM1D using the participating mechanisms (left); with the participating models using the BARTH mechanism (right).

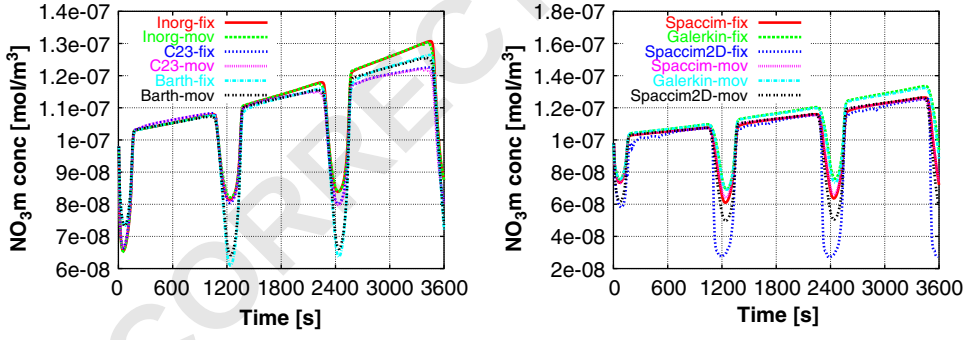

Fig. 12. Time evolution of NO_3^- concentration during the WAVE AEROSOL1 simulation: with SPACCIM1D using he participating mechanisms (left); with the participating models using the BARTH mechanism (right).

mechanisms concerning the maximum concentration level. These discrepancies are reflected also on NO_3^- (Fig. 12). The periods of NO_3^- concentration sink correspond to valley periods where a transfer into the gas phase occurs. A more detailed analysis shows that NO_3^- is mainly formed by the HNO_3 uptake and, during cloudy periods, by oxidation processes. The partitioning between gas and particle/droplet phase is mainly controlled by the pH values. The BARTH mechanism, which tends to the highest acidity (Table 5), simulates less NO_3^- than the two other mechanism. Furthermore, the pH dependency entails also to differences between the models. The GALERKIN models produce more particulate NO_3^- during cloudy period caused by the higher pH values. Altogether, SPACCIM1D, GALERKIN and SPACCIM2D-MOV show a relative good agreement. Again SPACCIM2D-FIX simulates less NO_3^- for the times corresponding to HNO_3 peaks.

Fig. 13 summarizes the nitrogen processing. A global decrease tendency of gaseous nitrogen and, consequently, a global increase for aqueous nitrogen from cycle to cycle is observed. This increase contributes mainly to the NWM production discussed above. Deviations between the models are not substantial and occur during the valley periods. These observations are also valid for AEROSOL2 where less initial NO_3^- is included. Tables 6 and 7 summarize some aqueous

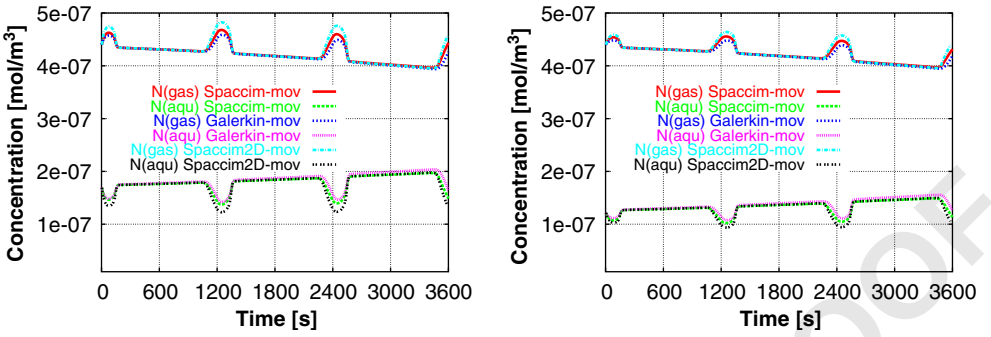

Fig. 13. Comparison of nitrogen processing in the gas and aqueous phase between the participating models (moving bin) during WAVE using BARTH mechanism: AEROSOL1 (left) and AEROSOL2 (right). N(gas) = $HHO_3 + HNO_4 + HONO + NO + NO_2 + NO_3 + N_2O_5 + NH_3$, N(aqu) = $HNO_3(aq) + NO_3^- + NH_4^+$.

Table 6
Relative deviation of selected aqueous phase species to the average concentration for the involved models in % at the end of the cycle during WAVE AEROSOL1

Mechanism	SO_4^{2-}		HSO_4^-		NO_3^-			OH(aq)	
	INORG	C23	INORG	C23	INORG	C23	BARTH	C23	BARTH
AVERAGE	2.018e−9	2.803e−9	2.032e−8	2.864e−8	8.994e−8	8.399e−8	7.759e−8	1.000e−20	3.449e−19
SPACCIM1D-FIX	−6.0	−15.6	0.0	−1.5	−2.6	−3.6	−7.1	0.0	+1.7
SPACCIM1D-MOV	+2.0	+14.9	−0.5	−3.7	−2.5	−4.5	−5.2	0.0	−10.1
GALERKIN-FIX	−18.8	−25.3	+2.9	+7.4	+6.8	+5.4	+20.1	0.0	+24.7
GALERKIN-MOV	−12.7	−13.8	+2.8	+5.4	+4.6	+2.4	+14.0	0.0	+18.4
SPACCIM2D-MOV	+35.6	+39.9	−4.9	−7.5	−6.2	+0.3	−21.8	0.0	−34.7
SPACCIM2D-FIX	+317.7	+217.4	−33.7	−38.5	−25.6	−20.3	−64.9	0.0	−36.9

Average concentrations are in mol m^{-3}.

Table 7
Relative deviation of selected aqueous phase species to the average concentration for the involved models in % at the end of the cycle during WAVE AEROSOL2

Mechanism	SO_4^{2-}		HSO_4^-		NO_3^-			OH(aq)	
	INORG	C23	INORG	C23	INORG	C23	BARTH	C23	BARTH
AVERAGE	2.496e−9	3.593e−9	1.594e−8	2.456e−8	7.569e−8	6.926e−8	5.780e−8	1.000e−20	2.601e−19
SPACCIM1D-FIX	−7.2	−18.1	−0.6	−1.2	−3.4	−4.9	−9.1	0.0	+0.2
SPACCIM1D-MOV	+22.4	+36.9	−3.6	−8.7	−3.6	−6.7	−6.1	0.0	−15.6
GALERKIN-FIX	−23.1	−30.7	+3.6	+10.3	+7.2	+5.4	+20.2	0.0	+31.0
GALERKIN-MOV	−20.5	−23.8	+6.1	+8.9	+5.5	+3.2	+14.8	0.0	+21.0
SPACCIM2D-MOV	+28.5	+35.9	−5.2	−9.1	−5.6	+3.0	−19.6	0.0	−36.4
SPACCIM2D-FIX	−39.7	−57.2	+82.0	+65.2	−31.9	−25.6	−66.5	0.0	−37.2

Average concentrations are in mol m^{-3}.

phase species concentrations during WAVE at the end of the cycles for AEROSOL1 and AEROSOL2.

4.3. Numerical aspects

The simulations offer the opportunity to examine the sensitivity of the model results to the applied numerical schemes and the way the coupling of microphysics with chemistry is implemented. A fair and reliable numerical comparison between the six approaches is not possible since they are implemented and optimized for different kinds of applications. For instance, GALERKIN focuses on the description of aerosol-dynamical and multiphase chemical processes for non-activated particles. In the SPACCIM1D approach, an "optimal" choice of several control parameters (coupling time step Δt_{cpl}, required tolerance for the BDF scheme) can reduce the numerical costs markedly (Wolke et al., 2005). In this case, the numerical error is often increased. The compromise between accuracy and computational cost depends on the application as well as the objective of the simulation. In SPACCIM2D, the used implementation of the coupling scheme (especially the computation of the microphysical flux matrix) works well, but not very efficiently. An improvement should reduce the costs substantially.

Altogether the following remarks can be stated about the numerical efficiency. More processing costs are needed for "fixed bin" runs in comparison to the "moving bin" ones. The microphysical fluxes vanish during the last and no "remapping" to the original grid is done. In general, the computational costs are much lower for AEROSOL1 than for AEROSOL2. SPACCIM1D and GALERKIN yield comparable results. Usually, an "optimal" choice of Δt_{cpl} in the SPACCIM approach depends on the considered scenario. Large coupling time steps reduce the number of restarts which are expensive for higher order implicit solvers. Otherwise, the increased deviations between the interpolated microphysical variables and their real values can adulterate also species chemical evolution. The benefit in the computational effort is bought by a lower accuracy (Wolke et al., 2005). In this study, a coupling time step of 10 s seems to be reasonable and gives satisfactory results. Due to the detailed 2D microphysical structure, SPACCIM2D is much more expensive than the two others. As expected, the INORG mechanism simulations run faster than BARTH which also runs faster than CAPRAM2.3 although the number of right hand side and Jacobian evaluations remain comparable for the three mechanism. Less time is spent for calculating the expensive Arrhenius terms in INORG. A numerical sensitivity study for SPACCIM1D can be found in Wolke et al. (2005).

5. Conclusion

The objective of this study was to figure out discrepancies between several detailed cloud chemistry models related to the use of different microphysical size-resolved approaches and numerical schemes with a focus on the "fixed bin" and "moving bin" representations. For that aim, various scenarios, initial aerosol mixing and chemical mechanisms of different complexity were involved with initial data taken from field measurements. It was shown that five out of the six participating models agree in an appreciable way in all scenarios and cases. In principle, the SPACCIM2D models allows a more realistic description of the mixing state regarding hygroscopic properties of the particles. However, SPACCIM2D-FIX shows a singular behavior when calculating species concentrations. Further investigations including 2D chemistry discretization should be carried out to get a better evaluation. Moreover, the "fixed bin" models where a "remapping" to original grid is considered, simulate less uptake of gas phase species during RISING (cumulus type cloud). That has obviously a direct effect on the aqueous phase species evolution. During WAVE calculations imitating the natural cycle of air parcels going into and out of clouds in the boundary layer, the differences stated above for the gas uptake between the "fixed bin" and "moving bin" representations are not observed. The pH values are in good agreement for all participating models with lower ones for WAVE. The loss of accuracy due to the use of "splitting" between microphysics and multiphase chemistry in the case of SPACCIM1D approach and the accompanying numerical cost are not significant in comparison with the fully coupled approach in GALERKIN. That indicates that the coupling strategy is robust and reliable.

References

Barth, M.C., Sillman, S., Jacobson, M.Z., Kim, C.-H., Monod, A., Liang, J., 2003. Summary of the cloud chemistry modeling intercomparison: photochemical box model simulation. Journal of Geophysical Research 108 (D7), 4214.

Bott, A., 2000. A flux method for the numerical solution of the stochastic collection equation: extension to two-dimensional particle distribution. Journal of Atmospheric Science 57, 284–294.

Chaumerliac, N., Leriche, M., Audiffren, N., 2000. Modeling of scavenging processes in clouds: some remaining questions about the partitioning of gases among gas and liquid phases. Atmospheric Research 53, 29–43.

Djouad, R., Sportisse, B., Audiffren, N., 2002. Numerical simulation of aqueous-phase atmospheric models: use of non-autonomous Rosenbrock method. Atmospheric Environment 36, 873–879.

Gelbard, F., Seinfeld, J.H., 1980. Simulation of multicomponent aerosol dynamics. Journal of Colloid Interface Science 78, 485–501.

Herrmann, H., Ervens, B., Jacobi, H.-W., Wolke, R., Nowacki, P., Zellner, R., 2000. CAPRAM2.3: a chemical aqueous phase radical mechanism for tropospheric chemistry. Journal of Atmospheric Chemistry 36, 231–284.

Herrmann, H., Wolke, R., Müller, K., Brüggemann, E., Gnauk, T., Barzaghi, P., Mertes, S., Lehmann, K., Massling, A., Birmili, W., Wiedensohler, A., Wieprecht, W., Acker, K., Jaeschke, W., Kramberger, H., Syrcina, B., Bächmann, K., Collett, Jr J.L., Galgon, D., Schwirn, K., Nowak, A., van Pinxteren, D., Plewka, A., Chemnitzer, R., Rüd, C., Hofmann, D., Tilgner, A., Diehl, K., Heinold, B., Hinneburg, D., Knoth, O., Sehili, A.M., Simmel, M., Wurzler, S., Mauersberger, G., Majdik, Z., Müller, F., 2005. FEBUKO and MODMEP: field measurements and modelling of aerosol and cloud multiphase processes. Atmospheric Environment, this issue.

Hindmarsh, A.C., 1983. Scientific Computing. Chapter ODEPACK: A Systematized Collection of ODE Solvers. North-Holland, Amsterdam, pp. 55–74.

Hirsch, C., 1992. Numerical computation of internal and external flows. Computational Methods for Inviscid and Viscous Flows, vol. 2. Wiley, Chichester.

Jacobson, M.Z., 2002. Analysis of aerosol interactions with numerical techniques for solving coagulation, nucleation, condensation, and reversible chemistry among multiple size distributions. Journal of Geophysical Research 107 (D19), 4366.

Knoth, O., 2005. A parcel model for the combined treatment of microphysical and multiphase chemical processes. Atmospheric Environment, this issue.

Kreidenweis, S.M., Walcek, C.J., Feingold, G., Gong, W., Jacobson, M.Z., Kim, C.-H., Liu, X., Penner, J.E., Nenes, A., Seinfeld, J.H., 2003. Modification of aerosol mass and size distribution due to aqueous-phase SO_2 oxidation in clouds: comparison of several models. Journal of Geophysical Research 108 (D7), 4213.

Roelofs, G.J.H., 1993. A cloud chemistry sensitivity study and comparison of explicit and bulk cloud model performance. Atmospheric Environment 27A-15, 2255–2264.

Sandu, A., Potra, F.A., Charmichael, G.R., Damian, V., 1996. Efficient implementation of fully implicit methods for atmospheric chemical kinetics. Journal of Computational Physics 129, 101–110.

Sandu, A., Verwer, J.G., van Loon, M., Charmichael, G.R., Potra, F.A., Dabdub, D., Seinfeld, J.H., 1997. Benchmarking stiff ODE solvers for atmospheric chemistry problems I: implicit versus explicit. Atmospheric Environment 31, 3151–3166.

Schwartz, S.E., 1986. Mass transport considerations pertinent to aqueous phase reactions of gases in liquid water clouds. Chemistry of Multiphase Atmospheric Systems, vol. G6. NATO ASI Series. Springer, Berlin, pp. 415–471.

Simmel, M., Wurzler, S., 2004. Condensation and nucleation in sectional cloud microphysical models based on the linear discrete method. Atmospheric Research, submitted.

Simmel, M., Diehl, K., Wurzler, S., 2005. Numerical simulation of the microphysics of an orographic cloud: comparison with measurements and sensitivity studies. Atmospheric Environment, this issue.

Simmel, M., Trautmann, T., Tetzlaff, G., 2002. Numerical solution of the stochastic collection equation—comparison of the linear discrete method with other methods. Atmospheric Research 61, 137–150.

Stockwell, W.R., Kirchner, F., Kuhn, M., Seefeld, S., 1997. A new mechanism for regional atmospheric chemistry modelling. Journal of Geophysical Research 102 (D22), 25847–25879.

Tilgner, A., Majdik, Z., Sehili, A.M., Simmel, M., Wolke, R., Herrmann, H., 2005. SPACCIM: simulations of the multiphase chemistry occurring in the FEBUKO hill cap cloud experiments. Atmospheric Environment, this issue.

Wolke, R., Knoth, O., 2002. Time-integration of multiphase chemistry in size-resolved cloud models. Applied Numerical Mathematics 42, 473–487.

Wolke, R., Sehili, A.M., Simmel, M., Knoth, O., Tilgner, A., Hermann, H., 2005. SPACCIM: a parcel model with detailed microphysics and complex multiphase chemistry. Atmospheric Environment, this issue.

Available online at www.sciencedirect.com

SCIENCE DIRECT®

ELSEVIER

Atmospheric Environment ▮ (▮▮▮▮) ▮▮▮–▮▮▮

ATMOSPHERIC ENVIRONMENT

www.elsevier.com/locate/atmosenv

H_2O_2 and organic peroxide measurements in an orographic cloud: The FEBUKO experiment

J. Valverde-Canossa[a], W. Wieprecht[b], K. Acker[b], G.K. Moortgat[a,*]

[a]*Max-Planck-Institut für Chemie, Division of Atmospheric Chemistry, P.O. Box 3060, D-55020 Mainz, Germany*
[b]*Air Chemistry Group, Brandenburg Technical University Cottbus, Volmer-Str. 13, D-12489, Berlin, Germany*

Abstract

The H_2O_2 and organic peroxides are known to be important oxidants in cloud-water, influencing the oxidising capacity of the atmosphere. Measurements of H_2O_2 in cloud-water have shown a wide range of concentrations depending on the season and measuring site. Moreover, organic peroxide measurements are scarce in spite of their importance. Measurements of peroxides were carried out in the Thuringian Forest, Germany, during the FEBUKO research cluster in the Fall 2001. The measuring stations were located at three sites: upwind (gas phase), summit (cloud-water and gas phase) and downwind (gas phase). Analysis was achieved by high performance liquid chromatography (enzymatic method). From the different peroxides only H_2O_2 was detected in the gas phase at the upwind site with mixing ratios <130 ppt. In the cloud-water, besides hydrogen peroxide (H_2O_2), hydroxymethylhydroperoxide (HMHP), 1-hydroxyethylhydroperoxide (1-HEHP) and methylhydroperoxide (MHP) were also detected with concentrations normalised with the liquid water content up to 1.30, 0.075, 0.065 and 0.015 nmol m^{-3}, respectively. Organic peroxides (HMHP + 1-HEHP + MHP) constitute up to 80% of the total peroxides during nighttime while during daytime they accounted for about 14%. Consequently, organic peroxides might play an important role in nighttime cloud chemistry.

Keywords: Organic peroxides; Hydrogen peroxide; Ozonolysis; Sulphate production

1. Introduction

H_2O_2 and organic peroxides (ROOH) are key components in the photooxidation of volatile organic compounds. They act as a sink for HO_2 and RO_2 radicals and thus influence the HO_x cycle. Another major role of H_2O_2 and the organic peroxides in the atmosphere is the efficient oxidation of sulphur dioxide (SO_2) to sulphuric acid (H_2SO_4) in cloud droplets and in wet aerosol surfaces (Penkett et al., 1979). In the gas phase, during daytime, the main source of H_2O_2 is the recombination of HO_2 radicals and the major source of ROOH is the $HO_2 + RO_2$ reaction. The only known mechanism to the formation of peroxides in the absence of light is the ozonolysis reaction of alkenes (Großmann, 1999; Valverde-Canossa, 2004), which involves the reaction of the Criegee Intermediate with water vapour. This reaction is the main source of 1-hydroxyalkylhydroperoxides (1-HAHP) such as hydroxymethylhydroperoxide (HMHP) and 1-hydroxyethylhydroperoxide (1-HEHP) and a source of OH radicals (Atkinson and Aschmann, 1993; Paulson et al., 1999).

In the aqueous phase, most of the pathways proposed for the formation of peroxides in cloud-water involve

*Corresponding author.
E-mail address: moo@mpch-mainz.mpg.de (G.K. Moortgat).

1352-2310/$ - see front matter © 2005 Elsevier Ltd. All rights reserved.
doi:10.1016/j.atmosenv.2005.02.040

sunlight (Finlayson-Pitts and Pitts, 2000). As for the gas phase, the main source of H_2O_2 is the HO_2 radicals, via $HO_2 + O_2^-$ reaction. CH_3OOH is formed by an analogous reaction, $CH_3O_2 + O_2^-$. Cloud chemistry involves gas and aqueous phase chemistry; the link between both phases is described in detail by Lelieveld and Crutzen (1991).

Several investigators have measured H_2O_2 in cloud-water from mountain sites (Watanabe et al., 2001). Samples taken throughout the year show significantly seasonal variation i.e., with higher concentrations in summer than in winter (Olszyna et al., 1988). Additionally, measurements carried out in the eastern United States at several non-urban sites show differences between H_2O_2 concentrations measured in rain samples (0.1–100 μM), precipitating clouds (0.1–100 μM) and non-precipitating clouds (median values $<10\mu M$) (Kelly et al., 1985). A summary of observed concentrations of H_2O_2 and other compounds in cloud-water can be found in Gunz and Hoffmann (1990), Pruppacher and Klett (1997) and Lee et al. (2000). Measurements of speciated organic peroxides are scarce and to our knowledge, besides this study, only Sauer et al. (1996) carried out such measurements. They found the contribution of HMHP + 1-HEHP to the total peroxides to be between 0% and 81%, pointing out that these compounds play also a major role as oxidants in cloud-water and should be included into modelling studies of the aqueous phase oxidation of S(IV).

The general objective of Field Investigations of Budgets and Conversions of Particle Phase organics in Tropospheric Cloud Processes (FEBUKO) is to investigate the fate of organic substances in front of, inside and behind an orographic cloud under conditions of connected flow (= "flow reactor"). The results will serve as a database for a comparison of current knowledge on the budget of organics in multiphase environments in central Germany and in tropospheric multiphase models (Müller et al., 2005). The specific objective of this work is the study of the fate of H_2O_2 and ROOH in an air mass during its passage through an orographic cloud. In this paper the in-cloud production and/or destruction of the peroxides will be assessed from the influence of physical (i.e., temperature, pH, liquid water content (LWC), cloud base height) and chemical parameters (i.e., sulphate, sulphur dioxide, carbonyl compounds) on the peroxides concentrations. Additionally, the peroxides concentrations measured at the upwind and calculated at the downwind sites are compared in order to give further insight into the understanding of the influence of cloud processing on these compounds.

2. Experimental

2.1. Site description

FEBUKO took place at the DWD (German Weather Service)/UBA (Umweltbundesamt) mountain station 'Schmücke', located in the Thuringian Forest near Zella-Mehlis, Germany. The measuring stations were selected prior to the field campaign by means of modelling and tracer experiments showing that identical air masses flow over Goldlauter, Schmücke and Gehlberg at a wind direction range of 210°–240° (Heinold et al., 2005). Goldlauter is located upwind of the Schmücke (summit) at 605 m a.s.l, 10° 45′ 20″ E and 50° 38′ 25″ N and Gehlberg is located downwind of the summit at 732 m a.s.l at 10° 47′ 32″ E and 50° 40′ 21″ N. The cloud measurements took place at the Schmücke (summit located at 937 m a.s.l at 10° 48′ 15″ E and 50° 39′ 19″ N) at a tower height of 20 m.

2.2. Meteorology and cloud events description

The air masses characterised at the DWD/UBA station Schmücke are comprised of aged air masses, which have been anthropogenically influenced first and then exposed to biogenic emissions on their way southeast from the Rhein-Main area to the Thuringian forest. The DWD/UBA research station at the Schmücke Mountain is found to be within an orographic cloud for 170 days in a year and should therefore be well suited for a cloud experiment. Furthermore, the months of October and November have the highest probability of cloud formation, which is about 80% (Müller et al., 2005). The field campaign took place from 1st October to 8th November 2001 (6 weeks). Our measurements took place between 25th October to 8th November. During this period two main cloud events took place, i.e. on the 26 October and the 26/27 October hereafter referred as EIV and EI. From these cloud events only the EI satisfied the criteria described in detail by Tilgner et al. (2005) and Heinold et al. (2005), which included suitable synoptical conditions, completeness of the data and adequate flow characteristics. The latter allows the comparison between the three stations. EI took place on the 26/27 October in a timeframe between 2200, 26.10.01 UTC and 1300, 27.10.01 UTC and lasted 15 h. This event was characterised by low stratiform clouds in a moist boundary layer, air mass from the Mid-Atlantic and stable flow conditions particularly after the front passage at 0600, 27.10.01 UTC (Heinold et al., 2005). EIV did not satisfy the above criteria due to the large Froude number, which indicated stagnant flow (Heinold et al., 2005). Nevertheless, these measurements are also of relevance due to the scarcity of organic peroxide measurements in cloud-water. EIV took place on the 26th October

between 08:30–16:30 UTC and had a total duration of 8 h. This event was characterised by air masses from the Mid-Atlantic, constant southwesterly flow and was not influenced by frontal processes. In addition, a *stratus nebulosus* bank was formed, which is characterised by a marked stability in the planetary boundary layer and decoupling from the free atmosphere (Heinold et al., 2005).

2.3. Gas phase and cloud-water sampling

The air samples in Goldlauter were collected by the Leibniz-Institut für Troposphärenforschung (IfT-1). The equipment was set up in a container and the samples were collected using PFA tubing at a height of 2.5 m, where the air was directed through the sampling coil. Since the H_2O_2 and the ROOH are stable in cold aqueous acid, they are stripped from the gas phase by drawing the air sample and scrubbing solution through a thermostated helix-shaped coil (Lazrus et al., 1986). The scrubbing solution is 18 M Ω water acidified with H_3PO_4 (pH 3.5), which also has metal-complex forming properties, inhibiting the decomposition of the peroxide. The coil itself is approx. 25 cm long and the tube has an effective length of about 100 cm, 24-turn and 2 mm internal diameter (Sauer et al., 1999). The collection was performed using an airflow of 3.2 L min^{-1} (STP), a stripping-solution flow (Fa) of 0.17 L min^{-1} and a coil temperature of 2 °C (Sauer, 1997; Valverde-Canossa, 2004). The sampling interval was between 5 and 15 min. The samples collected upwind and transported by the IFT-1 to the Schmücke (~20 min) at an ambient temperature ~7 °C, where they were analysed (see analytical system). During this 20 min the samples decompose ~10% (the sample was given twice). The air samples in Gehlberg (downwind site) were collected and analysed by Zentrum für Umweltforschung/Universität Frankfurt/(ZUF) with the flow injection chemiluminescence technique (Jaeschke et al., 2005), which is based on reaction of H_2O_2 with bis-trichlorophenyloxalate.

Cloud-water was collected with the Single-Stage slit jet Impactor (SSI) and the Two-Stage Cloud-water Impactor (TSCI). The collectors were always conditioned 1 h before starting the measurements. The SSI has a cut-off drop diameter of 5 μm and the air enters the device through two parallel slit jets at 120 $m^3 h^{-1}$. The TSCI operation is based on the principle of inertial impaction on plane surfaces, a standard technique for the collection of dry aerosol particles (Schell, 1998). The air is sampled isokinetically and enters the device through three vertical slit impaction stages at 180 $m^3 h^{-1}$, one to collect the larger droplets (cut-off diameter 12 μm), followed by two identical stages in parallel (cut-off diameter 5 μm). The sampling interval was of 30 min or 1 h, depending if the amount of sample necessary for the different analyses was collected within this time interval. The team of the Brandenburgische Technische Universität Cottbus (BTU) collected these samples.

2.4. Analytical system

The gas and aqueous phase samples were analysed immediately after sampling by high performance liquid chromatography, (HPLC) (Jasco) using post-column derivatisation with horseradish peroxidase (HRP) and fluorescence detection (Valverde-Canossa, 2004). The HRP catalyses the reduction of H_2O_2 (Guibault et al., 1968) in the presence of p-hydroxyphenyl ethanoic acid (POPHA), a hydrogen donor molecule. H_2O_2 and alkylhydroperoxides react directly with the enzyme. Nevertheless, other peroxides, i.e. 1-HAHP and peroxy acids are temperature- and pHdependent and do not react directly with peroxidase. Therefore, to favour their decomposition into compounds that can later react with the enzyme, the post-column derivatisation reaction takes place at 40 °C and at a pH between 8.5 and 9.5. For every hydroperoxide consumed, one dimer is formed. The fluorescence of this dimer is directly proportional to the peroxide concentration and is detected in a fluorescence detector. Multipoint calibration for the peroxide analysis was performed twice a day using H_2O_2 standard solutions (5×10^{-8}–1.6×10^{-5} M). Additionally, before every sample a 3 μM H_2O_2 standard solution was injected. For the sampling conditions a quantification limit of 5 ppt for H_2O_2 and organic peroxides was obtained. As no standards are available on the market with the exception of H_2O_2 and peracetic acid and since the HPLC responds to organic hydroperoxides and H_2O_2 with equal sensitivity, the calibration of the system were performed with H_2O_2 (Kurth, 1992; Staffelbach and Kok, 1993). The organic hydroperoxides were identified by comparing the relative retention times of the organic peroxides (elution time of the organic hydroperoxide/elution time of the H_2O_2) obtained experimentally (Valverde-Canossa, 2004).

A comparison of the H_2O_2 concentrations measured in cloud-water samples with the fluorescence and chemiluminescence methods was performed during the field campaign. The results are shown in an accompanying paper in this issue (Jaeschke et al., 2005) and despite the different methods; cloud samplers and sample intervals the concentrations are in general in good agreement.

3. Results

3.1. Measurements in goldlauter (upwind site)

The measurements in Goldlauter took place from 30 October to 4 November 2001 when no clouds were present and were not performed simultaneously with the cloud events. No other peroxides besides H_2O_2 were detected in the gas phase. The mixing ratios of H_2O_2 were below 130 ppt with an average mixing ratio of 49 ppt and maximum mixing ratios around 1400 UTC. Table 1 contains a summary of the mixing ratios observed.

3.2. Measurements at the schmücke (summit)

The measurements at the Schmücke took place from 26 to 29 October 2001. Cloud-water samples were taken with the SSI and the TSCI. Most of the samples were taken with the SSI for which the LWC (Liquid Water Content, mg of waterper m^3 air) was also measured. The peroxide concentrations measured in μM were normalised with the LWC to nmol m^{-3} as recommended by Möller et al. (1996). Both the normalised and the μM concentrations of H_2O_2, HMHP, 1-HEHP and MHP are shown in Fig. 1. The time denotes the average time of the interval measured. Results of the measurements carried out with the TSCI are not shown here (for details see Valverde-Canossa, 2004) but in general the peroxide concentrations from the second stage of the TSCI show a similar trend to those collected with the SSI but are consistently higher in most of the samples. The latter is attributed to the different values of LWC, which is not available for the TSCI at the present time and it is not yet possible to verify this. Only three samples of cloud-water from the first stage of the TSCI are available since it was not always possible to collect enough sample volume for the peroxide measurements. Due to the few samples collected from the first stage of the TSCI, a comparison with the second stage of the TSCI is limited and it was not possible to establish a clear tendency of the concentrations of H_2O_2, HMHP and 1-HEHP measured in the two stages.

The H_2O_2 was detected during the daytime (06:00–18:00 UTC) as well as during the nighttime (18:00–06:00 UTC). A clear day profile can be observed on the 26th of October, with daytime concentrations between 0.04 and 13.6 μM (0.02–1.30 nmol m^{-3}) and night-time concentrations (26th/27th of October) between 0.04 and 2.76 μM (0.02–0.65 nmol m^{-3}). Normalised concentrations do not show always the same trend as the μM concentrations, showing that other factors besides the LWC may control the H_2O_2 concentrations.

Daytime concentrations of HMHP oscillate between 0.009 and 0.114 μM (0.003–0.0078 nmol m^{-3}) and night-time concentrations between 0.048 and 0.319 μM (0.022–0.075 nmol m^{-3}). Normalised concentrations of HMHP show the same trend as the μM concentrations; therefore the main factor controlling the HMHP concentrations is the LWC. Daytime 1-HEHP concentrations are between 0.015 and 0.177 μM (0.006–0.012 nmol m^{-3}) and concentrations between 0.028 and 0.277 μM (0.013 and 0.065 nmol m^{-3}). The 1-HEHP concentrations are in the same order as the ones found for HMHP but higher concentrations were observed during the day-hours.

The MHP was detected just in a few samples, predominantly during nighttime. Daytime concentrations were lower than 0.037 μM (0.0025 nmol m^{-3}) and night-time concentrations lower than 0.046 μM (0.015 nmol m^{-3}).

The H_2O_2 and the organic peroxides have similar daily patterns differing in the maxima occurrence. In the case of H_2O_2 the maxima occur during the daylight, whereas organic peroxides maxima occur during night-time. Organic peroxides (HMHP + 1-HEHP + MHP) constitute up to 80% of the total peroxides during nighttime, while during daytime they accounted for about 14%. Organic peroxides might play an important role in nighttime chemistry.

3.3. Measurements in gehlberg (downwind site)

The H_2O_2 measurements in the gas phase at this station were carried out by the ZUF. The H_2O_2 concentrations measured were below the detection limit (300 ppt) during the entire field campaign (Jaeschke et al., 2005).

Table 1
Measurements of peroxides in the gas phase

Date	Number of samples	Time interval (UTC)	H_2O_2 (ppt)	Organic Peroxides (ppt)
30.10.01	2	11:45–12:15	n.d.	n.d.
02.11.01	3	10:30–15:10	n.d.-34	n.d.
03.11.01	3	10:30–14:00	6-126	n.d.
04.11.01	3	09:00–15:00	n.d.-30	n.d.

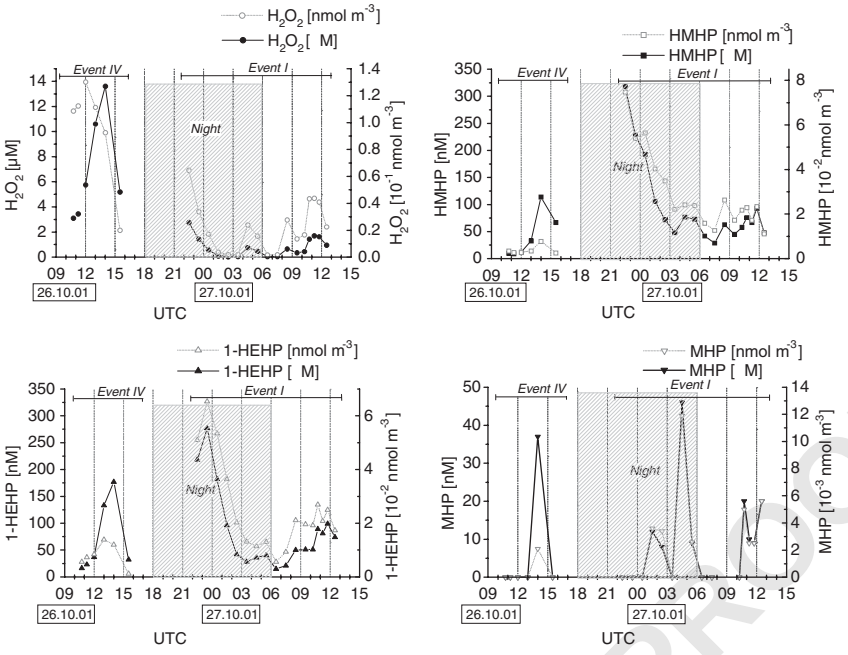

Fig. 1. Time profiles of the H_2O_2, HMHP, 1-HEHP and MHP measurements in cloud-water sampled with the SSI. Left axis: concentration and right axis: normalised concentration.

4. Discussion

Gas phase peroxide mixing ratios in FEBUKO were <130 ppt. The mixing ratios are comparable with the ones measured at the Kleiner Feldberg, Germany, which not only took place in the fall but were also influenced by anthropogenic emissions: H_2O_2 mixing ratios during the Kleiner Feldberg Cloud Experiment were <70 ppt (Fuzzi et al., 1994) and during the FELDEX field campaign <45 ppt (Sauer et al., 1996). In the latter field campaigns no organic peroxides were observed in the gas phase. A summary of measurements of gas phase H_2O_2 and ROOH measurements in the troposphere can be found in Lee et al. (2000).

In *cloud-water*, organic peroxides have only been measured by Sauer et al. (1996). They observed concentrations of HMHP $<1\,\mu$M and of 1-HEHP $<0.01\,\mu$M. During FEBUKO, concentrations of HMHP were $<0.32\,\mu$M, 1-HEHP $<0.28\,\mu$M and MHP $<0.046\,\mu$M. HMHP, MHP, 1-HEHP and EHP have also been measured in rain water at concentrations $<0.8\,\mu$M during the same season (Hellpointner and Gäb, 1989; Hewitt and Kok, 1991; Sauer et al., 1996).

Measurements in the fall show concentrations of $H_2O_2 < 3.2\,\mu$M in the FELDEX field campaign (Sauer et al., 1996), $<1\,\mu$M in the Kleiner Feldberg Cloud experiment (Fuzzi et al., 1994) and $<130\,\mu$M (Olszyna et al., 1988) at Whitetop Mountain. The latter concentrations are quite different to the ones observed in FEBUKO during the same season, where we observed concentrations $<15\,\mu$M. These variations give an indication of the complexity of cloud-chemistry.

4.1. Influence of physical and chemical parameters of clouds on the peroxide concentration

A description of the temporal evolution of the cloud events can be found in Fig. 2. This figure shows the time profiles of the cloud-base height above Goldlauter Station, the LWC measured at the Schmücke Station at 352 m above Goldlauter, and the time profiles of the H_2O_2 concentrations measured in cloud-water. During EIV the cloud progressively thins during the early morning until the afternoon 16:30 UTC. The concentrations of H_2O_2 in cloud-water increase at a rate of $3.6\,\mu M\,h^{-1}$ peaking at 14:00 UTC and later decreasing until the cloud breaks. Therefore, it is possible to recognize a very marked H_2O_2 diurnal cycle, which could be a result not only of the inversion separating the boundary layer from the free troposphere and/or transport of pollutants, but also of an enhanced production or decomposition of the peroxides in the water phase. During this event the measurements took place in the cloud as well as at the cloud base height, and higher concentrations were observed near the base of the cloud, where the LWC is lower. During EI, in the 26.10.01 at 22:00 UTC, the cloud thickens progressively during the night until the early morning hours ~08:00 UTC after which it starts thinning, finally breaking at 13:00 UTC. In addition, from 03:30 to

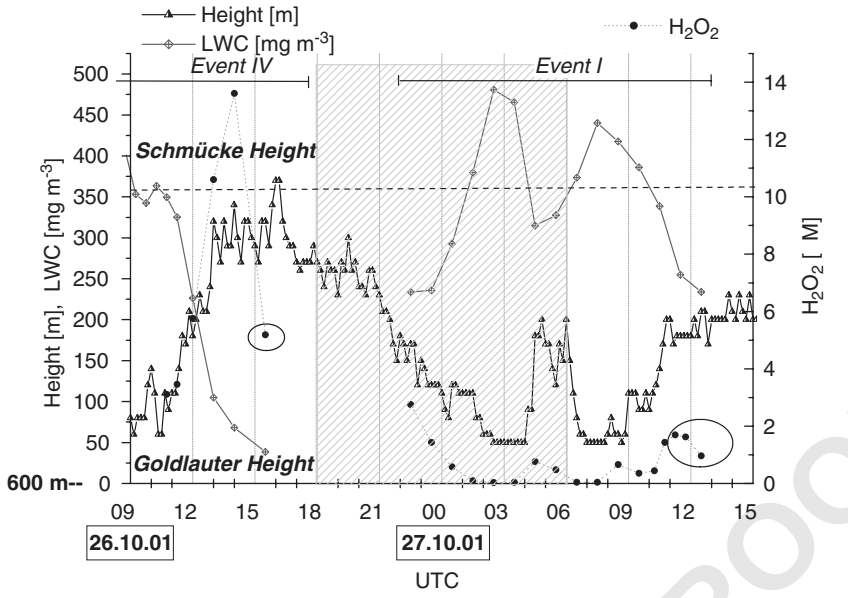

Fig. 2. Time profiles for EI and EIV. Right axis: H_2O_2 time profiles, left axis: LWC measured at Schmücke and cloud base height (H) measured at Goldlauter (see also Wieprecht et al., 2005).

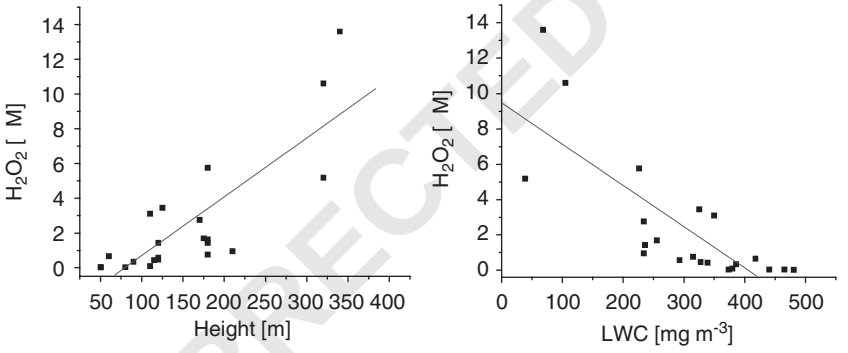

Fig. 3. Correlations between H_2O_2 concentration and LWC and cloud-base height.

05:00 UTC a decrease in the peroxides concentrations is accompanied by an increase in the wind speed from 7 to 10 m s^{-1}, an increase in O_3 of 8 ppb and a decrease of NO_x of 3.3 ppb in less than two hours (see also Brüggemann et al., 2005). This could be the product of vertical mixing and air entrainment resulting in a decrease in the LWC from 475 to 320 mg m^{-3} at this time.

In general, the H_2O_2 concentrations measured are correlated with the LWC ($r^2 = 60\%$, negative correlation) and cloud-base height ($r^2 = 67\%$, positive correlation) as can be observed in Fig. 3. Nevertheless, if the last points when the cloud breaks on the 26th and on the 27th are excluded (these points are circled in Fig. 2), the correlations of H_2O_2 with the LWC ($r^2 = 69\%$) as well as with the cloud-base height ($r^2 = 77\%$) are stronger. This stronger correlation is expected, since from Fig. 2 it can be qualitatively observed that these points have a different behaviour. This observation together with the residual correlation (31% in the case of the LWC and 23% in the case of cloud base height) means that other factors besides the variability in LWC and cloud-base height are linked with the variance of the concentrations of H_2O_2, for instance, a very efficient release of trace gases towards the end of the event.

Temperature and pH are plotted in Fig. 4 together with the peroxide concentrations. The low temperatures ($<7\,^{\circ}$C) increase the solubility of the trace gases and the stability of the peroxides is directly related to the pH. From the organic peroxides observed, HMHP and 1-HEHP will decompose into H_2O_2 and the corresponding aldehyde at pH > 5 and pH > 3, respectively (O'Sullivan

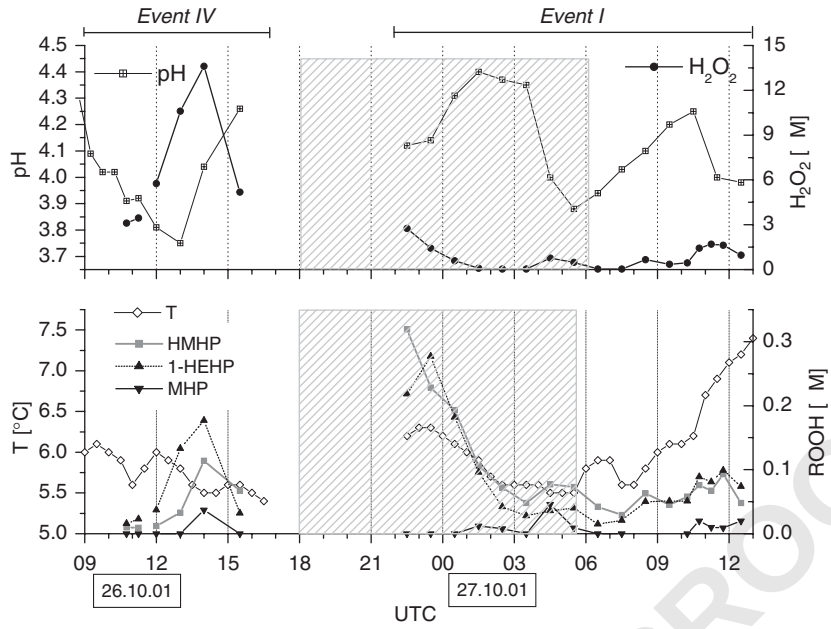

Fig. 4. Temperature and pH time profiles and their comparison with peroxide time profiles (details of the *T* and pH measurements can be found in Wieprecht et al. (2005).

et al., 1996). The pHs measured are between 3.7 and 4.4. Therefore, H_2O_2, HMHP and MHP are stable and will not tend to decompose, but the 1-HEHP will start decomposing after contact with the cloud and its decomposition will contribute to H_2O_2 and acetaldehyde formation. Additionally, the S(IV) oxidation pathways are dependent on the pH and temperature, preferring the oxidation by dissolved H_2O_2 at $pH < 5$ (Finlayson-Pitts and Pitts, 2000). The faster decrease of the concentrations of 1-HEHP in comparison with HMHP towards the end of EIV could be explained as an effect of the solubility; where the 1-HEHP due to its lower solubility is released faster into the gas phase.

In Fig. 5, H_2O_2 and organic peroxides are plotted together with a series of carbonyl compounds, which were grouped according to their concentration and included: formaldehyde (HCHO), acetaldehyde (CH_3CHO), unsaturated carbonyl compounds: methyl-vinylketone (MVK) and methylethylketone (MEK), hydroxycarbonyls: glycolaldehyde and hydroxyacetone and dicarbonyls: glyoxal, methylglyoxal and biacetyl (van Pixteren et al., 2005).

During the two events, for the following carbonyl compounds glyoxal, biacetyl, HCHO, CH_3CHO, methylglyoxal, MVK and MEK the maxima clearly occurred during daylight as for H_2O_2. However, in the case of hydroxyacetone and glycolaldehyde during EI nighttime and daytime maxima are comparable in magnitude. The dominant source of aldehydes in rain or in cloud-water is thought to be transfer from the gas phase, where they are either photochemically produced or directly emitted. Some of these compounds are primary (HCHO, MVK) or secondary products (hydroxyacetone, methylglyoxal and glycolaldehyde) of the photooxidation of isoprene, which is one of the major hydrocarbons of biogenic origin. Methylglyoxal and glyoxal are degradation products of aromatic organic compounds and are readily photooxidised during the daytime (Großmann et al., 2003). The chemistry of the carbonyl compounds is strongly related to that of the peroxides. The formaldehyde is immediately hydrated after dissolution in water forming methylene glycol, which later participates in a series of reactions leading to the production of H_2O_2 (Lelieveld and Crutzen, 1991). In addition the carbonyl compounds and the peroxides have a common source, the ozonolysis of alkenes reaction. This reaction is known to be the main source of peroxides, especially of hydroxyalkylhydroperoxides in the absence of HO_2 radicals, but is not expected to take place in the aqueous phase due to the low solubility of the precursors.

The common pattern observed for organic peroxides and carbonyl compounds can be attributed to chemical reactions occurring near to the measuring station, where these compounds are later taken up by the cloud or due to transport of aged air masses. The fact that the reaction of MVK with OH is the solely source of hydroxyacetone and that this reaction will occur only during daylight indicates that the pattern observed can be attributed mainly to transport of aged air masses,

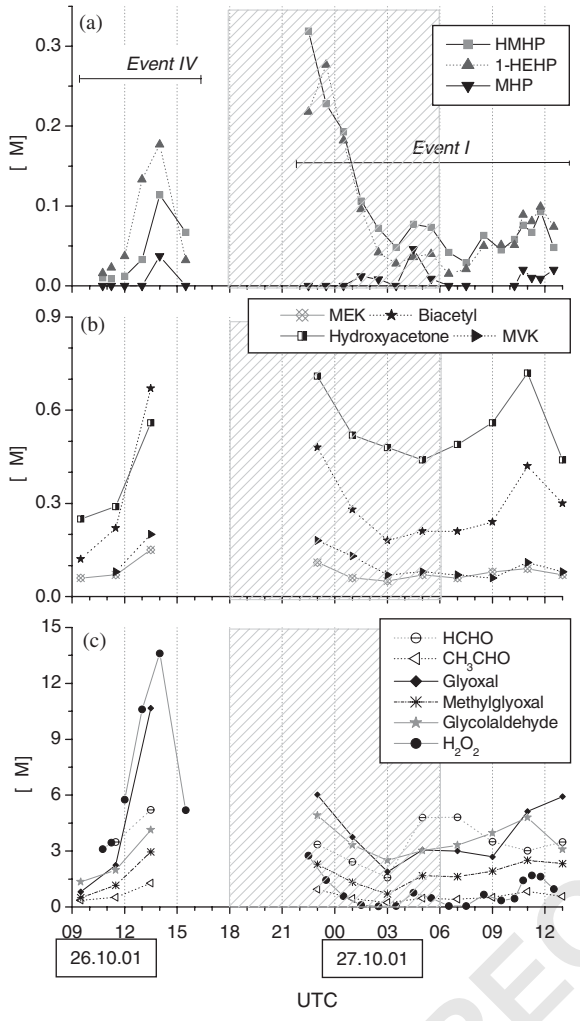

Fig. 5. Several carbonyl compounds found in cloud-water at the Schmücke (the carbonyl compounds were measured by Brüggemann et al. (2005).

which was also implied from the observations of SO_2, O_3, HCl, HNO_3 and CO by Brüggemann et al. (2005). Nevertheless, HMHP and 1-HEHP show relative higher concentrations than those measured for the carbonyl compounds during nighttime. Therefore, other factors may also be controlling the nighttime organic peroxide concentrations such as the ozonolysis reaction in the interstitial phase.

Fig. 6 shows SO_2 mixing ratios measured at the three stations (measurements at the summit and downwind were performed by Brüggemann et al. (2005) and sulphate (SO_4^{2-}) and H_2O_2 measured at the Schmücke. During the night of the 26/27th of October 2001 (EI), the cloud was formed together with an injection of high mixing ratios of SO_2 ~2 ppb. SO_2 mixing ratios measured at Gehlberg are lower than those measured upwind and at the summit stations. Therefore it seems that SO_2 was effectively scavenged during its passage through the cloud. In this event the concentrations of H_2O_2 were very low, including in the morning hours when an increase in H_2O_2 concentrations is expected. Scavenging of SO_2 may be one of the reasons for this process since at the pH measured (<4.4), SO_2 will be preferentially scavenged by H_2O_2. In EI at the Schmücke, H_2O_2 aqueous-phase concentrations were <3 μM, which correspond to calculated gas phase mixing ratios of <5 ppt, while SO_2 has gas phase mixing ratios <1 ppb and calculated aqueous-phase concentrations $<5\times10^{-3}$ μM. The gas phase H_2O_2 as well as the aqueous phase SO_2 concentration were calculated from the Henry's Law constant. The high mixing ratios in the gas phase of SO_2 compared to the one of H_2O_2 shows that the reaction was oxidant limited. Nevertheless, during this event it is not possible to observe an anti-correlation between SO_2 and H_2O_2, probably because of changing air masses. During EIV an apparent anti-correlation between H_2O_2 and SO_4^{-2} can be observed. Nevertheless, this cannot be attributed to in-cloud oxidation of SO_2 since the sulphate-time profile in the aqueous phase is similar to the one for the anions and cations measured (Wieprecht et al., 2005), where dilution seems to be the controlling factor. Therefore,from the product of $SO_2+H_2O_2$ reaction, SO_4^{-2}, cannot be quantified since it is not possible to distinguish which is its origin: the latter reaction or from dissolved SO_4^{-2} from aerosols. In addition, due to the large formaldehyde concentrations, the HSO_3^- and SO_3^{2-} reaction in cloud-water with dissolved formaldehyde producing hydroxymethanesulfonic acid (HMSA) also could be of importance (Gunz and Hoffmann, 1990).

4.2. Comparison between the three stations

This comparison is limited since even though simultaneous measurements in the three stations were performed, the concentrations measured by the ZUF downwind were always below the detection limit (300 ppt). In addition, gas phase upwind concentration measurements did not take place simultaneously. Therefore, NO_x, O_3 and SO_2 mixing ratios are used as indicators of pollution and similar concentrations of these compounds were set as a requisite to enable a comparison between these stations. During the gas-phase measurements upwind, on 30th October high NO_x (6–14 ppb) and SO_2 (0.6–1.2 ppb) mixing ratios and low O_3 mixing ratios ~25 ppb were measured. The 2nd November was characterised by average mixing ratios of O_3 of 25 ppb, SO_2<0.6 ppb and very high NO_x mixing ratios during the morning hours peaking 25 ppb at 0722 UTC with mean values of 10 ppb between the time scales measured. The 3rd November was characterised

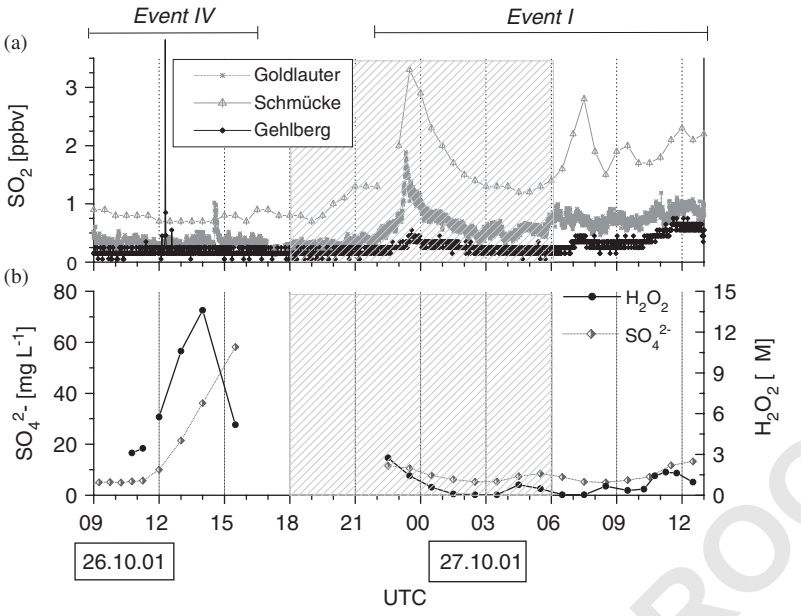

Fig. 6. Sulphur dioxide oxidation in clouds at Schmücke (details of the measurements of SO_2 and SO_4^{-2} can be found in Wieprecht et al. (2005) and Brüggemann et al. (2005).

by SO_2 mixing ratios <1 ppb, $O_3 \sim 30$ ppb and average NO_x mixing ratios of about 9 ppb during the measured interval. The 26/27 October at the summit station mean O_3 and NO_x mixing ratios were 21 and 7 ppb, respectively, together with SO_2 mixing ratios between 0.5 ppb and 2.0 ppb (Brüggemann et al., 2005). Therefore, the peroxide mixing ratios were measured under similar conditions of NO_x, O_3 and SO_2 mixing ratios and are used to enable a comparison between these stations. Additionally, for comparison purposes the mixing ratios of the peroxides in the gas phase at the summit station were estimated from the cloud-water measurements, by assuming that aqueous–gas phase equilibrium is reached. The Henry's Law constants (H) for H_2O_2, HMHP, 1-HEHP and MHP at 25 °C have been determined by several different authors (Lind and Kok, 1986), but there is still some uncertainty. Even though the measurements took place at an average temperature of 279 K, we took for our analysis the experimentally determined Henry constants from O'Sullivan et al. (1996), since all the peroxides of interest were measured by these authors under the same conditions, i.e., pH = 3 and $T = 278$ °C. The calculated mixing ratios (Fig. 7) in the gas phase are very low: $H_2O_2 < 30$ ppt, HMHP < 0.020 ppt, 1-HEHP < 3.5 ppt and MHP < 40 ppt. Therefore, gas-phase measurements at the Schmücke can provide information about H_2O_2 and MHP if available but not for 1-HEHP and/or HMHP since they are under the detection limit of the analytical instrument (DL = 5 ppt). H_2O_2 and the HMHP have very high Henry's Law constants, and thus remain mainly in the aqueous phase. However, this will not be the case for 1-HEHP and MHP since the former occurs in both phases and the latter one mainly in the gas phase. According to the gas–aqueous phase fractions, the fraction of A that exists in the aqueous phase X_{aq}^{A} is given by

$$X_{aq}^{A} = f_A/(1+f_A)$$

where f_A is the distribution factor for a species A, defined as the ratio of its aqueous-phase mass concentration c_{aq}^{A} (g L_{air}^{-1}) to its gas- phase mass concentration c_g^{A} (g L_{air}^{-1}). Assuming Henry's Law equilibrium:

$$f_A = 10^{-6} HRTLWC = HRTw_L,$$

where H is the Henry's Law constant (M atm^{-1}), R is the ideal gas constant (0.08205 atm L mol^{-1} K^{-1}), T is the temperature (K) and LWC is the liquid water content (g m^{-3}). The conversion factor 10^{-6} results of the units since w_L (vol water/vol air) $= 10^{-6}$ LWC (Seinfeld and Pandis, 1998).

The fraction in the aqueous phase will then depend not only on the Henry's constant but also on the LWC. During the field campaign, for LWC between 0.1 and 0.48 g m^{-3} the average fraction of peroxides in the aqueous phase are: $X_{aq}^{H_2O_2}$ is 96%, $X_{aq}^{HMHP} = 100\%$, $X_{aq}^{MHP} = 8\%$ and $X_{aq}^{1-HEHP} \approx 82\%$, assuming the H chosen to be correct. The latter means that H_2O_2 and HMHP are completely dissolved in the cloud. 1-HEHP is moderately soluble and is in both phases in significant fractions, 80% of the aqueous phase and 20% in the gas

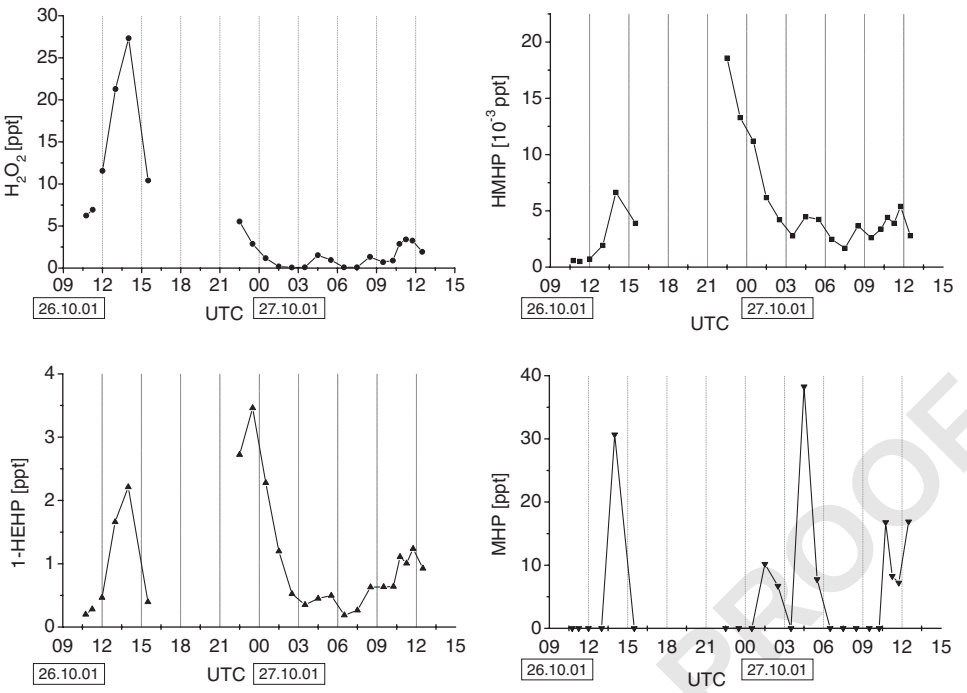

Fig. 7. Calculated gas phase mixing ratios of H_2O_2 and ROOHs from the measured concentrations in cloud-water at the Schmücke.

phase. MHP is rather insoluble since only 8% is in the aqueous phase; the remaining 92% is in the gas phase. Furthermore, even though the mixing ratios of MHP in the summit are high enough to be measured upwind, only H_2O_2 was observed. The MHP concentrations can be influenced by a single event, probably linked to anthropogenic influence but due to the low solubility of its precursors it is unlikely to be caused by in-cloud production.

If all the H_2O_2 in the water phase evaporates after cloud dissipation, calculated H_2O_2 mixing ratios during EI are <125 ppt, which is in agreement with the downwind measurements, where H_2O_2 concentrations were always below the detection limit of the instrument (300 ppt) (Jaeschke et al., 2005) and also agrees with our measurements upwind mixing ratios of $H_2O_2<130$ ppt. Moreover, it agrees with the measurements carried out by Jaeschke et al. (2005) in 2002, where he observed similar concentrations of H_2O_2 upwind and downwind. Measurements of organic peroxides in the upwind station are below the detection limit (<5 ppt) and were not carried out at the downwind site. Nevertheless, our calculations show that if the peroxides measured in cloud-water are entirely evaporated HMHP and 1-HEHP will not be detected, since the HMHP, 1-HEHP and MHP expected maximum mixing ratios are in the order of 2, 20 and 42 ppt, respectively. Therefore, more sensitive equipment downwind will give information about the fate of H_2O_2 and MHP but not necessarily of the fate of HMHP and 1-HEHP at this site and at this time of year.

5. Conclusions

In cloud water H_2O_2 and the following organic peroxides: HMHP, 1-HEHP and MHP were observed. These measurements are in agreement with the findings of Sauer et al. (1996) and show that these compounds are common constituents of cloud-water. The low temperatures and pH values measured favours the detection especially of H_2O_2, HMHP and 1-HEHP. In addition, it was found that these organic peroxides (HMHP + 1-HEHP + MHP) constitute up to 80% of the total peroxides during nighttime , while during daytime they accounted for about to 14%. Therefore, organic peroxides might play an important role in the nighttime chemistry. It is believed that the ozonolysis reaction is the main source of H_2O_2 during nighttime and of HAHP throughout the day. Therefore their detection during nighttime indicates that this reaction took place. Due to the low solubility of the precursors, the appearance of these peroxides cannot primarily be attributed to in-cloud ozonolysis reaction. In addition, whether the ozonolysis occurred in the gas phase previous to cloud contact or in the cloud-interstitial phase cannot be established.

The carbonyl compounds presented similar patterns to those of the peroxides. Hydroxyacetone was one of these, its presence indicates that this pattern can also be attributed to transport of air masses.

The role of H_2O_2 in the SO_2 oxidation to SO_4^{-2} was also studied, but the amount of sulphate produced by this reaction cannot be quantified since it is not possible to distinguish its origin: the latter reaction or from dissolved SO_4^{-2} from aerosols.

Besides the in-cloud chemistry, H_2O_2 concentrations were also found to be strongly linked to the cloud physics. It was observed that the H_2O_2 concentration strongly decreased upon cloud dissipation, which can be attributed to evaporation of this compound, and higher H_2O_2 concentrations were observed in the basis of the cloud, which normally coincided with low liquid water content.

It is not possible to establish the fate of the H_2O_2 and organic peroxides after passage through the cloud due to the lack of data in the downwind site, where more sensitive equipment is needed or a site or time of the year where higher concentrations of these compounds are expected. In addition, future experiments should be planned by selecting different measuring stations in the cloud, another measuring station at the side of the cloud should be useful to determine if entrainment took place and a higher sampling resolution should be applied mainly towards the beginning and end of the cloud event for a better understanding of the uptake of gases by the cloud and the effect of cloud dissipation on the concentration of trace components.

Acknowledgements

The authors wish to thank the organisers of FEBUKO for allowing us to take part in this project. Special thanks to Erika Brüggemann for collecting the gas phase samples and the team of the ZUF for the transport of the equipment. Funding was provided by the German Academic Exchange Service (DAAD), the Ministerio de Ciencia y Tecnología (MICIT) and the Max-Planck-Institute for Chemistry, Mainz.

References

Atkinson, R., Aschmann, S.M., 1993. OH production from the gas-phase reactions of O_3 with a series of alkenes under atmospheric conditions. Environmental Science And Technology 27 (7), 1357–1363.

Brüggemann, E., Chemnitzer, R., Rüd, C., Gnauk, T., Mertes, S., Acker, K., Auel, R., Wieprecht, W., Möller, D., Junek, R., Collett, J.L., Herrmann, H., 2005. Schmücke hill-capped cloud and valley stations areosol chemical composition during FEBUKO (I): Standard trace gases, main components and metals. Atmospheric Environment (this issue).

Finlayson-Pitts, B.J., Pitts, J.N., 2000. Chemistry of the Upper and Lower Atmosphere. Academic Press, New York.

Fuzzi, S., Facchini, M.C., Schell, D., Wobrock, W., Winkler, P., Arends, B.G., Kessel, M., Mols, J.J., Pahl, S., Schneider, T., Berner, A., Solly, I., Kruisz, C., Kalina, M., Fierlinger, H., Hallberg, A., Vitali, P., Santoli, L., Tigli, G., 1994. Multiphase chemistry and acidity of clouds at Kleiner-Feldberg. Journal of Atmospheric Chemistry 19 (1–2), 87–106.

Großmann, D., 1999. Die Gasphaseozonolyse von Alkenen in Gegenwart von Wasserdampf als Quelle für Wasserstoffperoxid und organische Peroxide in der Atmosphäre. Ph.D. Dissertation, Johannes Gutenberg-Universität Mainz.

Großmann, D., Moortgat, G.K., Kibler, M., Schlomski, S., Bächmann, K., Alicke, B., Geyer, A., Platt, U., Hammer, M.U., Vogel, B., Mihelcic, D., Hofzumahaus, A., Holland, F., Volz-Thomas, A., 2003. Hydrogen peroxide, organic peroxides, carbonyl compounds, and organic acids measured at Pabstthum during BERLIOZ. Journal of Geophysical ResearchAtmosp 108 (D4), 8250.

Guibault, G.G., Brignac, P.J., Juneau, M., 1968. New substrates for the fluorimetric determination of oxidative enzymes. Analytical Chemistry 40 (8), 1256–1263.

Gunz, D.W., Hoffmann, M.R., 1990. Atmospheric chemistry of peroxides: a review. Atmospheric Environment, Part A (7), 1601–1633.

Heinold, B., Tilgner, A., Jaeschke, W., Knoth, O., Wolke, R., Herrmann, H., 2005. Meteorological characterisation of the FEBUKO hill capped cloud experiments, Part II: Tracer Experiments and Flow Characterisation of the FEBUKO measurement periods with nested non-hydrostatic atmospheric models. Atmospheric Environment (this issue).

Hellpointner, E., Gäb, S., 1989. Detection of methyl-, hydroxymethyl- and hydroxyethyl- hydroperoxides in air and precipitation. Nature 337, 631–634.

Hewitt, C.N., Kok, G.L., 1991. Formation and occurrence of organic hydroperoxides in the troposphere: laboratory and field observations. Journal Of Atmospheric Chemistry 12 (2), 181–194.

Jaeschke, W., Haunold, W., Salkowski, T., Sitals, R., Moortgat, G.K., Valverde-Canossa, J., 2005. Formation and decomposition of H_2O_2 in FEBUKO hill-capped cloud experiment 2002. Atmospheric Environment (this issue).

Kelly, T.J., Daum, P.H., Schwartz, S.E., 1985. Measurements of peroxides in cloudwater and rain. Journal of Geophysical Research 90 (D5), 7861–7871.

Kurth, H.H., 1992. Bestimmung von Wasserstoffperoxid und organischen Hydroperoxiden in pg-Mengen: Entwicklung und Anwendung von flüssigkeitschromatographischen Methoden zur Analyse von Umweltproben. Doktorarbeit, Technische Universität München.

Lazrus, A.L., Kok, G.L., Lind, J.A., Gitlin, S.N., Heikes, B.G., Shetter, R.E., 1986. Automated fluormetric method for hydrogen peroxide in air. Analytical Chemistry. 58 (3), 594–597.

Lee, M.H., Heikes, B.G., O'Sullivan, D.W., 2000. Hydrogen peroxide and organic hydroperoxide in the troposphere: a review. Atmospheric Environment 34 (21), 3475–3494.

Lelieveld, J., Crutzen, P.J., 1991. The role of clouds in tropospheric photochemistry. Journal Of Atmospheric Chemistry 12, 229–267.

Lind, J.A., Kok, G.L., 1986. Henry's law determinations for aqueous solutions of hydrogen peroxide, methylhydroperoxide, and peroxyacetic acid. Journal of Geophysical Research 91 (D7), 7889–7895.

Möller, D., Acker, K., Wieprecht, W., 1996. A relationship between liquid water content and chemical composition in clouds. Atmospheric Research 41 (3–4), 321–335.

Müller, K., Brüggemann, E., Gnauk, T., Mertes, S., Lehmann, K., Massling, A., Wiedensohler, A., Wieprecht, W., Acker, K., Jaeschke, W., Kramberger, H., Svrcina, B., Bächmann, K., Galgon, D., Nowak, A., vanPixteren, D., Plewka, A., Hoffmann, D., Herrmann, H., 2005. FEBUKO Eexperiment design and measurements. Atmospheric Environment this issue.

Olszyna, K.J., Meagher, J.M., Bailey, E.M., 1988. Gas-phase, cloud and rain-water measurements of hydrogen peroxide at a high-elevation site. Atmospheric Environment 22 (8), 1699–1706.

O'Sullivan, D.W., Lee, M.Y., Noone, B.C., Heikes, B.G., 1996. Henry's law constant determinations for hydrogen peroxide, methyl hydroperoxide, hydroxymethyl hydroperoxide, ethyl hydroperoxide, and peroxyacetic acid. Journal of Physical Chemistry 100 (8), 3241–3247.

Paulson, S.E., Chung, M.Y., Hasson, A.S., 1999. OH radical formation from the gas-phase reaction of ozone with terminal alkenes and the relationship between structure and mechanism. Journal of Physical Chemistry 103 (41), 8125–8138.

Penkett, S.A., Jones, B.M.R., Brice, K.A., Eggleton, A.E.J., 1979. The importance of atmospheric ozone and hydrogen peroxide in oxidising sulphur dioxide in cloud and rainwater. Atmospheric Environment 13 (1), 123–137.

Pruppacher, H.R., Klett, J.D., 1997. Microphysics of Clouds and Precipitation. Kluwer Academic Press, Dordrecht.

Sauer, F., 1997. Bestimmung von H_2O_2 und organischen Hydroperoxiden. Ph.D. Dissertation, Johannes Gutenberg-Universität Mainz.

Sauer, F., Schuster, F., Schäfer, C., Moortgat, G.K., 1996. Determination of H_2O_2 and organic peroxides in cloud- and rain-water on the Kleiner Feldberg during FELDEX. Geophysical Research Letters 23 (19), 2605–2608.

Sauer, F., Schäfer, C., Neeb, P., Horie, O., Moortgat, G.K., 1999. Formation of hydrogen peroxide in the ozonolysis of isoprene and simple alkenes under humid conditions. Atmospheric Environment 33, 229–241.

Schell, D., 1998. Untersuchungen zur Durchmesserabhängigkeit der Lösungskonzentration von Wolkentropfen, Berichte des Zentrums für Umweltforschung. Zentrum für Umweltforschung, Frankfurt, Germany.

Seinfeld, J.H., Pandis, S.N., 1998. Atmospheric Chemistry and Physics: from air Pollution to Climate Change. Wiley Interscience Publication,Wiley, New York.

Staffelbach, T.A., Kok, G.L., 1993. Henry's law constants for aqueous solutions of hydrogen peroxide and hydroxymethyl hydroperoxide. Journal of Geophysical Research 98 (D7), 12713–12717.

Tilgner, A., Heinold, B., Nowak, A., Herrmann, H., 2005. Meteorological characterisation of FEBUKO hill capped cloud experiments, Part I: Synoptic Characterisation of Measurement Periods. Atmospheric Environment (this issue).

Valverde-Canossa, J., 2004. Sources and sinks of organic peroxides in the planetary boundary layer. Ph.D. Dissertation, Johannes Gutenberg-Universität Mainz.

van Pixteren, D., Plewka, A., Hoffmann, D., Müller, K., Kramberger, H., Svrcina, B., Bächmann, K., Jaeschke, W., Mertes, S., Collett, J.L., Herrmann, H., 2005. Schmücke hill-capped cloud and valley stations aerosol characterisation during FEBUKO (II): Organic compounds. Atmospheric Environment (this issue).

Watanabe, K., Ishizaka, Y., Minami, Y., Yoshida, K., 2001. Peroxide concentrations in fog water at mountainous sites in Japan. Water Air and Soil Pollution 130 (1–4), 1559–1564.

Wieprecht, W., Mertes, S., Collett, J.L., Acker, K., Brüggemann, E., Hofmann, D., Jaeschke, W., Herrmann, H., 2005. Cloud Physics and Cloud-water Sampler Comparison during FEBUKO. Atmospheric Environment (this issue).